2000

Control of the short-circuit gas metal arc welding process using instantaneous current regulation

Dominic Cuiuri
University of Wollongong

CONTROL OF THE SHORT-CIRCUIT GAS METAL ARC WELDING PROCESS USING INSTANTANEOUS CURRENT REGULATION

A thesis submitted in fulfilment of the requirements for the award of the degree:

Doctor of Philosophy

from

University of Wollongong

by

Dominic Cuiuri

School of Electrical, Computer and Telecommunications Engineering

2000

Acknowledgements

I would like to thank Professor Chris Cook and Professor John Norrish for their guidance and assistance during the course of this project. Thanks also to Dr. Lawrence Sanders for his knowledge, assistance and cooperation in the early stages of the project. I am indebted to Dr Yi Mao for the design and construction of the visualisation system flash head. The assistance of Joe Tiziano, Frank Mikk, Brian Webb and Joe Abbott at various stages in the construction of the equipment is gratefully acknowledged. I also had a number of good-humoured and pertinent discussions with Milenko Carapic about the nuances of current-controlled short circuit GMA welding behaviour.

I also wish to thank the Co-operative Research Centre for Welded Structures (CRC-WS) for infrastructural and financial support during this project.

Last, but certainly not least, I must thank my long suffering wife Marina. This thesis would not have been completed without her unwavering support and considerable patience.

University of Wollongong

Thesis Declaration

This is to certify that I, Dominic Cuiuri, being a candidate for the degree of Doctor of Philosophy, am fully aware of the University of Wollongong's rules and procedures relating to the preparation, submission, retention and use of higher degree theses, and its policy on intellectual property.

I acknowledge that the University requires the thesis to be retained in the Library for record purposes and that within copyright privileges of the author, it should be accessible for consultation and copying at the discretion of the Library officer in charge and in accordance with the Copyright Act (1968).

I authorise the University of Wollongong to publish an abstract of this thesis.

I declare that the work reported in this thesis is my own, except where explicitly specified and referenced. I further declare that this thesis has not been submitted for a degree at any other university or institution.

Signed:

Date: 1/12/00

Table of Contents

Volume I

Volume II

Abstract

The performance of the short-circuit gas metal arc welding (GMAW) process under the control of two current-controlled techniques is investigated in detail using a custom built, high performance power source. The objective of these techniques is to provide significant improvements in process control compared to that obtained by using conventional constant voltage power sources.

The first control technique, described as "open loop", has a fixed, pre-programmed response to key events within the process that define various states of the weld cycle. The response parameters are adjusted to suit the wire feed speed, welding travel speed and shielding gas mixture. Adaption to the requirements of the process occurs automatically, since the timing of the responses is determined solely by events at the weld. This technique produces stable, low-spatter welds with excellent bead appearance across a very wide range of wire feed speeds and contact tip to workpiece distance (CTWD) values. Operation does not depend on synchronising the weld cycle frequency with the natural frequency of the weld pool. The technique also significantly decouples key welding parameters such as peak arc length, fusion area, and short-circuit metal transfer characteristics.

Following investigation of this technique, a new approach is proposed. This "closed loop" control aims to regulate the size of the droplet formed at the end of the electrode on a cycle-by-cycle basis. A model of the instantaneous melting rate is developed to predict droplet size. A novel method is used to estimate the CTWD using "through the arc" sensing techniques. The objectives of this technique are to increase process stability and to further reduce spatter. These aims were achieved under a limited set of operating conditions. The performance of this second technique is influenced by weld pool oscillation but the key benefit of parameter decoupling is retained.

The theoretical development of both techniques and experimental validation of their performance is detailed in this thesis.

Publications, Reports and Patents

Due to the commercial interests of the financial contributors to this project, there has been a restriction on the publications arising from the work detailed in this thesis.

The internal reports, publications and patents resulting from the work carried out in this project are listed below.

Publications

Cuiuri D, Norrish J and Cook C D, "Developments in short circuit metal transfer gas metal arc welding power sources", Welding Technology Institute of Australia (WTIA) 47th Annual Conference, 17-20 October 1999, Brisbane Qld., Australia. Paper No.38, pp1-10.

Dean G, Cuiuri D, Norrish J and Cook C D, "An alternative approach for dip transfer GMAW", WTIA Advances in Welding Research Symposium, 16 February 2000, Sydney NSW, Australia. Session 4, Paper No.2, pp1-4.

Internal Reports

CIGWELD Optimised Arc Welding Systems (OptArc) Project 96.30
Phase 1 Technical Report: Description of experimental controller. June 1997

CIGWELD Optimised Arc Welding Systems (OptArc) Project 96.30
Phase 2 Report: Real time arc length control in Pulsed GMAW and Dip transfer stability assessment. July 1998.

Patents

Australian Provisional Patent PQ5284
Dean G, Cuiuri D, Norrish J and Cook C D, "A welding control system".
27th January, 2000

Glossary

α (alpha)

Arc related melting rate constant. Units: $mA^{-1}s^{-1}$

Average arcing current

Average welding current during the arcing period only, with current during the short circuit taken to be zero.

$$I_{arc\_avg} = \frac{1}{T}\int^{Ta} I(t)dt$$

where T is the total weld cycle and T_a is the arcing period.

Argoshield 51

GMAW shielding gas mixture sold by BOC Ltd in Australia. Contents are 81% Argon, 16% CO_2, 3% O_2.

Argoshield 52

GMAW shielding gas mixture sold by BOC Ltd in Australia. Contents are 77% Argon, 23% CO_2.

β (beta)

Resistive melting rate constant. Units: $A^{-2}s^{-1}$

CTWD

Contact tip to workpiece distance, measured along the centre line of the electrode, from the end of the contact tip to the nominal surface of the work. Weld bead build up is not taken into account. Units: millimetres (typically).

ΔL (Delta L)

The equivalent length of electrode which has melted to form the droplet at the end of the electrode. Units: millimetres (typically).

DSP

Digital signal processor. A type of microprocessor initially designed for speech processing, now widely used in small systems applications requiring high processing speeds.

Form factor

Used in relation to a voltage or current waveform. The ratio of RMS value to mean or average value. Waveforms of different "shape" have different form factors. Form factors are independent of frequency. Units: dimensionless.

GMAW

Gas Metal Arc Welding, also known as Metal Inert Gas (MIG) welding, or Metal Argon Gas (MAG) welding.

GTAW

Gas Tungsten Arc Welding, also known as Tungsten Inert Gas (TIG) welding.

Iarc_max

Maximum arcing current, applied during the initial stage of the arcing period for time Tarc_max. Units: Amperes.

Iarc_min

Steady state arcing period current. Units: Amperes.

Iarc_ramp

Rate at which current is reduced from Iarc_max to Iarc_min at the end of Tarc_max. Units: Amperes/millisecond.

Isc_ramp

Rate at which current is increased during the short circuiting period.
Units: Amperes/millisecond.

Premonition circuit/unit

Circuit used in this project to reliably predict the onset of the short-circuit rupture just prior to the actual event.

Tarc_max

Time for which the maximum arcing current is applied during the initial stage of the arcing period.

Transit time τ

Time taken for an element of material in the electrode to travel from the contact tip to the workpiece.

Transit time τ = CTWD/(Wire Feed Speed). Units: seconds.

T_rupture

The time allowed by the welding controller for the short circuit to rupture at low current after the onset of the short circuit rupture is detected by the premonition unit, and the main current has been turned off. If the short circuit does not rupture within this time, the main current is re-applied at value Iarc_max, to force the rupture.

T_sc

The "active" duration of the short circuit. The time from when the current exceeds 50A to the time that the main current is turned off and drops below 50A. T_sc is the total short circuit time less the T_wetting and T_rupture.

T_wetting

The wetting-in time at the start of the short-circuit, when the current is reduced to 20A (Typically) to allow for wetting-in of the droplet at the end of the electrode into the weld pool.

WFR

Wire feed rate, or wire feed speed. Units: metres per minute

Chapter 1

Introduction

The gas metal arc welding (GMAW) process is widely used in industry for the fusion joining of a wide range of metals, with low carbon steel being the most common. The process is favoured because of its ease of use, potentially high deposition rate, and its suitability to a variety of welding positions such as downhand, vertical and overhead. Depending on the current density in the consumable electrode, the process operates in a distinct number of metal transfer modes. For applications where the weld must be performed "out of position" against gravitational forces, where thin sections need joining, or where root gaps need to be bridged, the most commonly used mode of operation is the short-circuiting transfer mode. This mode is also colloquially referred to as "dip transfer" mode, and operates at the lowest current densities that are sustained by the GMAW process.

The short-circuit GMAW process has been in commercial use since the late 1950s, when it was established that the process could be made to operate satisfactorily by using a simple constant voltage (CV) power source with suitable static and dynamic characteristics. By adjusting the open circuit voltage, slope and inductance of the power source to suit a particular electrode feed rate, a stable weld can be easily achieved in argon-based shielding gases and also in carbon dioxide with somewhat more difficulty. In the 1960s and 1970s, this approach provided a simple, low cost solution which was readily achievable with the available technology. Even today, the conventional CV power source is the most widely used form of power source for operating the GMAW process. The apparent simplicity is an attractive feature to many fabricators within the welding industry. In fact, most commercial power sources only have operator adjustments for the open-circuit voltage and electrode feed rate.

The apparent simplicity of a conventional CV power source masks an underlying complexity in the operation and control of the short-circuit GMAW process. A large amount of research has been undertaken since the 1950s towards gaining an understanding of the key physical events within the process, and determining the factors that influence the behaviour of the process. There have been extensive investigations into aspects such as:

- dynamic forces involved with metal transfer during the short circuit

- weld pool oscillation, prediction and measurement
- temperatures, forces, flows and potentials within the arc column
- boundary conditions of the arc, and sheath voltages
- causes of instabilities and explosions
- prediction of electrode melting behaviour
- physical mechanisms causing changes in transfer mode
- optimisation of process stability through control of process parameters.

None of these areas can be considered trivial. A tremendous amount of knowledge and insight into the short-circuit transfer process has been gained through cumulative research efforts. At present, some aspects of the process can be modelled and simulated, and the results show good agreement with experimental measurements. Yet the understanding is not sufficiently developed to enable the process to be modelled or simulated in a way that gives realistic and detailed results. Prediction of process behaviour is made more difficult by the complex interaction of the process with the current delivered by the power source. The dynamic response of the CV power source is influenced by the welding process to such an extent that key arcing properties such as peak arc length, electrode melting rate and heat input are determined by the events of the previous short circuit period. The intimate coupling of short-circuit (metal transfer) parameters to arcing (heating) parameters adds extra complexity to the process. Parameter coupling makes the short-circuiting process difficult to control in a manner that is not encountered in the regulation of current-controlled open arc processes such as pulsed spray transfer.

Since the mid-1960s, a number of researchers have recognised the difficulties that have been imposed on the control of the short-circuit GMAW process by using a constant voltage approach. Problems that were encountered in practical applications included lack-of-fusion defects, unacceptable spatter production (particularly with CO_2 shielding gas) and a narrow window of operational stability. To tackle these problems, these researchers used current-controlled power sources to minimise coupling of key welding parameters. As the understanding of the process improved, and electrical engineering technology also improved, the control methods used by these researchers also became more sophisticated. Although the theoretical knowledge of the process was (and remains) incomplete, it was sufficiently advanced that control techniques could be devised to overcome or avoid many of the problems. The performance of "advanced"

current-controlled power sources has been improved to a state where they significantly outperform conventional CV power sources.

However, the properties and benefits of these advanced power sources have not been widely reported in the literature, nor have they been widely exploited in the market place. There are a number of reasons for this. Firstly, the design of these advanced power sources is appreciably more complex than both conventional CV power sources and inverter-based power sources. The entry barrier for research is high, since there are very few of these power sources available for purchase. Even if a commercial power source is obtained, the manufacturer is understandably reticent to divulge design information which would allow the researcher to make any significant changes to the operation of the equipment, so that meaningful research could be conducted. The ability to perform detailed equipment modification and also to carry out the basic welding research requires multi-disciplinary skills which may not be available during the course of such a research project. If the rather bold decision is made to construct an experimental power source "from scratch", the same (or greater) multi-disciplinary skills are needed to complete the project. Secondly, limited information has been published regarding the details of the operation and performance of "advanced" power sources. Again, this is simply a result of manufacturers preserving "commercial confidentiality" to avoid the benefits of in-house development being given away to competitors. Finally, the added equipment complexity that is required by the "advanced" power source makes it significantly more expensive than even a standard inverter-based power source, let alone a conventional CV power source. In a cost-sensitive market, this price penalty ensures that "advanced" power sources do not achieve widespread use. As few of these machines are in use, there is less incentive for research to be conducted. Consequently, research and development in this area tends to be the province of the equipment manufacturers.

This thesis involves the construction of an advanced power source and the subsequent investigation of the performance of the short-circuit GMAW process under the control of two advanced current-controlled techniques. The first technique is referred to as "open loop" since it responds in a fixed, pre-programmed way to key events which are detected during the weld cycle. The second technique is a "closed loop" scheme which regulates the size of the droplets formed at the end of the electrode on a cycle-by-cycle basis. The objectives of both control techniques are to produce

stable, low-spatter welds over a wide operating range, and to minimise or remove the coupling of key parameters such as peak arc length, heat input and metal transfer characteristics during the short circuit. The advantages and limitations of both techniques are assessed. The differences in behaviour compared to conventional CV power sources are also discussed.

This report is presented in two volumes. All chapters are contained in Volume I. Volume II consists of appendices which contain supporting data, figures, diagrams and experimental results for the chapters. The lists of figures and tables are also included in the second volume. Although the figures in Volume II assist in clarifying fine details and provide significant documentation for the project, the chapters can be read with only infrequent referral to the second volume.

Chapter 2 gives a physical description of the short-circuit GMAW process and summarises previous research into the factors that affect process behaviour. The interaction with CV power sources is also discussed. Chapter 3 is a brief history of the development of short-circuit power sources and control techniques. Chapter 4 describes the experimental power source and associated equipment that has been custom-built to conduct the research. The control techniques that are programmed into the power source are documented in Chapter 5. In order to perform closed loop control of the process, key parameters need to be estimated from the welding voltage and current feedback signals. A robust method of estimating the contact tip to workpiece distance (CTWD) is presented in Chapter 6. A means of estimating the size of the droplet formed at the end of the electrode is developed in Chapter 7. Chapter 8 documents the measurement of voltage-current arcing characteristics of various shielding gases using a novel technique involving the experimental power source of Chapter 4. Chapter 9 describes a novel process visualisation system that was developed during the course of this thesis, which is capable of producing excellent quality photographs of the process at any desired time during the weld cycle. The performances of the "open loop" and "closed loop" control techniques are evaluated in Chapters 10 and 11, respectively. As these chapters involve lengthy discussion, the findings are summarised in the last section of each chapter. The major accomplishments, findings, and recommendations for future work are contained in Chapter 12.

Chapter 2

Description of the Short-Circuit Gas Metal Arc Welding Process

2.1 Scope

The GMA welding process is known to operate in a number of distinct modes of metal transfer, depending on the current density in the consumable electrode. This chapter gives a qualitative description of the process operating under the short-circuiting, or "dip", transfer mode. This mode is encountered at the lowest values of welding current, and is the transfer mode of interest in this thesis. The following description relates to physical events within the process and factors that affect behaviour at these key events. In particular, the influence of power source dynamics on the performance of the process are considered. The limitations placed on performance by use of conventional "constant voltage" power sources are also discussed.

2.2 Process Description

2.2.1 Physical Implementation

The gas-shielded metal arc welding (GMAW) process utilises an electric arc struck between the workpiece(s) and a consumable electrode to fuse the joint area, thereby accomplishing the goal of joining two or more metal objects. The consumable electrode is almost always fed into the weld area at a constant speed, and constitutes the filler material or filler "wire" for the weld. The energy required to sustain the arc is provided by a power source having suitable electrical static and dynamic characteristics [1, 2, 3]. The molten metal at the tip of the electrode and at the weld pool formed on the workpiece surface are protected from reaction with the ambient atmosphere by a column of relatively inert gas which is directed onto the weld area by a nozzle on the end of the welding torch, as shown in Figure 2.1. The electrical connection from the power source to the electrode is made at the copper contact tip. The electrode is biased against one side of the hole in the contact tip so that a connection to the power source is always maintained. In the vast majority of GMA welding using solid wires, the wire or electrode is positive (anode) and the workpiece is negative (cathode). Except for very specialised applications [4], the polarity is not changed during the weld.

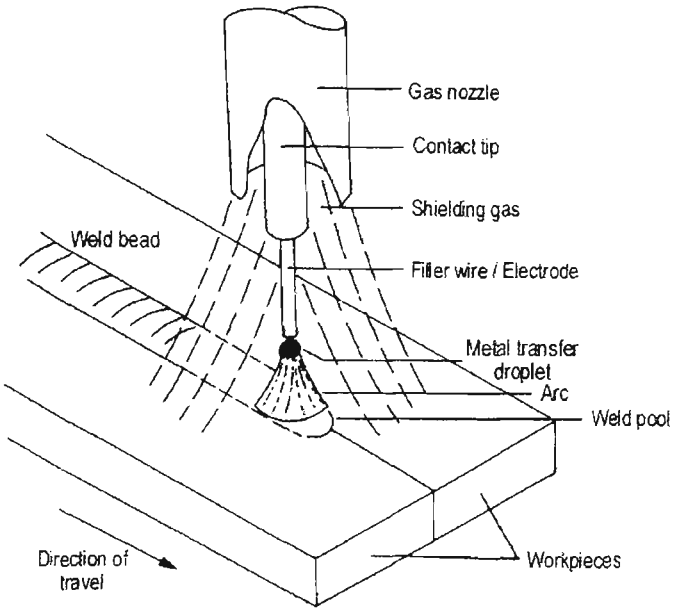

Figure 2.1 Implementation of the GMAW process

2.2.2 The Short-Circuiting Transfer Mode

The GMA weld is stabilised by balancing the welding current with the wire feed speed, so that the rate at which the electrode is melted by the action of the arc and transferred to the weld pool is matched by the feed speed, and the arc length is kept constant. The use of a power source with a "constant voltage" characteristic makes this easy to achieve in practice [1]. An increase in arc length (due to a small reduction in wire feed speed) causes the arc voltage to increase, which in turn will cause the delivered current to decrease. Since the electrode melting rate is determined by the current [5], then the electrode melting rate will also decrease, and the arc length will be maintained relatively constant. The regulation of arc length is necessary to produce an even weld bead with consistent fusion area, controlled metallurgical properties, and a smooth, "pleasing" appearance.

At high wire feed speeds and high welding currents, the filler metal is transferred from the wire to the weld pool through the arc as fine droplets. The end of the wire never touches the weld pool, and the process is generally described as "open arc". The high current transfer modes are generally referred to as "spray" transfer. The specific type of spray transfer mode produced, such as projected, streaming or rotating, depends on the current density within the electrode [6]. As the current and wire feed speed are reduced (to maintain a constant arc length), the diameter of the droplets exceeds that of the wire, and the globular transfer region is entered. This particular mode is characterised by large droplets forming at the end of the electrode, and

detaching at irregular intervals under gravitational force and falling into the weld pool. This mode is generally avoided for practical welding applications because of the irregular metal transfer properties. Further reduction of the current causes the wire feed speed to exceed the rate of electrode melting, so a constant arc length can no longer be maintained. The arc gap closes and the end of the electrode eventually contacts the weld pool. The welding process then operates by alternately cycling between open arc and short-circuiting on a regular basis. This characterises the short-circuiting transfer mode, which produces a small, fast-freezing weld pool and is especially suited for joining thin sections, out-of-position welding and for bridging root openings. In this mode, the dynamics of the power source become very important to the behaviour of the process, since the required welding current is no longer constant as for the open-arc transfer modes described previously.

If the key welding parameters of wire feed speed, open circuit voltage, internal resistance and output inductance are carefully chosen, it is possible to induce stable, regular short-circuiting events at frequencies of 50 to 200Hz using a conventional "constant voltage" (CV) power source. Figure 2.2 shows typical current and voltage waveforms for the short-circuiting GMAW process using an electronic power source operating in CV mode. The sawtooth ripple which is evident in the current waveform and less visible in the voltage is due to the switching action of the transistors within the power source. The operation of the power source is described in more detail in Chapter 4. The equivalent circuit used by the electronic power source to emulate a truly conventional power source (using a variable voltage transformer, diode rectifier and output inductor) is shown at the top of Figure 2.2. This model was used by the controller to generate these waveforms, as described in Chapter 5. For the purposes of the following description of the welding process, it should be recognised that the current and voltage waveforms for a truly conventional CV power source are the same as those of Figure 2.2, but without the presence of switching ripple. Examples of such waveforms are abundant in the literature [2, 3, 7, 8].

Figure 2.2 also illustrates diagrammatically the various events that occur during a short-circuit transfer weld cycle. Figure 2.3 shows photographs taken during the weld at the various stages, using the equipment and techniques described in Chapter 9. These high quality photographs demonstrate that the diagrammatic representations of Figure 2.2 are essentially correct. It should be noted that the images in Figure 2.3 are not derived from the same weld cycle, so some variations in detail are to be expected.

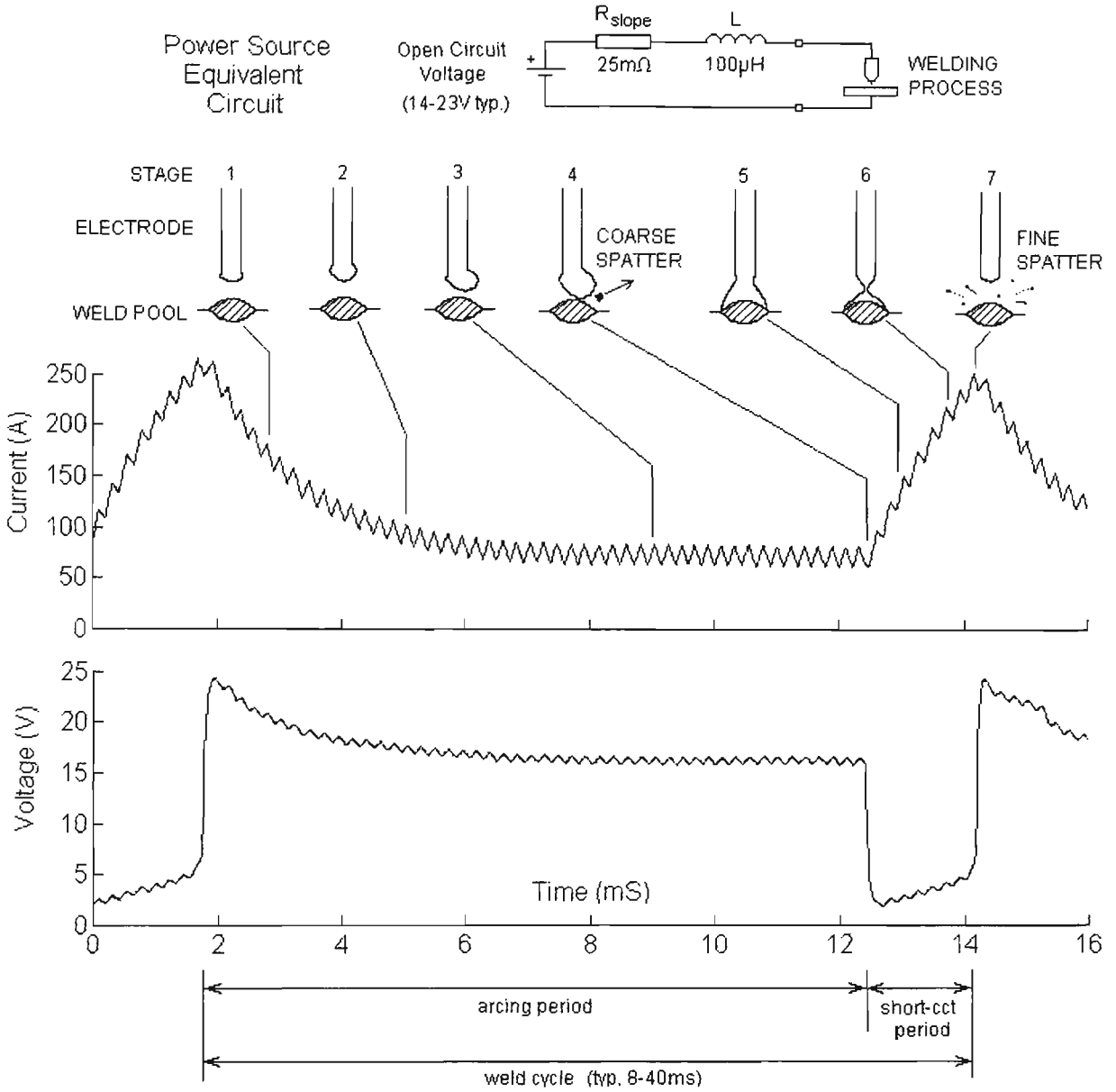

Figure 2.2 Typical GMAW waveforms for conventional CV power source

2.2.3 The Arcing Period

During the arcing period, which constitutes the majority of the weld cycle, a droplet of molten metal is formed at the end of the electrode. The energy required to heat the solid metal from room temperature to a liquid above melting point is generated by two mechanisms. The first mechanism is resistive heating of the metal as it transits from the end of the contact tip to the end of the electrode "stickout" (the length of the electrode protruding from the contact tip). During the transit time, which is a function of the wire feed speed and the stickout length, the metal is heated by the welding current, but remains a solid. The energy input due to resistive heating by current is a complex

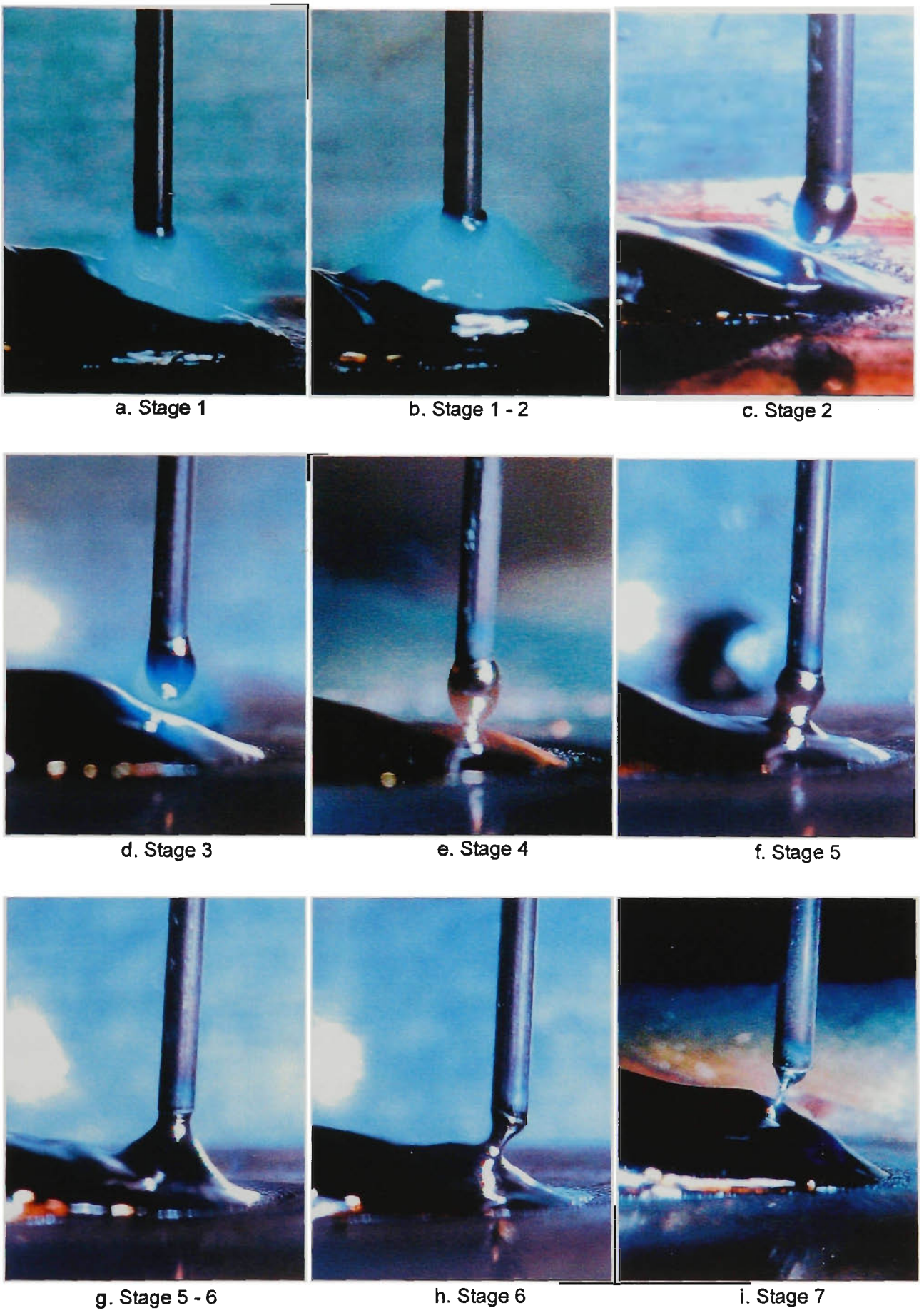

a. Stage 1 b. Stage 1 - 2 c. Stage 2

d. Stage 3 e. Stage 4 f. Stage 5

g. Stage 5 - 6 h. Stage 6 i. Stage 7

Figure 2.3 Photographs of weld area at various stages in welding cycle

function of current for the case of ferrous electrodes, since the resistivity of the metal is a function of its temperature [9]. When the preheated metal reaches the end of the electrode, it is turned to a liquid by the second mechanism of anodic heating by the arc. According to Halmoy [10], the volume of metal that is molten by these two mechanisms can be expressed as the instantaneous wire melting rate $v_m(t)$. This can be considered to be the velocity of the solid/liquid interface of the droplet and electrode end, relative to the stationary workpiece.

$$v_m(t) = i(t)\frac{K_1}{K_1 - S(t,t_m)}\left[\sqrt{1 - \frac{K_3(K_1 - S(t,t_m))}{K_2^2}} + 1\right] \tag{2.1}$$

Constants K_1, K_2 and K_3 are compound constants whose values depend on the work function of the electrode material and the non-linear relationship between resistivity and enthalpy. The effect of electrode resistive preheating is described by the term $S(t,t_m)$, which is the integral of the square of the current during the transit time t_m.

$$S(t,t_m) = \int_{t-t_m}^{t} i^2(t)dt \tag{2.2}$$

Equation 2.1 indicates that the melting rate for a given current is increased if the electrode preheating S is higher. Experimental studies have shown that electrode preheating can account for changes of more than 50% in melting rate [5] when steel electrodes are used. Once the melting rate is calculated, the volume of the formed droplet V_d can be calculated by integrating melting rate during the arcing period t_{arc}:

$$V_d(t) = A\int_0^{t_{arc}} v_m(t)dt \tag{2.3}$$

where A is the cross sectional area of the electrode. A more complete treatment of droplet size estimation is given in Chapter 7. The distance h of the solid/liquid interface from the workpiece surface is the integral of the difference between instantaneous wire melting rate $v_m(t)$ and wire feed rate v_f (assumed constant). The instantaneous arc length is difficult to estimate because of indeterminate factors such as the shape of the droplet, distortion of the droplet due to arc forces, depression of the weld pool and disturbances of the weld pool surface due to oscillations. These effects are visible in Figure 2.3.

$$h(t) = \int_0^t \left(v_m(t) - v_f\right)dt \tag{2.4}$$

Returning to Figure 2.2, the effects of instantaneous current on arc length and droplet size can be predicted using the above equations. At stage 1, immediately following the rupture of the previous short circuit, the current is high, so the distance

$h(t)$ rapidly increases, as does the droplet size. The depression of the weld pool due to arc force is evident in Figures 2.3a and 2.3b. The circuit inductance L prevents the current from changing rapidly, so a high arcing current is sustained for the first two to three milliseconds of the arcing period. This ensures that a sufficient arc length can be generated so that a short circuit does not occur prematurely. During the arcing period, a droplet of sufficient size needs to be produced so that a successful transfer of metal can take place during the short circuit [8, 11, 12]. If the droplet is too small, a stable metal bridge is formed during the short-circuiting period between the pool and electrode, which can only be cleared at extremely high current [8]. The formation of stable bridges causing long short-circuiting duration is discussed further in Chapter 6. Other research [13] indicates that small droplets are more easily repelled from the weld pool for a given current in the initial stages of the short circuit. This results in unsuccessful metal transfer and excessive spatter. The production of a droplet of sufficient size during the arcing period is essential for the successful transfer of metal during the short-circuiting period.

Stages 2 and 3 in Figure 2.2 correspond to periods of significant droplet growth. The current is lower than at stage 1, but the growth time is sufficiently extended. At some point in stage 2, the electrode melting rate becomes less than the wire feed rate, so the solid/liquid interface of the electrode stops receding and begins to approach the weld pool. Some time later, the current reaches a steady-state value. At this point, the inductor L has no influence on the circuit behaviour, assuming there is no disturbance to the process. The welding current is determined by the difference between the power source open-circuit voltage and the arcing voltage, and the internal resistance R_{slope} of the power source. During stage 3, the droplet continues to grow and the solid/liquid interface of the electrode approaches the weld pool. The combination of these factors gradually reduces the arc length, as illustrated in Figures 2.3c, 2.3d and 2.3e, until a short circuit occurs.

In addition to determining the electrode melting rate, the current during the arcing period also has a significant influence on weld bead properties, particularly bead width and fusion area (see Chapters 10 and 11). The heat input to the workpiece is supplied mainly by the cathode voltage drop and contribution from the arc column through radiation, conduction and convection [14, 15]. Consequently, the current during the short-circuiting period has negligible effect on workpiece heating. As part of the experimental work in later chapters, it will be shown that the workpiece fusion area for

a given welding travel speed is determined by the electrical energy input to the process, and not the mean welding current, which contains a significant component from the short-circuiting period. When analysing the effects of current, it is prudent to assess the impact on workpiece heating as well as metal transfer dynamics. Addition of filler material to the weld area without adequate fusion will not produce a weld of adequate strength. Lack-of-fusion defects are more frequently encountered in dip transfer welding than in any other mode.

2.2.4 The Short-Circuiting Period

During the short-circuiting period, the developed droplet is transferred to the weld pool. From stage 4 to stage 5 in Figure 2.2, the contact area between droplet and pool is enlarged by surface tension forces, as shown in Figures 2.3e and 2.4f. According to [13], this will occur if the resultant reduction in surface energy is greater than the increase in electromagnetic energy when the contact radius is increased (i.e. the system settles to a state of lower energy). The electromagnetic energy is related to the current while the surface energy is determined by the surface tension. The worst case scenario for production of coarse "ball repulsion" spatter in dip transfer welding is experienced when using CO_2 shielding gas at high shorting currents. Carbon dioxide is known to reduce the surface tension of molten steel [16]. Figure 2.4 shows a photograph of a repulsion event taken 0.5ms after the start of the short circuit at 90A using CO_2, dramatically illustrating the production of this type of spatter. In general, this type of spatter can be reduced by having a low steady-state arcing current prior to the short circuit, or using an argon-based shielding gas which does not reduce surface tension to the same degree as CO_2.

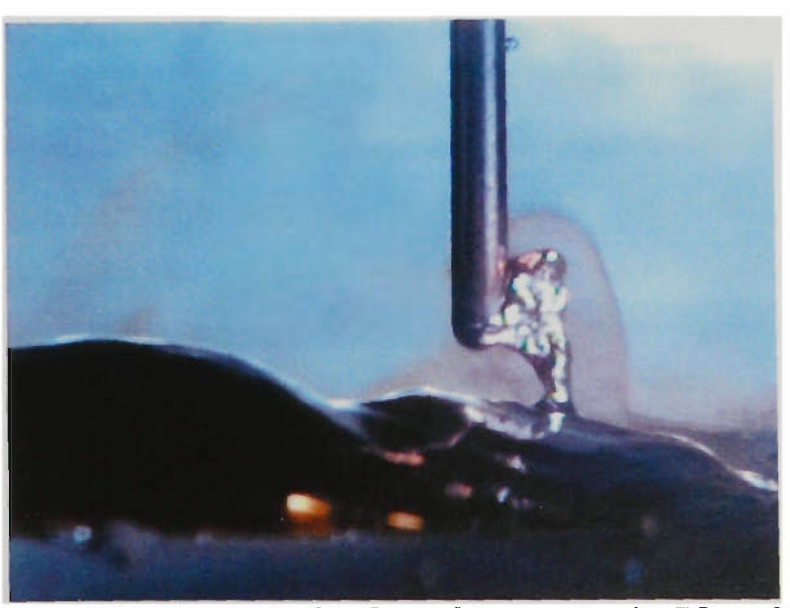

Figure 2.4 Photograph of ball repulsion spatter in CO_2 at 90A

From stage 5 to stage 6 in Figure 2.2, the current increases rapidly since the process voltage is low; typically less than 5V during the short circuit. The rate of rise of current is determined by the value of inductance and the open circuit voltage. While surface tension forces work to transfer the molten metal to the workpiece, the $\underline{\boldsymbol{J}}\times\underline{\boldsymbol{B}}$ Lorentz force (or electromagnetic pinch force) becomes dominant as the current increases during the short [6, 12, 17, 18]. The electromagnetic pinch force on the molten metal bridge is directed inward at right angles to the current flow when the current flux lines represented by $\underline{\boldsymbol{J}}$ are straight and parallel, and this force is counterbalanced by internal fluid pressure. Such a condition may exist temporarily between stages 5 and 6, as shown in Figures 2.3f and 2.3g. At all other times during the short circuit, the shape of the bridge causes the current flux lines to become divergent or convergent, depending on the exact shape. The complex sum of force vectors resulting from this electromagnetic geometry induces a pressure gradient along the axis of the bridge, and effectively pumps metal through the bridge and into the weld pool [12]. Figures 2.3h and 2.3i clearly illustrate the transfer of material. As this occurs, the bridge is reduced in diameter, and the process is accelerated by the combination of reduced bridge radius and increased current. According to [19], the inwardly-directed pressure G (dynes/cm^2) at a distance r (cm) from the axis of a conductor of radius R (cm) is described by equation 2.5:

$$G = I^2 \frac{R^2 - r^2}{100\pi R^4} \tag{2.5}$$

Since the pressure is proportional to the square of the current and inversely proportional to the square of the radius, transfer of metal to the weld pool becomes very rapid as the bridge is reduced. This effect can be observed in high-speed films of the process.

At stage 7 in Figure 2.2 (photograph Figure 2.3i), metal transfer is virtually complete. A residual droplet remains on the end of the electrode, and an extremely thin neck connects it to the weld pool. The resistance of the short circuit is high and rapidly increasing, while the current is also near its maximum. Under these conditions the bridge will rupture violently, producing fine spatter and a distinct, audible noise transient which is the main cause of the characteristic "crackling" sound produced by the gas-shielded GMAW process. Research [20, 21] indicates that in the very last stages of the short circuit (the last 15μs), the neck diameter drops to a point where the current density exceeds 10^7 A/cm^2. The metal temperature can reach over 8000 K, which is sufficient to cause instantaneous vaporisation, causing an electrical explosion. The

shock wave spreads to a radius of up to 11 mm, generating a force of up to several hundred grams on the weld pool. Apart from the metal contained in the neck, spatter can also result from material ejected from the weld pool under extreme circumstances.

2.2.5 The Role of Inductance

The importance of selecting the correct inductance value has been known since the late 1950s [2, 3, 22]. The inductance must be high enough to limit the rate of rise of current (dI/dt) at the commencement of the short circuit so that the current does not rise significantly while the droplet is "wetting" into the weld pool, otherwise ball repulsion spatter is encouraged. It must also be sufficiently high so that the current at the end of the short circuit is not excessive, thus limiting the energy involved with the neck rupture. If the inductance is excessive, the current does not rise rapidly enough during the short circuit to assist in metal transfer to the pool, so the short circuit is artificially extended. The inductance is also important during the arcing period. If it is too low, the current will drop rapidly to its final steady-state arcing value. The integral of the melting rate will be lowered, so the generated arc length will be insufficient to sustain an arc length of reasonable duration. The droplet formed at the end of the electrode will be too small, and a stable bridge may form at the next short circuit which is difficult to clear, thereby destabilising the welding process. Workpiece heating is also reduced, increasing the likelihood of lack-of-fusion defects. Excessive inductance does not adversely affect the arcing period per sé, except that the overall weld cycle frequency may be reduced to a value that is unacceptable to an operator. In extreme cases, the dipping frequency can become so low that excessively large droplets are formed. Under these conditions, the operator may not be able to manually produce an acceptable weld bead. In general, however, high inductance during the arcing period can be considered beneficial for welding thicker sections because it enhances workpiece fusion through increased heat input.

2.2.6 Causes of Instabilities

Since the short-circuiting GMAW process is cyclical by nature, instabilities in the process appear as variations in the weld cycle times. A large number of studies have been carried out into these, with [23] being representative of the approach taken, which is to use the standard deviation of the weld cycle time as a measure of process regularity or stability. Ignoring external influences such as surface contamination or poor joint

preparation, the major factor influencing stability in a weld performed under near-optimum conditions is the presence of weld pool oscillations. These are initiated by the sudden increase in arc pressure immediately following arc reignition, and by the momentum of liquid metal transferred to the weld pool during the short circuit [23]. Experiments described in [23] show that stable welding occurs in a relatively small voltage/wire feed rate window, when the weld cycle frequency is equal to the weld pool oscillation frequency. Under these conditions, the standard deviation of the weld cycle time is minimised. When these frequencies are divergent, the process becomes irregular since the time at which the droplet touches the pool becomes unpredictable. This is not surprising when the effects of variations in the short-circuiting and arcing durations on the current waveform in Figure 2.2 are considered.

If a short circuit occurs "prematurely" in a given arcing period, only a small droplet would be formed on the end of the electrode. The lower-than-average volume would take less time to transfer to the pool during the next short circuit [18], so the final short-circuiting current would be lower than that for the previous short-circuit. Since the rupture current constitutes the initial arcing current, the time constant of the circuit is fixed by R_{slope} and inductance L, and the electrode melting rate is determined by the current, then the volume of the droplet produced in the next arcing period can be potentially lower, and the peak arc length will also be lower. The uncertainty introduced into the arcing period duration by random movements of the weld pool may cause the droplet to be smaller or larger than indicated by the initial arcing current. Under the most unfavourable conditions, the droplet may become so small that a stable bridge is formed with the weld pool, and "stubbing" occurs.

Conversely, if the short circuit occurs later in the arcing period than expected, the droplet will be larger and require more time during the next short circuit to transfer the metal to the weld pool. The initial arcing current for the following arcing period will be higher, creating a longer initial arc length and potentially larger droplet. The process is stabilised by a rise in arcing voltage at long arc lengths, which causes the arcing current to fall more rapidly during an arcing period immediately following a sustained short circuit. Alternatively, a shorter initial arc length tends to sustain the arcing current due to less process voltage opposing the open circuit power source voltage (see Figure 2.2).

The intimate coupling of one arcing event to the next arcing event via the short-circuit current imposes a severe limitation on the ability of a CV power source to

produce acceptable welds over a wide operating range. Overcoming this limitation is a major consideration of this research.

2.2.7 A Current-Driven Process

The importance of inductance to the short-circuiting GMAW process, and the limitations resulting from use of CV power sources, highlight a fact that is often overlooked. The process itself is driven by current, not the voltage produced as a result of current flowing through the arc and electrode. The melting rate is determined by the instantaneous current and the degree of electrode preheating, which in turn is a function of the history of the current. The arc length is a consequence of the melting rate (equation 2.4). The physics of metal transfer during the short circuit are determined by the current and surface tension. The open circuit voltage V_{oc} and internal resistance R_{slope} are important only because they determine the rate of change of current ($dI/dt=V_{oc}/L$) and limit the maximum short circuit current ($I_{max}=V_{oc}/R_{slope}$). The shape of the current waveform, in combination with the melting characteristics of the electrode and physical requirements of short-circuit metal transfer, determines the overall behaviour of the process. To support this view of the dip transfer process, a number of recent developments in the control of this process are summarised in Chapter 3. All of these developments use instantaneous current regulation to regulate the welding process, rather than the conventional "constant voltage" approach. This approach is used as the basis for control techniques which are described and assessed in later chapters of this thesis.

2.3 Summary

The short-circuiting GMAW process has been qualitatively described, and the mechanisms which cause metal transfer, spatter and instabilities have been discussed. From this, the reasons for limitations in the control of the process using conventional CV power sources can be understood. Improvements to the control of the process, described in the following chapters, can be reviewed on the basis of the information that has been briefly presented in this chapter.

Chapter 3

History of Developments in Short-Circuit Transfer GMAW Power Sources

3.1 Scope

This chapter summarises the major developments in the control of the short-circuit transfer GMAW process and places them into a historical perspective. The improvements in power source design and process control techniques are described. The sequence of these developments shows the evolutionary path that has been taken over the past 40 years. The improvements are discussed in relation to the physical aspects of the process described in Chapter 2, in particular the key process problem areas of metal transfer, spatter, and instability. The changes required to power source topology in order to achieve improved process control are also described.

3.2 Developments in Power Sources

3.2.1 Developments in Conventional Power Sources

The earliest power sources for GMA welding in the late 1940s consisted of a DC supply with a steeply drooping voltage-current (V-I) characteristic, as had previously been used for the manual metal arc welding (MMAW) process [24]. These "constant current" power sources had a large series inductance, and therefore a very slow response to changes in the process such as disturbances in the wire feed rate or alteration of electrode extension (stickout). The process itself was initially limited to spray transfer, and setting the arc length involved the operator balancing power source current against the wire feed rate to obtain a consistent, stable welding condition. While this arrangement was satisfactory for automated welding, it was not satisfactory for manual welding because the arc length would not remain constant as the contact tip to workpiece distance (CTWD) varied. The electrode melting rate is a function of the current and electrode extension [5], so as long as the current remains constant then the electrode extension would also remain constant so that the melting rate matches the wire feed rate. The difference between CTWD and electrode extension would be taken up by the arc length.

Research in the early 1950s by Needham and Hull [1] showed that a far better power source for the Gas Metal Arc process was a DC supply with a much smaller

droop (or "slope") in its V-I characteristic, preferably 3 to 5 Volts per 100A. This allowed the operator to set arc length via the source voltage almost independently of the wire feed rate. The current would then automatically adjust to maintain a near-constant arc length. This occurs because of two mechanisms which contribute to the self-adjustment of the process. The first is the interaction of the arc voltage and the current. As the arc length increases, the output current is reduced, as shown by the circuit output characteristic in Figure 3.1. The second mechanism is the relationship of melting rate to current. As current reduces, the melting rate decreases and the arc length is stabilised. The operating point of arc length and current is set by the intersection of the power source characteristic with the arc characteristics. The arc length is altered simply by adjusting the open-circuit voltage of the power source (E and E' in Figure 3.1). Changing the output resistance, or slope, also affects the arc length to a lesser degree. Using this type of "constant voltage" power source improved process stability tremendously for both automatic and manual welding.

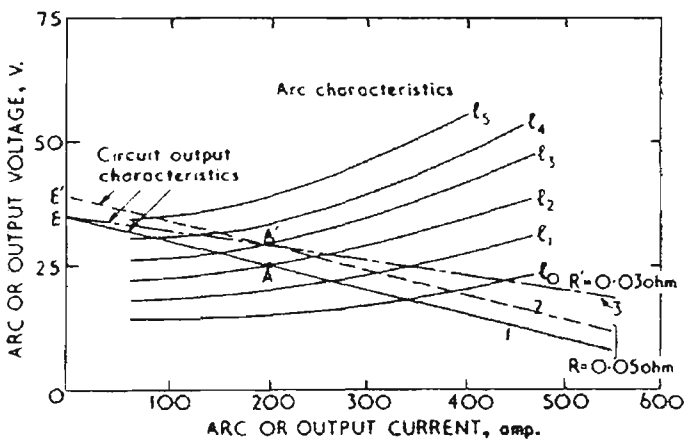

Figure 3.1 Interaction of CV power source and arcing characteristics [1]

Satisfactory spray (or "free flight") transfer was obtained with these early "constant voltage" power sources, as the spray process is relatively insensitive to the dynamic characteristics of the power source. Consequently, spray transfer GMAW was the first process to be used widely. However this process mode was limited to downhand applications, since the threshold current for spray transfer of 1.6mm diameter steel in argon is approximately 300A. At this current, the pool is too liquid and the deposited metal simply runs out of the pool in vertical or overhead positions [3]. Additionally, the high currents would cause burn-through in thinner section workpieces, limiting the application of this process to thicker sections.

At lower operating voltages, it was known that the short-circuit transfer of metal to the workpiece was possible at greatly reduced mean current, and that it could be applied to vertical and overhead positions. However, process stability remained a

problem, let alone being able to operate the power source over a variety of electrode sizes and types. In many cases, spatter was unacceptably high.

It was found that different electrode sizes and materials required different power source dynamic characteristics, or time constants, to reduce spatter and increase process stability [2, 22, 25]. This was achieved by adding an adjustable inductor in series with the output of the rectifier, yielding rates of response in current of 50 to 150 A/msec, depending on wire size. Matching current response times to the process produced current waveforms such as those described in Chapter 2. Spatter was reduced by avoiding excessive short-circuiting rupture currents, while stability was improved by ensuring that the consistent droplets of adequate size were produced [8] at frequencies matching those of the weld pool oscillations [23, 26]. Smaller wire sizes were found to be most effective and exhibited greater operational stability. It was now possible to weld thick sections as well as thin sheet in all positions using the technique which was aptly named "dip transfer" [2].

By the mid-1960s, the more sophisticated commercial GMAW power sources had the ability to adjust open circuit voltage, slope and inductance. To the present day, these "basic" power sources using simple transformer/rectifier/inductor circuit topologies are still produced. Manufacturers have developed these designs [27] to achieve acceptable welding performance over a reasonably wide process range (refer to Figure 3.2).

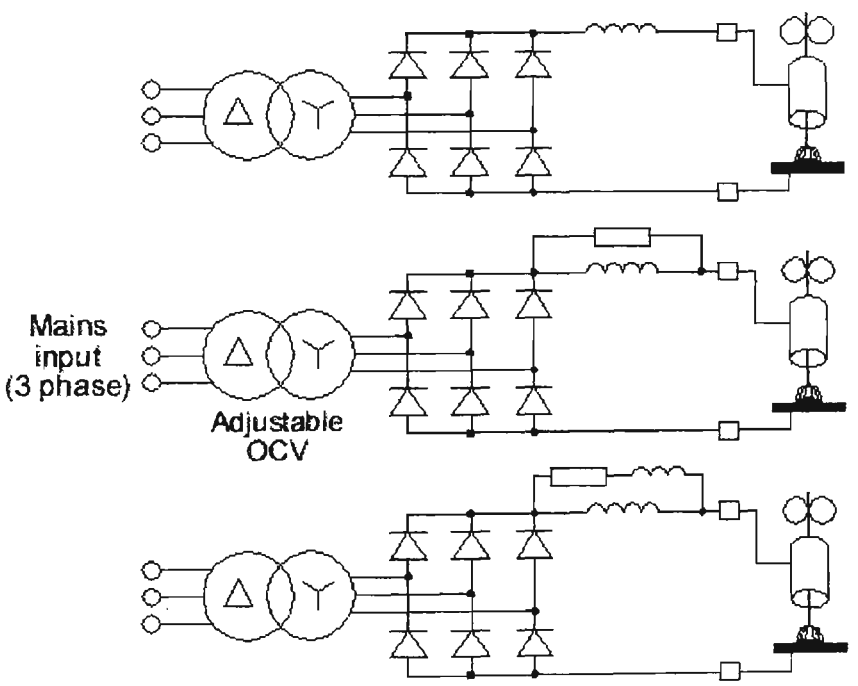

Figure 3.2 Some variations on conventional CV power source topology [Abe92]

3.2.2 The decoupling of short circuit and arcing parameters

The greater stability and higher deposition rate of thinner (0.8mm) wires led to their use on thicker sections as well as the thin sheet to which they were better suited. Positional welding on plate material revealed a tendency for lack-of-fusion defects [28, 28a], forcing the use of the larger 1.2 and 1.6mm wires for plate work, with their inherently poorer stability and higher spatter levels. In an effort to use thinner wires for plate applications the concept of a duplex power source was investigated by Smith in 1966 [25]. This was the first attempt at controlling fusion in the short-circuiting transfer process by independently adjusting arcing current independently of the short-circuiting current. The power source consisted of a constant current source to provide the steady state arcing current, and a constant voltage source to provide the short-circuiting current (Figure 3.3). Importantly, the dynamic response during the short circuit was decoupled from the steady-state arcing current, although the current in the initial stages of the arcing period was still dependent on the final short-circuiting current.

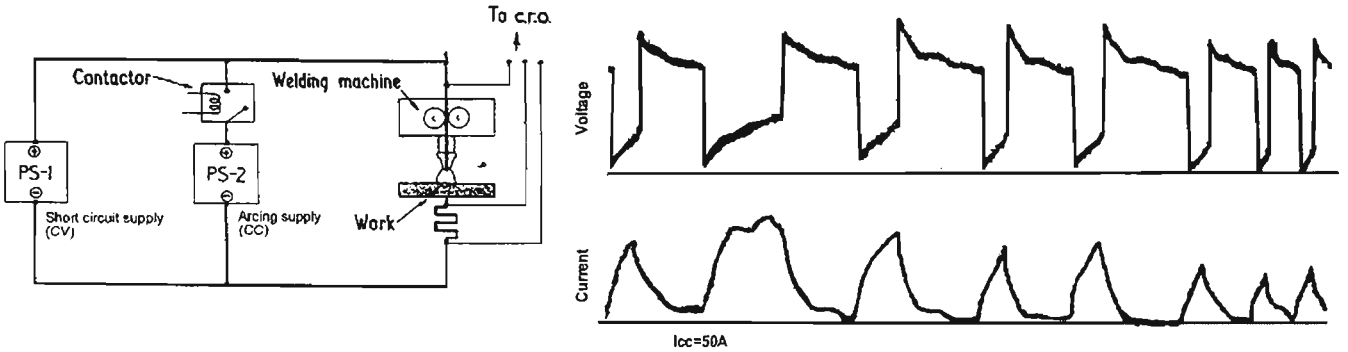

Figure 3.3 Duplex power source and waveforms [25]

The duplex power source was successful in that it proved that the objective of decoupling the arcing parameters from the short-circuit parameters and adjusting one set of parameters independently of the other was a valid concept. The duplex power source enabled use of thin 0.8mm electrodes at high mean current (160A) to produce a smooth weld bead with excellent penetration and a stable operating arc in carbon dioxide. Arguably, CO_2 is the most difficult shielding gas for obtaining a stable weld with satisfactory bead properties. In comparison, using a conventional CV power source with the same mean current produces a peaky, narrow weld bead with poor penetration and stability. Additionally, while the 0.8mm wire with the duplex power source operated at similar peak currents to 1.6mm wire with conventional power sources, the duplex power source produced a markedly "softer" arc. This was perceived to be of benefit in applications such as all-positional pipe welding where blow-through must be avoided.

Yet despite these advantages, the cost, bulk and increased operational complexity of the duplex power source made it unattractive for a conservative, price-sensitive market.

The next, and arguably most significant, step forward was the development of an experimental power source specifically for better control of short-circuiting transfer [29, 30]. The work performed by Boughton and MacGregor for the British Welding Research Association in the early 1970s had the objective of eliminating spatter and "regularising" the short-circuiting process; i.e. reducing the statistical variations found with conventional power sources. In the experimental power source (Figure 3.4), many parallelled transistors were used as switches, to provide a resistor-limited shorting current during the short circuiting period (current *i3* in Figure 3.5), while an independent constant-current supply maintained the steady-state current *i1* throughout the arcing period.

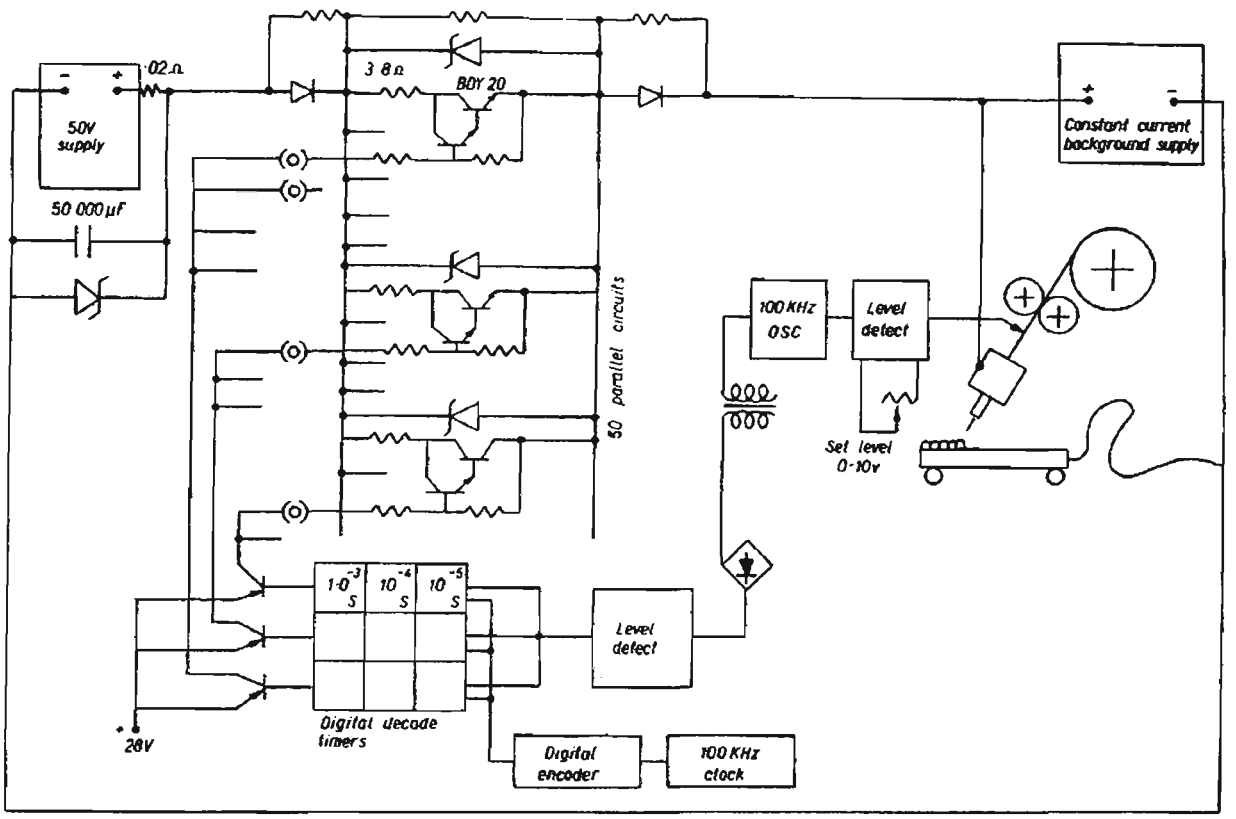

Figure 3.4 Power source schematic [31]

Specifically designed circuits detected the onset of the short-circuit rupture, and deactivated the transistors just prior to the rupture. The short-circuit rupturing current was reduced to a lower value *i4*, which may be lower than the arcing current *i1*. Current turnoff rates during the short-circuit of 4000 A/msec were obtained. During the last portion of the short-circuit period, the short circuit bridge was broken through the combined action of surface tension and a weakened electromagnetic pinch force due to the reduced current. Elimination of high current at the point of short-circuit rupture had

two positive effects. Fine fuse-burst spatter was almost totally eliminated, and the stability of the process was greatly improved due to the elimination of the explosive forces generated at the end of the short circuit. The ball repulsion spatter created at the start of the short circuit was also significantly reduced by including a "wetting-in" time at the start of the short-circuiting period. During time *t2*, the current was reduced to a low value *i2*, which is significantly lower than the steady-state arcing current *i1*. Wetting-in times of 0.5 milliseconds for Ar-20%CO_2 and 1.6 milliseconds for CO_2 were found to significantly reduce coarse spatter. The significantly longer wetting time required by CO_2 was thought to be due to the oxidising effect of the gas and the reduction of surface tension. This effect explained why it is far more difficult to obtain an optimum welding condition for CO_2 using a conventional CV power source, particularly with large wires which require higher currents.

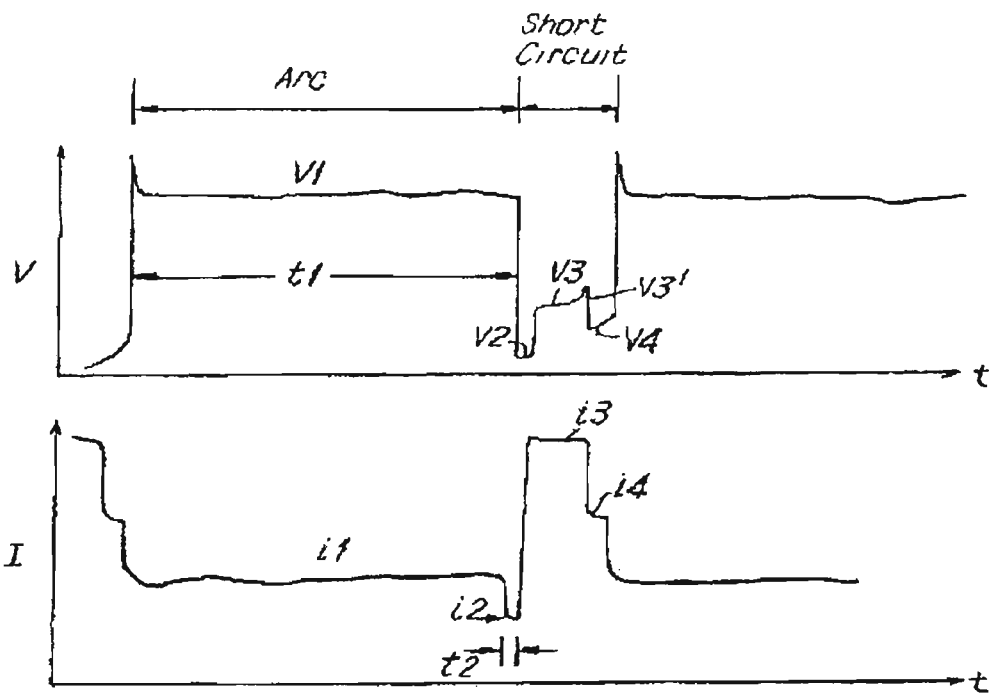

Figure 3.5 Power source waveforms [31]

Aside from the reduction in process disturbances due to spatter-producing mechanisms, the overall repeatability or stability of the process was thought to be improved because of the constant current aspect of the power source during arcing. The arcing current waveform remained constant for all arcing periods, so the melting rate would not alter greatly between short circuits. The weld pool was also quiescent because of the absence of violent short-circuit ruptures. The reduction in weld pool oscillations ensured that the arcing periods would be more consistent. Additionally, the arcing energy and hence fusion could be altered by altering the background current *i1*, whilst maintaining process stability at high levels.

As for the duplex power source, commercialisation was not economically feasible with the available technology. A major technical problem was that the detection of the onset of short-circuit rupture (critical to the operation of the process control) could not be done reliably in a system where the distance between contact tip and workpiece was variable; for example, a manual weld. In the experimental power source, the onset of rupture was detected by comparing the voltage against a fixed threshold, which was found by trial and error for a given welding condition. The threshold *v3'* was relatively easy to find (the current would reliably be reduced by the control circuit just before the actual rupture event). However, if the CTWD or wire type was altered, the value of *v3'* would also change, and the rupture detection would fail. This was a severe limitation, and the solution to this problem would not be found for another decade. Patents for the system were filed [31] but no further action was taken.

3.2.3 The introduction of power electronics to welding power sources

The advent of high voltage, high current switching bipolar transistors in the late 1970s and early 1980s allowed commercial production of fully electronic (primary rectifier inverter) power sources with feedback control of either voltage or current [32, 33]. These power sources were significantly smaller and lighter than conventional 50Hz transformer designs, due to their internal operation at high frequencies from 3 kHz up to 100 kHz. They were also designed to be either constant voltage or constant current types, depending on the mode selected by the operator. The concept of a high quality multi-process (MIG/TIG/Stick) power source was realised. The increasingly sophisticated control circuits were also able to provide output characteristics suitable for various materials, but the features were somewhat limited because microprocessors were still too expensive to be incorporated into the designs. Current ratings for these power sources were generally below 300A, and rates of response were 50-150 A/msec; similar to those of conventional power sources. In the latter half of the 1980s, costs of both power transistors and microprocessors dropped, while capabilities increased. Microprocessor controlled power sources of 500A rating became possible.

Despite the advent of these electronic "inverter-based" power sources, the control of the short-circuiting GMAW process did not improve, simply because these new power sources emulated the behaviour of conventional designs (Figure 3.2). Consequently, process stability with larger wires was still poor, and lack-of-fusion defects (amongst others) remained a persistent disadvantage of dip transfer welding.

3.2.4 Combining welding research with improvements in electronics

As more sophisticated control techniques became economically viable, previously experimental work was implemented commercially. In 1987, Ogasawara *et al.* [34, 35] reported development of a power source based on the work of Boughton and MacGregor for specialised control of short-circuit transfer welding in carbon dioxide. There had been an ongoing need in Japanese industry for improvement in this process using CO_2 because of the very high degree of factory automation. In large scale automation, the cost of shielding gas is a much more important factor in the total cost of the weld than for the more common Western practice of low volume production using manual welding, where labour costs dominate. Using a transistorised "inverter-based" power source with rapid current response (500 A/msec), spatter was claimed to have been reduced by up to 75% compared to that of a well-tuned conventional CV power source.

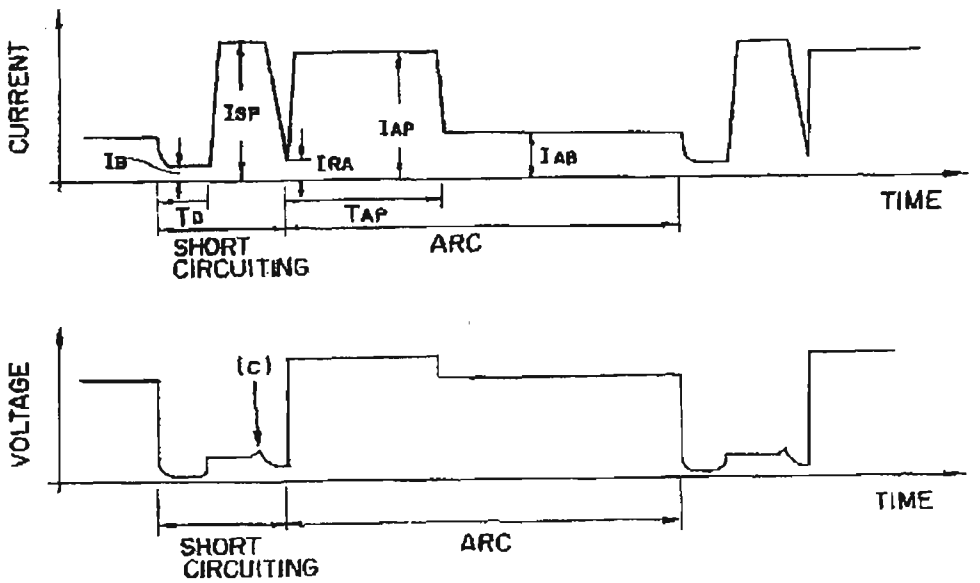

Figure 3.6 Waveforms for power source described in [35]

Figure 3.6 shows the waveforms for the improved process, in which the current is instantaneously regulated by the power source. The similarity of this approach to earlier work is evident. The major difference in the current waveform is the application of a pulse current I_{AP} for duration T_{AP} at the commencement of the arcing period, to ensure that a sufficiently long arc length is generated to avoid a premature short circuit. The pulse also promotes early droplet growth. In this respect, this new current waveform emulates the arcing behaviour of the CV power source.

Most importantly, the problem of reliable detection of the onset of short-circuit rupture (event "c" in Figure 3.6) was overcome. The detailed voltage and current

waveforms during the short-circuit period are shown in Figure 3.7. At a time after the short-circuit current reaches its steady-state value I_{SP}, the voltage V_L is sampled and retained as the "base" short-circuit voltage. The controller internally generates a voltage $V_N(t)$ which is proportional to the integral of the instantaneous voltage:

$$V_N(t) = k\int_0^t V(t)dt \tag{3.1}$$

A quantity $\Delta V(t)$ is calculated to represent the voltage component due to the formation of the narrowing short-circuit bridge.

$$\Delta V(t) = V(t) - V_N(t) - V_L \tag{3.2}$$

When $\Delta V(t)$ reaches a threshold value, the short-circuiting current is reduced to a low level I_{RA} until the rupture occurs. It was determined experimentally that for 1.2mm diameter wire and I_{SP} of 400A, V_N ramps at 0.20-0.25 V/ms and the threshold for ΔV is 0.3-0.6 Volts.

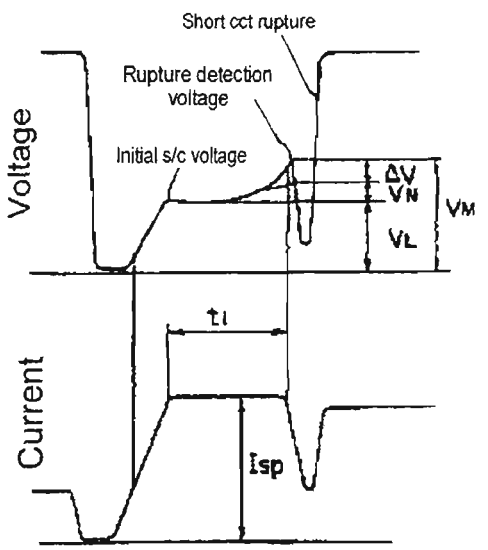

Figure 3.7 Short-circuit rupture detection waveforms [35]

The development of this method of rupture "premonition", which compensated for changes in CTWD, enabled the equipment to be applied in practical applications. There were also benefits gained by improving other aspects of power source control, such as improved arc starting and reduction of residual drop size at the wire tip after welding. These were of particular benefit in automated applications. Further development of the above control technique was reported in 1995 [36], adding main circuit polarity reversal to minimise burn-through in thin sheet.

The reduction of spatter reported by Ogasawara *et al.* was not as complete as that described by Boughton and MacGregor more than a decade earlier. The reason was

that the inverter-based power source used by Ogasawara *et al.* used a conventional output circuit topology consisting only of diodes and an inductor, with no other active switching devices present in the output stage. The use of a conventional "basic" circuit gave that power source a dynamic response of no better than 200 A/ms when operating into a short circuit. In comparison, the equipment used by Boughton and MacGregor achieved current reduction rates of 4000 A/ms under the same conditions, at the cost of a more complex and inefficient circuit. The ability to rapidly reduce the current once the short-circuiting event is predicted is vital to avoiding the production of spatter, since the time available between the premonition of the rupture and the actual event is typically around 500 μs or less (see Chapter 4). This fact was recognised by Nakanishi *et al.* in 1984 [37], and the circuit revision needed to achieve the high current turnoff rates is shown in Figure 3.8.

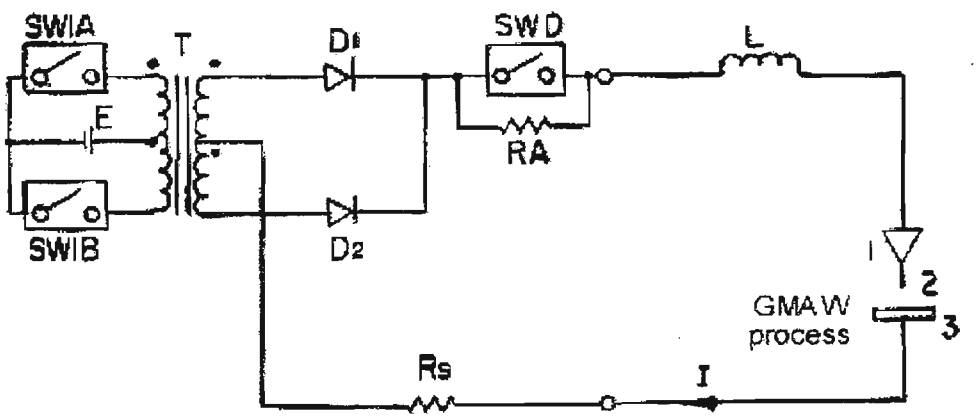

Figure 3.8 Power source circuit modification for rapid current turnoff [37]

The conventional inverter-based power source does not incorporate components SWD and RA. When a sudden reduction in output current is required during a short circuit, the control circuit will deactivate transistors SW1A and SW1B. The current will then "flywheel" through diodes D1 & D2, output & cable inductance L, and cable & short-circuit resistance R_S. The instantaneous current after turn-off is given by:

$$I(t) = I_o e^{-\frac{R}{L}t} \tag{3.3}$$

Using an initial current I_0 of 400A, a total inductance of 50μH (40μH for power source output inductance and 10 μH for cables), a total resistance of 40 mΩ (20mΩ for the electrode extension and short circuit bridge, 20mΩ for cables), and a rupturing time of 500μs, then the final current at the point of bridge rupture is 268A. This is not low enough to avoid spatter production.

If components SWD and RA are used, device SWD is "closed" during normal current output, so there are few losses in the output circuit. Device SWD is opened when rapid current turnoff is required, so that resistor RA is inserted into the output circuit to significantly reduce the time constant. Using the same initial current, inductance, rupturing time and resistances as above, and adding RA of 0.5Ω, the final current at the point of bridge rupture is dramatically reduced to 2A. If the rupturing time is reduced to 150μs, the final current is still acceptably low at 80A. Evidently, the inclusion of SWD and RA allow high current turnoff performance to be obtained at minimal cost or impact on the design of the power source.

In the late 1980s, a power source combining the features of earlier designs and the improved output circuit topology described above was developed by the Lincoln Electric Company (U.S.A.). Sold as the "Surface Tension Transfer (STT)" power source, it was designed solely for short-circuiting transfer GMA welding of steels. Patents [38] were filed in 1989. The commercial unit was reported in the literature in 1993 [19]. The waveforms are illustrated in Figure 3.9. Again, the welding current is instantaneously controlled by the power source in response to process conditions.

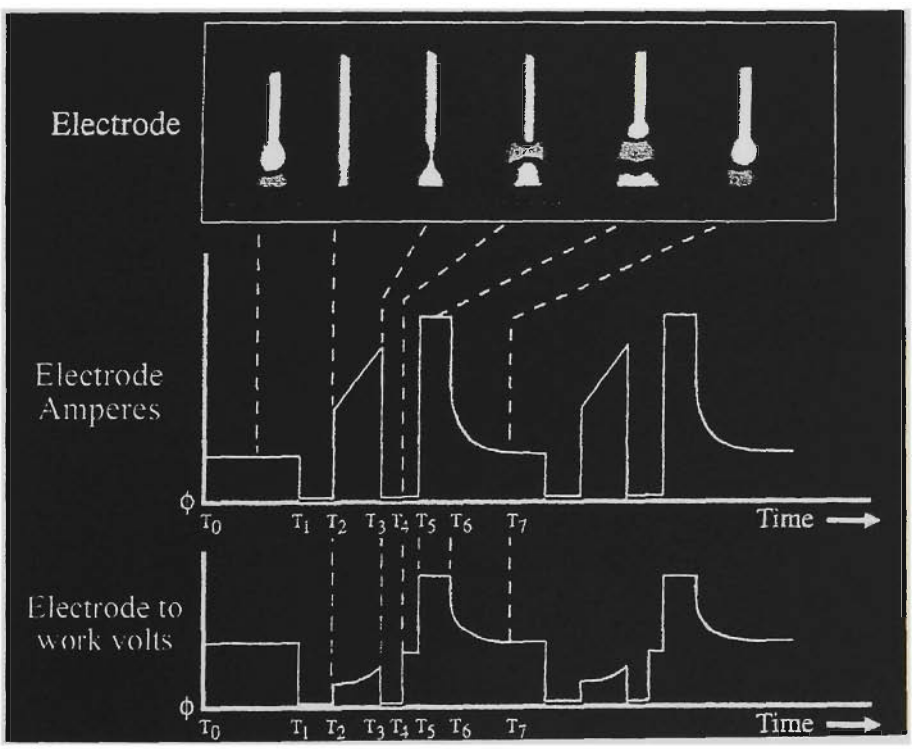

Figure 3.9 Waveforms for "STT" power source [19]

The differences between these waveforms and those of Figure 3.6 occur in the short-circuiting period. Here, the current is linearly ramped from a fixed level of around 150A after the wetting-in period. In earlier designs, the short-circuiting current was constant. The ramped current emulates the behaviour of conventional CV power sources

during the short circuit, and offers the advantage that metal transfer is achieved at lower current for most short circuiting events. The rupture premonition technique described previously is rendered ineffective by the use of a non-constant current, since the change in electrode resistance during the short-circuit is a complex function of time and current. To provide reliable premonition of the short-circuit rupture, the rate of change of voltage (dv/dt) is evaluated and compared to a threshold value, which depends on the electrode size and composition. This method has been proven to be very reliable, and is described in detail in Chapter 4.

The benefits of this power source were claimed to be low spatter levels (particularly for CO_2 shielding gas), maintenance of arc stability with variations in electrode extension, and reduced heat input on thin-gauge material.

3.3 Summary

This chapter has outlined the major developments of the short-circuit transfer GMA welding process, and the corresponding improvements in the power sources that were required to achieve enhanced process control. The history of these changes and an understanding of the reasons for these changes are necessary background information for the work that is described in Chapter 4 (equipment design) and Chapter 5 (process control techniques).

Chapter 4

An Experimental Advanced Power Source for Short-Circuit Transfer GMA Welding

4.1 Scope

This chapter describes the design and implementation of the custom-built, high-performance power source used to conduct the research documented in later chapters. The power source has been constructed specifically for use as a research tool for this project, and consequently incorporates all of the design improvements outlined in Chapter 3. Because the power source design is not constrained by commercial considerations such as cost and form, a number of improvements have been incorporated to increase performance and flexibility within the research environment. The design of the power source is modular, so that the operation of the welding test facility as a whole depends on the interaction between the basic power source and an array of associated test equipment. This associated equipment is also described.

Section 4.2 details the design and operation of the experimental power source. Section 4.3 describes the speed-regulated wire feed unit used with the power source. The computer controller, interfacing equipment and general arrangement of the welding test facility are described in section 4.4, while the short-circuit premonition unit is covered in section 4.5.

4.2 Power Source

To meet the likely requirements of ongoing research, and in view of the historical developments in power source technology described in Chapter 3, the specifications of the experimental power source are as follows:

1. Power source characteristic: DC Current-Controlled
2. Arrangement: Main current supply & Background current supply
3. Main current peak output: 600A
4. Main current mean output: 300A @ 60% duty cycle (10 minutes)
5. Main current ramping rate into 30V arc: +/- 300 A/ms
6. Main current turnoff rate: 20,000 A/ms minimum
7. Background current output: 0-50A @ 100% duty cycle
8. Interface: Analogue references and Digital (TTL) control signals

The electrical schematic diagrams of the power source are shown in Figure 4.1 (Appendix 1). Figure 4.2 shows photographs of the exterior and interior of the unit. The power source derives an internal DC bus of approximately 80V from a modified commercial constant voltage GMA power source. Two independent current controllers are used to supply the dynamic main current and the constant background current which is used as a "pilot arc" after the short-circuit rupture, as described in Chapter 3 and [38]. Both current supplies are based on hysteresis controllers. The background current supply has a fixed hysteresis of 5A, while the main current supply has a programmable hysteresis of 20A or 7A, determined by the external controller (section 4.4). Generally, the hysteresis is set at 20A during the arcing period to reduce switching losses within the power source. The hysteresis is reduced to 7A during the short-circuiting period to reduce ripple in the voltage feedback, so the onset of short-circuit rupture can be reliably detected. This is described further in section 4.5. The main and background current supplies can be activated or deactivated independently. The instantaneous output current of the power source is the sum of the outputs of the two current supplies, which are independently adjusted through 0-10V analogue signals from the controller.

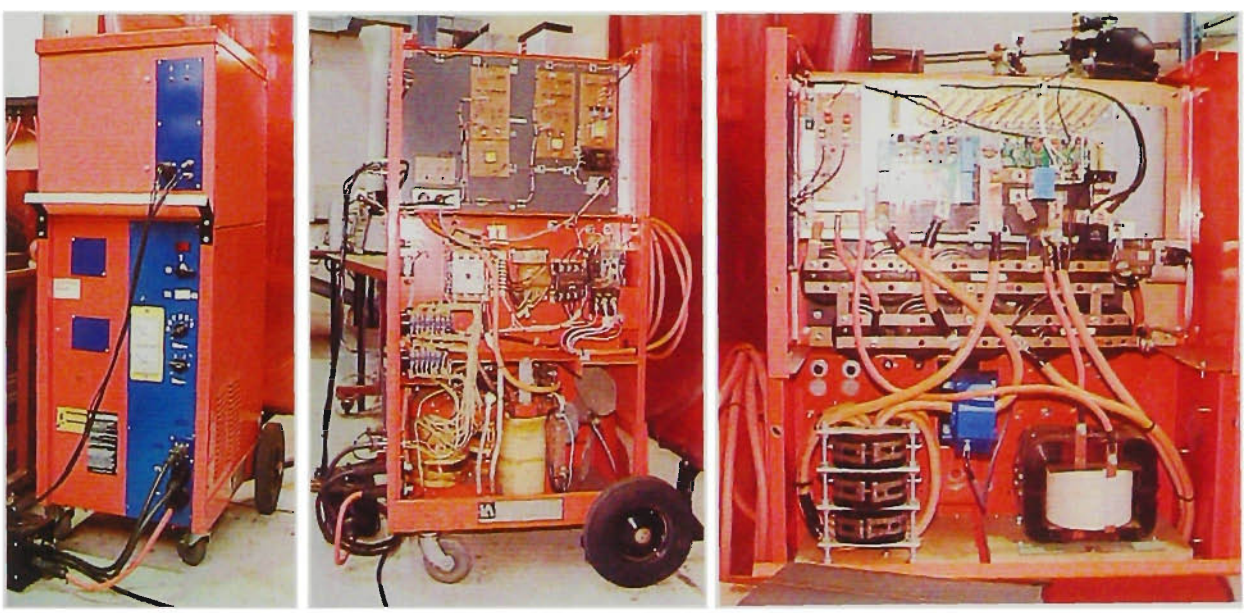

Figure 4.2 Photographs of Experimental Power Source

The ability to rapidly reduce the output current during a short circuit is provided by the topology of the main current supply output circuit. Figures 4.3b & 4.3c show the circuit operation in a simplified representation of the complete circuit shown in Figure 4.1a (Appendix 1). In comparison, Figure 4.3a is the equivalent output circuit of a conventional inverter-based power source. In all cases, the power source internal

inductance, cable inductance and total short circuit resistance are represented by L_m, L_c and R_{sc}, respectively.

For the case of the conventional power source, when the current in the output short circuit is to be reduced, the controller deactivates all switching devices, represented by SW1. The current then "flywheels" in the circuit as shown in Figure 4.3a. The exponential rate of decay of current is determined by the total inductance and resistance, as explained in Chapter 3. In the time available between premonition of the short-circuit rupture and the actual rupture, the current cannot be sufficiently reduced by this circuit to avoid spatter production. In recent years, the primary (input) circuit topology of electronic power sources has been improved to reduce losses and production costs [39, 40], but the output circuit has remained unchanged. The fundamental short-circuit response is therefore unchanged.

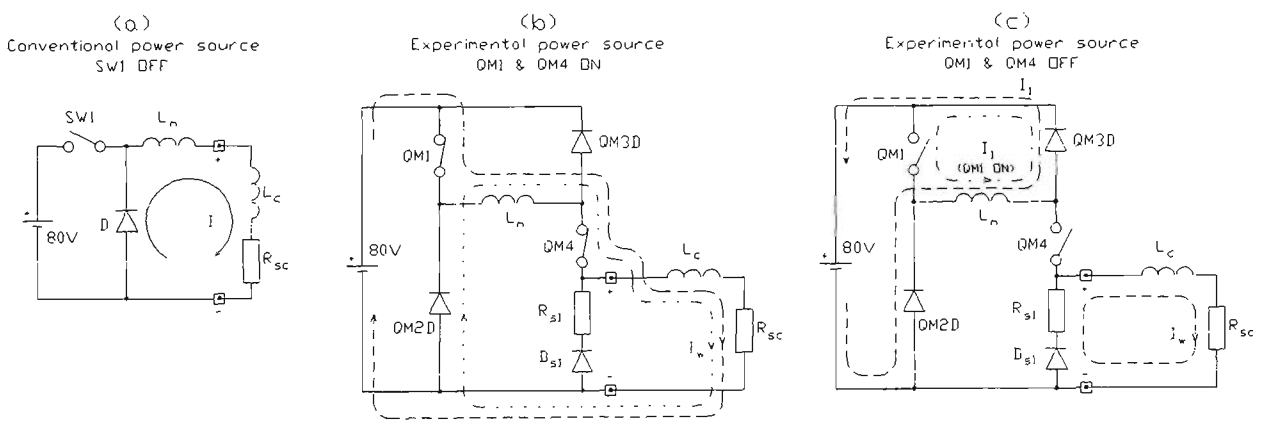

Figure 4.3 Main supply output circuit operation

Figure 4.3b shows the current path in the topology of the experimental power source when the current is being increased in the short circuit. In this case, QM1 and QM4 are closed ("on"), and the welding current I_w is conducted by L_m and L_c in the path indicated by the dashed line. When the desired current is reached, QM1 is opened, and the current flywheels in the path indicated by the dotted line. During normal operation in both short-circuit and arcing periods, QM4 remains closed. However, when a rupture event is predicted, QM4 and QM1 are opened, as shown in Figure 4.3c. The energy stored in L_m is returned to the DC supply through QM2D and QM3D via current flow I_1 (dashed line). More importantly, the welding current I_w is forced to flywheel through the independent circuit D_{S1}, R_{S1}, Lc and R_{sc}. As explained in Chapter 3, the value of R_{S1} is chosen to be much greater than R_{sc}, so than the time constant of the current decay is very small. This ensures that the welding current is reduced to below 20A within 50μs of the QM4 turnoff event. The majority of the energy stored in the

cable inductance is dissipated by R_{S1}. The current turnoff performance of the circuit is shown in Figure 4.4a. The initial rate of fall of current is 28,000 A.ms, and the current is reduced from 650A to 20A within 50μs.

Another benefit of rapid welding current recovery after the short-circuit rupture can be gained by appropriate control of the output circuit. As described above, when QM4 and QM1 are opened, the energy stored in L_m is returned to the DC supply at a rate determined by the inductance and supply voltage. However, if QM1 is kept closed, current I_1 flywheels in the path indicated by the dotted line in Figure 4.3c. The energy losses are limited to conduction losses in QM1 and QM3D. Furthermore, if the final short-circuiting current is greater than the initial current desired during the arcing period, QM1 can be opened at the point of rupture detection so that I_1 is reduced to the desired initial arcing current. When the desired initial arcing current is reached, QM1 is closed to hold this value of current in L_m. When the short-circuit rupture is complete, QM4 is reclosed and current I_1 is applied to the welding circuit at a rate which is much greater than that which could be achieved by building the current from zero through both inductors L_m and L_c. The improvement in current recovery depends on the ratio of L_m to L_c. For the experimental equipment, this ratio is approximately 7. Figure 4.4b shows the current recovery performance where energy storage in L_m is not used. Figure 4.4c clearly shows the improvement when energy storage is applied. It should be noted that the energy storage scheme cannot increase the current in L_m while QM4 is open. Therefore, the value to which the current can rapidly be restored is the final short-circuit current less any flywheeling losses during the time taken for the short circuit to rupture.

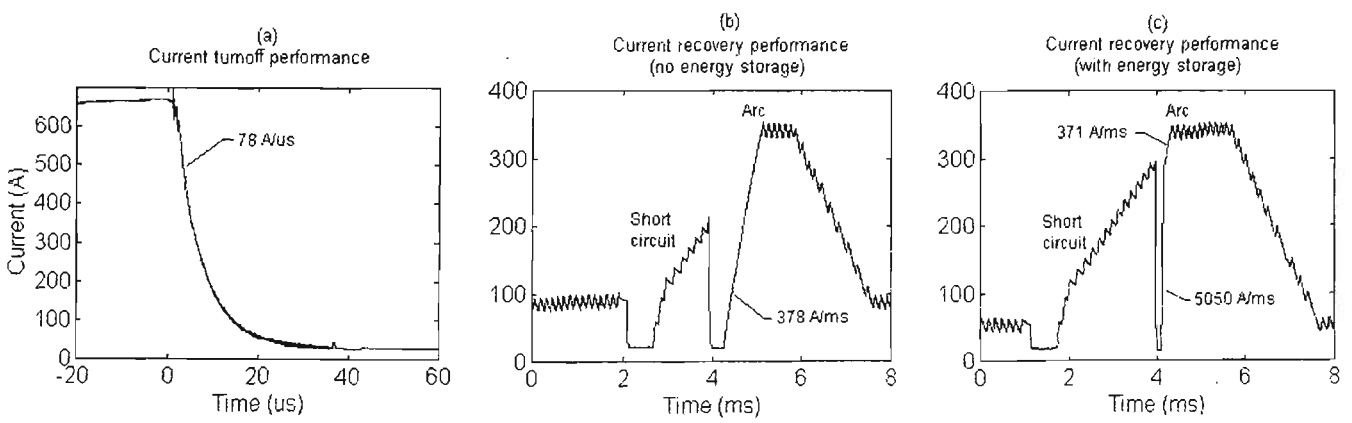

Figure 4.4 Current response of experimental power source

The very rapid application of welding current after the short circuit rupture has benefits for the welding process. Because the melting rate is immediately high, the likelihood of a premature short circuit occurring at the start of the arcing period is

greatly reduced. This is expected to be particularly important for situations where the transferred droplet was small, so the clearance between weld pool and electrode is also small. The instant application of significant current rapidly depresses the weld pool to avoid unwanted contact. Weld pool depression under these conditions is clearly illustrated in Chapter 10.

4.3 Wire Feed Unit

The wire feed rate is a key parameter in the GMAW process. In order to be able to validly compare the results of experiments conducted at different stages in a project using the same wire feed rate, it is vital that the wire feeding equipment is able to reliably reproduce the same feed conditions irrespective of factors such as frictional load and mains voltage variation. The repeatability of wire feed rate becomes even more important when using larger electrodes in longer torch conduit lengths. Since the equipment described here is used for a number of research activities, the stability of wire feed rate was considered sufficiently important to justify the construction of a wire feed unit with speed feedback control to ensure stability and repeatability of the drive roll speed under all practical conditions.

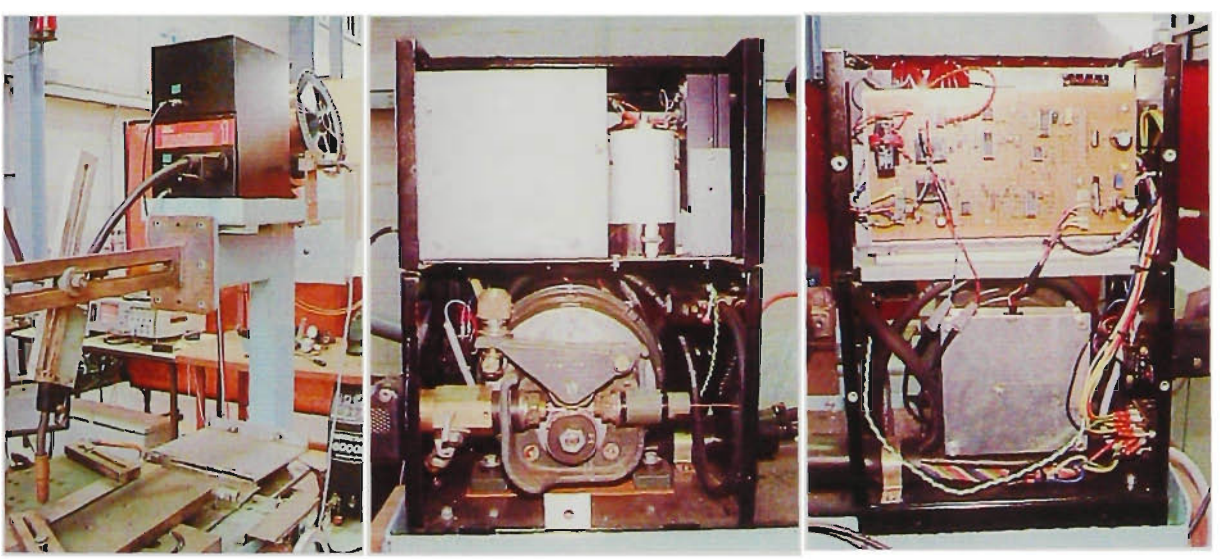

Figure 4.7 Photographs of Modified Wire Feed Unit

Figure 4.7 shows photographs of the commercial wire feeder which has been modified by the addition of new electronics housed in the extended upper section of the chassis. The electrical schematics are shown in Figures 4.5 and 4.6 (Appendix 2). The speed control system has a conventional structure of inner current loop to control the torque output of the DC drive motor, and an outer speed loop whose feedback is derived from a 500 pulse per revolution encoder mounted on the motor armature. The motor current is limited to 1.0 P.U. (per-unit, continuous full load rating), enabling the unit to

uniformly accelerate from rest to full speed of 20 m/min in 0.39 second with no wire feeding load. Testing showed that a step increase in output shaft load of 0.6 P.U. at 8 m/min causes a 0.16 m/min drop in speed, recovering to the correct speed within 0.2 seconds. This level of performance is considered adequate for an experimental wire feed unit. As a practical consideration, the wire feed unit is designed to operate from 24VAC and 110VAC supplies so that it can be used with a wide range of pre-existing and commercially available power sources, should this need arise for other projects.

4.4 Control System and Associated Equipment

The power source and wire feed unit described in the previous sections require a coordinated control system to allow a weld to be performed. The block diagram of the system which comprises the welding test facility is shown in Figure 4.8 (Appendix 3). At the heart of the system is a commercially available digital signal processor (DSP) based controller which is accommodated by a desktop personal computer (PC). The DSP controller comprises of a 32 bit floating point processor which is programmed in "C" high level language through the PC. The DSP controller operates independently of the PC operating system, so that consistent real time control of the welding process can be achieved. The process control program is regulated by interrupts generated within the DSP hardware, and for the work performed in this project the interrupt rate is fixed at 25 kHz (40μs period). Data is transferred between PC and DSP controller through a small region of dual port RAM, so that target settings can be downloaded to the controller and logged data can be uploaded to the PC. The transfer of data is handled by handshaking routines built into the DSP control program and the PC program which is written by the researcher to act as a user interface. Chapter 5 gives a description of the DSP control programs used for this project.

The DSP controller is configured with 16 digital inputs and 16 digital outputs that are TTL compatible. These can be directly connected to other equipment that has appropriate earthing or optical isolation. The DSP controller also has four analogue inputs and four analogue outputs designed for a fixed +/-3V operating range. These are interfaced to external equipment operating at +/-10V levels by the scaling unit. The scaled DSP analogue outputs are individually isolated electrically by the isolation unit to provide the two interference-free current references to the power source and the speed reference to the wire feed unit.

The analogue signals for voltage, current, wire feed speed and welding travel speed are provided by the instrumentation unit. The voltage feedback is produced by a differential amplifier with two filtered outputs. One is a "fast" signal with only a 1μs single pole time constant, while the other has a 40μs time constant. The former is used by the short circuit premonition unit as described in the next section, while the latter is used by the DSP controller and data acquisition equipment. The current feedback is produced by a closed loop Hall-effect sensor placed on the negative lead of the power source. The current output of the sensor is converted to a voltage by the instrumentation unit and minimal filtering with 1μs time constant is applied. The wire feed speed feedback is produced by a commercially available sensor specifically for this purpose, and the welding travel speed is generated from a pulse train produced by a digital encoder situated on the welding table drive screw. These two signals are scaled and then filtered to provide clean outputs with acceptable response times.

The primary data acquisition is performed by a digital storage oscilloscope with 12 bit resolution and sampling rates up to 10 MS/sec. Secondary data acquisition is performed by an existing data acquisition system that has been utilised for earlier research [41, 42]. As the equipment was fully operational, and the acquisition software was uprated by Dr. L Sanders as part of a concurrent project using the welding test facility, it was also used in this project. The initiation signal for both data acquisition systems is generated manually, or by a high-speed film camera which generates a synchronisation pulse when the film reaches its target speed. The latter feature was not used in this project.

The speed and weld length control is achieved by existing equipment consisting of the welding table, variable speed drive and PLC (programmable logic controller) cabinet. The welding table is a modified metal-working lathe with the chuck and gearbox removed, as described in [41, 42]. The welding torch, which is only 500mm from the wire feed unit, remains stationary. The workpiece, which is clamped to a flat table that replaces the original cutting tool holder of the lathe, is moved by the lathe feed screw. The speed is manually set by means of the variable speed drive. The desired length of a weld bead can be set from switches on the PLC cabinet. The welding process is automatically terminated when the required distance has been travelled.

The stationary welding torch is advantageous for photography of the welding process. This aspect of the project is detailed in Chapter 9. As shown in the system block diagram of Figure 4.8 in Appendix 3, the digital camera and lighting system are

triggered from a digital output of the DSP controller. The timing of the photograph is entirely under software control. The camera and flash trigger units provide signal isolation and adjustable delays so that the camera exposure can be synchronised to the light output from the flash unit. The facility also exists to use a helium-neon laser as a backlighting source as an alternative to the flash unit. The image captured by the camera is digitised by an inexpensive frame grabber card contained by the control computer.

Figures 4.9, 4.10 and 4.11 in Appendix 4 show the electrical schematics of the instrumentation unit, isolation unit, and scaling unit respectively. Figures 4.12 to 4.15 below are photographs of the various pieces of equipment.

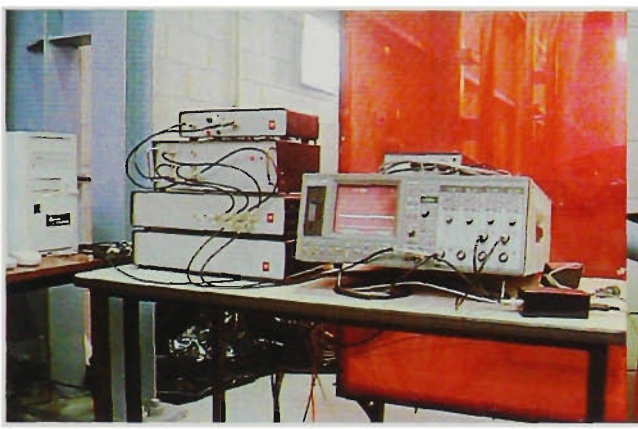

Figure 4.12
Premonition, instrumentation, scaling, & isolation units, digital storage oscilloscope

Figure 4.13
Data acquisition & control computers

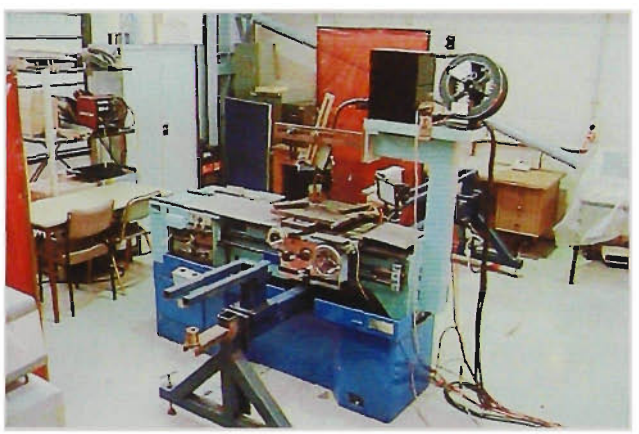

Figure 4.14
Welding table

Figure 4.15
PLC cabinet and power sources

4.5 Short-Circuit Premonition Unit

The ability to predict the short circuit rupture event, so that the current can be reduced prior to the actual rupture, is vital to the enhanced control of the short-circuit GMAW process. The "premonition" of the rupture event is performed by measuring the rate of rise of weld feedback voltage, as discussed briefly in Chapter 3. For successful control of the process, the rupture event must be reliably anticipated in every short-

circuiting period, otherwise the benefits of the improved process control will be lost. The premonition unit must operate successfully under conditions of changing short-circuit current. This section describes the development and operation of a premonition unit which has been proven to reliably predict the short-circuit rupture with a success rate of better than 96% under the operating conditions encountered in this project.

The short-circuiting voltage waveform produced by the experimental power source operating as a conventional CV supply is shown in Figure 4.16. In this particular case, the CTWD was 13mm and the electrode was 0.9mm diameter to AWS A5.18-ER70S-6 specification. Although not shown, the current waveform is similar to that of Figure 2.2. That is, the current is not constant during the short circuit. The current hysteresis band has also been reduced from 20A to 7A so that voltage ripple is also reduced. The voltage waveform in Figure 4.16 has been filtered using a 40μs single-pole filter to further reduce ripple without significant phase shift.

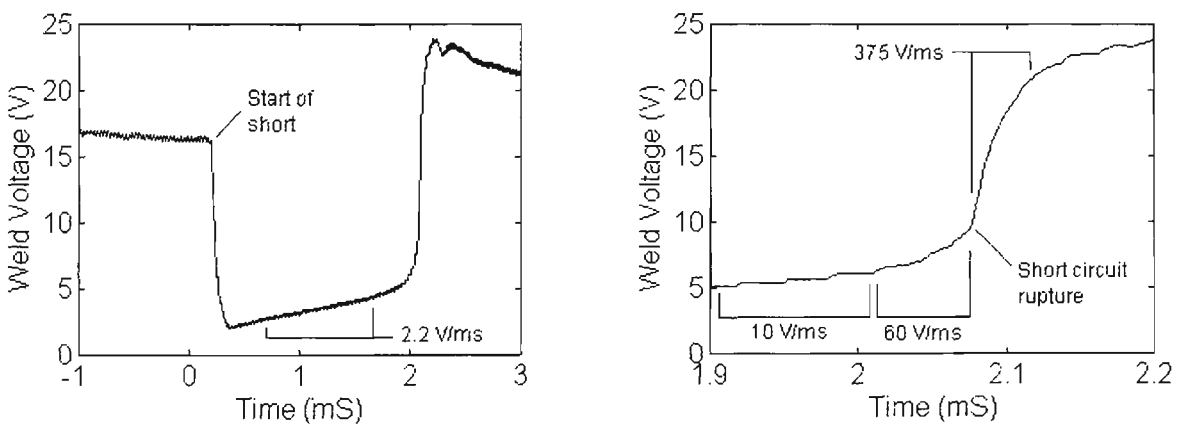

Figure 4.16 Short circuit voltage waveform

It is clear that in the final stages of the short circuit, the rate of change of voltage (dV/dt) increases from a minimum of 2.2 V/ms to over 60 V/ms. The values shown are averages taken over the indicated time period. It would seem that the rupture event could be predicted by evaluating the voltage derivative and comparing it to a threshold value between 10 and 60 V/ms. When this occurs, the main welding current produced by the experimental power source would be rapidly turned off, and the short circuit bridge could then rupture at the background current level of around 20A.

To physically implement this, a hardware circuit was constructed and inserted between the DSP controller and the power source, as shown in the system block diagram of Figure 4.8 (Appendix 3). The premonition unit uses voltage feedback signals from the instrumentation unit, and intercepts the "Main Enable" output from the DSP controller. When the premonition unit determines that a short-circuit rupture is

imminent, it de-asserts the "Main Enable" output to the power source. This is done asynchronously to the operation of the controller, which has a sampling and control period of 40μs (25kHz). By scrutinising the waveforms in Figure 4.16, it was judged at the time of system construction that the DSP controller would not have sufficient time resolution to reliably predict the rupture. In particular, this would be the case if the detection needs to be done at over 60 V/ms, where the window of opportunity is very narrow. To prevent the premonition unit from disabling the main current at other times in the weld cycle, a "Permit Disable" signal is sent from the DSP controller and is asserted only during the short-circuiting period when the current exceeds 135A. The premonition unit also provides digital feedback to the controller to indicate that the main current has been asynchronously disabled.

The first version of the premonition circuit used an analogue differentiator to instantaneously evaluate the dV/dt of the filtered short-circuit voltage. A great deal of care was taken to ensure that a noise-free signal was available to the differentiator, and that noise pickup from the power supply and adjacent circuits was not present. The waveforms produced by this method are shown in Figure 4.17.

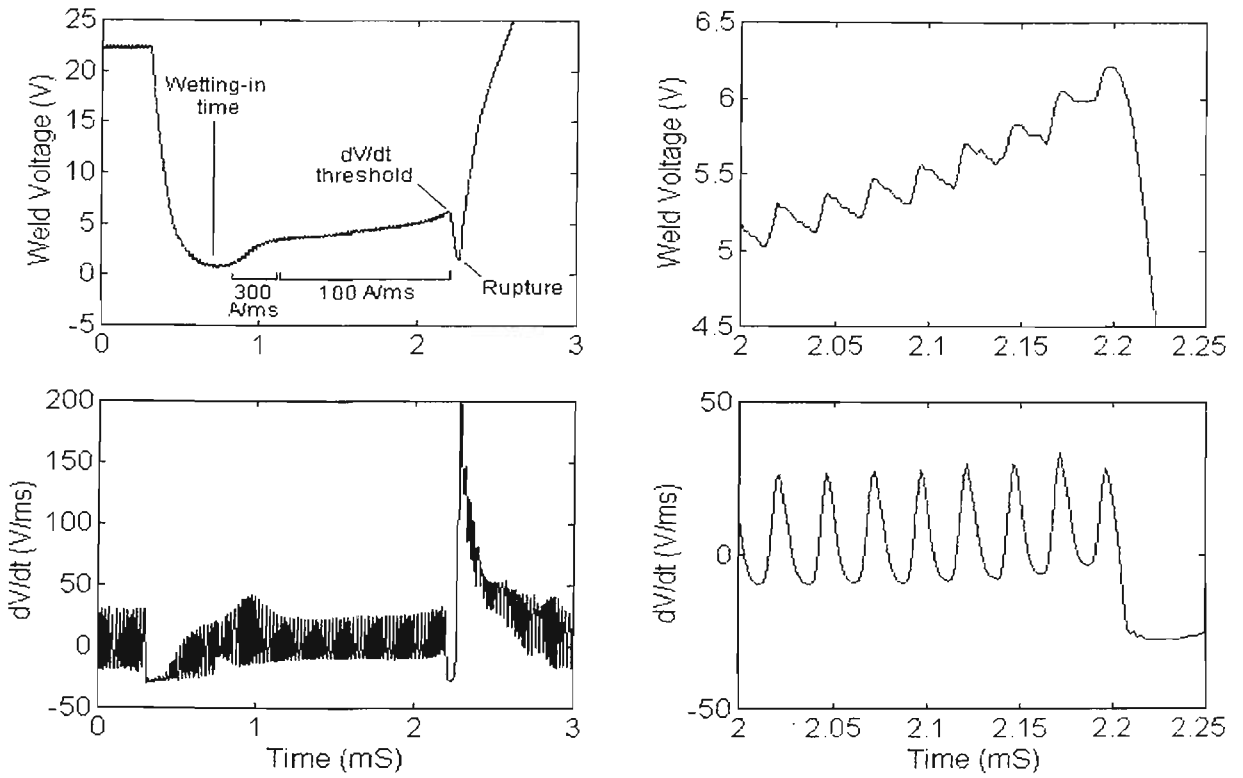

Figure 4.17 Waveforms for analogue differentiator

The welding voltage waveform is different from that in Figure 4.16 because the current waveform produced by the experimental power supply is now similar to that of the "STT" commercial power source described in Chapter 3 (Figure 3.9). In the initial stages of the short circuit, the main current is reduced to 20A. After the wetting-in time,

the main current is rapidly increased to 100A at a ramp rate of 300A/ms. After this, the main current is ramped linearly at 100A/ms until the rupture is predicted, at which time the main current is rapidly turned off until the rupture occurs and the arcing period starts. This control method is described in more detail in Chapter 5.

The operation of the analogue differentiator did not reliably predict the rupture event. The waveform captured in Figure 4.17 shows one of the few weld cycles where the premonition was successful. The success is indicated by the welding voltage rapidly dropping , then increasing a short time later after the short circuit ruptures under the influence of a low background current. For "late" premonitions, the welding voltage does not drop at all, so it appears as shown in Figure 4.16. The rupture occurs at full current as in a conventional weld. For "early" premonitions, the welding voltage drops but the rupture does not occur at reduced current. In this case, the welding controller software detects a fault condition after 1.0ms, and reactivates the main current to clear the short circuit so that the welding process can continue. The detail of the waveforms on the right hand side of Figure 4.17 shows that the differentiator responds to the small ripple in the voltage feedback, making the premonition unit insensitive to dV/dt values less than 20 V/ms. It was found that threshold values greater than 20 V/ms consistently produced "late" premonitions, so the process requires that the main current needs to be removed earlier in the short circuit. Increased filtering of the feedback signal did not improve the situation, since excessive phase delays were introduced which again produced "late" premonitions. These experiments showed that the analogue differentiator is not suitable for this task due to the presence of ripple in the voltage, which is an inevitable consequence of using an electronic power source.

To produce a dV/dt signal which is less sensitive to voltage ripple and provides resolution down to 1.0V/ms, a second and final version of the premonition unit was built, using a "sampling" differentiator. This circuit samples the filtered voltage at 25μs intervals and then produces an output which is the difference between the present input voltage and that at the sampling point. The waveforms for this circuit are shown in Figure 4.18. Using this approach, reliable premonitions could be obtained with success rates greater than 96%. That is, in any given sequence of 50 weld cycles, a maximum of two short circuits would not successfully rupture under the influence of background current. The premonition success rate was found to be determined by the dV/dt threshold value used. For the 0.9mm ER70S-6 electrode used, acceptable values ranged from 4 V/ms to 11 V/ms. The best value was found to be approximately 7.2 V/ms, and

this value was used in the experiments conducted in later chapters. The time taken for the short circuit to rupture after main current turnoff was found to vary between 0.1 and 0.6ms. Changes in CTWD and shielding gas composition did not discernibly affect premonition success rate, although this aspect was not rigorously investigated. It is expected that changes in electrode diameter will alter the optimum dV/dt threshold value. In the present design, the threshold is set manually by a potentiometer. In a commercial application where a variety of electrode sizes and types are likely to be encountered, an automated means of finding the optimum threshold is required. One possible method is to calculate the percentage of "successful" premonitions, where the rupturing time is between 0.1 and 0.6ms, say, and adjust the threshold so that the percentage is maximised.

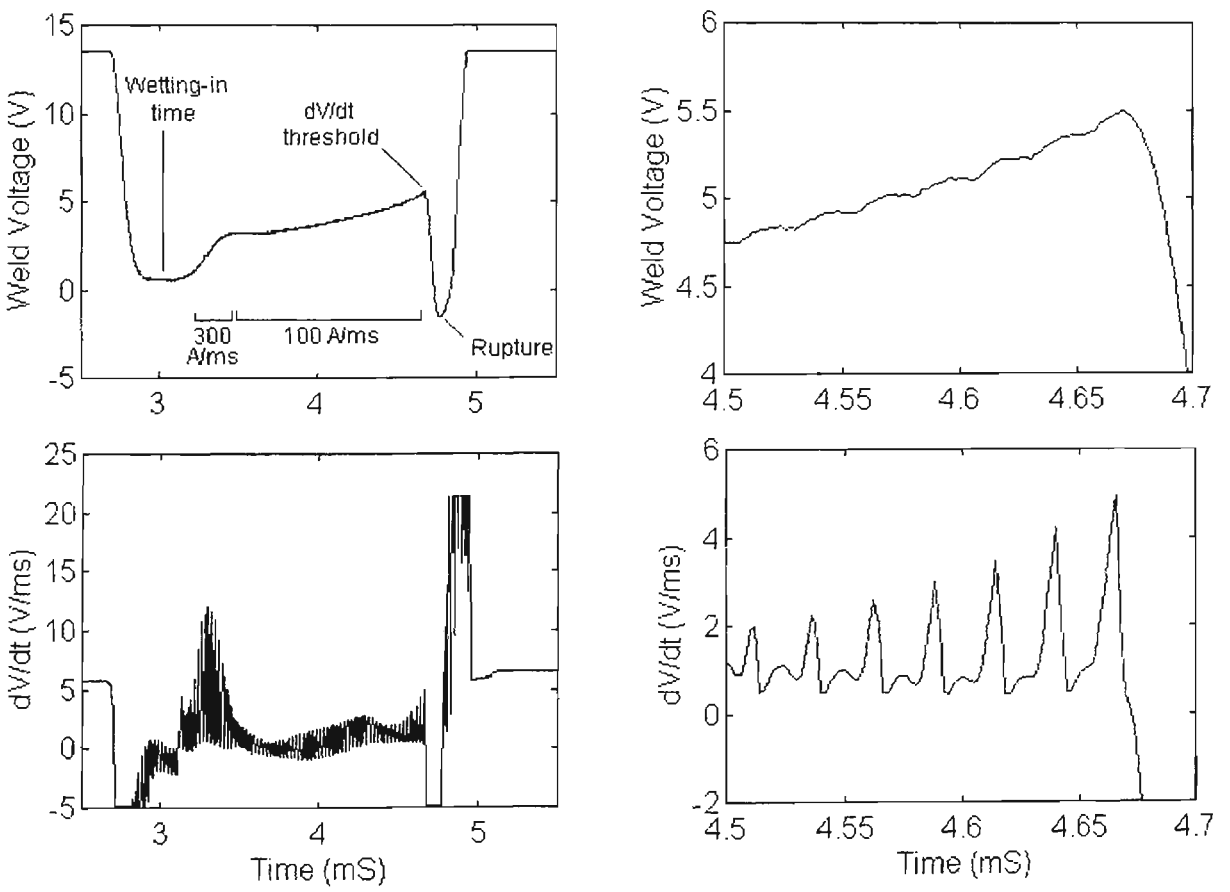

Figure 4.18 Waveforms for "sampling" differentiator

As shown in Figure 4.18, higher dV/dt values are produced during the time of rapid current ramping than at the end of the short-circuiting period. To avoid spurious premonitions, the DSP controller does not permit disabling of the main current until 0.35 ms after the fast current ramping is completed. By this time, the dV/dt settles to a value that is safely below the detection threshold.

The schematic diagrams of the premonition unit are shown in Figure 4.19 in Appendix 5. Perusal of these will show that there is additional circuitry which allows

the unit to asynchronously disable the main current at the start of a short circuit. This is done by using the voltage feedback signal that is filtered with only a 1μs time constant, and comparing it to a fixed threshold of 8V. This function, if enabled by the controller, can disable the main current within 10μs of the start of the short circuit. This is much faster than the sampling rate of the controller. This is intended to reduce ball repulsion spatter at the start of the short circuit. This function was a late addition, and is not used for experiments documented in the following chapters. The effect of this function on ball repulsion spatter is discussed in Chapter 11.

4.6 Summary

A current-regulated power source has been constructed specifically for optimised control of the short-circuiting GMA welding process. It has the very high dynamic performance, particularly in short-circuit current turnoff, that is needed to fully exploit the improvements that have been made to the control of the process in the past. A premonition circuit has been built to reliably predict the onset of a short-circuit rupture with a success rate of better than 96%. These form the basis of a welding test facility which also incorporates a custom-built speed-controlled wire feeder, data acquisition systems, and necessary interfacing hardware. Particular attention has been paid to system design so that all electrical signals are free from noise induced from the welding environment. At the heart of the facility is a flexible, programmable computer-based welding controller which regulates the welding process. The controller coordinates the function of the power source and associated equipment, and can be programmed to obtain the desired behaviour from the power source. With this array of hardware, a number of process control techniques can be investigated. These techniques are described in detail in the following chapter.

Chapter 5

Process Control Techniques

5.1 Scope

This chapter describes the control techniques that are programmed into the DSP controller for regulating the short-circuit GMA welding process. Three control schemes are discussed. Section 5.2 describes a method of emulating the behaviour of a conventional constant voltage power source using the current-controlled power source described in Chapter 4. It is presented to demonstrate the versatility of the welding test facility described in the previous chapter. Section 5.3 describes a current-regulated "open loop" process control technique that is very similar to the recently developed methods described in Chapter 3. The performance of this method is investigated in detail in Chapter 10. Section 5.4 describes a current-regulated "closed loop" process control technique which is based on the "open loop" method. The electrode melting rate is modelled in order to predict droplet size. The size of the droplets transferred to the weld pool can then be regulated on a cycle-by-cycle basis. The objective of this method is to improve process stability (or regularity) and reduce spatter. The performance of this method is investigated in detail in Chapter 11.

5.2 The Conventional Constant Voltage Process

The experimental power source described in Chapter 4 has a current-regulated output which can be dynamically adjusted to obtain any desired output characteristic (within the limitations of the power source). The instantaneous adjustment of the current is performed by the DSP controller, which can be programmed so that the system behaves as a conventional constant voltage power source. The controller has access to the power source output voltage and output current feedback signals. These are represented internally in floating point engineering units (i.e. Volts and Amperes). The simple model of an ideal CV power source, shown in Figure 5.1, can be used by the controller to generate the current reference for the power source so that the desired CV characteristic is achieved.

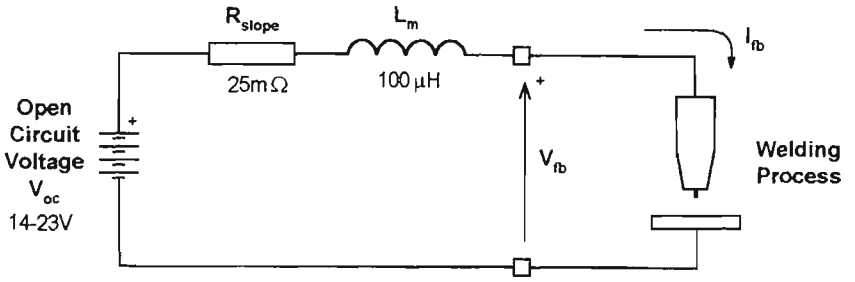

Figure 5.1 Model of ideal CV power source

In this model, R_{slope} is used to produce the slope in the static voltage-current characteristics as described in Chapter 3. The value of 25mΩ generates a slope of 2.5V per 100A. The value of inductance L_m (in Henries) produces the required dynamic circuit characteristics, as described in Chapter 2. The open circuit voltage V_{oc} is adjusted in the same way as would be done for a "real" CV power source, so that a stable welding condition is achieved. Using the available feedback signals V_{fb} and I_{fb}, the equations used by the controller to govern the process are:

$$\Delta I = \frac{(V_{oc} - V_{fb}) - I_{fb} \cdot R_{slope}}{L_m} T_S \tag{5.1}$$

$$I_{next} = I_{fb} + \Delta I \tag{5.2}$$

where T_S is the sampling & controlling period of the controller, ΔI is the change in current for a particular period, and I_{next} is the current reference supplied to the power source for the next controlling period. These governing equations were used by the controller to produce a weld from which the current and voltage waveforms shown in Figure 2.2 (page2-4) were obtained.

The ability to program the governing equations into the controller gives tremendous flexibility to emulate circuits of various design, as shown in Figure 3.2 (page 3-3). This has already been done by equipment manufacturers [27]. An interesting possibility is that the component values need not be static, but can be adjusted during the weld cycle. For example, the inductance L_m may be different during the early stage of the short circuit, the final stage of the short circuit, and the initial stage of the arcing period. Another possibility is that the entire equivalent circuit can be changed from the short-circuiting period to the arcing period, so that optimised circuits are applied to each phase of the weld cycle. These possibilities are not pursued further in this project because it is believed that the methods described in the following sections are superior control techniques that have not yet been adequately investigated in the literature. The

work in this thesis is confined to a detailed investigation of the control schemes described in the following sections.

5.3 The Current Controlled "Open Loop" Process

This section describes the programming of a current controlled waveform which incorporates the improvements in the short-circuit transfer GMAW process described in Chapter 3.

A major difference between this control method and that of the previous section lies in the concept that the welding cycle can be considered to occur in a finite number of sequential steps or states. The output current of the power source is controlled in different ways, depending on the state of the weld. In accordance with this concept, the controller is programmed as a finite-state machine. The transition between states is determined mainly by events within the welding process, and sometimes by pre-determined time limits. The state diagram for the current controlled "open loop" process is shown in Figure 5.2, along with the welding current waveform and a typical voltage waveform. It should be noted that the current is always determined by the controller and power source, while the voltage is a result of physical events within the process. The interpretation of voltage phenomena is discussed in detail in Chapters 10 and 11.

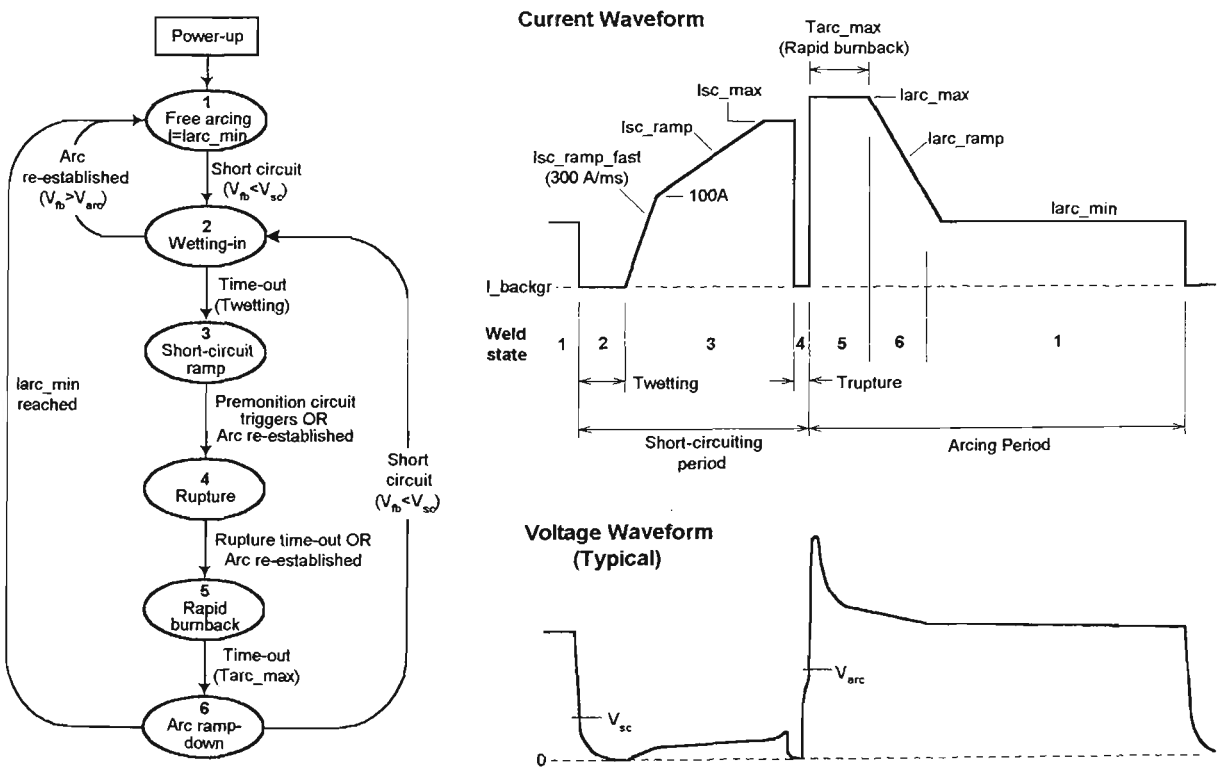

Figure 5.2 State diagram & waveforms for "open loop" control

The initiation of a short-circuit (state 2) is detected by the controller when the voltage drops below detection threshold V_{sc} (typically 5V). The main current is

immediately turned off so that only the background current I_backgr is flowing through the welding circuit. This background current is needed to produce the voltage necessary for detection of a short circuit rupture, should it occur. The immediate cessation of the short circuit is an unwanted event which may occur due to repulsion forces at the interface of the droplet and weld pool as described in Chapter 2. If the background current is not present, there is no way for this event to be detected, as no arcing voltage would be generated. If arcing is re-established in state 2, then the main current is reactivated, and steady-state arcing current Iarc_min is reapplied. This ensures continued droplet growth and workpiece heating. However, if the short-circuit is successful, the droplet at the end of the electrode "wets in" to the weld pool. A predetermined time T_wetting must expire before the transition is made to state 3, when the main current is reactivated.

In state 3, the current is rapidly raised to 100A at 300A/ms so that a significant electromagnetic pinch force is exerted on the short-circuit metal bridge. This provides partial compensation for the "lost time" during state 2 where no significant pinch forces are present, and metal transfer is accomplished mainly by surface tension. After the current reaches 100A, it is then ramped at a slower specified rate Isc_ramp (A/ms). The current is limited to Isc_max, but this value is set at 400A or higher. Almost all short circuits in a stable weld using 0.9mm mild steel electrode rupture at currents below 350A. The current limit is used to prevent power supply overcurrent trips (set at 660A) for unstable welds which tend to stub for a long period, or to limit the initial rupture current at the start of a weld.

When the current exceeds 135A in state 3, the premonition unit is enabled. The state is completed when the premonition unit has detected the onset of a short circuit rupture and asynchronously deactivated the main current, as described in Chapter 4. A digital signal to the controller confirms this action. Alternatively, if the premonition unit fails to predict the onset of rupture, the arc will re-establish and the voltage will exceed detection threshold V_{arc} (typically 12V). Either of these events will cause the controller to exit state 3. In all cases, the duration of state 3 is determined by the process' behaviour. The main factors which determine duration are initial droplet size, the wetting-in time, and the current ramping rate. The current during the short-circuiting event is not affected by the final arcing current prior to the short. This provides a useful decoupling from the previous arcing event, and allows the metal transfer process to be controlled independently.

If the short-circuit rupture has been successfully predicted, the voltage feedback during state 4 is low because only the background current flows through the short circuit. Even though the neck is very narrow and resistance is high, the voltage never exceeds 10V. The neck typically ruptures between 0.1ms and 0.6ms after the main current is turned off. When the rupture occurs, the voltage exceeds V_{arc}. If the arc is not established after time T_rupture (typically 1.0ms), the premonition unit is considered to have prematurely predicted the rupture. The short-circuit is unlikely to rupture within a reasonable time at the background current because the bridge remains too large and metal transfer is too slow. In this case, state 4 is terminated and the transition is made to state 5. If state 4 is entered after the premonition unit has failed to predict the rupture, the voltage will already exceed V_{arc}. Again, state 4 is immediately terminated and the transition to state 5 is made.

In state 5, the arc is established after a short-circuit rupture, so a high, fixed current Iarc_max is applied for specified time Tarc_max. This promotes weld pool depression and rapid melting of the electrode so that sufficient arc length is generated to avoid a premature short circuit. The presence of a suitable arc length at the end of this state also ensures an arcing period of acceptable duration, so that the workpiece will receive adequate heat input for good fusion. The only exit condition for state 5 is the expiry of time Tarc_max. If a short circuit occurs during this stage, it is considered to be a fault condition. The current is deliberately kept high so that the short is "blown clear". In practice, a short circuit occurs only if Iarc_max is too low for the welding conditions. The values of Iarc_max and Tarc_max determine the peak arc length that is achieved at the end of this state, since the instantaneous melting rate is a function of current and electrode preheating. The current Iarc_max is independent of the final short-circuiting current in state 3. The peak arc length for each arcing period is therefore expected to be more consistent across a wider set of operating conditions than could be achieved with a CV power source, provided the electrode preheating does not rapidly change. This caveat is discussed in detail in Chapters 6 and 7.

During state 6, the current is linearly reduced to steady state value Iarc_min at the specified ramping rate Iarc_ramp (A/ms). This state is terminated when Iarc_min is reached, or a short-circuit occurs. Again, the latter is a fault condition which occurs if Iarc_max is set too low. The "premature" short circuit occurs at high current, which generates excessive ball repulsion spatter as described in Chapter 2. If no fault occurs, the duration of state 6 is determined by Iarc_max and Iarc_ramp.

State 1 is the steady state arcing period, where the current is kept constant at Iarc_min. In almost all welding conditions it is the state with the longest duration. During this state there is significant droplet growth and greatest heat input to the workpiece. It can be expected that increasing Iarc_min will significantly increase droplet size, reduce dipping frequency, and measurably increase workpiece fusion area. These aspects of process behaviour are experimentally determined in Chapter 10. As for states 3 and 4, the duration of this state is determined by the process' behaviour. State 1 ends when the growing droplet makes contact with the weld pool, so that the voltage drops below threshold V_{sc}. The current Iarc_min is constant and independent of the arcing voltage, so the rate of droplet formation is not affected by arcing conditions, as would be the case for the CV process. Consequently, the "open loop" scheme is expected to produce a stable welding condition over a wider set of operating conditions.

Although the current and voltage waveforms in Figure 5.2 show the main features as described above, the scaling of the horizontal (time) axis has been slightly exaggerated for illustrative purposes. Actual current and voltage waveforms for a weld performed using 0.9mm mild steel electrode to AWS A5.18 ER70S-6 specification and Ar-23%CO_2 shielding gas are shown in Figure 5.3. The wire feed speed is 5.70 m/min, and the welding travel speed is 390 mm/min. The CTWD is 16mm, Iarc_max is 200A, Iarc_min is 70A, Isc_ramp is 100 A/ms, and Iarc_ramp is 150 A/ms. It is evident from Figure 5.2 that the duration of state 1 is the longest.

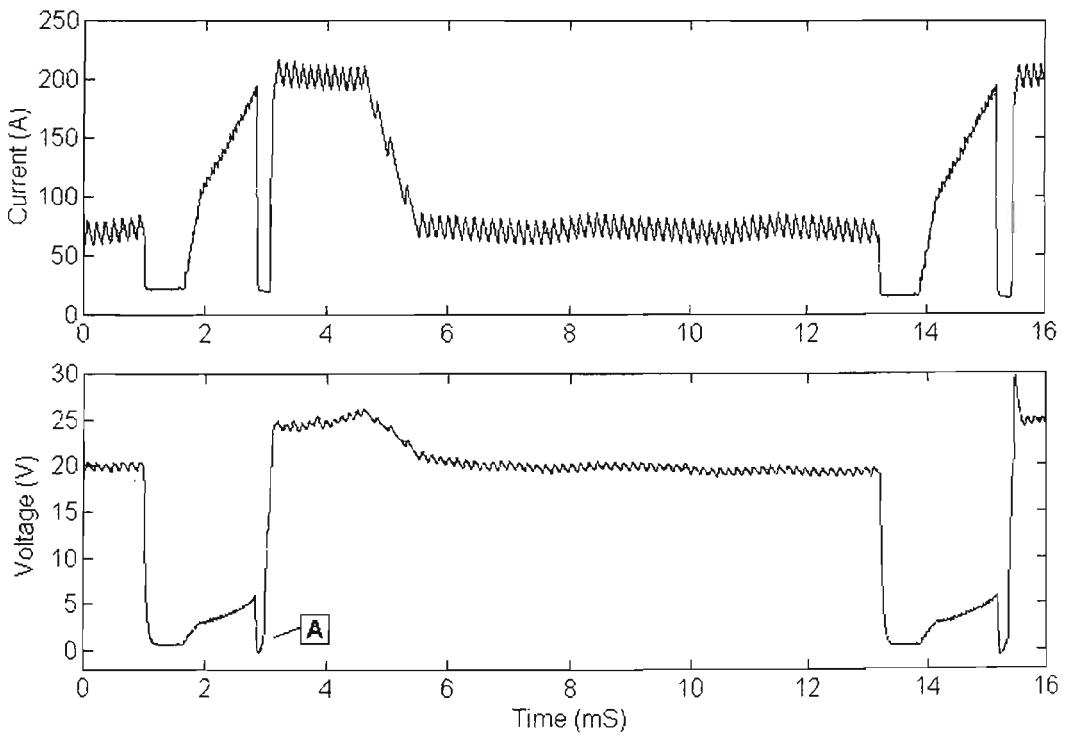

Figure 5.3 Typical waveforms for "open loop" control

The events surrounding a successful short-circuit premonition (labelled "A") are clearly visible. After the main current is rapidly turned off by the premonition unit, the voltage is reduced for a short time before the rupture occurs at 20A. The main current is reapplied by the controller only after the 12V arcing threshold is exceeded.

Further scrutiny of Figure 5.3 also shows other features of the experimental power source described in Chapter 4. During the short-circuiting period, the ripple in the current waveform is one third that of the arcing period. This ensures reduced ripple in the voltage signal for reliable rupture premonition. The current recovery after the short circuit is very rapid due to the internal energy storage ability of the power source. The low-frequency ripple of approximately 2.5ms period that is evident in the steady state arcing current waveform is a result of the hysteresis in the background current controller: The background current ripple is superimposed onto the main current waveform.

The various current settings, voltage thresholds and specified times are communicated to the DSP controller by a PC-based interface which may be programmed to suit the required control strategy. A typical user interface screen is shown in Figure 5.4.

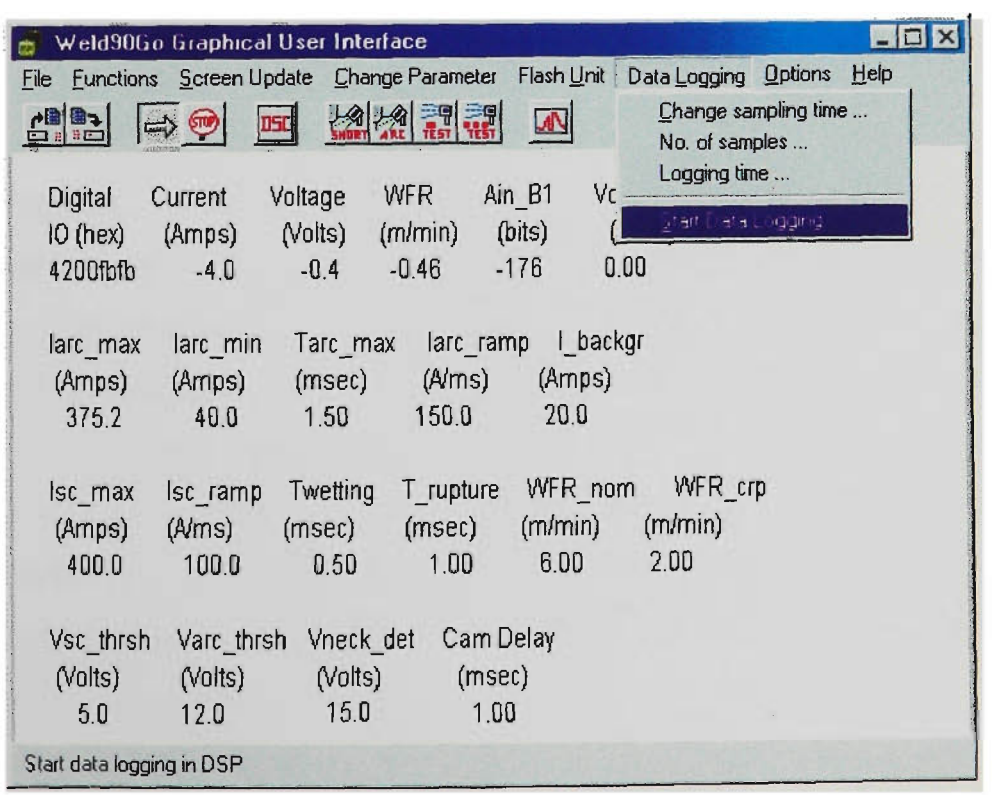

Figure 5.4 Typical user interface screen

The control strategy described in this section is considered to be "open loop" because no attempt is made to directly control any key parameter of the process, such as mean current, weld cycle frequency, or mean voltage. While certain control parameters strongly influence certain process parameters (e.g. Iarc_max determines peak arc length), no attempt is made to regulate these in a closed loop system so that the effects of disturbances are minimised (e.g. peak arc length is determined by Iarc_max but is affected by electrode stickout and preheating). With the exception of short-circuit premonition, the process control technique described in this section responds to events in the process after they occur, and the response is the same for each weld cycle. Despite this, the "open loop" control method is capable of producing excellent welds over a wide operating range. A detailed evaluation of the performance of this method is given in Chapter 10.

5.4 The Current Controlled "Closed Loop" Process

The "closed loop" control scheme described in this section is designed to regulate the size of the droplet formed at the end of the electrode on a cycle-by-cycle basis. To do this, the electrode melting rate is modelled within the controller. The instantaneous droplet size is calculated to be the integral of the electrode melting rate during the arcing period. When the desired droplet size is reached, further growth of the droplet is limited by reducing the arcing current from its steady-state value Iarc_min to a low, fixed value of 30A. This reduction in current hastens the onset of the next short circuit, since the melting rate is greatly reduced and pool depression force is also less.

One objective of this control scheme is to improve process stability. Process stability is often assessed from the degree of variation of the weld cycle time [23, 43, 44, 45]. Using this criterion, the duration of each weld cycle is identical in a maximally stable weld. If the wire feed speed is constant, the amount of metal transferred from electrode to weld pool per weld cycle should also be identical. If this was not the case, variations in arc length would exist from cycle to cycle, which would not be conducive to stable transfer. By actively regulating the growth of the droplet during each arcing period, it is anticipated that process regularity can be improved over that achieved by the "open loop" control scheme.

Another objective of the "closed loop" control scheme is to reduce spatter to lower levels than those achieved by the "open loop" method. As previously discussed, the use of a premonition circuit to reduce the current during short-circuit rupture is

expected to eliminate almost all of the fine spatter generated at the end of the short circuit. However, in the "open loop" scheme, the mechanism which produces ball-repulsion spatter remains. At the start of the short circuit, the current Iarc_min can still be high enough to promote repulsion. The "closed loop" scheme is designed to reduce the current to 30A prior to the short circuit, so that the likelihood of repulsion is minimised.

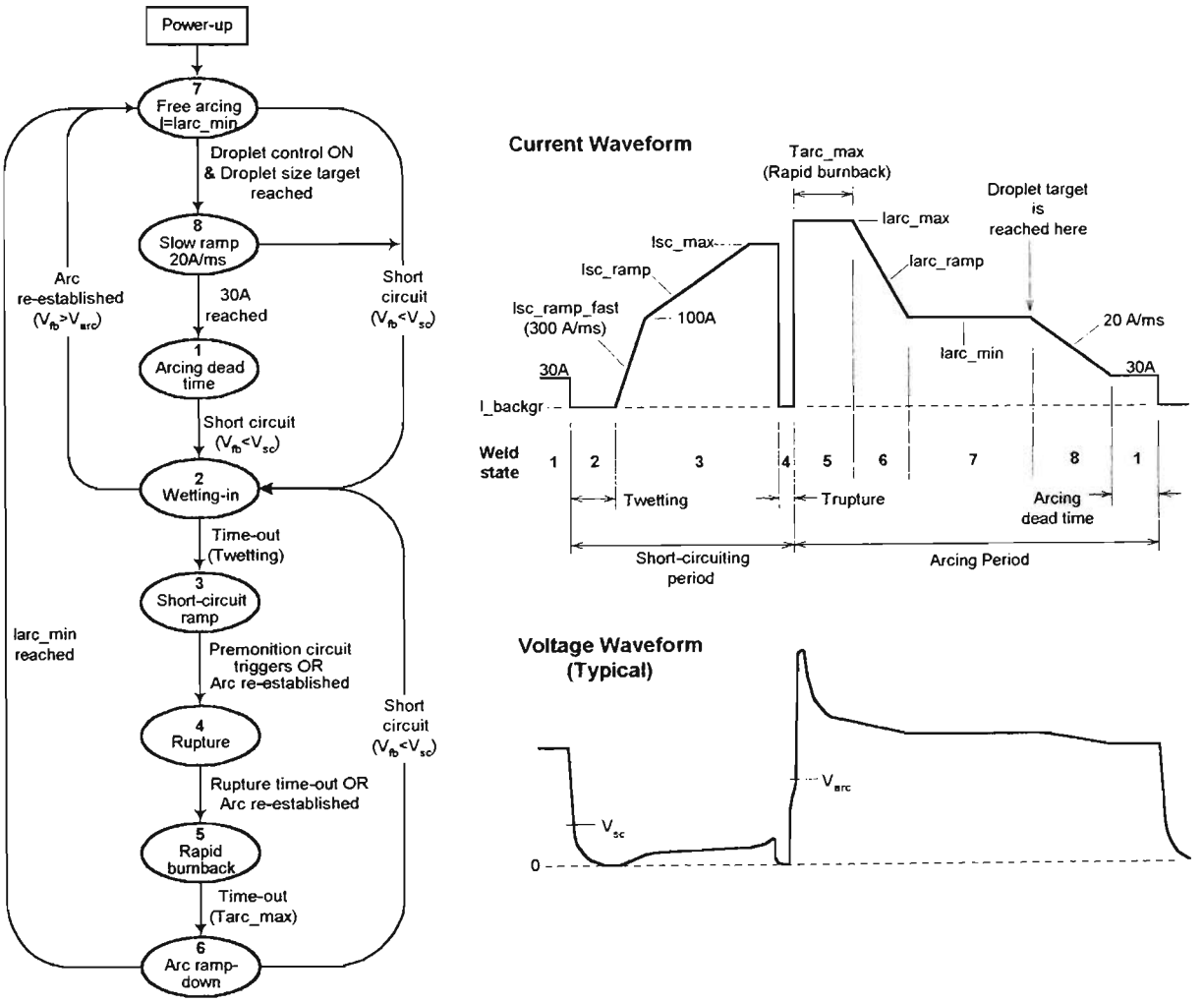

Figure 5.5 State diagram & waveforms for "closed loop" control

The state diagram and waveforms for the "closed loop" process are shown in Figure 5.5. Comparison with Figure 5.2 shows that states 2 to 6 are identical, and the changes involve the final part of the arcing period. The steady state arcing current Iarc_min is maintained in state 7 until the droplet size target is reached. The current is then reduced in state 8 at a fixed rate to the minimum of 30A, whereupon state 1 is entered. The duration of state 1 is referred to as the "arcing dead time", because the current is too low to promote significant electrode melting or workpiece heating. An ideal condition exists when the arcing dead time is minimised, since the loss of workpiece heating could be minimised, and the current at the start of the short circuit is low enough to avoid spatter production. However, achieving this involves precise

selection of the droplet target to suit the welding conditions, which may alter significantly simply by changing one parameter such as the CTWD or Iarc_min. The effects of parameters on the achievable droplet size is discussed in Chapter 10. The selection of an appropriate droplet target is detailed in Chapter 11.

Inspection and consideration of the current waveform may raise the question: Why ramp the current in state 8 at a such a slow rate, and why not reduce the current in state 1 to 20A or less? During preliminary testing of the "closed loop" control scheme, the main current was completely turned off at the end of state 7, so that only the background current remained in state 1. Two detrimental effects were observed. Firstly, the process is extremely sensitive to the selection of a suitable droplet size target. If the target is too large, the short circuit occurs at Iarc_min, so the benefit of reduced spatter is lost. If the target is too low by as little as 2.5%, the arcing dead time would be unacceptably extended to 5ms or more, resulting in a significant loss of workpiece heating. This could be clearly seen by visually comparing the width and height of the weld bead to that produced by the "open loop" control scheme using the same parameters. Unrealistically small changes in the droplet size target could alter the behaviour of the process in this way. Secondly, the abrupt removal of main current tends to initiate weld pool oscillations, which remain undamped at currents below 25 to 30A. This effect is particularly pronounced when using CO_2 shielding gas, and is described further in Chapter 10. The presence of weld pool oscillations can be seen in oscillations of the welding voltage (Figure 10.99, page 10-39). The presence of weld pool oscillations strongly affects the timing of the short circuit, so that any attempts made to regularise the weld cycle duration by droplet control are negated by the unpredictable timing of the next short circuit. To avoid these problems, the current is ramped at 20A/ms in state 8 to avoid pool disturbance and also to provide additional heat input. The current in state 1 is kept at 30A to minimise oscillations in CO_2 shielding gas.

Actual current and voltage waveforms for a weld performed using 0.9mm mild steel electrode to AWS A5.18 ER70S-6 specification and Ar-23%CO_2 shielding gas are shown in Figure 5.6. The conditions are the same as those for Figure 5.3.

To determine the instantaneous droplet size during the arcing period, an estimate is made of the instantaneous electrode melting rate by the welding controller during every sampling period. The development of this model is described in Chapter 7. The electrode melting rate is significantly affected by the stickout length, which is equal to

the CTWD during the short-circuiting period. A method of estimating the CTWD by using the voltage and current feedback signals is the subject of Chapter 6.

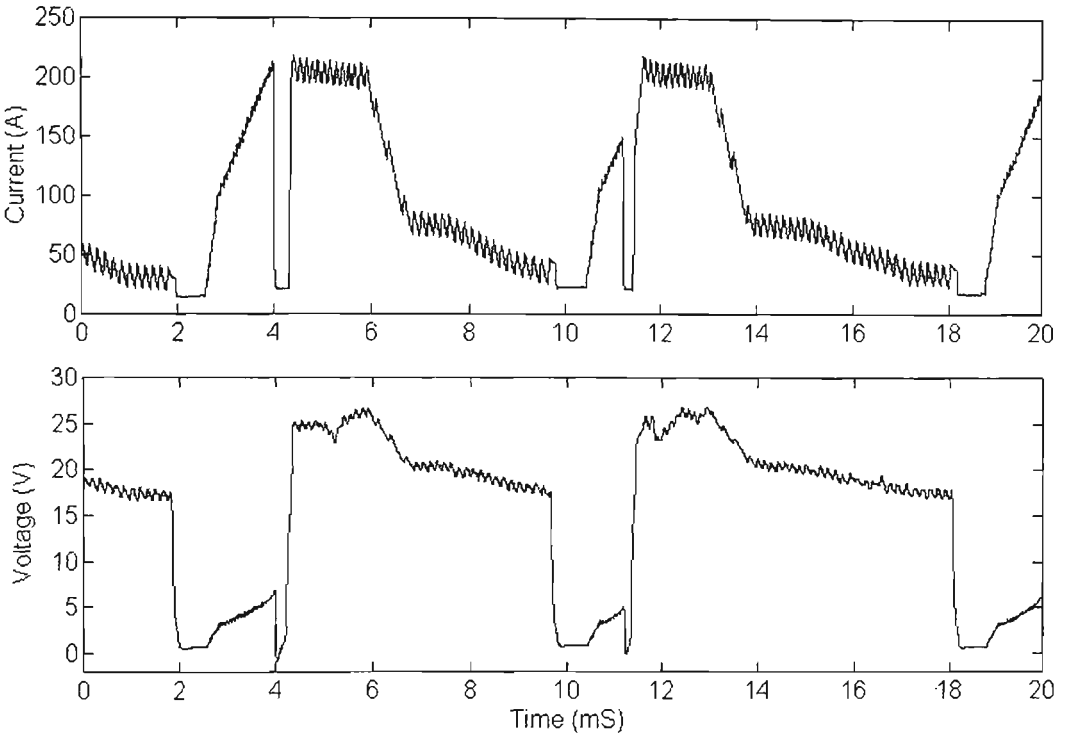

Figure 5.6 Typical waveforms for "closed loop" control

5.5 Summary

This chapter has described a number of process control techniques which have been implemented through the DSP-based welding controller. The first of these emulates the conventional constant voltage (CV) power source. The flexibility of the power source controller allows for any number of circuit topologies to be emulated, and the value of the components within such circuits can also be altered at any time during the welding process, so that performance can be optimised. Although there is tremendous scope for research using such methods, these possibilities are not explored in this project. It is believed that there are superior control methods which can deliver better performance. Unlike the CV process, these have not been widely investigated in the literature. The emulation of the CV process has been used as a means of testing the system, and to demonstrate the flexibility in control afforded by the experimental equipment which has been described in the previous chapter.

The control schemes investigated in this thesis are the "open loop" and "closed loop" current-controlled schemes described in sections 5.3 and 5.4, respectively. The operation of these has been covered in detail. The "open loop" method considers the welding process to occur in distinct states, and responds to each state in a repeatable,

predetermined way. The response (current) parameters are set by the operator to obtain a satisfactory welding condition. The expected benefits of this control method are stable operation over a wide range conditions, low spatter, and significant decoupling of key parameters such as peak arc length, fusion and metal transfer characteristics in the short-circuit.

The "closed loop" method proposes to regulate droplet size on a cycle-by-cycle basis by reducing the current during the arcing period when the desired size is reached. This approach is expected to further improve process regularity and reduce spatter produced at the start of the short-circuiting period.

The performance of these current controlled schemes will be assessed in subsequent chapters.

Chapter 6

Online Measurement of Contact Tip to Workpiece Distance

6.1 Scope

This chapter describes the development and implementation of a method of contact-tip-to workpiece-distance (CTWD) measurement that is suitable for the short-circuit transfer mode. The proposed method can be described as "through the arc sensing", as it uses the voltage and current feedback signals from the welding process. It measures the minimum resistance during the short circuit period, and uses this to estimate the CTWD after applying a correction factor for the duration of the short circuit. The effect of wire feed speed, actual CTWD and shielding gas on the correction factor is determined experimentally.

Sections 6.2 and 6.3 provide a brief summary of research that has been carried out in the area of CTWD estimation. Section 6.4 uses computer modelling of electrode resistance changes for complex non-constant welding current waveforms to predict the relationship between resistance and CTWD under varying conditions. In particular, the instantaneous resistance changes for waveforms with variable period are analysed. Section 6.5 describes the experimental results from which the relationships between CTWD and minimum short circuit resistance are determined, and also the corrections which need to be applied to obtain consistent results for varying short circuit duration. The agreement (or otherwise) between experimental and simulation results is discussed. A photographic investigation of the short-circuiting phenomena is also documented. Section 6.6 evaluates the performance of the estimation technique implemented in the real-time welding controller.

6.2 Background

A large effort has been applied to finding a method of measuring the CTWD during a weld by using only the voltage and current feedback signals. These signals are readily available and not prone to failure, as are mechanical contact sensors or optical sensors. The methods that have been developed fall broadly into three categories.

The first category, as exemplified by [46, 47], model the CTWD as a function of other key operating conditions or variables such as wire feed speed, mean current, and

mean voltage. The CTWD is related to particular combinations of these variables by regression constants. Experiments are performed using a particular CV power source to collect a sufficient number of data points, and then the regression constants are solved for a "best fit". Work presented in [46, 47] shows that this approach works well for conventional CV power sources. The main limitation of this method is that the regression constants will change depending on the power source characteristics (mainly slope), electrode type and shielding gas. Experiments need to be repeated when a major system component is altered. This method is also well suited to open arc processes, particularly spray transfer, where arcing conditions are constant.

The second category [48, 49, 50, 51] involves extensive use of physical relationships to model key components of the process such as the power source dynamics, arcing voltage and melting rate. The conventional CV power source equation is:

$$V_{oc} = I(R_S + R_C) + V_{arc} + M\frac{dI}{dt} \tag{6.1}$$

where V_{oc} is the open circuit voltage, R_S and R_C are source and cable resistances, M is the power source inductance. The arc voltage is described by Ayrton's relationship [52]:

$$V_{arc} = K_1 L_a + K_2 + (K_3 L_a + K_4) I \tag{6.2}$$

where L_a is the arc length, and constants K_1 to K_4 define the arcing characteristics of the shielding gas. The melting rate is modelled by Halmoy's linearised model [53]:

$$v = \frac{1}{H_m + b}\left(\varphi j + \rho_L L_e j^2\right) \tag{6.3}$$

where H_m, b and ρ_L are constants, and j is the current density in the electrode. It should be noted that use of equation 6.3 for the short-circuit transfer mode is fraught with error, and this is discussed in detail later in this chapter and also in Chapter 7.

Finally, the CTWD is given by:

$$CTWD = L_e + L_a \tag{6.4}$$

These equations can be used to derive a complex expression for CTWD in terms of the other parameters. The major drawbacks of this method are that a large number of constants must be known, and that an error in the values of the constants will affect the final CTWD estimate. This disadvantage can be mitigated if the "constants" are treated as variable and the system of equations is solved in real time during the weld [54, 55].

Errors may then be limited by the validity of assumptions that are implied in equations 6.1 to 6.3.

It was found that the method outlined above can give good results with open arc processes, including pulse spray transfer, but application in the short circuit transfer mode is limited [56, 57]. Assumptions concerning the melting rate relationship of equation 6.3 are no longer valid for low wire feed rates and low mean currents.

The third category of CTWD estimation techniques is particularly suited to the short-circuit transfer mode as it involves the use of short circuit resistance measurements. This is eminently sensible, as it removes possible error sources from melting rate estimates and arc characteristics as modelled in equations 6.3 and 6.2, respectively. Work presented in [58, 59, 60] indicates that a reliable and consistent estimate of CTWD can be obtained using short circuit resistance, and that the sampling rate of such a system is equal to the weld cycle frequency. Of this work, [60] is the most recent and detailed. It is considered to be the most relevant since it closely investigates and exploits the welding process' behaviour during the short circuiting period. There are clear physical explanations for all of the observed phenomena. Its findings are summarised in the next section, as these form the basis of the work described later in this chapter.

6.3 Summary of Recent Work in CTWD Estimation

This section is a summary of the findings in [60]. Figure 6.1 shows the welding torch to workpiece geometry. During the arcing period, a droplet of length L_d forms at the end of the electrode. During the short circuit, a molten metal bridge of similar length is formed between the end of electrode stickout and the weld pool. The CTWD, or L, is the sum of the solid wire length L_S and the liquid drop length L_d. Variations in L_d can be expected between short circuits, since the arcing period varies and thus affects the size of the droplet formed.

During the short circuiting period, the instantaneously calculated resistance varies in a typically U-shaped curve as shown in Figure 6.2. Six short-circuits of similar duration are represented, with the short-circuiting time normalised to a dimensionless 0-100%. The minimum value R_{smin} during each short is very similar, although it may not occur for all shorts at the same time relative to duration. The measurement of R_{smin} during a number of welds at various values of CTWD produces the graphs of Figure

6.3. Plotting these values against CTWD shows that R_{smin} is linearly related to CTWD within acceptable error bands (Figure 6.4).

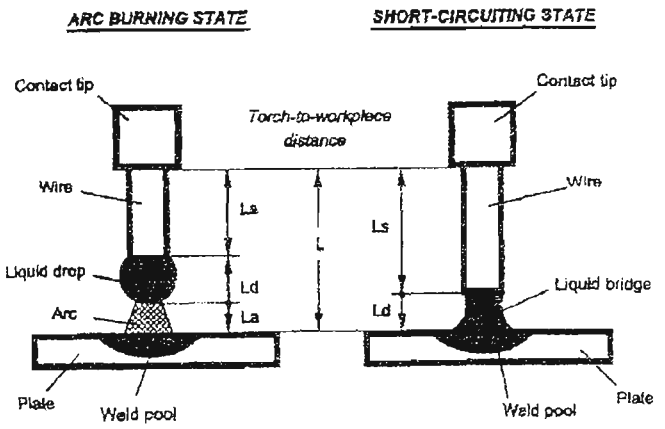

Figure 6.1 Torch to workpiece configuration [60]

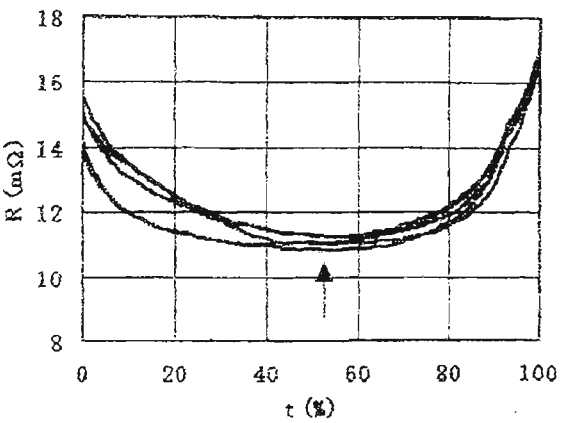

Figure 6.2 Resistance waveform in short circuit state [60]

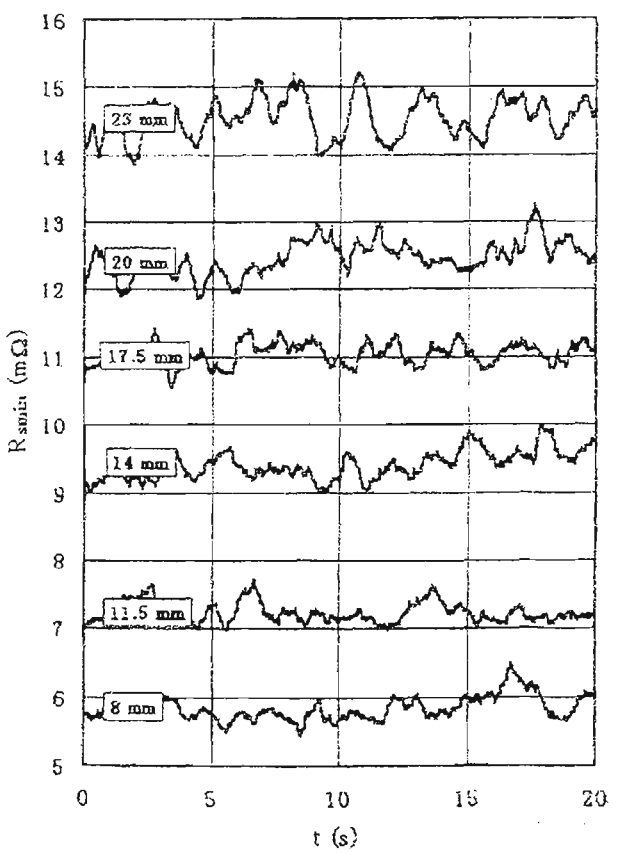

Waveform of sensor output at various torch-to-workpiece distances
(I=165A, U=20V, L=8-23mm, v_d=4m/min, MS wire, Ø1.2 mm, CP mode, K_I=60kA/s)

Figure 6.3 R_{smin} variation for various CTWD [60]

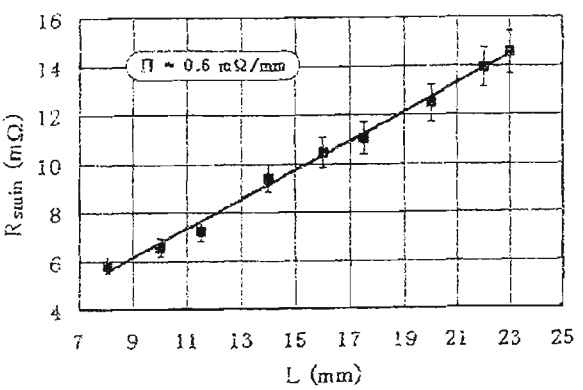

Sensor output vs. torch-to-workpiece distance
(I=165A, U=20V, L=8-23mm, v_d=4m/min, MS wire, Ø1.2 mm, CP mode, K_I=60kA/s)

Figure 6.4 R_{smin} versus CTWD [60]

The value of R_{smin} for a given value of CTWD is affected by the rate of rise of current K_I during the short circuit, shown in Figure 6.5. As K_I is increased, the

electromagnetic pinch force acting on the bridge are higher at any given time into the short circuit period. There is more metal transferred to the pool before the drop-pool contact reaches its maximum, so the maximum area of this contact is reduced and the resistance is higher. For a conventional CV power source, the rate of rise of current during the short circuit is affected by the open-circuit voltage setting. In the current-controlled method described in chapter 5, K_I is constant at 100 A/ms, or 100kA/s under all conditions. This eliminates this source of resistance variation.

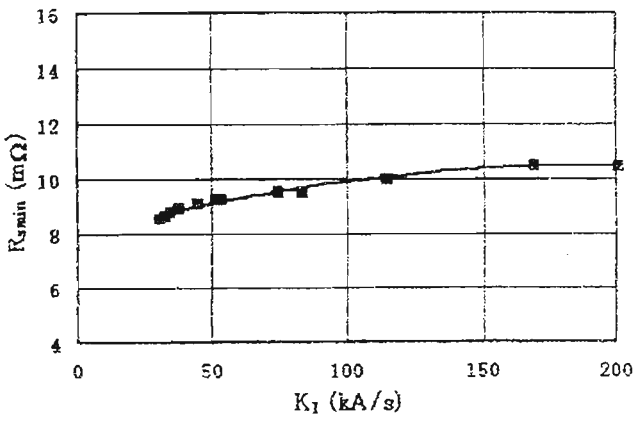

The sensor output (R_{smin}) vs. current slope (K_I)
(I=175A, U=20.5V, L=14mm, v_d=5.2m/min, MS wire, Ø1.2 mm, CP mode, K_I=31-200kA/s)

Figure 6.5 R_{smin} vs. Current Slope K_I

[60]

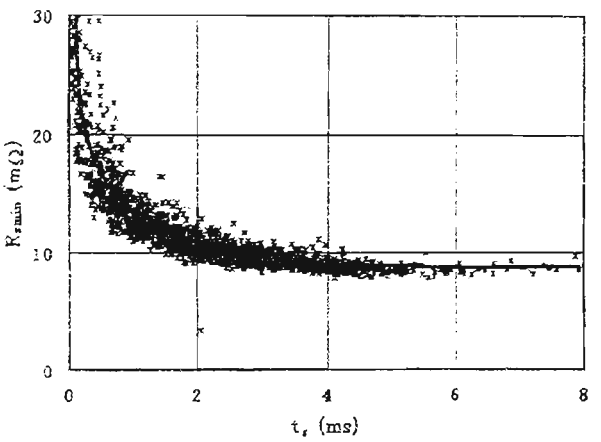

Sensor output (R_{smin}) vs. short-circuit duration (t_s)
(I=160A, U=20V, v_d=5.2m/min, L=14mm, MS wire Ø1.2 mm, CP mode, K_I=60kA/s)

Figure 6.6 R_{smin} vs. Short circuit duration

[60]

Figure 6.6 shows that R_{smin} is highly dependent on the short circuit duration t_s. This is attributed in [60] to small contact area and narrowed necking of the bridge. It is believed that variations in the droplet size formed during the arcing period are the actual cause of the changed bridge profile. No attempt is made in [60] to compensate for this effect. The high dependence on t_s can easily account for the ripple seen in Figure 6.3. Indeed, the weld would need to be exceptionally stable (small variation in t_s) for the ripple to be minimised.

6.4 Analysis and Simulation of CTWD Resistance Variation

6.4.1 Mechanisms for Resistance Variation

Consideration of the geometry shown in Figure 6.1 suggests several possible mechanisms which will influence the repeatability of the CTWD estimation based on resistance measurement. The first is the variation in L_d, depending on the size of the formed droplet. From experiments which are detailed in Chapter 10, the dipping frequency varied from 38 Hz to 110Hz at a wire feed speed of 5.7 m/min. This corresponds to average droplet lengths L_d of 1.45mm and 1.02mm, respectively, assuming a perfectly spherical droplet suspended from the end of the solid electrode. So if L in Figure 6.1 is constant, Ls is altered by approximately 0.4mm for a very large change in dipping frequency. This represents a 3.3% variation if L is 12mm.

A second mechanism for resistance variation is the change in liquid bridge profile as the size of the droplet changes during the welding process. This is identified in [60] and is believed to be responsible for the trend in Figure 6.6. For large droplets, the short circuit time is longer as more time is required to transfer the molten material from the bridge to the weld pool. The cross section of the bridge at the point of lowest resistance (Figure 6.2, arrow) is large. As droplet size reduces, the transfer time is reduced due to lower material volume, and the maximum bridge cross section is expected to be much smaller than that for a larger droplet. This is photographically verified in section 6.5.4. The results of Figure 6.6 indicate that the resistance of the liquid bridge can become higher than the resistance of the solid electrode for small droplet sizes. Compensation is made for this in section 6.5, using experimental results.

A third mechanism for resistance variation is attributable to variations in electrode preheating caused by the instantaneous changes in the welding current waveform. The waveform for a conventional CV power source is described in Chapter 2, while that for the current-controlled process is described in Chapter 5. The following section analyses this aspect in detail.

A further mechanism which may affect the measured resistance is variation in weld pool height due to oscillation. In Figure 6.1, pool oscillation affects L_d and consequently liquid bridge profile. The effect of oscillations is difficult to model because a large number of factors influence oscillation amplitude and frequency. Weld pool dimensions, surface tension and pool depression forces due to the initial arcing current Iarc_max are key factors. The effects of weld pool oscillation on the welding

process are detailed in Chapter 10. However, no modelling of pool oscillation is carried out in this thesis.

6.4.2 Modelling Resistance Variation due to Changes in Joule Heating

This section simulates the non-linear resistance ("Joule") heating of the solid electrode under the influence of a complex current waveform such as that described in Chapter 5. Of particular interest is the variation in the instantaneous resistance of the electrode stickout under ideal conditions. This will indicate whether the resistance method of CTWD estimation described in section 6.3 is susceptible to intrinsic and unavoidable variations. If so, this can be used to explain the variations in the waveforms of Figure 6.3, and also places a fundamental limit on the possible accuracy of such a CTWD estimation technique. Also, the dependence of electrode resistance on the RMS welding current is investigated.

According to [61, 62], the voltage drop across the electrode stickout is

$$V_L = j\int_0^L \rho(x)dx \tag{6.5}$$

where j is the current density in the electrode, L is the length of the solid electrode, and x is the distance along the axis of the electrode from the contact tip. Resistivity ρ is a function of the material temperature, or heat input (Figure 6.7). The electrode stickout resistance is

$$R_L = \frac{1}{A}\int_0^L \rho(x)dx \tag{6.6}$$

where A is the cross-sectional area of the electrode. In short-circuit GMA welding, the current varies during the transit time τ (the time taken for an electrode element dx to travel from the contact tip to the end of the electrode through distance L). The heat input applied to an electrode element dx varies as a function of the distance x and the time t_x when the element is in position x. To obtain $\rho(x,t_x)$, it is necessary to calculate $H(x,t_x)$ using Figure 6.8 to relate the history of current flow in the electrode to the heat input H. Figure 6.7 can then be used to find ρ. Once $\rho(x,t_x)$ is known, the integral in equation 6.6 can be evaluated to find R_L.

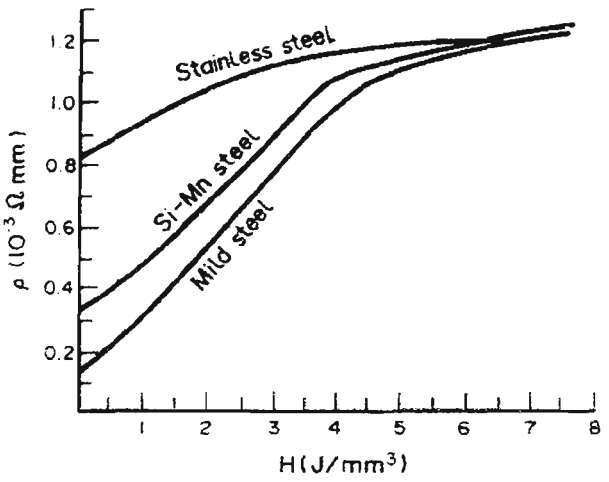

Figure 6.7 Resistivity vs. Heat Input (from [62])

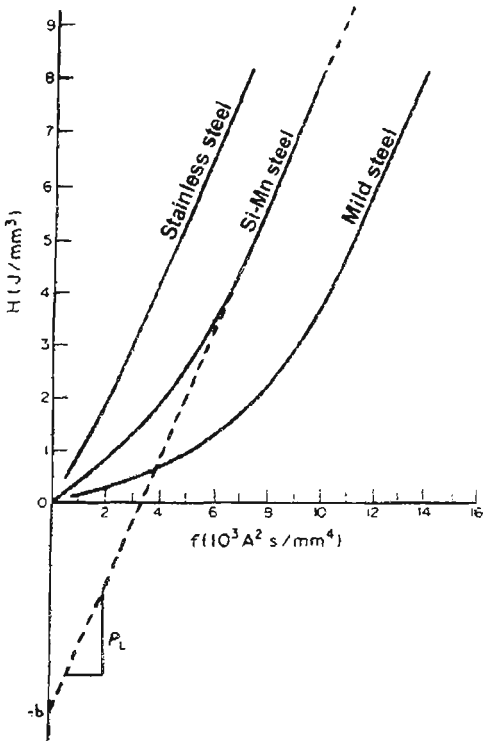

Figure 6.8 Heat input versus Action Integral (from [62])

The x-axis of Figure 6.8 is referred to as the action integral in [63]. It is the integral of the square of the current that has passed through an element of electrode during the time τ it has been in transit from the contact tip and along the stickout.

$$W(x,t) = \frac{1}{A^2} \int_{t-\frac{x}{v}}^{t} i^2(T)dT \tag{6.7}$$

Note that the transit time $\tau = x/v$ can apply to any point along the electrode. For simplicity, the wire feed speed v is assumed to be constant. The relationship of Figure 6.8 for Si-Mn steel is divided into linear and non-linear sections, delineated by the transition action W_T of 6500 A^2smm^{-4}.

$$H_L = 4.615\text{x}10^{-8}W^2 + 3.154\text{x}10^{-4}W \qquad \text{for } W \le 6500 \tag{6.8a}$$

$$H_L = 1.176\text{x}10^{-3}W - 3.647 \qquad \text{for } W > 6500 \tag{6.8b}$$

A more detailed description of the above is given in Chapter 7. It is worth noting that equation 6.3 for the average melting rate is derived by assuming that the end of the electrode operates at action integral values above W_T. It is shown in this chapter and also Chapter 7 that the short-circuit transfer mode often operates in the non-linear region of Figure 6.8.

To evaluate theoretical variations in electrode resistance under ideal conditions, computer simulations are performed incorporating the non-linear modelling of electrode material resistivity detailed above. The simulations were performed using programs

written in the "C" programming language. The current waveform is assumed to be perfectly periodic, with the form and values indicated in Figure 6.9. The mean and RMS values of such a waveform are 81A and 123A, which are reasonably representative of real welding conditions at 5.7 m/min wire feed speed and a CTWD of 20mm (section 6.5). With the assumed current waveform of Figure 6.9, the action integral and heat input are evaluated using equations 6.7 and 6.8, respectively. The relationship between resistivity and heat input is represented in a piecewise linear fashion with data points listed in Table 6.1. Linear interpolation is carried out between these defining points.

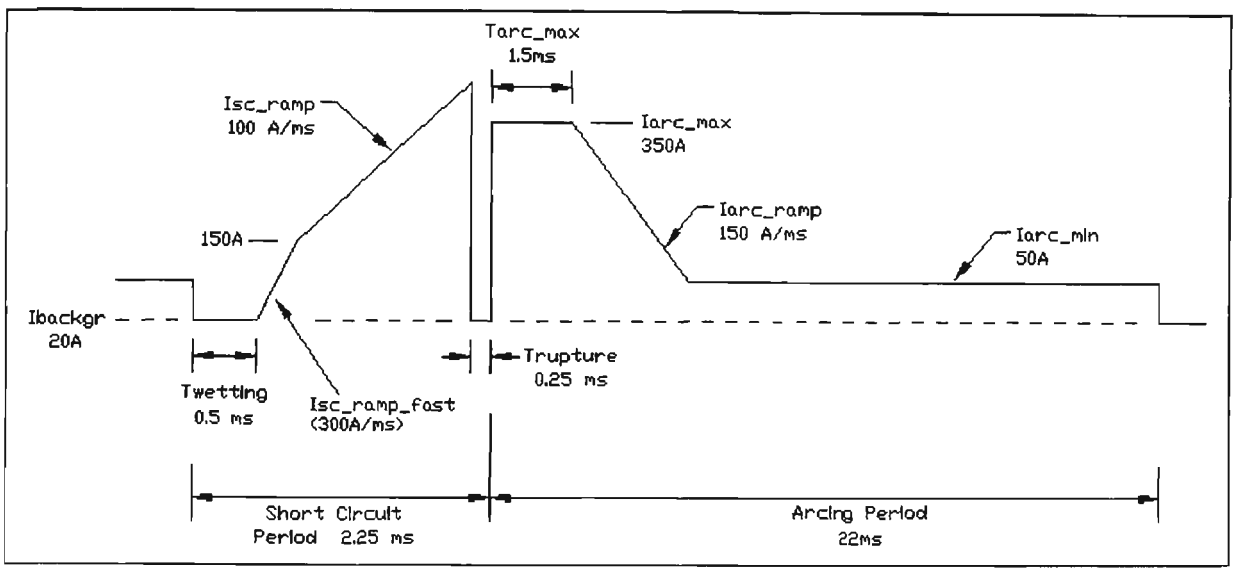

Figure 6.9 Simulation Current Waveform (Current vs Time)

Table 6.1 Defining Data points for ρ versus H

H (J/mm^3)	ρ (mΩ-mm)	H (J/mm^3)	ρ (mΩ-mm)	H (J/mm^3)	ρ (mΩ-mm)
0	0.33	3	0.90	6	1.20
1	0.47	4	1.09	7	1.23
2	0.68	5	1.16	8	1.26

Figure 6.10 in Appendix 6 shows the simulated value of $H_L(x,t_x)$ as it varies in time for a number of points along the electrode stickout, as calculated using equations 6.7 and 6.8. For the simulation calculations, the electrode stickout is divided into 20 elements of equal length. The total length is equal to the CTWD being simulated, in this case it is 20mm. It is evident that for electrode elements close to the contact tip, the action varies significantly with time. As the distance from the contact tip increases, the percentage variation decreases, and H_L can be considered essentially constant. The rises in $H_L(x,t_x)$ occur during the short-circuit and at the start of the arcing period when the current is high. The rises correspond to increases in ohmic heating due to the action of

the current on the entire length of the stickout. The drops in $H_L(x,t_x)$ can be attributed to the "loss" of material from the end of the stickout at x=L, when an old element of electrode has transited through the "measurement point" at x=L and is no longer relevant to the resistance calculation up to that point. The action due to the particular part of the current waveform which caused the increase in H_L occurred before t_x=τ, and is no longer a part of the history of action applied to the material which is presently between x=0 and x=L. The rises in $H_L(x,t_x)$ occur whenever the current increases, but drops in $H_L(x,t_x)$ are determined by the history of the current waveform and transit time τ. Since the current waveform is periodically uniform in these simulations, the drops in $H_L(x,t_x)$ occur at regular intervals. When the transit time is a multiple of the current period, the ripple in $H_L(x,t_x)$ may disappear entirely.

Figure 6.11 in Appendix 6 shows the variation in resistance along the electrode stickout, as calculated from $H_L(x,t_x)$ using equation 6.6 and Table 6.1. Again, as the distance from the contact tip increases, the resistance variation with time is less, when expressed as a percentage of the average value. Close inspection of the simulation waveforms in Figure 6.12 shows that during the short-circuiting period, the resistance does not vary from cycle to cycle. So if the resistance is sampled at approximately the middle of the short circuiting period as described in section 6.3, then the stickout resistance would be seen as constant from cycle to cycle, provided that the current waveform is periodic.

Figure 6.13 in Appendix 6 maps the calculated average stickout resistance as a function of the distance x along the stickout, assuming that the welding current waveform remains unchanged. Each curve represents the results using RMS current values measured in experiments described later in this chapter. As expected for a material whose resistivity varies with temperature, the resistance is not a linear function of L for a given RMS current. Prima facie, it would not seem possible to estimate CTWD linearly from the short-circuit resistance as described in section 6.3. However, in reality the welding current is altered as CTWD is changed, irrespective of the current parameters of the waveform in Figure 6.9. The arcing and short circuit times are affected by the requirements of the process (i.e. they are not set by the controller) and these alter the RMS and mean current values. The form of equation 6.7 is based on the RMS current value, which is by definition:

$$I_{RMS} = \sqrt{\frac{1}{t}\int_0^t i^2(T)dT} \qquad (6.9)$$

So it is the RMS welding current which is indicative of the electrode preheating, not the mean welding current. Figure 6.14 in Appendix 6 shows how the RMS welding current changes for various values of CTWD and wire feed rate. The data is obtained from experiments detailed in section 6.5. The RMS current is higher for low values of CTWD where the transit time is correspondingly low. The RMS current is also higher for higher wire feed speeds, where the transit time is inversely lower.

Combining the data in Figure 6.13 and 6.14, it can be seen that in real welding, the relationship between stickout resistance and CTWD will not be as non-linear as indicated in Figure 6.13. The increasing RMS current at low CTWDs will apply greater preheating to the electrode at a given distance from the contact tip, increasing the resistivity. The resistance of the shorter electrode stickout is consequently higher than the resistance of the same length of electrode considered as part of a longer stickout subjected to a lower RMS current.

Figure 6.15 summarises the results of a number of simulations where the mean electrode stickout resistance has been estimated for values of RMS currents and transit times which are the same as those in experiments (Figure 6.14).

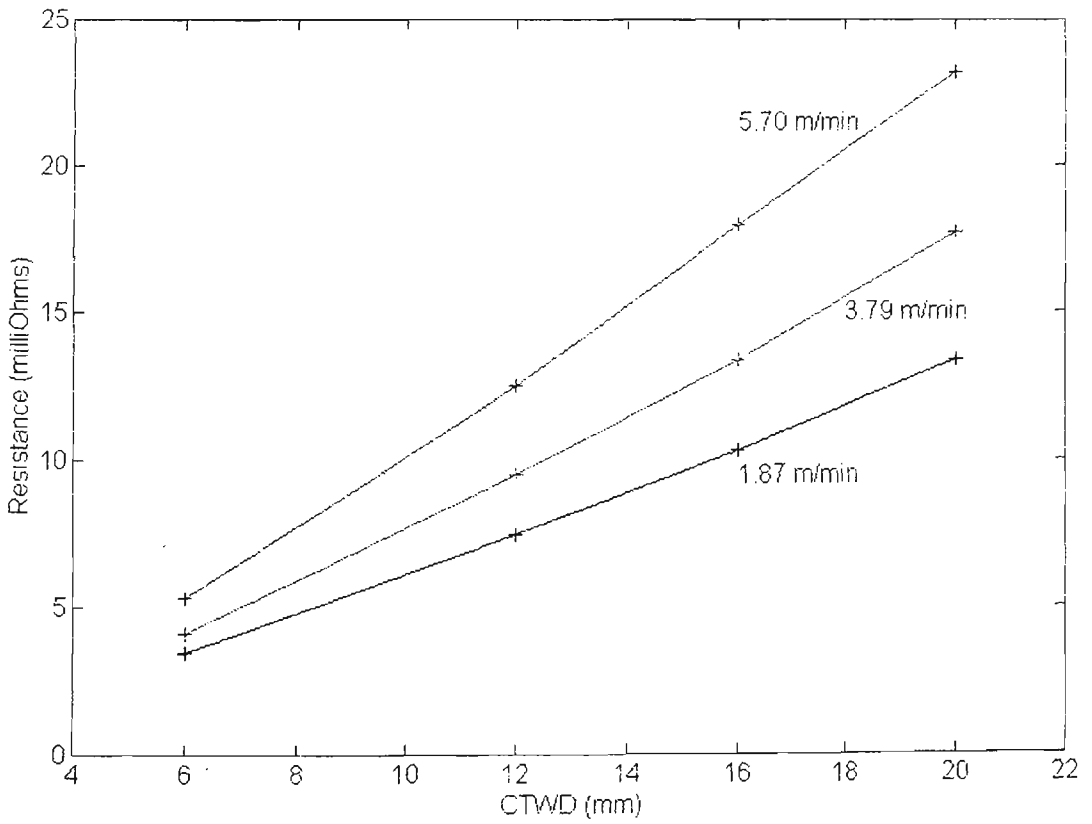

Figure 6.15 Calculated stickout resistance vs CTWD and wire feed speed

As expected, the relationship between stickout resistance and CTWD (x=L=CTWD) is much more linear than the results of Figure 6.13, particularly for higher wire feed speeds. So the inherent increase of RMS current as CTWD is reduced

in a real weld causes additional electrode ohmic heating, which linearises the relationship between stickout resistance and CTWD. This agrees with the results shown in section 6.3. The simulations have also shown that the ratio of stickout resistance to CTWD will change as the wire feed speed is altered.

The simulations so far have assumed a perfectly periodic current waveform, and the results have indicated that there is no variation in stickout resistance from cycle to cycle, when measured at the same point in the short-circuit period. Figure 6.16 in Appendix 6 shows the results of a simulation performed under the same conditions as that of Figures 6.10 and 6.11, except that the duration of the arcing and short-circuiting has been "randomised" by up to 25%. The calculations assume that x is 20mm. A random variation in arcing duration occurs in any type of short-circuit transfer GMAW [7, 43, 44, 45]. To make the conditions more realistic, the degree of randomisation of the short-circuiting period is made equal to the randomisation of the previous arcing period. Simulations and experiments by other researchers [8, 12, 17, 64] show that transfer time (short circuit duration) depends on droplet size (integral of melting rate during previous arcing period). Figure 6.16 shows that H_L at the electrode tip is relatively constant despite significant variations in the duration of arcing and short-circuiting periods. Experiments in Chapter 7 will verify that this occurs in real welds, provided that the weld is stable. But the variation in H_L is not consistent, so the electrode resistance also varies in an unpredictable manner. The signal R_{sample} in Figure 6.16 is produced by sampling the electrode resistance in the middle of the short-circuiting period, as described in section 6.3. It is evident that there is a significant (5%) variation in the electrode resistance with time when the arcing period duration varies by up to 25%.

In conclusion, calculations in this section have shown that there are a number of factors which cause the electrode stickout resistance to vary. It has been shown that under a non-constant but periodic current waveform, the resistance at any point along the stickout will vary in time, but if sampled at the same time during the short circuit period, the value will be constant. If the arcing period is varied, the stickout resistance, as sampled during the short-circuiting period, will also show variation due to the changing action applied during the transit time. This explains the variation in electrode resistance seen by [60] in Figure 6.3, even though the CTWD remains constant. It has also been shown that the resistance varies non-linearly along the stickout for a given RMS current, due to large changes in resistivity of the electrode material with

temperature (Figure 6.7). However, as the CTWD is reduced in practice, the RMS current increases and tends to linearise the relationship between stickout resistance and CTWD, particularly for higher currents (Figure 6.15). The relationship between stickout resistance and CTWD is expected to alter with wire feed speed. At low wire feed speeds, the RMS current is much lower. Even though the transit time is higher, the total action applied to the electrode is lower, so the resistance per unit length is reduced.

Another factor which will influence the stickout resistance is the value of the RMS current. As shown in Figure 6.14, the RMS current for a given CTWD and wire feed speed varies within a range of values as indicated by the error bars, depending on the parameters such as Iarc_max, Iarc_min and Tarc_max. This is covered in more detail in Chapters 10 and 11. The inherent variation of RMS current for a given CTWD will inevitably affect the mean value of electrode resistance.

In this analysis, the effects on resistance of the molten droplet and weld pool have not been taken into account. The experimental results presented in the next section will show these effects. The modelling has also not accounted for conduction of heat to the electrode from the molten droplet and the arc. Some researchers [66, 67] have done this and claim more accurate results. Conduction effects may be more pronounced at low wire feed speeds, where there is sufficient time during the transit time for the conduction to occur.

6.5 Experimental Investigations

6.5.1 Scope

This section documents experiments carried out to assess the ability to estimate the CTWD via the short circuit resistance under a wide range of operating conditions, using the "open loop" current control method described in Chapter 5. Compensation is used to account for the effects of variable short circuit duration. The linearity of the compensated minimum short circuit resistance as a function of CTWD is investigated.

6.5.2 Methodology

A number of welds were performed using different CTWD, wire feed rate, shielding gas, and current waveform parameters, as listed in Tables 6.1 to 6.4 in Appendix 6. The tests were arranged into four groups: Ar-23%CO_2 shielding gas at 5.70 m/min wire feed speed, CO_2 at 5.70 m/min, Ar-23%CO_2 at 3.79 m/min, and Ar-23%CO_2 at 1.87 m/min wire feed speed. In all cases, the electrode was 0.9mm diameter

mild steel conforming to ER70S-6 AWS specification, and the travel speed was 390 mm/min. During each weld, the current and voltage waveforms were recorded for 3.0 seconds at a sampling rate of 20kHz using a 12 bit digital storage oscilloscope. The current was measured using a closed loop Hall effect sensor with a response time of 1μs. The positive voltage was measured at the torch cable connection to the wire feeder, as shown in Figure 6.17. The negative voltage was measured at the welding table to which the workpiece is firmly clamped. The differential voltage signal was filtered using a single pole filter with a 40 μs time constant, to reduce switching ripple in the signal. The equivalent resistive circuit during the short circuit, also shown in Figure 6.17, has a large number of components. By placing the contact tip firmly against a clamped workpiece and applying a large pulsed current of low duty cycle (with no electrode being fed), the total resistance of components R5 to R9 was measured at 0.23mΩ, which is inconsequential.

From the voltage and current recordings, the instantaneous resistance during each short circuit was evaluated off-line. The minimum resistance during each short circuit R_{smin} was noted, along with the "active" duration of the short circuit T_{sc}. Figure 6.18 shows typical waveforms for a single short-circuiting event. For brevity, the arcing period waveforms have been removed. For the purposes of correlation, T_{sc} was measured as the time between when the current rises above 50A and when the current falls back below 50A. Thus the wetting-in time and the rupture time are excluded. T_{sc} represents the time during which a significant Lorentz (electromagnetic pinch) force is active on the short-circuit bridge.

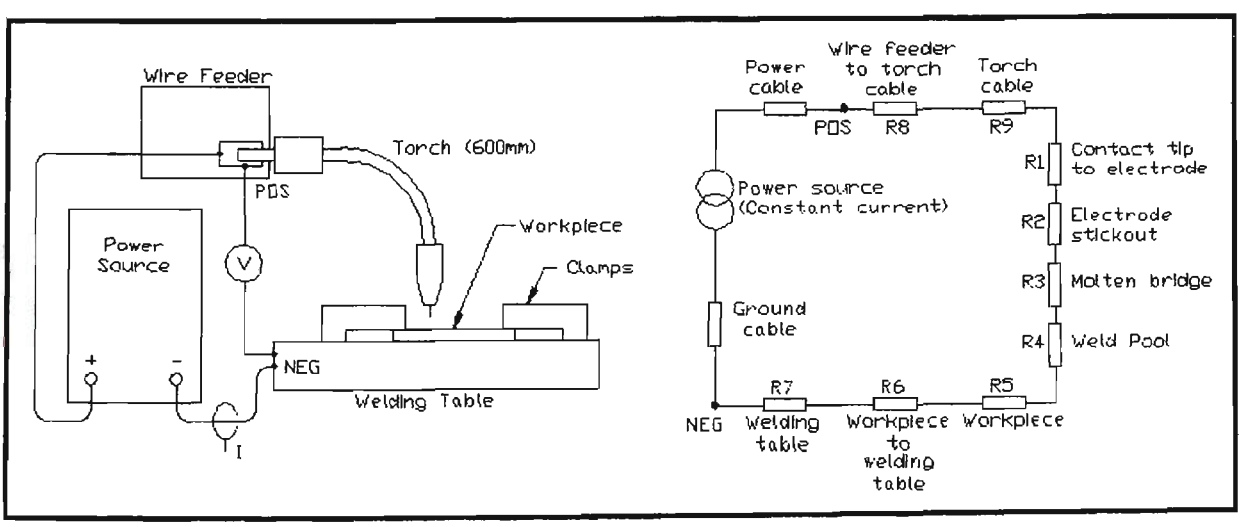

Figure 6.17 Current & Voltage measurement , and Equivalent circuit

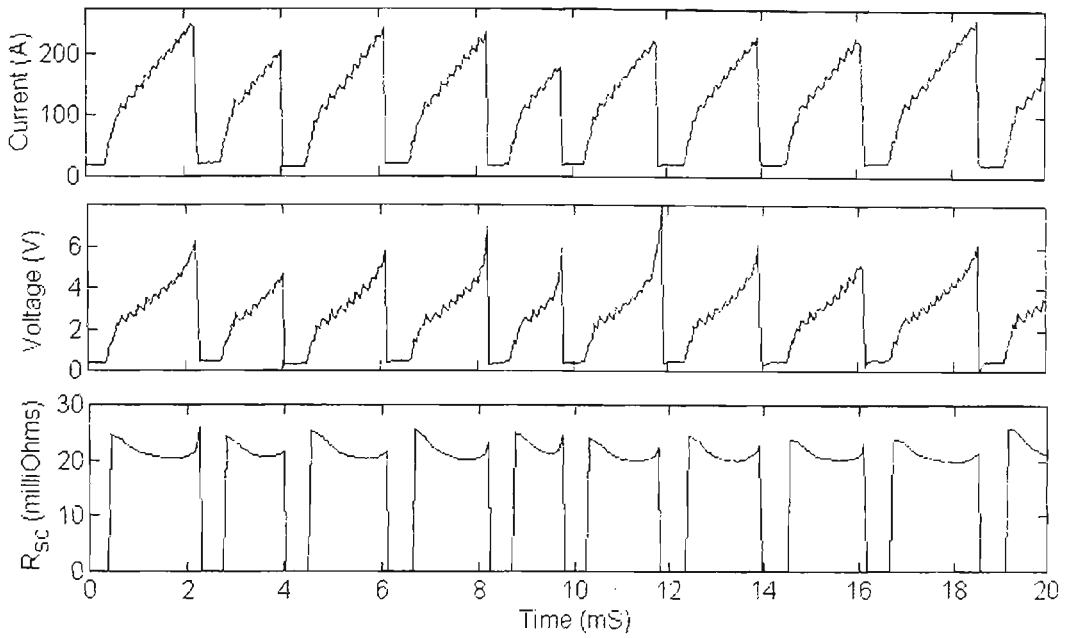

Figure 6.18 Typical current, voltage and short circuit resistance waveforms

The following subsection describes the correlation between R_{smin} and T_{sc} for each of the test groups.

6.5.3 Test Results and Analysis of Results

The relationship between R_{smin} and T_{sc} for the case of Ar-23%CO_2 shielding gas and 5.70 m/min wire feed speed is shown in Figure 6.19 in Appendix 6. The current waveform parameters, listed in Table 6.1, are varied over a reasonably wide range. This ensures that the dipping frequency and hence droplet size varies significantly for each value of CTWD tested. The results in Figure 6.19 show that there is a significant increase in R_{smin} for T_{sc} below 2ms. These results agree well with those of Figure 6.6 from [60]. The physical interpretation is that the resistance of a narrow short-circuit bridge is higher, and this corresponds to a smaller droplet which requires less time for metal transfer to the weld pool. This is investigated further in section 6.5.4. These results also show that a CTWD estimate based solely on R_{smin} will contain large errors and signal swings where there are large changes in T_{sc}. This is particularly evident for a CTWD of 6mm. The errors would be less noticeable for larger values of CTWD, where the process is more stable and produces tighter groups of data points. It is evident that a correction for short circuit duration needs to be made.

Modelling of short-circuit metal transfer has been carried out by a number of researchers [12, 17, 64], but there is insufficient data in the public domain at this time to predict the relationship between transfer time and bridge resistance. Despite the lack of

theoretical predictions in this area, the data in Figure 6.19 indicate that a suitable curve of best fit is of the form:

$$R_{s\min} = \frac{C_t}{T_{sc}} + R_{corr} \qquad (6.10)$$

The term C_t is a correction factor for the transfer time T_{sc}, and has units of mΩ.ms in the above equation. The term R_{corr} is the corrected minimum short circuit resistance, and is the asymptote of equation 6.10 for large values of T_{sc}. Physically, it is the minimum possible short circuit resistance which would be obtained if the resistance of the bridge was either at a minimum (very large droplet and very wide bridge) or possibly not present at all.

Equation 6.10 was fitted using the least squares method to the data from each of the four test groups in Figure 6.19. Data points with T_{sc} below 0.25ms were ignored, since these are considered to be incipient shorts with unreliable characteristics. The best fit values of C_t and R_{corr} for each value of CTWD are listed in Table 6.6 in the left hand columns. The dotted lines in Figure 6.19 are the lines of best fit using these values. However, if a CTWD estimation algorithm is implemented in practice, the correction factor cannot be made a function of CTWD, since the CTWD is not known until the calculations are completed. One value of C_t must be used, so it is set to the average of those in Table 6.6, the average being 7.67.

Using the value of 7.67 for C_t, equation 6.10 was again fitted to the data points, yielding the value of R_{corr} shown in the right hand column of Table 6.6. The solid lines in Figure 6.19 are the resulting lines of best fit using the single value of Ct and the corresponding best-fit values of Rcorr. It can be seen that there is little difference between the two groups of lines.

Table 6.6 C_t and R_{corr} (Ar-23%CO_2, 5.70m/min wire feed speed)

Curve fitting to individual data groups			Fixed C_t (average value)		
CTWD (mm)	C_t (mΩ.mm)	R_{corr} (mΩ)	CTWD (mm)	C_t (mΩ.mm)	R_{corr} (mΩ)
20	7.22	24.68	20	7.67	24.41
16	8.70	18.05	16	7.67	18.70
12	8.05	13.78	12	7.67	14.13
6	6.70	7.85	6	7.67	7.14

Figure 6.20 in Appendix 6 shows the correction applied to the data in Figure 6.19 by using equation 6.10. The average value of the corrected data in each group is equal to the value of R_{corr} in the right hand column of Table 6.6. The correction "flattens

the data out", but for a given CTWD the short circuit resistance is distributed in a "cloud" rather than a flat line. This indicates that as the short circuit resistance data is processed in real time during a weld, the resultant signal will contain appreciable ripple as the resistance changes from short to short. This has already been observed in Figure 6.5 from [60], and appears to be unavoidable. From simulations in section 6.4, variations of +/- 0.5mΩ are expected at a CTWD of 20mm purely from variations in action applied to the electrode stickout. The experimental results show variations of 3 to 5 mΩ, indicating that the majority of variation is attributable to changes in the dynamic geometry of the bridge. Weld pool oscillation is expected to be a contributing factor. Chapter 10 discusses the effects of pool oscillation in more detail.

Figures 6.21 to 6.26 in Appendix 6 show the corresponding experimental data for the other three test cases (CO_2 at 5.70m/min wire feed speed, Ar-23%CO_2 at 3.78m/min, and Ar-23%CO_2 at 1.87m/min). Tables 6.7 to 6.9 list the derived values of C_t and R_{corr}. Figure 6.21 shows that a greater variation in R_{smin} exists for CO_2 than for the argon-based gas. A larger variation in the estimated CTWD can be expected when using carbon dioxide as the shielding gas. The differences between the dotted and solid equation lines in Figures 6.19, 6.21 and 6.23 are small, which means that only very small errors are introduced into the compensating function by assuming one value of Ct for each wire feed speed. However, Figure 6.25 shows that for very low wire feed speeds (1.87m/min), this approximation introduces more significant errors. The error is greatest for small CTWDs, where the shape of the data group in Figure 6.26 indicates that over-compensation is applied for short circuits with low T_{sc}.

Table 6.7 C_t and R_{corr} (CO_2, 5.70m/min wire feed speed)

Curve fitting to individual data groups			Fixed C_t (average value)		
CTWD (mm)	C_t (mΩ.mm)	R_{corr} (mΩ)	CTWD (mm)	C_t (mΩ.mm)	R_{corr} (mΩ)
20	6.16	23.98	20	6.21	23.95
16	7.03	19.30	16	6.21	19.89
12	6.28	14.73	12	6.21	14.78
6	5.39	8.66	6	6.21	8.12

Table 6.8 C_t and R_{corr} (Ar-23%CO_2, 3.79m/min wire feed speed)

Curve fitting to individual data groups			Fixed C_t (average value)		
CTWD (mm)	C_t (mΩ.mm)	R_{corr} (mΩ)	CTWD (mm)	C_t (mΩ.mm)	R_{corr} (mΩ)
20	9.87	24.16	20	8.69	25.10
16	8.15	19.94	16	8.69	19.51
12	9.25	13.54	12	8.69	13.98
6	7.50	9.35	6	8.69	8.48

Table 6.9 C_t and R_{corr} (Ar-23%CO_2, 1.87m/min wire feed speed)

Curve fitting to individual data groups			Fixed C_t (average value)		
CTWD (mm)	C_t (mΩ.mm)	R_{corr} (mΩ)	CTWD (mm)	C_t (mΩ.mm)	R_{corr} (mΩ)
20	16.10	21.06	20	11.43	24.14
16	14.15	16.32	16	11.43	18.12
12	9.18	14.51	12	11.43	12.98
6	6.31	9.29	6	11.43	5.64

There is a difference between the average value of C_t for the same wire feed speed but different shielding gases (Tables 6.6 and 6.7). This is not surprising, since the wetting-in time for the carbon dioxide tests is 1.5ms, compared to 0.5ms for the argon-based gas. Combined with the fact that shielding gas composition changes surface tension of the molten metal, it is surprising that the C_t values are so similar.

There is a significant change in the value of Ct as wire feed speed is altered. It appears that a greater degree of compensation for short-circuit duration needs to be applied as wire feed speed is reduced. Stated another way; for a given T_{sc}, the measured resistance R_{smin} is greater for a lower wire feed speed. No good explanation of this phenomenon can be offered at this time. Simulations [17] have shown that wire feed speed is an insignificant factor in metal transfer during the short circuit, since the velocity of the material being transferred is much greater than the wire feed speed. It is observed that the width of the weld bead is greatly reduced for lower wire feed speeds. At 5.7m/min, the bead width is 5-7mm, at 3.79m/min it is 4-5mm, and at 1.87m/min it is reduced to 2-3mm. The narrowing of weld pool width at low wire feed speeds may have two effects. Firstly, the pool resistance may increase sufficiently to start making a noticeable contribution to the total resistance, since the cross-sectional area of the molten material in the pool is less than 20% of that at 5.70m/min. Secondly, the volume of the molten weld pool is perhaps 10% of that at 5.70 m/min. This may affect the amount of material transferred during the wetting-in period, where there are no major electromagnetic pinch forces at work, and the transfer is dominated by surface tension. The remainder of the droplet is transferred during T_{sc}, but the altered transfer conditions during the wetting-in time will have altered the relationship between R_{smin} and T_{sc} in the same way that it would with a change of $T_{wetting}$ or shielding gas composition. Modelling in [12, 17, 64] assumes an unbounded or infinite weld pool, so these effects, if significant, are not considered.

The relationship between the average corrected short-circuit resistance and the CTWD is shown in Figures 6.27 to 6.30 in Appendix 6. The error bars in these figures

indicate the data point scatter one standard deviation either side of the average. In a normal distribution with moderate skew, this represents approximately 70% of the data. Equations 6.11 and 6.12 were fitted to the data points using a least squares approach. The values of a, b and s are listed in Table 6.10.

$$R_{corr} = a.CTWD + b \tag{6.11}$$

$$R_{corr} = s.CTWD \tag{6.12}$$

Table 6.10 Corrected resistance to CTWD relationship constants

Shielding Gas	Wire feed speed (m/min)	a (mΩ/mm)	b (mΩ)	s (mΩ/mm)
Ar-23%CO_2	5.70	1.22	-0.45	1.19
Ar-23%CO_2	3.79	1.19	0.70	1.24
Ar-23%CO_2	1.87	1.32	-2.53	1.15
CO_2	5.70	1.14	1.25	1.22

Figures 6.27 to 6.30 show that, with the exception of 1.87m/min wire feed speed, the use of equation 6.12 gives a valid approximation for the relationship between the corrected resistance and CTWD. It is interesting to note that the ratio of resistance to CTWD is almost constant not only for all values of CTWD at a given wire feed speed, but is almost unchanged for all wire feed speeds. The latter is not an expected result from simulations carried out in section 6.4, which indicate that the resistance per unit length should change noticeably with different wire feed speeds (Figure 6.15). This has not occurred. No good explanation is offered for this. The reduction of the weld pool width as explained earlier may create an increase in resistance, but it is unlikely to contribute 5 to 10 mΩ at a CTWD of 20mm (see Figure 6.15). At the lower wire feed speeds where the transit time is high, conduction effects may be significant. Analysis which takes this into account [66, 68] may give a more accurate prediction of stickout resistance.

It is worth noting that the proposed method of CTWD estimation will not work if the weld is unstable. Figure 6.31 in Appendix 6 shows the relationship between R_{smin} and T_{sc} for two unstable welds at 5.70m/min and a CTWD of 20mm. From the discussion in section 6.4, it follows that an unstable weld produces large variations in $H_I(x,t_x)$ because the current waveform has very large variations in period. The variation in stickout resistance is correspondingly large, so scatter in the data points of Figure 6.31 is the expected result.

6.5.4 Photographic Investigation

In this section the photographic equipment described in Chapter 9 is used to verify that the variation of R_{smin} with T_{sc} are caused by changes in the short circuit bridge profile.

A number of photographs of the short circuit were taken under a condition that is known to produce a large range of T_{sc} values: Test condition 14 in Table 6.3 (Appendix 6). The objective is to obtain images of the short circuit bridge at the mid point of the "active" short circuit, when the current is above 50A. Unfortunately, the short circuit duration cannot be predicted before the event. Also, the delay between the start of the short circuit and the camera exposure time is programmable but fixed for a given exposure. If a photograph of a short circuit with a T_{sc} of 2ms is required, and the wetting-in time is 1.5ms, then the camera delay is set to 2.5ms and a number of photographs are taken until a short circuit event with a suitable T_{sc} is captured. For rare events with very short or very long T_{sc}, this may require over 20 attempts.

Figures 6.32 to 6.34 in Appendix 6 are photographs of a short circuits with T_{sc} of 0.78, 2.06 and 6.28ms, respectively. The exposure time is 1/8000 sec, or 125μs. The accompanying waveforms shows the variation in instantaneous resistance and the camera exposure timing. In all cases, the exposure is taken close to the region where the minimum resistance occurs, so the images are indicative of the bridge geometry at minimum resistance. The "glitch" in the resistance is due to induction of a small voltage spike on the voltage feedback signal during operation of the flash unit. The flash head is only 100mm from the weld, and generates a pulse current of 1000A for 90μs. The current signal was unaffected by the flash unit's operation. The figures clearly show that the bridge geometry is quite variable, and clearly show why the geometry strongly influences R_{smin}. The photographic equipment is not able to take an exposure just before the short circuit, which would show the size of the droplet formed at the end of the electrode. However, from observing the shape of the short circuit bridge and nearby weld pool, it is reasonable to deduce that the bridge in Figure 6.32 is a result of a much smaller droplet than for the case of Figure 6.33.

The extended short circuit shown in Figure 6.34 is an atypical case which is not found in a highly stable weld. R_{smin} is clearly minimised because the bridge is very short and there in no actual necking of molten material. But because the solid-to-liquid interface is so close to the weld pool, the surface tension forces tend to maintain the bridge. The electromagnetic pinch force required to push material out of this bridge is

very high. Since the power source current limit was set to 400A during this test, the short circuit duration was greatly extended. This condition is "stubbing" of the electrode into the workpiece. It is a result of a short circuit occurring before a droplet of sufficient size is developed on the end of the electrode. The extended short-circuiting at high current destabilises the welding cycles after the event because the preheating of the electrode stickout is abnormally high. After this short circuit is cleared, the following cycles will be abnormally extended, until the overheated material in the stickout is consumed. These phenomena agree with the assertion by Kiyohara [8] that a stable welding condition requires a minimum bridge length (or droplet size) to be maintained for successful metal transfer.

6.6 Implementation of CTWD Estimation in Real Time

In section 6.5, the relationship between the CTWD, R_{smin} and T_{sc} has been quantified for 0.9mm diameter ER70S-6 electrode operating with Ar-23%CO_2 and CO_2 shielding gases. The relationships are described by equation 6.10 and 6.11, the values of a and b in Table 6.10, and the average value of C_t in Tables 6.7 to 6.9. These relationships were implemented in the DSP-based welding controller described in Chapter 4, to produce a subsystem capable of estimating the CTWD in real time while also controlling the process. To produce a signal with acceptable response and reduced "ripple" or signal swing, the simple single-pole filter of equation 6.13 was added:

$$CTWD_{filt} = 0.2\,CTWD_{new} + 0.8\,CTWD_{filt.last} \qquad (6.13)$$

The sampling frequency is equal to the weld cycle frequency, so the time constant of the filter varies accordingly. Short circuits with values of T_{sc} below 0.25ms are not used for estimating CTWD. For testing purposes, the filtered CTWD estimate was copied to a spare analogue output of the controller, and sampled with a digital storage oscilloscope.

Welds were performed at various values of CTWD using both Ar-23%CO_2 and CO_2 shielding gases. The wire feed speed was kept at 5.70 m/min. The CTWD estimation output was sampled for 3.0 seconds. Figure 6.35 shows the variation in the estimates operating with Ar-23%CO_2, while Figure 6.36 shows the results for CO_2.

The amount of signal variation is acceptable, but could not be considered outstandingly low. Variation in the CTWD estimate is expected, because of variations in electrode preheating as simulated in section 6.4, and also because of variations in molten bridge geometry as shown in section 6.5. The bridge geometry is affected by

factors such as weld pool oscillation (position of pool wave at time of contact with droplet), and asymmetrical distortion/repulsion of the droplet, particularly for CO_2 shielding gas.

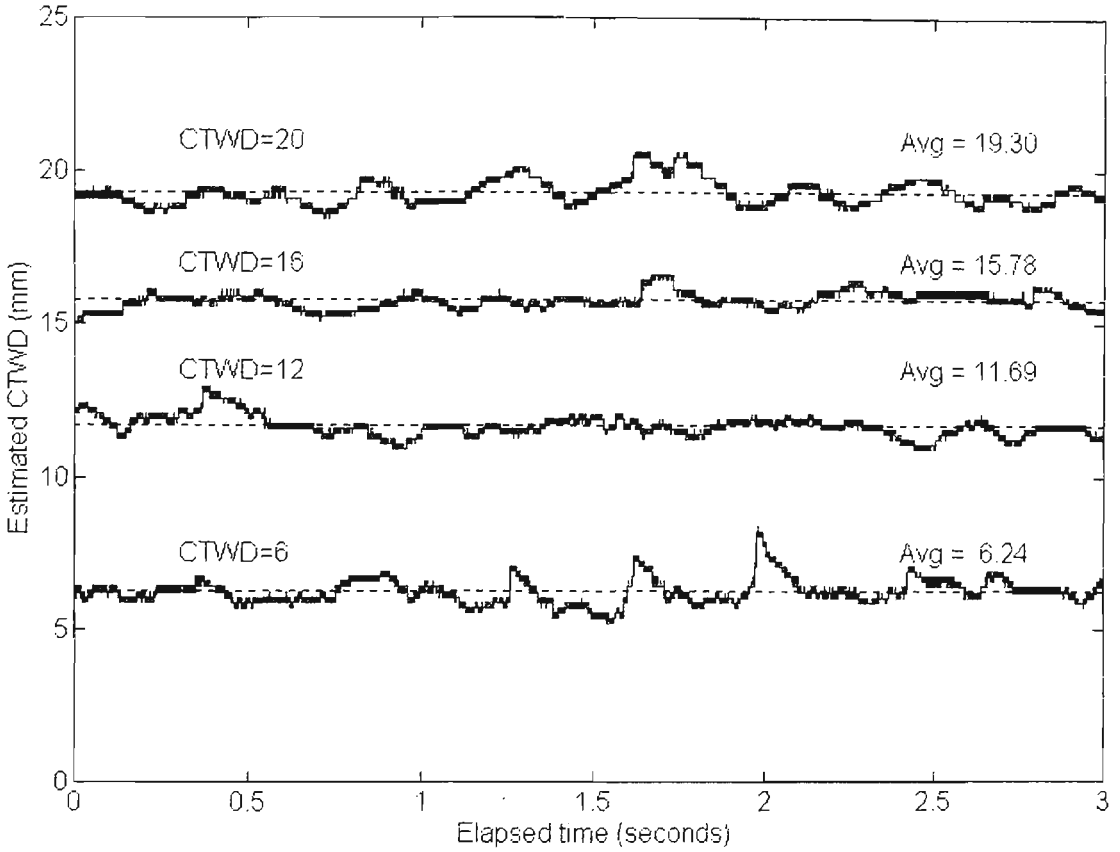

Figure 6.35 Filtered CTWD estimation signal (Ar-23%CO_2, 5.70m/min)

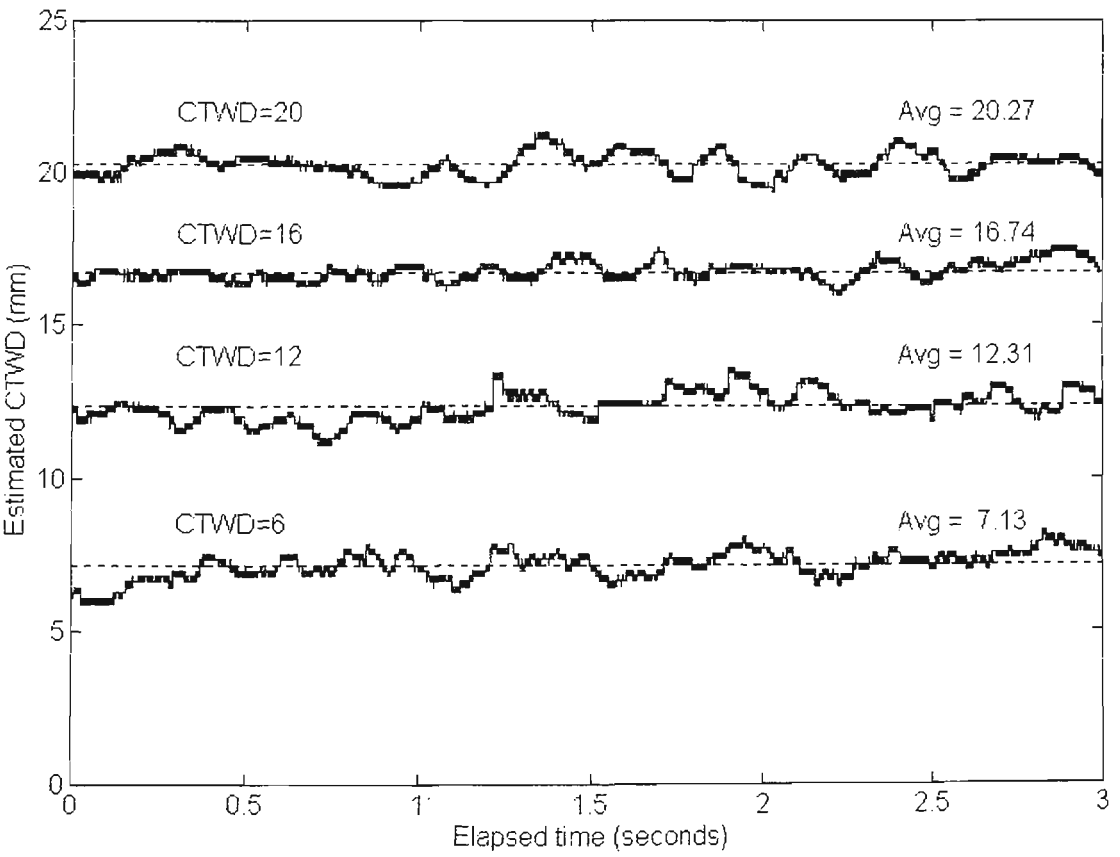

Figure 6.36 Filtered CTWD estimation signal (CO_2, 5.70m/min)

In view of the results shown in Figures 6.35 and 6.36, the instantaneous error in the CTWD estimate can be conservatively quoted to be +/-2mm. The greatest errors occurred for low values of CTWD in the argon-based gas, where the weld was slightly less stable than those at higher CTWDs.

6.7 Summary

This chapter has described and experimentally verified a method of estimating the CTWD based on the minimum short circuit resistance (R_{smin}) which is corrected for the active duration of the short circuit (T_{sc}). Accurate and consistent results were obtained in both CO_2 and argon based shielding gases, at CTWD values from 6mm to 20mm, using 0.9mm mild steel (AWS A5.18 ER70S-6) electrode at wire feed rates from 1.87 m/min to 5.70 m/min.

The relationship between the CTWD and corrected resistance (R_{corr}) has been found to be effectively linear for a number of wire feed speeds, and is not significantly affected by a change of shielding gas. The linearity of the experimental results agrees with computer simulations in section 6.4. The simulations indicate that the stickout resistance is non-linearly related to length for a given RMS current, but the relationship becomes almost linear when the increase of current for a decrease of CTWD is taken into account. However, the experimental relationship between CTWD and R_{corr} remains almost unchanged for large changes in wire feed speed. This is in conflict with the simulations, which predict a reduction in the stickout resistance for a given CTWD at low wire feed speeds (hence low currents). The discrepancy may be explained by accounting for thermal conduction in the electrode at low feed speeds, and/or increased resistance of the narrowed weld pool. Further investigation of this aspect is required. Notwithstanding the discrepancy, the almost constant relationship of CTWD to corrected resistance R_{corr} across a very wide range of wire feed speeds is most advantageous for a practical measurement system.

The short circuit time correction factor (C_t) changes significantly with wire feed speed. This is thought to be caused by changes in the weld pool geometry. The value of C_t is also altered by changing the shielding gas and/or the wetting-in time at the start of the short circuit. In the absence of detailed dynamic modelling of metal transfer under ramped current-controlled conditions, the value of C_t must be determined

experimentally for each combination of electrode type, wire feed speed, shielding gas mixture, and wetting-in time that will be encountered in normal operation.

The CTWD estimation technique was implemented in the DSP-based real time welding controller described in Chapter 4. Under the test conditions documented in section 6.6, the maximum instantaneous error in the CTWD estimate was found to be +/-2mm. Despite the corrections and mild filtering applied to the raw data, variations in the CTWD estimate are expected from at least three sources: Firstly, there are instantaneous changes in electrode preheating due to non-periodic waveforms, as predicted in section 6.4. Secondly, the process operates within a certain range of RMS currents for a given CTWD and wire feed rate, depending on the current waveform parameters. Although the range is not large in most cases, the change in RMS current will affect the average electrode resistance. Thirdly, there are inherent variations in the bridge geometry even for short circuiting periods of the same duration. When these types of process effects are considered, it is difficult to envisage a method of CTWD estimation which will yield a more accurate estimate and maintain an acceptable dynamic response to changing conditions.

In conclusion, the proposed method of CTWD estimation has been shown to produce very good results in current-controlled welds of average stability in both CO_2 and argon-based shielding gases. It has been shown that the technique cannot work where the weld is unstable. The advantage of this estimation method, or any technique based on short-circuit events, is that it is not reliant on arcing behaviour. The shielding gas arcing characteristics or melting rate constants are not required, so they cannot introduce additional errors into the results. Conversely, the proposed technique cannot be used in open arc processes. Finally, the proposed technique is well suited to the current-controlled process outlined in Chapter 5 using the equipment described in Chapter 4. The wetting-in time and current is guaranteed to be consistent for each short circuit, as is the rate of rise of current (dI/dt). The repeatability of the short circuit current waveform aids process consistency, which is expected to minimise variations in behaviour between short circuiting events.

Chapter 7

Melting Rate Relationships and Droplet Size Estimation

7.1 Scope

This chapter describes the development of the droplet size estimation algorithm necessary to implement the closed loop control function that is described in Chapter 5 and investigated in Chapter 11. The algorithm is designed to be used in real-time control of the welding process. As a first stage of development, a formula to calculate the average melting rate specifically for short-circuit GMAW using melting constants α and β, the RMS current and the average arcing current is derived and tested. The tests are performed using current waveforms with variable form factor, and the results are compared to those using the conventional formula with mean current only. In the second stage, the melting rate formula is modified to estimate the instantaneous droplet size. An action integral is used to evaluate the degree of electrode preheating at any point in time. Since this method is based on a linearised approximation for process behaviour, the range of errors introduced by the approximation is evaluated, using simulations based on actual voltage and current recordings of the process. In the third stage, a more accurate model of electrode preheating is used to account for non-linear electrode heating effects caused by changes in resistivity with temperature. The errors incurred by this model are compared to those of the previous model. From these results, a simplified method of droplet size estimation is developed which is not prone to error from CTWD estimation, but has intrinsic steady-state errors which must be compensated by other techniques. Finally, the estimation technique is implemented in the real-time welding controller. The performance is evaluated, and the limitations in assessment of this performance are discussed.

7.2 A Formula for the Average Melting Rate in Short-Circuit GMAW

7.2.1 Background

Early investigations in the 1950s of the GMAW process operating with open arcs established that the electrode melting rate is strongly dependent on mean current and almost totally independent of arc length, or voltage [5]. These results apply to the electrode-positive process. The effect of electrical resistance heating had been known

for some time [69], so extensive experiments in [5] led to an empirical equation for the electrode melting rate of the form:

$$M_{RP} = C_a I_{mean} + C_r L I_{mean}^2 \tag{7.1}$$

M_{RP} is the deposition rate in lb/hr, and L is the electrode extension in inches. Constants C_a ($lbA^{-1}hr^{-1}$) and C_r ($lbA^{-2}hr^{-1}in^{-1}$) were evaluated for a particular type of mild steel wire and aluminium. The first term C_aI_{mean} describes the anode heating of the electrode, while the second term $C_rLI^2_{mean}$ models the electrode resistance heating. It was shown that for resistive materials such as mild steel, the second term can account for over half of the total melting rate. For aluminium, the contribution made by resistive heating is far less. Equation 7.1 has since been used extensively to accurately calculate the average melting rate for electrode-positive open-arc GMAW processes, where current is almost constant in time.

Later work [9, 61] has shown that the melting rate in terms of wire feed speed v can be derived from fundamental physical considerations of electrode material properties and current flow:

$$v = \frac{1}{H_m + b}\left(\varphi j + \rho_L L j^2\right) \tag{7.2}$$

Here, v is expressed in mm/s, j is the current density (A/mm^2), φ is the work function of the electrode material (Volts), ρ_L is the resistivity of the hot end of the electrode (Ω-mm), L is the electrode stickout (mm), and H_m is the heat input per unit volume (J/mm^3) needed to melt and detach droplets. Both H_m and b are constants (in J/mm^3) resulting from linearisation in modelling of electrode heat content as a function of resistivity. For a given electrode material, H_m, ρ_L, b and φ are constant provided that the electrode heating is sufficiently high. Section 7.3.2.1 discusses this assumption in more detail. Both terms in equation 7.2 are independent of arc length or arc voltage.

For a given electrode diameter, the relationship between current density j and current i is determined by the cross-sectional area of the electrode. Thus equation 7.2 can be rewritten as:

$$v = \alpha^*.j + \beta^*.L.j^2 \tag{7.3a}$$

$$v = \alpha.i + \beta.L.i^2 \tag{7.3b}$$

where $\alpha^* = \alpha.A$, $\beta^* = \beta.A^2$, and A is the electrode cross-sectional area.

Equation 7.3a represents the "normalised" result that is valid for all electrode diameters for a given material. In this equation, v is expressed in m/s, α is the arc

heating constant ($m^3A^{-1}s^{-1}$), and β is the resistive melting constant ($m^4A^{-2}s^{-1}$). Equation 7.3b is the familiar form of the melting rate equation used to accurately estimate melting rate for open arc GMAW electrode positive processes using pulsed current waveforms even at low currents [70, 71, 72]. Equation 7.3b is applicable to specific electrode sizes for given values of α and β. Here, v is expressed in m/s, α in m/As, and β in $A^{-2}s^{-1}$. Equation 7.3 can yield good results if it is applied to the process where electrode preheating is above a certain value. If the preheating is below this value, the equation may still be applied provided that the process operates in a restricted current range and the values of α and β are chosen appropriately. Section 7.3.2 covers this in more detail.

7.2.2 A Melting Rate Formula for Short-Circuit GMAW

The first term in equation 7.3 describes anode heating at the end of the electrode, which is valid whenever the welding arc is present. In the short-circuit transfer mode, this term does not contribute to the melting rate during the short circuit period. Using the mean current I_{mean} in this term to calculate the average melting rate will create an error since the short-circuiting current can contribute significantly to I_{mean}. The second term in equation 7.3 accounts for resistive heating in a conductor. Use of the mean current also creates errors for the case of a non-constant current waveform. As shown below, the RMS current should be used in the second term.

Integrating equation 7.3 as current varies with time yields the total length of electrode consumed during that time. The average wire feed rate is thus:

$$v_{avg} = \alpha \frac{1}{t}\int_0^t i(T)dT + \beta L \frac{1}{t}\int_0^t i^2(T)dT \tag{7.4}$$

For the first term, the contribution to the integral during the short-circuiting period must be ignored. The "average arcing current" is defined for each welding cycle as the integral of the current during the arcing period t_a, divided by the total weld cycle duration T_c. This integration is performed for all n weld cycles during time t in equation 7.4.

$$I_{arc\_avg} = \frac{1}{n}\sum_1^n \left[\frac{1}{T_{c,n}} \int_{}^{t_{a,n}} i(T)dT \right] \tag{7.5}$$

The RMS current is, by definition:

$$I_{RMS} = \sqrt{\frac{1}{t}\int_0^t i^2(T)dT} \tag{7.6}$$

Substituting equations 7.5 and 7.6 into equation 7.4 yields an equation suitable for the evaluation of the average melting rate for the short-circuit GMAW process.

$$v_{avg} = \alpha.I_{arc\_avg} + \beta.L.I_{RMS}^2 \qquad (7.7)$$

Equation 7.7 is the recommended form of equation 7.1 for processes where an open arc is not always present [61].

7.2.3 Verification of Melting Rate Formula for Short-Circuit GMAW

This section shows that equation 7.7 can model the average melting rate for the short circuit GMAW process more accurately than the traditional equation 7.1 used for open arc GMAW processes. Melting rate constants α and β are also evaluated and compared to previously published values.

A number of experiments were conducted using the "open loop" control scheme described in Chapter 5, in both Ar-23%CO_2 and CO_2 shielding gases. The electrode was 0.9mm mild steel conforming to ER70S-6 specification. Oscilloscope recordings of current and voltage were taken, and processed to obtain mean, average arcing and RMS current values for each experiment. These recordings have a vertical resolution of 12 bits, a sampling time of 50μs, and cover a time of 3.0 seconds, so the accuracy and time span of the data is considered to be acceptable. Table 7.1 in Appendix 7 lists the parameters for each test using Ar-23%CO_2, and Table 7.2 lists those for CO_2. A least squares minimisation technique was used to find values of α and β which minimise the error in estimating the average melting rates, for each test group and each type of formula. This approach was used so that the best (least error) result could be obtained for each formula independently of the other. The respective melting rate constants, and the resulting sum of squares of the errors for each test group are listed in Table 7.3.

The sum of the squares of the error show that equation 7.7 is significantly better at estimating the actual melting rate, for the given experimental data. Inspection of the mean current values in Tables 7.1 and 7.2 shows that this is an expected result, since the mean current can vary significantly for tests conducted at the same wire feed speed and CTWD. This is a property of the "open loop" current-controlled process, since the form factor of the current waveform can be significantly altered by the current controller. This effect is expected to be less significant for conventional power sources with fixed inductance and resistance, but this has not been investigated here.

Table 7.3 Melting Rate Constants and Comparison of Errors

Shielding Gas	Formula Type	α ($mA^{-1}s^{-1}$)	β ($A^{-2}s^{-1}$)	Sum of Squares of error (m^2min^{-2})
Ar-23%CO_2	$\alpha I_{mean} + \beta LI^2_{mean}$	6.09×10^{-4}	1.69×10^{-4}	6.56
	$\alpha I_{arc\_avg} + \beta LI^2_{RMS}$	5.97×10^{-4}	1.59×10^{-4}	2.94
CO_2	$\alpha I_{mean} + \beta LI^2_{mean}$	2.55×10^{-4}	5.34×10^{-4}	7.18
	$\alpha I_{arc\_avg} + \beta LI^2_{RMS}$	5.46×10^{-4}	2.09×10^{-4}	0.77

For equation 7.1, the solutions for α and β with minimised errors for CO_2 are significantly different to those for the argon-based gas. This also shows that equation 7.1 cannot accurately model the melting rate under varying conditions. The melting rate constants obtained by data-fitting to equation 7.7 are reasonably similar for both shielding gases. Interestingly, the form of equations 7.2 and 7.3 suggest that α and β are determined from the electrode material characteristics, in particular resistance for β and work function for α [9]. These should not change with shielding gas composition. However, it is well known that arc root behaviour for CO_2 is quite different to that for argon-based gases [6, 73]. The arc envelopes the droplet being formed at the end of the electrode in argon-based gas, whereas in CO_2 there is a "spot" formed at the anode due to the dissociation of the gas, causing a large variation in thermal conductivity in the arc column. The arc is constricted to one point due to narrower high-temperature regions. An asymmetrical force on the droplet is easily generated, depending on the exact position of the arc root in the droplet. This causes asymmetrical distortion of the droplet and non-uniform heating of the droplet, and may alter the balance of resistive heating to anodic heating.

Table 7.4 compares the melting rate constants of Table 7.3 to previously published figures for mild steel, and corrections are applied so that α and β have the same units and are corrected for 0.9mm diameter electrode. The values are in reasonable agreement, considering the variations in experimental method and materials.

Figure 7.1 graphs the melting rate estimates listed in Table 7.1 for Ar-23%CO_2 shielding gas. The estimates generally follow similar trends. Figure 7.2 shows the results for CO_2. The dramatic improvement in the estimates using equation 7.7 compared to equation 7.3b is evident for CO_2 in particular. Surprisingly, the range of errors is greater for the argon-based gas. Maximum errors of +/-15% are experienced for Ar-23%CO_2, while those for CO_2 are +/- 10%. The implications of these errors to

the regulation of instantaneous droplet size are not serious provided that the percentage error experienced during a given operating condition is constant.

Table 7.4 Comparison of Melting Rate Constants from Various Sources

Refer-ence	Quoted Constants		Electrode Diameter	Corrected Values (Equation 7.3a)		Corrected Values (Eq 7.3b, 0.9mm dia)	
	Arcing	Resistive		$\alpha^* x10^{-10}$ ($m^3A^{-1}s^{-1}$)	$\beta^* x10^{-17}$ ($m^4A^{-2}s^{-1}$)	$\alpha \times 10^{-4}$ ($mA^{-1}s^{-1}$)	$\beta \times 10^{-4}$ ($A^{-2}s^{-1}$)
Table 7.3	$5.97x10^{-4}$ $mA^{-1}s^{-1}$	$1.59x10^{-4}$ $A^{-2}s^{-1}$	0.9mm	3.80	6.43	5.97	1.59
Table 7.3	$5.46x10^{-4}$ $mA^{-1}s^{-1}$	$2.09x10^{-4}$ $A^{-2}s^{-1}$	0.9mm	3.47	8.46	5.46	2.09
[72] (p.147)	0.30 $mm.A^{-1}s^{-1}$	$5.0x10^{-5}$ $A^{-2}s^{-1}$	1.2mm	3.39	6.40	5.33	1.58
[70,71]	0.023 $mA^{-1}min^{-1}$	$2.86x10^{-6}$ $s/minA^2ms$	1.2mm	4.33	6.10	6.81	1.51
[63]	0.23 $mm^3A^{-1}s^{-1}$	$93x10^{-6}$ $mm^4A^{-2}s^{-1}$	0.9mm	2.31	9.30	3.63	2.30
[9] (Note 1)	0.232 $mm^3A^{-1}s^{-1}$	$79.5x10^{-6}$ $mm^4A^{-2}s^{-1}$	---	2.32	7.95	3.65	1.96
[5]	$1.86x10^{-2}$ $lb.A^{-1}hr^{-1}$	$54.7x10^{-6}$ $lb.A^{-2}hr^{-1}in^{-1}$	1/16" 1.59mm	3.01	6.92	4.73	1.71

Note 1: H_m=11.1J/mm^3, b=4.0J/mm^3, φ=3.5V, ρ_L =$1.2x10^{-3}\Omega$-mm in equation 7.2

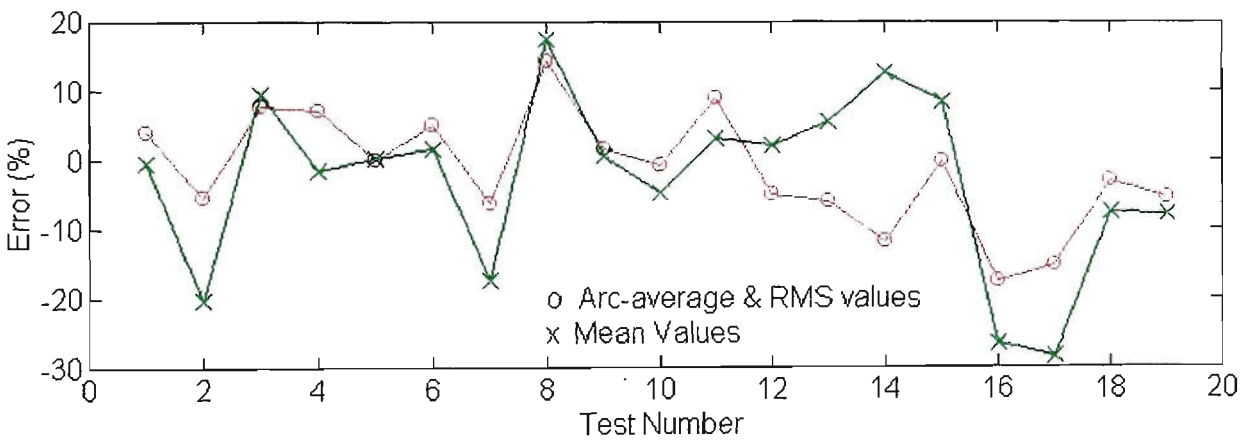

Figure 7.1 Percentage error in melting rate estimates for Ar-23% CO_2

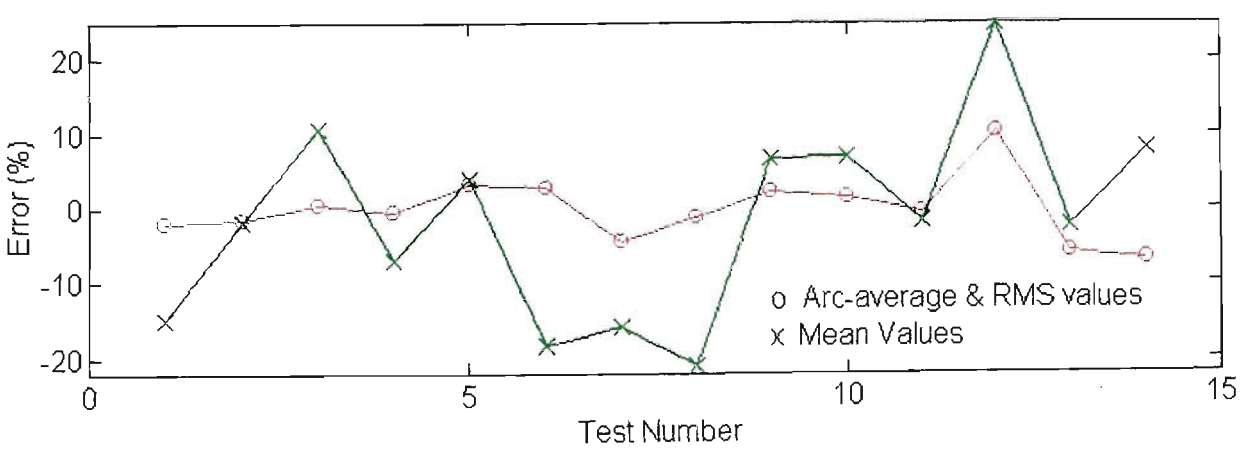

Figure 7.2 Percentage error in melting rate estimates for CO_2

7.3 Instantaneous Droplet Size Estimation

7.3.1 First Method for Determining Instantaneous Melting Rate

7.3.1.1 Development of First Method

Earlier work by Shepard and Cook [63] focused on developing a model for burnoff rate under dynamic conditions. This model expresses instantaneous melting rate in terms of the instantaneous current. The steps outlined below show the development of the first method for determining instantaneous melting rate, based heavily on the work presented in [63].

Exploding wire experiments in the 1950s [53, 68] established that the action integral, defined in equation 7.8, provides a useful representation of the energy accumulated in heated conductors. Work described in [9, 68] uses a similar experiment.

$$W(t) = \int_0^t j^2(T)dT = \frac{1}{(Area)^2}\int_0^t i^2(T)dT \tag{7.8}$$

Here, t is the time over which current has been flowing through the conductor, and the action integral has units A^2s/m^4. For convenience, if a constant cross-sectional area is assumed, the action integral can be modified to be expressed in terms of current instead of current density.

$$Action(t) = \int_0^t i^2(T)dT \tag{7.9}$$

The units of this modified action integral are A^2s. Equation 7.3 can be rewritten as:

$$v(t)\left(1 - \beta\frac{Li^2(t)}{v(t)}\right) = \alpha.i(t) \tag{7.10}$$

Under conditions of constant wire feed speed V and current I, where the melting rate is balanced by the wire feed speed, the modified action integral at the electrode tip is:

$$Action(L) = \frac{LI^2}{V} = \tau I^2 \tag{7.11}$$

The term τ is the transit time; the time taken for an element of the electrode to travel from the contact tip to the end of the electrode. The transit time is typically an order of magnitude greater than the duration of a weld cycle for short-circuit GMAW process. In the short-circuit transfer mode, the current is not constant, but the wire feed speed does remain relatively constant during the transit time. The action integral at the

tip of the electrode at any time is a function of the current that has flowed through the electrode during the transit time.

$$Action(t) = \int_{t-\tau}^{t} i^2(T)dT \tag{7.12}$$

This calculation is used to evaluate the RMS current during the transit time (cf equation 7.6). Substituting (7.12) into (7.10) and rearranging gives the model equation for the instantaneous burnoff rate:

$$v(t) = \frac{\alpha}{1 - \beta.Action(t)} i(t) \tag{7.13}$$

This model suggests that the instantaneous melting rate is proportional to current, but the constant of proportionality is modified by the action integral, or the RMS welding current evaluated during the transit time. The action integral reflects the amount of preheating experienced by the material at the end of the electrode during the transit time. A higher preheat minimises the denominator in equation 7.13, therefore increasing the melting rate for a given welding current. The form of this equation places a limitation on the action integral. It must not exceed $1/\beta$ A^2s. From section 7.2, the value of β for 0.9mm ER70S-6 electrode operating in Ar-23%CO_2 is $1.69 \times 10^{-4} A^{-2}s^{-1}$, corresponding to an action integral limit of 5917 A^2s. For a wire feed speed of 5.7 m/min and a CTWD of 20mm, the RMS current must be less than 167A. In experiments conducted under these conditions, the RMS current did not exceed 125A. Nevertheless, the form of equation 7.13 inherently places limitations on the electrode preheating.

The size of the droplet forming on the electrode is represented by the length of electrode ΔL which has been melted since the start of the arcing period, having the same volume as the actual droplet.

$$\Delta L(t) = \int_{t_{arc}} v(t)dt \tag{7.14}$$

In the development of this model, a number of simplifying assumptions have been made to derive equation 7.13. These simplifications produce a model which can be evaluated relatively simply in a real time controller where calculation time is limited. Firstly, it has been assumed that the electrode extension L is equal to the contact tip to workpiece distance (CTWD). This is true during the short circuit, but not true during the arcing period. Secondly, it has been assumed that the electrode extension L remains constant. This is valid for open arc processes, at least for the duration of the transit time,

if the welding torch is moved slowly in relation to the workpiece. In the short-circuiting process, L varies by the peak arc length, which may be approximately 2mm (see Chapter 10 Figures 10.124 to 10.131). For a CTWD of 20mm, this is only a 10% error, but for a CTWD of 8mm the error is 25%, which is significant. This assumption is necessary for the derivation of equation 7.13 from equation 7.10. Due to these simplifications, errors in the estimation of droplet size are expected. These are assessed in subsequent sections.

7.3.1.2 Error Analysis in Calculation of Action Integral

A method for evaluating equation 7.12 is required which is efficient and capable of being implemented in the DSP-based control system with minimal inherent computational error and minimum execution time. Due to the discrete sampling and execution of the control software, errors are introduced in the calculation of equation 7.12 over a time period equal to the transit time. This section describes the steps taken to minimise these errors, which can significantly influence the final estimated droplet size. A further source of error in evaluating equation 7.12 is the value of the CTWD. The range of CTWD errors is covered in Chapter 6, and no further improvements are made here.

An efficient method of calculating the action integral uses a circular array of fixed size (N_a elements) to store the individual action integral values for time intervals of duration (τ/N_a). The entire array covers the transit time τ, which is calculated from the wire feed speed (constant) and CTWD (variable). The sum of all the array elements is the desired action integral value, and is stored in a single variable Action_Value. A pointer into the array indicates the oldest recorded value. During each time increment (τ/N_a), the "local" action integral is calculated at each controller time sample T_s.

$$Local\ Action\ Integral = \sum_{1}^{N_{local}} \left[i_n^2(t).T_s \right] \tag{7.15}$$

The number of samples for which the local integral is evaluated is in integer value:

$$N_{local} = Int\left[\frac{\tau}{T_s.N_a} + 0.5 \right] \tag{7.16}$$

After N_{local} samples, the local action integral value is stored in the action integral array at the pointed location. Before this is done, the old value at that location is subtracted from Action_Value, and the new local action integral is added to it. The local

action integral then overwrites the oldest value. The array pointer is finally incremented so it points to the oldest array value. Figure 7.3 shows this diagrammatically.

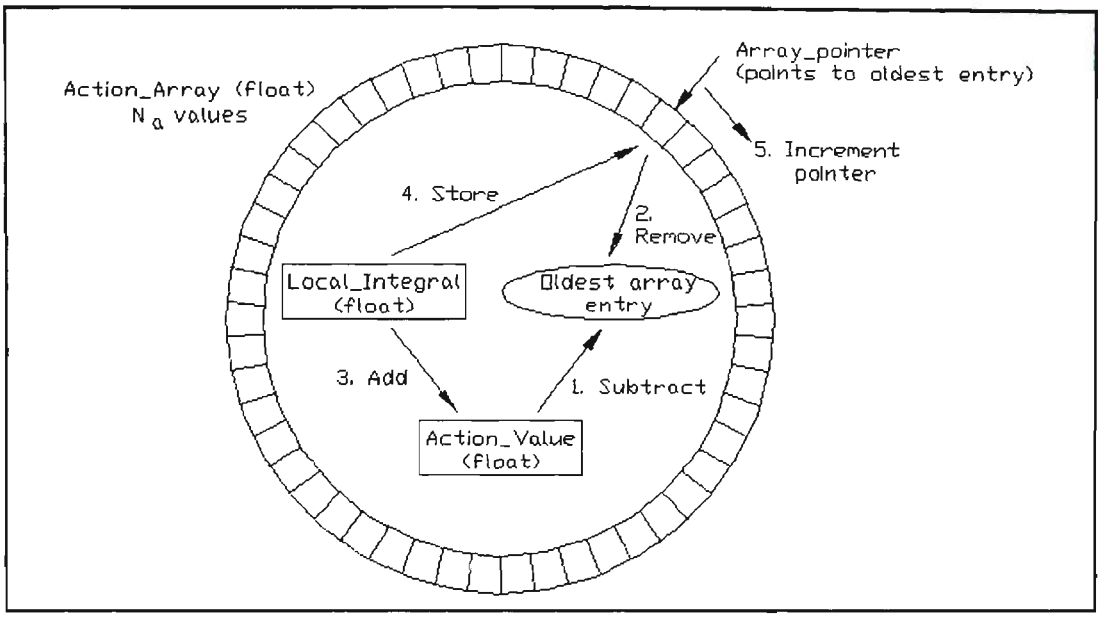

Figure 7.3 Structure of Action Integral Calculations

If the CTWD changes, the time period covered by each array element ($T_s.N_{local}$) is modified, so that each array element does not necessarily cover the same time interval. Assume, for the purposes of error evaluation, that CTWD remains constant. Due to the discrete sampling of the control, the array will cover a total time of:

$$T_{array} = N_{local}.T_S.N_a \tag{7.17}$$

This time is not necessarily the same as the transit time τ. Substantial errors can arise from this discrepancy. The percentage error in evaluation of the action integral due solely to the discretisation of sampling is:

$$Error = 100 \text{ x } \frac{\tau - T_{array}}{\tau} \tag{7.18}$$

There is no error when the transit time is an exact multiple of time interval of each array element. At all other values, an error in the integration time will exist.

The magnitude of these errors are evaluated for the case where there are 400 elements in the array, and the sampling time is 50μs. This sampling time corresponds to that of oscilloscope recordings which are used elsewhere in this chapter to test the various droplet estimation methods. Figures 7.4 to 7.6 in Appendix 7 show the results. Figure 7.3 is a three dimensional representation of error as a function of CTWD and wire feed rate. The maximum error is 20%, and occurs at high wire feed speeds and small CTWD. Figures 7.4 and 7.5 show the dependence of error on wire feed speed and CTWD, respectively.

Figures 7.7 to 7.9 in Appendix 7 show the errors for the case where the sampling time is still 50μs but the number of array elements is reduced to 100. The maximum error is reduced to less than 7%. It is evident that making each array element cover a larger time interval generates less error since N_{local} in equation 7.16 is a larger number, effectively improving the resolution. The reduction in N_a to minimise error must be balanced against loss of resolution in the value of the action integral. If N_a is 10, the value of the action integral will change dramatically at the end of each time interval, and an error in the droplet size estimate of equation 7.14 will occur.

Finally, Figures 7.10 to 7.12 in Appendix 7 show the errors for the case of 100 array elements and a sampling time of 40μs. This represents the values implemented by the DSP controller described in Chapter 4. As expected, the maximum error is further reduced because of the slightly faster sampling rate (25kHz) of the DSP compared to the 20kHz sampling of the oscilloscope recordings. At CTWDs above 8mm and wire feed speeds below 6 m/min, the error is less than 2%. This is considered acceptable for the expected range of operating conditions for tests documented in Chapters 10 and 11.

7.3.1.3 Offline Testing of First Method

This section describes software tests that were performed to assess the accuracy of the first method in estimating the size of individual droplets and consequently the averaged electrode melting rate. It is not possible with existing equipment to compare a droplet size estimate to actual droplet size on a continuous cycle-by-cycle basis over an extended time period of, say, 2 seconds. However, if the droplet estimates for each weld cycle are summed over an extended time and then compared to the actual amount of electrode deposited during that time, an indication of the accuracy of the estimates may be obtained. Such tests are documented in this section for both Ar-23%CO_2 and CO_2 shielding gases.

The offline tests are done with software that simulates the behaviour of a controller that would use the model described in section 7.3.1.1, and designed in accordance with the error minimisation techniques discussed in section 7.3.1.2. To simulate controller signal inputs, the software uses current and voltage data from the oscilloscope recordings taken during the tests used in section 7.2.3. These recordings were used to test the melting rate formula for the short-circuit GMAW process, and the key parameters are listed in Table 7.1 and Table 7.2 in Appendix 7. The sampling rate of the simulated controller is equal to the oscilloscope sampling rate of 20kHz

(T_s=50μs). The action integral array uses 100 elements. The values of melting rate constants α and β are those shown in Table 7.3, determined by using arc-average and RMS currents. The outputs of the simulation are calculated quantities such as action integral and instantaneous droplet size, expressed as the equivalent length of melted electrode, ΔL(t).

The accuracy of the simulated first method is assessed by comparing the sum of the individual estimated droplet equivalent lengths divided by the elapsed time of the simulation to the actual average melting rate, which is of course the wire feed speed. The recordings cover 3.0 seconds, but the simulation results are considered valid for 2.7 seconds. The first 300ms are not used since quantities such as estimated CTWD and action integral have not reached steady state values, as indicated by the offline tests.

The simulations are performed in two stages. The first stage uses a fixed CTWD value ("L" in equations 7.1 to 7.11) so that there is no possibility of an error in the estimated CTWD inducing additional errors in the droplet size estimate. This first stage gives droplet size estimates under favourable conditions where the CTWD value is certain. The second stage of simulation replaces the fixed CTWD with an estimated value which is calculated from the recorded data according to the methods described in Chapter 6. In this second stage, the influence of errors in the CTWD estimate on the accuracy of the droplet estimate can be evaluated.

Figures 7.13 and 7.14 in Appendix 7 show the calculation results of the simulation software when applied to Test 12 in Table 7.1. In this simulation, the estimated CTWD is utilised.

Figure 7.15 summarises the simulation results for the Ar-23%CO_2 tests. The percentage errors in estimating the average melting rate over 2.7 seconds of weld are compared for the three methods described so far. The "true" average melting rate is taken to be the wire feed speed during testing. The results using equation 7.7 can be considered to be the benchmark, since these results were used to obtain values of α and β which minimise the errors. The three sets of results are reasonably consistent, but it is evident that the introduction of the CTWD estimate does introduce additional error into the calculations.

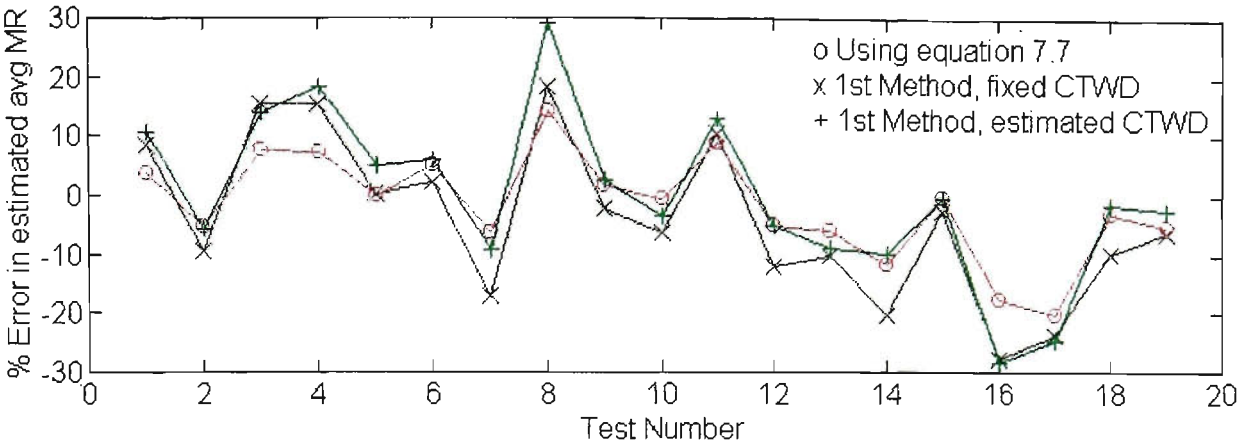

Figure 7.15 Percentage error in average melting rate estimates for Ar-23%CO_2 versus Test number (First Method)

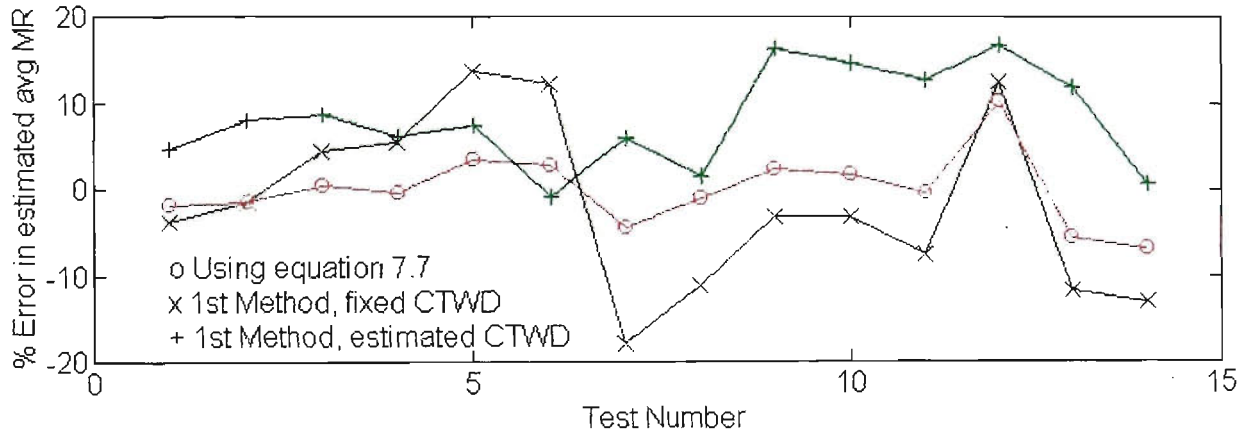

Figure 7.16 Percentage error in average melting rate estimates for CO_2 versus Test number (First Method)

The corresponding results for CO_2 shielding gas are shown in Figure 7.16. In this case, the range of errors in estimating the average melting are actually less than those for Ar-23%CO_2. However, the errors in estimates using the first method are significantly higher than those for equation 7.7. Also, errors in the estimated CTWD cause large changes in the estimated melting rate. Two factors contribute to this. Firstly, the variation in estimated CTWD tends to be greater in CO_2, as shown in Chapter 6. Secondly, the ratio β/α is greater for CO_2 than Ar-23%CO_2 (see Table 7.3), so errors in preheating calculations have a greater effect on errors in final melting rate estimates. This indicates that a better technique is required which reduces errors for CO_2 shielding gas.

The apparently random scatter of errors across the test range in Figures 7.15 and 7.16 can be correlated to the mean welding voltage. Figures 7.17 and 7.18 show this correlation most distinctly for Ar-23%CO_2 and specifically for the results of equation

7.7 in Ar-23%CO_2. A similarly strong correlation exists between error and average dipping frequency. The welds with high mean voltage have longer arcing times. No correlation was found between error and CTWD, indicating that the assumption of constant stickout length is not a primary source of error. The physical reason for the correlation of error to arcing time or mean voltage is not clear from this model. The next section presents a model which may provide a physical explanation for this.

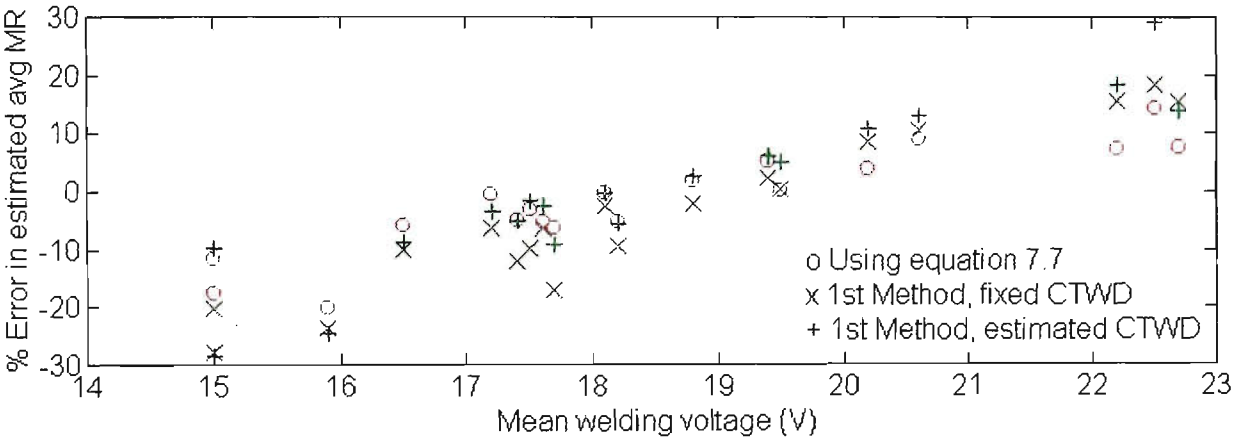

Figure 7.17 Percentage error in average melting rate estimates for Ar-23%CO_2 versus Mean welding voltage (First Method)

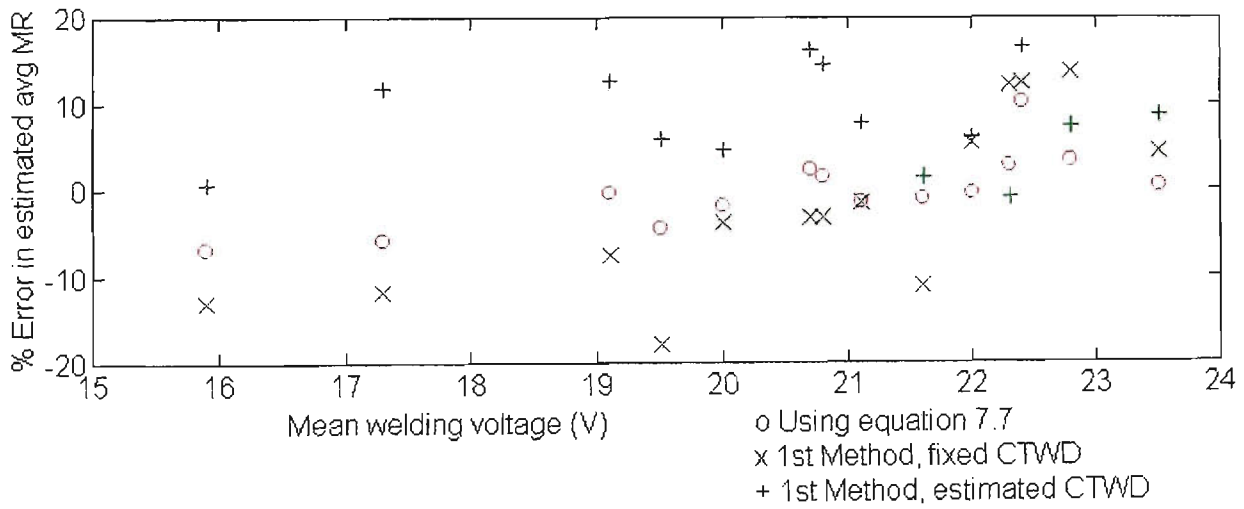

Figure 7.18 Percentage error in average melting rate estimates for CO_2 versus Mean welding voltage (First Method)

7.3.2 Second Method for Determining Instantaneous Melting Rate

7.3.2.1 Development of Second Method

The model derived in the previous section, based on the work presented in [63], may be considered unsuitable for the short-circuit GMAW process because it is based on an equation 7.10, which is derived for cases where the heat input to the electrode is above a particular threshold value. In the short-circuiting transfer mode, this value is

often not reached, so the fundamental modelling assumption is not valid. In this case, a linear model cannot accurately predict the degree of electrode preheating, so the instantaneous melting rate estimate is inherently incorrect. This section proposes a second model based on the work by Halmoy [9, 10, 61, 62] which accounts for the non-linear heating effect within electrodes.

From [61], the energy balance equation at the electrode tip exposed to the arc can be written as:

$$H_m = H_L + \frac{\varphi . j(t)}{v(t)} \tag{7.19}$$

This equation is valid instantaneously and is valid for a wide range of electrodes, currents and shielding gases. H_m is the energy per unit volume (J/mm^3) required to melt the electrode material and raise the temperature of the molten droplet to the final value before it is transferred to the weld pool. For a stable weld, whether in spray or short-circuiting transfer mode, this quantity is considered to be constant. H_L is the increase in specific heat content (J/mm^3) of a volume of electrode which has been generated by resistance heating as it travels from the contact tip to the end of the electrode through distance L. The term on the right hand side of equation 7.19 represents the remaining heat input due to anodic heating, as a result of electrons impinging on the anode surface during arcing. Equation 7.19 gives the instantaneous melting rate in terms of current:

$$v(t) = \frac{\varphi . i(t)}{A\left(H_m - H_L(t)\right)} \tag{7.20}$$

The form of this equation has a similar physical interpretation to that of equation 7.13. The instantaneous melting rate is influenced by the degree of electrode preheating (H_L). The term H_m is considered constant but $H_L(t)$ must be evaluated instantaneously.

The value of H_L is derived as follows. Consider an electrode element with resistivity ρ travelling from the contact tip to the end of the electrode at x=L, and is subjected to a time varying current density $j(t)=i(t)/A$, as shown in Figure 7.19. This element will receive an increase in specific heat content H at a rate:

$$\frac{dH}{dt} = \rho . j^2(t) \tag{7.21}$$

With common GMAW steel electrodes, the resistivity ρ is not constant, but a function of the heat content H, so $\rho=\rho(H)$. Figure 7.20, reproduced from [62] shows this relationship for a number of materials.

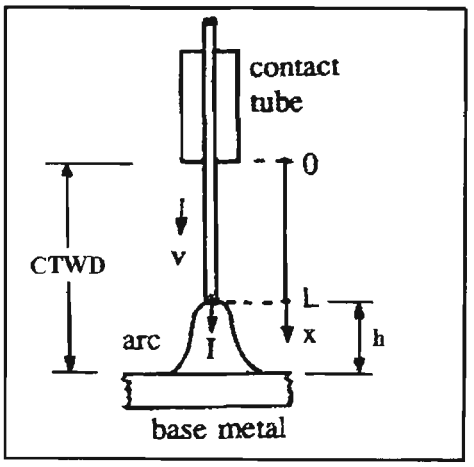

Figure 7.19 Arc and electrode coordinates (from [62])

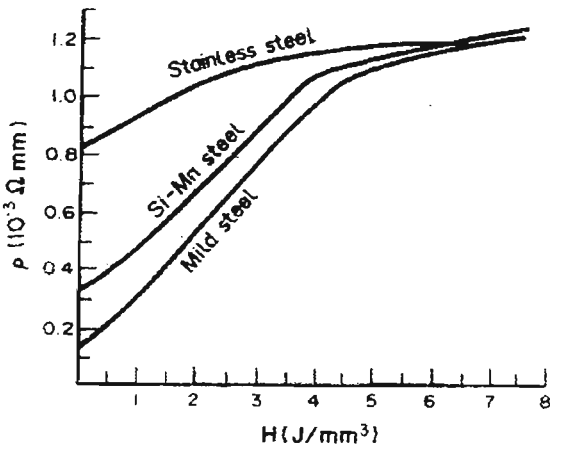

Figure 7.20 Empirical values for ρ(H) (from [62])

To assess the increase in heat content to the electrode element during the transit time τ=L/(wire feed rate), equation 7.21 is integrated over this time, accounting for the variation in ρ. The result is a function $f_1(H_L)$ which varies non-linearly with the action integral.

$$W(\tau) = \int_0^{\tau} j^2(t)dt = \int_0^{H_L} \frac{dH}{\rho(H)} = f_1(H_L) \qquad (7.22)$$

The relationship between $W(\tau)$ and H_L can be found experimentally by heating the wire electrically and instantaneously measuring energy input and resistance. This is the same experiment described in section 7.3.1.1. Figure 7.21, reproduced from [62], shows the relationship for a number of materials. An initial temperature equal to room temperature is implied. The specific heat due to resistance heating H_L is linearly related to $W(\tau)$ above a certain value, referred to in [63] as the transition action W_T. From Figure 7.21 (using Si-Mn steel, which is closest in composition to GMAW wires), this value is 6500 A^2s/mm^4. This is in good agreement with experimental results in [63], which lists W_T at 6591, 5958 and 6715 A^2s/mm^4 for 0.9mm, 1.2mm and 1.6mm diameter electrodes, respectively.

Equation 7.22 can be restated as:

$$H_L = f_2(W(\tau)) \qquad (7.23)$$

where f_2 is the inverse of f_1. For values below W_T, a quadratic curve can be fitted to f_2. Above W_T, a straight line is suitable. From Figure 7.21, data points for (W,H_L) are (0,0), (4000,2), (6500,4) and (9900,8). Thus equation 7.23 can be specified:

$$H_L = 4.615\text{x}10^{-8}W^2 + 3.154\text{x}10^{-4}W \qquad \text{for } W \le 6500 \qquad (7.23a)$$

$$H_L = 1.176\text{x}10^{-3}W - 3.647 \qquad \text{for } W > 6500 \qquad (7.23b)$$

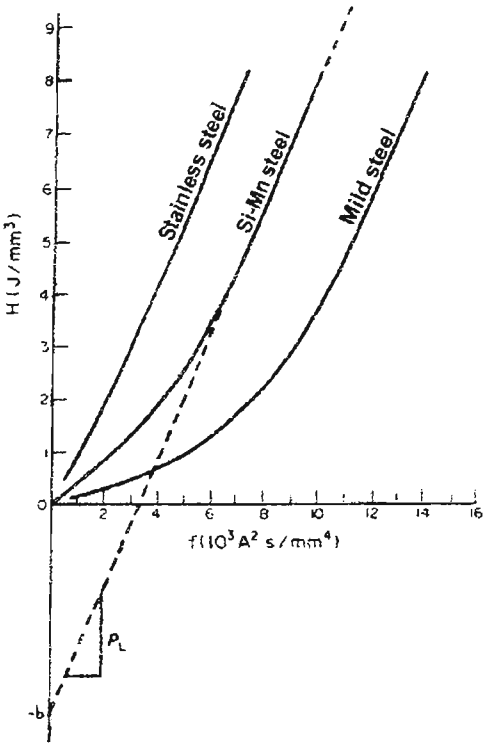

Figure 7.21 H_L as a function of W (from [62])

Substituting equations 7.8, 7.9, and 7.23 into 7.20 gives an expression for the instantaneous melting rate in m/s:

$$v(t) = \frac{\varphi . i(t)}{A\left(H_m - \mathrm{f}_2\left(\frac{Action(\tau)}{A^2}\right)\right)} \tag{7.24}$$

It is worth noting here that for the case of an open arc process with constant current and values of W above W_T, equation 7.23b is written as follows [9]:

$$W = \frac{H_L + b}{\rho_L} = j^2 \frac{L}{v} \tag{7.25}$$

Substituting equation 7.25 into 7.19 yield the familiar linearised equation for steady state wire feed speed, equation 7.2.

Returning to the non-linear case, equation 7.24 can be integrated during the arcing period to estimate the equivalent length of electrode that has been melted to form the droplet.

$$\Delta L(t) = \int_0^{t_a} v(t)dt = \frac{\varphi}{A}\int_0^{t_a} \frac{i(t)}{\left(H_m - \mathrm{f}_2\left(\frac{Action(\tau)}{A^2}\right)\right)} dt \tag{7.26}$$

From [9], φ is the constant anodic heating potential of 3.50V, and corresponds to the work function of steel. H_m is 11.1 J/mm^3, which is just above liquidus for steel.

7.3.2.2 Offline Testing of Second Method

To test the accuracy of the second method of droplet size estimation, the same techniques are used as for the first method (section 7.3.1.3). As before, the simulations are performed in two stages. The first stage uses a fixed CTWD ("L" in equations 7.19 to 7.26). This ensures that no CTWD estimation errors are introduced into the droplet size estimates. Unfortunately, this simplification introduces another error into the estimates, since in reality the stickout length L is up to 2mm less than the CTWD during the arcing period. The resultant error in H_L may be significant for cases where the CTWD is low, but for CTWD values of 16mm or greater, the error is reduced.. The second stage of simulations introduces the CTWD estimate to evaluate the sensitivity of droplet size estimates to changes in CTWD estimates.

When the first stage simulations were performed using φ=3.50V and H_m=11.1J/mm^3, it was found that all the average melting rate estimates were consistently lower than the actual wire feed rate value. The resultant errors were much larger than for the first method. To enable a valid comparison between the two methods, a correction factor C_1 is applied to all of the second method estimates for each shielding gas. The value of C_1 is calculated such that the sum of the squares of the error between actual wire feed rate and C_1-corrected estimates is minimised. So equation 7.24 is modified to:

$$v_1(t) = \frac{C_1 \varphi . i(t)}{A\left(H_m - \mathrm{f}_2\left(\frac{Action(\tau)}{A^2} \right) \right)} \tag{7.27}$$

For Ar-23%CO_2, the value of C_1 is 1.249, while for CO_2 it is 1.525. These are significant corrections, and indicate two things: There are significant errors in the estimation technique, and the melting behaviour is significantly altered by shielding gas composition. The latter can also be deduced from the fact that α and β values were altered by shielding gas in section 7.2. The second method does not anticipate this effect, as equation 7.19 is considered to be universally applicable and φ is related to the work function of the electrode material. The values of $C_1\varphi$ are 4.37 and 5.34 for Ar-23%CO_2 and CO_2, respectively. These values are close to the work function of iron as quoted in [74], which is 4.70. Furthermore, other researchers [75, 76] have modelled anodic heating with the term:

$$\varphi_w + \frac{5 k_B T_e}{2e} \tag{7.27a}$$

while other researchers [77] model anodic heating with:

$$\varphi_w + V_\alpha + \frac{3k_B T_e}{2e} \qquad (7.27b)$$

where φ_w is the work function of the material, k_B is Boltzmann's constant, V_α is the anode drop voltage, and T_e is the electron temperature at the anode, assumed to be 10^4 Kelvin. The term on the right hand side of (7.27a) is 2.16V under these conditions. A fixed value of 5.5V is used by [50] to represent anode heating effects. Although these values of anode potential are in general agreement, the results indicate that anode heating is not constant but is varied by welding conditions.

Having corrected the estimates using C_1, Figure 7.22 compares the results of the second estimation method to the first method for Ar-23%CO_2. Figure 7.23 shows the corresponding results for CO_2. The second method does not produce better results in the argon-based gas, but appears better in CO_2. The similarity in trends between the results is surprising, considering that the second method accounts for non-linearities in the electrode preheating, while the first method is based on a linearised approximation. A possible explanation for this is that all the test welds produce a similar degree of electrode preheating, as indicated by the action integral $W(\tau)$ or the calculated $H_L(\tau)$ using equation 7.23. Table 7.5 in Appendix 7 lists the average value of $H_L(\tau)$ calculated during the simulations for both shielding gases. The range is 2.2 to 5.6 J/mm^3, which is on the non-linear section of the H_L versus W curve of Figure 7.21. The selection of appropriate α and β terms for the first method will effectively linearise the melting rate equation 7.7 to this range of values, rather than the range above W_T. Thus the "constants" α and β of that model may be thought of as variables which need to be altered depending on electrode preheating conditions. The values of α and β listed in Table 7.3 give results which are comparable to a model which caters for nonlinearities only because the test range is restricted. If the operating range is widened, particularly into spray transfer mode, the first method would be expected to be less consistent.

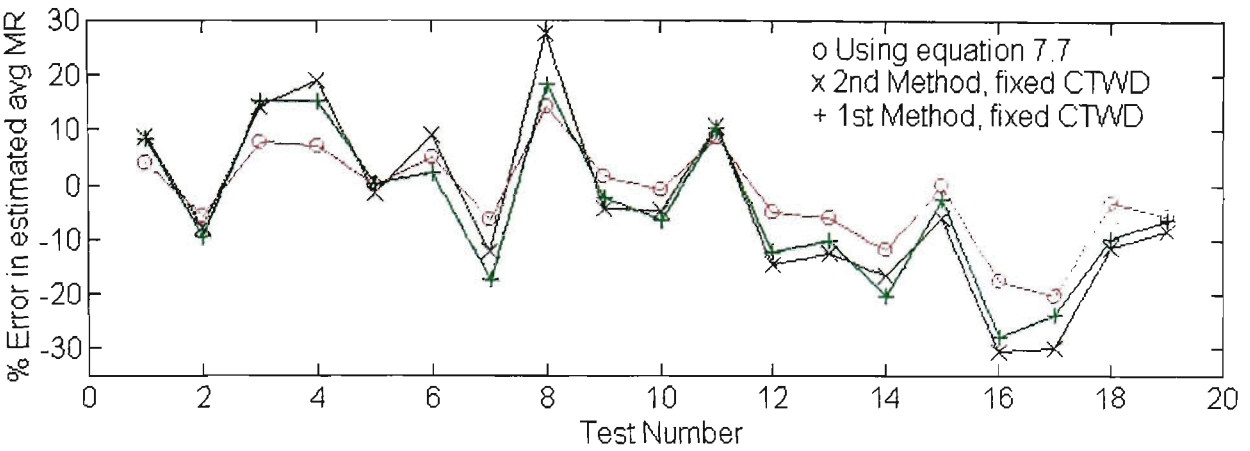

Figure 7.22 Percentage error in average melting rate estimates for Ar-23%CO_2 versus Test number (Second Method, fixed CTWD)

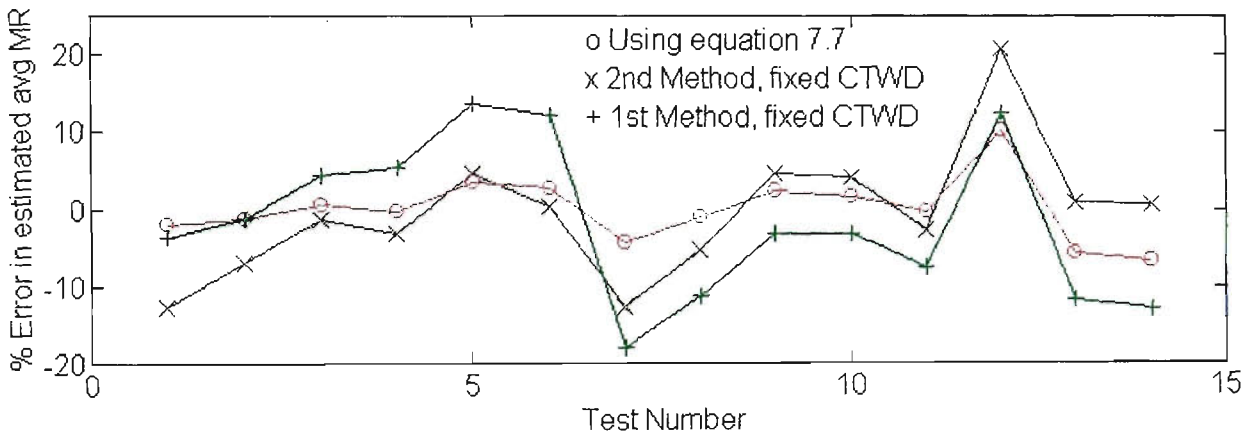

Figure 7.23 Percentage error in average melting rate estimates for CO_2 versus Test number (Second Method, fixed CTWD)

Figures 7.24 and 7.25 compare the estimates of the first and second methods for the case where the estimated CTWD is used instead of a fixed value. Again, the estimates for argon-based gas are similar, while for carbon dioxide the second method produces slightly better results. However, the spread of errors is still unacceptably high. As for the first method, errors in CTWD estimation will proportionately create errors in the evaluation of the action integral. Any errors in the action integral, present in the denominator of equation 7.27, will create disproportionate errors in estimates of melting rate and droplet size.

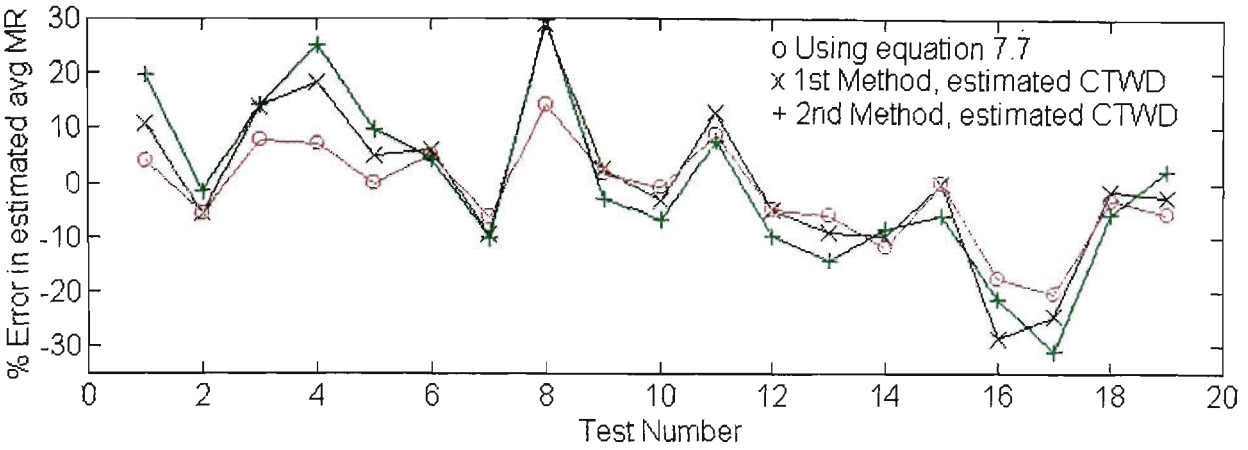

Figure 7.24 Percentage error in average melting rate estimates for Ar-23%CO_2 versus Test number (Second Method, estimated CTWD)

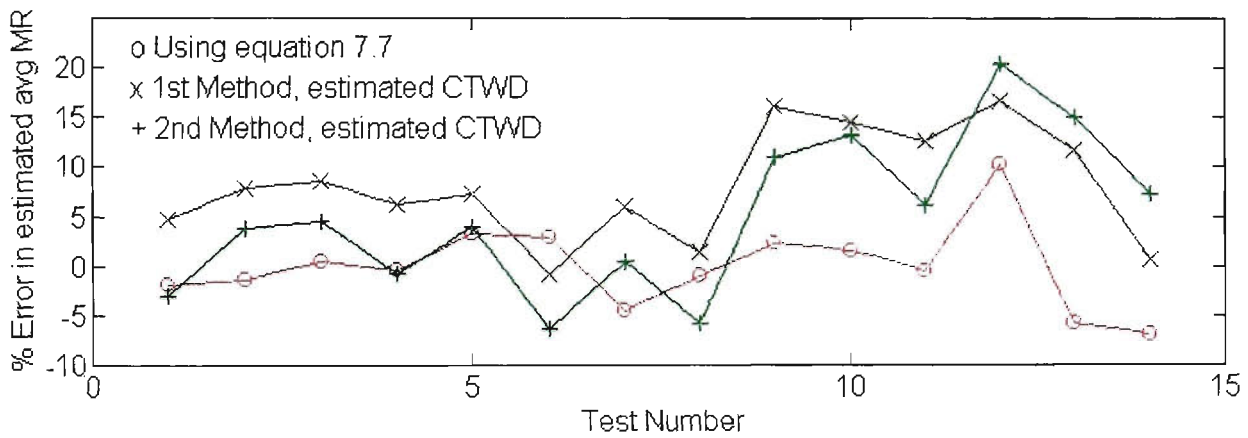

Figure 7.25 Percentage error in average melting rate estimates for CO_2 versus Test number (Second Method, estimated CTWD)

7.3.2.3 Relationship of Short Circuiting Time to Droplet Size

An investigation of the relationship between the droplet size and the time required for the short circuiting transfer of that droplet is not directly related to the development of the estimation method. However, for simulations performed in Chapter 11, this relationship needs to be quantified. In the process of performing the offline simulations in the previous section, it is a simple matter to correlate the estimated size of a droplet to the duration of the subsequent short-circuiting event. For continuity of discussion, the results are presented in this section.

Figures 7.26 and 7.27 in Appendix 7 show the correlation of ΔL to T_sc for Ar-23%CO_2 and CO_2 shielding gases, respectively. These figures contain all of the data obtained from the tests listed in Tables 7.1 and 7.2. The droplet size estimates are obtained by using the second method with fixed CTWD. It must be noted that T_sc is the time within the short circuit for which the current is above 50A. So T_sc for each droplet transfer starts at the end of the wetting-in period and ends when the Premonition

Unit predicts the short-circuit rupture event and turns off the main current. The total short circuit duration is the sum of T_wetting (fixed by the controller), T_sc and T_rupture (process dependent).

The relationship between T_sc and ΔL is clearly not very regular nor repeatable. The reasons for this are not investigated here. It is suspected that the amount of metal transferred from electrode to weld pool, for a droplet of given volume, may vary during the wetting-in time. This in turn may be influenced by the relative geometry at the time of contact, in particular the contact area. Greater variations exist for CO_2 because of the asymmetrical arc forces acting on the droplet during the arcing period, so the position of the droplet with respect to the weld pool is more variable than for Ar-23%CO_2. Another possible reason for the spread of data points is the error in droplet size estimation, as discussed in previous sections. Errors of up to 20% are generated in the estimation of average melting rates for the tests conducted (Figure 7.22). Assuming that the error for the average melting rate in each test can be applied to the estimation error of individual droplets, then a correction can be made to the droplet size information presented in Figures 7.26 and 7.27. The relationship of "corrected" ΔL to T_sc is shown in Figures 7.28 and 7.29 in Appendix 7. As before, the value of correction factor C_1 is 1.249 for Ar-23%CO_2, while for CO_2 it is 1.525. The data point scatter is not discernibly reduced. The line of best fit for each shielding gas is listed below. T_sc has units of milliseconds and ΔL has units of millimetres.

$$T\_sc = 0.35\Delta L + 1.21 \qquad (Ar\text{-}23\%CO_2) \qquad (7.28a)$$

$$T\_sc = 0.54\Delta L + 0.90 \qquad (CO_2) \qquad (7.28b)$$

The relationships are expected to be significantly different because the surface tensions are altered by the shielding gas composition [6, 16, 78], and the wetting-in times are different for the two sets of tests. For Ar-23%CO_2 the wetting-in time is set to 0.5ms, while for CO_2 it is set to 1.5ms, as described in Chapter 5.

7.3.3 Third Method for Determining Instantaneous Melting Rate

7.3.3.1 Development of Third Method

In an attempt to further reduce estimation errors, changes were made to the second method algorithm to account for changes in the stickout length during the arcing period. Simulations were performed for the CO_2 tests using the following refinements to the second method. The height h of the solid/liquid interface at the end of the electrode above the workpiece (refer to Figure 7.19) is estimated. It can be calculated without

consideration of droplet shape, since the melting rate model which estimates v(t) assumes that the molten material "disappears" from the end of the electrode. In fact, the model predicts the position of the unmolten end of the electrode.

$$h(t_a) = \int_0^{t_a} (v(t) - WFR)dt \tag{7.29}$$

The instantaneous value v(t) used in this calculation at every time step is that calculated in the last sampling period or time step of the simulation. The wire feed rate is assumed constant.

Once $h(t_a)$ is evaluated for the present sampling period, the present value of the action integral at the solid/liquid interface (x=L) is evaluated as a fraction of the action at x=CTWD. Note that the estimated CTWD remains constant during the arcing period, and is only updated at the end of the short circuiting period (see Chapter 6).

$$W_{(x=L)} = \frac{CTWD - h(t_a)}{CTWD} W_{(x=CTWD)} \quad \text{where} \quad L(t_a) = CTWD - h(t_a) \tag{7.30}$$

This can be done because the action integral, evaluated at a fixed distance from the contact tip, can be shown to be almost constant over time for a stable weld. This is shown in detail in section 7.3.4. Since the time integral of the square of the current is constant, the action integral is proportional to the distance from the contact tip, x. The instantaneous melting rate for the present sampling period or time step is then calculated using $W_{(x=L)}$ in equation 7.24.

7.3.2.2 Offline Testing of Third Method

Figures 7.30 and 7.31 show the simulation results for CO_2 using the third method. The estimates of the third method are slightly lower than the second method because the action integral is reduced, since L is less than CTWD. The differences are greater for tests where the CTWD is smaller. However, the trend of the errors remains the same, and the sensitivity to CTWD errors is unchanged.

These results indicate that the simplification of setting stickout length L equal to the CTWD throughout the arcing period does not significantly contribute to the error in droplet size estimation, nor does it alter the trends shown by the first and second methods.

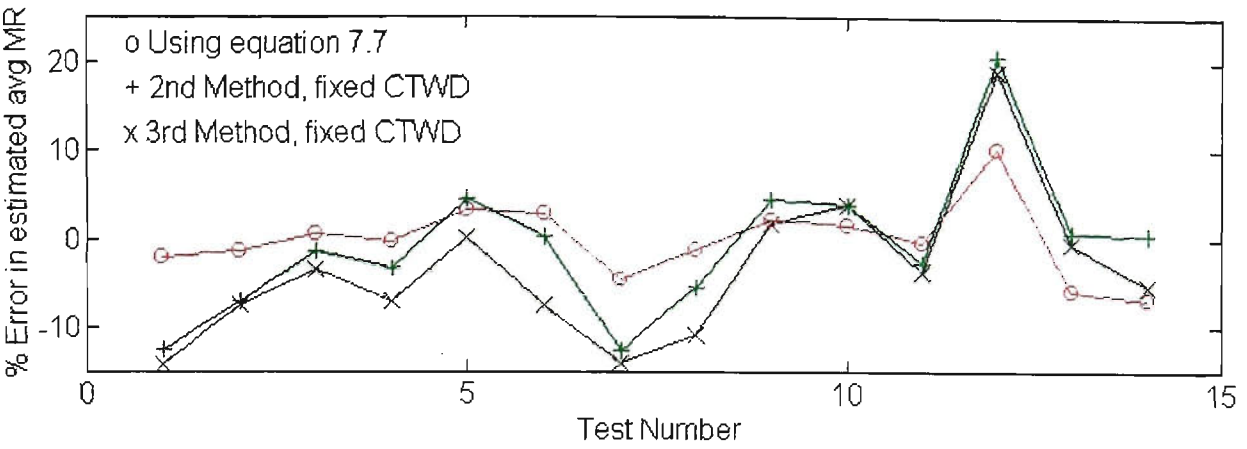

Figure 7.30 Percentage error in average melting rate estimates for CO_2 versus Test number (Third Method, fixed CTWD)

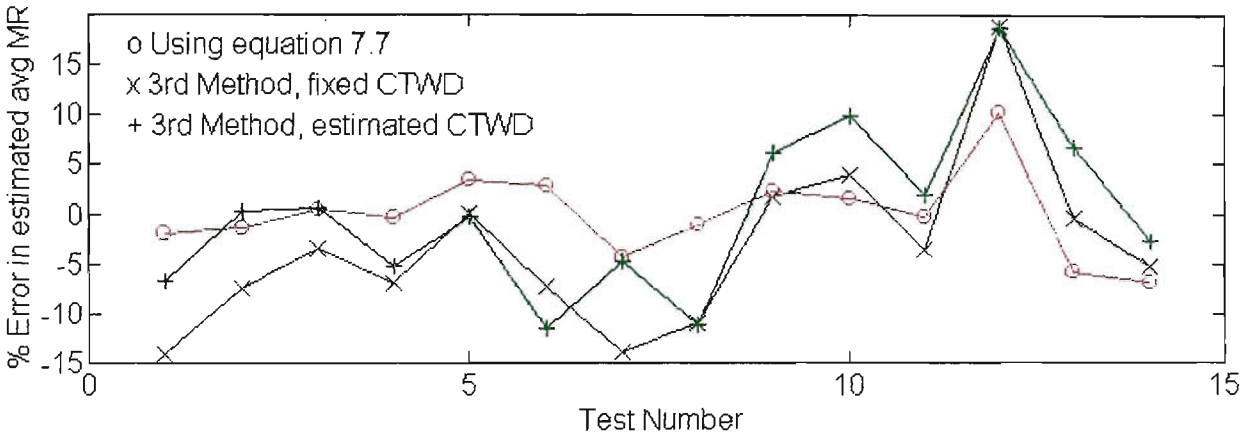

Figure 7.31 Percentage error in average melting rate estimates for CO_2 versus Test number (Third Method, fixed & estimated CTWD)

The testing of the first method showed that estimation errors can be correlated to mean voltage and arcing duration. Comparisons of the second method to the first method show that the error trends are unchanged, so the same mechanisms which introduce the errors still apply. The development of the second method gives a possible physical reason for the above correlation. In equations 7.19 to 7.27, the energy input per unit volume of molten material H_m is assumed constant at 11.1 J/mm^3. For welding tests with longer arc periods and correspondingly higher mean voltages, the heat input to the droplet may be higher. Overheating of the droplets has been previously reported [79, 80] and is thought to be the cause of higher fume generation due to metal vaporisation [81, 82, 83]. The energy input in long arcing periods may overheat the existing droplet rather than melting additional electrode material. This will cause the model to overestimate the droplet size, hence the results shown in Figures 7.17 and 7.18.

In conclusion, the three droplet estimation techniques that have been analysed here are sensitive to errors in CTWD estimation. Other estimation errors are also present. These are thought to be due to the inability of the models to account for

variations in anode heating and final droplet temperature. Section 7.3.4 devises a droplet size estimation method which is in principle less sensitive to changes in operating conditions such as CTWD and arcing duration.

7.3.4 Simplified Method for Droplet Size Estimation

This section proposes a simplified method of droplet size estimation which does not require the use of the estimated CTWD, thereby avoiding an unknown degree of error in the estimate. However, the simplifying assumptions made for this model give rise to other errors which must be compensated by the welding control algorithm.

During analysis of the first and second methods, it was observed that the action applied to the electrode at a fixed distance from the contact tip is almost invariant in time for a stable short-circuit transfer weld. Figure 7.32 in Appendix 7 shows the action integral (as per equation 7.12) calculated for Test 6 in Table 7.1. In this case, the CTWD is 16mm and the wire feed speed is 95mm/sec The action is evaluated for the corresponding transit time of 168ms. Figure 7.33 in Appendix 7 shows the action integral evaluated for Test 15 in Table 7.1. In this case, the CTWD is only 6mm, so the transit time is reduced to 63.2ms, which is approximately 5.5 times the average weld cycle time. Despite this, the action is relatively constant, indicating that the electrode preheating at any significant distance x along the stickout does not vary in time provided the weld remains stable. The qualification of "significant distance" is applied to this statement because at x=0.5mm, for example, the integration time τ is so small that the action is evaluated over less than one weld cycle, causing the value to change significantly. Figure 7.34 shows the action for an unstable (stubbing) weld at a CTWD of 6mm. The irregularity of the current waveform alters the value of action applied to the electrode, so the action varies greatly for an unstable weld.

Assuming that the weld remains stable and that the transit time is more than 5 times the average weld cycle duration, it may be assumed that $W(\tau)$ and thus H_L are constant. Under these conditions, the value of H_L can be calculated from the RMS welding current and equation 7.23:

$$H_L = 4.615\text{x}10^{-8} W^2 + 3.154\text{x}10^{-4} W \qquad \text{for } W \leq 6500 \qquad (7.31a)$$

$$H_L = 1.176\text{x}10^{-3} W - 3.647 \qquad \text{for } W > 6500 \qquad (7.31b)$$

$$W = \frac{I_{RMS}.CTWD}{A.V} \qquad (7.31c)$$

Here, V is the (constant) wire feed speed. The results in Table 7.5 show that the value of H_L calculated using the above equation is very close to the average value of H_L calculated instantaneously during the offline simulations of section 7.3.2.2. Together with Figures 7.32 and 7.33, this indicates that H_L remains constant throughout a stable weld where the operating conditions are not changing. Consequently, equation 7.27 can be rewritten as:

$$\Delta L(t) = \int_0^{t_a} v(t) = \frac{C_1 \varphi}{A(H_m - H_L)} \int_0^{t_a} i(t)dt \tag{7.32}$$

The term $C_1\varphi/A(H_m-H_L)$ may be considered constant, and the integral of current during the arcing period is defined in equation 7.5 as the average arcing current. Equation 7.32 can be averaged over a long period of time to obtain the average melting rate.

$$v_{avg} = \frac{C_1 \varphi}{A(H_m - H_L)} I_{arc\_avg} \tag{7.33}$$

Figures 7.35 and 7.36 compare the results of using this equation and the "bulk" values of RMS and average arcing current to the second method simulations and the linearised melting rate equation 7.7. The results of equation 7.33 show little deviation from the results of the second method simulations, indicating that the term $C_1\varphi/A(H_m-H_L)$ does remain essentially constant during a stable weld.

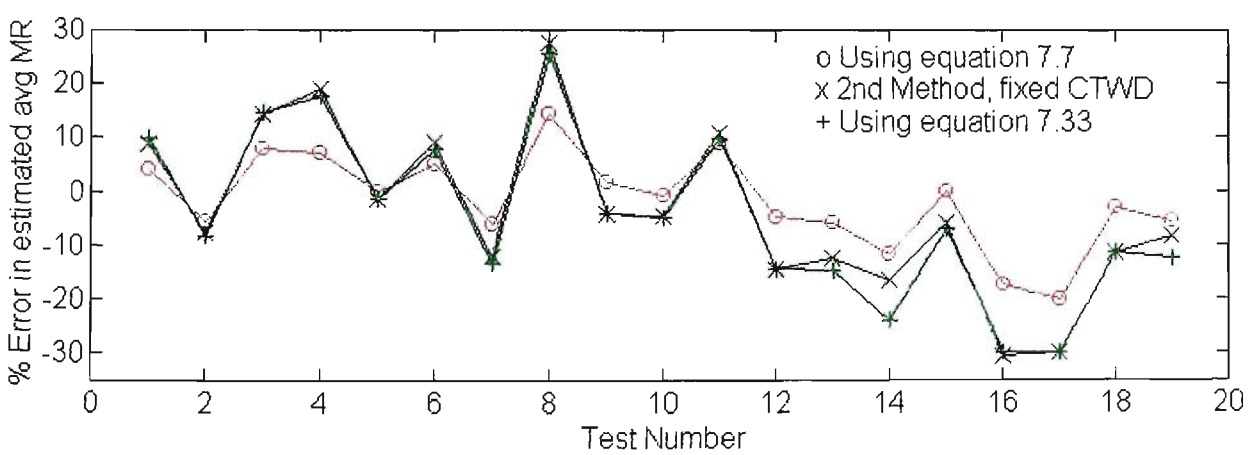

Figure 7.35 Percentage error in average melting rate estimates for Ar-23%CO_2 versus Test number (using "bulk" values)

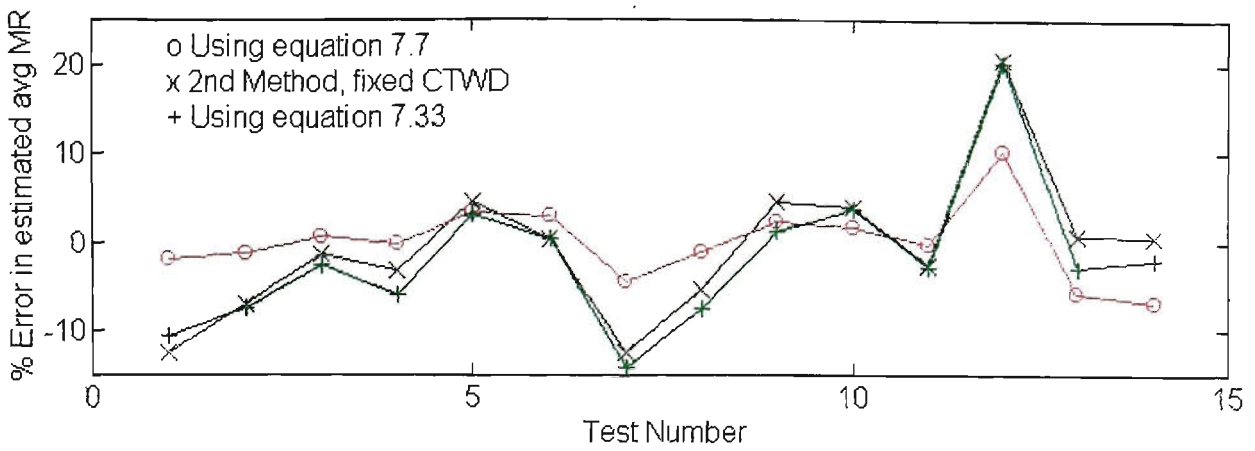

Figure 7.36 Percentage error in average melting rate estimates for CO_2 versus Test number (using "bulk" values)

In view of these results, a simplified method of droplet size estimation is proposed which assumes that for a number of weld cycles corresponding to the transit time τ (say, 5 to 15) the operating conditions remain unchanged and the weld remains stable. This is a reasonable assumption for either a mechanised welding process or a manual process being performed by a reasonably skilled operator. In either case, the CTWD is not expected to change significantly in 200 milliseconds. From equation 7.32, the term $C_1\varphi/A(H_m-H_L)$ is considered constant but unknown, since H_L is not known. Thus equation 7.32 can be expressed as:

$$\Delta L(t) = K\int_0^{t_a} i(t)dt \qquad (7.34)$$

The size of the droplet, as represented by an equivalent length of molten electrode, is proportional to the integral of the current during the arcing period. Since K is unknown, there exists an error in this constant of proportionality at any time during the weld. The error is expected to change little during the transit time. As discussed in Chapter 5, the objective of the "closed loop" control is to generate droplets of consistent size rather than a specific size. Implementation of equation 7.34 in the controller generates a signal which is proportional to the droplet size, but contains a proportionality error which may vary slowly as conditions change. This situation is preferable to the first and second methods of estimation, which introduce an unknown and rapidly changing error related to the estimated CTWD. The disadvantage of the simplified method is that the closed loop control algorithm must be designed to automatically compensate for the proportionality error. The engineering solution to this practical problem is presented in Chapter 11.

For the purposes of implementation, the fixed values of C_1, j, H_m and H_L are assumed to be 1.4, 3.50V, 11.1 J/mm^3 and 4.5 J/mm^3, respectively. The value of K is 1.17 mmA^{-1}s^{-1} for a 0.9mm diameter electrode.

7.4 Photographic Verification of Droplet Size Control

The simplified droplet size estimation technique of equation 7.34 was implemented in the controller described in Chapter 4. The software was written so a fixed droplet size target could be specified to the controller, which would immediately reduce the arcing current to 30A when the target size had been reached. The software was also modified to trigger the photographic equipment (described in Chapter 9) at the instant that the target is reached. The camera delay is known to be 400μs, and the exposure time is 125μs (1/8000 sec). Slow ramping of the current as described in Chapter 5 was not used after the target size is reached. The immediate reduction of current to 30A allows for a clearer photograph of the droplet which is not obscured by the arc.

Fifteen welds were performed using the settings listed below.

Shielding gas:	Ar-23%CO_2	CTWD:	16 mm
Wire feed rate:	5.70 m/min	Travel speed:	390 mm/min
Iarc_max:	250 A	Iarc_min:	80 A
Iarc_ramp:	150 A/ms	I_backgr:	20A
Isc_max:	375 A	Isc_ramp:	100 A/ms
T_wetting:	0.5 ms	Tarc_max:	1.5 ms
Electrode type:	0.9mm ER70S-6	ΔL target:	0.95mm

At each weld, a photograph was taken of the droplet immediately after the specified target was achieved. The volume of each droplet was estimated from the photograph. To do this, the droplet is assumed to be axisymmetrical. The image of the droplet was divided into approximately 20 cylindrical "slices", and the scale of the photograph was determined from the image of the non-molten electrode, which is known to be 0.9mm in diameter.

Figure 7.37 in Appendix 7 shows the welding current, welding voltage and camera trigger waveforms for one of the tests. Figure 7.38 in Appendix 7 illustrates some of the photographs taken, showing the variation in droplet shape encountered in testing.

Figure 7.39 summarises the droplet volumes estimated from the photographic images. The volumes were found to be reasonably consistent at around 1.0 mm^3. Measurement errors can account for most of the variation. The greatest source of error occurs in determining the scaling of the image. At high magnification, it is difficult to determine the exact edges of the electrode due to blurring. A good estimate can be made, but a 2.5% error in diameter estimation can produce a 7.5% change in calculated volume. The error bars in Figure 7.39 indicate such an error band. Smaller errors can arise from changing the determined boundary of the droplet (up to 2% change in calculated volume was observed). Further errors are made in guessing a straight line of best fit for the solid/liquid boundary between electrode and droplet (approximately 1.5% changes observed). Finally, the photographs had to be taken with the camera lens at an angle of approximately 10^0 to the horizontal, in order to achieve images of suitable size with the available magnification while avoiding interference with the moving welding table. The image plane is at an angle to the electrode/droplet axis, introducing another source of variation, particularly for droplets deflected away from the camera.

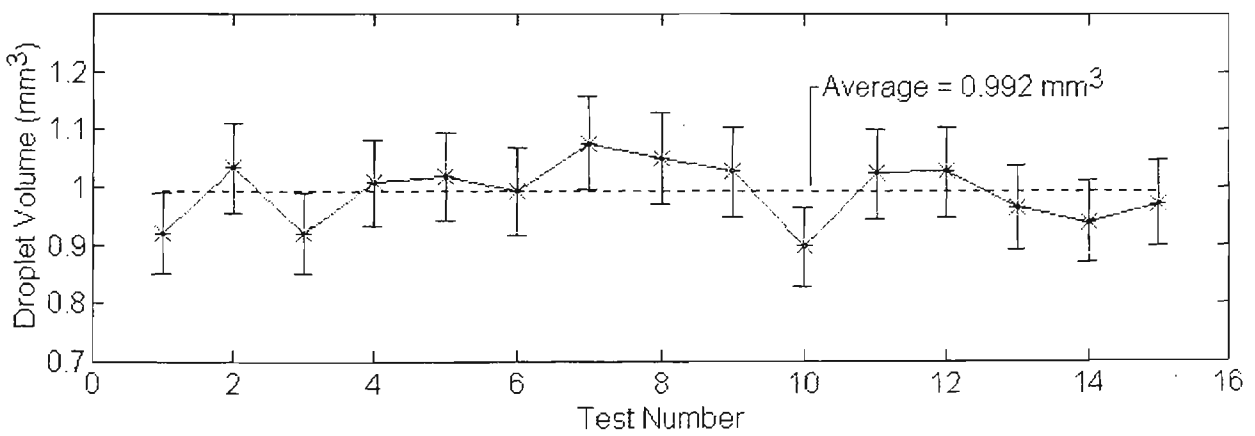

Figure 7.39 Droplet volumes calculated from photographs

Despite the non-ideal measurement conditions, the results indicate that the volume of droplets formed using the simplified estimation technique is sufficiently consistent that variations can be explained by measurement error. The photographic technique used here is believed to be the best one developed to this date for this type of measurement. However, the resolution of the images would need to be improved significantly if droplet size consistency is to be absolutely proven.

7.5 Summary and Discussion

This chapter has investigated a number of methods to instantaneously estimate the size of the droplet being formed at the end of the electrode. The first method uses a modified form of the linearised Halmoy melting rate formula. The values of constants α and β are found from the application of a formula for the average melting rate in short circuit transfer mode using RMS and average-arcing currents. The second method models the non-linear relationship between electrode resistance heating and the action applied to the electrode by the non-constant welding current during the transit time. For both of these methods, the electrode stickout is assumed to be equal to the CTWD throughout the arcing period. A third method uses the non-linear electrode heating modelling of the second method, and also accounts for variation in the electrode stickout during the arcing period.

It has been shown that the estimates produced by these three methods are prone to error from at least two sources. Firstly, the estimates are affected in a consistent manner by the mean voltage, or the arcing period duration. It is believed that a higher final droplet temperature is reached for welds with long arcing periods, so the central modelling assumption of constant specific heat content is violated. Secondly, errors in CTWD estimation produce unacceptable errors in the estimated droplet size since the melting rate is dependent on the electrode stickout. The stickout is equal to the CTWD during the short circuit and not greatly different during most of the arcing period. The errors are unacceptable because they are large under certain conditions and also not easily predictable in the case of CTWD errors.

In view of these limitations, a simple estimation method has been implemented based on the time integral of current. The CTWD estimate is not used, so there are no stray errors introduced from this variable. However, the estimate is no longer a true estimate of the droplet size, but is proportional to the droplet size. Both fundamental modelling and test results indicate that the proportionality remains constant provided that operating conditions such as CTWD and wire feed speed do not change, and that the weld is stable. This is true even when accounting for changes in final droplet temperature and non-linear variations in electrode preheating. For the simple model to be useful in a practical closed loop system which aims to maintain a *consistent* droplet size, the operating conditions must remain almost unchanged during the transit time (typically 200ms or less). Conditions can change significantly over longer periods of over one second as this allows time for the controller to adjust for changes in the

relationship between estimate and true drop size. Such an adaption method is described in Chapter 11. The simple estimation method was implemented in the welding controller and tested under one set of conditions. Within the limitations of the equipment and test method, the volume of the generated droplets was found to be 0.99 mm^3 +/- 0.09 mm^3.

The simple estimation method is expected to work well with the current-controlled processes described in Chapter 5 because the current waveform is exactly the same at the start of each arcing period. This is not true for conventional CV power sources, where initial arcing current is determined by duration of the short circuit. The repeatability of the arcing current in the current controlled processes makes the development of each droplet repeatable, provided the CTWD does not rapidly change and that the weld remains stable. In principle, this should also be the case if some non-linear behaviour exists in the early stages of arcing, which has not been accurately measured or modelled, provided that the behaviour is always the same. The reproducible current waveform ensures that the formed droplet is the same at a given time into each arcing period. The overall performance of the "closed loop" droplet size regulation system is assessed in Chapter 11.

Chapter 8

Measurement of Arc Characteristics

8.1 Scope

This chapter describes the measurement of the voltage-current characteristics of various shielding gases using a novel technique. The advanced power source described in Chapter 4 is utilised because of its rapid current turn-off capability. This power source allows the use of a testing method similar to that which has been used in the past to measure V-I characteristics for the GTAW process. A stationary electrode of desired composition and size is used in a test geometry which closely resembles the physical conditions encountered in practical GMA welding. Problems with erosion of the small electrode during testing are minimised. The novel testing technique does not operate as a welding process, so errors due to factors such as variable arc gap and uncertain stickout resistance are avoided. Tests at low currents and small arc gaps are easily performed.

The measurement of instantaneous arc characteristics was undertaken at an early stage in the project, as it was anticipated that the information could be used to control arc length during the initial stage of the arcing period. As the project progressed, preliminary testing of this approach showed that process stability was not improved. The data documented in this chapter is therefore not used in later chapters, and other control methodologies which showed greater promise are explored in Chapters 10 and 11. Nevertheless, the novel method of arc characteristic measurement described in this chapter represents a significant improvement over existing methods, and offers a very efficient way of collecting data over a wide range of test conditions.

Details of the experimental method are given in section 8.3. The results are presented in section 8.4 and discussed in section 8.5.

8.2 Background

8.2.1 Some Physical Aspects of the Arc

An electric arc may be defined as "a sustained electrical discharge through a high temperature conducting plasma, producing sufficient thermal energy so as to be useful for the joining of metals by fusion" [84]. The electrical conduction takes place through a highly conductive gaseous column, or plasma. The plasma contains a mixture

of electrons, ions and neutral atoms all at temperatures of up to 30,000K [73]. However, the temperature of the electrodes is much lower than this, usually around 3,000K. So there are regions near the surfaces of anode and cathode where the temperature rapidly drops from 30,000K to 3,000K. A much higher thermal gradient exists in these regions compared to that in the plasma column. The thickness of these surface regions may be as little as 0.02mm [85], so a high potential difference (or electric field) also exists due to changing electrical conductivity. The potential differences in the anode and cathode regions are often called "sheath voltages". The arc can be divided into the anode, plasma and cathode regions [86]. Early physical analysis [87] indicates that the plasma voltage is strongly affected by arc length and shielding gas composition, while anode and cathode sheath voltages are dependent on the electrode material composition [6]. More recent research [88] shows that the sheath voltage is fairly independent of electrode material and influenced by shielding gas composition. The exact nature of the processes at work in the sheath region are not yet fully understood. Notwithstanding this, the total arc voltage consists of the contributions from the plasma column, anode sheath and cathode sheath, which are separate and distinct regions within the arc.

$$V_{arc} = V_{anode} + V_{plasma} + V_{cathode} \tag{8.1}$$

Measurement of this total arc voltage is the objective of the work described in this chapter.

8.2.2 Background of V-I characteristic Measurement

The voltage-current relationship for GTA welding with tungsten electrodes and argon shielding gas has been investigated by a number of researchers [84, 89]. Figure 8.1 shows a typical characteristic. The V-I characteristics for GTAW are abundant in the literature and are reasonably easy to obtain experimentally. Steady currents of 250A can be passed through the large water-cooled tungsten electrodes for long periods of time with little or no deterioration of the electrodes, hence no change in the test geometry [89]. The test geometry of the electrodes closely resembles that used in practice, as the cathode is a pointed tungsten electrode of 2.4mm diameter or more, and the anode is a comparatively large, flat surface. The operating current is usually a fixed DC current for steels, or a pulsed current of low frequency. The main difference between the experimental apparatus and a practical weld is the anode material, which is usually tungsten or copper in experiments, but steel in practice.

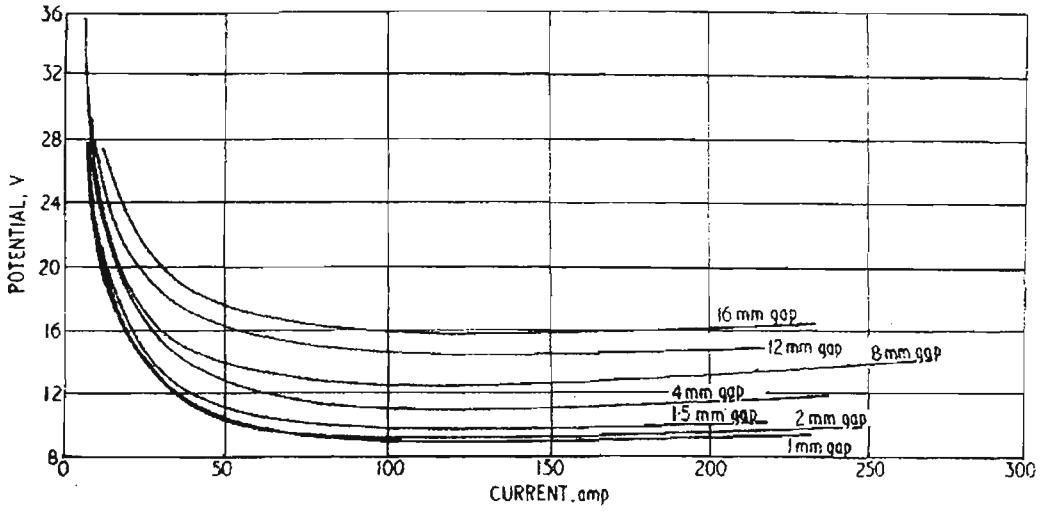

Figure 8.1 GTAW arc characteristics: tungsten in argon [89]

In comparison to the GTAW process, there is a dearth of comparable, detailed V-I characteristics for the GMA process [90]. Figure 8.2 shows experimental results summarised by Jackson in 1960 [84], while Figure 8.3 shows more recent experimental results by Halmoy [9]. Figure 8.4 shows simulation results from [76] using the model of [85] applied to argon with 2% iron vapour. Sheath voltages are not included in this model.

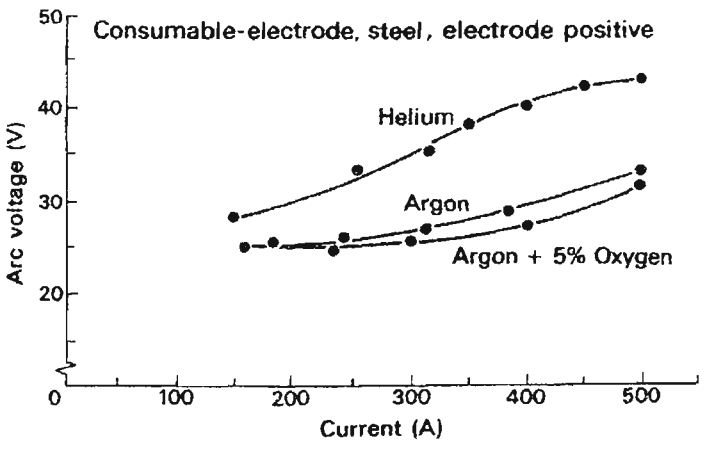

Figure 8.2 GMAW V-I characteristics [84]

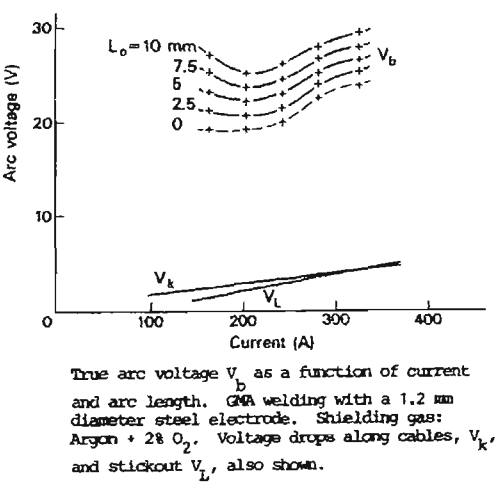

True arc voltage V_b as a function of current and arc length. GMA welding with a 1.2 mm diameter steel electrode. Shielding gas: Argon + 2% O_2. Voltage drops along cables, V_k, and stickout V_L, also shown.

Figure 8.3 GMAW V-I curves [9]

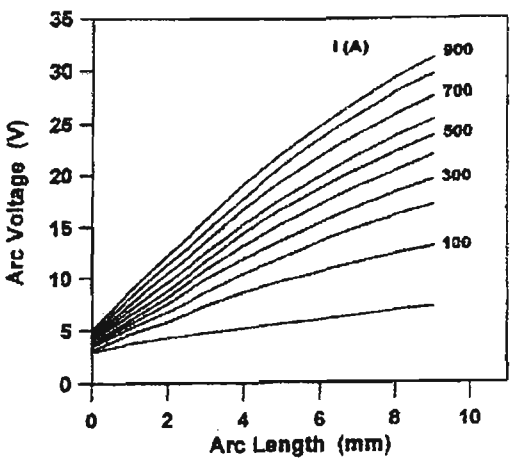

Figure 8.4 Simulation arc characteristics (from [76])

The characteristics of the form shown in Figures 8.1 to 8.3 can be represented by equation 8.2 [49, 91] or equation 8.3 [92]. The latter is also known as Ayrton's equation, and does not model the rise in arc voltage at very low arcing currents.

$$V_{arc} = K_1 L_a + K_2 + K_3 I + \frac{K_4}{I} \tag{8.2}$$

$$V_{arc} = K_1 L_a + K_2 + K_3 L_a I + K_4 I \tag{8.3}$$

In these equations, L_a is the arc length, and constants K_1 to K_4 are evaluated for the set of test results obtained for a given set of physical conditions.

The V-I characteristic data is more difficult to obtain for the GMAW process than the GTAW process. The electrode used in GMAW is much smaller than that used in GTAW for a given current. It is difficult to apply a test current to a stationary GMAW electrode without the electrode being overheated, causing the loss of the test geometry. If the characteristics are obtained by performing continuous welding, then the spray transfer mode must be used. The arc length must be stable long enough to obtain valid voltage and current measurements, and the arc length must be verified visually. This type of testing cannot be done below the transition current, as the arc length is variable in globular and short-circuit transfer modes. Furthermore, there is a greater variety of shielding gas mixtures and electrode materials used for GMAW compared to GTAW, so there are fewer opportunities for correlation of results between various research activities.

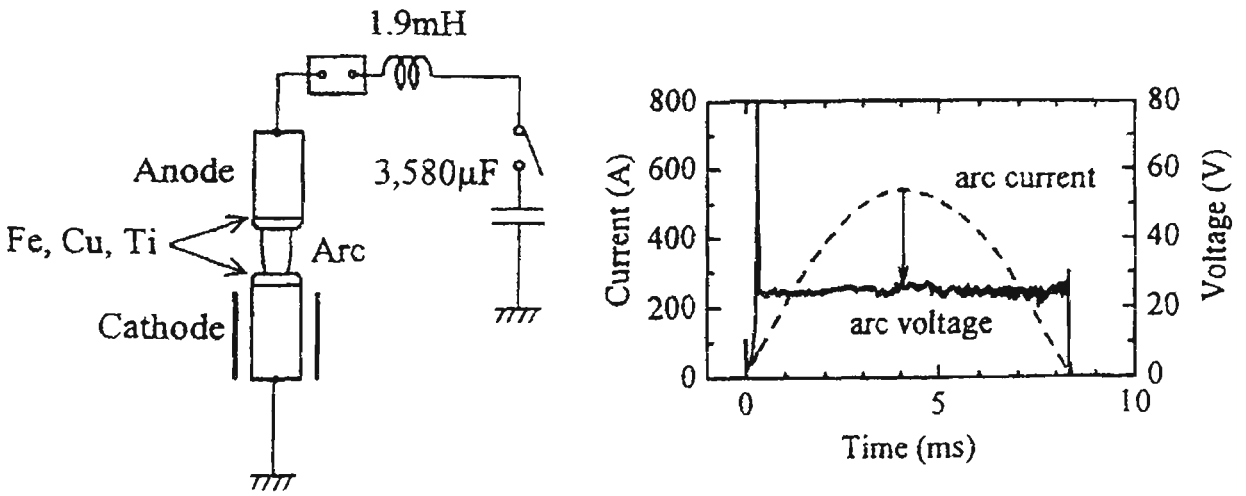

Figure 8.5 Circuit and waveforms of method by [88]

A different approach to obtaining V-I characteristics has been described in [88]. This approach involved the limited discharge of energy from a capacitor through an inductive circuit and the arc gap. The anode and cathode diameters were 26mm, enough to avoid excessive erosion by repeated arcs at high current. The arc was initiated by

rupturing a very thin copper wire placed across the electrodes. Figure 8.5 shows the circuit and waveforms for this technique. The technique used in the current work is a logical extension of this approach.

8.3 Experimental Equipment and Procedure

This section describes the procedure and equipment that were used in conjunction with the advanced power source described in Chapter 4 to obtain the arcing characteristics.

The testing procedure involves striking an arc between a test electrode (anode) and a workpiece specimen (cathode). The electrode is a short length of the desired GMAW wire held firmly in a modified contact tip by two "grub" screws. The cathode is a sample of the desired workpiece material approximately 70mm square, fastened to a larger sample support plate which is spring-loaded upward in the vertical direction against upper end-stops. This support plate is attached to two electrical solenoids which can rapidly pull it down against adjustable lower end-stops when required. Figure 8.6 in Appendix 8 shows the mechanical arrangement of the arc characterisation test rig, and Figure 8.6a below is a photograph of the test rig. Figure 8.7 in Appendix 8 shows the electrical arrangement. The height of the welding torch/contact tip is adjusted prior to testing so that the end of the electrode is just touching the workpiece. The lower end-stops are adjusted so that when the solenoids are activated, the workpiece is withdrawn to the required distance from the end of the electrode (i.e. the test arc gap).

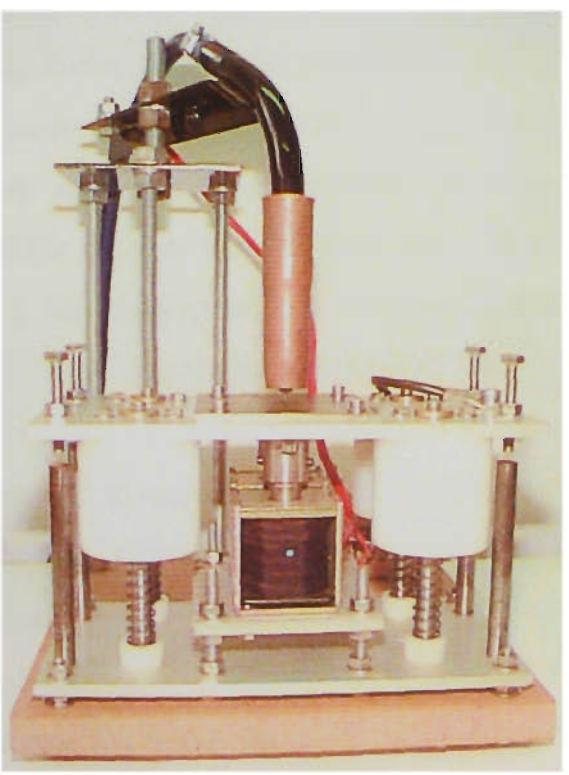

Figure 8.6a Photograph of Arc Characterisation Test Rig

The test sequence is automated and operates as follows. Initially, the electrode is in contact with the workpiece, and a small pilot current of 10A to 20A is established using the background current controller of the power source. After a 10ms delay to allow for build-up of this current, the test rig solenoids are activated to separate the electrode from the workpiece and establish the desired arc gap. A further 50ms is allowed for this step, as other tests have established that the solenoids can move the sample support plate against spring pressure by 10mm within 50ms. After a total delay of 60ms from the start of the sequence, the main current controller of the power source is enabled for 2 to 4ms, allowing the main testing current to be applied across the established arc. During this time, the current and voltage waveforms are recorded using a 12 bit digital storage oscilloscope. The main current on-time must be sufficiently long to allow the current to ramp to its final value (the rate of rise is limited by the internal inductance of the power source), and also to allow the voltage reading to settle to a steady-state value. After this is achieved, the main current, pilot current and solenoids are simultaneously deactivated. The total test time must be minimised to avoid erosion of the electrode during the test sequence, as the electrode is only 0.9mm to 1.6mm in diameter. Erosion of the larger workpiece is not a problem. The rapid turnoff capability of the advanced power source is definitely advantageous in this type of testing, as the main current can be quickly turned off at the completion of the test sequence, limiting the degree of electrode erosion.

For each combination of test current and arc gap, the above test sequence is carried out four times. Between each test, the degree of electrode erosion is evaluated both visually and by using feeler gauges to measure the arc gap setting (the sample support plate is manually pushed against the end-stops). If necessary, the end-stops are adjusted to correct for any erosion of the electrode. In tests, it was found that the greatest correction applied for erosion was 0.17mm (one sixth of a turn using M6x1.0 hex-head adjusting screws). This was necessary only for the highest test currents using the smallest diameter electrodes. The setup accuracy of the arc gap is realistically +/- 0.1mm.

After the last arcing test at each value of test current, the sample support plate end stops and torch height are adjusted so that the end of the electrode is firmly in contact with the workpiece. The solenoid driver is disconnected. The same current waveform that was applied during the arcing tests is applied to the short circuit. The voltage and current waveforms are again recorded, and these are used in the processing

of results to account for the voltage drops between the measurement points due to resistance of the various components. The primary consideration is the resistance of the test electrode, and in particular the variation in resistance at different testing currents and durations. At a test current of 400A applied for 3ms, the I^2t value is $480A^2s$. From the calculations of Chapters 6 and 7, the electrode resistance is not expected to alter significantly during the test sequence. The test results showed this to be the case. The short circuit resistance varied between test sets at different currents because either the electrode length changed as the electrode tip was "dressed" at the start of each test set, or the electrode was replaced whenever it became too short.

The arcing characteristics of a number of shielding gases were obtained, as summarised in Table 8.1. Arc lengths of 1mm, 2mm, 3mm and 4mm were tested. Unfortunately, the characteristics of carbon dioxide using a 0.9mm diameter electrode could not be obtained due to the high degree of erosion at the tip.

Table 8.1 Summary of Arc Characterisation Tests

Figure No.	Shielding Gas Composition	Electrode Diameter & Material	Workpiece Material	Arc Gap Range (mm)	Current Range (Amperes)
8.9	Ar-16%CO_2-3%O_2	0.9mm MS	Mild steel	1.0 – 4.0	40 - 375
8.10	Ar-16%CO_2-3%O_2	1.2mm MS	Mild steel	1.0 – 4.0	40 - 475
8.11	Ar-23%CO_2	0.9mm MS	Mild steel	1.0 – 4.0	40 - 375
8.12	Ar-23%CO_2	1.2mm MS	Mild steel	1.0 – 4.0	40 - 475
8.13	CO_2	1.2mm MS	Mild steel	1.0 – 4.0	40 – 525
8.14	CO_2	1.6mm MS	Mild steel	1.0 – 4.0	40 - 525

8.4 Results

Figures 8.9 to 8.14 in Appendix 8 show the data points for the V-I characteristics of each shielding gas, as listed in Table 8.1. The dotted lines in these figures are the family of curves representing the equation:

$$V_{arc} = V_0 + E_a L_a + R_a I \tag{8.4}$$

This equation is a simplified version of Ayrton's equation (8.3), since it does not account for a contribution to the arcing voltage by the term L_aI. V_0 is the arc voltage at zero arc gap and no current, and may be considered to be the minimum sheath voltage. E_a is the voltage gradient in the arc column, in V/mm. R_a is the arc resistance. The

values of V_o, E_a and R_a are found by performing a least-squares fitting of the data points in the figures to equation 8.4. It can be seen that the dotted lines provide a reasonable fit to the data, considering the degree of scatter. The omission of an L_aI term appears justified: The distance between data points for 1, 2, 3 & 4mm at a given current does not significantly change as the current is increased from 50A to 400A. The values of V_o, E_a and R_a determined from the data are listed in Table 8.2.

Figure 8.8 in Appendix 8 shows two typical sets of voltage and current recordings taken during the tests. The left-hand graphs show the response of the arc voltage to an 80A step, with the ramp rate being 483 A/ms. The arc voltage stabilises after approximately 1ms. The right-hand graphs show that when the arc is excited with a 480A step at a ramp rate of 409 A/ms, the response of the arc voltage is completely different, and far less time is required for the voltage to stabilise once the current reaches its steady state value. In both cases, the voltage and current data used in the arc characteristic graphs is found by taking the average value of each variable between the time when the voltage has settled and the time just prior to current turnoff.

Table 8.2 Summary of Arc Constants

Figure No.	Shielding Gas Composition	Electrode Diameter & Material	V_0 (Volts)	E_a (V/mm)	R_a (mΩ)
8.9	Ar-16%CO_2-3%O_2	0.9mm MS	15.3	1.82	21.4
8.10	Ar-16%CO_2-3%O_2	1.2mm MS	14.5	2.00	18.3
8.11	Ar-23%CO_2	0.9mm MS	15.2	1.87	25.9
8.12	Ar-23%CO_2	1.2mm MS	14.3	1.95	21.9
8.13	CO_2	1.2mm MS	17.2	3.35	19.0
8.14	CO_2	1.6mm MS	15.8	3.34	19.3

8.5 Discussion of Results

This section compares the results of the previous section to those of earlier research, and also discusses the errors and limitations of this method of arc characteristic measurement.

The voltage measurements carried out in this chapter are in broad agreement with those shown in Figures 8.2 and 8.3 from earlier experimental research in GMAW arc characteristics. It is evident that the GMAW arc generates higher voltages than the GTAW arc (Figure 8.2). There are, however, significant detail differences in the

characteristics found in this chapter compared to earlier work. Both Figures 8.2 and 8.3 show clear non-linear V-I relationships, whereas our results in Figures 8.9 to 8.14 tend to indicate more regular and linear behaviour across a very wide current range (there are, of course, some data which show exception to this). The minima found in Figure 8.3 do not appear in the results of this chapter. Also, the rise in voltage for very low currents was not observed in our tests, which operated down to 40A.

There are obviously large differences in experimental procedures used to obtain these characteristics. In particular, earlier results were obtained from stable open-arc welding processes, while the results presented here use an arc which is sustained at high current for only a few milliseconds. There are at least two effects at work under these two extremes. Firstly, the initial surface temperature of anode and cathode are lower under pulse testing. The anode surface is expected to heat up more rapidly than the cathode due to its lower thermal mass. The "erosion" of the anode observed during testing was actually the end of the "dressed" anode being molten to form a smooth hemispherical end. The sample cathode showed some minor pitting, indicating that the localised heating was also sufficient to melt the material at the arc root. Thus it might be concluded from the physical evidence that the surface temperature by the end of the test approaches that encountered in steady state welding. Secondly, the arc roots are not guaranteed to form in positions which minimise the arc length, so that it is equal to the arc gap set up in the experiment. Mobility of the cathode spot is influenced by surface oxides and their location [78], and tungsten-argon experiments have shown that arcs at low currents are positionally unstable [89]. During the initial stage of our testing, a low pilot current of 10 to 20A is used to sustain the arc while the cathode is drawn away from the anode. This condition may encourage arc wandering. When the main current is applied, the arc tends to "straighten" as thermal and surface conditions stabilise. The above phenomena may explain the waveforms shown in Figure 8.8 (Appendix 8). It was observed that in about 25% of tests conducted using argon-based shielding gas, the arc voltage did not stabilise as shown in Figure 8.8, but continued to oscillate throughout the duration of the main current pulse. The voltage was always higher than the final voltage of "successful" tests. For CO_2 shielding gas, this phenomenon occurred for over half of the tests. Increasing the main current pulse time to allow the arc more time to stabilise did not solve the problem. When longer pulse times were used, the anode tip would be excessively heated and the arc gap would increase during the test.

Interestingly, the arc characterisation tests performed in this chapter simulate electrical conditions encountered at the start of the arcing period in short-circuit transfer welding as described in Chapter 5. At the short circuit rupture, the current is in the order of 10 to 20A. Shortly after the rupture is completed, the current is increased rapidly to Iarc_max, which is in the order of 250 to 400A, and is applied for Tarc_max of 1.5ms. If some or all of the same mechanisms are at work in a "hot" weld as in these pulsed tests, then the arcing voltage can be expected to vary in the initial stages of each arcing period even though the arc gap may be the same. If this is the case, then the instantaneous feedback voltage cannot be successfully used during Tarc_max to adjust the current in order to instantaneously regulate arc length accurately.

The electric field strength E_a was found to be approximately 1.90 V/mm for argon-based shielding gases, and 3.35 V/mm for CO_2. In imperial terms, these are 48 V/in. and 85 V/in., respectively. These values are significantly higher than those obtained by Lesnewich [5], quoted at 20 V/in for argon and 45 V/in for CO_2. The conditions under which these figures were obtained are not specified, but from other tests it can be inferred that spray transfer was used with arc lengths of up to 0.5in. (12.7mm). The simulation results of Jonsson *et al.* [78] indicate that in argon-based shielding gases with 2 to 5% oxygen, the electric field intensity at the centre of the arc is a minimum of 0.8 V/mm at a distance of 6mm from the anode, where the arc gap is 10mm. However, the field intensity increases dramatically for distances of 3mm or less from the anode. Similar results in [93] show an average field strength of 1.8 V/mm over a distance of 4mm from the anode for a 100A arc in argon using aluminium electrodes. This increases to 2.3 V/mm at 250A. Over an arc gap of 10mm, these average figures are reduced to 1.2 and 1.5 V/mm, respectively, while over a 2mm arc gap they increase to 2.6 and 3.6V/mm, respectively. It should be noted that these figures include the effects of "arc resistance" (ie the increase of voltage with current for a constant arc length) but not sheath voltages. Since the data in [93] is very limited, a direct comparison between these calculated figures of field strength and those in Table 8.2 cannot be made, because E_a and R_a components cannot be separated. However, the variable field strength along the arc axis, weakening as distance from the anode is increased, indicates that the linear approximation of equation 8.4 to model this effect will not be valid over long arc lengths. Its use in modelling the experimental data over more than 3mm of arc length is likely to introduce significant errors. Having stated this, it is worth noting that the experimental results of Halmoy (Figure 8.3) show that there is

a linear increase in arc voltage with arc length for a given current, for arc lengths of up to 10mm. The differences between experimental results and simulation studies need to be reconciled.

All of the arc characteristics in Figures 8.8 to 8.14 indicate that the arc resistance is independent of arc length. The change in voltage produced by a given change in current does not significantly alter for different arc lengths. The empirical results in Figure 8.3 also reflect this. However, the simulation characteristics of Figure 8.4 show that a 300A change in current will produce a significantly different change in voltage at, say, an arc length of 1mm than at 4mm. Again the differences between experiment and theory do not agree, and no good reason can be offered at this time.

The values of R_a listed in Table 8.2 indicate that the arc resistance in argon-based gases is decreased as electrode size increases, while for carbon dioxide the electrode size is inconsequential. This might be expected if the differences in arc shapes are considered. In argon-based gases, the arc tends to envelop the end of the electrode [6, 73], so the arc root is expected to be influenced by the geometry of the electrode. For CO_2, the arc is severely constricted due to dissociation of the diatomic gas, so the anodic area, or arc root, is confined to a narrower area. The high temperature regions of the arc are also narrower [73], and the current enters the anode at a point rather than on a surface distribution. Thus electrode size is not expected to significantly alter arcing conditions. Based on the data collected in this chapter, it cannot be conclusively stated that electrode size has an effect on the apparent "arc resistance" in argon-based gases, especially when taking into account the scatter in data and the simple modelling of equation 8.4.

The form of equation 8.4 implies that at zero arc length, the sum of anode and cathode sheath voltages is a function of current:

$$V_{sheath} = V_0 + R_a I \tag{8.5}$$

This is extrapolated from the collected data, and is represented by the zero arc gap line in Figures 8.9 to 8.14. The dashed line in Figure 8.3 by Halmoy is an equivalent result. The sheath voltages are considered to be current dependent. However, other experimental work [88] has shown that the sum of sheath voltages is almost independent of current, in the range of 30A to 550A. The tests in [88] used a pulsed current of approximately 10ms duration, the electrodes were 26mm in diameter, and the tests were conducted with argon, helium, air and sulphur hexaflouride (SF_6). Despite the differences in test equipment and procedure, it is difficult to see how such a difference

in results can arise. To resolve these differences, further tests could be performed using our equipment with larger electrodes and longer arcing times, so that valid comparisons can be made with the findings of [88].

8.6 Summary

A method using a stationary electrode with a high current pulse of short duration has been used to obtain the arcing characteristics of various shielding gases with a range of electrode sizes, closely reproducing conditions encountered in the gas metal arc welding process. The results show the same trends as those obtained experimentally by other researchers, but there are some discrepancies with the findings of theoretical studies. Further testing is needed to assess the effect of factors such as pulse duration and electrode size on the repeatability of the results. Valid comparisons also need to be made between results of this method and more conventional techniques using the same combination of consumables.

As stated in section 8.1, the work described in this chapter was undertaken at an early stage in the project, in anticipation of using the results as part of a closed loop process control strategy later in the project. Unfortunately, preliminary testing of arc length control during the initial stages of the arcing period did not show any improvement in process stability. Other, more promising control techniques were investigated and the arc characteristic data is not used elsewhere in this report.

Nevertheless, the pulsed-current method of arc characterisation has been show to produce results that are in general agreement with previous empirical results. This novel method overcomes many disadvantages of previous methods, and offers a very convenient and efficient way of measuring the arcing characteristics over a very wide range of conditions. Furthermore, it simulates the prevailing conditions during transient arcing in short circuit transfer more closely than any of the previously reported methods.

Chapter 9

Visualisation of the GMAW Process

9.1 Scope

The ability to observe the GMAW process visually can be a very powerful tool for gaining an understanding of the process' behaviour. This chapter describes the development and function of the photographic equipment used to obtain single still photographs of the metal transfer behaviour during the weld. The camera used is a progressive-scan CCD type with the ability to take an exposure that is externally synchronised via a simple electrical signal. When used in conjunction with the welding controller described in Chapter 4, exposures can be synchronised to key events in the process, rather than being taken at random. A novel approach to this type of photography is to use a high-powered xenon flash unit to front-light the subject, so that a high quality "natural" colour image of the weld pool, electrode and droplet can be obtained, giving unprecedented detail of the molten metal and surrounding area. The flash unit is described in this chapter, as well as various technical problems that needed to be addressed. The results of this approach to process visualisation are shown at the end of this chapter, and are also used extensively in this thesis to illustrate various phenomena.

9.2 Background

Process visualisation has been used as a research tool since the earliest investigations of the arc welding process [94, 95]. Powerful arc lamps have been used to backlight the weld, altering the high contrast between the arc and surrounding objects. The profile of the weld pool, electrode and metal droplets is made clearly visible to high speed photographic equipment, providing that the correct exposure is used. The arc becomes almost invisible against the bright background and the metal can be filmed in silhouette [96, 97, 98]. The back lighting must be rated at several kilowatts to be suitable for observation of welds at currents of up to around 300A. The backlighting method is not considered adequate for very high current GMAW observations since the power requirements for the back light become prohibitive.

The "laser shadow-graph" or "laser backlighting" technique overcomes the problem of observation at very high welding currents. Typically, a helium-neon laser is

used to backlight the weld and various narrow band-pass filters are used to remove the arc light, so only the laser light reaches the camera to record what is visible. The He-Ne laser operates at 633nm, while the arc light is spread over a very wide spectrum. Thus only a low power light source is needed (usually 20-50mW). One of the first uses of this method was by Quigley *et al.* in 1971 [99]. This method has since been widely used by many researchers because it is effective and relatively inexpensive.

To capture images of the process with reasonable clarity, high speed photographic equipment must operate at 2,000 to 10,000 frames per second, and recording may be film-based or electronic. Faster shutter speeds reduce exposure time, which minimises blurring of images of rapidly moving objects. This benefit must be offset against the need for more light if the film or vision sensor is not sufficiently sensitive.

Results using the more traditional film-based techniques have been presented by [96, 98, 100, 101], while [102] shows results using video. At present, the cost of a high framing speed video system is several times greater than a film camera of comparable framing rate. The resolution of current high speed video systems is far less than that of 16mm film, and 8 bit (256 level) video systems cannot convey the large differences in contrast that film can. Conversely, the filming technique is less convenient to use because the film must be processed before the results can be evaluated. Several attempts may be needed to find the exposure settings which give the best results as judged by the human eye. This becomes more critical for filming short-circuit GMAW transfer with a tungsten arc backlight, but is less important for He-Ne laser backlighting.

Recent work in [103] uses a 35mm SLR (single lens reflex) camera with neutral density filters to obtain excellent colour photographs of pulsed GMA welding. The subject is back-lit with a 2kW tungsten-arc floodlight. Interestingly, the camera lens does not need to be in line with the light source and welding arc, so photographs can be taken "looking down" at the weld pool at angles of up to 30^0 from horizontal. The weld pool surface is illuminated by the combination of arc light and floodlight. The greatest contribution appears to come from the latter. The advantage of this method is very low cost, but the image is only a still photograph, and it cannot be synchronised to an event of interest during the weld cycle.

9.3 Objectives and Requirements of Visualisation System

The success of [103] in obtaining exciting high quality colour photographs of the GMAW process at low cost encouraged the development of a more sophisticated electronic system with these features:

CCD-based camera for instant result evaluation (no film processing)

Full colour capability, minimum resolution 640 x 480 pixels per colour

Initiation of exposure controlled from DSP welding controller

Low cost (relative to high speed filming)

Subject illumination by xenon flash front lighting.

The use of reflective front lighting to illuminate the weld area to obtain additional surface detail is the main novelty of this approach. This proved more difficult to achieve than initially anticipated. The reflectivity of the electrode, droplet, weld pool and workpiece surface is expected to be less than 0.33, which is the reflectivity of molten steel. So the light reflected from the solid surfaces and incident on the camera CCD array must be at least equal in intensity to the arc light which is emitted directly to the CCD array. The matching of these two sources of light requires a very powerful front-lighting source concentrated on the subject; two to three orders of magnitude greater than can be provided with a flood light. This is discussed in the next section.

The ability to synchronise the exposure to the process based on any event which can be detected through the electrical signals (e.g. 1.50ms after the start of the short circuit) is used as partial compensation for the fact that this system allows only one exposure to be taken, whereas filming can capture tens of milliseconds of welding, during which a number of events can be observed.

Finally, the cost of the final system is approximately one quarter that of a conventional high speed film camera. For research carried out on a limited budget, the cost factor cannot be ignored.

9.4 System Description and Development

Figure 9.1 is the electrical block diagram of the photographic system. The command to take an exposure is given by a digital output of the DSP welding controller, so the timing of the photograph is under software control. The synchronisation unit generates a delay between triggering signals to the flash unit and the camera, so that the camera exposure and flash light output coincide. The flash unit is custom made, and is

known to have a 50μs delay between triggering and maximum light output. Synchronisation was achieved by experimentation, and the camera was found to have an internal delay of 500μs. So the total delay between the trigger command from the DSP controller and the start of the exposure is set at 500μs, or 0.5ms.

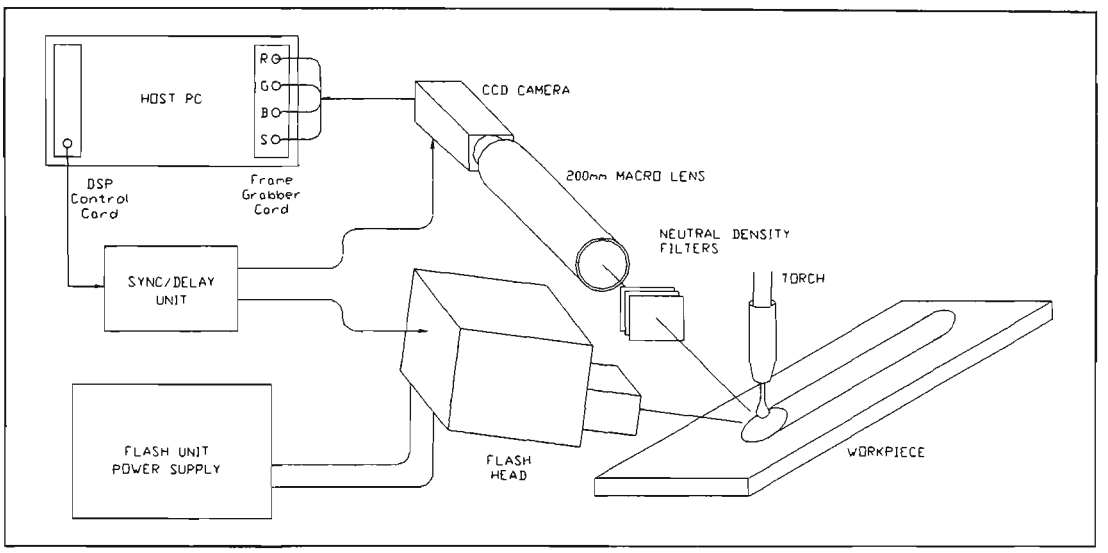

Figure 9.1 Block Diagram of Photographic System

The subject area of weld pool, arc and electrode is no more than a 20mm square, so a suitable macro lens is required to focus the image onto the CCD camera array. The correct exposure for a given photographic condition is determined experimentally by adjusting the lens aperture and adding or removing neutral density filters. To maximise the depth of field, an aperture of f16 to f32 is used.

Correct operation of the camera/lens/filter/frame-grabber system proved to be relatively straightforward. However, providing sufficient lighting of the subject was much more difficult. Before the custom high-powered flash unit was constructed, a number of alternative lighting schemes were tested. The first test consisted of using a 2kW tungsten arc floodlight to front-light the weld area, and a 500W floodlight for backlighting. Exposures were taken during the short circuit, when light output from the welding process is minimal. Figure 9.2 in Appendix 9 shows a typical result, with the camera looking down on the subject at an angle of approximately 10^0. Clearly, there is insufficient reflected light from the surface for a balanced photograph. The amount of radiated light from the molten metal bridge is much higher than the nearby weld pool, let alone the workpiece. The "ghosting" around the electrode is called "smear" by the camera manufacturer, and is due to very bright objects captured on a dark background. It is more pronounced at high shutter speeds ($1/4000^{th}$ sec in this case) because of

electronic charges generated beneath the CCD array vertical shift registers being comparable to the short light integration signal. This can be avoided by reducing the contrast of the subject, or increasing the general lighting level.

The amount of lighting required for an improved photograph makes the use of floodlighting impractical. The possibility of using xenon flash lighting was initially explored by comparing the light intensity of a 2kW flood light to that of a medium power commercial hand-held flash unit. This was done using an inexpensive photodiode with an acceptable response time of 3.5μs. Measurements at a distance of 750mm from the light sources (to avoid saturation of the sensor) showed that the xenon flash produced a peak light output 24 times greater than that of the floodlight. The duration of the pulse was approximately 1.2ms, measured at 25% of peak output. The peak was reached at 250μs after the trigger signal, making the commercial flash very easy to synchronise with the camera, whose shutter time would be set to $1/8000^{th}$ sec (125μs). Figures 9.3 and 9.4 in Appendix 9 are photographs of GMAW short circuits, using the commercial flash to front-light the weld area. The increase in light output over the flood-light is evident. The surface details of workpiece and weld pool are much clearer, and the bright glow from the molten bridge is tamed, so the bridge shape is clear.

Attempts to take photographs during the arcing period using the commercial flash were not successful, as there was excessive contrast between the arc light and the reflected light from the metal surfaces, even for low arcing currents of 20 to 30A. If the exposure was adjusted to obtain good rendering of the metal surfaces, the arc would be over-exposed to the point where the CCD array would be "saturated", showing the arc as pure white. If the exposure was adjusted so that the arc appeared transparent, the metal surfaces were too dark and details were lost. (These details could not be recovered by post-processing the image, because the dynamic range of the camera is limited to 8 bits per colour, or 256 levels. Unfortunately, contemporary CCD-based vision systems lack the dynamic range of film.) The difference in exposure settings of the two extremes was between 7 and 8 f-stops, indicating that the light output of the flash unit would need to be increased by a factor of 2^7 (128) to 2^8 (256).

An investigation of the electrical aspects of the commercial flash unit showed that the electrical energy stored in the 6.8μF capacitor charged to 400V is 0.54J. Enquiries with flash tube and capacitor manufacturers indicated that with the time and resources available for this aspect of the project, it would be feasible to construct a custom high-powered xenon flash unit which would use 163J of stored energy (145μF

capacitor charged to 1500V). The flash duration was designed at 100μs, so that all of the light produced by the unit is used within the camera exposure time of 125μs. The flash tube was derated for a minimum operational life of 10,000 flashes. Figure 9.6 in Appendix 9 is the electrical schematic of the unit. Due to the bulk of the transformer, capacitor, inductor and diodes, the unit is constructed in two sections; the flash head and the power supply. Electrical testing of the completed unit verified that the peak electrical input to the flash tube is approximately 2.1MW. The current and voltage and power waveforms are shown in Figure 9.7. The flash tube manufacturer specifies a typical conversion efficiency of 60%, so around 98J of light energy is produced, at a peak rate of 1.2MW. Of course, not all of this light is in the visible spectrum, and not all of the visible light can be directed onto the subject area.

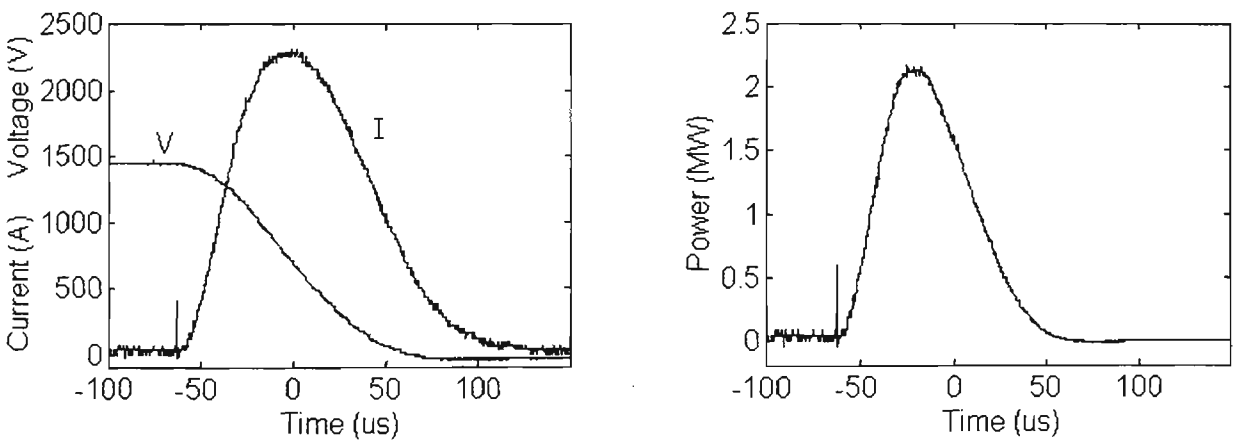

Figure 9.7 V, I and P waveforms for flash unit

The concentration of light onto the subject area proved to be a major technical hurdle. The first-design flash head, based on a pseudo-parabolic reflector aiming the reflected light at a focal point (Figure 9.5 in Appendix 9), was found to be ineffective. The utilisation of the available light was so poor that no improvement in subject lighting was gained over the less powerful commercial flash unit. The second-design flash head uses a different principle. Mechanical details are shown in Figures 9.8 and 9.9 in Appendix 9. The optics, consisting of a cylindrical mirror and two plano-convex lenses, are designed to produce an image of the flash tube at a distance of 76mm from the front of the flash head. Thus the subject can be placed anywhere on the axis of the image so that it is maximally illuminated. The arc contained within the flash tube is 76mm long and 7mm in diameter, so the "target area" would be of similar size. Calculations were performed to calculate the ratio of light incident on the camera lens due to direct radiation from the arc (Q_{arc}) compared to that due to reflection of the flash light from the

metal surfaces (Q_{refl}). Based on assumptions of 2200W power dissipation in the welding arc, 60% conversion efficiency for the flash tube, 0.33 reflectivity of the metal surfaces, and various geometrical considerations of the optical system, the ratio Q_{arc}/Q_{refl} was estimated to be 20. The dynamic range of the CCD camera is 2^8 or 256 levels, so it is expected that a usable image could be obtained of a 22V, 100A arcing condition.

At the time of the design, it was known that a better configuration would use two custom cylindrical mirrors to focus the light onto a smaller "target" of , say, 10mm square, thereby improving the light utilisation even further. However, the cost and time delay of having such lenses constructed precluded this option. The design shown uses readily available circular lenses, and was constructed within the available time. The author is greatly indebted to Dr. Y. Mao for the optical design and mechanical construction of the flash head.

Figure 9.10 below is a photograph of the completed flash unit as installed on the welding test bed.

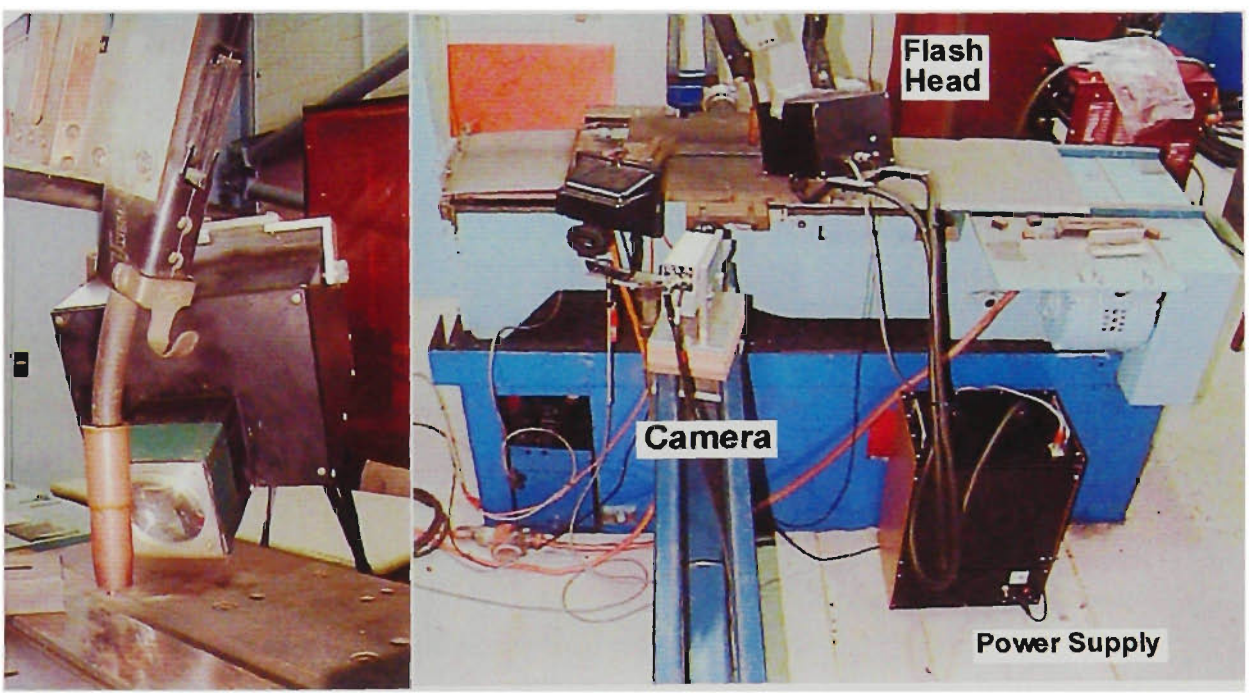

Figure 9.10 Photograph of installed flash unit

9.5 Results and Conclusions

The photographic system described in this chapter is able to produce clear and visually exciting images of the GMAW welding process under short-circuit and low current arcing conditions. Figure 9.11 is a photograph of a short-circuiting event taken 2.5ms after the start of the short with an exposure time of $1/8000^{th}$ second. Figure 9.12 shows the droplet on the end of the electrode at an arcing current of 20A.

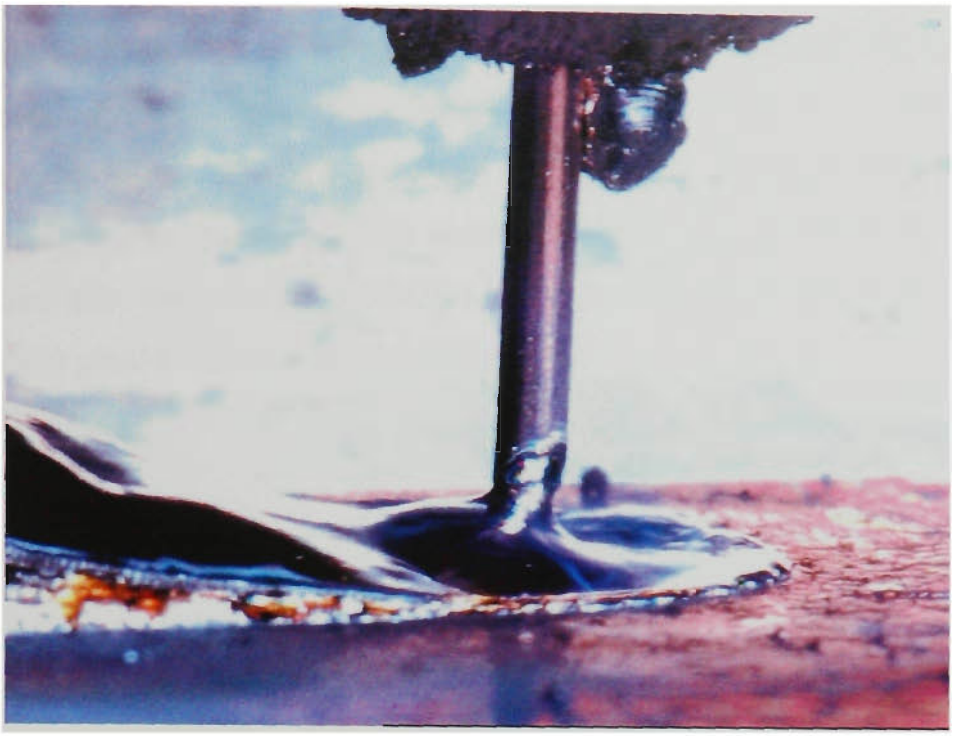

Figure 9.11 Photograph of short-circuiting event

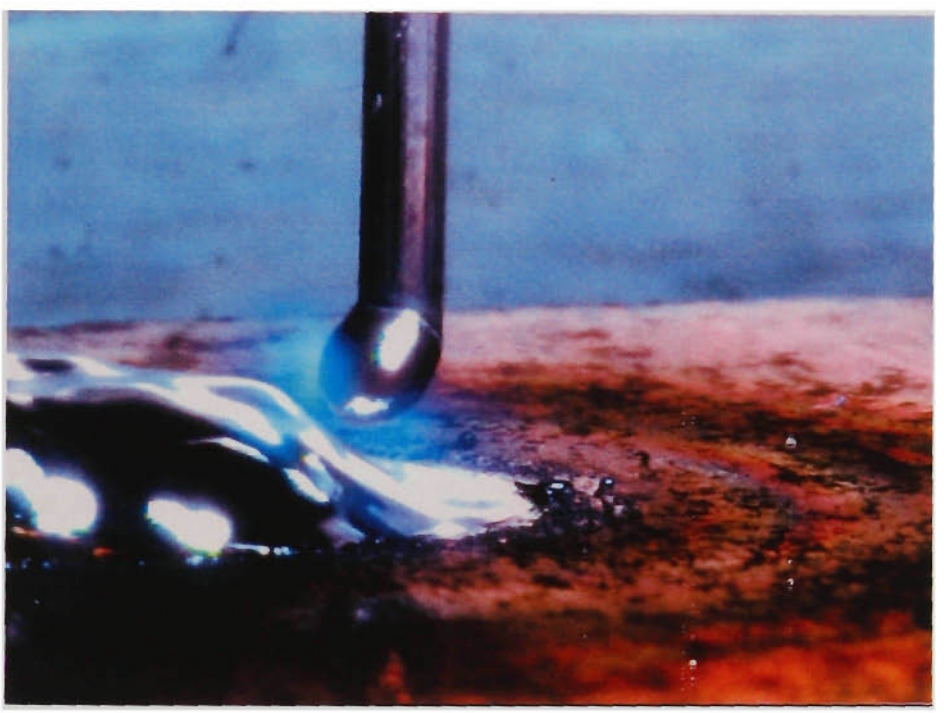

Figure 9.12 Photograph of arcing event at 20A

Unlike Figures 9.3 and 9.4, the short-circuit bridge in Figure 9.11 does not appear to glow, since the subject lighting is much more intense. In Figure 9.12 the arc is almost invisible, so the reflected light produced by the flash unit is more intense than the arc itself, at least at these low arcing currents. It was observed during various photographing sessions that the image could be improved if a reflective object was placed behind the workpiece, so that "excess" or "untargeted" light from the flash unit was redirected back onto the workpiece. Figures 9.11 and 9.12 exemplify this method.

Figures 9.13 to 9.15 are images obtained at arcing currents of 100A, 225A and 400A, respectively. The diminishing effectiveness of the flash unit at higher arcing current becomes evident. At 100A, the shape of the droplet can be readily distinguished, although the light from the arc partially obscures the side of the droplet that faces away from the flash unit. Under these conditions, the light reflected from the droplet surface is only slightly greater than that produced by the arc.

Figure 9.13 Photograph of arcing event at 100A

At an arcing current of 225A, the visibility of the droplet is not significantly degraded. The depression of the weld pool is evident in Figure 9.14. The rim of the pool "crater" is illuminated by a combination of arc light and flash light. At 400A (Figure 9.15), the arc becomes opaque and obscures detail of the droplet and weld pool. To obtain results under high current conditions that are comparable to those at lower currents, the optical design of the flash head would need to be improved as discussed in the previous section. If this proves inadequate, then the light output from the flash tube could be increased, at the expense of operational life.

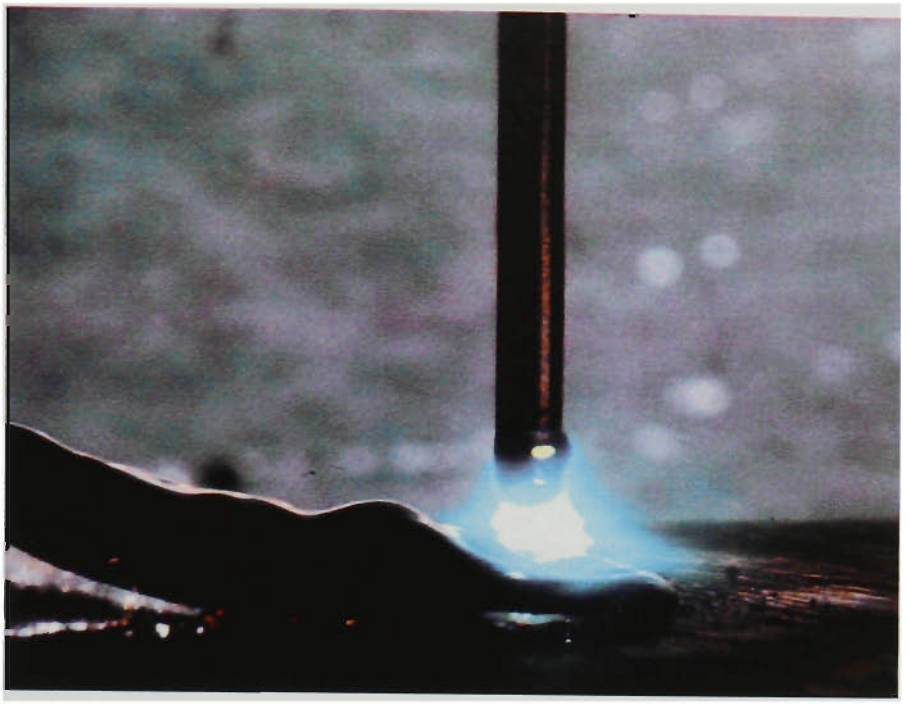

Figure 9.14 Photograph of arcing event at 225A

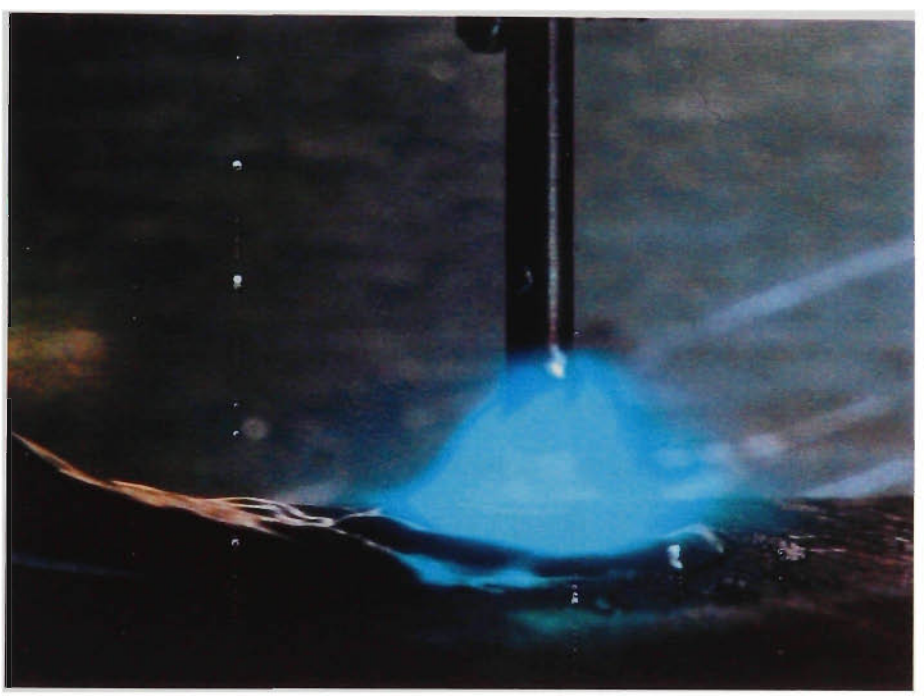

Figure 9.15 Photograph of arcing event at 400A

In summary, a novel visualisation system has been built which can produce outstanding, detailed images of the GMAW process across a wide range of conditions. The system is synchronised to the process by the controller described in Chapter 4, so exposures can be obtained at the desired point within the weld cycle. The images produced by this system, used extensively in other chapters, provide an effective means of evaluating process behaviour.

Chapter 10

Investigation of the "Open Loop" Controlled Short Circuit GMAW Process

10.1 Scope

This chapter investigates the performance of the "open loop" control method described in Chapter 5. A large number of welding trials were performed using 0.9mm mild steel electrode with both CO_2 and Ar-23%CO_2 shielding gases. The information obtained from these trials is used for three purposes. Firstly, the behaviour of the process using this type of current waveform control is explored in detail, to determine the behavioural differences and advantages over conventional power sources. Secondly, the results are compared against those of computer simulations which predict process behaviour based on melting rate considerations. Thirdly, a process performance benchmark is established, against which the "closed loop" control method can be compared. The analysis of process performance presented here takes a "wholistic" approach to evaluating process performance, encompassing disparate parameters such as stability index, spatter levels, fusion areas and "quality" of the weld bead. The aim is to convey as complete an assessment of the weld process as possible.

The major findings of this chapter are summarised in section 10.7. Sections 10.3 and 10.4 present the results and detailed discussion of process behaviour. Section 10.5 uses the photographic techniques developed in Chapter 9 to verify hypotheses regarding arc length and pool depression formed in sections 10.3 and 10.4. Section 10.6 compares simulation results of the "open loop" process to actual experimental results to show that process behaviour is dominated by melting rate considerations.

10.2 Test Conditions

10.2.1 Physical Process Conditions

All welds are performed with CIGWELD Autocraft LW1-6 0.9mm copper-coated mild steel electrode wire to AWS A5.18 ER70S-6 specification. The welding geometry is downhand bead on plate using 6mm descaled hot-rolled plate. The electrode angle is always 90^0 to the workpiece surface.

The wire feed speed is 5.7 m/min for all tests, being consistent with tests performed in previous chapters. It would be desirable to perform comprehensive tests at more than one wire feed speed. However, the amount of work required to thoroughly investigate process performance at just one speed precluded comparable tests at other speeds. A limited number of tests were performed at lower wire feed speeds for comparative purposes (section 10.3.9).

The weld travel speeds are 390mm/min for Ar-23%CO_2 and 195mm/min for CO_2. The reason for the difference is partly historical and partly due to process requirements. When the testing was commenced, all Ar-23%CO_2 welds were found to perform satisfactorily at 390 mm/min. When the CO_2 tests were subsequently attempted, it was not possible to obtain a satisfactory weld bead at the same travel speed using similar electrical parameters because of excessive "flash" at the weld toe for all reasonable arcing parameters. However, a reduction in travel speed with no other changes gave a dramatic improvement in bead appearance, so all CO_2 tests were continued at this speed. Refer to section 10.3.7 for further discussion of this issue.

Contact tip to workpiece distances (CTWDs) are 8mm & 16mm for Ar-23%CO_2 and 12mm & 20mm for CO_2. The reasons for the difference are similar to those above. Initial tests using Ar-23%CO_2 were performed at CTWD values of 8mm and 16mm with satisfactory results. When the CO_2 tests were attempted at the same travel speed and CTWD, the initial results were unsatisfactory. A satisfactory condition was found for a CTWD of 12mm and a travel speed of 195mm/min. It was desirable to perform another set of tests for an 8mm difference in CTWD, leaving 4mm or 20mm as options. The former was impractically low, so the latter was chosen.

Although the differences in CTWD and travel speed do not make the results directly comparable, this is of little consequence. As the results of sections 10.3 and 10.4 demonstrate, the same important behavioural trends are followed under all the different conditions.

10.2.2 Electrical Parameters

The "open loop" control method used in these tests is described in Chapter 5. The current waveform is illustrated in Figure 10.1.

As discussed in Chapter 6, correct function of the CTWD estimation algorithm requires that the short-circuit welding parameters be kept constant. Their values are:

Isc_ramp	100A/ms	Short circuit current ramp-up rate
T_wetting	0.5ms	Wetting-in time for Ar-23%CO_2
T_wetting	1.5ms	Wetting-in time for CO_2.

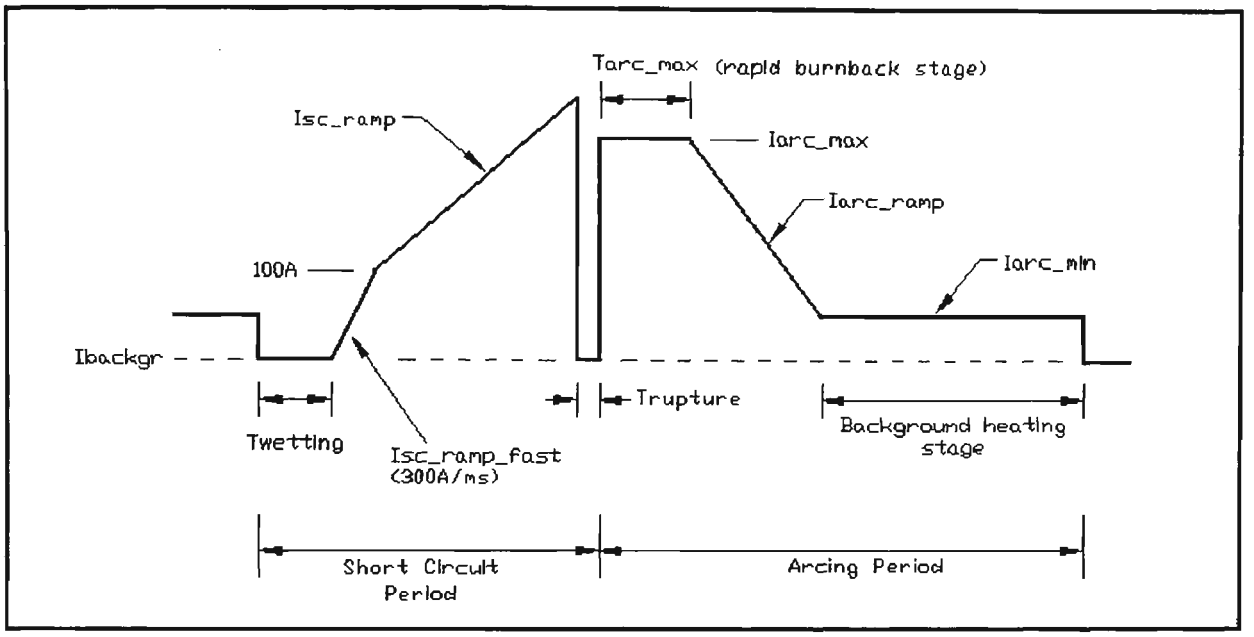

Figure 10.1 "Open Loop" controlled current waveform
Current (vertical) vs Time (horizontal)

These parameters were found to be suitable for 0.9mm MS electrodes, although it should be noted that for differing electrode materials or diameters, the wetting time and ramp rate would be modified, and the CTWD estimation factors would require recalculation.

The arcing parameters which could potentially be adjusted during the testing or "mapping" of the process are:

I_backgr	Background current during wetting-in & short-circuit rupture
Iarc_max	Arcing current immediately after short-circuit rupture
Tarc_max	Time for which Iarc_max is applied
Iarc_ramp	Rate of current fall from Iarc_max to Iarc_min.
Iarc_min	Steady-state arcing current.

The complete mapping of the process by individual adjustment of each parameter is beyond the scope of this project, even for a very limited investigation at one wire feed speed. To make the exercise realistic, three of these parameters were fixed, for the following reasons:

I_backgr 20A Adjusting this would be the same as varying Iarc_max &

		Iarc_min. A sufficiently high current is required to ensure the arc does not extinguish at the end of the short-circuit rupture. From experience, 20A meets this requirement for both CO_2 and Ar-23%CO_2.
Tarc_max	1.5ms	Adjusting this value is expected to significantly influence the arc length at the end of the rapid burnback stage, but this can also be done by adjusting Iarc_max. A time of 1.5ms was found to produce stable stub-free welds for a wide range of Iarc_max, but its value is not claimed to be optimum. Values from 0.75 to 2.0ms achieve similar results. Values higher than this may cause unwanted droplet detachment during arcing as the Iarc_max-Tarc_max parameter pair essentially emulates I_p-T_p parameters of pulse spray transfer [72, 104, 105].
Iarc_ramp	150A/ms	Adjustment of this parameter influences the burnoff rate just after the rapid burnback stage, and is also claimed to affect weld pool oscillation damping [19]. The chosen value is similar to the dI/dt measured for conventional power sources during the first quarter of the arcing period. Again, this value is not claimed to be optimal, but has been found to work satisfactorily.

Thus the two remaining parameters Iarc_max and Iarc_min are the variables to be adjusted during the arcing period, as these were found to have the greatest effect on the process.

10.2.3 Experimental Procedure

To ascertain the operating area of the process, a large number of tests were performed for various combinations of Iarc_max and Iarc_min. Current Iarc_max was adjusted in 25A increments and Iarc_min in 10A increments, to yield a test matrix with sufficient resolution to accurately determine the edges of the operating area.

Two 100mm long weld beads were laid down for each Iarc_max/Iarc_min combination. At approximately the midpoint of each weld, both oscilloscope and data

acquisition recordings of 1.0 second duration were taken of voltage and current. These were used to determine quantities such as stability index, mean current, average voltage, energy input and so on. The sampling time for oscilloscope recordings was set to 50μs (20kHz), while for the data acquisition system it was hardware-limited to 400μs (5kHz).

The stability index of each weld was defined by:

$$Stability\ Index = 1 - \frac{\sigma}{\mu} \tag{10.1}$$

where σ is the standard deviation of the weld cycle duration, and μ is the mean value of weld cycle duration. This measure of stability has been used by other researchers [43, 44, 45] to measure weld stability for conventional power sources.

It has been noted from experience that values of stability index above 0.65 correspond to good welds using the current waveform shown in Figure 10.1. Stability indices above 0.80 result in very high quality welds.

During each weld run, the process was visually observed by two operators, and a qualitative assessment of the amount of visual spatter noted. Although this is not a quantitative measure, it became evident during testing that due to the low amounts of spatter generated by this control method, it is easy for an operator to reliably judge the spatter level.

The levels of spatter were classified into one of six categories, each with a weighting from 0 to 5, as shown in Table 10.1. Since two welds were performed at each test condition, a spatter index ranging from 0 to 10 could be assigned to that condition.

Table 10.1 Spatter Assessment & Weighting

SPATTER ASSESSMENT	DESCRIPTION	WEIGHTING
low	Short, very fine sparks ejected from weld pool. No ball spatter. No sparks reach the surrounding work.	5
low - medium	Fine sparks with small glowing ball spatter. Small spatter may reach baseplate while still glowing. Typically less than 2 spatters per second	4
medium	Larger glowing ball spatter approx 1mm diameter. No more than 2-3 spatters per second.	3
medium - high	Larger ball spatter >1-2mm diameter. Typically 2-3 spatters/second. Sustained glow after coming to rest	2
high	Larger ball spatter >1-2mm diameter. Typically >5 spatters/second. Sustained glow after coming to rest	1
very high	Large ball spatter >2mm. Frequent ejection from weld, sustained glow after coming to rest.	0

Whilst a more accurate method such as mass measurement of captured spatter would have been preferable, it could not have been applied to hundreds of welds with the human resources available. Furthermore, this method is used daily by experienced operators as one of the key process quality indicators, in situations where quantitative measurement is impractical. From experimental experience, a spatter rating of 8 or higher can be considered to give a "low spatter weld". A rating of 10 is truly a "spatterless weld", where no material is visibly ejected from the welding area.

When all tests were completed, the beads for each weld condition were evaluated for appearance. Table 10.2 describes the weighting for each attribute considered important to the overall appearance. A bead quality index ranging from 0 (very poor and highly unlikely) to 15 (very good and quite possible) is assigned to each condition.

Table 10.2 Bead Quality Assessment & Weighting

PROPERTY	ASSESSMENT	WEIGHTING
Bead Ripple (as seen on surface of bead)	very low (not visible)	3
	low (visible)	2
	medium (evident/pronounced)	1
	high (unattractive)	0
"Flash" at Weld Toe	none (not visible)	3
	low (just visible)	2
	medium (quite plain/evident)	1
	high (unacceptable)	0
Ropiness of bead (variation in overall width or height)	none (not noticeable)	3
	low (noticeable)	2
	medium (evident)	1
	high (extreme)	0
Overall bead shape	good (flat u shape, large contact angle>150^0)	6
	OK (higher bead, moderate contact angle)	4
	poor (high bead, contact angle ~90^0)	2
	bad (high bead or v shape evident)	0

As a guide, the loss of one point in each category (total rating 11) would produce a weld bead that would be considered to have a "good" appearance. A weld with only one or two point loss would be considered "excellent".

The key properties of stability index, spatter index, and bead quality were then combined for each weld to produce an Overall Weld Quality Index calculated as follows:

$$Overall\ Weld\ Quality\ Index = \left(Stability\ Index \times \frac{Spatter\ Index}{10} \times \frac{Bead\ Quality}{15} \right) \qquad (10.2)$$

This gives a figure between 0 and 10, a useful indicator of the weld quality. Using the threshold values of 0.65, 8 and 11 cited previously, the overall weld quality threshold

would be 3.8. This may seem easy to exceed, but a deficiency in one area (eg stability) is usually manifested in other areas as excessive spatter and high bead ripple, reducing the overall rating rapidly. The above definition of overall weld quality is used only as an indicator. As will be discussed in later sections, there are a number of situations where this particular evaluation method is not applicable.

Finally, one material cross-section was cut from each weld bead pair. The end of the section was polished and etched with 15% Nital solution (85% ethanol, 15% nitric acid) to expose the fusion area of the weld. An electronic photograph was taken of each macrosection, and image analysis software was used to accurately measure fusion area, penetration depth, bead width and bead height.

10.3 Process Performance with Ar-23%CO_2 Shielding Gas

10.3.1 Scope

Tests were conducted to establish the operating range of the Ar-23%CO_2 process for a wire feed speed of 5.7 m/min at CTWD=16mm and CTWD=8mm. Figure 10.2a represents the test matrix for CTWD=16mm, while Figure 10.2b is for CTWD=8mm. These matrices can be considered to show the maximum extents of the process operating area for either case, using the fixed parameters specified in section 10.2.2. A subset of these settings would represent the "useful" operating area, where the combination of key characteristics such as stability, spatter and bead quality would be considered satisfactory by an operator. The "useful" operating area is calculated later.

Iarc_min	Iarc_max												
	150	175	200	225	250	275	300	325	350	375	400	425	450
10						Region1							
20					Cold workpiece								
30					X	X	X						
40					X	X	X	X		X			
50	Region 2			X	X	X	X	X	X	X			
60	Low		X	X	X	X	X	X	X	X		Region 4	
70	arc length		X	X	X	X	X	X	X	X			
80			X	X	X	X	X	X					
90			X	X	X	X	X	X					
100			X	X									
110													
120						Region 3							

Figure 10.2a Test matrix of Ar-23%CO2 process, wire speed=5.7 m/min, CTWD=16mm, Travel speed=390mm/min, 6mm MS plate

Iarc_min	Iarc_max												
	150	175	200	225	250	275	300	325	350	375	400	425	450
10						Region1							
20					Cold workpiece								
30													
40							X	X	X				
50	Region 2					X	X	X	X	X			
60	Low				X	X	X	X	X	X		Region 4	
70	arc length				X	X	X	X	X	X	X		
80				X	X	X	X	X	X	X	X		
90			X	X	X	X	X	X	X	X	X		
100			X	X	X	X	X	X	X	X	X		
110		X	X	X	X	X	X	X	X	X	X		
120						Region 3							

Figure 10.2b Test matrix of Ar-23%CO2 process, wire speed=5.7 m/min, CTWD=8mm, Travel speed=390mm/min, 6mm MS plate

Large amounts of welding process data from oscilloscope recordings, data acquisition recordings, visual observation and macrosections were compiled. Table 10.3 lists the relevant figures representing this data.

Table 10.3 Summary of Figures for Ar-23%CO2 Process "Open Loop" Tests

Figure Description	Figure No. CTWD=16mm	Figure No. CTWD=8mm
Mean welding current vs Iarc_min & Iarc_max	10.3	10.27
RMS welding current vs Iarc_min & Iarc_max	10.4	10.28
Average arcing current vs Iarc_min & Iarc_max	10.5	10.29
Mean voltage vs Iarc_min & Iarc_max	10.6	10.30
Average dipping frequency vs Iarc_min & Iarc_max	10.7	10.31
Avg wire melting incremental length ΔL vs Iarc_min & Iarc_max	10.8	10.32
Fusion area vs Iarc_min & Iarc_max	10.9	10.33
Penetration depth vs Iarc_min & Iarc_max	10.10	10.34
Weld bead width vs Iarc_min & Iarc_max	10.11	10.35
Weld bead height vs Iarc_min & Iarc_max	10.12	10.36
Energy input per unit length of weld vs Iarc_min & Iarc_max	10.13	10.37
Fusion area vs Energy input per unit length of weld	10.14	10.38
Fusion area vs Mean welding current	10.15	10.39
Fusion area vs Average wire melting incremental length ΔL	10.16	10.40
Stability index vs Iarc_min & Iarc_max (2D)	10.17	10.41
Stability index vs Iarc_min & Iarc_max (3D)	10.18	10.42
Spatter index vs Iarc_min & Iarc_max (2D)	10.19	10.43
Spatter index vs Iarc_min & Iarc_max (3D)	10.20	10.44
Bead quality index vs Iarc_min & Iarc_max	10.21	10.45
Weld overall quality index vs Iarc_min & Iarc_max	10.22	10.46
Useful operating area	10.23	10.47
Arcing duty cycle vs Iarc_max & Iarc_min	10.24	10.48

10.3.2 Test Results for Ar-23%CO_2 Shielding Gas, CTWD=16mm

Figures 10.3 to 10.24 represent the detailed results of all experiments performed under the conditions specified in section 10.2.

[Refer to Appendix 10 for Figures 10.3 to 10.24]

10.3.3 Discussion of Results for Ar-23%CO_2 Shielding Gas, CTWD=16mm

This discussion will make references to Figures 10.2 to 10.24.

As the welding tests were performed, the factors limiting the process operating range quickly became evident. In region 1 of Figure 10.2a, Iarc_min is low and consequently workpiece heating is also low. This is shown in Figure 10.13, where the energy input[1] to the process is seen to be lowest for a given Iarc_max. Other indicators of reduced energy input to the process are mean voltage (Figure 10.6) and mean current (Figure 10.3). The results of insufficient energy input were welds with higher bead height (Figure 10.12), reduced bead width (Figure 10.11) and most importantly reduced fusion area (Figure10.9). These welds also tend to "stub" and sound unsteady over long periods (2 seconds or more), indicating that workpiece heating conditions are not stable in the long term. The amount of ripple on the bead surface increased significantly, this being the main detractor of the bead quality index. An increase in spatter levels is also observed, and is discussed later in detail. The stability index is reduced by approximately 0.10 to 0.15 under these "cold plate" conditions.

In Figure 10.2a, process performance in region 2 is thought to be poor due to insufficient arc length being established by the end of the rapid burnback stage, where the melting rate is ostensibly determined by Iarc_max. The weld process sounded unsteady over a 2-3 second period, yet the stability index measured over 1 second remained satisfactory (over 0.70) for Iarc_min above 60A. Bead quality was also high

---

[1] Note that the mean energy input is *not* the arithmetic product of average voltage and mean current, but must be calculated as:

$$E = \int_0^t V(t)I(t)dt \qquad (10.3)$$

Use of the incorrect calculation method yields significant errors. For example, for the case of Iarc_max=250A & Iarc_min=70A, the mean voltage, current and calculated power using equation 10.3 were : V_{mean}=17.9V, I_{mean}=105.7A, P_{mean}=2120W, respectively. However, $V_{mean}I_{mean}$=1892W, giving an error of -11%. The general trend is for the $V_{mean}I_{mean}$ method to underestimate the average power delivered to the process, and the errors tend to be larger (up to 20%) for waveforms with higher values of Iarc_max.

(above12) and spatter levels acceptable (spatter index 8 or more). However, at Iarc_min=60A the stability index and bead quality abruptly declined. This is thought to be caused by insufficient energy input to the workpiece. Despite the good bead appearance for Iarc_min greater than 60A, good short-term stability and low spatter, an operator would rate Iarc_max=200A as the lower limit for satisfactory welding. Low fusion would also be a discounting factor in all applications except thin sheet metal.

Region 3 (high Iarc_min) limits process application because of significant increases in spatter and greatly reduced dipping frequency. The latter is not as critical for automated welding, but to a manual operator the low frequency can be disturbing, and an unsteady hand will result in poor weld beads. The bead quality did not deteriorate in these tests because of the automation. The only "fault" was a small amount of ripple on the bead surface. Fusion area and penetration depth are maximised at the boundary of this region.

Region 4 (high Iarc_max) is characterised by higher spatter, lower dipping frequency, longer arc length and increased ripple on the bead surface. The combination of these factors makes operation of the process in this area unsatisfactory.

Referring to each of Figures 10.3 to 10.22, a number of observations can be made about trends in process behaviour.

Mean welding current (Figure 10.3)

The results show that for a fixed wire feed speed, the mean current can be significantly altered by adjusting Iarc_min. The range of adjustment is around 25A. Also, for a given value of Iarc_min, variations of 175A in Iarc_max correspond to only 7A change in the mean current.

This data shows that, as discussed in Chapter 7, use of the "simple" melting rate equation:

$$\text{Melting Rate} = \alpha.I_{mean} + \beta.L.I^2_{mean} \qquad (10.4)$$

yields significant errors in the case of a current waveform with a variable form factor.

RMS welding current (Figure 10.4)

The variable form factor of the current waveform is evidenced by a rising mean value and a falling RMS value. As expected, RMS value is greatest for lower values of Iarc_min, where the peak-to-peak variation in current is highest. The change in RMS value is not significant for a given Iarc_max: approximately 5A being the largest. As discussed in Chapter 7, the RMS current is an intrinsic part of the action integral, used

to estimate the electrode preheating. The degree of preheating affects the relationship between instantaneous melting rate and instantaneous current. For a given Iarc_max, the variation in electrode preheating is small for large changes in Iarc_min. This provides a useful decoupling of process parameters: The instantaneous melting rate of the electrode at the start of the arcing period is virtually constant irrespective of Iarc_min. So for a given Iarc_max, the electrode burnoff achieved at the end of Tarc_max is also virtually constant, meaning that the peak arc length will also remain unchanged. Thus peak arc length is determined by Iarc_max, and is relatively insensitive to Iarc_min.

Apart from electrode preheating considerations, there does not appear to be any other useful information in the RMS current values.

Average arcing current (Figure 10.5)

Comparing this with Figure 10.3, distinctions in process behaviour for varying Iarc_max can be seen. For low values of Iarc_max, the average arcing current is significantly less (up to 15A) than for higher Iarc_max, even though the mean current may be slightly greater for low Iarc_max than for high Iarc_max. This is caused by the contribution of short-circuiting currents to the mean, absent from the average-arcing value. This result implies that for a given Iarc_min, as Iarc_max is reduced, a greater portion of the weld cycle is spent in short circuit. Stated another way, the arcing duty cycle is reduced as Iarc_max is reduced. Figure 10.24 shows the variation in arcing duty cycle for varying Iarc_max at constant Iarc_min values, supporting the above claim.

Although the peak short circuit current is proportional to the time spent in the short circuit, it cannot readily be concluded that the peak short circuit current is greater for low Iarc_max. While a greater portion of the weld cycle may be spent in short circuit, the overall weld cycle time is also shorter (see Figure 10.7).

Mean welding voltage (Figure10.6)

The mean welding voltage V_{mean} shows variations for both Iarc_max and Iarc_min.

The variation in V_{mean} with Iarc_min can be explained by two phenomena. The first is the change in arcing duty cycle shown in Figure 10.24: As Iarc_min is increased, a greater fraction of the weld cycle is spent in the arcing phase. The higher electrode melting rate increases the time between short circuits, while the short circuit duration is not similarly extended. The second contributing factor is due to the arcing characteristic of the shielding gas (Chapter 8). A higher arcing current generates a greater arc voltage (and a greater voltage drop across the electrode stickout). Although the arcing

characteristic makes a smaller contribution than melting rate effects, it is not insignificant.

The variation of V_{mean} with Iarc_max can be explained by similar phenomena. The result of the higher current at the start of the arcing period causes the arc length to be greater by the end of the rapid burnback stage, due to a higher instantaneous melting rate. The longer arc length will generate a higher arcing voltage for a given current. Also, the longer initial arc length will extend the time required for the droplet at the end of the electrode to reach the weld pool: 5.7m/min corresponds to 95mm/s, or 0.95mm per 10 milliseconds. An additional 0.5mm of arc length will extend the arcing period by around 5 milliseconds, all other factors being equal. Although the droplet size will have been increased due to the longer arcing period at identical Iarc_min, from investigations in Chapter 6 it is known that the short circuiting time will not be similarly extended, so in overall terms the mean voltage will rise as the duty cycle is increased.

It is noticeable that for a given Iarc_min, the change in mean voltage diminishes for the highest values of Iarc_max. This is again explained by the variations in duty cycle. As Iarc_max is increased, the arc length is increased and arcing time is also increased. Since the short-circuit time changes far less than the arcing time, the duty cycle displays a non-linear characteristic, as shown in Figure 10.25. For this curve, the short-circuiting time is fixed at 3.0ms. That the mean voltage displays a similar trend demonstrates that voltage changes due to arc length are a secondary consideration.

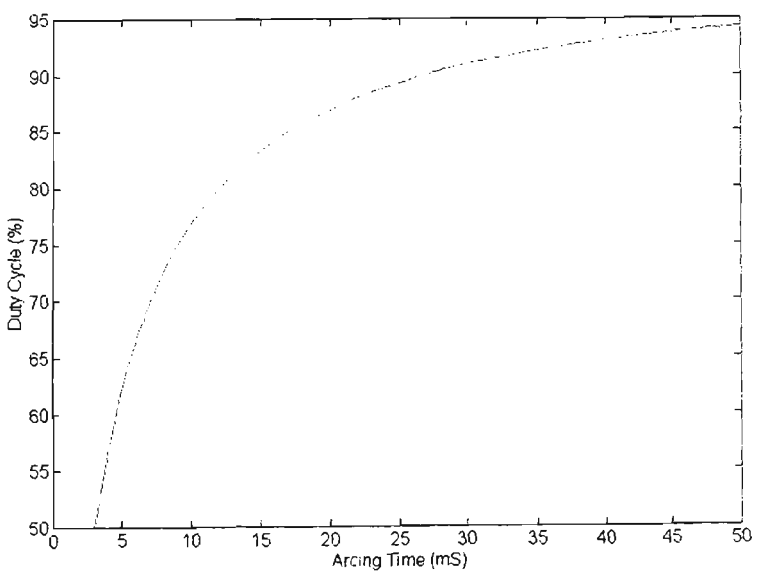

Figure 10.25 Duty cycle variations with arcing time ($T_{short\text{-}circuit}$=3.0ms)

The explanation given above shows that voltage variations can largely be explained in terms of current, arc characteristics, and melting rate.

As has been emphasised in earlier chapters, this "open loop" process is driven by current delivered by the power source independently of welding circuit characteristics. Consequently, voltages are purely the result of events at the arc, and are not determined by power source dynamics.

Average dip frequency (Figure 10.7)

Dip frequency is a function of Iarc_max and Iarc_min.

For a given Iarc_min, frequency decreases with increasing Iarc_max for the same reason that mean voltage rises: The initially higher current creates a longer arc length during the rapid burnback stage, requiring more time for the electrode tip to re-touch the weld pool.

Similarly, for a given Iarc_max, frequency increases with increasing Iarc_min for the same reason that mean voltage rises: The higher steady-state arcing current increases the electrode melting rate and extends the time to the next short circuit.

It is worth noting that the frequency change with Iarc_min for a given Iarc_max is not linear. It is also evident that weld cycle period (inverse of frequency) is also non-linear. This is shown in Figure 10.8, where the average wire melting incremental length is proportional to the period:

$$\Delta L_{avg} = \frac{Wire\ Feed\ Speed}{Average\ Dip\ Frequency} \tag{10.5}$$

This behaviour can be predicted from melting rate considerations alone, as shown in section 10.6.

It is also worth mentioning that the change of frequency with increasing Iarc_max or Iarc_min is monotonic. This contrasts with the frequency-voltage behaviour of a conventional CV power source such as that shown in Figure 10.26 [7], where the welding current conditions are determined by the interaction of power source dynamics with the process characteristics. As already mentioned, the "open loop" process being investigated here avoids this type of interaction which often obscures the actual welding process behaviour.

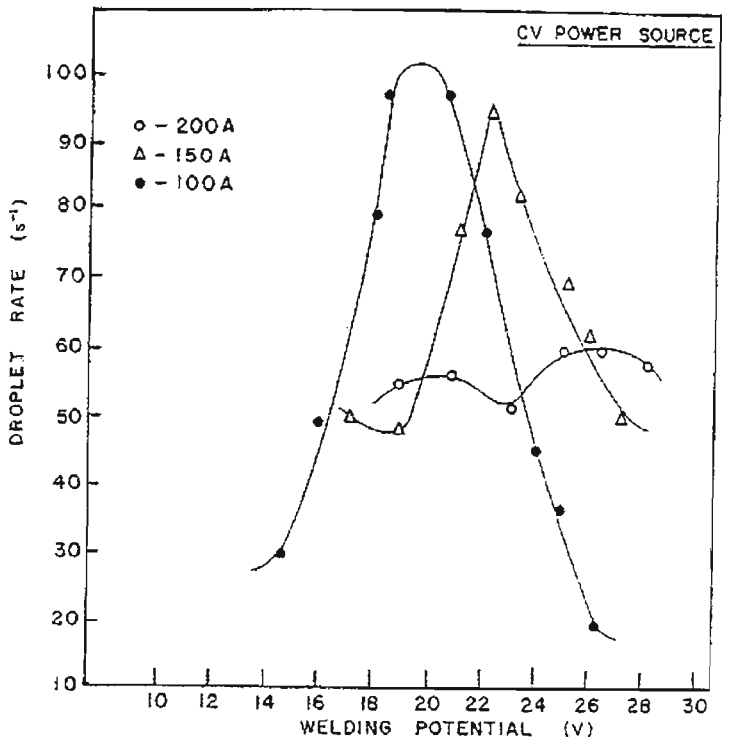

Figure 10.26 Frequency vs Open circuit voltage for conventional CV power source [7]

Average wire melting incremental length ΔL (Figure 10.8)

As described in equation 10.5, this quantity is the average length of electrode which is transferred to the weld pool at each short circuit. It increases in a non-linear manner for both increasing Iarc_min and Iarc_max. The consequence of this behaviour is that in the proposed "closed loop" control scheme of Chapters 5 and 11, it would be difficult to assign a target/reference value of ΔL for every conceivable combination of Iarc_max and Iarc_min. Other major parameters such as CTWD and wire feed speed would also have a large influence on the size of the formed droplet, making assignment of a ΔL target impractical for two reasons. Firstly, the size of the lookup table in a commercial controller would be too large (even in these days of inexpensive memory). Secondly, the time required to experimentally determine the optimum ΔL target for the entire process operating range is prohibitive.

Fusion area (Figure 10.9)

These results are of major importance since they show a method of regulating the fusion area while maintaining a constant wire feed speed. There is some scatter in the data points of this graph, and this is to be expected since only one macrosection per weld was taken. Variations of fusion area along the weld are expected, particularly for the reasonably high travel speed of 390mm/min. Nevertheless, it can be stated with confidence that for a given Iarc_max, the fusion area is linearly related to Iarc_min. Results for CTWD=8mm and for CO_2 CTWD=12mm show this trend more clearly. The

main benefit of this behaviour is that it allows the operator a straightforward method of adjusting fusion to avoid lack-of-fusion defects in thicker sections, or burn-through in thinner sections. This adjustment is possible without altering wire feed speed or travel speed, thus maintaining the same bead cross-section and deposition rate. Since Iarc_max is the major determining factor of maximum arc length, the changes to fusion area have no major effect on arc length.

The range of adjustment is significant. For Iarc_max=225A, the fusion area was varied from 3.0 mm^2 at Iarc_min=50A to 5.1 mm^2 at Iarc_min=100A, representing a 70% increase. This also influences dip frequency and spatter levels, but these may be of secondary importance in many applications.

Penetration depth (Figure 10.10)

These results reflect those of Figure 10.9. Again, there is scatter in the data points, but the increase in penetration depth can be seen for an increase in Iarc_min. Increases of 30% are typical for various values of Iarc_max.

Bead Width (Figure 10.11)

These results confirm the common visual observation that a wider weld bead has greater fusion area. Increasing Iarc_min widens the weld bead by up to 20% for a given Iarc_max.

The results also show that for a given Iarc_min, increasing Iarc_max will widen the weld bead. This effect can be seen with the eye during manual welding: a longer arc length produces a conical arc column with a wider base at the workpiece, widening the weld pool.

Bead Height (Figure 10.12)

Reinforcing the results of Figure 10.9 to 10.11, increasing Iarc_min gives a wider, flatter bead with greater fusion area and penetration depth. . Increasing Iarc_min reduces weld bead height by around 15% for a given Iarc_max. The bead height appears to be the least affected dimensional attribute of the bead for changing arcing conditions.

Energy input (Figure 10.13)

Commonly called "heat input", the electrical energy input to the process per unit length of deposited weld is a key factor affecting fusion. This figure illustrates why the "open loop" control process allows control of fusion. Adjustment of Iarc_min allows linear variation in total energy input to the process. For a given Iarc_min, there is non-linear variation in energy input as Iarc_max is changed, and the variation is less for

higher values of Iarc_max. This follows from the similar behaviour of mean voltage (Figure 10.6).

Fusion area vs Energy input (Figure 10.14)

These results show a strongly linear relationship between fusion area and the electrical energy input per unit length of weld, demonstrating the availability of an adjustment mechanism for fusion area.

Fusion area vs Mean current (Figure 10.15)

These results were compiled to show that there is not a consistent relationship between fusion area and mean welding current when Iarc_max is altered. It is worth presenting, since observation of Figure 10.3 (mean current) together with Figure 10.9 (fusion area) might tempt the casual observer to conclude that fusion area may be controlled simply by the mean current. This does not appear to be the case. Results for CTWD=8mm and CO_2 CTWD=12mm support this claim.

The inconsistent relationship between fusion area and mean current is due to the very low energy produced during the short circuit, even at high shorting currents, because there is no arcing voltage component. Also, most of the energy produced in the short occurs in the electrode stickout rather than at the workpiece. Therefore, the mean current is not closely linked to the energy, as it would be in open-arc processes. As Iarc_max is changed, the duty cycle is altered, and the relationship between mean current and energy is also changed.

Fusion area vs ΔL (Figure 10.16)

As for Figure 10.15, these results show that there is not a consistent relationship between fusion area and the average wire melting incremental length ΔL when Iarc_max is changed. If the results for Iarc_max=375A were not present, the data groupings would be more regular. Even so, there is a significant change in fusion area for a small change in ΔL, making the regulation of fusion area through control of ΔL impractical.

Stability and Spatter Indices , Bead Quality Index (Figures 10.17-10.21)

Welds with Iarc_max of 225A and 250A exhibit the highest stability indices generally, although an optimally tuned conventional CV power source can easily produce stability indices of 0.90 to 0.95. In terms of maximum stability index alone this advanced control scheme does not pose any advantages over a conventional CV power source. Advantages arise from a combination of other aspects such as low spatter and bead quality. Very low spatter levels are achievable across a wide operating range, and

the quality of the weld beads is high even for welds with low stability indices. Figure 10.18 shows the optimum operating "ridge" along Iarc_max = 250A.

Figures 10.19 and 10.20 show that spatter is acceptably low (rating 8 or more) for a region bounded by Iarc_max=[200,275] and Iarc_min=[50,90]. The increase in spatter for increasing Iarc_min can be explained by the increasing arc forces causing repulsion of material from the weld pool at the very start of the short circuit period. It appears that even the rapid turn off of current (delay measured at 150μs) cannot totally eliminate this effect. In a limited number of tests conducted during the course of these experiments, it was found that reducing the turn-off delay from 150μs to 12μs did not discernibly reduce the spatter levels. However, the reason for an increase in spatter for low values of Iarc_min is not as obvious. This is discussed further in section 10.3.7, where the effects of weld pool oscillations on spatter levels are investigated.

Figure 10.21 represents an unexpected result, since it indicates that across the entire range of test currents, there was only one weld bead whose appearance would have been considered unsatisfactory (rating less than 11). This is surprising considering the variations in stability index, spatter levels and fusion areas throughout the test range. This ability to lay down a good bead despite sub-optimum conditions makes this type of process control feel very "forgiving" to a manual operator.

Overall weld quality index (Figure 10.22)

As described in section 10.2.3, this index is an attempt to evaluate the "useful" operating area, which is a subset of the test matrix shown in Figure 10.2a. If a minimum value of 3.8 is chosen as the threshold (corresponding to a stability index of 0.65, a spatter index of 8 and a bead quality of 11), then the "useful" operating area is represented in Figure 10.23.

It must be emphasised that this definition of useful operating area is valid only for the narrowly defined conditions of these tests. As will be seen in section 10.3.7, the single act of reducing travel speed from 390 mm/min to 195 mm/min causes an almost total elimination of spatter down to Iarc_min=20A, thus radically modifying the useful operating area. The fact that changes in certain key process parameters (eg travel speed, workpiece thickness) have dramatic effects on the process makes it impossible to impose rigid boundaries for Iarc_min and Iarc_max.

10.3.4 Test Results for Ar-23%CO_2 Shielding Gas, CTWD=8mm

Figures 10.27 to 10.48 represent the detailed results of all experiments performed under the specified conditions.

[Refer to Appendix 10 for Figures 10.27 to 10.48]

10.3.5 Discussion of Results for Ar-23%CO_2 Shielding Gas, CTWD=8mm

This discussion will make references to Figures 10.27 to 10.48, and will draw comparisons to results for CTWD=16mm where appropriate.

Test Matrix (Figure 10.2b)

Comparison with the test matrix of CTWD=16mm shows that the possible operating area has been broadened in regions 3 & 4. The process at CTWD=8mm can be operated at higher values of Iarc_max because there has been less preheating of the electrode during the shorter material transit time from contact tip to workpiece. Hence more arcing current is required to form the maximum arc length and final droplet size. The other consequence of lower electrode preheat is that operational ability is lost in regions 1 & 2 , where the weld becomes too "cold" and has a tendency to sound unsteady and occasionally stub, since insufficient arcing current is available to form an adequate arc length or droplet size.

Mean welding current (Figure 10.27)

There is a linear variation of mean current for Iarc_max=300A and above, but for lower values of Iarc_max, the mean current actually increases above the linear trend line as Iarc_min is reduced. This coincides with the "cold" regions at the boundaries of regions 1 & 2 in Figure 10.2b. The reasons for this are partly explained by Figure 10.48, which shows a more rapid decrease in arcing duty cycle for low values of Iarc_max, as Iarc_min is reduced. Unfortunately, what is not shown in any figures is the extended short-circuiting times under the "cold" conditions, where more current is required to break the short circuit. The high short-circuit currents contribute to the mean current, making it an unreliable indicator of arc heating effect.

In comparison with CTWD=16mm (Figure 10.3), the mean current is approximately 15A higher for a given combination of Iarc_max & Iarc_min.

RMS welding current (Figure 10.28)

As for CTWD=16mm (Figure 10.4), the RMS current is generally decreasing while the mean current increases. The change in RMS current is greater for

CTWD=8mm than for CTWD=16mm, and generally, the RMS current is approximately 20A more for a given combination of Iarc_max & Iarc_min.

The RMS current in combination with the transit time gives a quantitative indication of the electrode preheating. Taking the example of Iarc_max=275A and Iarc_min=80A, the RMS currents for CTWD=16mm and 8mm are 126A and 149A respectively. As shown in Chapter 7, the average action integrals are:

$$Action_{CTWD=16} = \frac{CTWD.I_{RMS}^2}{WFR} = 2674\ A^2s$$

$$Action_{CTWD=8} = \frac{CTWD.I_{RMS}^2}{WFR} = 1870\ A^2s$$

Since the instantaneous melting rate is modified according to:

$$MR(t) = \frac{\alpha}{1 - \beta.Action} I(t) \qquad (10.6)$$

where $\beta = 0.000159\ A^{-2}s^{-1}$ for Ar-23%CO_2, then the ratio of melting rates is:

$$\frac{MR_{CTWD=16}}{MR_{CTWD=8}} = 1.22$$

$$\frac{MR_{CTWD=8}}{MR_{CTWD=16}} = 0.82$$

So for a given instantaneous arcing current *I(t)*, a 19% decrease in melting rate is predicted due to the reduction in CTWD.

Average arcing current (Figure 10.29)

When the effect of the short-circuiting current is removed, the results of this figure compare well with those of Figure 10.5. The increase in I_{arc_avg} is linear with Iarc_min, and the diminishing change in I_{arc_avg} as Iarc_max increases (for a given Iarc_min) is the same as for CTWD=16mm. I_{arc_avg} is higher by 10-15A for CTWD=8mm. Comparison of duty cycles shows that they are generally lower for CTWD=8mm, so this cannot explain higher I_{arc_avg} values. However, comparison of dipping frequencies (Figures 10.7 & 10.31) may help. For a given Iarc_max/Iarc_min combination , the frequency is significantly lower for CTWD=8mm. Using the case of Iarc_max=275A and Iarc_min=80A, the frequencies for CTWD=16mm and 8mm are 52Hz and 86Hz, respectively. The duty cycles for CTWD=16mm and 8mm are 85% and 76%, respectively. The arcing period is therefore much shorter for CTWD=8mm. Thus the effect of Iarc_max applied for fixed Tarc_max=1.5ms on the average of the arcing current is more for the shorter arcing period, yielding a higher result for I_{arc_avg}.

Mean welding voltage (Figure10.30)

The same behaviour is exhibited as in Figure 10.6 (CTWD=16mm). The voltages in Figure 10.30 are generally 1.0 to 1.5V lower for a given current condition, because of reduced arc lengths which in turn are due to lower melting rates resulting from lower electrode preheating.

Average dip frequency (Figure 10.7)

Because of reduced electrode preheating, the dipping frequency is markedly higher for given Iarc_max/Iarc_min conditions. In most cases, the frequency was well above 50Hz, which many operators may consider the lowest acceptable frequency for manual welding. The non-linear variation of frequency (and ΔL - see below) with Iarc_min is still evident, as the same mechanisms are still valid.

Average wire melting incremental length ΔL (Figure 10.32)

Comparison with Figure 10.8 (CTWD=16mm) shows that a change in CTWD greatly influences the average droplet size. The change is so great that a control system proposing to maintain a fixed droplet size under changing CTWD conditions would only be able to do this by altering the current conditions, which would also significantly change fusion area and bead geometry.

Figure 10.32 also shows less variation in droplet size for changes in Iarc_min. This is probably due to reduced electrode preheating during transit. The non-linear change of ΔL with Iarc_min is the same as for Figure 10.8, but less pronounced.

Fusion area (Figure 10.33)

The ability to alter fusion area by adjusting Iarc_min is even more evident in these results than for Figure 10.9 (CTWD=16mm). With the shorter CTWD, fusion area appears to be more sensitive to changes in Iarc_max. A greater fusion area was obtained using CTWD=8mm by using higher values of Iarc_max, and these would be satisfactory from an operator's point of view since the dipping frequency is not excessively low.

Figure 10.49 compares the fusion areas for current conditions where there are enough overlapping data points in the test matrices to make valid comparisons. It can be seen that for given Iarc_max/Iarc_min settings, if CTWD is increased then fusion area generally decreases. This behaviour is similar to that for conventional power sources, where manual operators can avoid burn-through by deliberately increasing CTWD.

Energy input (Figure 10.37)

The linear adjustment of energy input with Iarc_min is the same as for CTWD=16mm (Figure 10.13). Figure 10.50 compares the energy input for the same

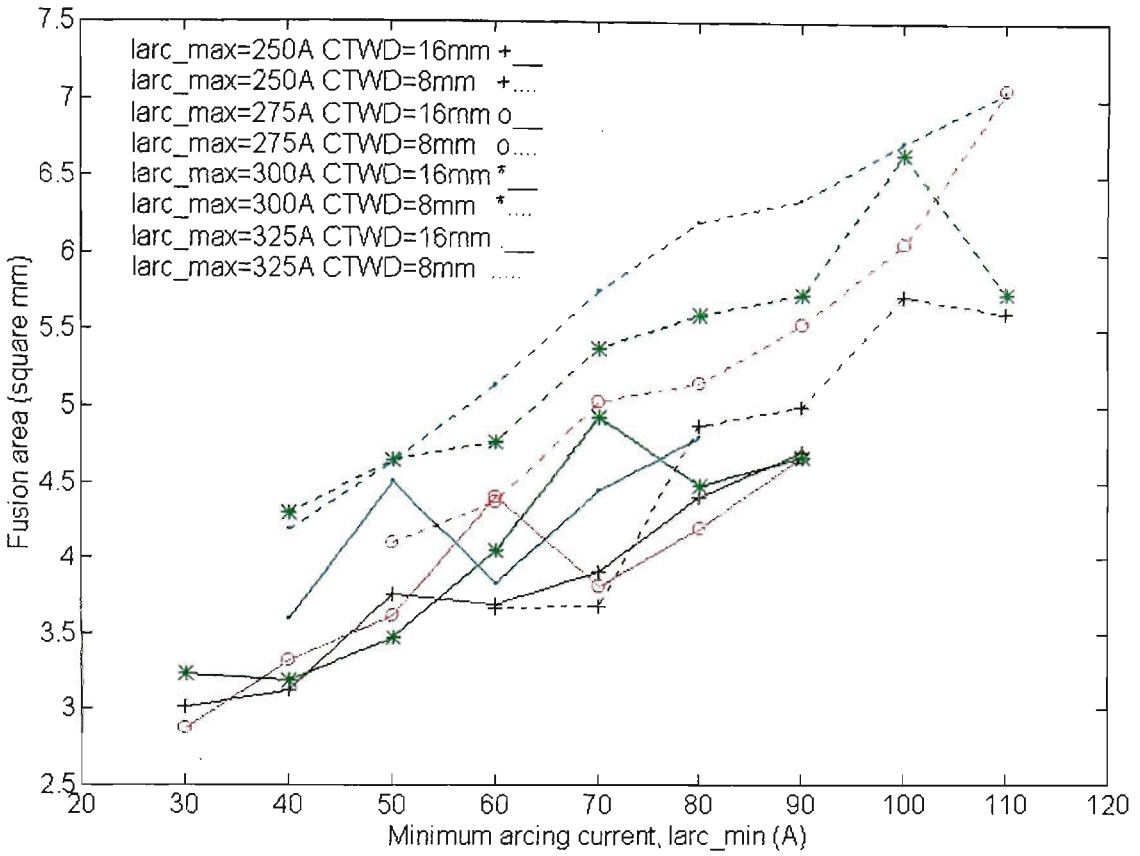

Figure 10.49 Fusion area vs Iarc_min for CTWD=8mm & CTWD=16mm

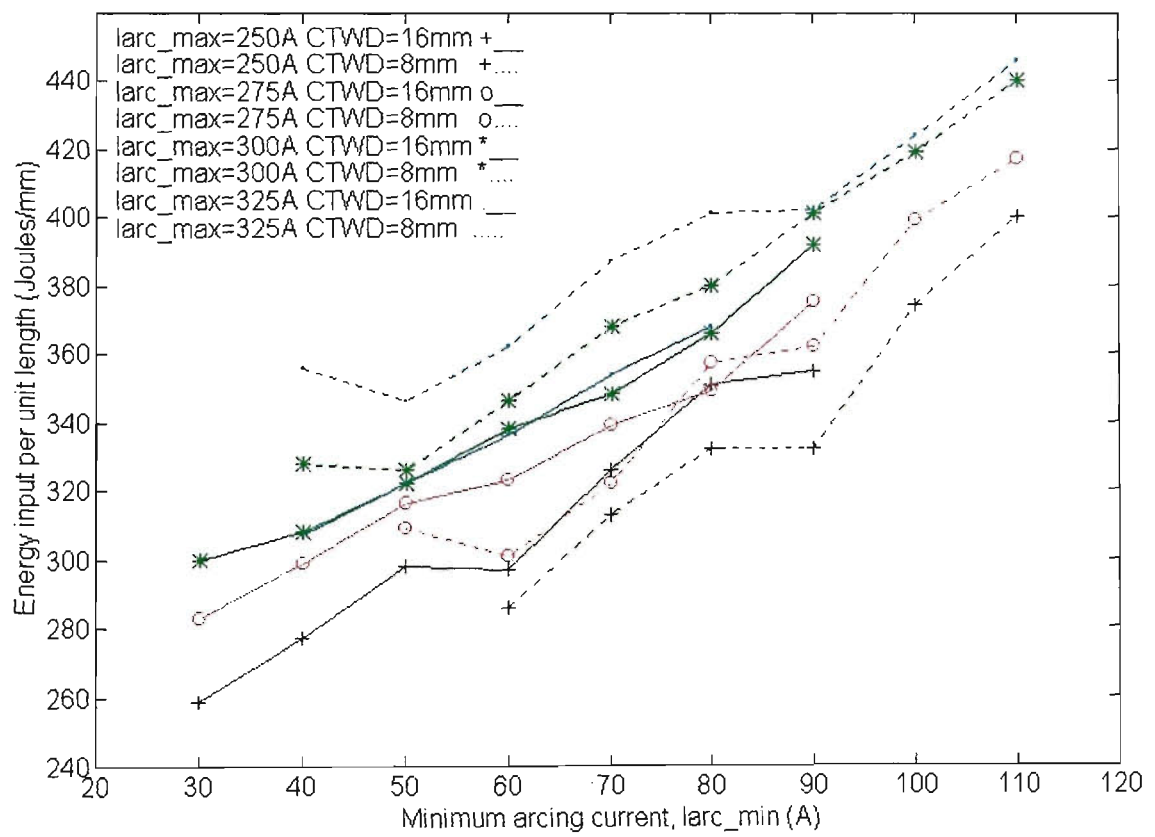

Figure 10.50 Energy input vs Iarc_min for CTWD=8mm & CTWD=16mm

current settings as those of Figure 10.49. As would be expected, higher energy inputs for Iarc_max=300A & 325A correspond to the higher fusion areas of Figure 10.49. Surprisingly, for Iarc_max=250A & 275A at CTWD=8mm, a similar or larger fusion

area is generated by a lower energy input. No reason can be presented with certainty for this phenomenon at this time. One possible explanation is the increased arc efficiency at shorter arc lengths, allowing greater heat transfer to the workpiece for less overall energy input to the process.

Fusion area vs Energy input (Figure 10.38)

The strongly linear relationship established in Figure 10.14 (CTWD=16mm) is repeated. Figure 10.51 combines the results of both sets of experiments to demonstrate the continuity of results. This shows that the relationship between fusion area and energy input is not greatly altered by significant changes in the CTWD, provided that all other welding parameters remain constant.

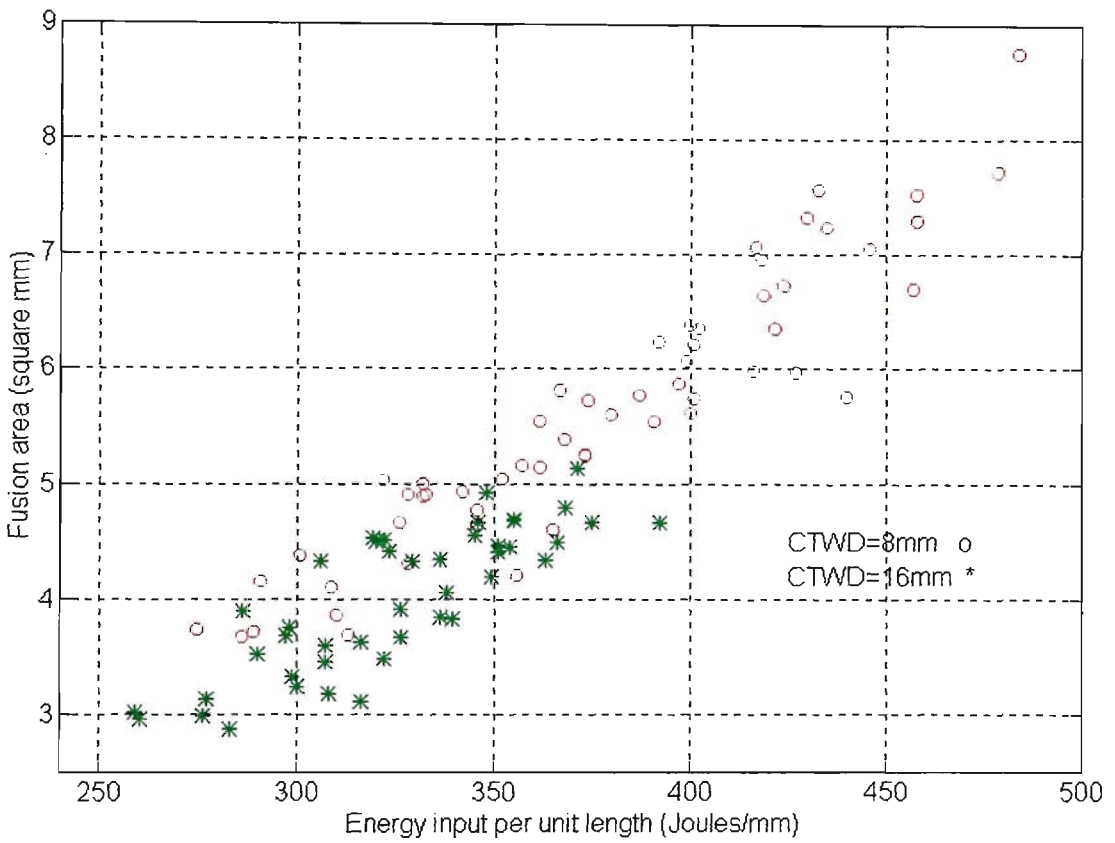

Figure 10.51 Fusion area vs Energy input for CTWD=8mm & CTWD=16mm

Fusion area vs Mean current (Figure 10.39)

As for Figure 10.15 (CTWD=8mm), these results show that there is no consistent relationship between fusion area and mean welding current when Iarc_max is significantly changed. Results for CO_2 CTWD=12mm will also support this claim.

Fusion area vs ΔL (Figure 10.40)

These results show a more defined trend than Figure 10.16 (CTWD=16mm. There is still a significant change in fusion area for a small change in ΔL, which shows

that regulating the fusion area through control of ΔL would be difficult. This figure does confirm two previously discussed results: an increase in fusion area (from higher energy input) is accompanied by a reduction in dipping frequency, hence an increase in average droplet size. The decoupling of droplet formation and workpiece heating is not possible in GMAW since the current which provides workpiece heating inevitably promotes electrode heating. In contrast, the GTAW process can independently adjust workpiece fusion and filler wire application since the welding current does not pass through the filler material.

Stability and Spatter Indices , Bead Quality Index (Figures 10.41-10 .45)

Comparison with CTWD=16mm show that the stability is generally improved at the lower CTWD. Figure 10.42 shows a "plateau" of high stability, compared to Figure 10.18 which shows an optimum operating "ridge" for CTWD=16mm.

Figure 10.43 shows that the general spatter levels are similar to CTWD=16mm. There are slightly less operating conditions for which spatter levels are classed as "low" (rating 10, indicating a spatterless weld). However, enough conditions exist with rating above 8 to make a low spatter weld easily achievable.

The high bead quality indices of Figure 10.45 again demonstrate the ability of this type of process control to lay down good beads. As stated previously, a rating of 10 or above indicates a bead of good appearance. The welds which fail on bead appearance are those at the lowest values of Iarc_min, for Iarc_max less than 350A. These correspond to "cold" conditions where the fusion is least: In Figure 10.2b, these are at the boundary of region 1.

Overall weld quality index (Figure 10.46)

As in section 10.3.3, this index is assigned a minimum value of 3.8 to evaluate the "useful" operating area, and the results are represented in Figure 10.47.

Comparisons with Figure 10.23 show that the process operates over a wider current adjustment range when the CTWD is less, at least under the conditions of these tests. The reduction in electrode preheating requires greater arcing current (either Iarc_max, Iarc_min, or both) to produce the same droplet size. The additional current increases workpiece fusion, producing a wider and deeper weld pool. This may enhance the metal transfer capabilities of the process, particularly for small droplet sizes (high dipping frequencies). As described in section 10.3.3 (CTWD=16mm), for low values of Iarc_min and Iarc_max less than 300A, stability index was reduced and spatter levels increased over optimum settings. The corresponding dipping frequencies were 85-95 Hz

under these conditions, and bead widths were consistently below 6.0mm. For CTWD=8mm, it was possible to obtain very stable, low spatter transfer of small droplets at 85-110 Hz provided the pool conditions were satisfactory. For example, for Iarc_max=200-250A and higher values of Iarc_min, stability, spatter & bead quality were good or acceptable, and bead widths were above 6.0mm. As Iarc_min was reduced, bead widths dropped below 6.0mm (Figure 10.35), and welding conditions deteriorated.

This evidence suggests that weld pool conditions have a significant effect on the stable transfer of small droplets with minimal spatter. Sections 10.3.6 & 10.3.7 present results which support this assertion.

10.3.6 Test Results for Ar-23%CO_2 at Reduced Travel Speed

A limited set of tests were performed at reduced travel speed for two reasons:

1. To investigate the effects of changes in weld pool conditions on process behaviour.
2. To provide an "open loop" benchmark for comparison with "closed loop" tests described in Chapter 11.

The electrical parameters were the same as for previous tests, with the exception of Iarc_max & Iarc_min, of course. Iarc_max was set to 250A, this being a value which produced good results for both CTWD=8mm & 16mm. The travel speed was 195mm/min, this being the speed at which all CO_2 tests were later performed. The CTWD was set to 16mm. Figures 10.52 to 10.60 compare key results for travel speeds of 195mm/min and 390mm/min.

[Refer to Appendix 10 for Figures 10.52 to 10.60]

10.3.7 Discussion of Results for Ar-23%CO_2 at Reduced Travel Speed

The following discussion makes comparisons between results for the different travel speeds, and focuses on the observed decrease in spatter levels for low values of Iarc_min as the travel speed is reduced.

Figures 10.52 & 10.53 show that for a change of travel speed with no other parameter changes, the mean current and dipping frequencies remained the same, allowing for some small variations inherent in the welding process. Thus the average droplet size formed at the end of the electrode did not change significantly as travel speed was altered.

This discounts the possible explanation that the droplets are of insufficient size and forms a molten bridge of sufficient length for successful metal transfer [8, 11, 12, 18] for low values of Iarc_min. If this were true, then spatter levels would not be affected by changes in travel speed.

Figures 10.54 and 10.55 show that workpiece heating conditions were significantly altered. The fusion area increased by up to 60%, while the bead width was increased by 1.5 - 2.0 mm. Figure 10.56 shows the expected doubling of electrical energy input per unit length of weld. Figure 10.57 shows a significant change in the relationship of energy input and fusion area. To achieve the same fusion area at the slower travel speed requires almost twice the energy input. This rules out the possibility of a fusion control system based simply on regulating the energy input without accounting for travel speed [106]. In a manual welding operation, significant changes in fusion are an inevitable consequence of (unmeasured) travel speed changes.

Figures 10.58 - 10.60 show the process changes that are of primary interest. For 390mm/min travel speed, as Iarc_min was reduced below 60A, the process behaviour deteriorated significantly. Stability index dropped from 0.86 to 0.62, and spatter increased from "spatterless" to "medium" levels. Bead appearance also deteriorated, with increases in surface ripple, ropiness and bead height/width ratio. At 195mm/min travel speed, stability indices were maintained above 0.75, and bead appearance was diminished only by a reduction in height/width ratio. Most importantly, spatter levels were maintained at "spatterless" levels. This supports the assertion made in section 10.3.5 that weld pool conditions appear to have a significant effect on the stable transfer of small droplets with reduced spatter. In the comparisons made in this section, droplet sizes were very similar, and steady state arcing currents (Iarc_min) just prior to the short circuit were identical. Spatter generating mechanisms at the start of the short circuit have been described in the literature as being dependent on initial short-circuiting current [13, 107, 108]. The increase in spatter levels for high Iarc_min values is explained by this mechanism, but the observed reduction in spatter from changes to the travel speed do not seem to be explained.

Further investigation of this phenomenon began with inspecting the current and voltage waveforms of welds with Iarc_max=250A and Iarc_min=30A for travel speeds of 390mm/min and 195mm/min. It was found that premature short circuits occurred occasionally, as shown in Figure 10.61. They would occur at currents well above Iarc_min, and sufficiently high to cause ball repulsion spatter. For 390mm/min, there

were 7 occurrences in 1.0 second sample, while for 195mm/min, there was only one occurrence.

The timing of the short circuit is entirely process-dependent, and not defined by the "open loop" control system, so the process was visually examined using the visualisation equipment described in Chapter 9. The shape of the weld pool was observed towards the end of the short circuiting period. Figure 10.62 shows the appearance of the bead at the end of the short circuit, for 390mm/min travel speed. Figure 10.63 shows the bead for 195mm/min. These photos are typical of many taken for each case.

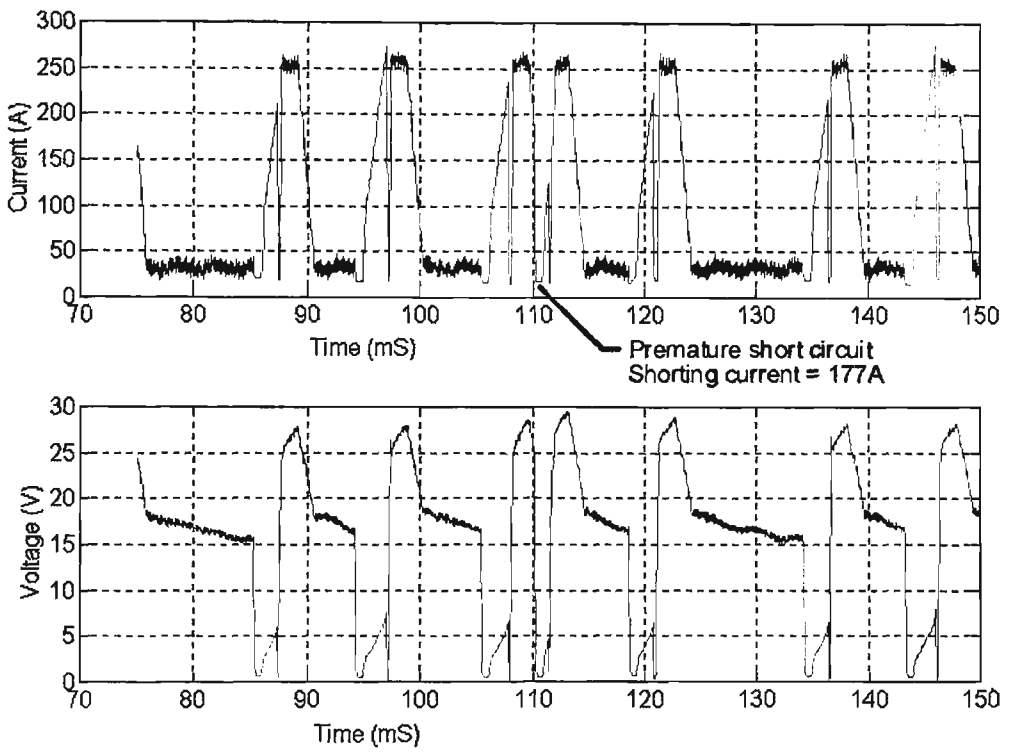

Figure 10.61 Current & voltage waveforms (Iarc_max=250A, Iarc_min=30A)

Figure 10.62 Bead for 390mm/min

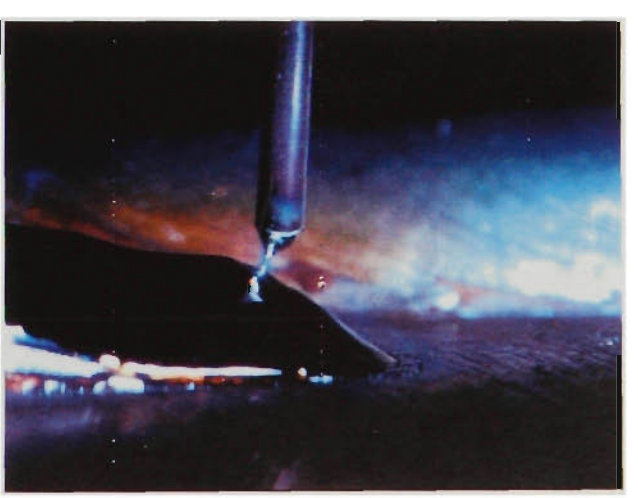

Figure 10.63 Bead for 195mm/min

In Figure 10.62, the weld pool is severely raised by the addition of droplet material. It is postulated that the release of the short circuit in combination with the depression of the pool during the rapid burnback stage of the arcing period can initiate large pool oscillations, creating conditions conducive to premature shorting. Figure 10.63 shows a larger, flatter pool which is not grossly distorted by the addition of a similar amount of material. The lower ratio of peak pool height to pool width is expected to produce smaller oscillations, lowering the probability of a premature short.

10.3.7.1 The Role of Weld Pool Oscillations

It is worth noting here that under all welding conditions, pool oscillations of varying amplitude do occur, and the moving pool surface makes small variation of arcing period duration unavoidable in the constant-current burn-off regime used in these tests. The role of weld pool oscillation can greatly influence the overall behaviour of the weld with conventional power sources [26, 109], and they are still important to the process control employed here. A benefit of this control technique is that it is less sensitive to these oscillations. As has been seen from earlier results, the changes to spatter and stability levels is not significant, merely worthy of investigation.

With further reference to [26], experiments using a conventional CV power source showed that the dipping frequency for optimally stable welds coincided with the calculated weld pool oscillation frequency f_o (for a partially-penetrated weld) given by:

$$f_0 = 5.84\left(\frac{\gamma}{\rho}\right)^{0.5} D^{-1.5} \qquad (10.7)$$

where γ is the surface tension coefficient, ρ is the molten metal density, and D is the "equivalent diameter" of the weld pool (the diameter of the circle having an area equal to the surface area of the weld pool). Figure 10.64 shows the results reproduced from [26] showing correlation of dipping frequency to f_o.

Figure 10.65 illustrates the equivalent results for the tests performed in sections 10.3.2 & 10.3.4 (travel speed of 390mm/min), and also the results of additional tests to be described in section 10.3.9 (low wire feed speeds). In this figure, the "equivalent diameter" of the weld pool is assumed to be equal to the bead width, and ρ is 7800 kg/m^3. According to [13, 64], the surface tension may lie between 0.75 and 1.2 N/m, and these extremes are shown in the Figure.

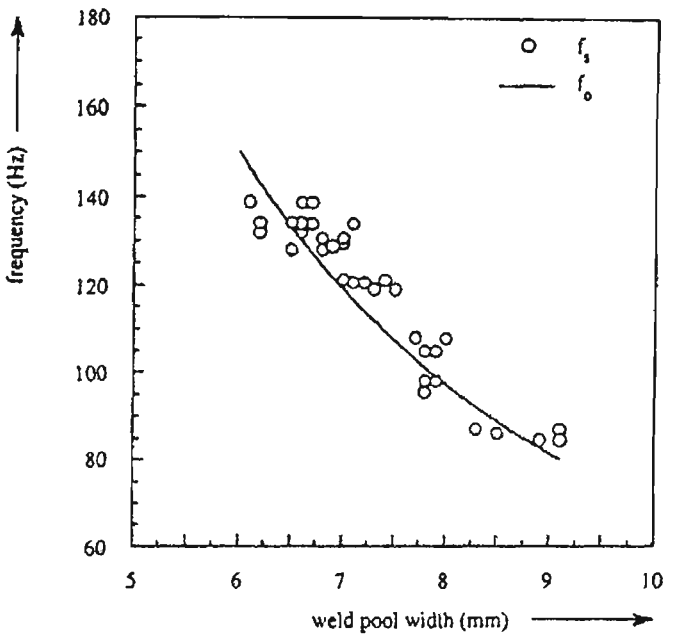

Figure 10.64 F_{dip} versus f_0 for CV power source & Ar-15%CO_2 (reproduced from [26])

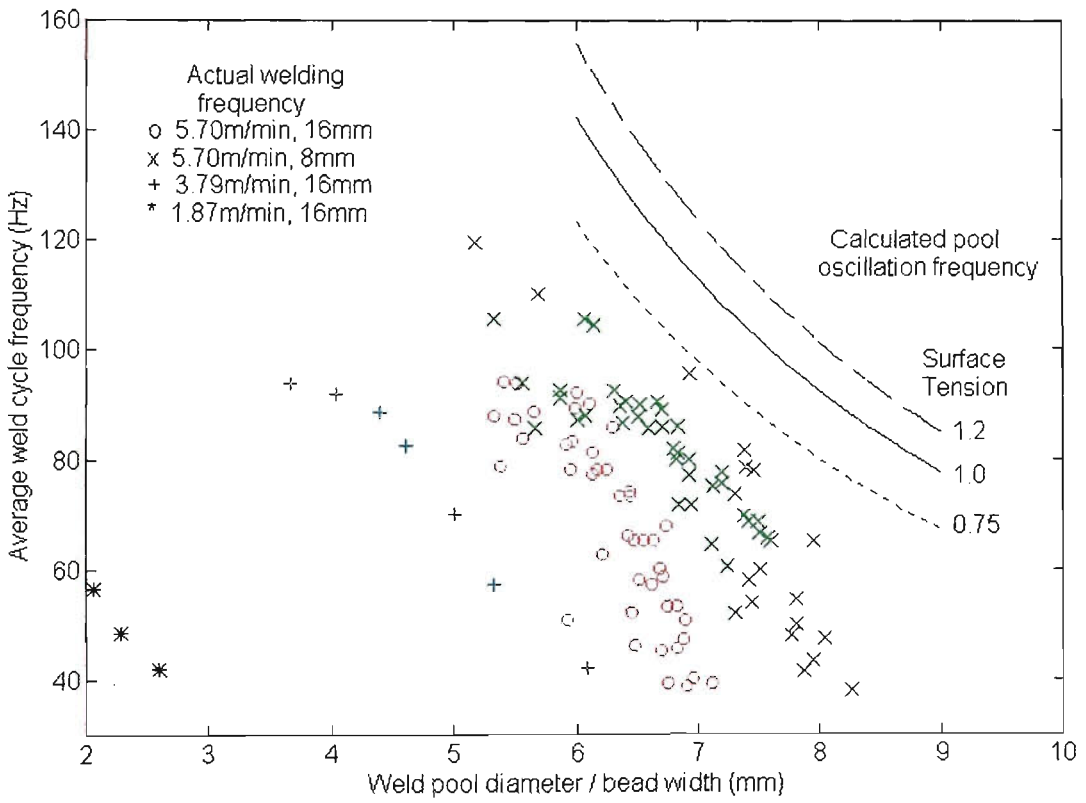

Figure 10.65 F_{dip} versus f_0 for Ar-23%CO_2 , circular weld pool

It can be seen that each welding condition produces results that appear to lie on different f_{dip}/D characteristic lines, and that these lines are significantly different to the pool oscillation frequency. The assumption that the "equivalent diameter" of the weld pool is equal to the bead width is questionable. There is sufficient evidence to suggest that the weld pool is extended or elongated as travel speed increases. Photos taken of welds, some of which are presented in this report, consistently show weld pools whose lengths are greater than the measured bead width. To address this, Figure 10.66 presents

the same results as Figure 10.65, but the weld pool is assumed to be the extended shape shown in the figure. The "equivalent diameter" D of the weld pool is calculated as:

$$D = W\sqrt{\frac{4}{\pi}+1} \tag{10.8}$$

where W is the bead width.

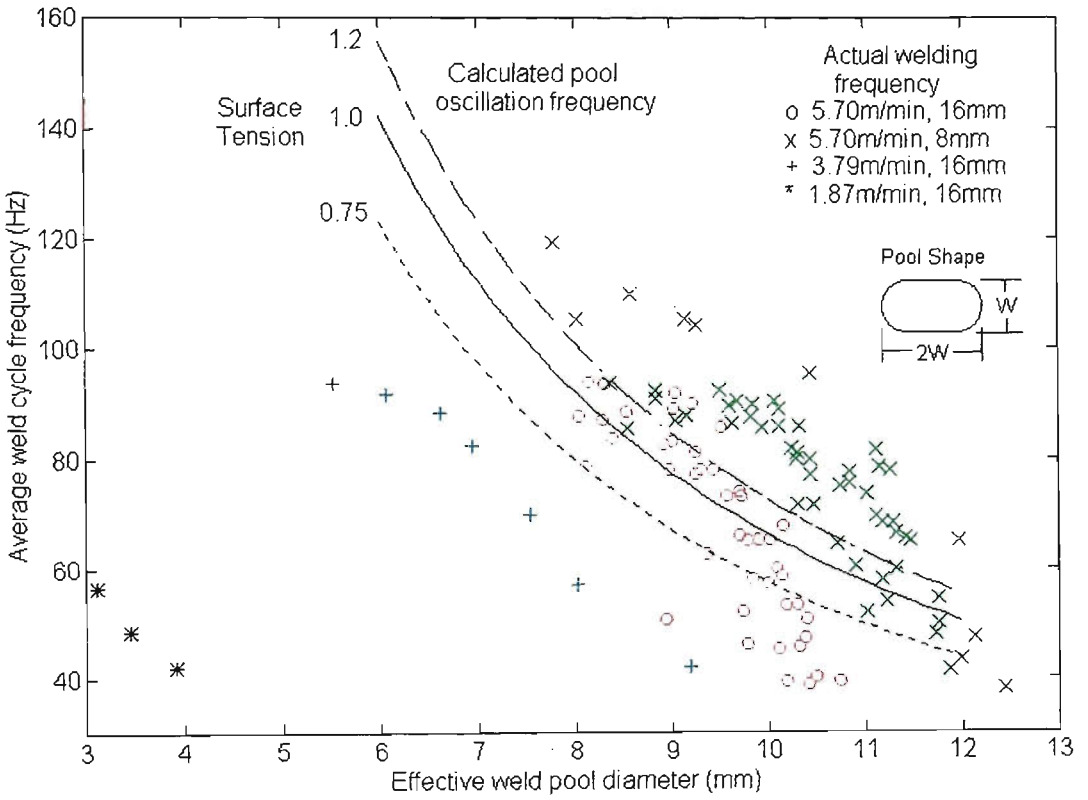

Figure 10.66 F_{dip} versus f_0 for Ar-23%CO_2 , extended weld pool

Figure 10.66 shows a closer correlation of experimental data to estimated pool oscillation frequency. However, there is sufficient spread of data points, particularly for lower wire feed rates, to conclude that this type of welding process control can produce welds of high quality, good stability and excellent appearance without the need to be closely synchronised with weld pool oscillation frequency. Despite this, from earlier explanations for variations in spatter levels, it cannot be stated that the effects of weld pool oscillation have been totally negated.

Since the dependence on weld pool events has been reduced, then it could be postulated that the process behaviour is predominantly dictated by electrode melting rate considerations. If this is the case, then the dipping frequency could be estimated by using the simple melting rate models described in Chapter 7. Section 10.6 investigates this hypothesis further.

10.3.8 Test Results for Ar-23%CO_2 at Reduced Wire Feed Speed

Up to this point, the documented tests have been restricted to a wire feed speed of 5.7 m/min, which is considered to be a typical setting suited to 5.0mm or 6.0mm plate. In practice, an operator may need to weld much thinner material using the same electrode size. One possibility is to retain the same wire feed rate and increase the travel speed, to reduce both bead size and heat input. This may not be possible for manual welding, since travel speeds become too high for the human hand, particularly on small or intricate objects. The practical option is to reduce the wire feed rate.

To briefly investigate the process behaviour at reduced wire feed speeds, a number of tests were performed at 1.87 m/min and 3.79 m/min using Ar-23%CO_2 shielding gas. Travel speed was 390 mm/min, CTWD=16mm, and the electrical parameters specified in section 10.2.2 were also unchanged. Only Iarc_max and Iarc_min were adjusted to obtain good welding conditions. The results are summarised in Table 10.4 below.

Table 10.4 Results for Ar-23%CO2 at Reduced Wire Feed Speed

WFR (m/min)	Iarc_max (A)	Iarc_min (A)	Bead Width (mm)	Avg Dip Freq (Hz)	ΔL avg (mm)	Stabil Index	Spatter Index	Mean Current (A)	Heat Input (J/mm)
1.87	90	20	2.06	56.5	0.55	0.595	8	37.1	72.3
"	"	25	2.29	48.5	0.64	0.720	10	38.9	82.6
"	"	30	2.60	42.0	0.74	0.800	9	39.7	94.5
3.79	175	20	3.66	94.0	0.67	0.835	6	67.0	161
"	"	30	4.03	92.0	0.69	0.810	8	69.5	172
"	"	40	4.39	88.5	0.71	0.780	9	71.9	186
"	"	50	4.60	82.5	0.76	0.800	9	63.1	203
"	"	60	5.0	70.0	0.90	0.785	10	79.7	219
"	"	70	5.32	57.0	1.11	0.745	9	86.5	242
"	"	80	6.09	42.0	1.50	0.680	7	92.6	279

10.3.9 Discussion of Results for Ar-23%CO_2 at Reduced Wire Feed Speed

Unlike the tests at higher wire feed speeds, these tests do not propose to "map" the operating range of the process at these wire feed speeds. The objective is to determine if the stability of the process, or the ability of the process to produce a good weld beads, is degraded by a reduction in wire feed speed.

It can be stated with confidence that the process operates extremely well at reduced wire feed speeds. Figure 10.67 shows photographs of the beads produced by the

welds analysed in Table 10.4. In all cases the bead appearance is very good, even for 1.87 m/min. Spatter levels are very low for most cases, and stability levels are acceptably high. The trend of a widening weld bead for increasing Iarc_min is similar to that experienced for 5.7 m/min wire feed speed, and is explained by the rise in heat input as Iarc_min is increased. For the welds performed at 3.79 m/min, the spatter is minimised for Iarc_min=60A, and increases as Iarc_min is reduced. This is likely to be caused by high amplitude weld pool oscillations, as described in section 10.3.7.

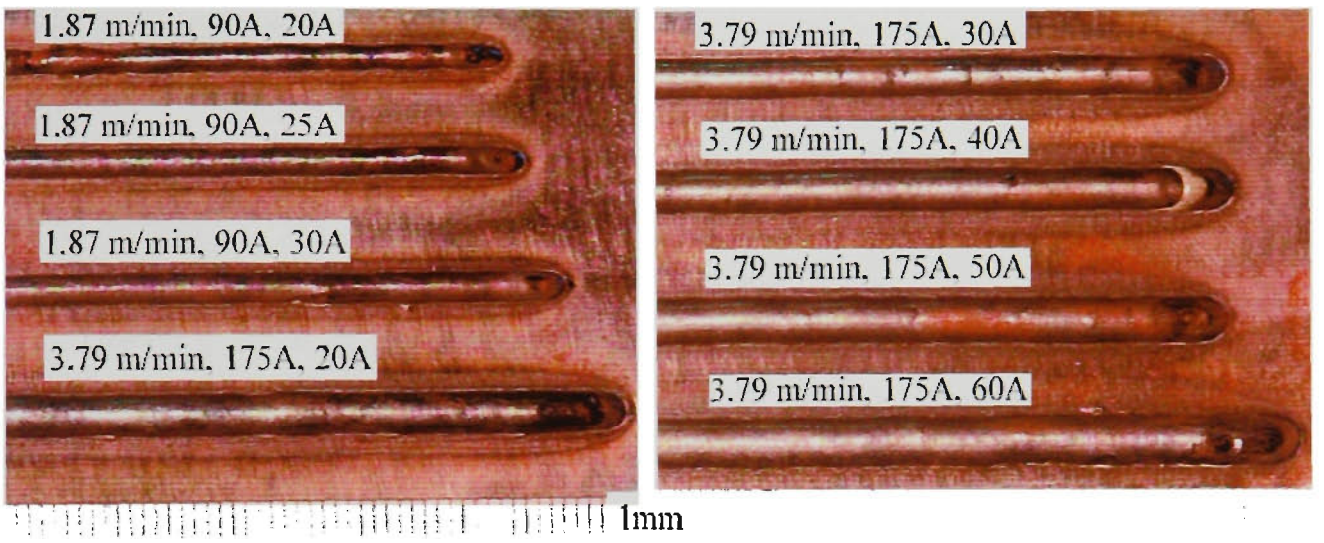

Figure 10.67 Photograph of weld beads for reduced wire feed speeds

Figure 10.68 is a photograph taken just prior to a short circuit rupture. Figure 10.69 shows the weld pool just after a rupture (though not of the same short circuit as Figure 10.68) and prior to application of Iarc_max. For these welds, Iarc_min=20A.

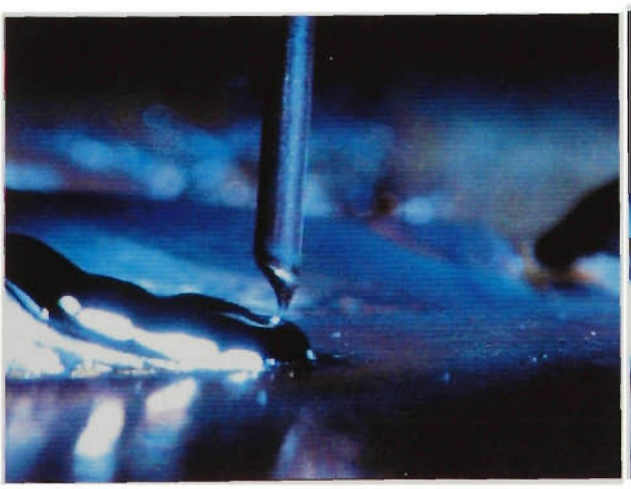

Figure 10.68 Pool just prior to rupture

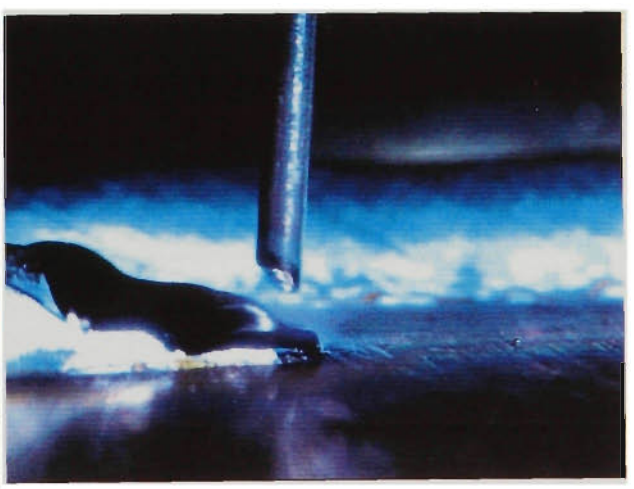

Figure 10.69 Pool just after rupture

The high wave front at the rear of the weld pool in Figure 10.69 will travel forward, and may cause a premature short circuit if the clearance between the pool and

electrode is not sufficient. The application of Iarc_max will simultaneously increase the clearance and depress the pool surface. The combination of these causes a premature short circuit to be avoided in most weld cycles, otherwise the spatter and stability would be unacceptable.

It can be deduced that the process at 3.79 m/min is able to operate over a wide range of current settings, since Iarc_min can be adjusted from 20A to 80A and still produce good welds. This is not the case for 1.87 m/min, where the value of Iarc_min is restricted to 30A or less. This is due to the reduced wire feed rate not being able to balance the melting rate of the electrode for high values of Iarc_min. In turn, this causes the dipping frequency to be reduced to values below 40Hz, which are not acceptable to a manual operator. The range of Iarc_min is likely to be increased by reducing the CTWD. The transit time is reduced, so electrode preheating is less, and the melting rate for a given Iarc_min is correspondingly reduced (section 10.3.5).

Discounting the limited operating range at 1.87 m/min, the high quality of welds produced was surprising nonetheless. Inspection of the electrical waveforms show why the process is stable and produces little spatter despite occasional failures to correctly predict the onset of short circuit ruptures. Figure 10.70 shows the current, voltage and camera synchronisation signal for a "failed" short circuit prediction. Figure 10.71 is a photograph of that event.

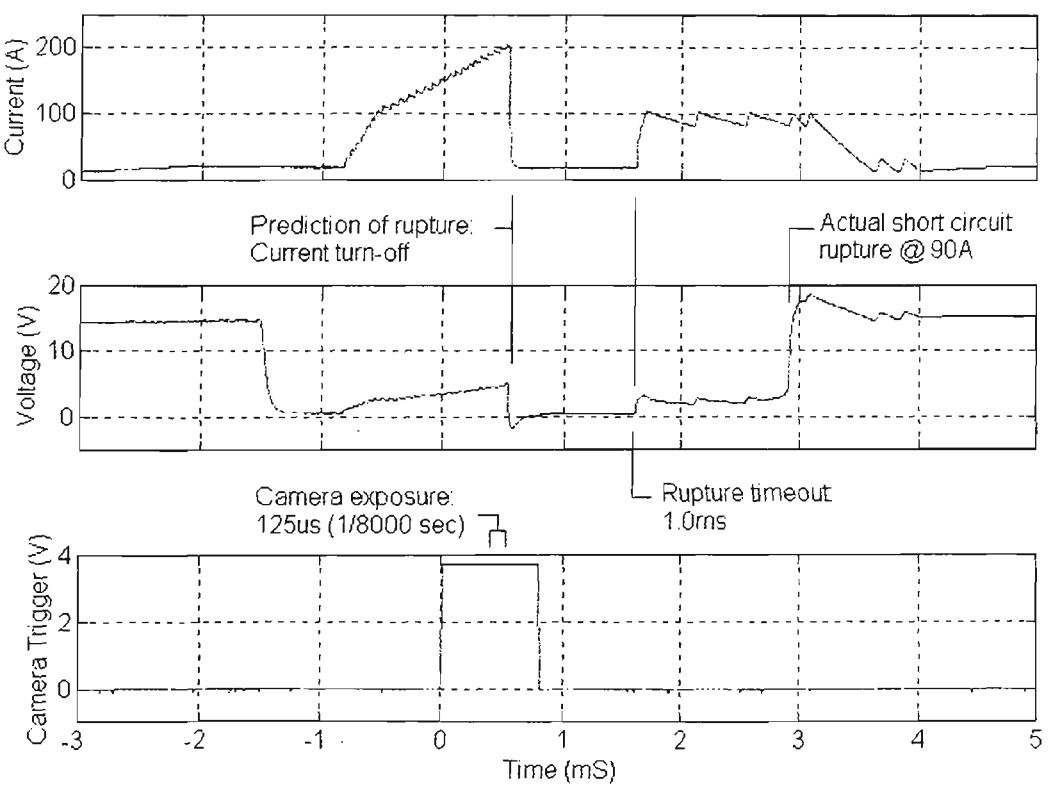

Figure 10.70 Current & voltage waveforms for WFR=1.87 m/min (Iarc_max=90A, Iarc_min=25A)

As shown in Figure 10.70, at time t=0.5ms, the premonition circuit predicts the onset of short circuit rupture, and the current is rapidly reduced to the background level (20A). However, the short circuit does not rupture, so after the programmed timeout of 1.0ms the initial arcing current Iarc_max is applied. From the voltage waveform, it can be seen that the short circuit finally ruptures at t=2.9ms, when Tarc_max has almost expired. Despite the rupture occurring at Iarc_max, little spatter is expected since the current is so low. At 90A, the arc forces do not appear to generate significant disturbances to the welding process. Figure 10.71 illustrates the failure of the short circuit detection. The exposure occurs 400μs after the camera trigger signal is asserted, and this corresponds to only 200μs before the short circuit current is removed, yet the short circuit neck is far from being pinched.

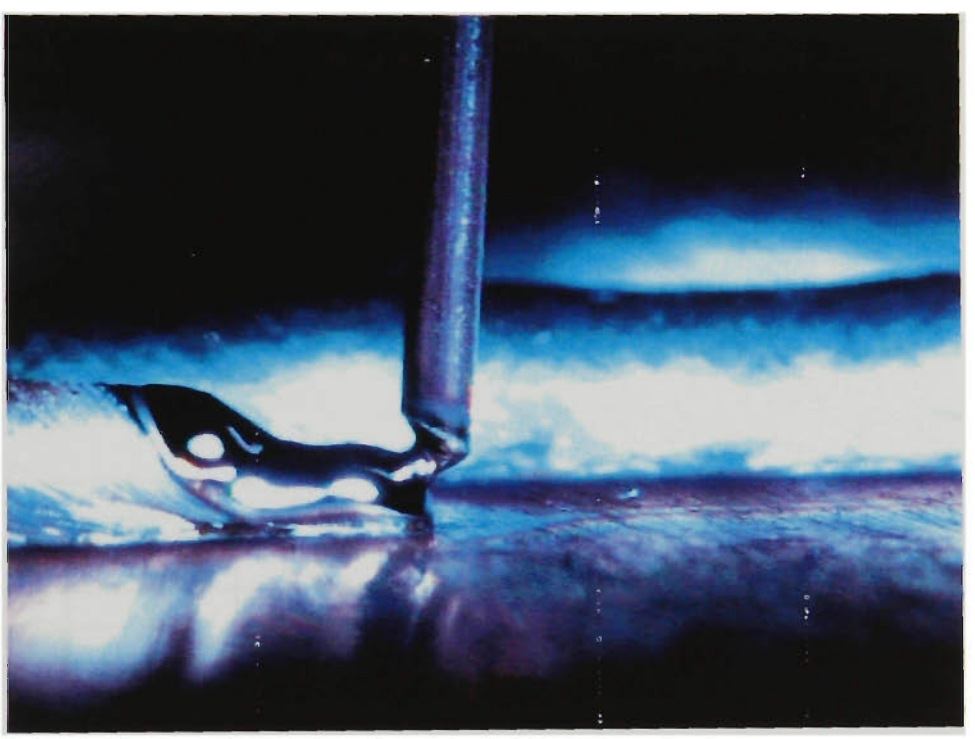

Figure 10.71 Photograph of weld prior to short circuit rupture

Inspection of waveforms recorded over 1.0 second periods show that the "fault" event described here occurs infrequently (typically less than once per second). Capturing the event photographically was a matter of luck as much as persistence.

10.4 Process Performance with CO_2 Shielding Gas

10.4.1 Scope

Tests were conducted to establish the operating range of the process operating with CO_2 shielding gas. Wire feed rate was 5.7 m/min and test values of CTWD were 12mm and 20mm. Parameters were set as per section 10.2.3. Figure 10.72a shows the test matrix for CTWD=12mm, while Figure 10.72b is for CTWD=20mm.

Iarc_min	Iarc_max												
	150	175	200	225	250	275	300	325	350	375	400	425	450
10						Region1							
20				X	X	X	X	X	X	X	X		
30				X	X	X	X	X	X	X	X		
40				X	X	X	X	X	X	X			
50	Region 2			X	X	X	X	X	X				
60	Low			X	X	X	X	X	X			Region 4	
70	arc length			X	X	X	X	X					
80				X	X	X	X						
90				X	X	X							
100													
110													
120						Region 3							

Figure 10.72a Test matrix of CO2 process, wire speed=5.7 m/min, CTWD=12mm, Travel speed=195mm/min, 6mm MS plate

Iarc_min	Iarc_max												
	150	175	200	225	250	275	300	325	350	375	400	425	450
10						Region1							
20			X	X	X	X	X	X					
30			X	X	X	X	X	X					
40				X	X	X	X	X					
50	Region 2				X	X	X	X					
60	Low				X	X	X					Region 4	
70	arc length												
80													
90													
100													
110													
120						Region 3							

Figure 10.72b Test matrix of Ar-23%CO2 process, wire speed=5.7 m/min, CTWD=8mm, Travel speed=390mm/min, 6mm MS plate

Results using data collected from oscilloscope recordings, data acquisition recordings, visual observation and macrosections were compiled. Table 10.5 lists the relevant figures representing this data.

Table 10.5 Summary of Figures for CO2 Process "Open Loop" Tests

Figure Description	Figure No. CTWD=12mm	Figure No. CTWD=20
Mean welding current vs Iarc_min & Iarc_max	10.73	10.103
RMS welding current vs Iarc_min & Iarc_max	10.74	10.104
Average arcing current vs Iarc_min & Iarc_max	10.75	10.105
Mean voltage vs Iarc_min & Iarc_max	10.76	10.106
Average dipping frequency vs Iarc_min & Iarc_max	10.77	10.107
Avg wire melting incremental length ΔL vs Iarc_min & Iarc_max	10.78	10.108
Fusion area vs Iarc_min & Iarc_max	10.79	10.109
Penetration depth vs Iarc_min & Iarc_max	10.80	10.110
Weld bead width vs Iarc_min & Iarc_max	10.81	10.111
Weld bead height vs Iarc_min & Iarc_max	10.82	10.112
Energy input per unit length of weld vs Iarc_min & Iarc_max	10.83	10.113
Fusion area vs Energy input per unit length of weld	10.84	10.114
Fusion area vs Mean welding current	10.85	10.115
Fusion area vs Average wire melting incremental length ΔL	10.86	10.116
Stability index vs Iarc_min & Iarc_max (2D)	10.87	10.117
Stability index vs Iarc_min & Iarc_max (3D)	10.88	10.118
Spatter index vs Iarc_min & Iarc_max (2D)	10.89	10.119
Spatter index vs Iarc_min & Iarc_max (3D)	10.90	10.120
Bead quality index vs Iarc_min & Iarc_max	10.91	10.121
Weld overall quality index vs Iarc_min & Iarc_max	10.92	10.122
Useful operating area	10.93	10.123
Arcing duty cycle vs Iarc_max & Iarc_min	10.94	-

10.4.2 Test Results for CO_2 Shielding Gas, CTWD=12mm

Figures 10.73 to 10.94 represent the detailed results of all experiments performed under the conditions specified in section 10.2.

[Refer to Appendix 10 for Figures 10.73 to 10.94]

10.4.3Discussion of Results for CO_2 Shielding Gas, CTWD=12mm

This discussion will make references to Figures 10.72 to 10.94. Where appropriate, comparisons will be made to results for the Ar-23%CO_2 process.

Mean welding current (Figure 10.73)

As for the Ar-23%CO_2 process, changes in Iarc_min produce significant changes in the mean current, and the relationship is linear. The mean current for low Iarc_max (short arc lengths) is noticeably different to that for higher values of Iarc_max (275A and above). This can be explained by significantly lower arcing duty cycle for low values of Iarc_max, as seen in Figure 10.94: A significantly larger fraction of the

weld cycle is spent in short circuit. This indicates that the geometry of the short circuit bridge is not conducive to efficient metal transfer. At first glance, it might be expected that the average weld cycle frequency would be higher for low values of Iarc_max. However, the significant extension in short-circuit duration adds to the total cycle time, so average frequencies for Iarc_max=225A and Iarc_max=275A do not differ greatly (Figure 10.77).

During welding trials, operation of the process for Iarc_max=225A was judged unsatisfactory from an operator's point of view. Oscillations in arc length were obvious, and the weld sounded quite "unsteady". The arc length oscillations became worse as Iarc_min was increased. The poor process behaviour is reflected in stability and spatter indices for Iarc_max=225A that are lower than Iarc_max=250A & 275A (see Figures 10.87 & 10.89). Bead quality was also degraded (Figure 10.91), with "flash" at the weld toe being the main detractor. The Iarc_max=250A condition did not exhibit this poor behaviour, even though the mean currents show similar trends. Some minor traces of "unsteadiness" were audible. No such problems existed for Iarc_max=275A. Figure 10.95 shows the differences in current waveforms for Iarc_max=225A and Iarc_max=275A, both at Iarc_min=60A. The large variation in short circuit duration and duty cycle is evident.

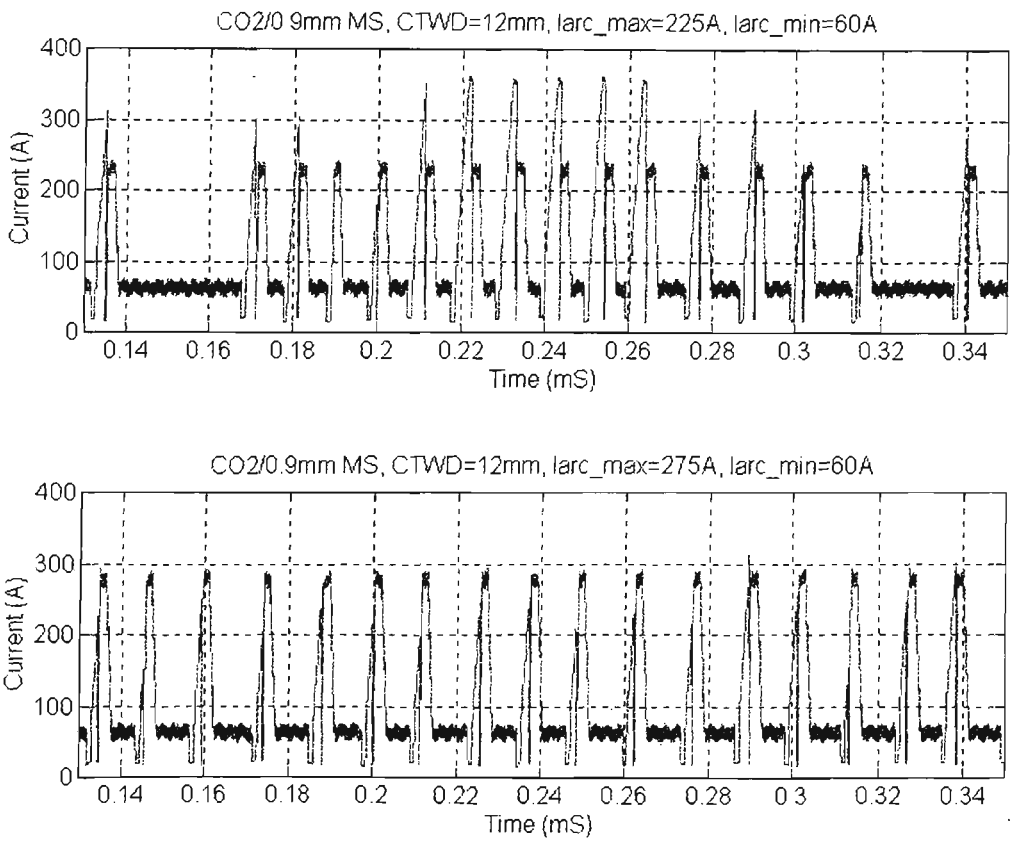

Figure 10.95 Waveforms for Iarc_max=225A and Iarc_max=275A (Iarc_min=60A)

Figure 10.96 is a photograph taken 400μs after the start of the short circuit for Iarc_max=275A, Iarc_min=60A, and the Figure 10.97 is the corresponding photograph for Iarc_max=225A, Iarc_min=60A. In Figure 10.96, the weld pool is relatively quiescent and the molten metal bridge length is long. These are conditions conducive to successful metal transfer [8]. In Figure 10.97, the weld pool is severely raised, presumably due to oscillations, and the resultant bridge length has been significantly reduced. If the period of weld pool oscillations is significantly longer than the short-circuiting duration, then for the duration of the short circuit the bridge length will remain shortened. As predicted by [8, 11, 12, 64], this makes the short circuit more difficult to rupture. The weld pool oscillations are not synchronised with the electrode melting rate, so the degree of bridge shortening varies with each short circuit. The resulting variations in short circuit duration are evident in the current waveform of Figure10.95. The weld pool oscillations for Iarc_max=225A are thought to be initiated and perpetuated by insufficient arc length. Increasing Iarc_max reduces or removes this problem. The effect of Iarc_max on arc length is investigated further in section 10.5.

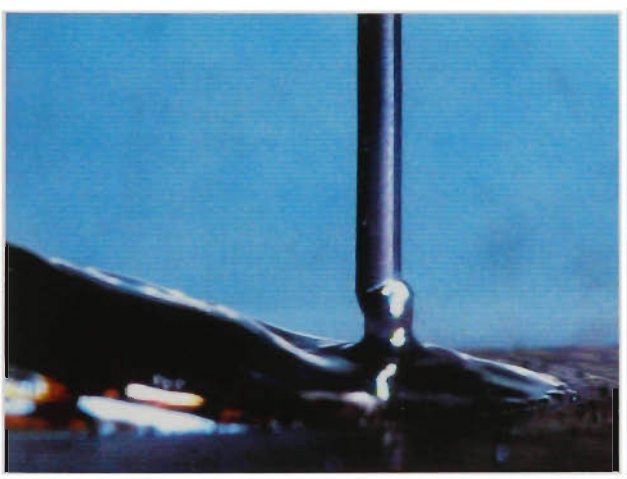

Figure 10.96 Pool at 400μs after short circuit for Iarc_max=275A

Figure 10.97 Pool at 400μs after short circuit for Iarc_max=225A

As a final comment on Figure 10.73, mean currents for the CO_2 process with CTWD=12mm are very similar to those for the Ar-23%CO_2 process at CTWD=16mm.

RMS welding current (Figure 10.74)

As for the Ar-23%CO_2 process, the RMS current generally falls as Iarc_min is increased. Aside from the intrinsic presence of RMS calculations in the action integral, there appears to be no other useful information in the RMS values.

Average arcing current (Figure 10.75)

This follows the same trends established for the Ar-23%CO_2 process. The currents are very similar to those for Ar-23%CO_2 CTWD=16mm.

Mean welding voltage (Figure 10.76)

Behavioural trends are the same as those of the Ar-23%CO_2 process. As expected, voltages for the CO_2 process are 2-3 volts higher than those for Ar-23%CO_2 for a given Iarc_max/Iarc_min condition. The differences are due mainly to different arcing characteristics of the shielding gases (Chapter 8), and partially due to differences in CTWD.

Average dipping frequency (Figure10.77)

Frequencies produced by the CO_2 process are similar to those of Ar-23%CO_2. This is expected because of the similarity of α and β melting rate constants. The results for Iarc_max=225A are aberrant because of reasons already discussed.

The frequency is monotonically decreasing with increasing Iarc_min except for the particular cases of Iarc_max above 275A and Iarc_min below 30A. Under these conditions, the weld cycle times became very bimodal, as shown in Figure 10.98. The current and voltage waveforms are shown in Figure 10.99.

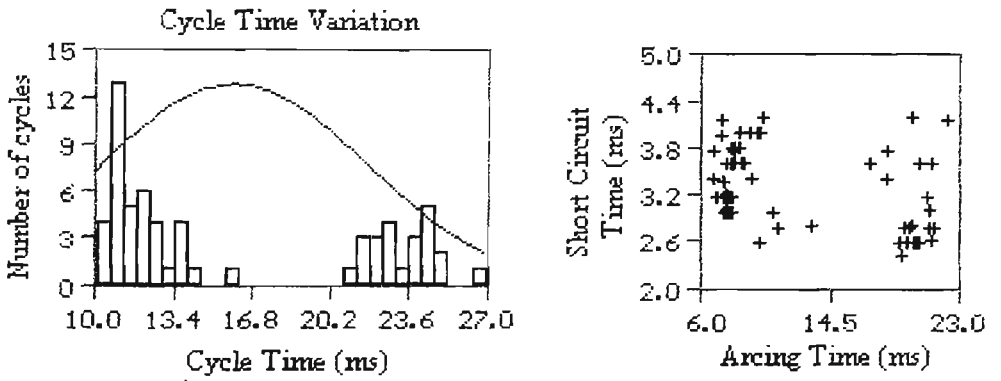

Figure 10.98 Cycle times statistical distribution for Iarc_max=325A, Iarc_min=20A

The large changes in cycle times are considered to be due to severe weld pool oscillations. These are initiated by the high value of Iarc_max (which applies a large depression force to the weld pool) and the rapid rate of current drop Iarc_ramp (which releases the force very rapidly). The very low value of Iarc_min does not provide any restraining force on the pool during free arcing, so oscillations are free to continue. The weld pool oscillations are evident in the voltage waveforms. Increasing Iarc_min tends to reduce these pool oscillations, as shown by the voltage waveforms in Figure 10.100 (Iarc_min=60A). A form of constant voltage control may be required to dampen these oscillations in a controlled manner, but this possibility is not investigated in this project.

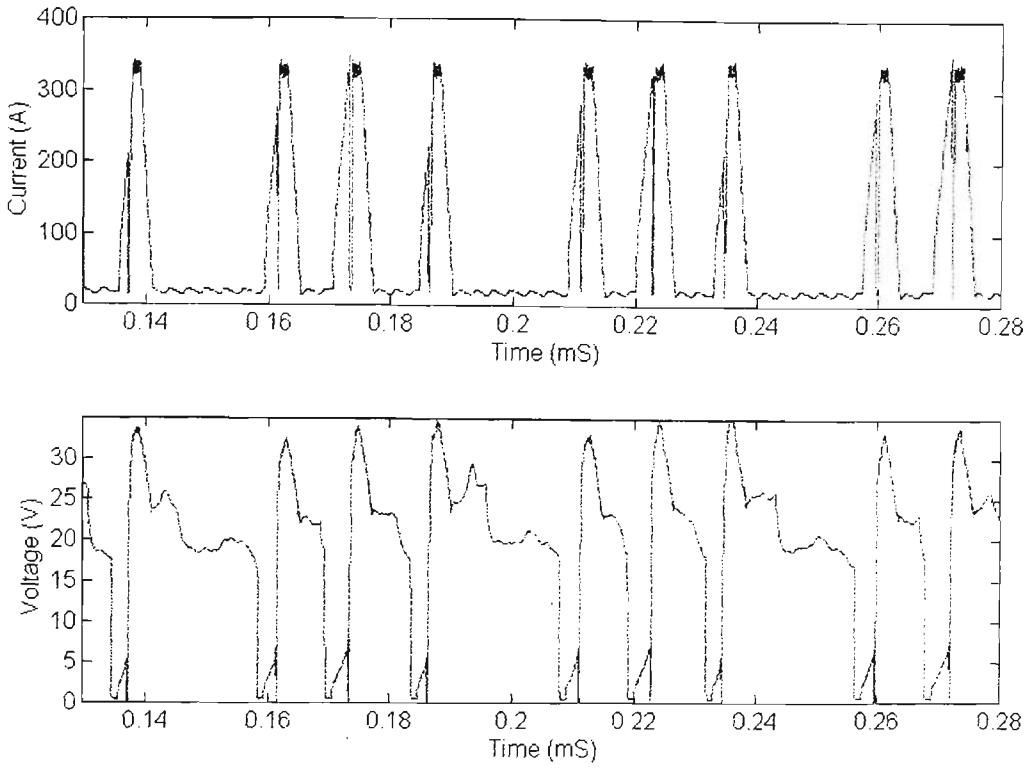

Figure 10.99 Waveforms for Iarc_max=325A, Iarc_min=20A

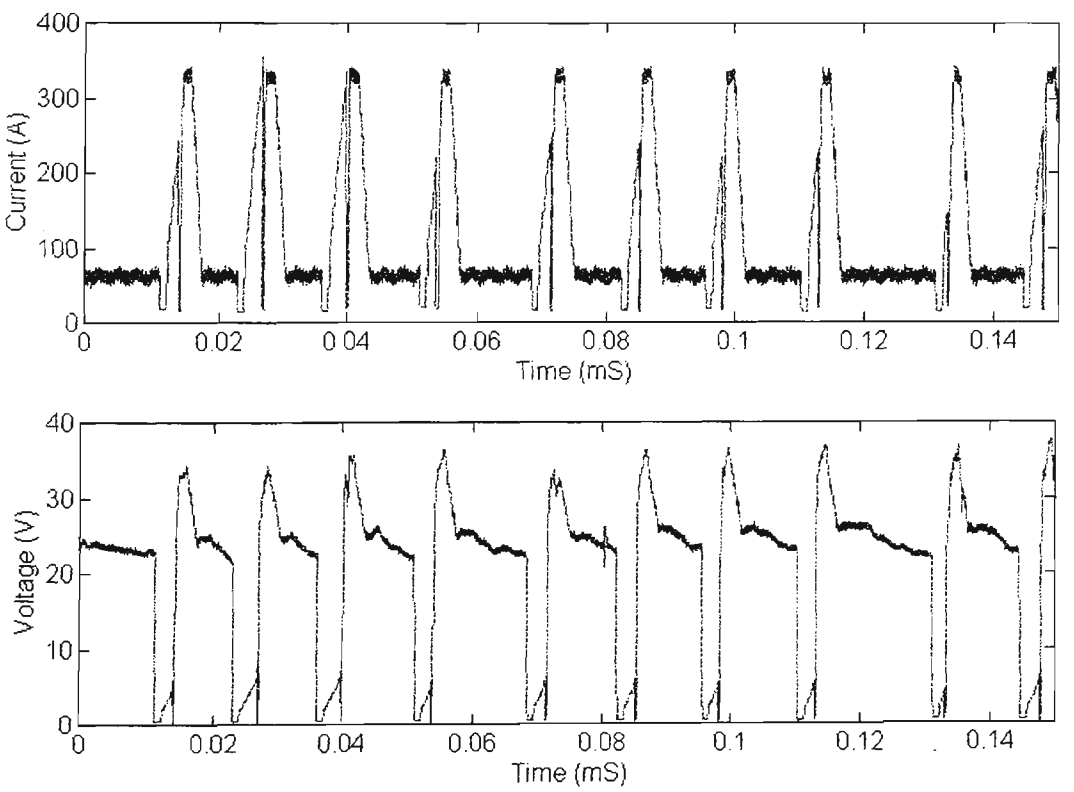

Figure 10.100 Waveforms for Iarc_max=325A, Iarc_min=60A

From a human perspective, the changes in dipping frequency as Iarc_min is adjusted are far less noticeable than for Ar-23%CO_2. The CO_2 process produces a much "softer" arc sound, which tends to mask the short circuit rupture sound transients, so a

45Hz weld does not sound much "slower" than a 90Hz weld. This property makes changes in frequency (which are necessary for achieving greater fusion) far more tolerable to an operator.

Average wire melting incremental length ΔL (Figure 10.78)

The change in ΔL for changes in Iarc_min are not as large as for the Ar-23%CO_2 process at CTWD=16mm (Figure 10.8). However, the overall range of values is similar, from 1.0mm to 2.5mm. As stated previously, determining values of ΔL to use as references in a closed loop droplet control system for all conceivable combinations of Iarc_max, Iarc_min and CTWD would be impractical.

Fusion area, Penetration depth, Bead width, Bead Height (Figures 10.79 – 10.82)

These results show the linear relationship of fusion area to Iarc_min more clearly than the results for the Ar-23%CO_2 process (figures 10.9 and 10.33). This is probably due to the slower travel speed used for CO_2, resulting in less variation of fusion area along the bead length. The range of fusion adjustment is quite remarkable. The maximum fusion area is over 2.5 times the minimum fusion area for a given Iarc_max, without altering the wire feed rate, peak arc length or short-circuit rupturing characteristics. It is doubtful that such a range of adjustment could be achieved with the same ease using a conventional CV power source. The change in circuit inductance required to alter arc heating would significantly affect the behaviour during the short circuit, degrading the stability of the process. Other factors such as maximum arc length would also be inadvertently affected.

Linear relationships of penetration depth, bead width and bead height to Iarc_min are also evident.

Energy input (Figure 10.83)

The linear variation of energy input to the process for changes in Iarc_min is the same as for the Ar-23%CO_2 process (Figures 10.13 & 10.37). For CO_2, the increase of energy input for increases in Iarc_max (assuming fixed Iarc_min) is far less than for Ar-23%CO_2. That is, the lines on the graph are closer together for Iarc_max above 275A. It is unclear if this is due to the slower travel speed, or a result of the differences in shielding gas properties. Nonetheless, this does not detract from the desirability of the process' behaviour.

Fusion area vs Energy input (Figure 10.84)

The linearity between fusion area and energy input is again confirmed. As expected, the fusion areas produced by the CO_2 tests are higher than those of Ar-

23%CO_2, but the major factor is travel speed. When comparisons are made for similar travel speeds (see Figure 10.57), the fusion areas for CO_2 and Ar-23%CO_2 are not vastly different. Although there are insufficient comparative results to draw a definite conclusion, it appears that the relationship of fusion area to energy input is the same for both shielding gases ie, it is material dependent. The CO_2 process can achieve greater fusion only because it can generate greater energy for a given Iarc_max/Iarc_min setting. This in turn is due to the arcing characteristic of the gas (Chapter 8).

Fusion area vs Mean Current (Figure 10.85)

As for the Ar-23%CO_2 process, the relationship between fusion area and mean current is not consistent for different values of Iarc_max. If the results of Iarc_max=[225,250] are ignored, the results may appear encouraging. However, the results are not sufficiently robust to make a closed loop control system practical.

Fusion area vs ΔL (Figure 10.86)

The data again indicates that the fusion area will not be inherently controlled via adjustment of the average wire melting increment length ΔL.

Stability and Spatter indices (Figures 10.87-10.90)

The stability indices are generally highest for low Iarc_min, and steadily degrade as Iarc_min is increased. Stability indices have a similar range of values to the Ar-23%CO_2 process, with the exception of Iarc_max=225A, which has been explained as an aberrant result.

The spatter is lowest at low Iarc_min, and rapidly increases as Iarc_min is raised. Unlike the Ar-23%CO_2 process, Iarc_max does not significantly affect the spatter levels, indicating that the primary spatter production mechanism is likely to be ball repulsion spatter at the start of the short circuit: As Iarc_min is increased, these repulsion forces tend to be increased [13]. Figure 10.96 shows the appearance of a short circuit bridge formed without repulsion for Iarc_max=275A, Iarc_min=60A. Figure 10.101 below shows extreme repulsion taking place for Iarc_max=255A, Iarc_min=90A. The exposure is taken 400μs after the start of the short. This degree of repulsion was observed for Iarc_min above 60A. The frequency of these events increases with Iarc_min, creating noticeable increases in spatter levels.

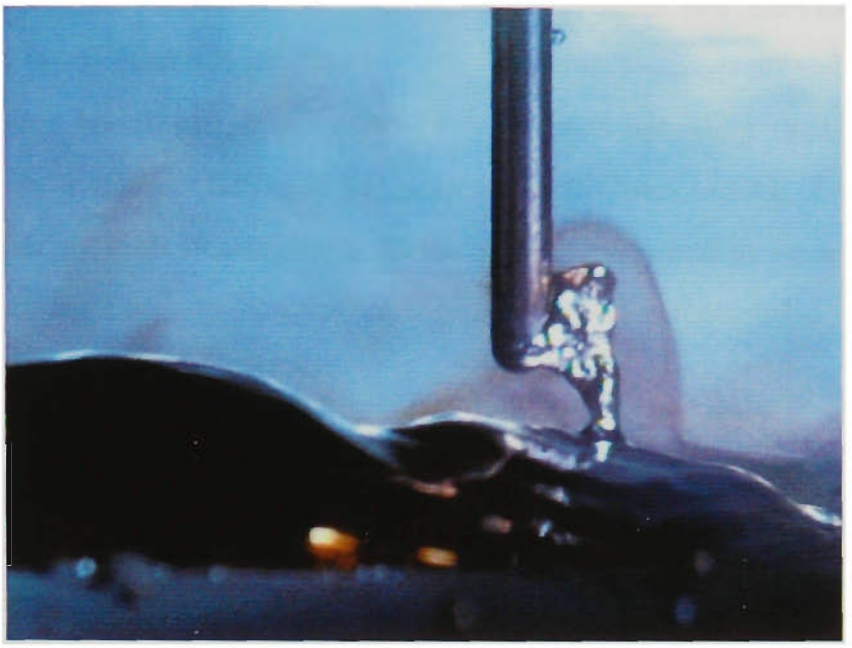

Figure 10.101 Photograph showing short circuit repulsion. Iarc_max=275A, Iarc_min=90A

Bead quality index (Figure 10.91)

The bead quality is good to excellent across the entire test range. Irrespective of stability index or spatter level, this type of process control can lay down a bead of good appearance with CO_2. Figure 10.102 shows some beads with higher bead quality indices.

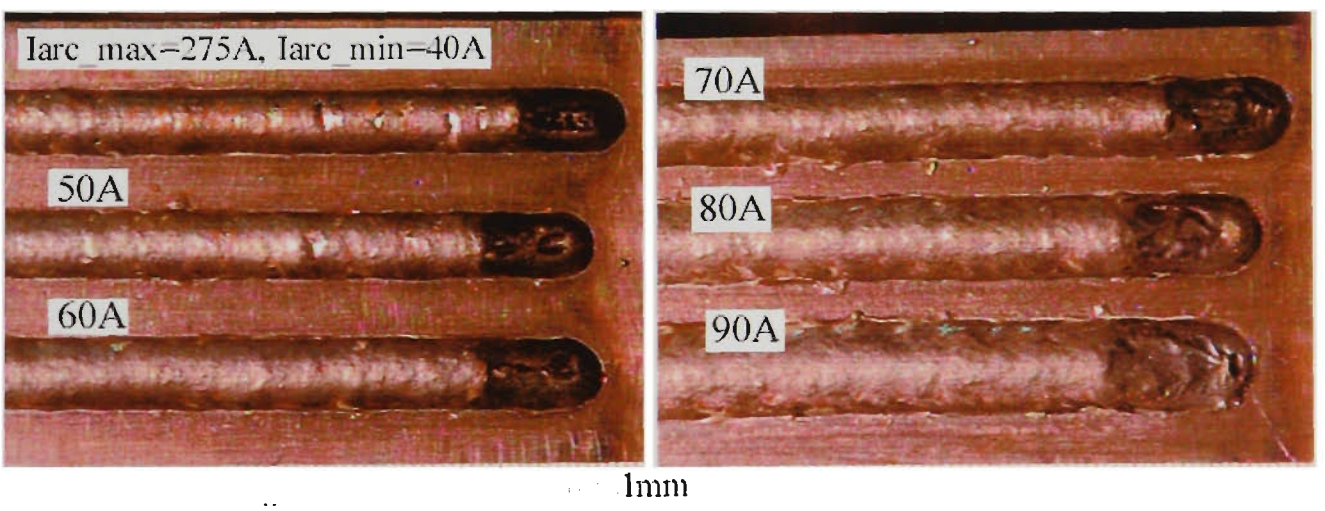

Figure 10.102 Photograph of weld beads for CO_2, CTWD=12mm

Overall weld quality index (Figure 10.92)

Overall weld quality indices are lower than for Ar-23%CO_2. This is almost entirely due to the increase in spatter levels, which is the common experience with all types of CO_2 welding. Using the same criteria as Ar-23%CO_2 for determining a satisfactory weld, the useful operating area is presented in Figure 10.93. Note that an

additional condition has been added: Iarc_max=225A does not provide satisfactory operation due to insufficient arc length.

Despite this additional qualification, this derived operating area could not be considered a truthful representation of the process' capabilities in CO_2. For example, in applications requiring high fusion, high values of Iarc_min need to be used. The high spatter is undesirable, but must be accepted if greater fusion is required.

10.4.4 Test Results for CO_2 Shielding Gas, CTWD=20mm

Figures 10.103 to 10.123 represent the detailed results of all experiments performed under the conditions specified in section 10.2.

[Refer to Appendix 10 for Figures 10.103 to 10.123]

10.4.5 Discussion of Results for CO_2 Shielding Gas, CTWD=20mm

This discussion will make references to Figures 10.102 to 10.123.

The results for CTWD=20mm follow the same trends established for CTWD=12mm. Generally, stability indices were significantly lower than for CTWD=12mm, and as Iarc_min is increased the weld would be judged unstable by an operator. Negative stability indices were obtained, indicating an unacceptably large variation in weld cycle times. As expected, bead quality was degraded, yet only 3 of the beads would be judged unacceptable in appearance (Figure 10.121). Again, the process shows its ability to produce acceptable beads under adverse conditions.

The useful operating area for CTWD=20mm (Figure 10.123) is much narrower than for CTWD=12mm (Figure 10.93). The main reason for this is the loss of stability as Iarc_min is increased, contributing to the drop in overall weld quality indices (Figure 10.122).

The energy input to the process (Figure 10.114) is much lower than for CTWD=12mm (Figure 10.84), so fusion area is correspondingly reduced. The reduction in energy is a result of the additional electrode preheating (longer transit time) increasing the melting rate per unit current, thus lowering the average current since more time is spent in steady state arcing (Iarc_min). Figure 10.123a shows that the relationship between fusion area and energy input is unaffected by CTWD. The Ar-23%CO_2 process exhibits similar behaviour (Figure 10.51).

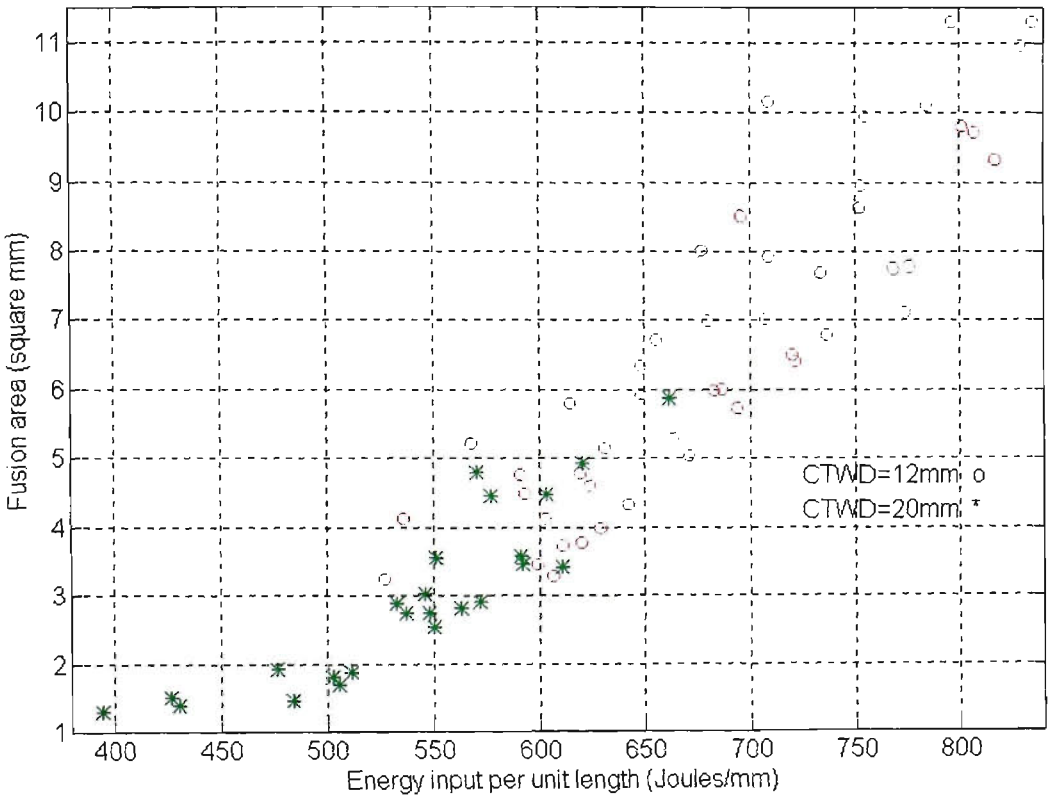

Figure 10.123a Fusion area vs Energy input for CTWD=12 & 20mm (CO_2)

In summary, operation of the CO2 process at high CTWD values is not desirable. In manual welding, excessive CTWD should be avoided because of low fusion despite a deceptively acceptable weld bead appearance.

10.5 Photographic Investigation of Arc Length and Pool Depression

In the discussions of sections 10.3 and 10.4, deductions concerning arc length and pool depression were drawn from the experimental data. This section presents photographic verification of these deductions, using the visualisation equipment described in Chapter 9. In particular, the following claims are investigated:

1. The maximum arc length is determined by Iarc_max current setting.
2. Pool depression is significant for high values of current (above 200A) and not significant for low values of current (below 100A).

10.5.1 Arc Length Variations in CO_2 Shielding Gas

A series of photographs were taken of the CO_2 process operating with 0.9mm ER70S-6 (AWS A5.18) electrode , 5.7 m/min wire feed rate, 195 mm/min travel speed, and 12mm CTWD. The photograph exposure is 1/8000 second (125μs) starting at 1.50 ms after the start of the arcing period. This corresponds to the end of Tarc_max, the

rapid burnback stage. All electrical parameters are those specified in section 10.2. Steady state arcing current Iarc_min was kept at 50A.

Figures 10.124 to 10.127 show the arc appearance for Iarc_max=225, 250, 375 and 400A, respectively. They are presented to the same scale. It is evident that arc length is increasing with the current level, and that the higher arcing currents create significant weld pool depression. The diameter of the weld pool "crater" increases as Iarc_max is raised, so the distance of the crater "floor" to crater "rim" is expected to be greater. The droplet at the end of the electrode becomes larger for increasing Iarc_max, due to the higher instantaneous melting rate. Asymmetrical deflection of the molten droplet material is also evident for higher currents, particularly 400A.

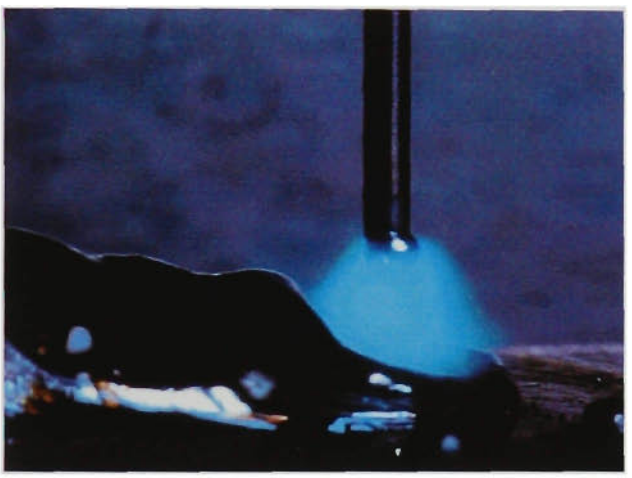

Figure 10.124 Iarc_max=225A

Figure 10.125 Iarc_max=250A

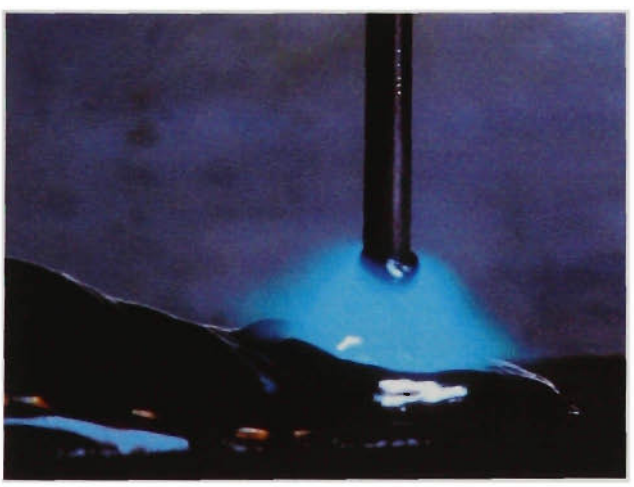

Figure 10.126 Iarc_max=375A

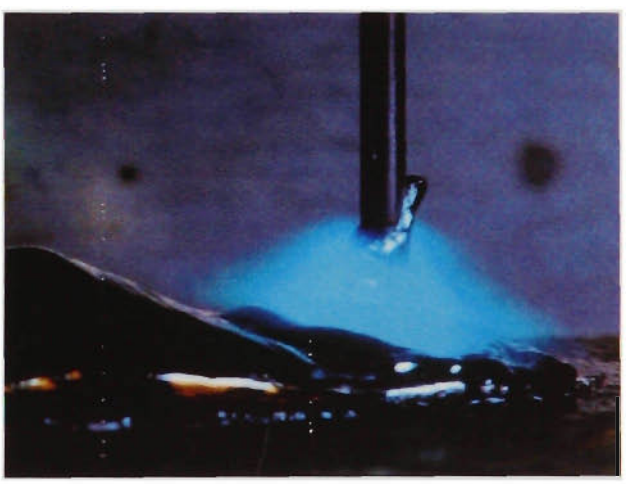

Figure 10.127 Iarc_max=400A

Accurate measurement of arc length is not possible using these photographs, since the pool depression hides the floor of the weld pool "crater". The camera viewing angle is approximately 10^0 to the horizontal. These photographs show that a far greater angle would be required to view the crater floor, but this may consequently obscure the bottom of the droplet. Accurate measurement of droplet volume is also difficult at high

Iarc_max due to material deflection as shown in Figure 10.127. If material is deflected behind the electrode or the droplet, it cannot be measured.

Despite these limitations, these photographs support the assertion that Iarc_max determines the peak arc length during arcing.

10.5.2 Arc Length Variations in Ar-23%CO_2 Shielding Gas

A series of photographs were taken of the Ar-23%CO_2 process operating with 0.9mm ER70S-6 (AWS) electrode , 5.7 m/min wire feed rate, 390 mm/min travel speed, and CTWD of 8mm and 16mm. As for previous photographs, the exposure is 1/8000 second (125μs) starting at 1.50 ms after the start of the arcing period. All electrical parameters are unchanged except for Iarc_max & Iarc_min.

Figures 10.128 and 10.129 shows the arc appearance for Iarc_max=200A and 350A, respectively. For these photographs, CTWD is 16mm and Iarc_min is 70A.

Figure 10.128
Iarc_max=200A CTWD=16mm

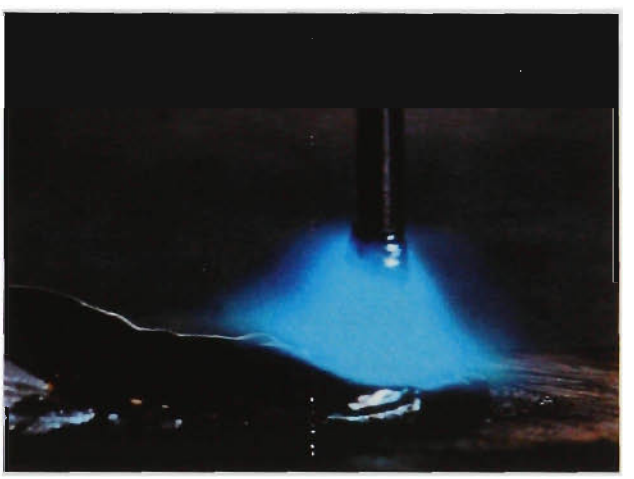

Figure 10.129
Iarc_max=350A CTWD=16mm

Figures 10.130 and 10.131 shows the arc appearance for Iarc_max=225A and 400A, respectively. For these photographs, CTWD is 8mm and Iarc_min is 90A. Note that these two sets of photographs are not intended to be directly comparable, since the degree of electrode preheating (and hence melting rate) would be significantly different for each value of CTWD. The degree of pool depression is less than that for the CO_2 process, due to the higher travel speed and thus lower bead height above the workpiece surface. As a result, the arc length differences are more evident. As before, increasing Iarc_max results in greater pool depression and a larger droplet on the electrode at the end of Tarc_max. These results strongly support the assertion that peak arc length is determined by Iarc_max in the Ar-23%CO_2 process.

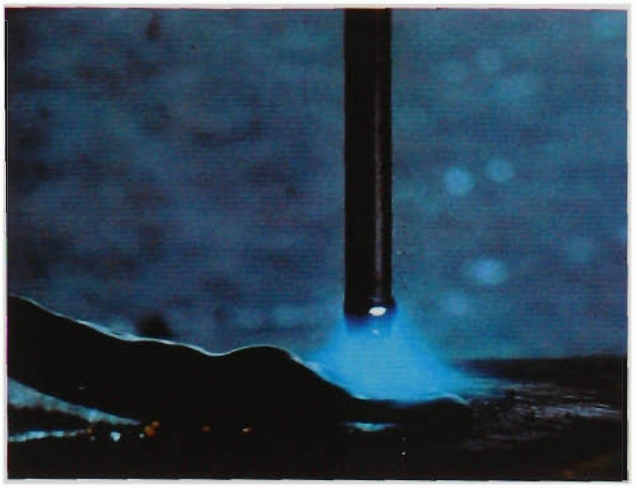

Figure 10.130
Iarc_max=225A CTWD=8mm

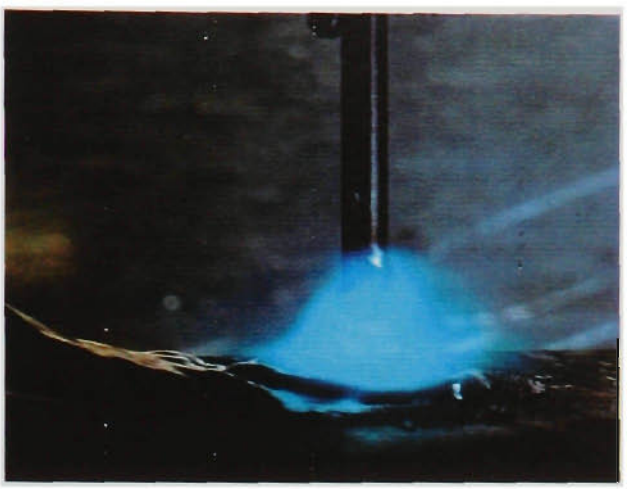

Figure 10.131
Iarc_max=400A CTWD=8mm

10.5.3 Pool Depression during Steady State Arcing

This section investigates the degree of pool depression experienced during steady state arcing (at current Iarc_min).

Figure 10.132 shows the Ar-23%CO_2 process operating at Iarc_min=100A. The exposure occurs 10.0ms after commencement of arcing, so any pool oscillation transients due to initial pool depression will have diminished. The total arcing time for this event is 12.1ms. The travel speed is set to 195mm/min, so that a high weld bead is produced, tending to exaggerate pool depression (see previous section). It can be seen that pool depression due to Iarc_min is minimal, and not readily distinguishable from small pool oscillations.

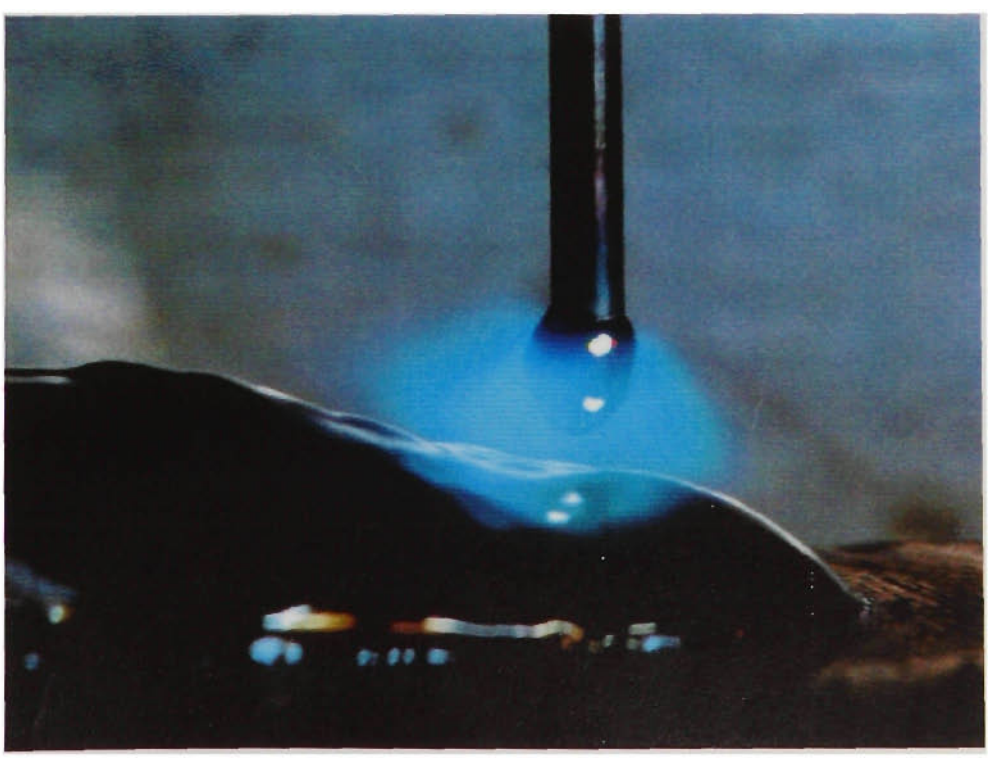

Figure 10.132 Pool depression in Ar-23%CO_2, Iarc_min=100A

Figure 10.133 shows the CO_2 process operating at Iarc_min=100A. This exposure occurs 40.0ms after commencement of arcing, so any pool oscillation transients due to initial pool depression will have diminished. The total arcing time for this event is 49.9ms. The travel speed is also set to 195mm/min, this being the travel speed for all CO_2 test. Here, some pool depression is evident, although it is far less than that produced in Figures 10.124 to 10.127.

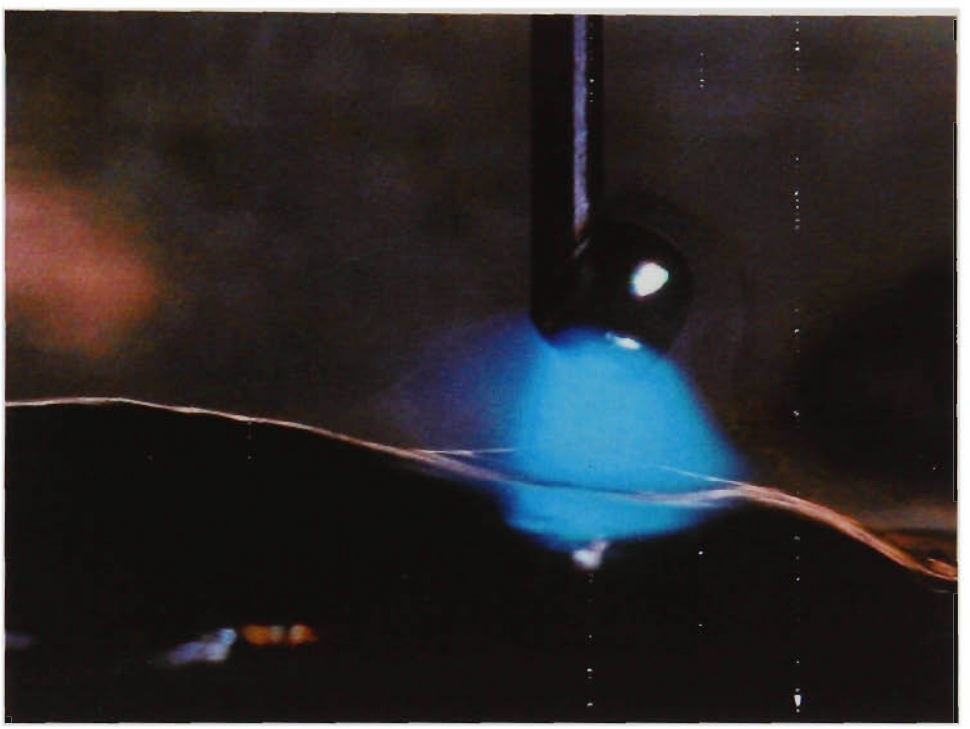

Figure 10.133 Pool depression in CO_2, Iarc_min=100A

As has been shown in section 10.4.3, Iarc_min=100A represents the highest probable steady state arcing current, due to the high spatter levels. At lower currents, pool depression is not expected to play a significant part in the process.

10.6 Simulation of the Open Loop Process using Melting Rate Considerations

In earlier sections of this chapter it has been postulated that the behaviour of the open loop process is dominated by melting rate considerations, while pool oscillations have a smaller role to play. To test this theory, a number of software simulations were performed using a relatively simple model of the process. This section presents the simulation results and compares them to the experimental results shown in section 10.3 and 10.4.

10.6.1 Description of Process and Power Source Model

A number of simplifying assumptions are made regarding the process:

1. The instantaneous melting rate of the electrode is determined using the action integral described in Chapter 7 to model the electrode preheating:

$$Melting\ Rate(t) = \frac{\alpha}{1 - \beta \int_0^{\tau} i^2(t)dt} i(t) \tag{10.9}$$

where τ is the transit time from contact tip to workpiece. The values of melting rate constants α and β depend on the type of shielding gas being modelled.

The wire melting incremental length $\Delta L(t)$ at any time during the arcing period is thus:

$$\Delta L(t_a) = \int_0^{t_a} Melting\ Rate(t)\ dt \tag{10.10}$$

where t_a is the time from the start of arcing.

2. The molten material at the end of the electrode represented so far as a cylinder of length ΔL and diameter equal to the electrode diameter d_e is converted to a sphere of diameter d_s of equal volume. This sphere is suspended below the non-molten end of the electrode.

$$d_s(t_a) = 2.\sqrt[3]{\frac{3d_e^2 \Delta L(t_a)}{16}} \tag{10.11}$$

3. The weld pool is considered to have zero height and depth at the workpiece surface. No oscillation or depression dynamics are modelled.

4. The wire feed rate is assumed to be perfectly constant. During the arcing period, the arc length is calculated as:

$$L_{arc}(t_a) = \Delta L(t_a) - d_s(t_a) - \int_0^t (WFR)dt + L_{rupture} \qquad (10.12)$$

where t is the time from the start of the short circuit.

The wire feed rate is integrated from the start of the short circuit. The arc length at the start of the arcing period is non-negative due to $L_{rupture}$. This simulates the clearance between pool and electrode at the end of the short circuit rupture (see Figure 10.69) by setting $L_{rupture}$ to be equal to the final value of d_s in the last arcing period. Thus the initial arc length at the start of arcing is:

$$L_{arc}(t_a = 0) = L_{rupture} - \int_0^{T_S} (WFR)dt \qquad (10.13)$$

where T_S is the short circuit duration. Thus the advance of the electrode during the short circuit is taken into account.

5. The arcing period is considered to be ended when the arc length is zero. At the start of the short circuit, ΔL is reset to zero.

6. The total short circuit time is based on the results obtained in Chapter 7:

$$T_S = T\_wetting + (1.21 + 0.35\Delta L_{LAST}) + T\_rupture \quad (\text{Ar-23\%}CO_2) \qquad (10.14a)$$

$$T_S = T\_wetting + (0.9 + 0.54\Delta L_{LAST}) + T\_rupture \quad (CO_2) \qquad (10.14b)$$

where: T_wetting = 0.5ms for Ar-23%CO_2, 1.5ms for CO_2

T_rupture = 0.25ms (fixed)

ΔL_{LAST} is the value of ΔL at the end of the last arcing period.

The modelling of the power source is straightforward, since it acts as a current source under all circumstances. The rules for power source behaviour are as follows:

1. At the start of the short circuit, reduce current to I_backgr (20A) for time T_wetting. Then increase current at 300A/ms up to 100A, after which current is ramped up at 100A/ms. Clamp short circuit current to 400A. This is done for time T_S calculated using equation 10.14. During T_rupture, current is set to I_backgr.

2. After the short circuit time expires, Current is Iarc_max for time Tarc_max (1.5ms), and is then ramped down to Iarc_min at the rate Iarc_ramp (150A/ms). Steady state arcing is continued at Iarc_min until the next short circuit (zero arc length is reached).

The resultant current waveform is similar to that in Figure 10.1.

It is worth noting that in the modelling of this type of process control, the current-voltage characteristics of the arc are not relevant, since they do not influence the output current of the power source. This removes a major source of error from the simulation. Because of this, it can be stated that this simulation bases its results solely on modelling of electrode melting rates.

10.6.2 Results of Simulations

Figures 10.134 to 10.141 compare the results of simulations to the experimental results presented in sections 10.3 and 10.4. The CO_2 process is modelled for Iarc_max=275A, while the Ar-23%CO_2 process is modelled for Iarc_max=250A.

The simulation results are remarkably similar to the experimental data, considering the gross simplifications of the process model. The case of Ar-23%CO_2 at CTWD=8mm shows the greatest deviation, mainly for dipping frequency. In all cases, the simulation overestimates values at low values of Iarc_min. This trend corresponds to the simulation results presented in Chapter 6, where use of the action integral and assigned values of α and β tended to underestimate the melting rate for lower welding voltages (shorter average arc lengths produced by low Iarc_min). An underestimation of melting rate in the simulations of this section would indeed result in predicted dipping frequencies being higher than experimental values. The mean and RMS currents would also be higher than actual values, due to the increased ratio of short circuit current-time integral to arcing current-time integral.

In conclusion, the good agreement between simulations and experimental data support the hypothesis that process behaviour is dominated by electrode melting rate considerations, while weld pool dynamics play a less significant role.

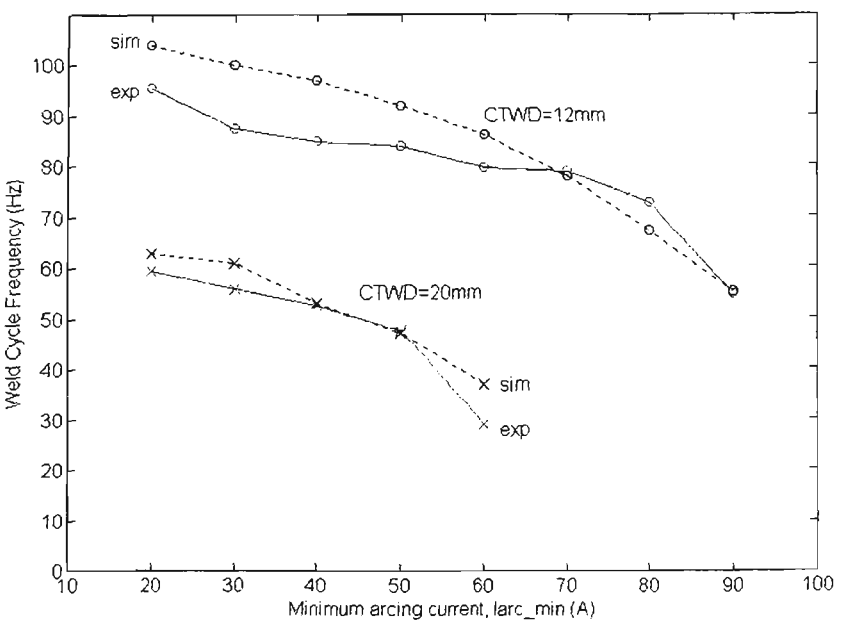

Figure 10.134 Simulation of dipping frequency for CO_2 (Iarc_max=275A)

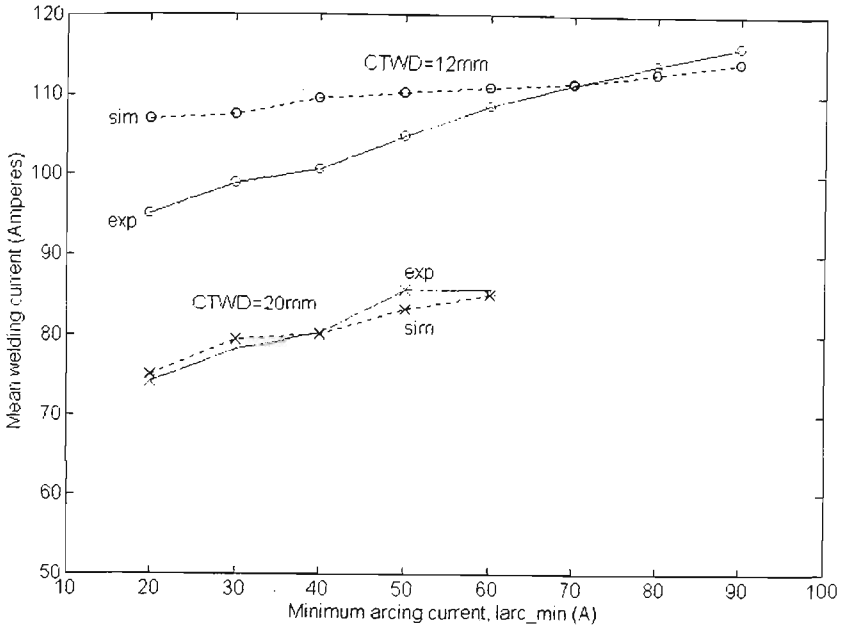

10.135 Simulation of mean welding current for CO_2 (Iarc_max=275A)

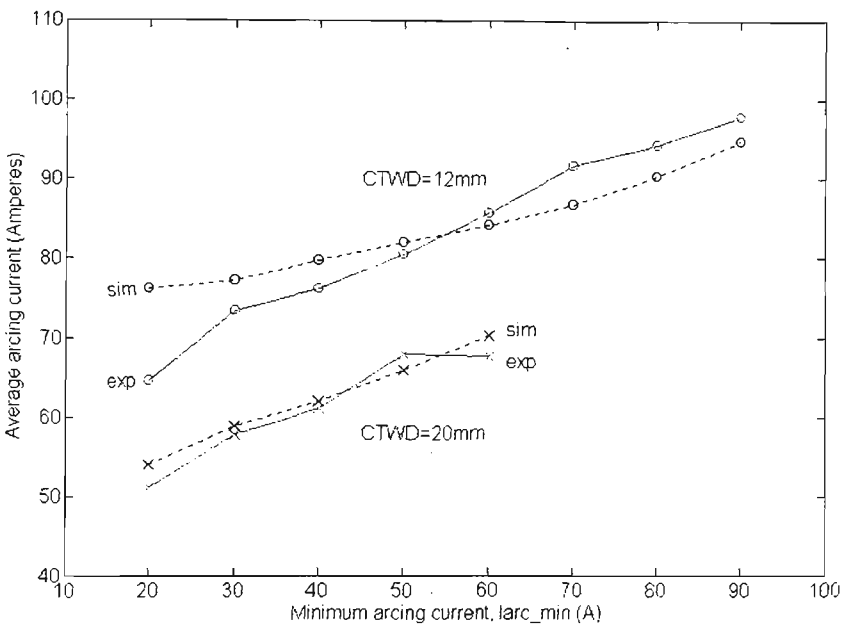

10.136 Simulation of average arcing current for CO_2 (Iarc_max=275A)

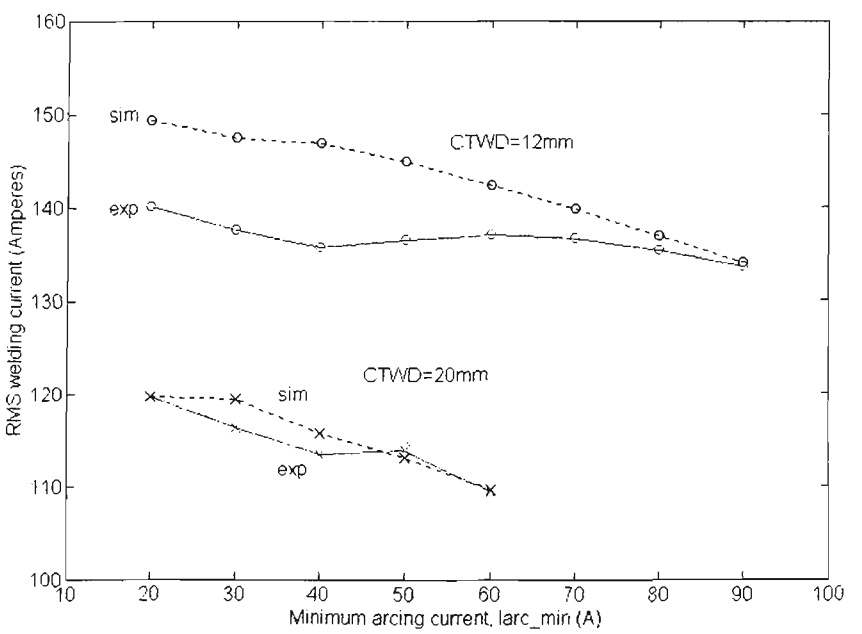

10.137 Simulation of RMS welding current for CO_2 (Iarc_max=275A)

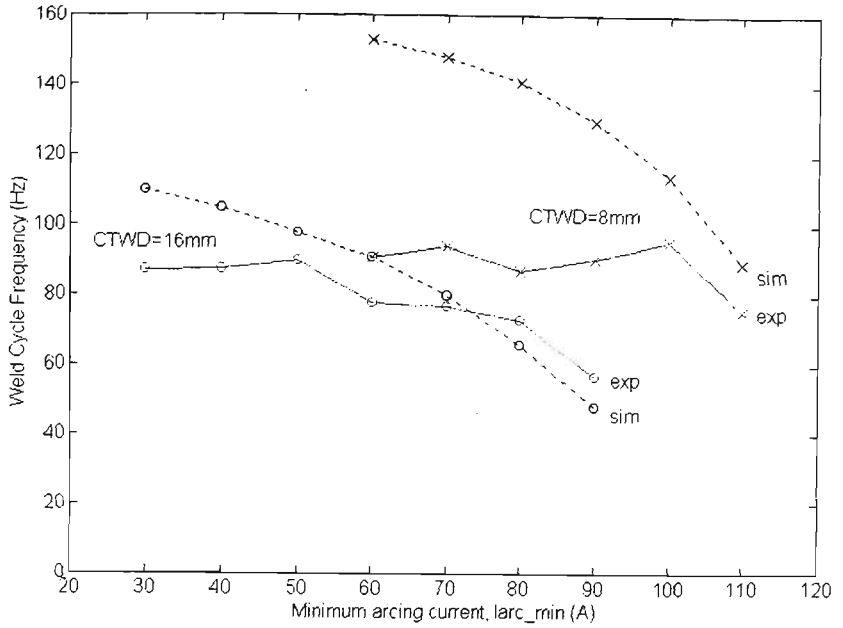

10.138 Simulation of dipping frequency for Ar-23%CO_2 (Iarc_max=250A)

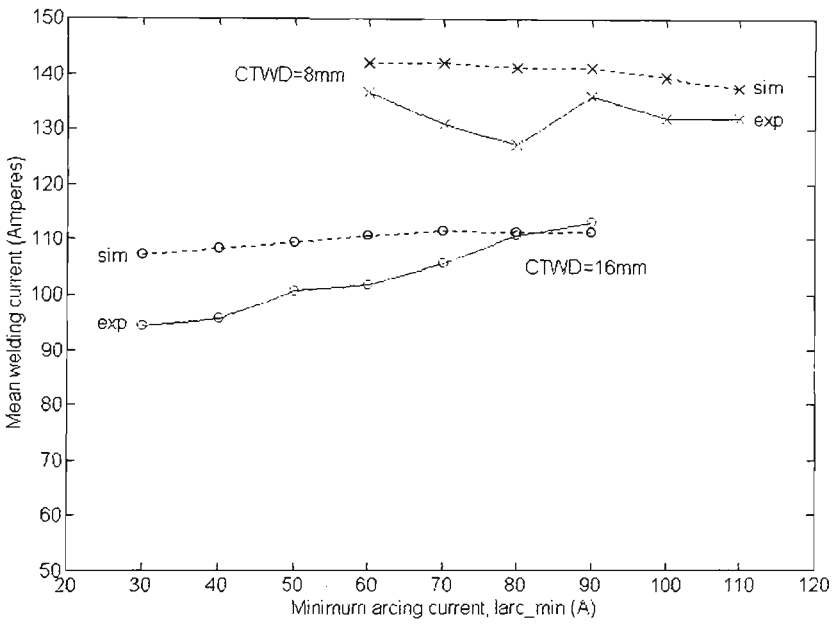

10.139 Simulation of mean welding current for Ar-23%CO_2 (Iarc_max=250A)

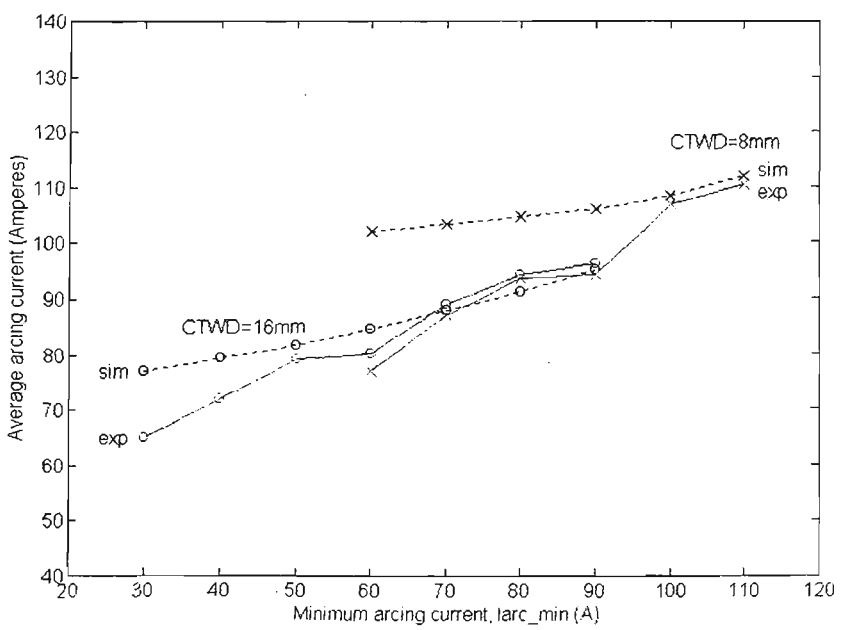

10.140 Simulation of average arcing current for Ar-23%CO_2 (Iarc_max=250A)

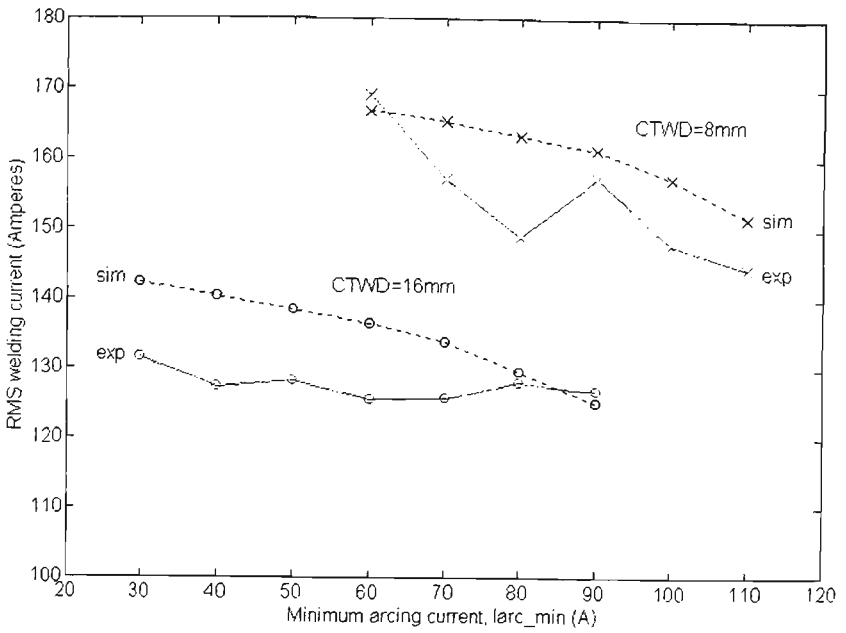

10.141 Simulation of RMS welding current for Ar-23%CO_2 (Iarc_max=250A)

10.7 Summary and Discussion of Results for the "Open Loop" Process

This section summarises the key findings presented and discussed in detail throughout this chapter.

The major benefit delivered by the "open loop" controlled short circuit GMAW process is the ability to significantly decouple key process parameters such as peak arc length, energy input, fusion area, and short-circuit rupturing characteristics. The degree of decoupling is not absolute (for example, an increase in arc length also causes some small increase in energy input), but the interplay between parameters is minimised. This allows greatly improved process control compared to a conventional CV power source. Importantly, the dependence of welding process behaviour on power source dynamics has been removed.

Peak arc length is determined by current Iarc_max. For a given setting of Iarc_max, the RMS current remains almost constant as Iarc_min is adjusted from 30A to 100A. This means that the electrode preheating is also almost constant, since electrode preheating is determined by the RMS current. From Chapter 7, the preheating determines the relationship between instantaneous electrode melting rate and instantaneous current (equation 10.9 in section 10.6). Thus Iarc_max determines the peak arc length almost independently of Iarc_min. In addition, the variation of peak arc length with changes in Iarc_max (with no other parameter changes) has been verified by photography in section 10.5.

The maximum value of current Iarc_min is limited by two considerations. The first limiting factor is that the peak arc length produced during the rapid burnback phase (Tarc_max) must be limited, to avoid low dipping frequencies and excessively large droplets. This limit is determined subjectively and varies with changes in CTWD, as a result of changes to electrode preheating. The second consideration is to avoid unintended pulse-spray transfer of material across the arc. This would occur if the Iarc_max-Tarc_max parameter pair are set to values which essentially emulate I_p-T_p parameters suitable for pulse spray transfer. This limit has already been determined by earlier research [72, 104, 110, 111].

Fusion area can be varied significantly by adjusting steady state arcing current Iarc_min. Fusion area can be adjusted without altering wire feed speed or travel speed, hence keeping bead cross-section and deposition rate constant. For CO_2, the maximum fusion area was over 2.5 times the minimum fusion area for a given Iarc_max, without altering the wire feed rate, peak arc length or short-circuit rupturing characteristics. It is doubtful that such a range of adjustment could be achieved with the same ease using a conventional CV power source. The change in circuit inductance required to alter arc heating would significantly affect the behaviour during the short circuit, degrading the stability of the process. Other factors such as maximum arc length would also be inadvertently affected using the conventional CV power source. The complete decoupling of arcing and short-circuit parameters is a major advantage of the current-controlled short circuit GMAW process.

Fusion area is proportional to energy input for a given travel speed. The constant of proportionality is not greatly affected by changes in CTWD. The relationship between fusion area and mean current was found to be inconsistent, and varied with the value of Iarc_max (section 10.3.5). This is an expected result for the short-circuiting process with a current waveform of variable form factor (shape), because very little energy is produced at the workpiece during the short circuit, even at high current. High short-circuiting currents contribute to the mean current value, but not to energy input. Changes in Iarc_max alter the duty cycle, which causes a change in the relationship between mean current and energy input. These effects do not occur in open-arc processes, where the relationship between mean current and fusion area is more consistent and predictable [106].

Although fusion area is determined by energy input, experiments have shown that fusion area cannot be controlled to a particular value under all circumstances solely

by regulating the energy input to the process. A change in travel speed significantly alters the relationship between fusion area and energy input (section 10.3.7). However, if travel speed can be kept constant, then changes in CTWD do not significantly affect the relationship between fusion area and energy input (section 10.3.5). In situations where the travel speed can be either controlled or measured, the current-controlled short circuit GMAW process allows tremendous scope for regulation of fusion area without altering the deposition rate (change of wire feed speed). This is an improvement over systems which alter wire feed rates to regulate welding current [112].

The experimental results have shown that the relationship between fusion area and energy input is not significantly altered by large changes in CTWD for a given wire feed speed and travel speed (refer to Figure 10.51, page 10-22). If travel speed is constant, the fusion area can be controlled by regulating the energy input through Iarc_min adjustment, even though the CTWD may be changing. However, if a large fusion area is required for thicker sections, it may only be achievable at low CTWD values. In this case, the value of CTWD would need to be constrained. For welding of thin sections where avoidance of burn-through is of primary importance, the CTWD can be allowed to vary over a very wide range, since the energy input can be controlled to the required level over this wide range of CTWD values.

The open loop current controlled short-circuit GMAW process produced stability indices in the range of 0.70 to 0.90 for welds of good quality. In comparison, an optimally tuned conventional power source can achieve stability indices of 0.90 to 0.95. However, the weld bead quality is not measurably higher, and the optimal state of tune occurs in a very narrow operating range. It appears that the current control scheme tested in this chapter can intrinsically adapt to changes in arc length and droplet size on a cycle-by-cycle basis, and provide stable metal transfer during the short circuit. Changes in arc length and droplet size alter the duration of the weld cycle, which would alter the instantaneous current output of a conventional CV power source at each weld cycle. The current controlled power source used here produces the same current waveform profile for each short circuit and arcing period, so the metal transfer mechanism operates more consistently irrespective of the weld cycle duration, which is the only variable used in calculating the stability index. Stable operation is therefore possible even when the short-circuiting frequency is grossly dissimilar to the frequency of weld pool oscillations (section 10.3.7.1). The result is a very "forgiving" process for

the manual operator, which can produce high quality welds over a wide range of operating conditions.

The predominant spatter production mechanism appears to be ball repulsion spatter, generated at the start of the short circuit. Spatter is generally low or nonexistent for low Iarc_min, and increases markedly for high Iarc_min. However, spatter can also be relatively high for low Iarc_min under certain conditions such as faster travel speeds. This is investigated in section 10.3.7, and is a result of premature shorting at high arcing currents, caused by large weld pool oscillations. Fusion area is greatest for high values of Iarc_min, so in many applications, zero or low spatter levels may need to be traded for high fusion.

Reduction of wire feed speed reduces the range of current settings which will produce satisfactory welds (sections 10.3.8 and 10.3.9). However, high quality welds using 0.9mm mild steel electrode can be produced at wire feed speeds of 1.87 m/min and a travel speed of 390mm/min (Figure 10.67). These welds were produced on 5.0mm plate, which usually creates conditions that are too "cold" for currents of 35 to 40A. Spatter levels at reduced wire feed speeds are zero to low. The flexibility of this type of process control is pleasantly surprising to an operator accustomed to conventional CV power sources.

The range of tests carried out in this chapter show that a wide range of average droplet sizes (ΔL_{avg}) are produced, depending on wire feed speed, shielding gas, Iarc_max, Iarc_min, and CTWD. In particular, an 8mm change in CTWD produces a large change in ΔL values, with all other parameters remaining unchanged. Consequently, it would be impractical to assign target values of ΔL for every conceivable operating condition in a closed loop system attempting to regulate the droplet size, as has been proposed in Chapter 5. Such a system would require an alternative method of selecting the appropriate ΔL target value. This is discussed in Chapter 11.

Simulations in section 10.6 show that the process behaviour can be predicted with reasonable accuracy by considering only electrode melting rate and ignoring weld pool dynamics such as depression and oscillations. Photographs of pool depression at low currents (section 10.5.3) show that weld pool depression is minimal. Weld pool dynamics (such as pool depression and oscillations under extreme conditions) make a secondary but important contribution to behaviour. Where present, oscillations are thought to determine the timing for short circuiting events. In cases of mild oscillations,

the dipping frequency is made bimodal (section 10.4.3) but spatter remains relatively low since shorting occurs at low currents. Process stability remains relatively unchanged. In more extreme cases, shorting is premature and occurs at higher currents than Iarc_min, creating spatter and further pool disturbances (section 10.3.5), significantly reducing process stability and degrading bead appearance.

Simulation of the "open loop" controlled short circuit GMAW process is greatly simplified by the constant current characteristic of the power source. The instantaneous welding current is independent of the voltage at the arc (or short circuit), and is determined only by the control algorithm. This removes major sources of error in simulation introduced by the shielding gas current-voltage characteristics, and the need to accurately estimate the arc length at all times. The simulations performed in section 10.6 do not require an accurate estimate of the instantaneous arc length. The short circuit is deemed to occur when the length of electrode fed in to the process is balanced by the length of electrode molten by the welding current. Simulation of a conventional power source requires accuracy in data for arc I-V characteristics and instantaneous arc length, since these affect the output current, which determines the instantaneous melting rate. The unimportance of voltage related factors in the simulation of the controlled short circuit GMAW process is another example of parameter decoupling.

In conclusion, the "open loop" process has been investigated in detail across a range of wire feed speeds, CTWD values and travel speeds in both CO_2 and argon-based shielding gases. The findings summarised in this section show that this type of control has many significant performance advantages over the conventional CV power source. The current controlled process is also much simpler to model, therefore allowing more accurate simulations to be undertaken in the future. Finally, a performance benchmark has been established, against which the "closed loop" process described in Chapter 11 can be compared.

Chapter 11

Investigation of the "Closed Loop" Controlled Short Circuit GMAW Process

11.1 Scope

This chapter investigates the performance of the "closed loop" control method described in Chapter 5. This control method has two objectives. The first is to improve process regularity, hence stability index, by controlling the size of the droplet formed at the end of the electrode on a cycle-by-cycle basis (i.e. instantaneously). The second objective is to reduce spatter levels by ensuring that the short circuit always occurs at very low arcing current, typically 30 Amperes.

The performance of the closed loop control is compared to the performance benchmark established in Chapter 10 for the "open loop" control. As in Chapter 10, assessment of process performance encompasses diverse parameters such as spatter levels, stability indices, fusion area and weld bead "quality". Detailed analysis is undertaken in this chapter to explain various behavioural aspects of the closed loop process.

Section 11.2 defines the test conditions, while section 11.3 describes refinements made to the closed loop control in order to overcome estimation errors described in Chapter 7 and also problems that became evident during initial testing. Sections 11.4 and 11.5 compare the closed loop and open loop system performances using Ar-23%CO_2 and CO_2 shielding gases, respectively. The main findings are summarised in section 11.6. Possibilities for further enhancements to control of the process, based on these findings, are also discussed.

11.2 Test Conditions

11.2.1 Physical Process Conditions

All of the physical conditions are identical to those of the "open loop" tests of Chapter 10. The electrode material is CIGWELD Autocraft LW1-6 0.9mm mild steel,

conforming to AWS ER70S-6 specification. The electrode angle is 90^0 to the workpiece surface, and all welds are bead on 6mm descaled hot-rolled plate.

The wire feed speed is maintained at 5.7 m/min. Tests using Ar-23%CO_2 shielding gas are performed at travel speeds of 390 mm/min & 195 mm/min, and at CTWD values of 8mm & 16mm. Tests using CO_2 shielding gas are performed at travel speeds of 195 mm/min, and at CTWD values of 12mm & 20mm. These allow direct comparison with the results compiled in Chapter 10.

11.2.2 Electrical Parameters

The "closed loop" control technique used in these tests is described in Chapter 5. The current waveform is shown in Figure 11.1. All of the electrical parameters retain their previous function and values:

I_backgr	Background current at wetting-in & short cct rupture	20A
T_wetting	Short circuit wetting-in time for Ar-23% CO_2	0.5 ms
	Short circuit wetting-in time for CO_2	1.5 ms
Isc_ramp	Short circuit current ramp-up rate	100 A/ms
T_rupture	Maximum allowable short-circuit rupturing time	1.0 ms
Iarc_ramp	Rate of current fall from Iarc_max to Iarc_min	150 A/ms

The two remaining parameters Iarc_max and Iarc_min are varied during testing, as they have been shown in Chapter 10 to control arc length and fusion area, respectively.

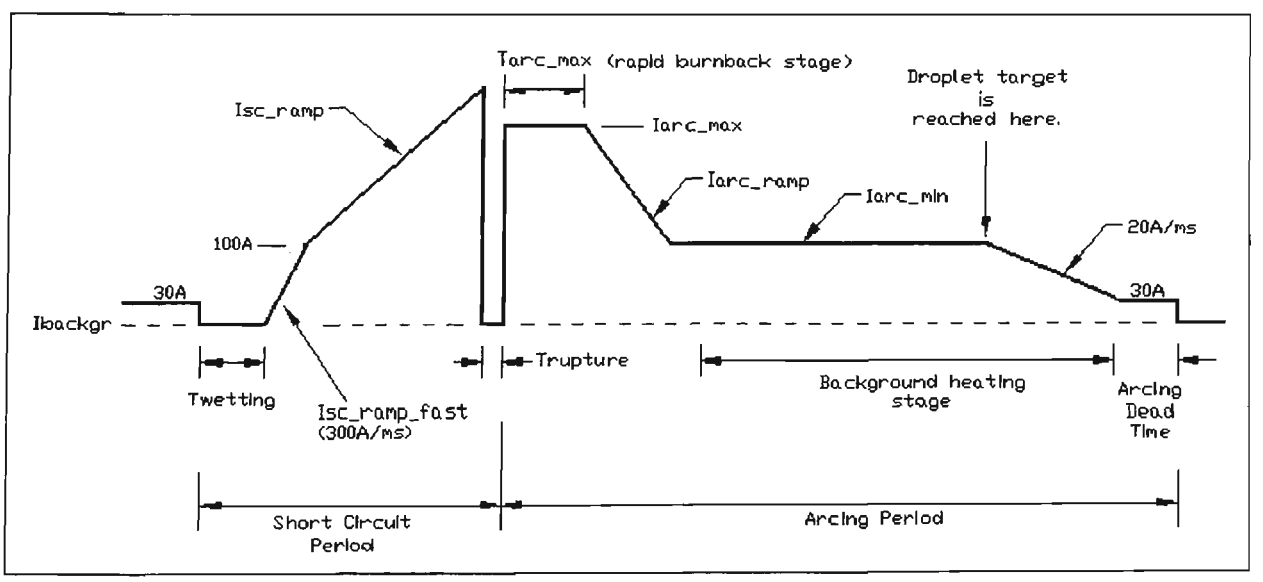

Figure 11.1 "Closed Loop" controlled current waveform

Current (vertical) vs Time (horizontal)

11.2.3 Experimental Procedure

Detailed testing of the closed loop control using a test matrix of Iarc_max and Iarc_min values is not undertaken. Instead, a single value of Iarc_max is selected for each test case which is considered to correspond to the best performance "group" of the open loop control for the same physical and electrical conditions. Refer to Table 11.1 for the test values of Iarc_max. The key indicators used to assess performance are stability index, spatter levels and bead quality. For the selected value of Iarc_max, tests are conducted as parameter Iarc_min is adjusted in 10A increments.

Other aspects of the experimental procedure, such as assessment of stability, spatter and bead quality, are the same as those described in section 10.2.3.

Table 11.1 Values of Iarc_max for Closed Loop Tests

Shielding Gas	CTWD (mm)	Travel Speed (mm/min)	Iarc_max (Amperes)
Ar-23%CO_2	16	390	250
Ar-23%CO_2	8	390	250
Ar-23%CO_2	16	195	250
CO_2	12	195	275
CO_2	20	195	250

11.3 Automatic Selection of Droplet Size Target

11.3.1 Background

As discussed in Chapter 7, the droplet size is represented by an equivalent length of electrode ΔL of equal volume, and this length varies in a non-linear relation to the droplet volume. The results of Chapter 10 show that the average dipping frequency varies significantly as key parameters are altered. This implies a significant variation in droplet size. The average equivalent length ΔL_{avg} is affected by wire feed speed, CTWD, Iarc_min and Iarc_max. Furthermore, there is an unknown but constant fractional error between the estimated ΔL and the actual value, for a given operating condition. As described in Chapter 7, this is due to the estimation algorithm not accounting for the electrode preheat, which is strongly dependent on stickout length or CTWD, and is prone to significant errors. In a closed loop control system that aims to regulate ΔL, it is not practical to assign a reference value ΔL_{target} for each possible operating condition. Nor is it possible to use a single fixed value for ΔL_{target}, because

conditions often exist where either the target will never be reached, or the process is capable of generating a far larger droplet than the target value represents. This section describes the method devised to overcome these estimation and operational problems, and discusses other reasons why automatic selection of droplet size target is necessary.

11.3.2 Sensitivity to Changes in Droplet Size Target

The droplet size (represented by ΔL) varies significantly across the operating range of the process, and the target value must be altered depending on various conditions. The question arises: "How sensitive is the process control to small changes in ΔL_{target}?". A number of experiments were performed in which the droplet size target was set manually. The current and voltage waveforms were analysed to establish the degree of "success" of the control. The control is assumed to be "100% successful" if in all of the arcing periods, the current drops from Iarc_min to 30A before the start of the next short circuit. This indicates that the assigned target size is reached for each droplet, and that the current is at the minimum value just prior to the next short circuit, thereby minimising ball repulsion spatter. The success of the control is indicated by the presence of "arcing dead time", defined as the time between the current reaching 30A and the next short circuit (see Figure 11.1). Another requirement for success is that the arcing dead time must be minimised, otherwise the droplet size target is excessively low. In this case, the majority of the "background heating stage" indicated in Figure 11.1 would be spent at 30A. The result would be an unacceptable reduction in fusion area.

Figure 11.2 shows a current waveform for the case where ΔL_{target} is excessively low. Figure 11.3 shows the current waveform where ΔL_{target} approaches an optimum value. For these waveforms, the shielding gas is Ar-23%CO_2, wire feed speed is 5.7 m/min, travel speed is 390mm/min, CTWD=16mm, Iarc_max=250A and Iarc_min=80A. In Figure 11.2, the arcing dead time is excessive. While this does not significantly affect the stability of metal transfer from electrode to workpiece (in fact, stability index is increased - see Table 11.1), the workpiece heating is significantly reduced, increasing the probability of lack-of-fusion defects. For a value of ΔL_{target} which is near-optimum, the arcing dead time is minimised, so energy input and fusion area are maximised.

The results of repeating the above tests for various values of ΔL_{target} are summarised in Table 11.2. The conditions for all tests were kept the same so that the estimation error due to electrode preheating is almost unchanged. From tests in Chapter 10, it is known that the RMS current is not significantly altered by changes in the steady-state arcing current, provided that CTWD and Iarc_max are constant.

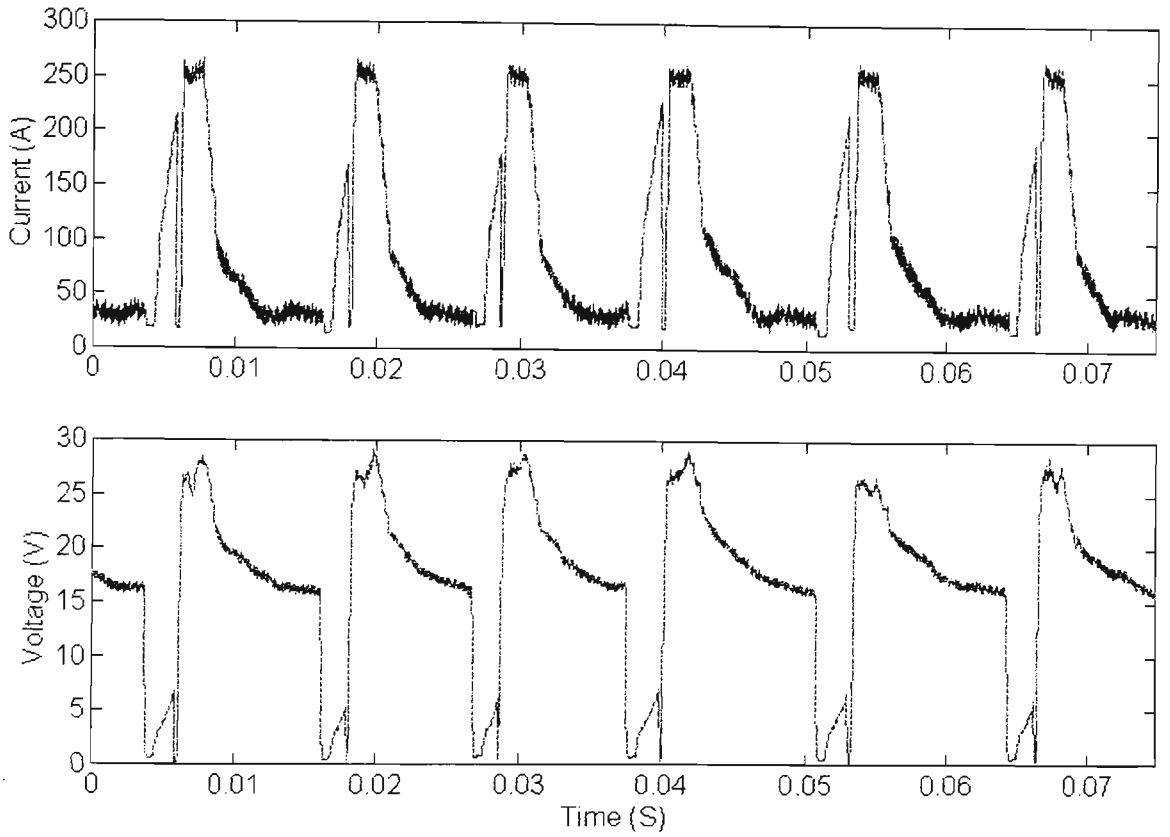

Figure 11.2 Current waveform for low ΔL_{target}

Table 11.2 Successful operation of fixed ΔL_{target}

ΔL_{target} (mm)	Percentage of weld cycles with dead time present	Dip frequency (Hz)	Stability Index (0.0 - 1.0)
0.55	97.4 %	78	0.90
0.70	100 %	76	0.92
0.80	97.2 %	71	0.89
0.90	84.3 %	70	0.81
1.00	84.4 %	64	0.83
1.10	77.9 %	68	0.87
1.20	49.3 %	67	0.78
1.40	45.0 %	60	0.78
1.60	31.6 %	57	0.79
Open loop	0 %	56	0.77

The results in Table 11.2 indicate that a small change in ΔL_{target} from the optimum value (approximately 0.90) can significantly affect the process' behaviour. An error of 0.25mm in setting the target causes unsatisfactory operation of the control system. These tests demonstrate the need for an automatic method of determining an

optimum ΔL_{target} which also adjusts the value to changing operating conditions, and inherently minimises problems created by the errors in ΔL estimation due to changes in electrode preheating conditions.

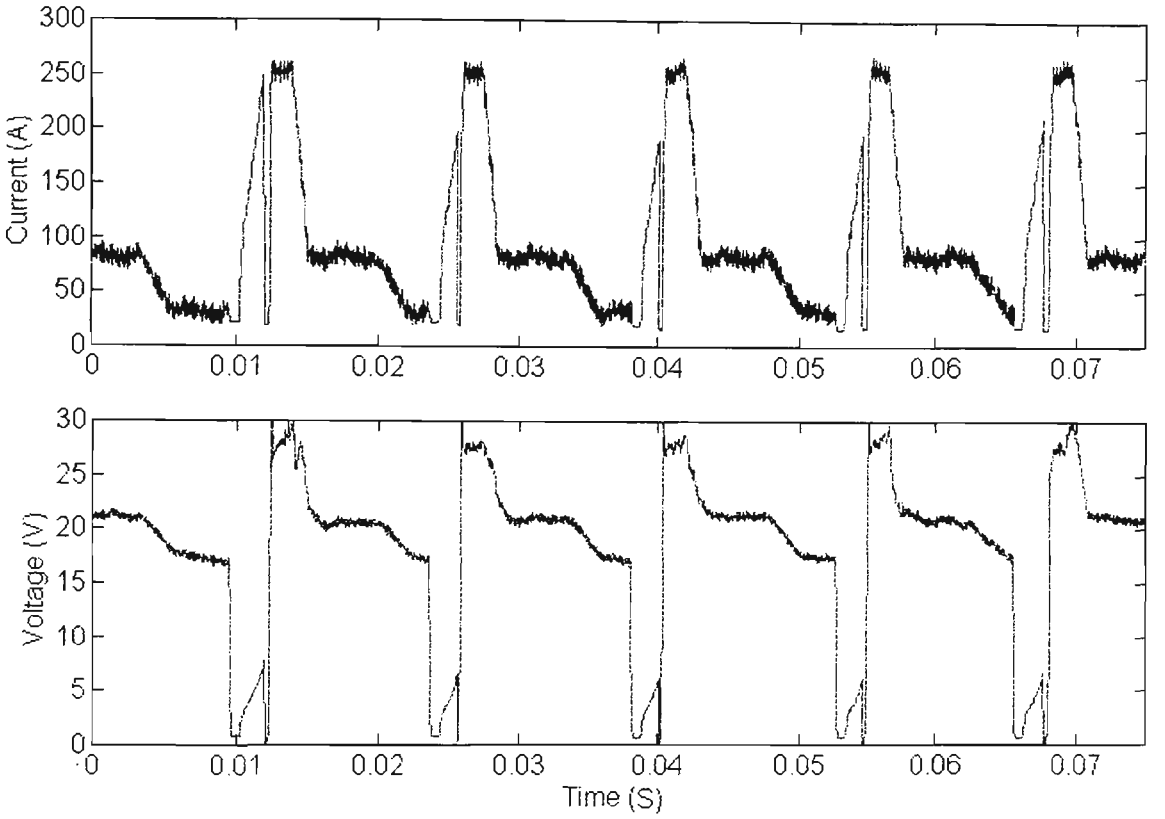

Figure 11.3 Current waveform for near-optimum ΔL_{target}

11.3.3 An Automatic Selection Method for Droplet Size Target

A number of techniques were devised to adjust ΔL_{target} to an optimum value. The most successful method was also the simplest. It involves following these rules, which are executed once at the end of every arcing period:

1. If an arcing dead time was not present in the previous arcing period, reduce ΔL_{target} by a fixed amount, ΔL_{sub}.
2. If an arcing dead time was present in the previous arcing period, then increase ΔL_{target} by a fixed amount ΔL_{add}.

The technique works well if ΔL_{sub} is greater than ΔL_{add}. Qualitatively, it functions as follows:

If the target is excessive, then an arcing dead time will not be present. As long as this condition persists, the target will be rapidly decreased until an arcing dead time is established. An extreme example of this occurs at the start of a weld, when the target is initialised to an arbitrarily high value such as 5.0mm. After an arcing dead time is

established, the target is slowly raised after each "successful" arcing period until it is too high, and the arcing dead time is not achieved during the arcing period with the available current waveform. In this way, the target is allowed to "float" up to its optimum (maximum) value which inherently minimises the arcing dead time. The optimum value is exceeded when the arcing dead time is no longer present, and short circuiting occurs at currents higher than 30A, increasing spatter.

A similar technique is used to control "detonation" or "pre-ignition" in spark-ignition internal combustion engines for passenger vehicles [113]. When the fault condition (detonation) is sensed, the spark ignition timing is reduced or "retarded" from the assigned value in relatively large steps, until the fault condition no longer exists. Once this occurs, the timing is allowed to increase gradually and return to the assigned value.

Tuning of the control involves selecting values of ΔL_{add} and ΔL_{sub} which avoid over-reaction of the controller to changes in arcing dead time. This was done subjectively by observing the current waveform after many trials, and adjusting both values so that target changes appeared "well damped". The final values chosen for ΔL_{add} and ΔL_{sub} are 0.005mm and 0.05mm, respectively. These are used for all tests performed in this chapter.

11.3.4 Example of Operation

The operation of the automatic droplet size target selector is shown in Figures 11.4 and 11.5. The operating conditions are the same as those for the tests performed in section 11.3.1. Figure 11.4 shows variations in the droplet size target over a small number of weld cycles. The operation of the control is evident from the changes in the reference. Figure 11.5 illustrates how ΔL_{target} varies over a long period of time. (NB: the waveform for ΔL_{target} is obtained from a spare analogue output of the DSP controller).

It is important to note that the actual average wire melting incremental length ΔL always exceeds the target, even for the case where there are no estimation errors. For the above waveforms, the average value of ΔL_{target} is 0.78 mm. The average frequency is 75 Hz, corresponding to $\Delta L_{avg} = 1.27$ mm. This is expected, since the short circuit does not occur immediately after the droplet size target is reached. While the current is ramped down to 30A, electrode melting continues until the short circuit

occurs. It might be concluded that a rapid shutdown of current when the target is reached would be preferable. However, this creates other problems, as explained in Chapter 5. The aims of this control technique are spatter minimisation and droplet *uniformity*, rather than achieving a specific droplet size.

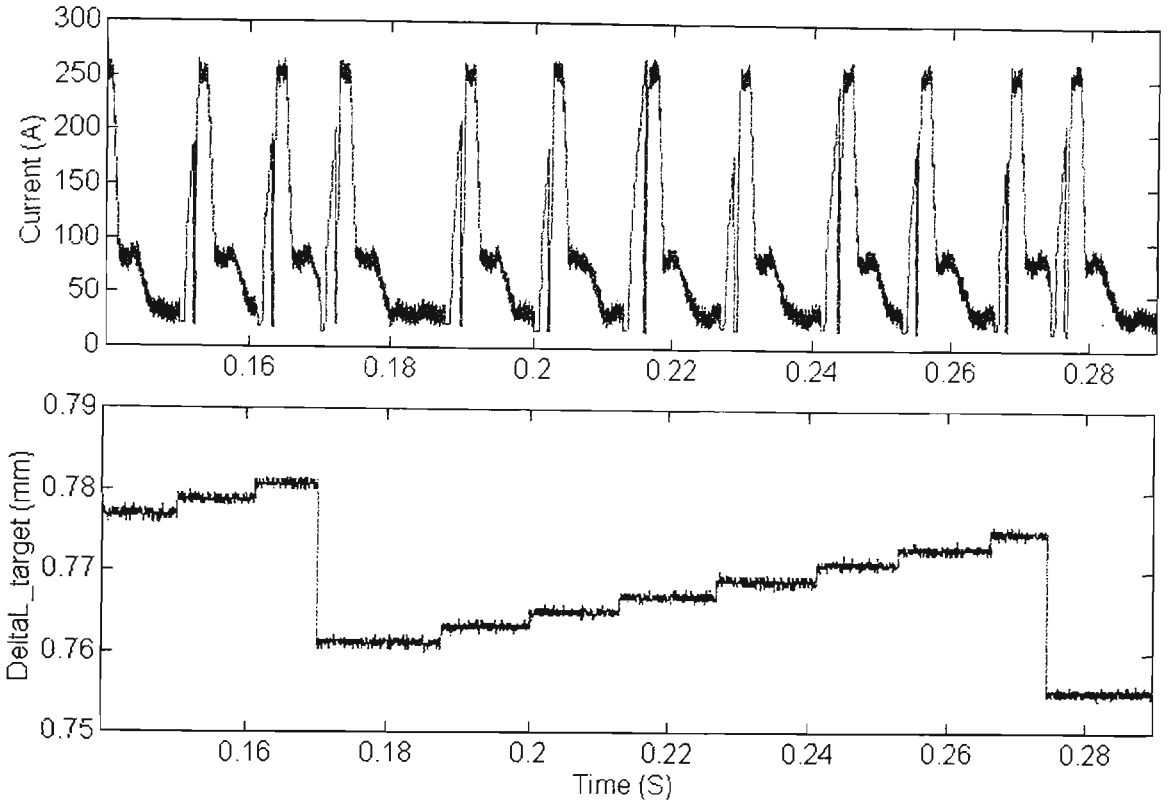

Figure 11.4 Variation in ΔL_{target} over several weld cycles

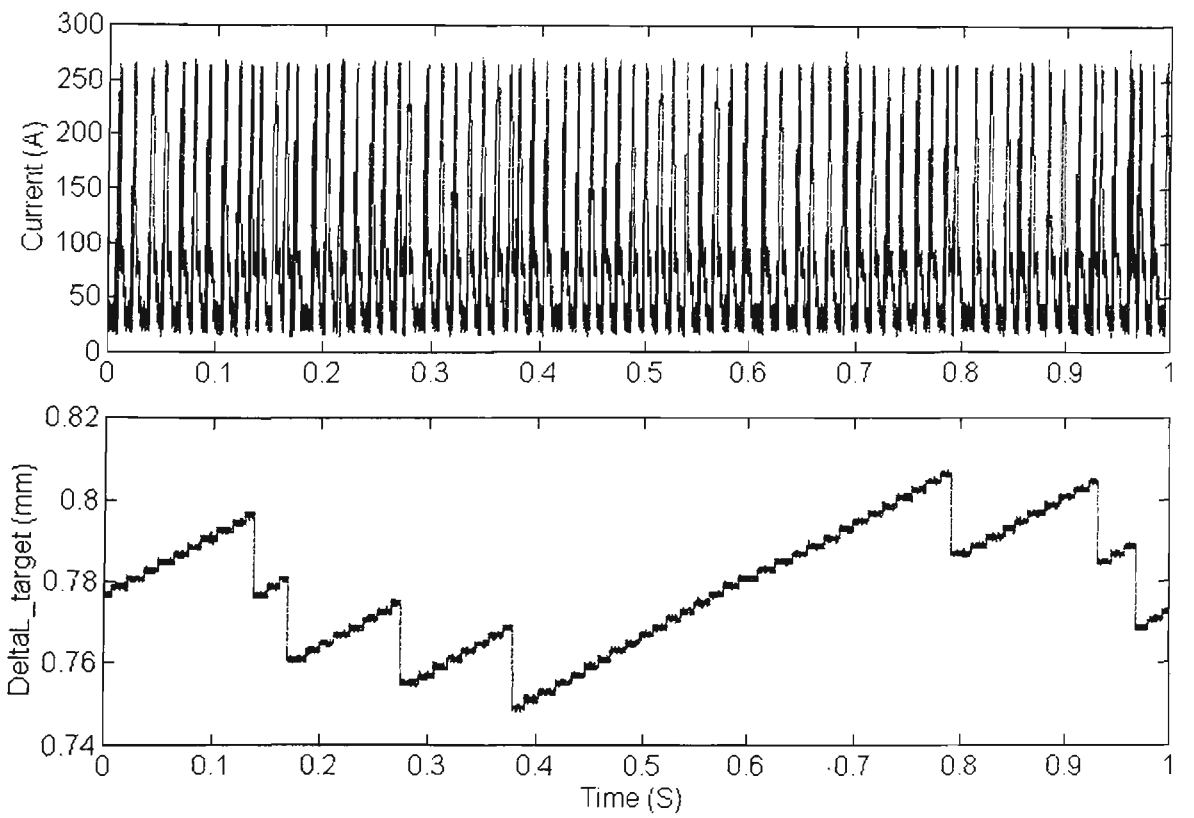

Figure 11.5 Variation in ΔL_{target} over 1.0 seconds

11.4 Process Performance with Ar-23%CO_2 Shielding Gas

11.4.1 Scope

This section compares performance of the closed loop control to open loop, operating at Iarc_max=250A under the conditions specified in section 11.2. Three "groups" of tests were performed. The relevant figures comparing various aspects of each group's performance, and the differing parameters for each group, are listed in Table 11.3.

Table 11.3 Summary of Figures for Ar-23%CO_2 Process "Closed Loop" Tests

Figure Description	Figure No. CTWD=16mm 390mm/min*	Figure No. CTWD=8mm 390mm/min*	Figure No. CTWD=16mm 195mm/min*
Stability index vs Iarc_min	11.6	11.20	11.33
Spatter index vs Iarc_min	11.7	11.21	11.34
Bead quality index vs Iarc_min	11.8	11.22	11.35
Fusion area vs Iarc_min	11.9	11.23	11.36
Penetration depth vs Iarc_min	11.10	11.24	11.37
Bead width vs Iarc_min	11.11	11.25	11.38
Energy input per unit length vs Iarc_min	11.12	11.26	11.39
Fusion area vs Energy input per unit length	11.13	11.27	11.40
Average dipping frequency vs Iarc_min	11.14	11.28	11.41
Mean welding current vs Iarc_min	11.15	11.29	11.42
Average arcing current vs Iarc_min	11.16	11.30	11.43
RMS current vs Iarc_min	11.17	11.31	11.44
Mean welding voltage vs Iarc_min	11.18	11.32	11.45

* = Travel speed

11.4.2 Test Results for CTWD=16mm, 390 mm/min Travel Speed

Figures 11.6 to 11.18 compare the results of closed loop control to open loop control under these conditions.

[Refer to Appendix 11 for Figures 11.6 to 11.18]

11.4.3 Discussion of Results for CTWD=16mm, 390 mm/min Travel Speed

The results represented by each figure are discussed in this section.

Figure 11.6 shows that there is some improvement in stability index for the closed loop system. However, the difference in stability indices for the two sets of tests is small, and not easily discernible to an operator. It was thought that the regulation of droplet size would cause the variation in arcing times to be reduced, since the amount

of material molten and detached from the electrode would be more consistent. Since the variation of arcing time is much greater than the variation in short-circuit time for variations of droplet size, it should follow that the variation of total cycle time would also be reduced. As the stability index is based on weld cycle time deviation, an improvement in stability index is expected.

There may be a number of uncontrolled factors at work which make this expectation unrealistic. As discussed in Chapter 7, there are inherent errors in the estimation of the droplet size. These may be significant in absolute terms, but the error magnitude is not important as long as the error itself is not changing on a cycle by cycle basis. As shown in section 11.3, the value of the droplet size target is automatically selected on the criteria of spatter minimisation. The very fact that the target is varied over time (Figures 11.4 and 11.5) also influences the stability index, calculated in these tests over a 1.0 second period.

Weld pool oscillations are thought to be the major factor which degrades stability index from the theoretical maximum value of 1.0. As explained in Chapter 10, the precise timing of a short circuit event at the end of an arcing period is "randomised" by movement of the weld pool surface. At a wire feed speed of 5.7 m/min, a 0.2 mm increase in the height of the weld pool surface will cause the short circuit event to occur 2.1 milliseconds sooner than if the pool surface did not move. If the average dipping frequency is 70 Hz, the change in arcing time is almost 15% of the total weld cycle time. Although these calculations are crude, they do demonstrate how very small weld pool oscillations can make high stability indices (greater than 0.90) difficult to achieve across a wide operating range, since dipping frequency cannot always be equal to the weld pool oscillation frequency.

Figure 11.7 shows that the spatter levels generated by the open loop and closed loop processes are similar, particularly at the extremes of their respective operating ranges. This indicates that the closed loop process has not reduced spatter levels below those of the open loop process. This is surprising, since the results of Chapter 10 show that reducing the steady state arcing prior to the short circuit definitely results in lower spatter levels. The waveforms in Figure 10.18 show the reason why overall spatter levels have not declined: As Iarc_min is increased to 150A to maintain fusion area (refer to Figure 11.9), the incidence of one "premature" short circuit at the elevated current generates a similar amount of spatter to that produced by a greater number of

short circuits occurring at lower steady state arcing current. In the closed loop control method, the short circuit is considered to be "premature" if the short circuit occurs before the target droplet size is achieved, so the short-circuiting current is Iarc_min rather than 30A. The premature short circuits are believed to be caused by weld pool oscillations. The same mechanism investigated in section 10.3.6 appears to be active here. The improvement in results presented for the closed loop process operating at reduced travel speed (sections 11.4.6 & 11.4.7) support this hypothesis.

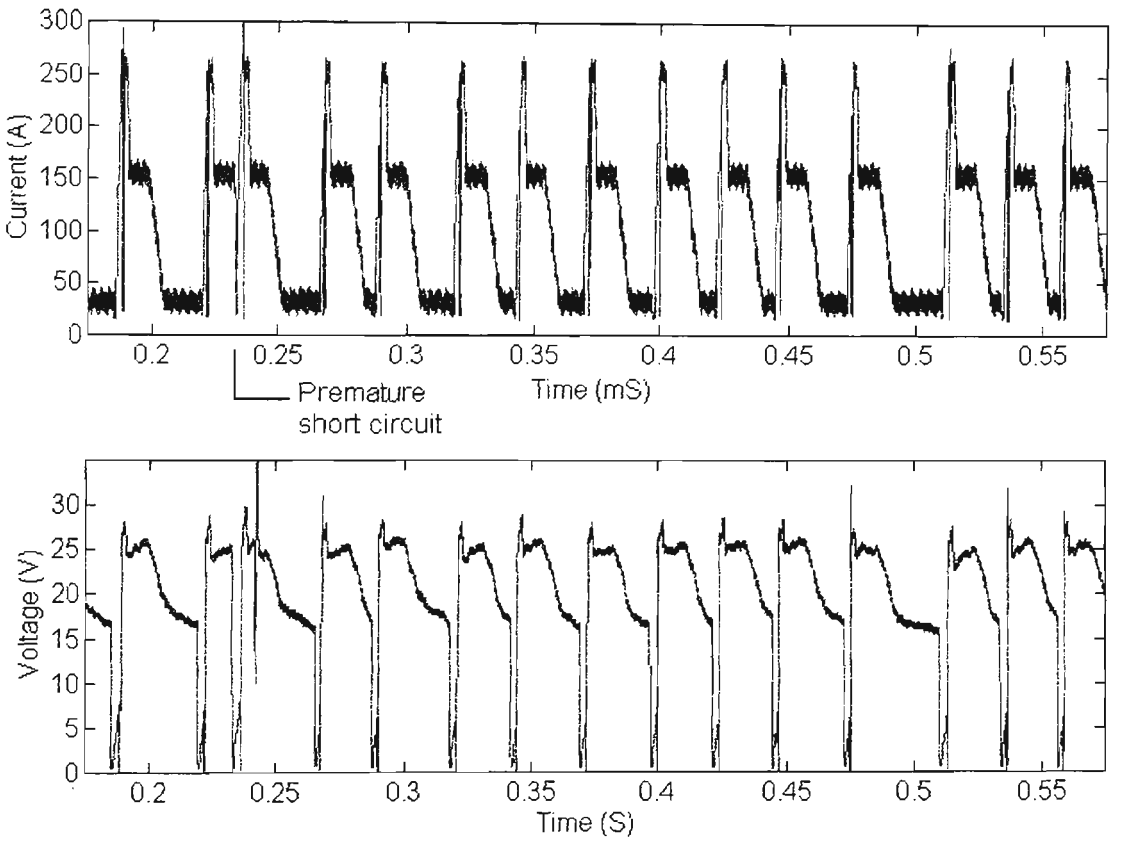

Figure 11.19 Waveforms for Iarc_min=150A

The bead quality (Figure 11.8) produced by the closed loop process is comparable to open loop, except for high values of Iarc_min. Above 130A, the dipping frequency is significantly reduced for the closed loop process (see Figure 11.14). This tends to produce a higher surface ripple on the weld bead. There was also some "flash" at the weld toe, and the overall shape of the bead became uneven.

Due to the reduction of current at the end of the arcing period, the closed loop process generates significantly less energy input (Figure 11.12) and consequently fusion area (Figure 11.9) for a given value of Iarc_min. The action of the automatic ΔL_{target} selection also makes the relationship between energy input and Iarc_min somewhat less repeatable: Iarc_min is no longer applied for the entire arcing period, but an

undetermined fraction of it. The loss of "certainty" in the predictable linear relationship between fusion area and Iarc_min is undesirable. Nonetheless, the fusion area generated by the closed loop process can still be adjusted through changing Iarc_min.

The closed loop process can produce a wider bead (Figure 11.11) but with less penetration depth (Figure 11.10). The increased width capability is a result of being able to sustain a longer arc length at the beginning of the arcing period by using high values of Iarc_min. This is reflected in the increased range of weld voltage (Figure 11.18) for the closed loop process. As seen in Chapter 10, wider weld beads are produced by increasing Iarc_max. The arc "cone" widens with current, as shown in Figures 10.124 to 10.131, in both argon-based and CO_2 shielding gases. The widening of arc radius with current is described in [114].

The linearity between fusion area and energy input (Figure 11.13) is maintained for the closed loop process. This is not surprising, as this behaviour should be intrinsic to the process and not dependent on the control methodology. There is scatter in the data points of this figure, but results presented in subsequent sections show the same result. There tends to be less scatter in the data points for lower travel speeds.

As expected, for a given value of Iarc_min the closed loop process produces a higher dipping frequency than open loop (Figure 11.14). Again, this is due to the reduction of current at the end of the arcing period. For Iarc_min above 120A, the closed loop process produces larger droplets than the open loop process' maximum size, but the fusion area is not greater than the open loop's maximum. This shows that the final portion of the arcing period (where the current is 30A) is underutilised. If maximisation of fusion area is important, an alternative control technique is needed, where the arcing current is reduced just prior to the short circuit. This should reduce spatter levels while maintaining maximum fusion area, and is discussed further in section 11.6.

Figures 11.15 and 11.16 verify that, as for the open loop control, mean current and average arcing current vary with Iarc_min in the same manner. Figure 11.17 shows that the variation in RMS current is small across the adjustment range of Iarc_min. As explained in Chapters 7 and 10, this indicates that the electrode preheating is almost constant, so the peak arc length is determined by Iarc_max, and is almost independent of Iarc_min. The continued decoupling of arc length and workpiece heating (fusion area) is a most desirable feature.

11.4.4 Test Results for CTWD=8mm, 390 mm/min Travel Speed

Figures 11.20 to 11.32 compare the results of closed loop control to open loop control under these conditions.

[Refer to Appendix 11 for Figures 11.20 to 11.32]

11.4.5 Discussion of Results for CTWD=8mm, 390 mm/min Travel Speed

This discussion makes references to Figures 11.20 to 11.32, and will draw comparisons to results for CTWD=16mm where appropriate.

There is no improvement in the stability indices (Figure 11.20) for the closed loop process operating at CTWD=8mm compared to the open loop process. As seen for CTWD=16mm, attempting to regulate droplet size does not guarantee that stability index will be improved under all conditions.

The spatter levels (Figure 11.21) are reduced for low and high values of Iarc_min. The reduction of spatter at high Iarc_min values is expected, but the reduction of spatter at low values of Iarc_min is an unexpected result. It did not occur for CTWD=16mm. As explained in Chapter 10, the primary cause of spatter at low Iarc_min and high travel speed for the open loop process is the presence of large weld pool oscillations. The oscillations cause premature short circuiting early in the arcing period when the current is being reduced from Iarc_max to Iarc_min (section 10.3.7). For the specific case of closed loop control operating at CTWD=8mm, it is suspected that the workpiece heating and current waveform (arc force/pool depression during Iarc_max) conditions are conducive to reduced pool oscillations, so that the premature short circuits occur less frequently, or not at all. Further investigation of this aspect of process behaviour was not carried out.

For the same reasons that spatter is reduced at low Iarc_min, bead quality (Figure 11.22) is also improved. The improvement in this case is attributable to a reduction in the ripple on the bead surface for the closed loop control. The bead quality for higher values of Iarc_min are comparable (within 1 point).

As for CTWD=16mm, the range of fusion areas (Figure 11.23) produced by the closed loop process is slightly less than for the open loop process. The penetration depth (figure 11.24) is also lower. The reduction in range of energy input to the process (Figure 11.26) is the reason. The bead width (Figure 11.25) is slightly more for high

values of Iarc_min, for the same reasons discussed in section 11.4.2. The relationship of fusion area to energy input (Figure 11.27) remains unchanged, as this is a physical property of the process that is not affected by the control technique. Figure 11.28 shows the reduction in average droplet size produced by the closed loop control. Again, this is attributable to the reduction of current at the end of the arcing period, which reduces the instantaneous electrode melting rate.

The behaviour of mean current (Figure 11.29) is the same for both open loop and closed loop systems. The variation in mean current is not monotonically increasing as for CTWD=16mm (Figure 11.15) because of the contribution of increasing short circuit duration at low values of Iarc_min. This is explained further in section 10.3.5. The average arcing current (Figure 11.30) shows the "removal" of the short circuit current contribution from the mean current. The linear increase of effective arcing current with increasing Iarc_min is evident for both open loop and closed loop systems.

The variation in RMS current (Figure 11.31) is less for the closed loop system. This is a desirable result, as explained in section 11.4.2. There is little variation in the electrode preheating for the range of Iarc_min adjustment, so the peak arc length is determined by Iarc_max almost independently of Iarc_min.

The mean voltage for CTWD=8mm (Figure 11.32) is 1.5V to 2.0V lower than for CTWD=16mm. The mean current is approximately 20A higher for CTWD=8mm, which would tend to increase the voltage due to resistance in the electrode and arc column if the CTWD change is not considered. Typical values of resistance are 1.16 mΩ/mm for 0.9mm mild steel electrode (Chapter 6) and 25.9 mΩ for Ar-23%CO_2 arc (Chapter 8). Accounting for an 8mm decrease in CTWD and a mean current of 100A for CTWD=16mm, a 20A increase in mean current for CTWD=8mm results in a 0.22V *drop* in resistance-related voltage. So the remainder of the voltage drop for CTWD=8mm must be a result of decreased arc length. As a crude calculation, from Chapter 8 the field strength in an Ar-23%CO_2 arc is 1.87 V/mm, corresponding to an arc length decrease of 0.7 mm for (1.5-0.22)V.

11.4.6 Test Results for CTWD=16mm, 195 mm/min Travel Speed

Figures 11.33 to 11.45 compare the results of closed loop control to open loop control under these conditions.

[Refer to Appendix 11 for Figures 11.33 to 11.45]

11.4.7 Discussion of Results for CTWD=16mm, 195 mm/min Travel Speed

In tests performed for Chapter 10, it was seen that travel speed affected one of the mechanisms responsible for spatter production; weld pool oscillation. For this reason, this set of tests is performed to compare the performance of the closed loop control system to open loop in a situation where pool oscillations are less influential: a slower travel speed of 195 mm/min. Under these conditions, any benefits of the closed loop control are expected to become evident.

The stability indices (Figure 11.33) for the closed loop system are slightly higher than those for the open loop control, the greatest difference occurring at the higher values of Iarc_min. To make a valid comparison, conditions for which fusion areas are similar need to be compared. Using Figure 11.36, the fusion areas for open loop control at Iarc_min of 40A and 70A produce fusion areas approximately equal to those for the closed loop control operating at Iarc_min of 70A and 150A respectively. When these operating points are compared for stability indices, it can be seen that the closed loop process does not produce any significant improvement in stability index.

However, the reduction of spatter levels (Figure 11.34) is remarkable, and is sustained throughout the operating range. At the reduced travel speed where weld pool oscillations have been reduced (but not entirely eliminated), the entire process becomes quiescent enough that premature short circuits such as those shown in Figure 11.19 do not occur at all. For the spatter index to consistently achieve a score of 10 (spatterless), the short circuits such as those shown in Figure 11.4 (occurring while the arcing current is being ramped down from Iarc_min to 30A and causing the droplet size target to be "knocked back") would have to consistently occur at the point where Iarc_min is almost completely ramped down to 30A. Figure 11.46 is the current waveform for Iarc_min=120A, and shows this behaviour. There is some visible variation in the arcing period duration, showing that weld pool oscillations are still present but have little influence.

The bead quality index (Figure 11.35) shows precisely the same trend for both open loop and closed loop systems, indicating no change in process performance as far as this aspect is concerned.

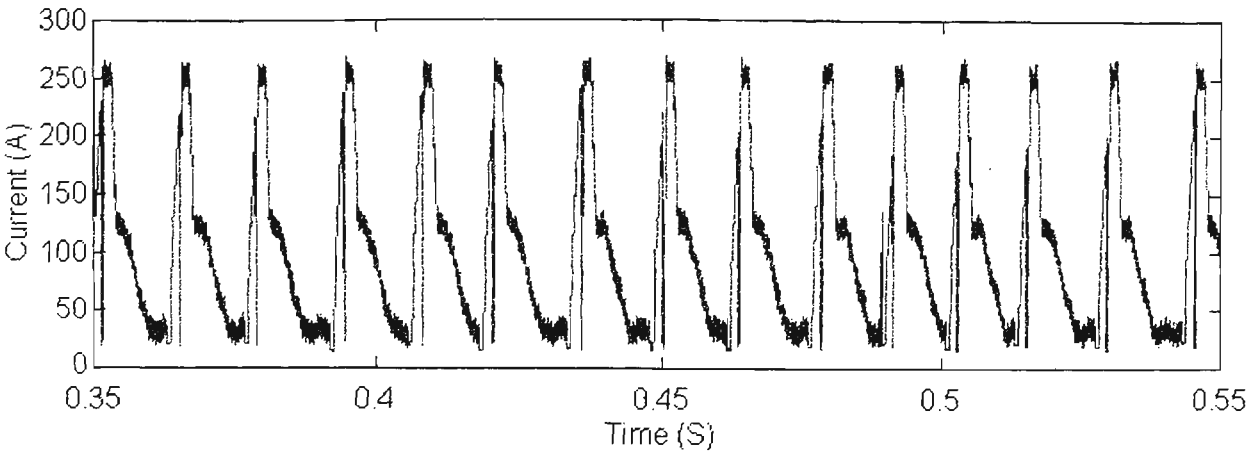

Figure 11.46 Current waveform for Iarc_min=120A

As for previous test sets, the closed loop system is not able to produce the same fusion areas (Figure 11.36) and penetration depths (Figure 11.37) as open loop control, due to the loss of energy input (Figure 11.39) during the final portion of the arcing period. The bead width (Figure 11.38) produced by the closed loop system is comparable only for the very highest values of Iarc_min. The relationship of fusion area to energy input (Figure 11.40) is unchanged, as expected.

The trends in mean current, average arcing current and RMS current (Figures 11.41 to 11.43) are the same as those described in section 11.4.2 for the higher travel speed of 390 mm/min.

11.5 Process Performance with CO_2 Shielding Gas

11.5.1 Scope

This section compares performance of the closed loop control to open loop, operating with CO_2 shielding gas, with the conditions specified in section 11.2. Tests were performed for CTWD values of 12mm and 20mm. For CTWD=12mm, Iarc_max is set to 275A since this was found to be a near-optimum value in tests conducted in Chapter 10 . At the higher CTWD value of 20mm, Iarc_max was reduced to 250A, for the same reason. Table 11.4 lists the relevant figures for each test condition.

11.5.2 Test Results for CTWD=12mm

Figures 11.47 to 11.59 compares the results of closed loop control to open loop control for the CO_2 process at CTWD=12mm and Iarc_max=275A.

[Refer to Appendix 11 for Figures 11.47 to 11.59]

Table 11.4 Summary of Figures for CO_2 Process "Closed Loop" Tests

Figure Description	Figure No. CTWD=12mm 195mm/min*	Figure No. CTWD=20mm 195mm/min*
Stability index vs Iarc_min	11.47	11.61
Spatter index vs Iarc_min	11.48	11.62
Bead quality index vs Iarc_min	11.49	11.63
Fusion area vs Iarc_min	11.50	11.64
Penetration depth vs Iarc_min	11.51	11.65
Bead width vs Iarc_min	11.52	11.66
Energy input per unit length vs Iarc_min	11.53	11.67
Fusion area vs Energy input per unit length	11.54	11.68
Average dipping frequency vs Iarc_min	11.55	11.69
Mean welding current vs Iarc_min	11.56	11.70
Average arcing current vs Iarc_min	11.57	11.71
RMS current vs Iarc_min	11.58	11.72
Mean welding voltage vs Iarc_min	11.59	11.73

* = Travel speed

11.5.3 Discussion of Results for CTWD=12mm

The results represented by these figures are discussed in this section. Where appropriate, comparisons are made with the Ar-23%CO_2 process.

Inspection of the results shows that the differences between the closed loop and open loop processes operating with CO_2 shielding gas are mostly similar to the differences exhibited for Ar-23%CO_2. However, there are areas where the CO_2 closed loop process appears to operate better than in open loop. The stability index (Figure 11.47) is the most improved factor. It is significantly improved for values of Iarc_min above 60A. But when accounting for the inevitable reduction in fusion area (Figure 11.50), the stability index for a given fusion area is only slightly improved by the closed loop system for the higher fusion area values. This is discussed further in section 11.6. The amount of spatter produced (Figure 11.48) for a given value if Iarc_min is reduced, though the change is not as impressive as for the case of Ar-23%CO_2 at reduced travel speed (Figure 11.34). The reason for the spatter level not being as low as for Ar-23%CO_2 is evident from the current waveform in Figure 11.60, for the case of Iarc_min=120A. A "premature" short circuit occurs at time t=0.16 seconds. The short circuit current is at the Iarc_min level (120A) rather than the desired 30A. As investigated in Chapter 10, the level of ball repulsion spatter in CO_2 is very high for currents above 80A (see Figure 10.101). The combination of premature short circuits

and violent ejection of material from the weld pool at high short circuit currents causes the overall spatter level for the closed loop CO_2 process to be significantly higher than for the Ar-23%CO_2 process operating under the same conditions. The premature short circuits need not be frequent to generate this level of spatter. In the 1.0 second recording from which Figure 11.60 is produced, there was only one premature short circuit in 74. There were 3 other short circuits which occurred at currents above 30A but less than 50A. This corresponds to the observations noted during the experiment: "Consistent fine spatter with infrequent bursts of high spatter". Because of the additional "bursts of high spatter", the weld was given a spatter rating of "medium" rather than "low". To obtain a more accurate assessment of spatter reduction under these conditions of intermittent spatter production, the spatter would need to be carefully collected and weighed for each test case. This was not possible with the available resources.

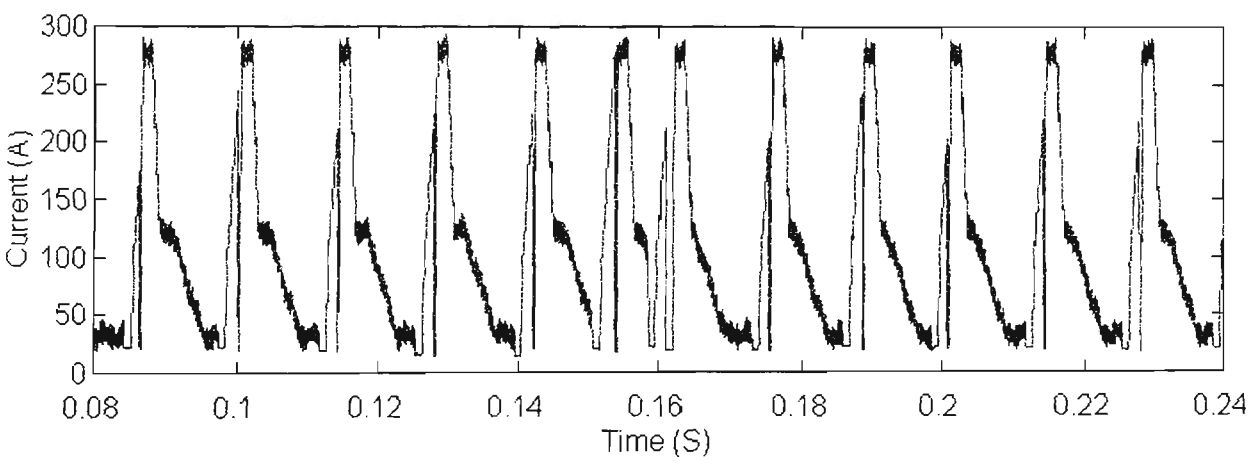

Figure 11.60 Current waveform for Iarc_min=120A

The significant improvement in stability index for a given value of Iarc_min can be explained in light of the preceding explanation of spatter generation mechanisms. For the majority of weld cycles, the arcing period terminates at low current levels of 30A. At this level, there is little disturbance to the weld pool due to generation of repulsive ball spatter. This keeps the weld pool quiescent, so that stability indices are kept between 0.80 and 0.90 across the entire operating range.

As for the closed loop Ar-23%CO_2 process at reduced travel speed, the bead quality index (Figure 11.49) maintains the same trend as for the open loop process. The fusion area (Figure 11.50) and energy input (Figure 11.53) are reduced for a given value of Iarc_min, so that penetration depth and bead width are correspondingly reduced. The

RMS welding current (Figure 11.58) remains relatively constant (+/- 2%) throughout the operating range, so the peak arc length is dependent almost solely on Iarc_max.

11.5.4 Test Results for CTWD=20mm

Figures 11.61 to 11.73 compares the results of closed loop control to open loop control for the CO_2 process at CTWD=20mm and Iarc_max=250A.

[Refer to Appendix 11 for Figures 11.61 to 11.73]

11.5.5 Discussion of Results for CTWD=20mm

The results represented by Figures 11.61 to 11.73 are discussed in this section.

In general, the behaviour of the closed loop process at a CTWD of 20mm follows the same pattern as that for CTWD=12mm. There are significant improvements in stability index (Figure 11.61) for the closed loop process over the open loop process. The stability of the open loop process at higher values of Iarc_min is poor because of long arc lengths developed due to high electrode preheating. By its operation, the closed loop process limits the amount of electrode burn-back during the arcing period while regulating the droplet size. This is reflected in the higher average weld cycle frequency (Figure 11.69). The spatter levels (Figure 11.62) are lowered for median values of Iarc_min, but the overall range of spatter produced by both processes is the same. Inspection of the waveforms show the same infrequent (1 to 2 per second) occurrence of the "premature" short circuits as described in section 11.5.3. The range of bead quality indices (Figure 11.63) is also unaltered, indicating that the closed loop process does not enhance the bead appearance. Unlike all other test groups, the fusion area (Figure 11.64) and penetration depth (Figure 11.65) achieved by the closed loop system matches that of the open loop. This can be attributed to the poor performance of the open loop system at 20mm CTWD. The range of bead widths (Figure 11.66) is slightly increased because of a widened arc column produced by higher Iarc_min values in the early stages of the arcing period, when the arc length is longest (see section 11.4.3).

Due to improved stability, the closed loop process can generate a slightly higher energy input (Figure 11.67) to the weld. The difference in maximum energy input between processes is only 6%. The graph of fusion area versus energy input (Figure 11.68) does not show a clear increase in fusion area for the closed loop process, due to

the data scatter. As indicated previously, scatter in fusion area data is expected since only one macrosection per weld is taken.

The RMS current (Figure 11.72) remains within 2A of 116A for most of the test range, deviating by 10A for the highest value of Iarc_min tested. The peak arc length is therefore not influenced by Iarc_min for most of the test range.

11.6 Summary and Discussion of Results for the "Closed Loop" Process

This section summarises the key findings presented in detail throughout this chapter, and also draws conclusions from these results.

To successfully implement the "closed loop" process in practice, a method has been devised to automatically select the optimum droplet size target. This method compensates for steady state scaling errors in the estimation of droplet size caused by varying CTWD and electrode preheating. The method also removes the need to predetermine an optimum value of droplet size target for every conceivable operating condition.

The main objective of the closed loop control system investigated in this chapter is to regulate the droplet size produced at the end of the electrode on a cycle-by-cycle basis. The expected benefits are reduced spatter levels and improved stability indices. Results presented in this chapter show that there are improvements in both areas, but not under all operating conditions. Furthermore, by attempting to reduce spatter and regulate droplet size, the modification of the current waveform results in a loss of fusion area for a given setting of Iarc_min.

The closed loop system produces lower spatter levels for a given value of Iarc_min under most operating conditions. This is particularly evident for Ar-23%CO_2 at reduced travel speed, and CO_2 generally. Under these conditions, it has been shown in Chapter 10 that weld pool oscillations are less influential on process behaviour. For Ar-23%CO_2 at reduced travel speed, all welds were truly spatterless across the tested operating range. For CO_2, spatter was reduced but not entirely eliminated because of infrequent "premature" short circuits occurring early in the arcing period, before the droplet target is reached and while the arcing current is still high. As described in section 11.5.3, this is likely to be a result of weld pool oscillation, and generates a large amount of ball spatter per single event. Despite these complications, there is sufficient

evidence to show that the reduction of arcing current to 30A prior to the short circuit event is an effective method of eliminating the single spatter-causing mechanism that remains in this type of process control. Spatter could not be eliminated from the Ar-23%CO_2 process operating at 390mm/min travel speed because "premature" short circuits tend to occur well before the droplet target is reached. The short circuit event occurs at the same high current as in the open loop control, so spatter is not reduced. The droplet estimation algorithm is designed to select the droplet size target so that the current is reduced to 30A just prior to the short. For the control algorithm to achieve reduced spatter, the process must consistently remain in the arcing state long enough for the droplet to grow to the target value.

The act of reducing arcing current when the droplet target is reached has the undesired effect of reducing energy input to the process at the tail end of the arcing period. The fusion area is reduced for a given value of Iarc_min. The closed loop process can achieve a similar fusion area to the open loop process only by increasing Iarc_min. In doing so, the amount of spatter inadvertently produced by infrequent "premature" short circuits at higher current can negate the spatter reduction in the majority of weld cycles where the current is successfully reduced to 30A. When the spatter levels for a given fusion area are compared, it can be seen that the closed loop process produces only minor improvements in spatter levels (refer to Figures 11.79 to 11.83 in Appendix 11). It can be concluded that weld pool oscillations play a significant part in the operation of the closed loop control.

For operating conditions where weld pool oscillations are not pronounced, the stability index for a given value of Iarc_min showed some improvement. The improvements were greatest for Ar-23%CO_2 at reduced travel speed and CO_2 operating at higher values of Iarc_min. Not coincidentally, these conditions also exhibited the most reduction in spatter. The improvement in stability index is believed to be due to reduced agitation of the weld pool, since most short circuits occur at reduced current, so the forces that generate ball repulsion spatter are avoided. However, when the stability indices of open loop and closed loop processes are compared for the same fusion area, it can be shown that in general there is no significant improvement in stability index (refer to Figures 11.74 to 11.78 in Appendix 11). The stability index is based on the variation in the weld cycle duration, which is mainly due to changes in arcing time. As explained in section 11.4.3, small movements in weld pool height in the order of 0.2mm

can alter arcing duration by up to 15%. In view of this degree of sensitivity, it is not surprising that the stability indices cannot be noticeably improved unless a control scheme is employed which specifically aims to reduce weld pool oscillation.

The fact that there is no significant improvement in stability index does not prove that the droplet estimation method functions poorly. It is quite possible that the closed loop control system is producing droplets of the same size when the ΔL_{target} is reached and arcing current begins to be reduced. Since some arcing current must always be present (to detect the short circuit event), additional electrode melting will occur, and the droplet will continue to grow at a reduced rate during the "arcing dead time". The timing of the short circuit is influenced by movement of the weld pool, hence variations in final droplet size will occur. The magnitude of the variations in size depends on the variation in arcing dead time and the instantaneous electrode melting rate. Experiments in Chapter 7 have shown that, within limitations of the test equipment, the implemented droplet estimation algorithm is able to generate droplets of consistent size.

The tests conducted in this chapter show no evidence that regulation of droplet size produces an improved weld bead. In the five test "groups", the profiles of bead quality index versus Iarc_min for the closed loop system follow the profile for open loop control. Bead quality was neither enhanced nor degraded across the test range. It was shown in Chapter 10 that the open loop process can produce high quality weld beads for stability indices that would be considered low for conventional CV power sources. It can be concluded from tests in this chapter that the attempt to regulate droplet size does not discernibly enhance bead quality. Combining the facts that bead quality is not strongly influenced by stability index, that good beads can be produced at moderate values of stability index, and that avoiding short-circuit spatter tends to improve stability index, it may be concluded that stability index by itself is not a sufficiently accurate indicator of process performance in these types of current-controlled processes. The focus may need to be removed from process regularity and more attention directed at removing non-ideal disturbance forces generated during the weld cycle, such as fuse rupture and ball repulsion. Increases in process regularity are likely to follow any such improvements. A moderate level of stability index (0.70 to 0.90) is satisfactory, since the current controlled process can successfully transfer a droplet of varying size from electrode to weld pool without affecting the subsequent

arcing period. The regularity of the melting rate in each arcing period is determined by the controller and the repeatable current waveform. This is completely different from a conventional CV power source, which relies on process regularity so that the initial and final arcing currents are kept almost the same.

The closed loop control system retains the major benefit delivered by the open loop system: decoupling of key parameters such as peak arc length, fusion area and short-circuit rupturing characteristics. It has been shown that for a given combination of Iarc_max, CTWD, wire feed rate and travel speed, the RMS current does not significantly vary as Iarc_min is adjusted and as the droplet size target is automatically varied by the control system. Thus the peak arc length is determined by Iarc_max. The fusion area is still predominantly determined by Iarc_min, although the closed loop system effectively adjusts the energy input to the process during the arcing period. As discussed in section 11.4.3, there has been some loss of "certainty" in the predictable relationship between fusion area and Iarc_min. Nevertheless, the fusion area can be adjusted over a wide range with reasonable predictability and repeatability by adjusting Iarc_min, without altering the short circuiting behaviour.

It can be concluded from the findings of this chapter that the greatest benefit of the closed loop system is its ability to reduce or eliminate ball repulsion spatter by reducing the arcing current to 30A prior to the short circuit. Ball repulsion spatter is the one remaining spatter-producing mechanism in the process, since spatter from short circuit fuse ruptures has been eliminated by the equipment described in Chapter 4. The lack of improvement in stability index for a given fusion area, combined with an improvement in stability index where the spatter is reduced, indicate that a control system which can reduce the arcing current just prior to the short circuit may be more successful than the droplet regulation scheme tested in this chapter. The current reduction must be done immediately before the short circuit, so that the energy input and workpiece heating is maximised (i.e., equal to that of the open loop process). If the onset of the short circuit can be reliably predicted, not only is the spatter expected to be reduced, but the stability index is also expected to be improved due to reduced pool disturbances at the short circuit, particularly for CO_2 shielding gas.

Although some claims have been made regarding prediction of the short circuit [34], close inspection of voltage and current waveforms of the open loop process operating in either CO_2 or argon-based shielding gases indicate that there is no apparent

"precursory event" which could be reliably used to predict the short circuit before it actually occurs. Figure 11.84 shows fine detail of a short-circuit event in Ar-23%CO_2 for Iarc_min at 70A, and Figure 11.85 shows the corresponding waveforms for CO_2 operating at Iarc_min=90A. The waveform sampling rate is 1μs. The filtering time constant applied to both current and voltage waveforms is also 1μs. The lack of a "precursory event" means that the prediction of the onset of short-circuiting may be a more difficult task than the prediction of the short circuit rupture, which is described in detail in Chapter 4. This problem has not been further investigated.

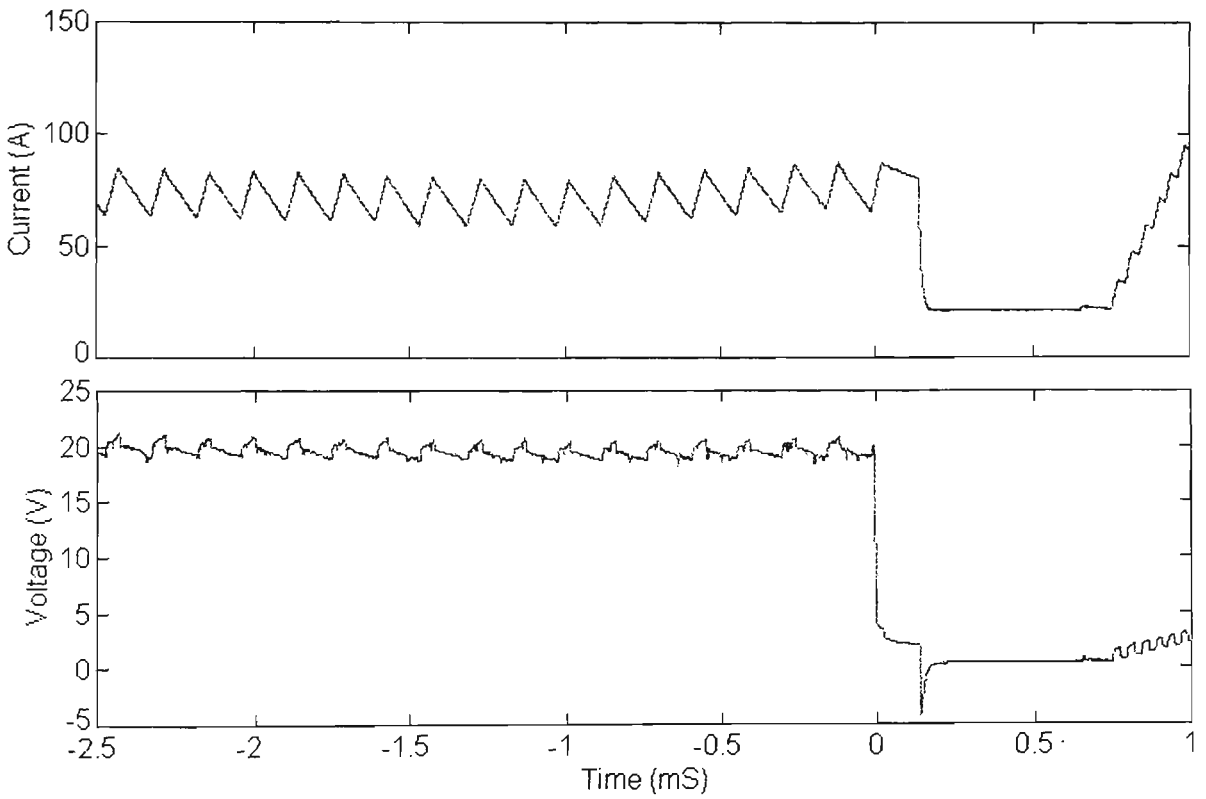

Figure 11.84 Short-circuit event waveforms for Ar-23%CO_2

Examination of Figures 11.84 and 11.85 shows that there is a 150μs delay between the start of the short circuit (as indicated by a sudden drop in the "unfiltered" voltage signal) and action taken by the control system to switch off the main arcing current. All tests performed in chapters 10 and 11 have exhibited this delayed response. The delay is present because the action to turn off the current is taken by the DSP processor, in response to a voltage signal with a 40μs time constant single-pole filter. The short circuit is not recognised until the filtered voltage signal drops below 5V. It is reasonable to suspect that a delay of 150μs may be enough to promote ball repulsion spatter at the start of the short circuit. To investigate this possibility, some enhancements were made to the Premonition Unit so that the main arcing current is switched off when the

"unfiltered" voltage shown in the figures drops below 8V. The resultant system response is shown in Figures 11.86 and 11.87, for CO_2 at Iarc_min=90A.

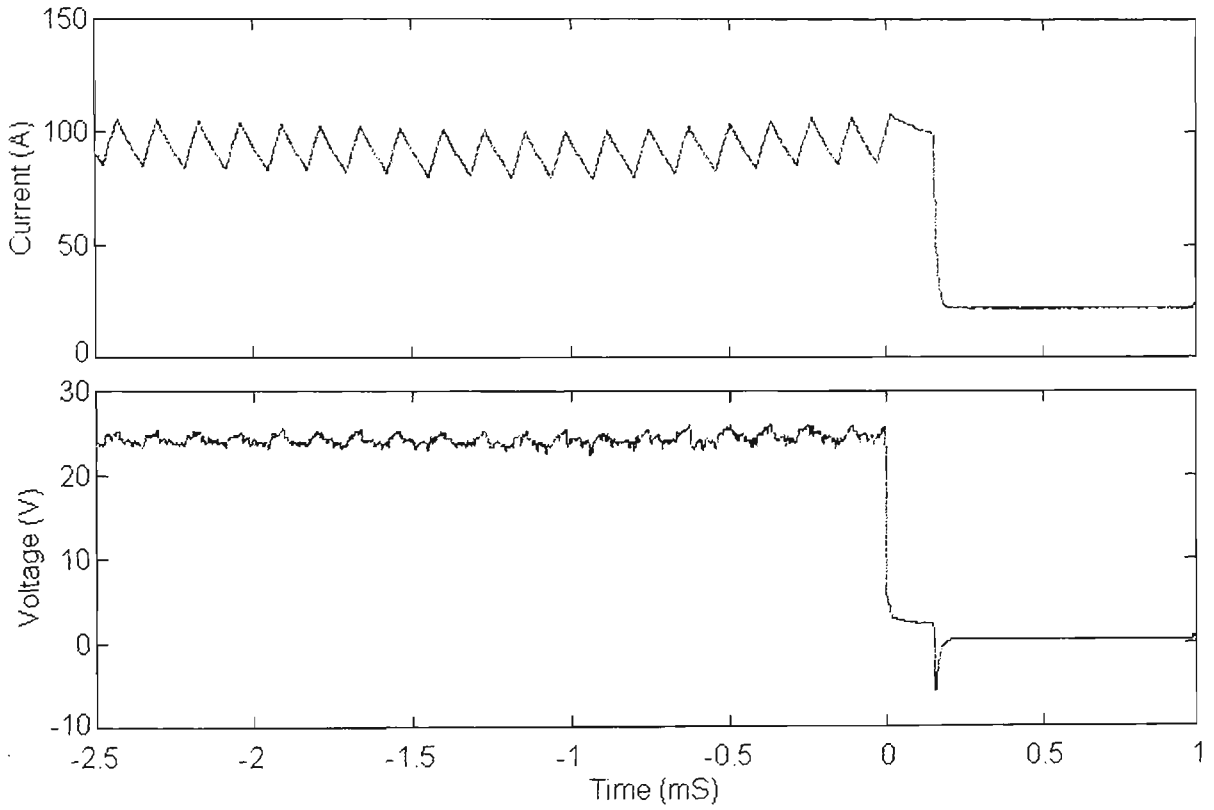

Figure 11.85 Short-circuit event waveforms for CO_2

The time delay between the start of the short circuit and the start of current turn-off is reduced to a mere 10μs. The current is reduced from 100A to 30A after a further 20μs. With this improved electrical performance, the spatter levels were compared to the unimproved system under the following conditions:

1. CO_2 shielding gas, Iarc_max=275A, Iarc_min=90A, CTWD=12mm
   Travel speed=195 m/min, Wire feed speed=6.0 m/min
2. CO_2 shielding gas, Iarc_max=275A, Iarc_min=40A, CTWD=12mm
   Travel speed=195 m/min, Wire feed speed=6.0 m/min
3. Ar-23%CO_2 shielding gas, Iarc_max=300A, Iarc_min=90A, CTWD=16mm
   Travel speed=390 m/min, Wire feed speed=6.0 m/min
4. Ar-23%CO_2 shielding gas, Iarc_max=350A, Iarc_min=110A, CTWD=8mm
   Travel speed=390 m/min, Wire feed speed=6.0 m/min

Three welds were performed at each condition for each system configuration. For cases 1, 2 and 3, there were no discernible changes in spatter levels using the visual assessment technique described in section 10.2.3. In case 4, there was a definite

reduction in spatter, from "very high" levels to "medium-high". The stability indices did not change significantly in any of the tests.

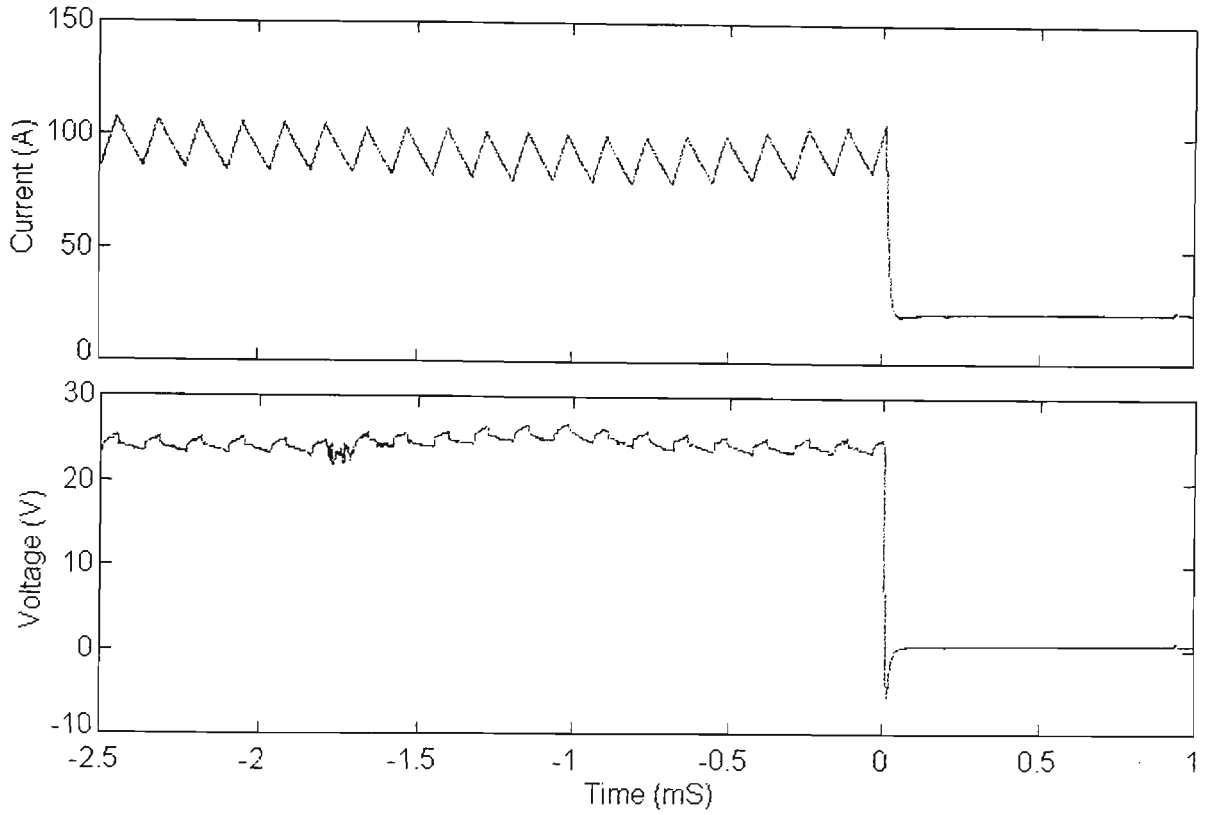

Figure 11.86 Short-circuit event waveforms for improved system (coarse)

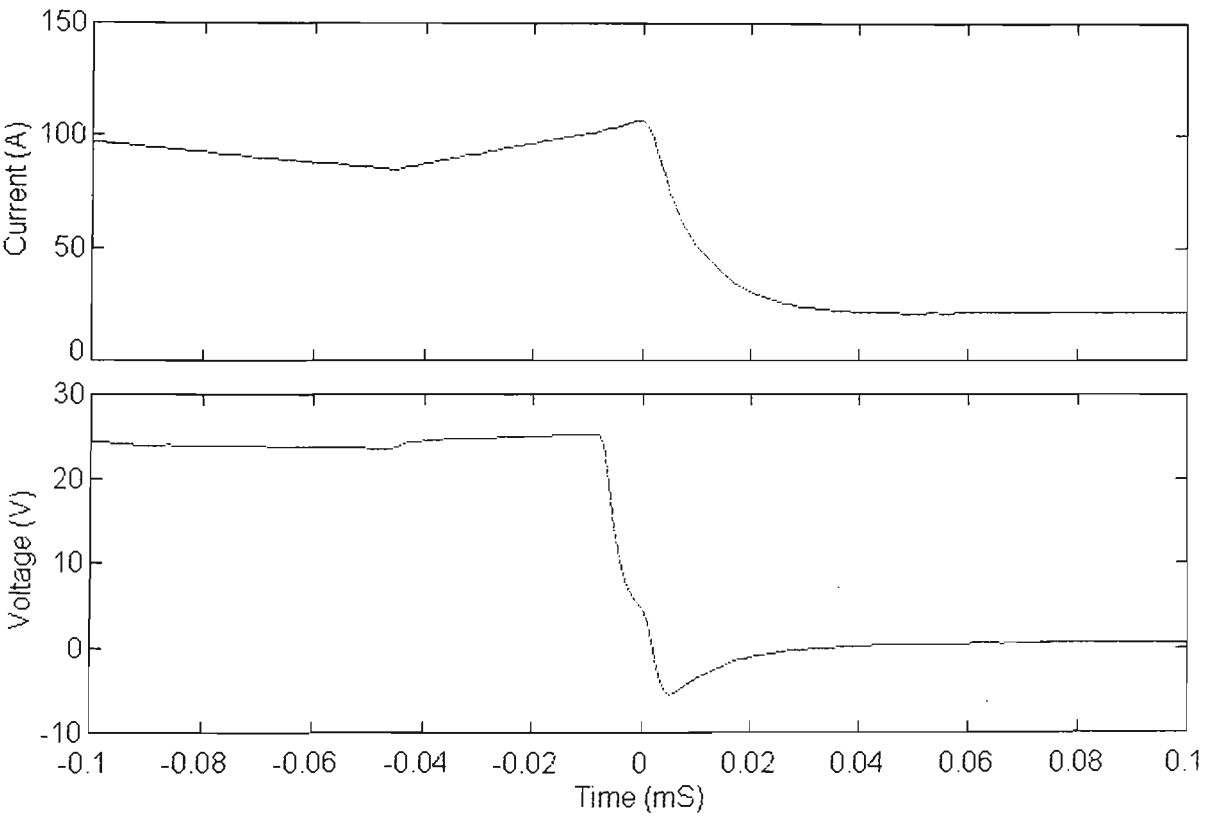

Figure 11.87 Short-circuit event waveforms for improved system (fine)

Although these tests are limited, their results indicate that even a very rapid current turn-off (<30μs) at the start of the short circuit is not sufficient to appreciably reduce ball repulsion spatter under most operating conditions. The results in this chapter indicate that to totally eliminate this type of spatter, the current must be reduced before the short circuit event.

It is recommended that future work should concentrate on the development of a method that can reliably predict the onset of a short circuit event, so that the arcing current can be reduced at least 100μs prior to the short circuit. Implementation of this method is expected to eliminate ball repulsion spatter in the same way that the Premonition Unit described in Chapter 4 has removed short-circuit rupture spatter from the process.

Chapter 12

Summary, Conclusions and Recommendations

12.1 Summary

This thesis has investigated the behaviour of the short-circuit gas metal arc welding process under the control of two advanced current-controlled techniques. The first of these, referred to as the "open loop" process, is very similar to control schemes that have been reported in the literature. This type of process control is available commercially in a very limited range of equipment, but has not previously been rigorously investigated in the literature. The second technique, referred to as the "closed loop" process, regulates the size of the droplet formed at the end of the electrode on a cycle-by-cycle basis. The objectives of both control techniques are to produce stable, low spatter welds over a wide operating range, and to reduce or remove the coupling of key parameters such as peak arc length, heat input and metal transfer characteristics during the short-circuit. The research conducted in this project has shown that these objectives can indeed be achieved.

The results of the work presented in this thesis have been discussed in detail in each chapter, and are summed up at the end of each chapter. The various stages of the work are further summarised below. The major conclusions follow in section 12.2.

In order to perform the research, an experimental current-controlled power source and auxiliary control equipment were specifically designed and constructed, as documented in Chapter 4. For reasons described in Chapters 2 & 3, the power source was required to have extremely fast current turnoff response, in the order of 20 kA/ms. A suitable "premonition unit" was developed to reliably predict the onset of short circuit rupture, so that the final stages of the short circuit were consistently completed at very low current levels to avoid spatter being generated at the rupture. Interfacing equipment was also constructed to provide accurate, noise-free signals representing voltage, current, wire feed speed and travel speed. The high quality of the signals has been crucial to the transient analyses conducted throughout the project. The power source and premonition unit were interfaced to a PC-based DSP welding controller so that virtually every aspect of the system's behaviour could be programmed (and easily reprogrammed) in a high level language. The "open loop" and "closed loop" control

techniques were programmed as finite-state processes, as detailed in Chapter 5. To assist in analysing and understanding process behaviour, a novel process visualisation system for the GMAW process has been developed and is described in Chapter 9. The welding controller is programmed to trigger a digital colour camera so that a photograph of the process is taken, and synchronised to desired events within the process. The weld area is illuminated by a custom-built high power xenon flashlighting unit, which overcomes the intense arc light to produce images of remarkable clarity and detail. These are used throughout this thesis to illustrate particular aspects of process behaviour.

In order to perform closed loop droplet size regulation, it was necessary to estimate the instantaneous electrode melting rate. This in turn required an estimate of the electrode stickout length, which is equal to the CTWD during the short circuiting period. Chapter 6 describes a novel method of online CTWD estimation. It is applicable specifically to the current-controlled short-circuit GMAW process, where the current is increased at a fixed rate during the short circuit. The CTWD is estimated by measuring the minimum resistance during the short circuit, and applying a correction factor which is a function of the duration of the short circuit, the type of shielding gas used, and the wire feed speed. The correction factor was determined for CO_2 and Ar-23%CO_2 shielding gases, for wire feed speeds from 1.9 m/min to 5.7 m/min. Experiments showed that this method can estimate the CTWD to within +/-2mm of the actual value in the range from 6mm to 20mm with both argon-based and carbon dioxide shielding gases.

Having obtained an estimate of the CTWD, Chapter 7 describes the development of three methods of predicting in real time the instantaneous size of the electrode droplet. Offline simulations of these methods (applied to actual welding voltage & current waveforms) showed that unacceptably large errors of +/-30% were introduced into the estimates. Analysis indicated that the errors stemmed from two sources. Firstly, unpredictable errors in CTWD estimation caused corresponding errors in the instantaneous melting rate estimate. Secondly, there was a consistent error caused by changes in dipping frequency, which was thought to change the final temperature of the droplets. This violated the central modelling assumption of constant specific heat content. To overcome these problems, a simplified model was adopted which provides an estimate that is proportional to the droplet size. The proportionality depends on the

operating conditions, but remains constant provided that operating conditions do not alter. This estimate may be implemented in a closed loop system whose aim is to produce droplets of a consistent size rather than a specific size. The automatic selection of an optimum droplet size target is described in Chapter 11. Using the process visualisation system, the droplet volume was measured to be within $0.09mm^3$ of the average volume. The variations were within the range of measurement errors.

Chapter 8 outlines a novel technique of measuring the current-voltage characteristics of various GMAW shielding gases. The experimental power source was used to apply a pulsed current of short duration to test electrodes which were positioned in a geometry which is the same as that encountered in actual short-circuit welding. Characteristics for Ar-23%CO_2, Ar-16%CO_2-3%O_2, and CO_2 shielding gases with electrode diameters from 0.9mm to 1.6mm were obtained using this convenient and efficient method. This work was undertaken to provide additional data for process modelling. Although the data was not utilised in the models which were subsequently developed, the work is reported in this thesis since it provides new data which may be of use in future research.

Chapter 10 documents an extensive experimental evaluation of the "open loop" control technique. Tests were carried out using 0.9mm mild steel electrode in Ar-23%CO_2 and CO_2 shielding gases under a variety of conditions.

The experimental evaluation of the "closed loop" droplet size control technique is described in Chapter 11. Tests were carried out using 0.9mm mild steel electrode in Ar-23%CO_2 and CO_2 shielding gases under a more limited range of conditions in comparison with the tests of Chapter 10.

12.2 Conclusions

1) An open loop control system for short circuiting GMAW has been implemented and experimentally evaluated in detail.

2) This control technique is able to produce stable, low spatter welds with excellent bead appearance across a very wide range of operating conditions. The test conditions ranged from wire feed speeds of 1.9 m/min to 5.7 m/min, and CTWDs of 8mm to 20mm.

3) It has been established that the "open loop" control technique meets its objective of significantly decoupling peak arc length from other parameters such as energy

input, fusion area and short-circuit transfer characteristics. Unlike the constant voltage process, the behaviour of the process does not rely on the dynamic characteristics of the power source.

4) Peak arc length is determined by current Iarc_max applied during the initial stages of the arcing period.

5) The fusion area can be significantly altered by adjusting the steady state arcing current Iarc_min. The fusion area can typically be adjusted over a 2:1 range without altering wire feed speed or CTWD. Lack-of-fusion defects in thick-section workpieces can be avoided by correct selection of Iarc_min. Conversely, burn-through in thin sections can be avoided by decreasing Iarc_min, whilst achieving the desired deposition rate.

6) As expected, the fusion area was found to be proportional to the energy output of the power source. By decreasing the CTWD while keeping all other parameters constant, the energy input can be greatly increased. Conversely, as the CTWD is increased, the energy that can be supplied to the process is reduced. In a practical application requiring high fusion, the CTWD must be constrained to low values. For welding of thin sections, the CTWD can vary over a wide range, since the required energy input can be supplied over this wide range of CTWD values through the adjustment of Iarc_min. (The welding travel speed must of course be kept constant).

7) The RMS current remains almost constant as Iarc_min is altered. This means that the electrode preheating is unaffected by changes to the fusion area at a given CTWD and wire feed speed. Thus the relationship of peak arc length to Iarc_max is unaffected, and arc length is decoupled from fusion control.

8) Increasing steady state arcing current Iarc_min causes a monotonic increase in average droplet size, hence a monotonic decrease of dipping frequency. The control of the process during the short-circuiting period is able to successfully transfer the material to the weld pool for a very wide range of droplet sizes. Thus process stability can be maintained across a wide range of metal transfer conditions, so short-circuit metal transfer is decoupled from arcing considerations. In contrast, the constant voltage process generates a maximum frequency at a particular voltage, and the maximum process stability is

experienced only in a narrow window of operating frequencies. This also limits the available fusion area to a small range at a given wire feed speed.

9) The "open loop" process produces stable welds and excellent weld beads with stability indices in the range of 0.70 to 0.90. In comparison, the constant voltage process can generate stability indices of 0.90 to 0.95 in its optimum operating window, where the dipping frequency equals the weld pool oscillation frequency. The ability of the "open loop" process to produce consistent arcing conditions and to successfully transfer a wide range of droplet sizes means that the process is not influenced by weld pool oscillations to the same extent as the CV process. As a result, the current-controlled process operates well even when pool oscillation frequency is grossly dissimilar to the dipping frequency. Under these conditions, the stability index will naturally be low, even though the weld quality is high.

10) Truly spatterless welds can be produced under some conditions, and welds with very low spatter levels are produced under most conditions. Spatter produced at the rupture of the short circuit has been virtually eliminated. The predominant spatter production mechanism was found to be ball repulsion spatter, produced at the start of the short circuit. Generally, the spatter level is related to the value of Iarc_min. However, high spatter could also be produced at very low values of Iarc_min if premature short circuits occur early in the arcing period, when the current is still high. This was found to be caused by large weld pool oscillations. In this respect, the welding process is still influenced by pool oscillations.

11) Because the instantaneous welding current is controlled by the power source and not determined by the arcing voltage, the process is governed by the melting rate behaviour of the electrode, and the timing of the short circuit events is influenced by weld pool oscillations. Simulations of the process were carried out where the electrode melting rate was modelled and weld pool dynamics were ignored. Despite this important simplification, the simulation results showed good agreement with experimental results. Discrepancies occurred in cases where pool oscillations were found to be more pronounced.

12) A closed loop control system which regulates droplet size has also been implemented and evaluated in detail.

13) A method of automatically selecting the optimum droplet size target is necessary for closed loop control, and this has been developed.

14) The technique in (13) above removes the need to predetermine a value for every conceivable operating condition, and also compensates for steady state errors in droplet size estimation.

15) The decoupling of key parameters (peak arc length, fusion area and short-circuit transfer characteristics) has been maintained.

16) The "closed loop" technique is able to significantly reduce or totally eliminate ball repulsion spatter in conditions where pool oscillations are not large. In situations where pool oscillations are significant, premature short circuits occur at high current, thereby reintroducing the mechanism which the control system attempts to avoid.

17) The "closed loop" control causes a loss of potential fusion area, as the current is reduced in the final stages of arcing. This makes the "closed loop" technique better suited to welding of thin sections. In thicker sections, the "open loop" technique can produce greater fusion at the cost of increased spatter.

18) The regulation of droplet size produces no discernible improvement in the stability index when comparisons are made of welds with equal fusion area. Stability index is based on weld cycle time, and simple calculations show that a 0.2mm change in pool height can alter arcing duration by up to 15% for a wire feed speed of 5.7 m/min. In the presence of even small oscillations, variations in weld cycle times are unavoidable where the dipping frequency does not coincide perfectly with pool oscillation frequency.

19) The regulation of droplet size neither improves nor degrades the bead quality when compared to the "open loop" technique. This is due to both process' ability to successfully transfer droplets of largely variable size to the weld pool without affecting the subsequent arcing period.

From the results of Chapters 10 and 11, some further conclusions can be drawn:

20) Firstly, the stability index by itself is not a sufficiently accurate indicator of process performance in these types of current controlled processes, where adaption is automatically made for variations in the timing of short-circuiting and arcing periods. This is indicated by the fact that stable welds with low

spatter and good bead appearance can be produced at stability indices that would be considered too low for conventional CV power sources. To properly assess process behaviour, a wholistic approach needs to be adopted, encompassing diverse aspects such as bead appearance, spatter levels and appropriate fusion levels.

21) Secondly, the results have shown that the predominant spatter production mechanism is ball repulsion, produced at the start of a short circuit occurring at high current. If the timing of the short circuit can be predicted within less than 1ms prior to the event, then spatter can be eliminated for a stable weld without significant loss of fusion area.

12.3 Recommendations for Future Work

While this thesis has examined the behaviour of the current-controlled short-circuit GMAW process in detail, a number of issues remain to be researched. It is suggested that future work should include:

a) Development of a method to reliably predict the short circuiting event to within 1.0 ms of the actual event. This appears to present the greatest challenge, and the greatest source of process improvement.

b) Further investigation of the "open loop" technique for smaller (0.6mm, 0.8mm) and larger (1.2mm, 1.6mm) electrode diameters in steel, and also further investigation of process behaviour with different materials (aluminium alloys and stainless steels).

c) Further development of the CTWD estimation technique for other electrode diameters and materials. In an automated, closed loop system which aims to control fusion area through energy input, the regulation of the CTWD is essential. There is also a need to resolve the differences between simulation and experimental results for CTWD estimation at low wire feed speeds, where conduction effects may be important.

d) Further testing and evaluation of the pulsed-current method of arc characteristic measurement, as described in Chapter 8.

References

1. Needham J C and Hull W G, "Self-adjusting welding arcs", *British Welding Journal* February 1954, pp71-77

2. Tuthill R W, "Dip transfer carbon dioxide welding", *Welding Journal* October 1959, pp976-981

3. Smith A A, "Characteristics of the short-circuiting CO_2 shielded arc", *British Welding Journal* November 1963, pp571-586

4. Yamamoto H, Harada S, Nishikawa W and Ueyama T, "MIG welding of aluminum [sic] – Process and power source", *IIW Document* XII-1433-96

5. Lesnewich A, "Control of melting rate and metal transfer in gas-shielded metal-arc welding, Parts 1 and 2", *Welding Journal*, August 1958 pp343s-353s, September 1958 pp 418s-425s

6. Lancaster J F, "The physics of welding", 1986 2nd Edition, *Pergamon Press*, ISBN 0-08-034076-8

7. Liu S and Siewert T A, "Metal transfer in gas metal arc welding: Droplet rate", *Welding Journal* February 1989 pp52s-58s

8. Kiyohara M, Okada T and Yamamoto H, "On the stability of metal transfer in short circuit arc welding and the new control systems", *IIW Document* 212-276-73

9. Halmoy E, "Current-voltage process characteristics in GMAW", *IIW Document* 212-773-90

10. Halmoy E, "Dynamics and instability in arc welding", *Advances in Welding Research 2000* Sydney Symposium (Australia) February 2000, Keynote address

11. Maruo H and Hirata Y, "Current and time required to break up a conducting liquid bridge", *IIW Document* 212-720-89

12. Maruo H and Hirata Y, "Bridging transfer phenomena of conductive pendant drop", *IIW Document* 212-833-93

13. Lebedev V K, Zaruba I I and Andreev V V, "Conditions of the formation of a liquid bridge in the droplet transfer of metal with short-circuiting of the arc gap", *Avt. Svarka* No.9 1975, pp1-3

14. Essers W G and Walter R, "Heat transfer and penetration mechanisms with GMA and plasma-GMA welding", *Welding Journal* February 1981, pp37s-42s

15. Jonsson PG, Szekely J, Madigan R B and Quinn T P, "Power characteristics in GMAW: Experimental and numerical investigation", *Welding Journal* March 1995, pp93s-102s

16. Keene B J, Mills K C and Brooks R F, "Surface properties of liquid metals and their effects on weldability", *Materials Science and Technology* Vol.1 1985, pp568-571

17. Choi S K, Yoo C D and Kim Y-S, "Dynamoc simulation of metal transfer in GMAW, Parts 1 and 2", *Welding Journal* January 1998, pp38s-51s

18. Hirata Y, Onda M, Osamura T and Ohji T, "Breakup time of liquid bridge in short-circuiting transfer process of GMA welding", *IIW 51st Annual Meeting* 1998 (Hamburg Germany), *IIW Document* 212-936-98

19. Stava E K, "A new, low spatter arc welding machine", *Welding Journal* January 1993, pp25-29

20. "The physics of spatter formation during dip transfer GMA welding", *IIW Document* 212-738-89

21. Zaruba I I, "Electrical explosions as the cause of metal spatter", Avt. Svarka 1970 No.3, pp12-16

22. Lewis P D and Bax D N A, "Effect of inductance on spatter loss in the CO_2 shielded welding of mild steel", *British Welding Journal*, April 1964 pp157-162

23. Hermans M J M and den Ouden G, "Process behaviour and stability in short circuit gas metal arc welding", *Welding Journal* April 1999, pp137s-141s

24. Houldcroft P T, "Welding Processes", *Cambridge University Press* 1967

25. Smith A A, "Features of short-circuiting CO_2 arc welding with a duplex power source", *British Welding Journal* April 1966, pp215-223

26. den Ouden G, Xiao Y H and Hermans M J M, "The role of weld pool oscillation in arc welding", *Int. J. for the Joining of Materials* Vol.5 (4) 1993, pp 123-129

27. Aberg P, "Computerised power sources make optimised welding characteristics more easily accessible", *Svetsaren (ESAB Review)* Vol.46 No.1 1992

28. Sibley C R, "All-position welding of HY-80 steel with the gas-shielded process", *Welding Journal* October 1960, pp433s-437s

28a. Smith A A, *British Welding Research Association Report* C94/4/63

29. Boughton P and MacGregor G, "Control of short circuiting in MIG welding", *British Welding Research Association Members' Report* P57/72

30. Boughton P and MacGregor G J, "Control of short circuiting in MIG welding", *Welding Research International* Vol.4(2) 1974, pp31-53

31. Needham J C and Boughton P, "Welding power source", *U.S. Patent* 3792225

32. Colens A, "Electronic Welder", *RCA Power Semiconductor, Application Engineering Report (Liege)* May 1976

33. Needham J C, "Evolution of power sources in arc welding- transition from passive to active role", *TWI Research Bulletin* April 1987

34. Ogasawara T, MaruyamaT, Saito T, Sato M and Hida Y, "A power source for gas shielded arc welding with new current waveforms", *Welding Journal* March 1987, pp 57-63

35. Ogasawara T, Maruyama T, Sato M, Hida Y and Saito T, "Output control of short circuit welding power source", *U.S. Patent* 4546234

36. Maruyama T, Okada M, Hida Y, Honma M and Minato T, "Current waveform control in gas shielded arc welding for robotic systems", *Kobelco Technology Review* No.18 April 1995, pp24-28

37. Nakanishi S, Nakajima Y, Kawano H, Ihochi A, Ogasawara T and Maruyama T, "Method and device for controlling welding power supply to avoid spattering of the weld material" ", *U.S. Patent* 4544826

38. Stava E K and Parks J M, "Apparatus and method of short circuiting arc welding", *U.S. Patents* 4717807, 4835360, 4866247, 4897523, 4954691, 4972064, 5001326, 5003154, 5148001,

39. Malesani L, Mattavelli P, Rossetto L, Tenti P, Marin W and Pollmann A, "Electronic welder with high frequency resonant inverter", *IEEE Trans. Ind. Appl.* Vol.31 No.2 1995, pp273-279

40. Pollock H and Flower J O, "Series parallel load-resonant converter for controlled-current arc welding power supply", *IEE Proc. Electr. Power Appl.* Vol.143 No.3 May 1996, pp211-218

41. Sanders L A, Ratto H, West M P, Soh W K and Norrish J, "Monitoring gas metal arc welding phenomena using high speed data acquisition techniques", *Proc. WTIA 45th Annual Conference* November 1997 (Melbourne Australia), Paper No.35

42. Sanders L A, "Process monitoring and on-line modelling of the gas metal arc welding process", *PhD Thesis*, Department of Mechanical Engineering, University of Wollongong, Australia, 1996

43. Buki A and Gorenshtein I M, "The stability and self adjustment of metal deposition with short circuits of the arc gap", *Automatic Welding* 11 1967

44. Shinoda T, Kaneda H and Takeuchi Y, "An evaluation of short circuiting phenomena in GMA welding", *Welding and Metal Fabrication* Vol.57 (10) 1989

45. Kuszelyko R, "An objective solution of the welding process stability evaluation", *IIW Document* XII-F208-79

46. Kim J W and Na S J, "A study on prediction of welding current in gas metal arc welding. Part2: Experimental modelling of relationship between welding current and tip-to-workpiece distance and its application to weld seam tracking system", *Proc. Instn Mech Engrs Part B: J. Eng. Manufacture* Vol.205 1991, pp64-69

47. Ogunbiyi T E B, "Process monitoring and adaptive quality control for robotic gas metal arc welding", *PhD Thesis*, Cranfield University, U.K., 1995

48. Kim J W and Na S J, "A study on prediction of welding current in gas metal arc welding. Part1: Modelling of welding current in response to change of tip-to-workpiece distance", *Proc. Instn Mech Engrs Part B: J. Eng. Manufacture* Vol.205 1991, pp59-63

49. Cook G E, "Robotic arc welding: Research in sensory feedback control", *IEEE Trans. Ind. Appl.* Vol IE-30 No.3 August 1983, pp252-267

50. Huismann G and Hoffmeister H, "Sensing the MIG process by measuring the wire feed rate and the current", *IIW 51st Annual Meeting* 1998 (Hamburg Germany), *IIW Document* 212-931-98

51. Fujimura H, Ide E and Inoue H, "Robot welding with arc sensing", *Sensors and Control Systems in Arc Welding, Technical Commission on Welding Processes, Japan Welding Society* 1991, pp II-91 to II-96

52. Ando K *et al.*, "Welding arc phenomena",1962, *Sanpoh*, (Tokyo)

53. Halmoy E, "Wire melting rate, droplet temperature and effective anode melting potential", *The Welding Institute International Conference on Arc Physics and Weld Pool Behaviour*, London, May 1979, pp49-59

54. Do K D, "Adaptive control of the robotic gas metal arc welding process", *M.E. Thesis*, Department of Mechanical Engineering, University of Wollongong, Australia, 1998

55. Do K D, De Boer F G and Norrish J, "On-line identification of gas metal arc welding process parameters", *Proc. WTIA 45th Annual Conference* November 1997 (Melbourne Australia), Paper No.34

56. Nomura H *et al.* (Ed.s), "Welding guide II – Sensors and control systems in arc welding – The state of the art in Japan", *Technical Commission on Welding Processes*, Japan Welding Society, 1991

57. Ushio M, Liu W and Mao W, "An experimental investigation of dynamic behaviour of arc sensor in GMA welding in short circuit transfer mode", *Transactions of Japan Welding Research Institute* 24(1) 1995

58. Philpott M L, "Robot MIG weld seam tracking by dip-resistance monitoring", *Washington State University 20th Conference of the North American Manufacturing Research Institution of the Society of Manufacturing Engineers (NAMRC)*, 20-22 May 1992 (Pullman, Wa., U.S.A.), pp355-360

59. Carvalho G C, "An adaptive control system for off-line programming in robotic gas metal arc welding", *PhD Thesis*, School of Industrial Science, Cranfield University U.K., 1996

60. Orszagh P, Kim Y C and Horikawa K, "Short-circuiting transient phenomena in GMA/CO_2 welding (I): Through-the-wire sensor for feedback torch height control", *Transactions of JWRI* Vol.26 No.1 1997, pp49-67

61. Halmoy E, Electrode wire heating in terms of welding parameters", *Appendix A* of [6], 1986

62. Halmoy E, "Simulation and instabilities in GMAW and SAW", *IIW Study Group 212: Physics of Welding* September 1996 (Budapest Hungary), *IIW Document* 212-895-96

63. Shepard M E and Cook G E, "A non-linear time domain simulation of self regulation in gas metal arc welding", *International Trends in Welding Science and Technology* 3rd International Conference 1992, pp905-910

64. Hirata Y, Osamura T, Goto N and Ohji T, "Numerical model of short-circuiting transfer process in GMA welding", *Proc. 7th International Conference on Computer Technology in Welding* San Francisco USA July 1997, NIST Special Publication 923, pp 279-287

65. Zhu P, Rados M and Simpson S W, "Theoretical predictions of the start-up phase in GMA welding", *Welding Journal* July 1997, pp269s-274s

66. Quinn T P, Madigan R B and Siewert T A, "An electrode extension model for gas metal arc welding", *Welding Journal* October 1994, pp241s-248s

67. Kim Y-S, McEligot D M and Eagar T W, "Analyses of electrode heat transfer in gas metal arc welding", *Welding Journal* January 1991, pp20s-31s

68. Waszink J H and van den Heuvel G J P M, "Heat generation and heat flow in the filler metal in GMA welding", *Welding Journal* August 1982, pp269s-282s

69. Wilson J L, Claussen G E and Jackson C E, "The effect of I^2R heating on electrode melting rate", *Welding Journal* August 1956, pp1s-8s

70. Midleton P, Oliveira Santos J F and Quintino L, "Synergic algorithms to relate wire feed rate to arcing current for conventional GMA welding", ", *Joining Sciences* Vol.1 No.2 1992, pp 87-93

71. Midleton P, Quintino L and Santos J, "A compensation factor for the resistive melting due to background current when using constant current-pulsed synergic algorithms", *Joining Sciences* Vol.1 No.2 1992, pp 94-99

72. Norrish J, "Advanced welding processes", 1992 *Institute of Physics Publishing*, ISBN 0-85274-326-2

73. Haidar J and Lowke J J, "Effect of CO2 shielding gas on metal droplet formation in arc welding", *IEEE Trans. Plasma Sc.* Vol.25 No.5 1997, pp 931-936

74. Michaelson H B, "The work function of the elements and its periodicity", *J. Appl. Phys.* Vol.48 No.11 November 1977, pp4729-4733

75. Simpson S W, Xu P and Rados M, "Transfer mode transitions in GMAW", *Proc. WTIA 45th Annual Conference* November 1997 (Melbourne Australia), Paper No.32

76. Zhu P, Rados M and Simpson S W, "A theoretical study of a gas metal arc welding system", *Plasm Sources Sci. Technol.* Vol.4 1995, pp495-500

77. Kim Y S and Eagar T W, "Analysis of metal transfer in gas metal arc welding"" *Welding Journal* June 1993, pp269s-278s

78. Jonsson P G, Murphy A B and Szekely J, "The influence of oxygen additions on argon-shielded gas metal arc welding processes", *Welding Journal* February 1995, pp48s-58s

79. Akulov A I and Spitsyn V V, "Rate of formation and transfer of a drop of electrode metal in CO2 welding", *Svar. Proiz* No.12 1968, pp7-12

80. Hirata Y, Onda M, Nagaki H and Ohji T, "In-situ measurement of metal drop temperature in GMA short-circuiting welding", *53rd Annual Assembly International Institute of Welding* July 9-14, 2000, (Florence, Italy), IIW Document 212-969-00

81. Gray C N, Hewitt P J and Dare P R M, "New approach would help control weld fumes at source", *Welding and Metal Fabrication* September 1982, pp 318-397

82. Wisniewski G, "The effect of MAG arc welding parameters on environmental pollution", *Welding International* Vol.5(12) 1991, pp949-953

83. Castner H R, "Gas metal arc welding fume generation using pulsed current", *Welding Journal* February 1995, pp59s-68s

84. Jackson C E, "The science of arc welding", *Welding Journal*, April 1960 pp129s-140s, May 1960 pp177s-190s, June 1960 pp225s-230s

85. Lowke J J, Kovitya P and Schmidt H P, "Theory of free-burning arc columns including the influence of the cathode", *J. Phys. D: Appl. Phys.* 25 1992, pp1600-1606

86. Mantel W, "Considerations on the importance of the physical processes in the welding arc", *Schweissen und Schneiden*, 8, No.8 1956, pp278-280

87. Lancaster J F, "Energy distribution in argon-shielded welding arcs", *British Welding Journal* September 1954, pp412-426

88. Yokomizu Y, MatsumuraT, Sun W Y and Lowke J J, "Electrode sheath voltages for helium arcs between non-thermionic electrodes of iron, copper and titanium", ", *J. Phys. D: Appl. Phys.* Vol.31 1998 pp880-883

89. Goldman K, "Electric arcs in Argon: Volt-amp and volt-arc gap characteristics", *Physics of the Welding Arc: A Symposium*, Institute of Welding London 1966

90. Comment by Einar Halmoy during keynote address, *Advances in Welding Research 2000* Sydney Symposium (Australia), February 2000

91. Fujimura H *et al.*, "Robot welding with arc sensing", in [56].

92. Ohshima K *et al.*, "Stability of pulsed current consumable electrode transfer by power source with periodically varying nonlinear characteristic (in Japanese), *Journal of Japan Welding Society* 51(2) 1982, pp91-97

93. Jonsson P G, Westhoff R C and Szekely J, "Arc characteristics in gas-metal arc welding of aluminum [sic] using argon as the shielding gas", *J. Appl. Phys.* 74 (10) November 1993, pp5997-6006

94. Spraragen W and Lengyel B A, "Physics of the arc and the transfer of metal in arc welding", ", *Welding Journal* Vol.22 1943, pp2s-42s

95. van der Willigen P C and Defize L F, "The determination of droplet size in arc welding by high speed cinematography", *Philips Technical Review* Vol.15 No.4 pp122-128

96. Needham J C, "Metal transfer in inert gas shielded arc welding", *British Welding Journal* 7 (2) 1960, pp101-114

97. Allemand C D, Schoeder R, Ries D E and Eagar T W, "A Method of filming metal transfer in welding arcs", *Welding Journal* January 1985, pp45-47

98. Woods R A, "Metal transfer in aluminum [sic] alloys", *Welding Journal* February 1980, pp59s-66s

99. Quigley M B C and Webster J M, "Observations of exploding droplets in pulsed-arc GMA welding", *Welding Journal* November 1971, pp461s-466s

100. Ueguri S, Hara K and Komura H, "Study of metal transfer in pulsed GMA welding", *Welding Journal* August 1985, pp242s-250s

101. Johnson J A, Carlson N M, Smartt H B and Clark D E, "Process control of GMAW: Sensing of metal transfer mode", *Welding Journal* April 1991, pp91s-99s

102. Rhee S and Kannatey-Asibu E, "Observation of metal transfer during gas metal arc welding", *Welding Journal* October 1992, pp381s-386s

103. Ratto H, "Visualisation study of metal transfer in gas metal arc welding", *M.E. Thesis*, Department of Mechanical Engineering, University of Wollongong, Australia, 1996

104. Allum C J, "Metal transfer in arc welding as a varicose instability: II. Development of model for arc welding", *J. Phys. D: Appl. Phys.* 1995, pp1447-1468

105. Nixon J H and Norrish J, "Determination of pulsed MIG process parameters", *Welding and Metal Fabrication* Synergic MIG Supplement April 1988, pp 4-7

106. Allum C J and Quintino L, "Control of fusion characteristics in pulsed current GMAW", *IIW Document* 212-582-84

107. Yamamoto H, Okazaki K and Harada S, "The effect of short circuiting current control on the reductin [sic] of spatter generation on CO_2 arc welding", *IIW Document* 212-649-1986

108. Yamamoto H, Harada S and Yasuda T, "The development of welding current control systems for spatter reduction", *Welding International* Vol.4(5) 1990, pp398-407

109. Hermans M J M, Sipkes M P and den Ouden G, "Characteristic features of the short-circuiting arc welding process", *Welding Review International* May 1993, pp80-86

110. Needham J C, "Pulse controlled consumable electrode welding arcs – General principles and operating characteristics", *British Welding Journal* April 1965, pp191-197

111. Needham J C and Carter A W, "Material transfer characteristics with pulsed current (for consumable electrode welding arcs with argon-rich gas shield)", *British Welding Journal* May 1965, pp229-241

112. Maruyama T, Okada M, Honma M and Sato E, "Steady current-controlled MAG/MIG welding power source", *Proc. Technical Commission on Welding Processes*, Automation Technology of Arc Welding, Japan Welding Society 1996, ppII-115 – II-120 (*IIW Doc.* XII-1471-96)

113. Dodd C R, "The design and service of automotive electronic equipment", *Autolec* 1988 revised second edition, ISBN 86889 103-7

114. Lowke J J, "Simple theory of free-burning arcs", *J. Phys. D: Appl. Phys.* Vol.12 1979, pp1873-1885

CONTROL OF THE SHORT-CIRCUIT GAS METAL ARC WELDING PROCESS USING INSTANTANEOUS CURRENT REGULATION

Dominic Cuiuri

VOLUME II

Table of Contents

List of Figures

List of Tables

Appendix 1

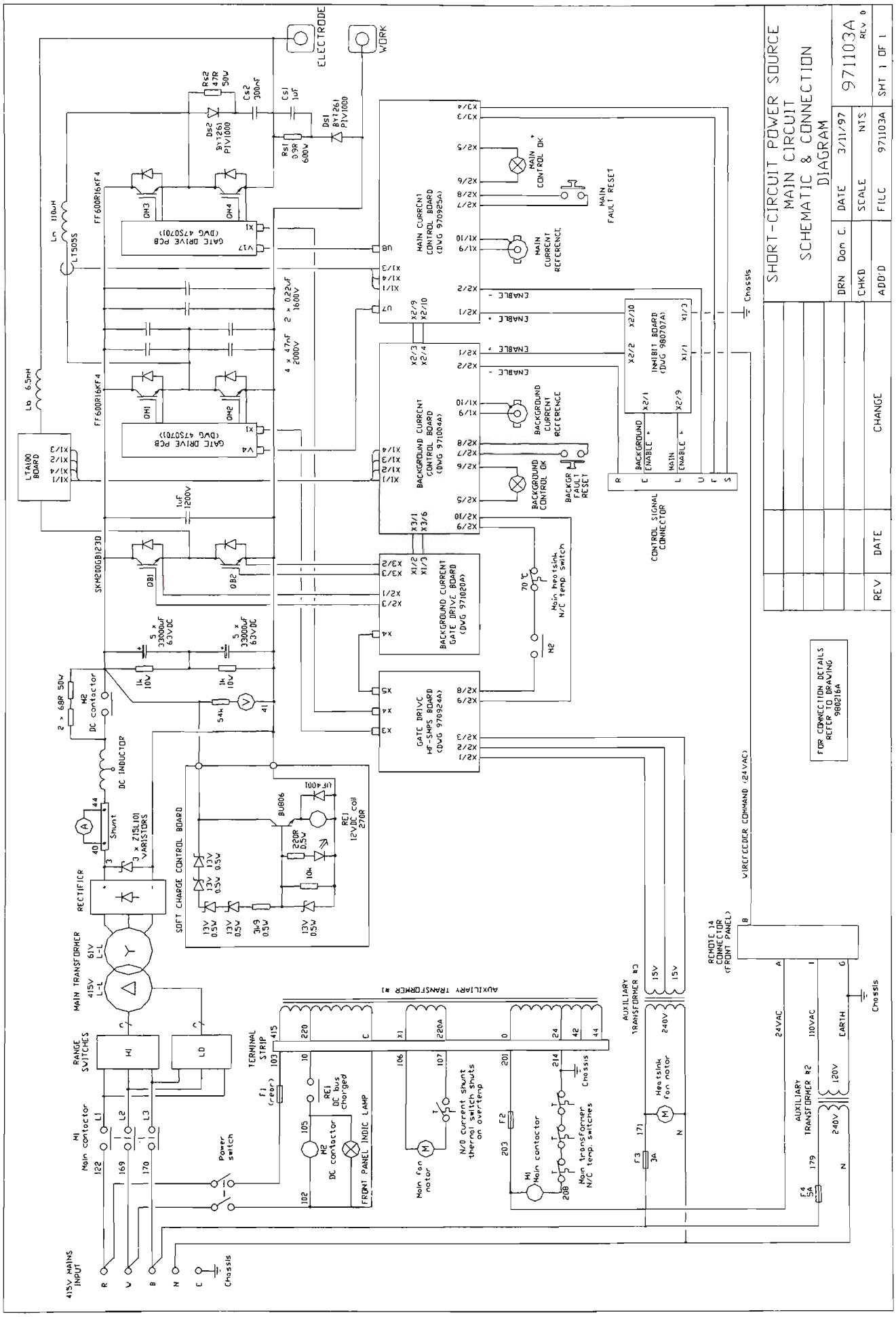

Figure 4.1a Power source main circuit schematic

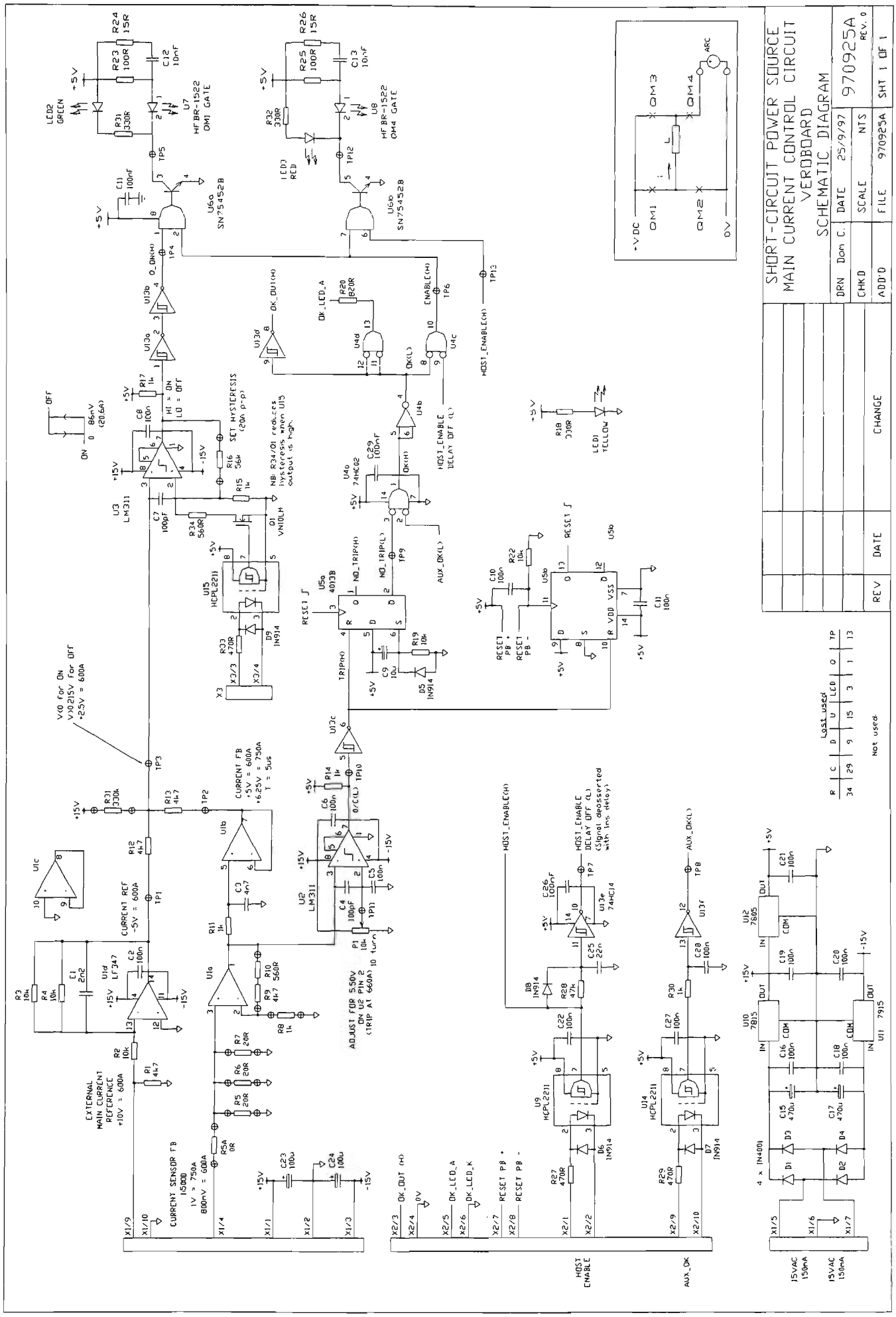

Figure 4.1b Power source main current controller schematic

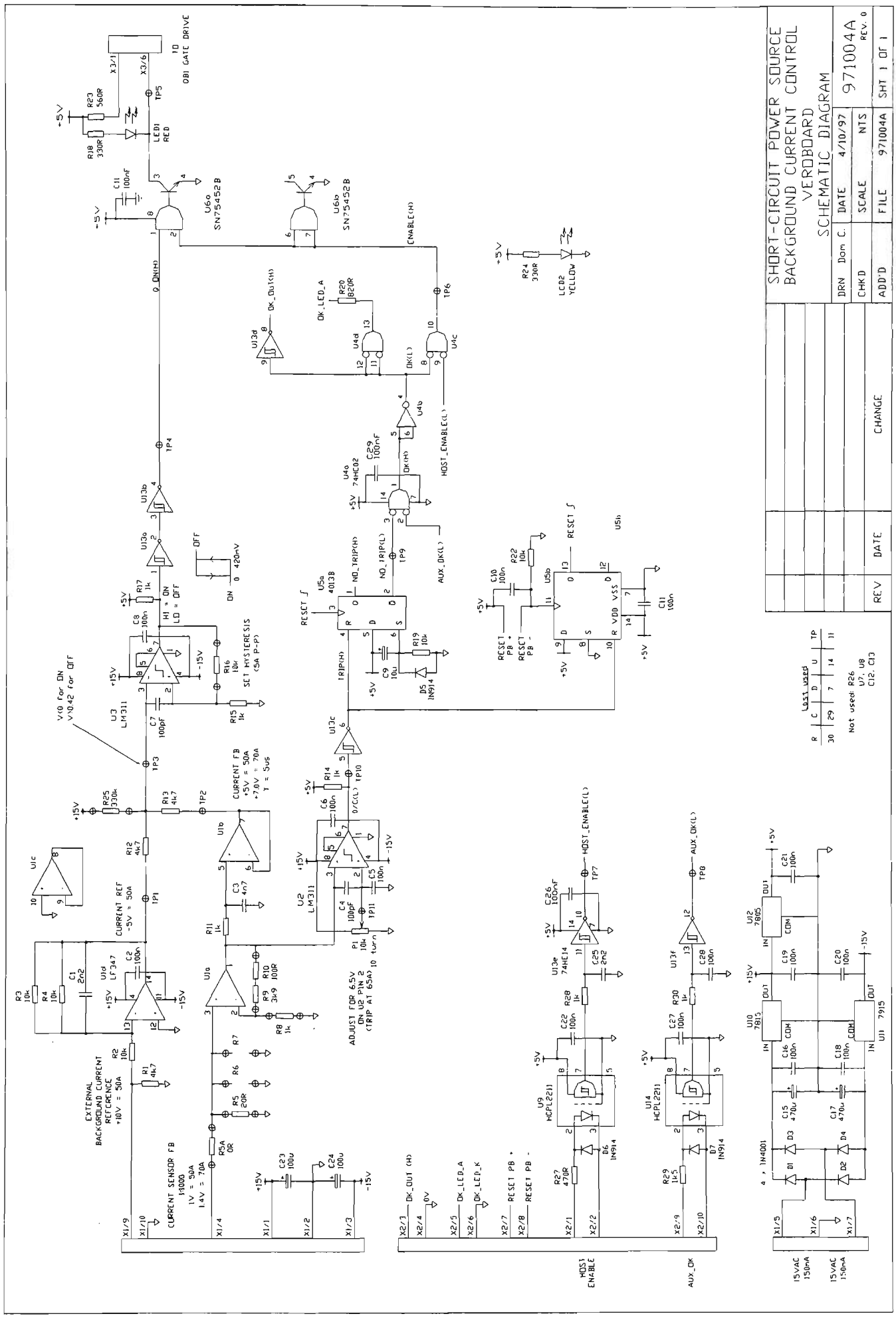

Figure 4.1c Power source background current controller schematic

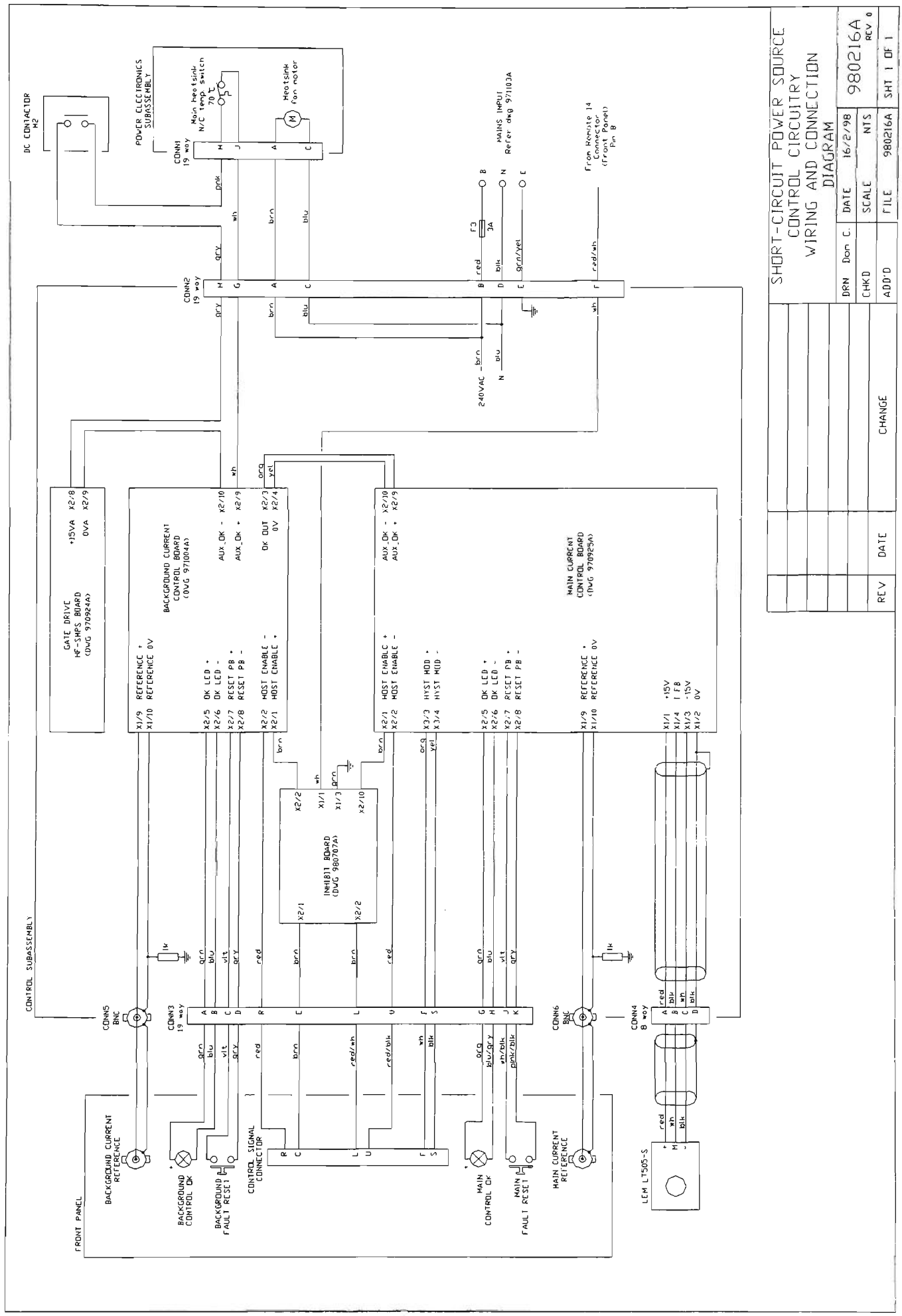

Figure 4.1d Power source control wiring and connection diagram

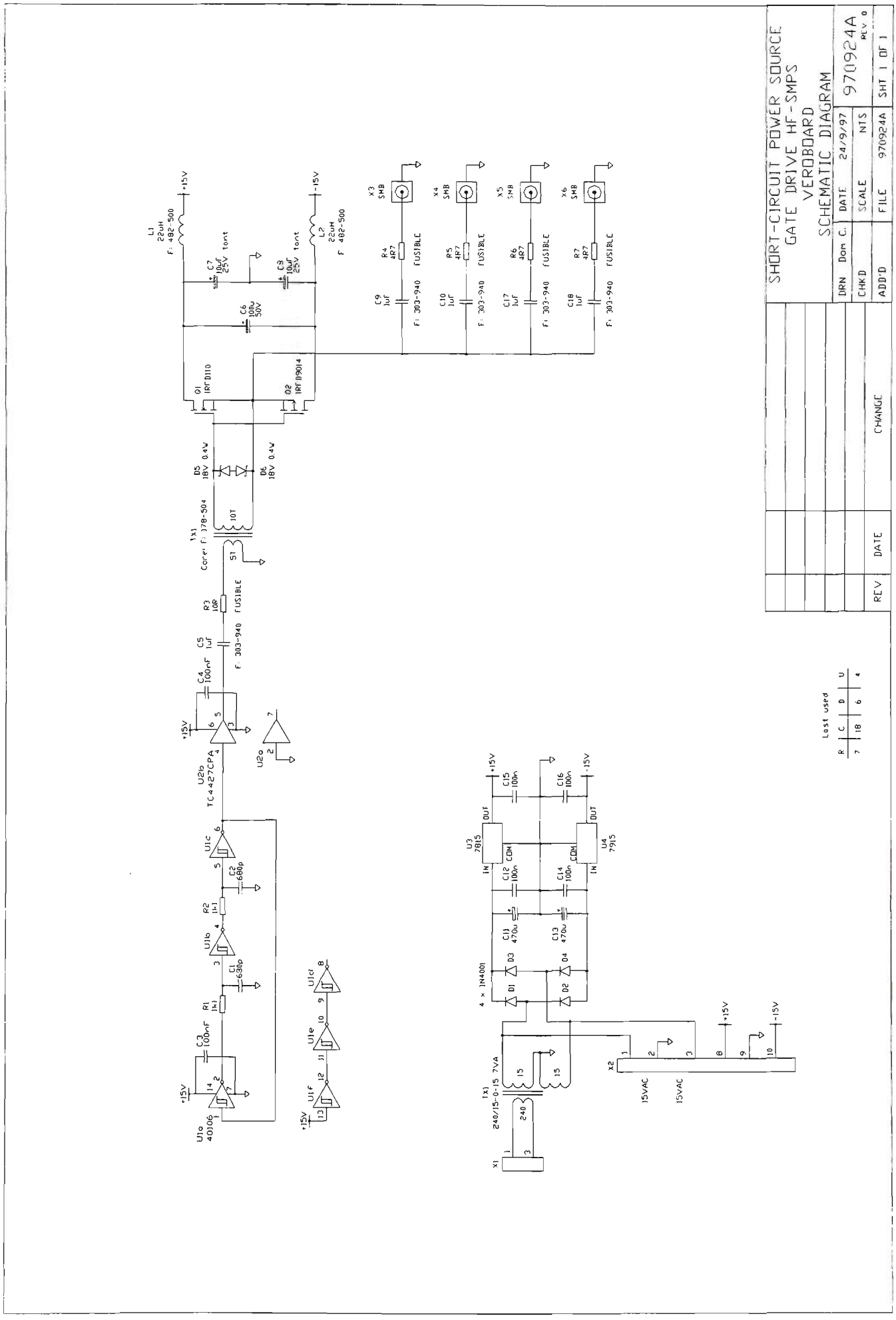

Figure 4.1e Power source gate drive supply

Appendix 2

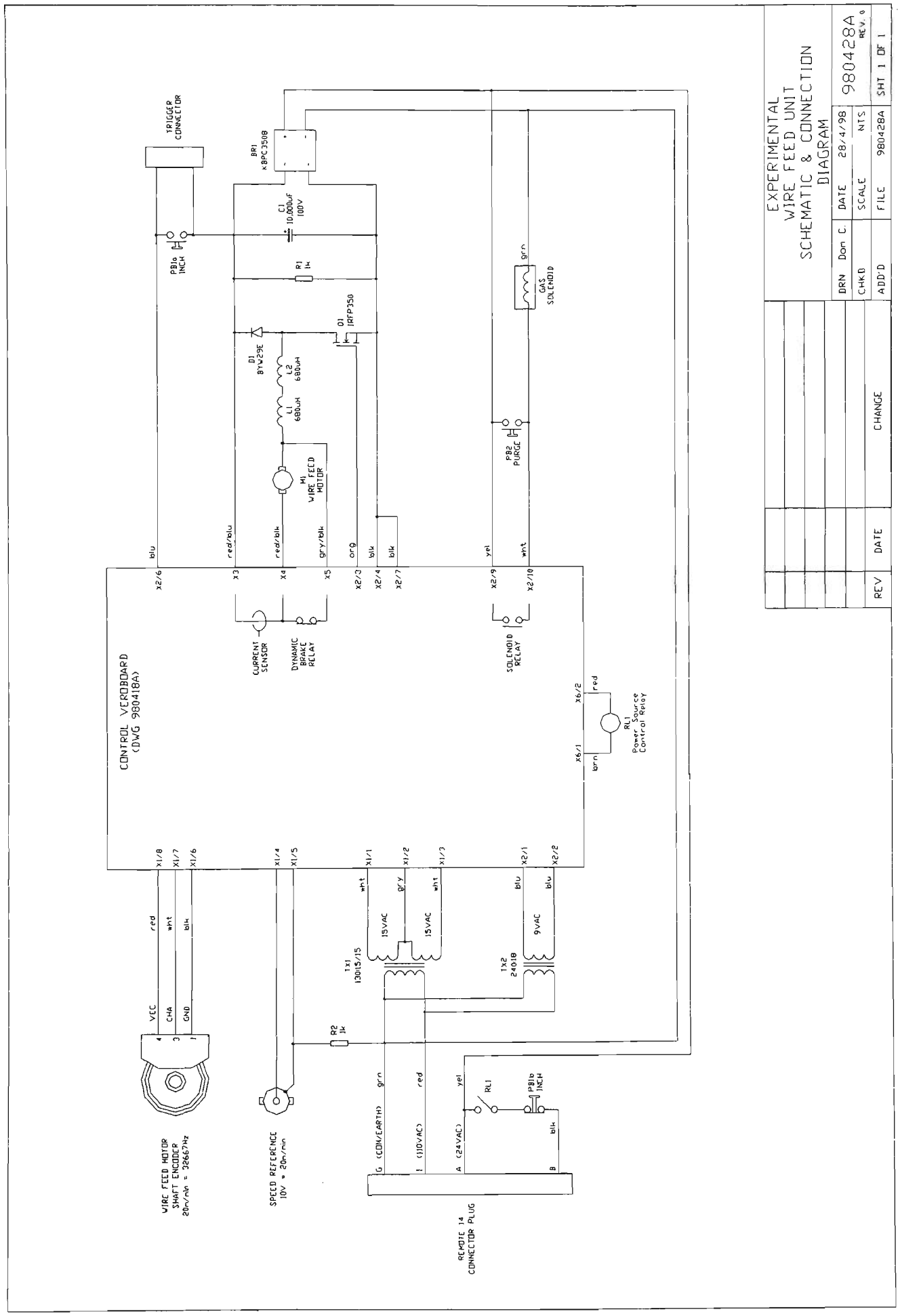

Figure 4.5 Wire feed unit main circuit schematic

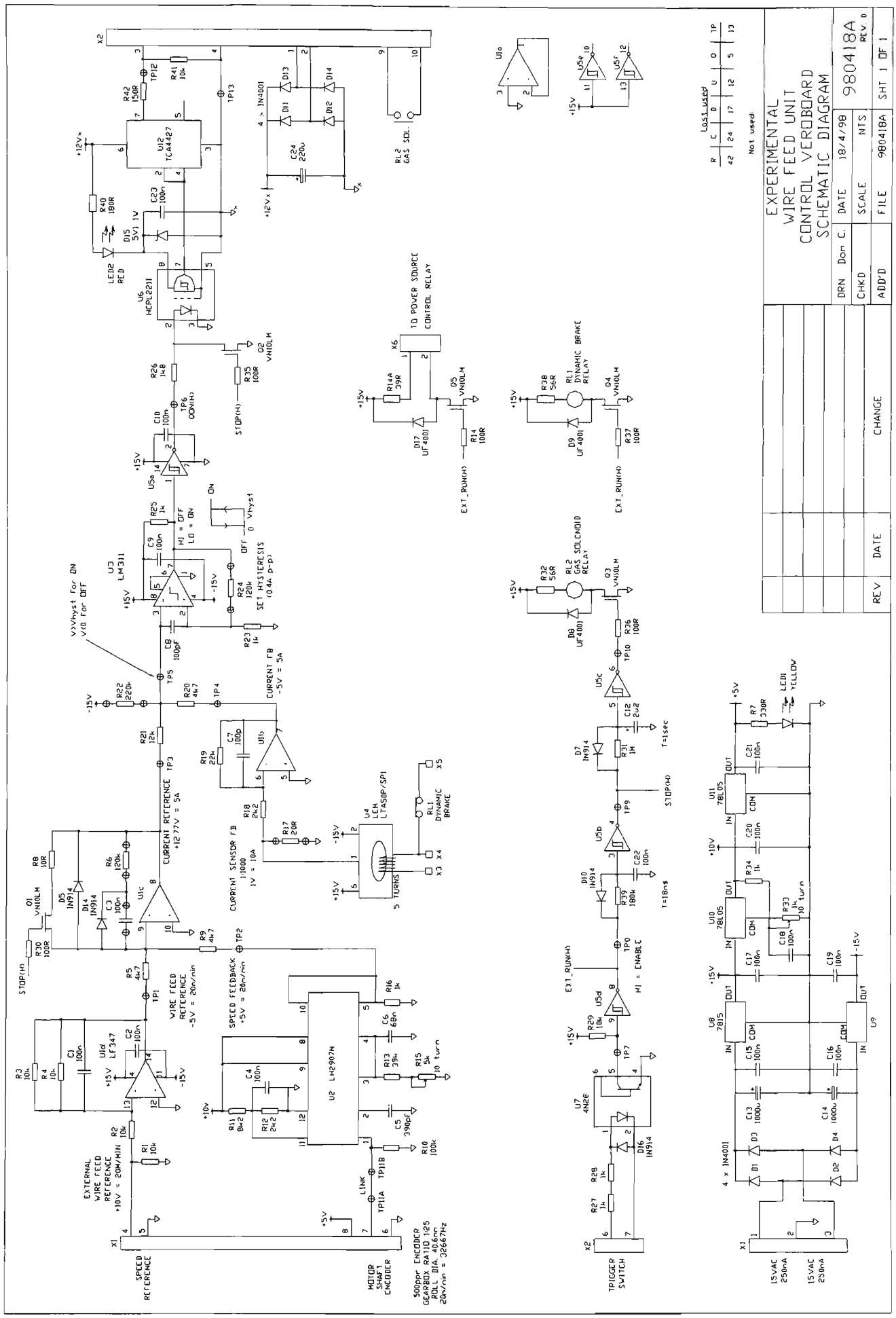

Figure 4.6 Wire feed unit control board schematic

Appendix 3

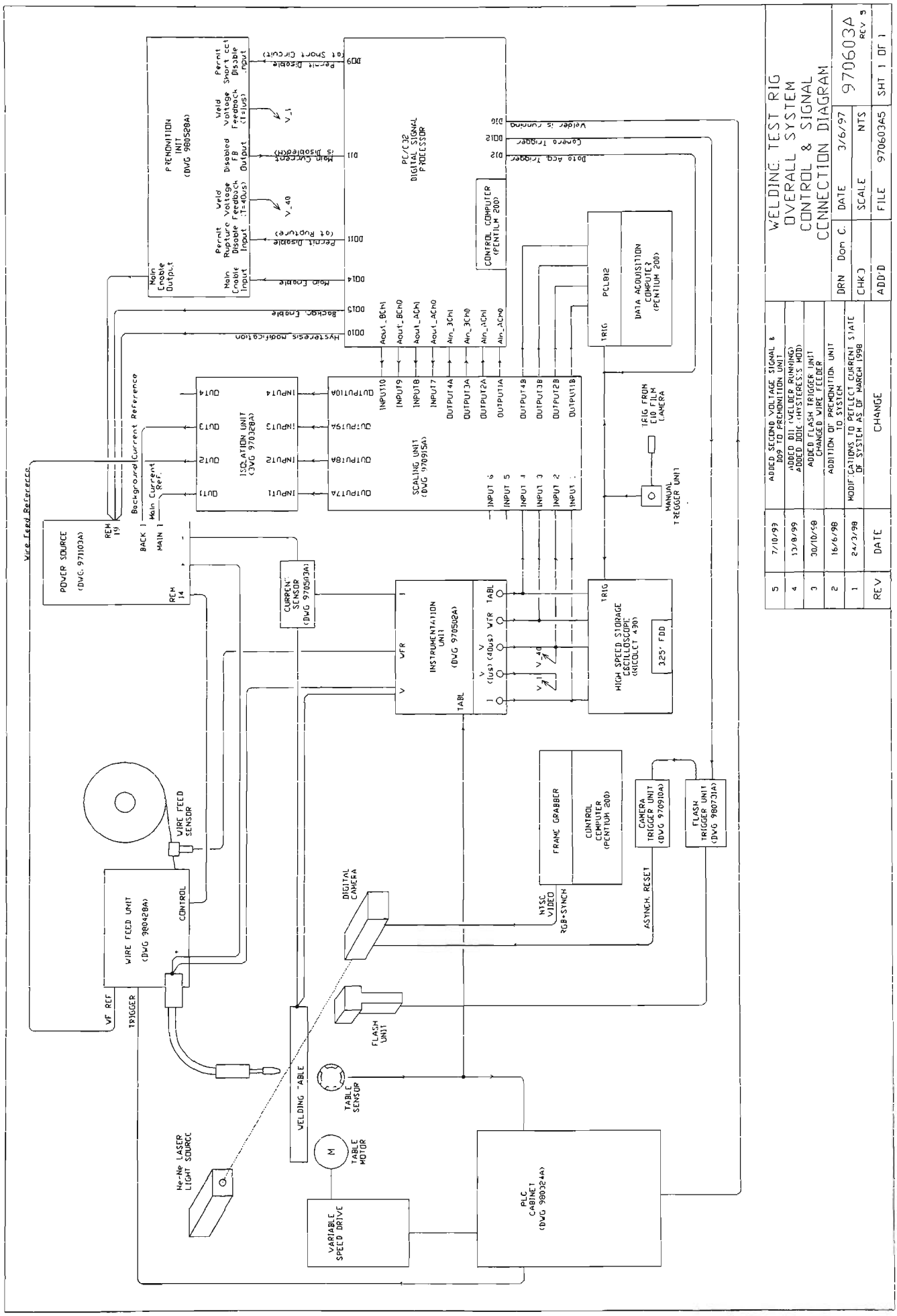

Figure 4.8 Welding test facility block diagram

Appendix 4

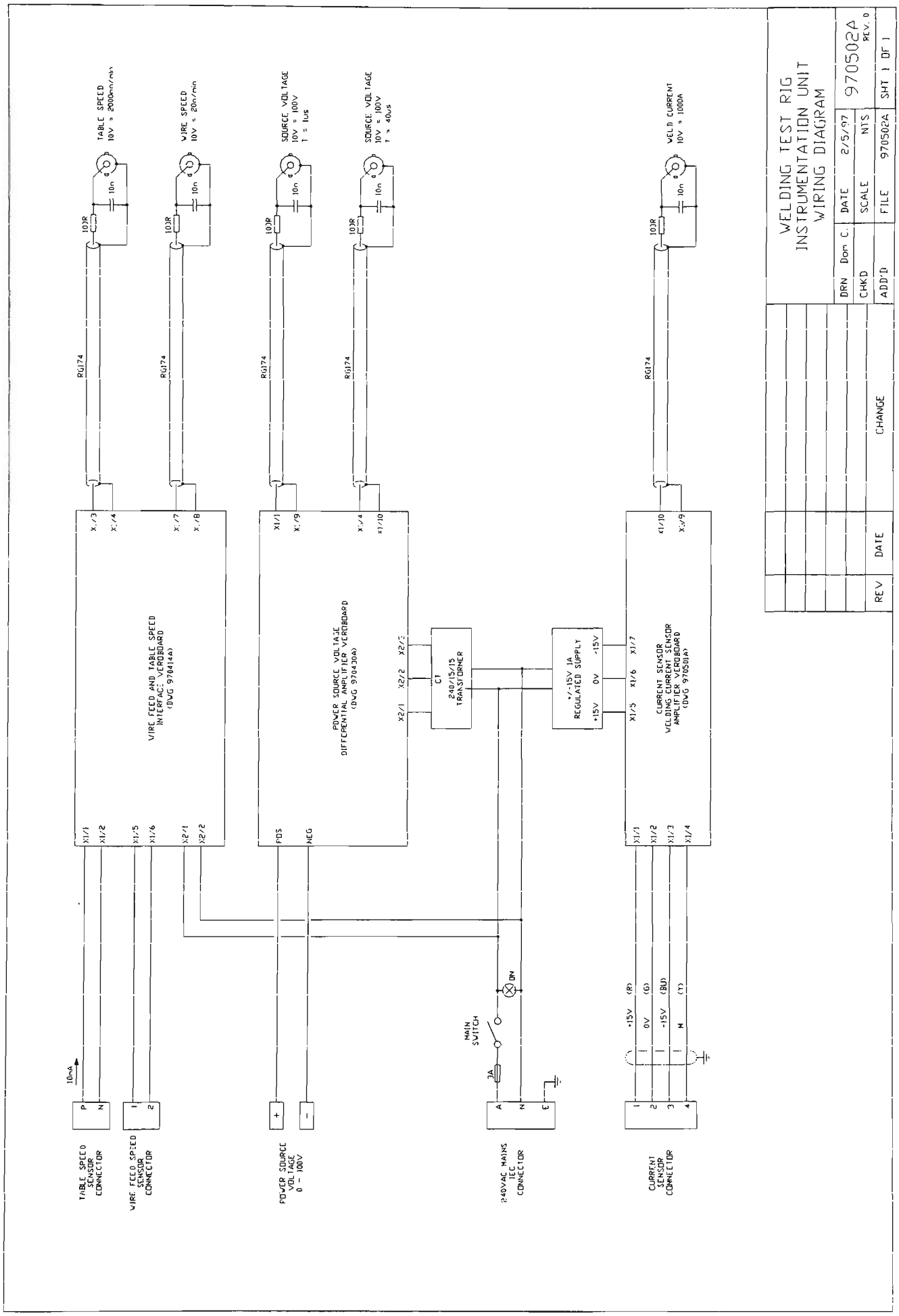

Figure 4.9a Instrumentation unit main schematic

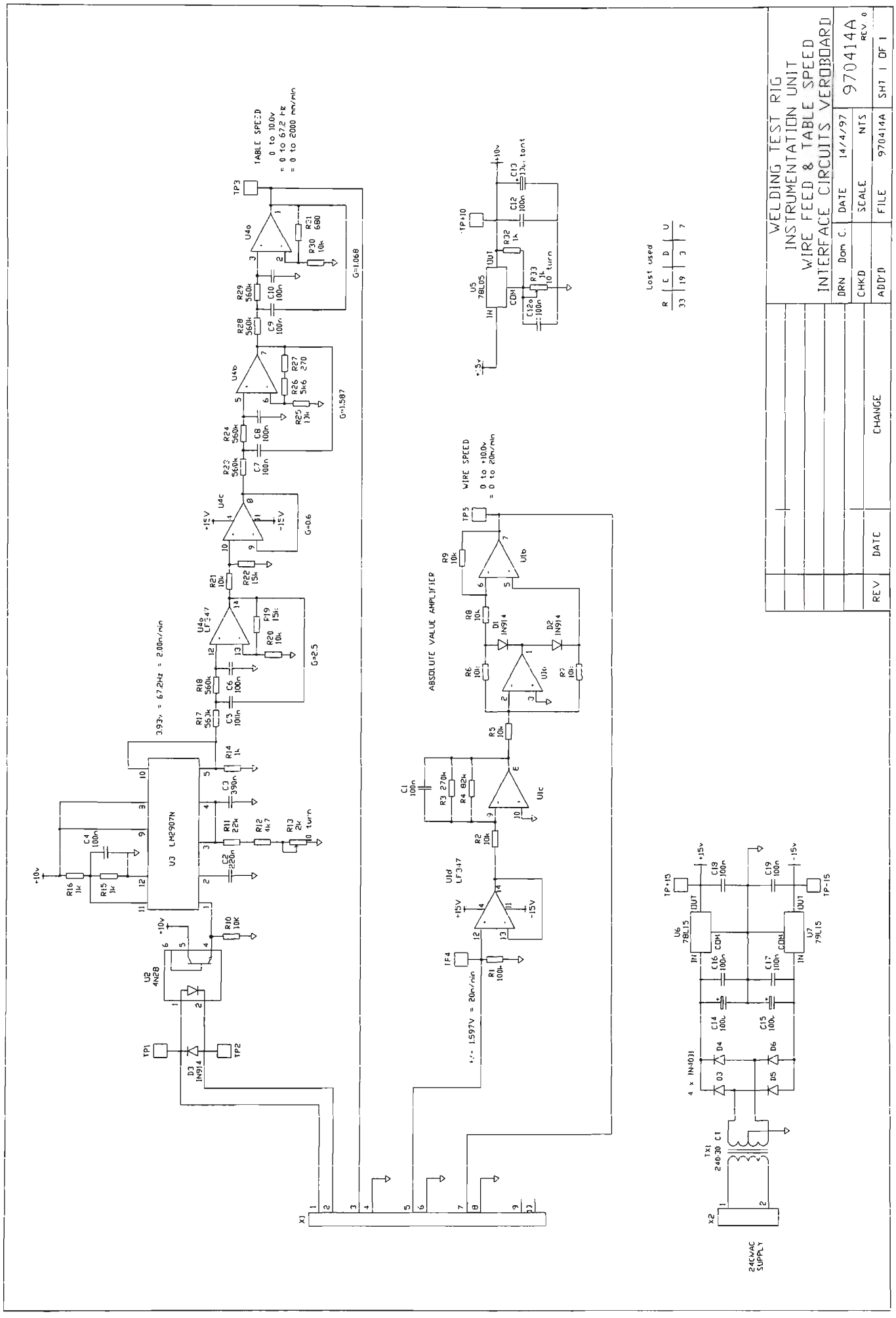

Figure 4.9b Instrumentation unit wire feed & table speed interface schematic

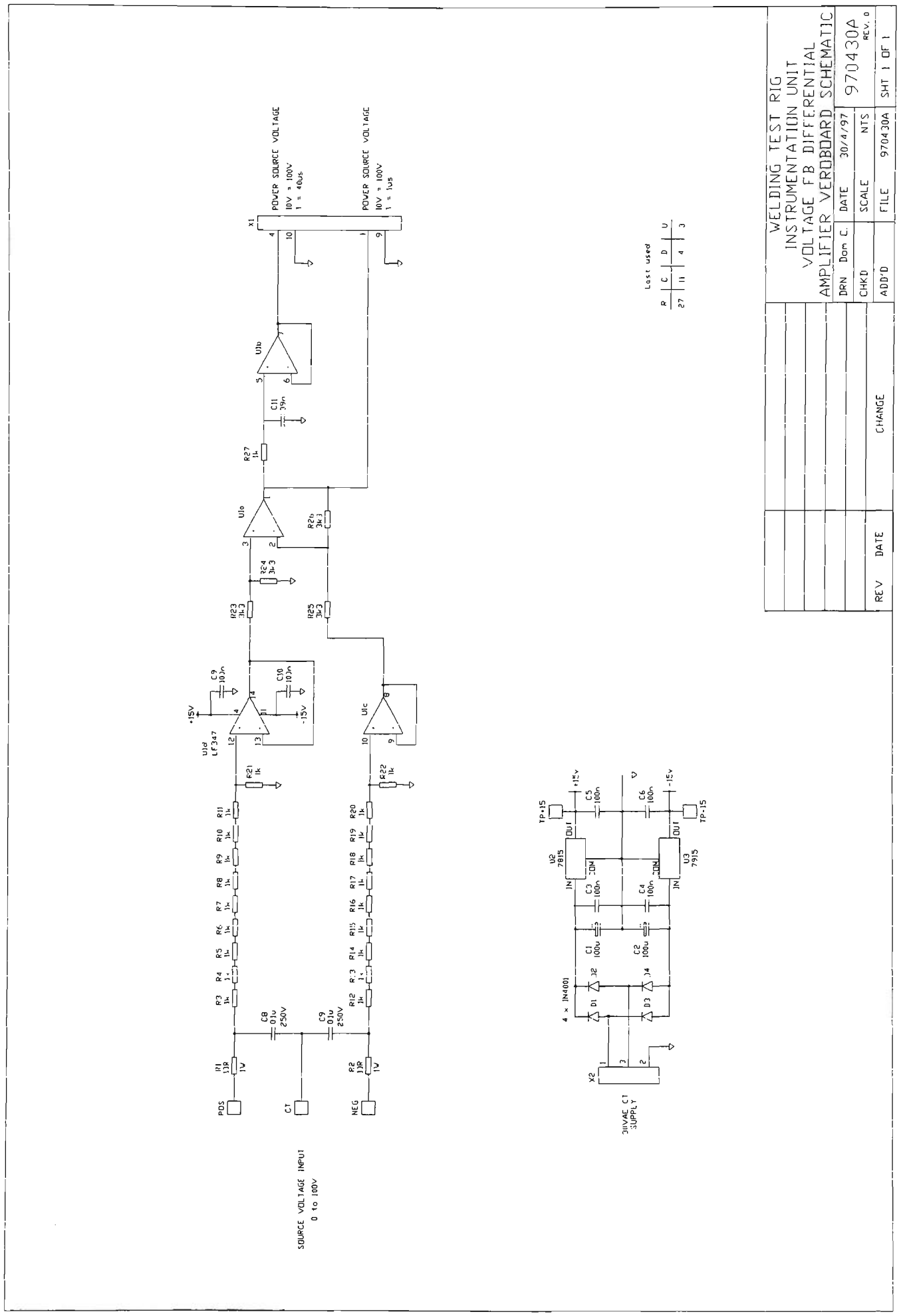

Figure 4.9c Instrumentation unit voltage interface schematic

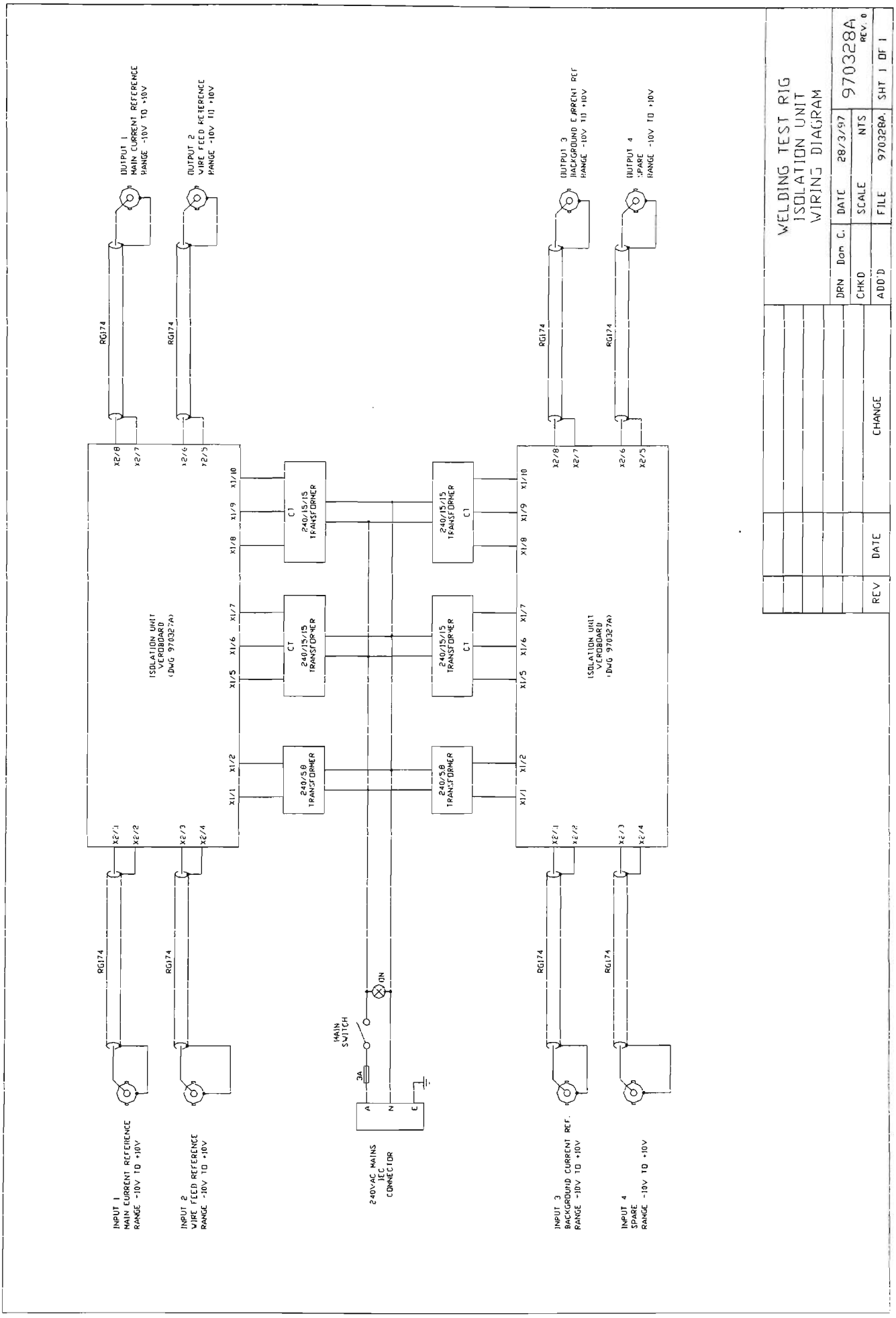

Figure 4.10a Isolation unit main schematic

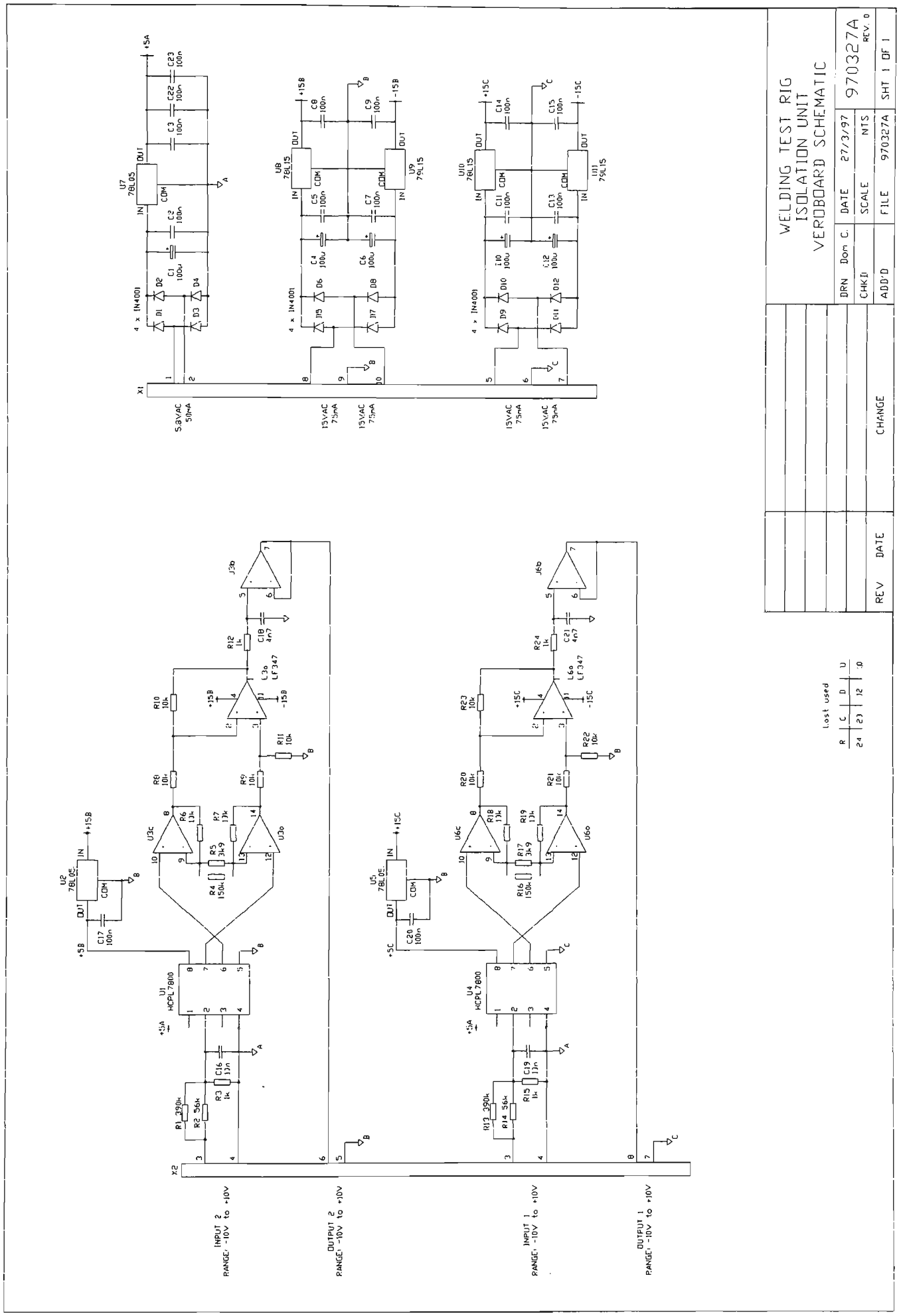

Figure 4.10b Isolation unit veroboard schematic

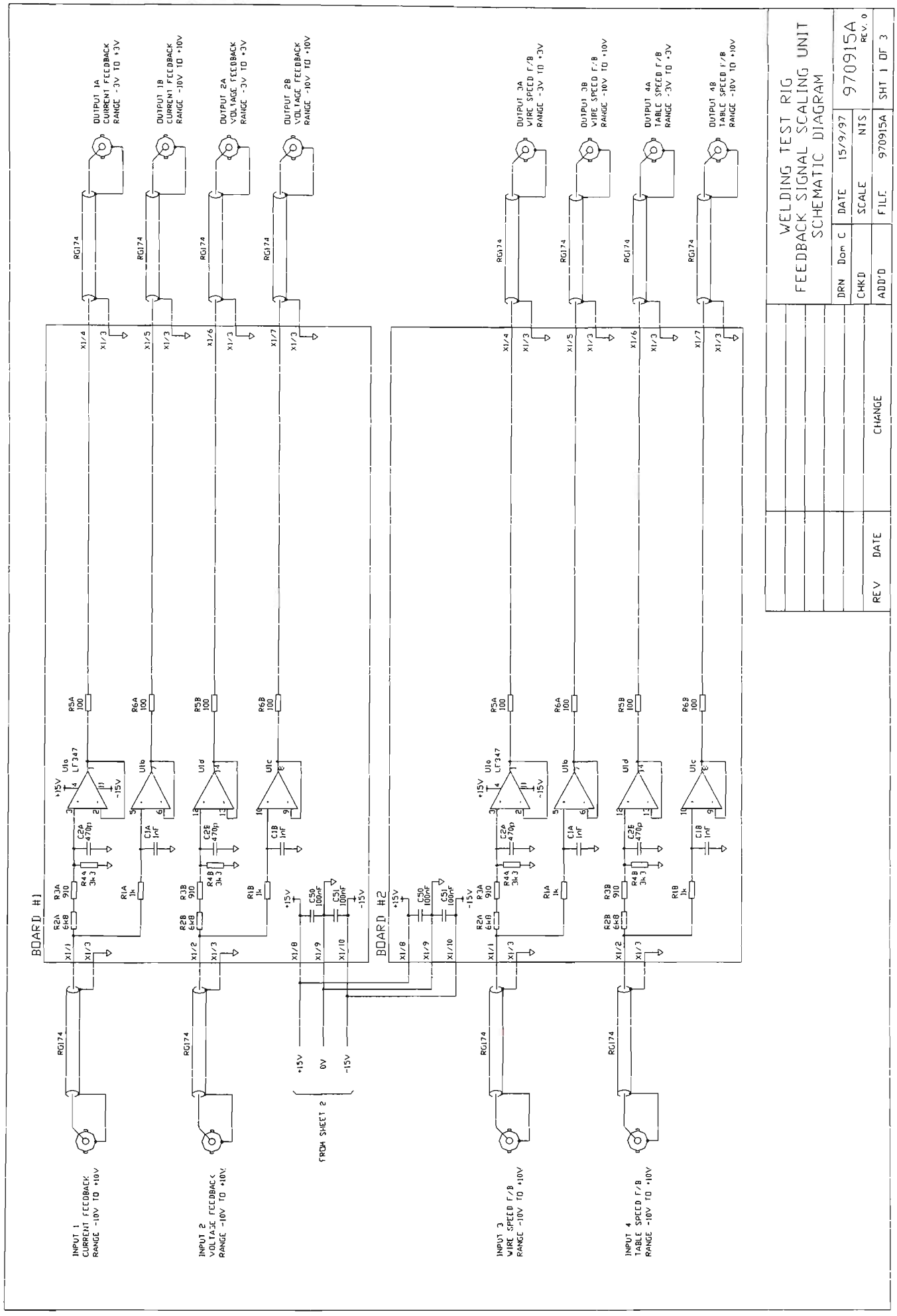

Figure 4.11 Scaling unit schematic

Appendix 5

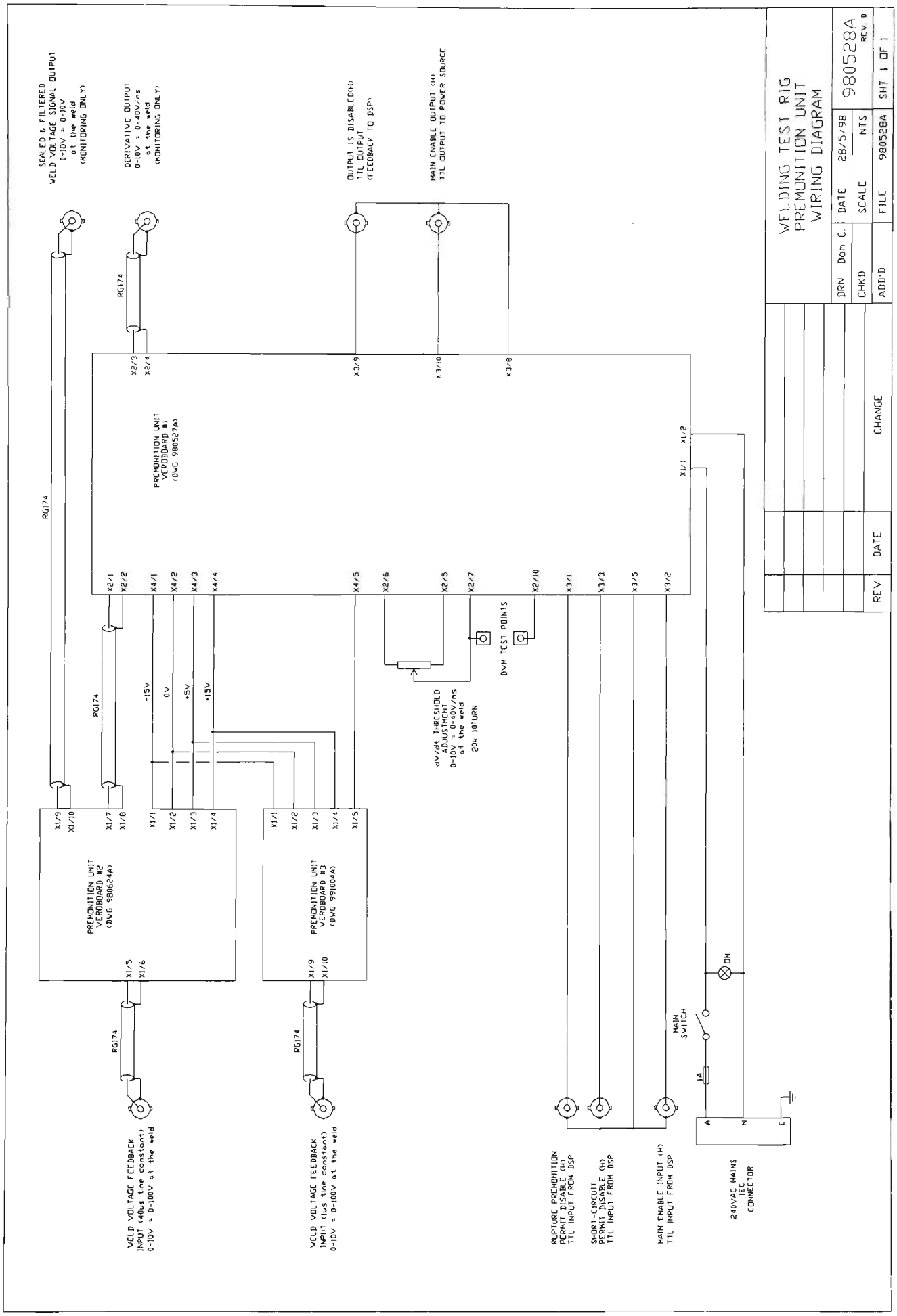

Figure 4.19a Premonition unit main schematic

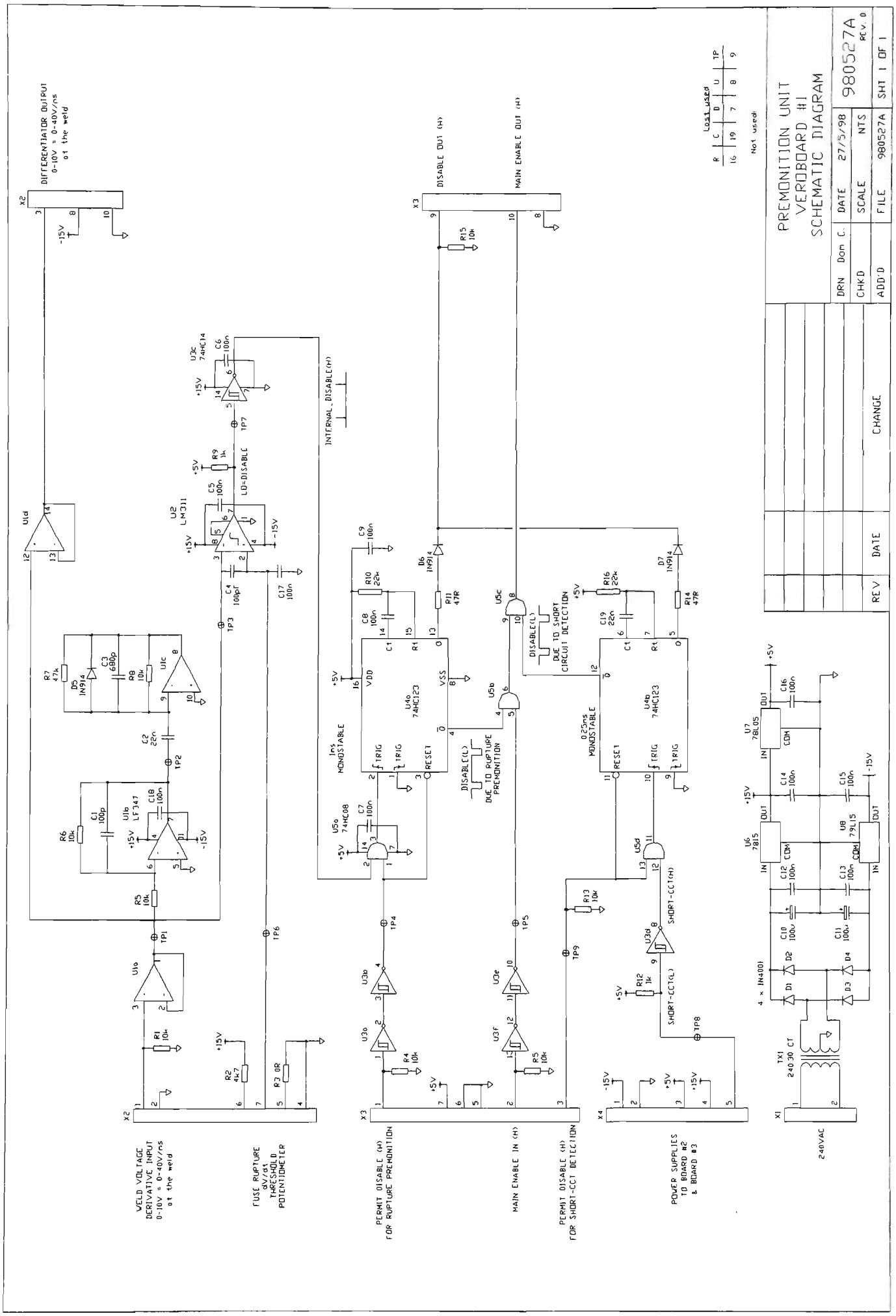

Figure 4.19b Premonition unit board #1 schematic

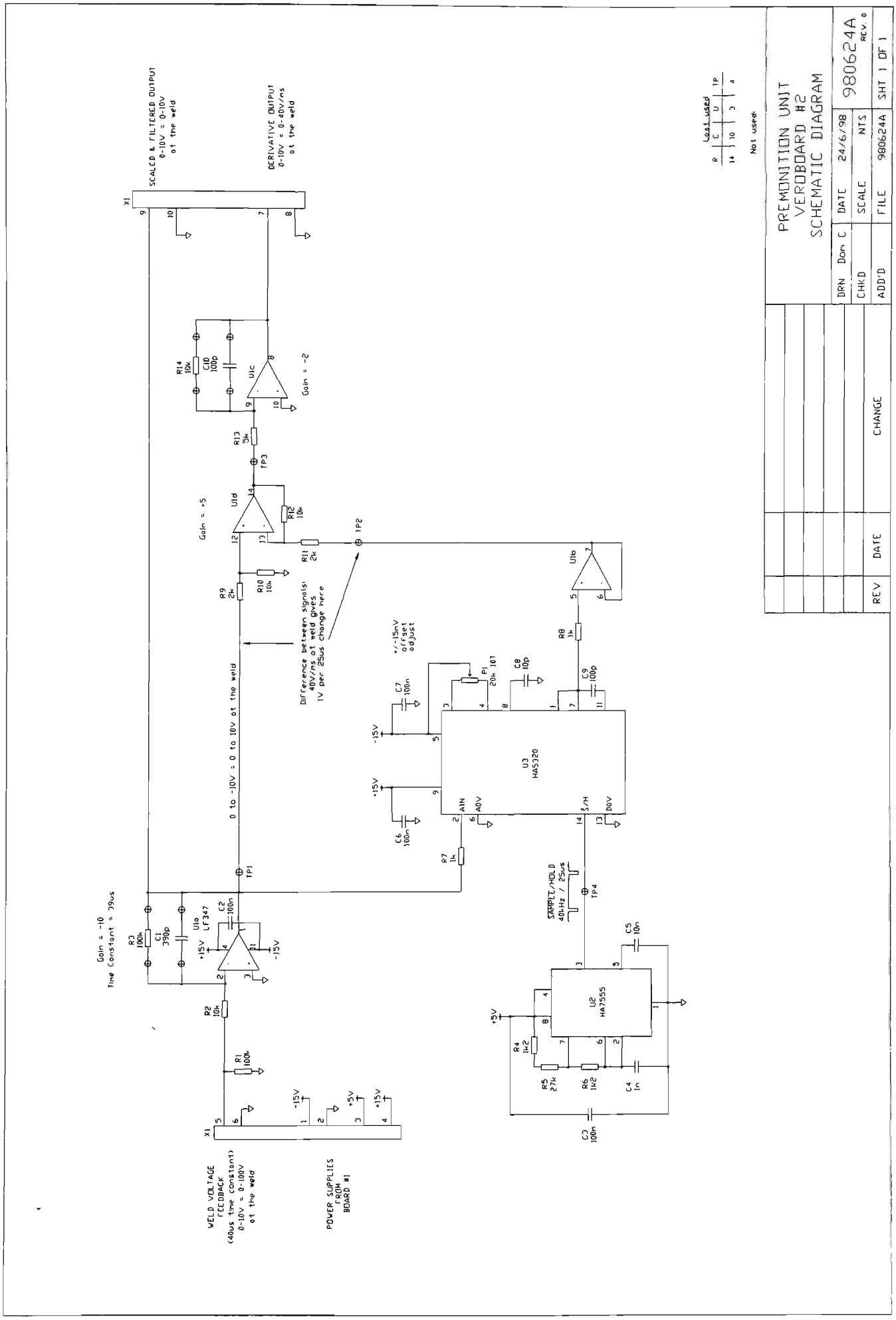

Figure 4.19c Premonition unit board #2 schematic

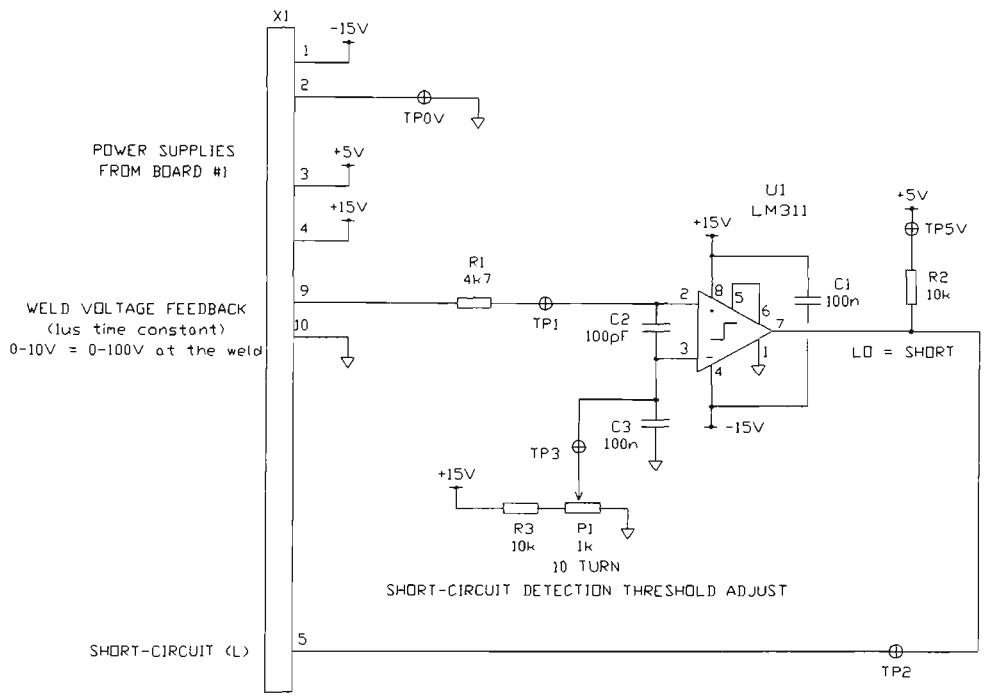

Last used

R	C	D	U	TP
3	3	-	1	2

Not used:

			PREMONITION UNIT VEROBOARD #3 SCHEMATIC DIAGRAM		
			DRN Dom C.	DATE 4/10/99	991004A REV. 0
			CHKD	SCALE NTS	
REV	DATE	CHANGE	ADD'D	FILE 991004A	SHT 1 OF 1

Figure 4.19d Premonition unit board #3 schematic

Appendix 6

This appendix contains Figures relevant to Chapter 6.

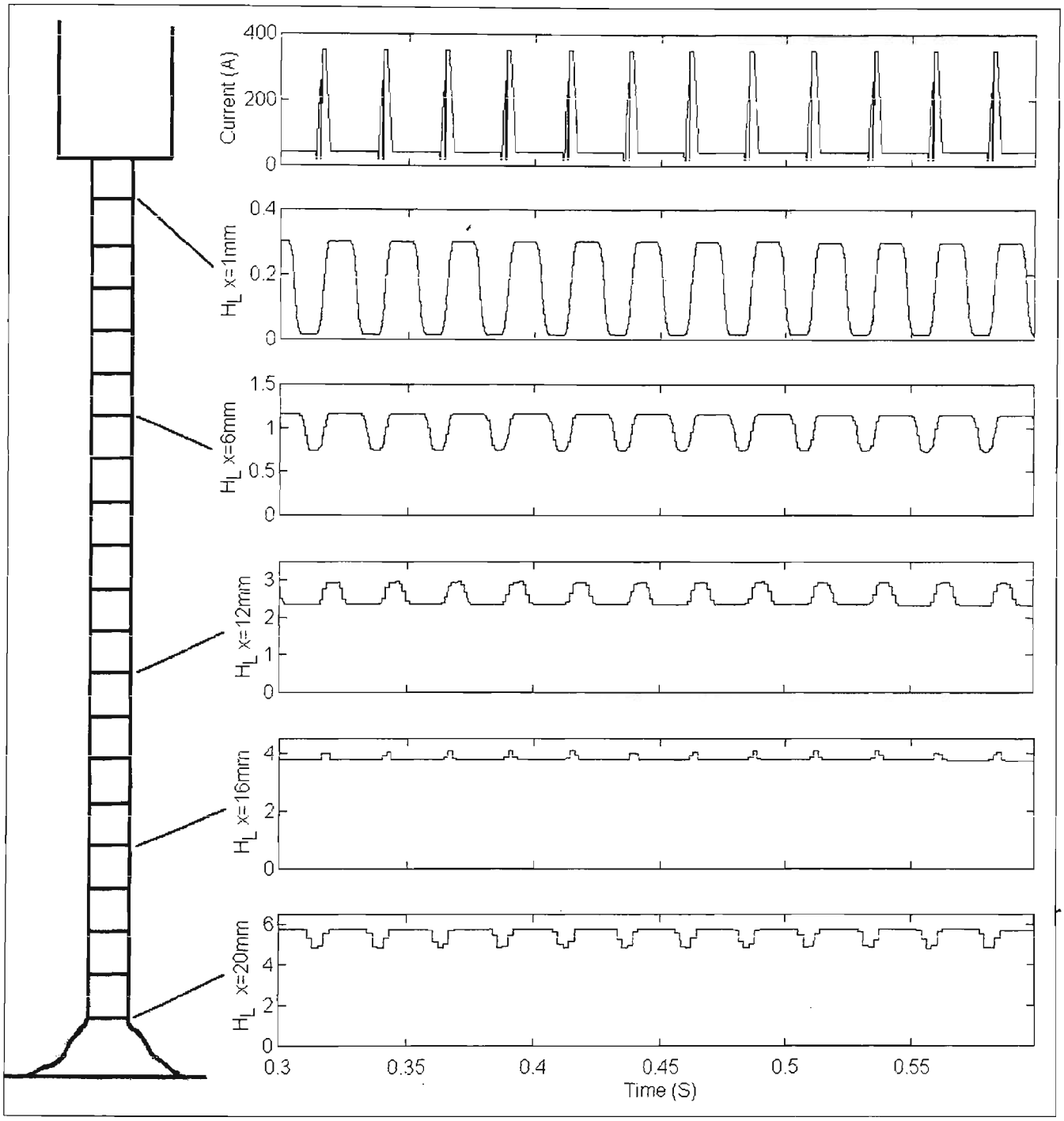

Figure 6.10 $H_L(x,t_x)$ as a function of time t and distance x from contact tip

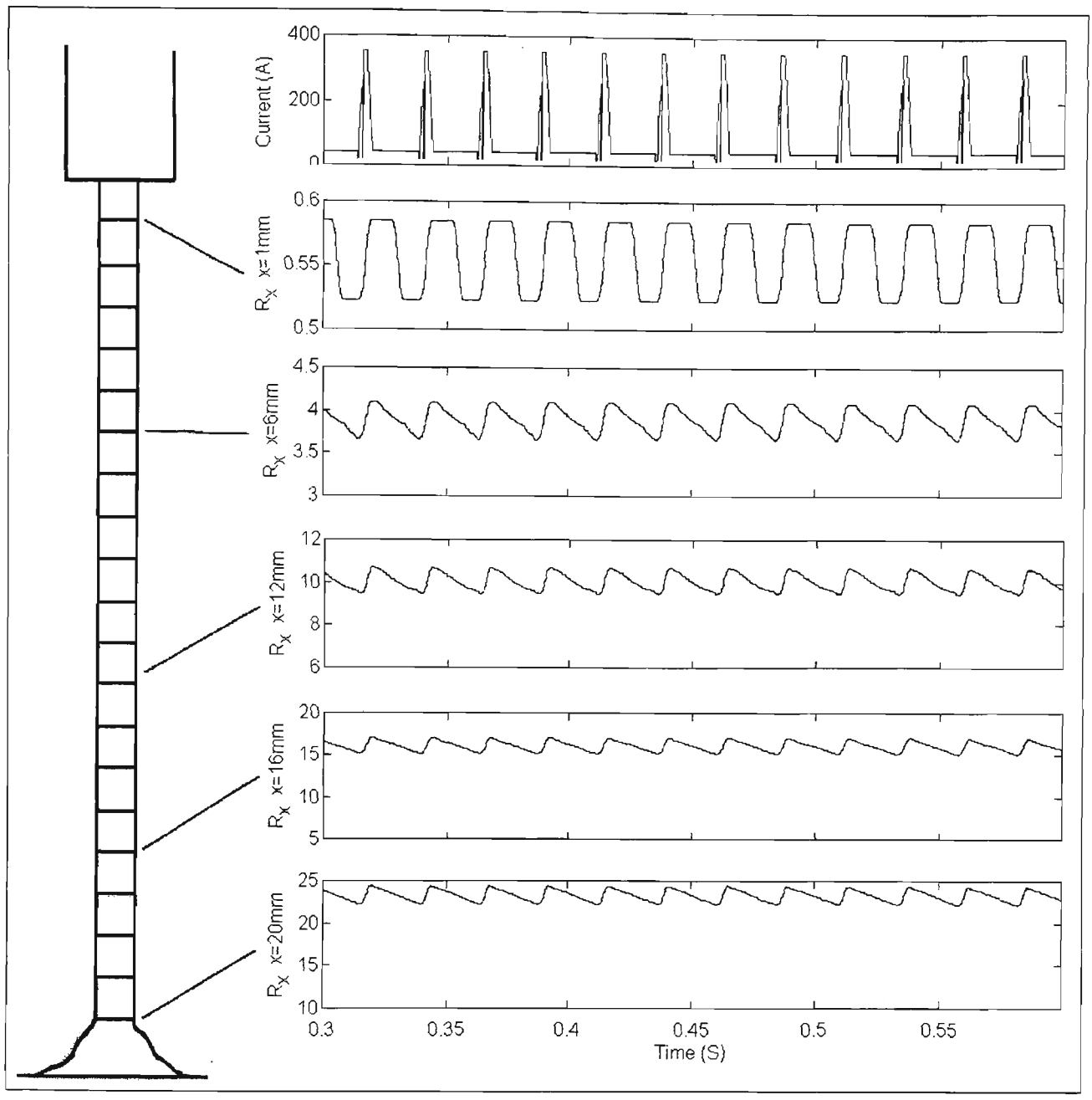

Figure 6.11 R(x,t_x) as a function of time t and distance x from contact tip

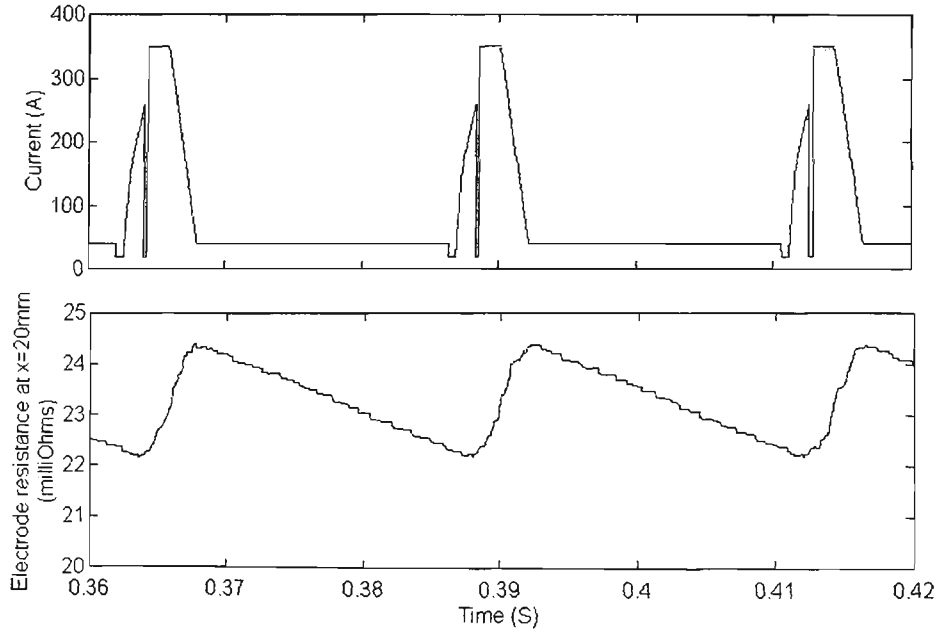

Figure 6.12 Detail of R(x,t_x) at x=20mm

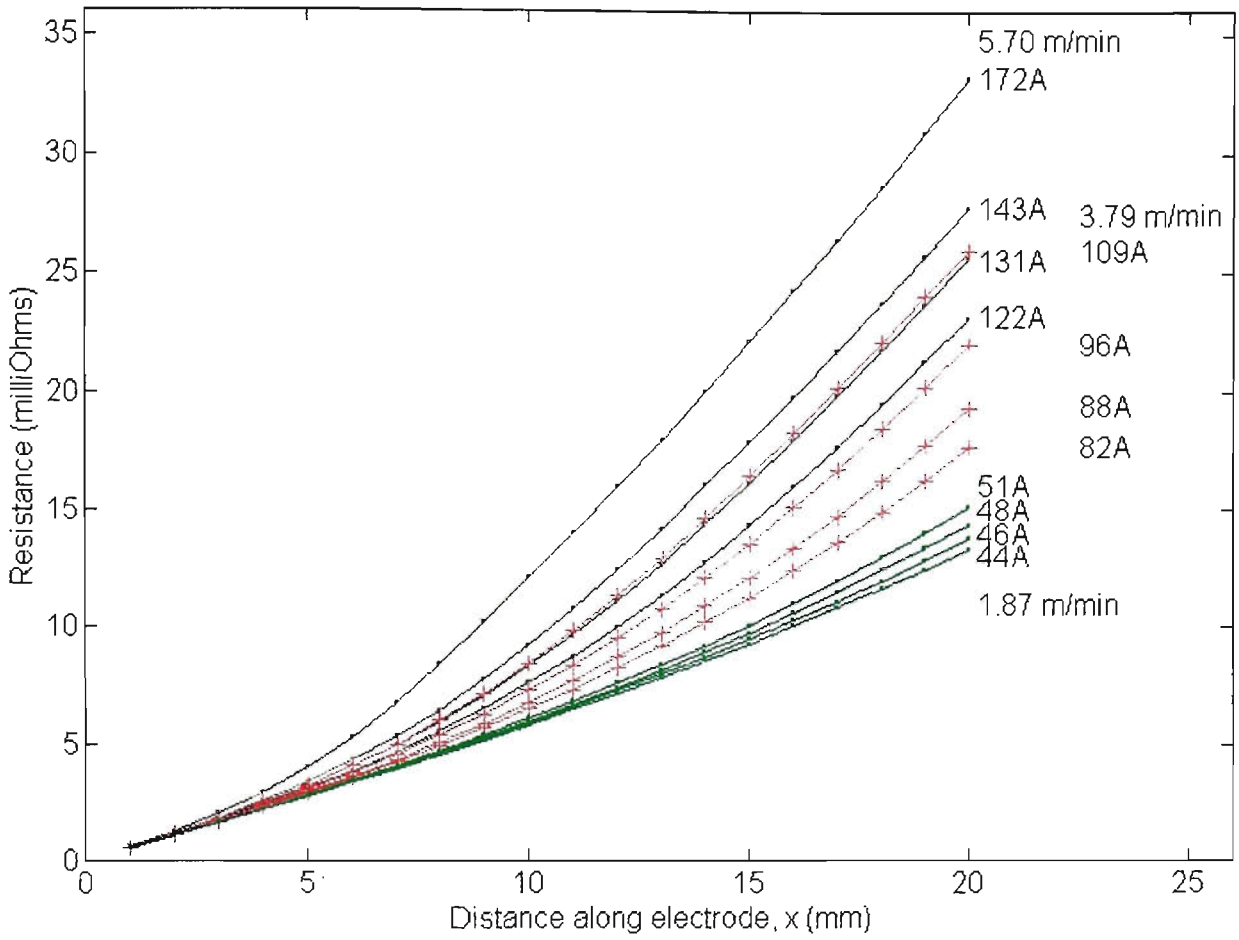

Figure 6.13 Resistance versus length for various RMS currents

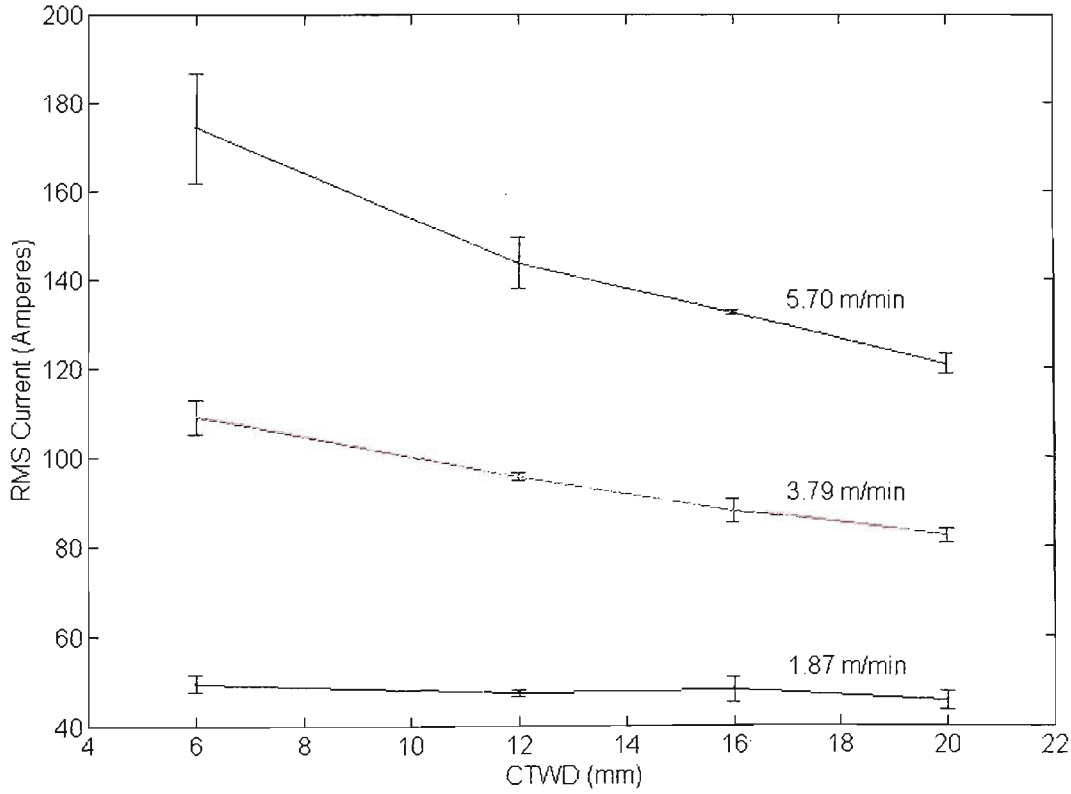

Figure 6.14 RMS current as a function of CTWD and wire feed speed

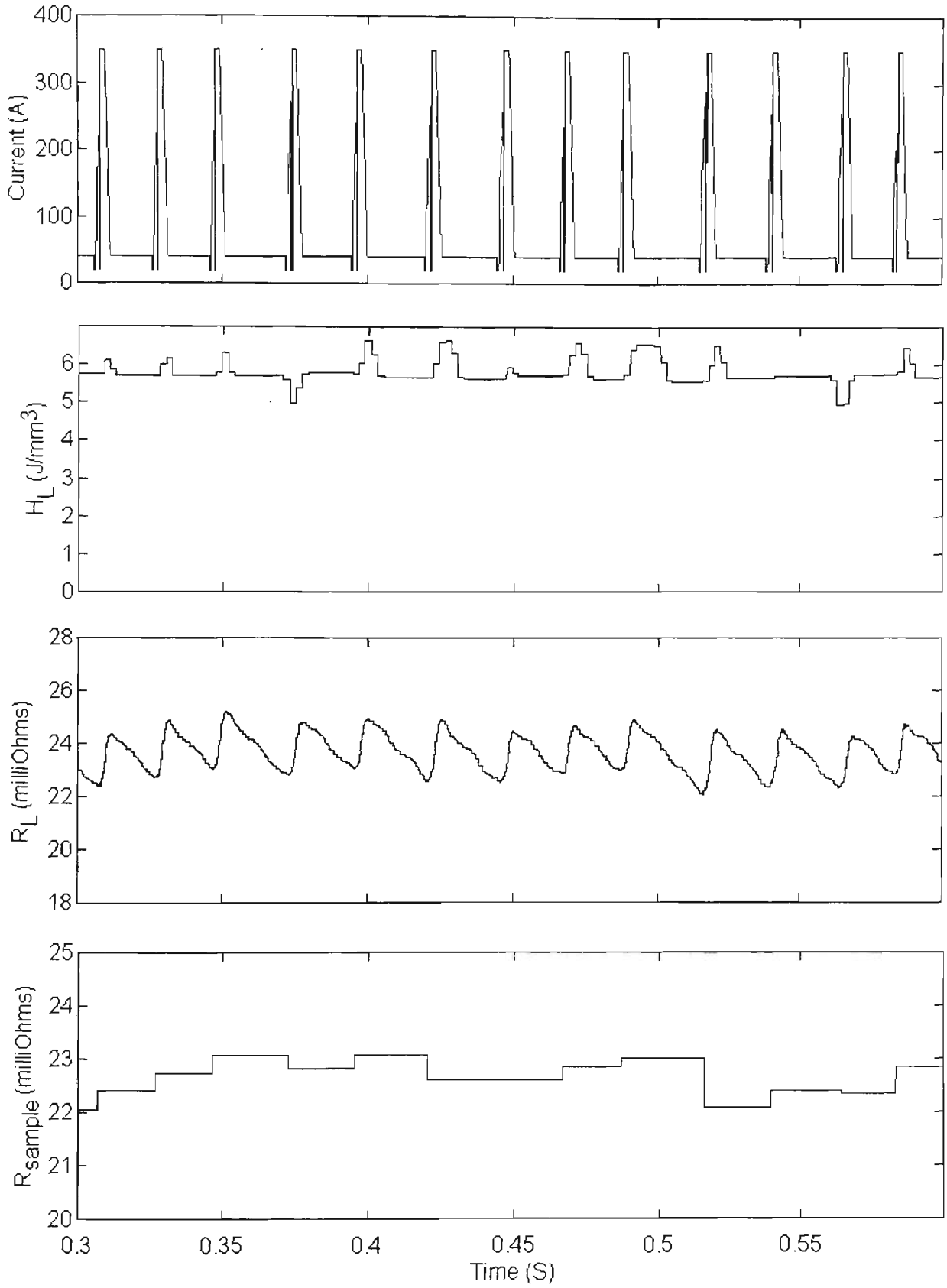

Figure 6.16 Current, H_L, R_L and sampled electrode resistance for variable arcing period duration

Table 6.2 Test Parameters for Ar-23%CO_2 at 5.70 m/min

Test No.	CTWD (mm)	Iarc_max (A)	Tarc_max (ms)	Iarc_min (A)	RMS Current (A)	Average Frequency (Hz)
1	20	350	1.5	75	122.2	45
2	20	350	1.5	40	123.0	54
3	20	350	1.5	95	119.8	18
4	20	350	3.5	75	123.1	19
5	20	275	1.5	75	118.6	59
6	16	350	1.5	75	132.4	56
7	16	350	1.5	40	131.8	62
8	16	350	1.5	105	133.1	29
9	12	350	1.5	75	141.3	68
10	12	350	1.5	40	149.4	75
11	12	350	3.5	75	146.9	35
12	12	275	1.5	75	137.9	88
13	6	350	1.5	75	167.4	92
14	6	350	1.5	40	186.8	79
15	6	350	1.5	100	161.7	84
Fixed parameters						
T_wetting (ms)	**Isc_max (A)**	**Isc_ramp (A/ms)**	**Iarc_ramp (A/ms)**	**T_rupture (ms)**	**Travel speed (mm/min)**	**Workpiece Thickness (mm)**
0.5	400	100	150	1.0	390	6

Table 6.3 Test Parameters for CO_2 at 5.70 m/min

Test No.	CTWD (mm)	Iarc_max (A)	Tarc_max (ms)	Iarc_min (A)	RMS Current (A)	Average Frequency (Hz)
1	20	350	1.5	30	119.0	52
2	20	350	2.5	50	115.1	45
3	20	350	2.5	75	113.8	33
4	20	350	2.5	45	117.8	33
5	20	350	2.5	60	117.3	32
6	20	350	2.5	30	122.8	28
7	16	350	1.5	30	127.8	59
8	16	350	3.5	30	130.3	33
9	16	350	1.5	60	127.5	52
10	12	350	1.5	75	136.5	56
11	12	350	1.5	50	141.9	65
12	12	350	1.5	100	138.0	49
13	6	350	1.5	90	171.8	70
14	6	350	1.5	75	182.7	70
Fixed parameters						
T_wetting (ms)	**Isc_max (A)**	**Isc_ramp (A/ms)**	**Iarc_ramp (A/ms)**	**T_rupture (ms)**	**Travel speed (mm/min)**	**Workpiece Thickness (mm)**
1.5	400	100	150	1.0	390	6

Table 6.4 Test Parameters for Ar-23%CO_2 at 3.79 m/min

Test No.	CTWD (mm)	Iarc_max (A)	Tarc_max (ms)	Iarc_min (A)	RMS Current (A)	Average Frequency (Hz)
1	6	200	1.5	50	105.3	83
2	6	250	1.5	70	110.0	45
3	6	225	1.5	60	107.4	63
4	6	225	1.5	30	113.0	79
5	12	200	1.5	50	95.0	65
6	12	250	1.5	70	96.4	20
7	12	225	1.5	40	96.1	60
8	12	175	1.5	40	94.6	87
9	16	175	1.5	40	86.2	76
10	16	200	1.5	60	89.4	38
11	16	150	1.5	40	85.1	88
12	16	175	1.5	60	90.4	59
13	20	175	1.5	40	82.0	67
14	20	150	1.5	40	80.6	81
15	20	175	1.5	60	84.0	29
16	20	150	1.5	60	83.5	56
Fixed parameters						
T_wetting (ms)	Isc_max (A)	Isc_ramp (A/ms)	Iarc_ramp (A/ms)	T_rupture (ms)	Travel speed (mm/min)	Workpiece Thickness (mm)
0.5	400	100	150	1.0	390	5

Table 6.5 Test Parameters for Ar-23%CO_2 at 1.87 m/min

Test No.	CTWD (mm)	Iarc_max (A)	Tarc_max (ms)	Iarc_min (A)	RMS Current (A)	Average Frequency (Hz)
1	6	125	1.5	30	51.5	35
2	6	100	1.5	30	49.6	44
3	6	75	1.5	30	47.6	56
4	12	75	1.5	25	47.8	61
5	12	90	1.5	27	46.8	47
6	12	105	1.5	28	48.1	38
7	16	75	1.5	20	50.8	50
8	16	85	1.5	20	49.0	55
9	16	85	1.5	25	45.1	47
10	20	75	1.5	25	43.4	46
11	20	100	1.5	25	45.1	30
12	20	75	1.5	20	47.5	65
Fixed parameters						
T_wetting (ms)	Isc_max (A)	Isc_ramp (A/ms)	Iarc_ramp (A/ms)	T_rupture (ms)	Travel speed (mm/min)	Workpiece Thickness (mm)
0.5	400	100	150	1.0	390	2

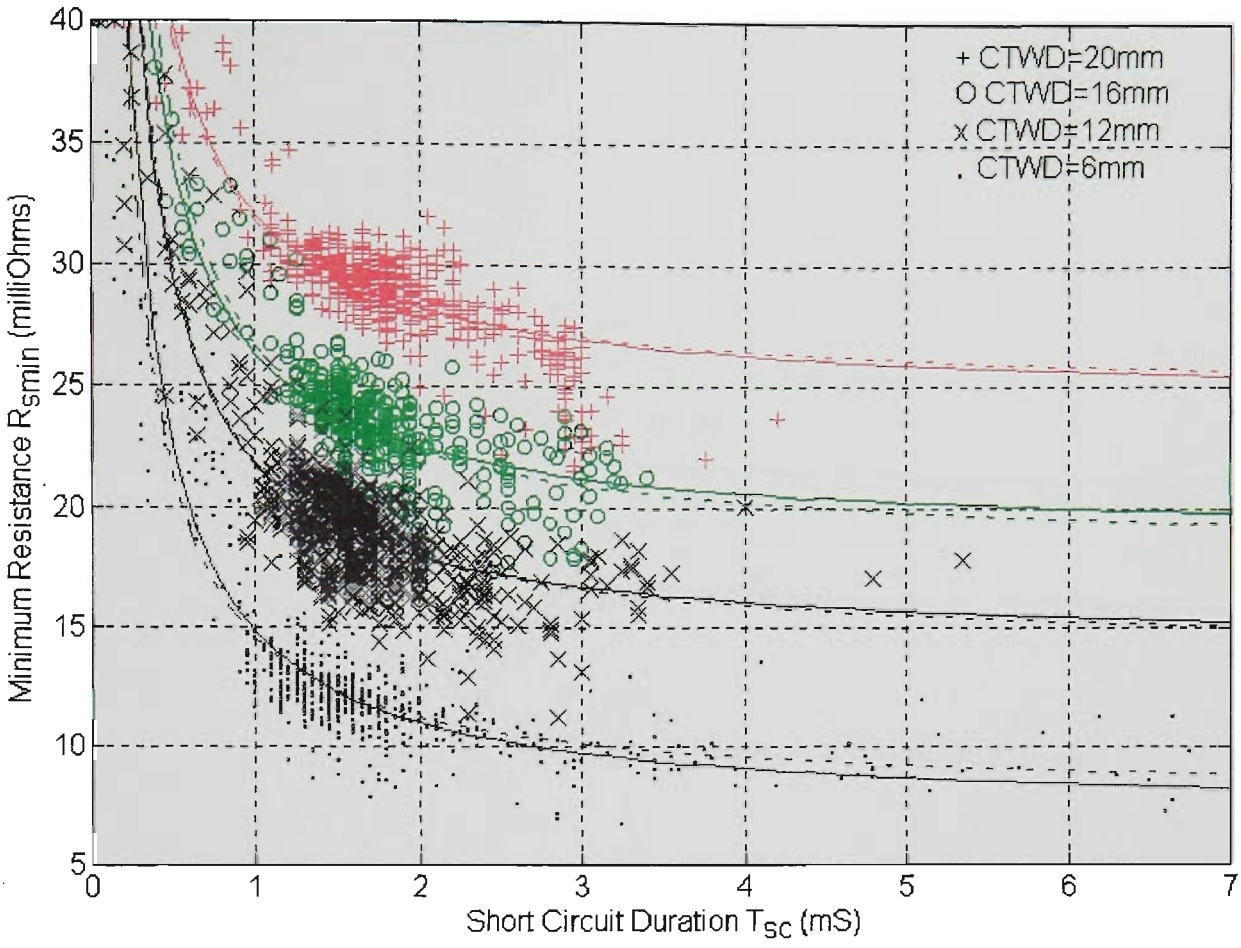

Figure 6.19 R_{smin} vs T_{sc} for Ar-23%CO_2 at 5.70 m/min

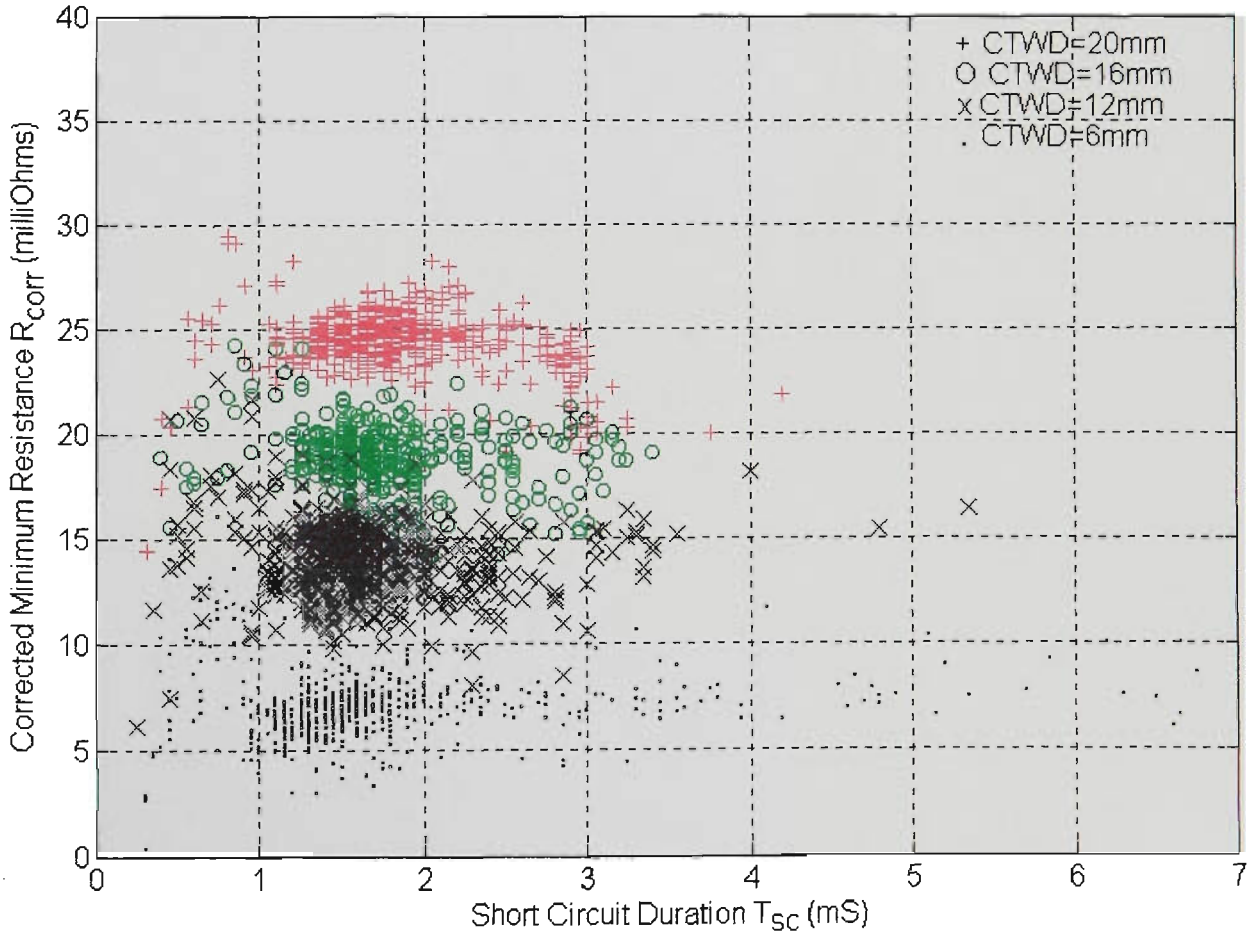

Figure 6.20 R_{corr} vs T_{sc} for Ar-23%CO_2 at 5.70 m/min

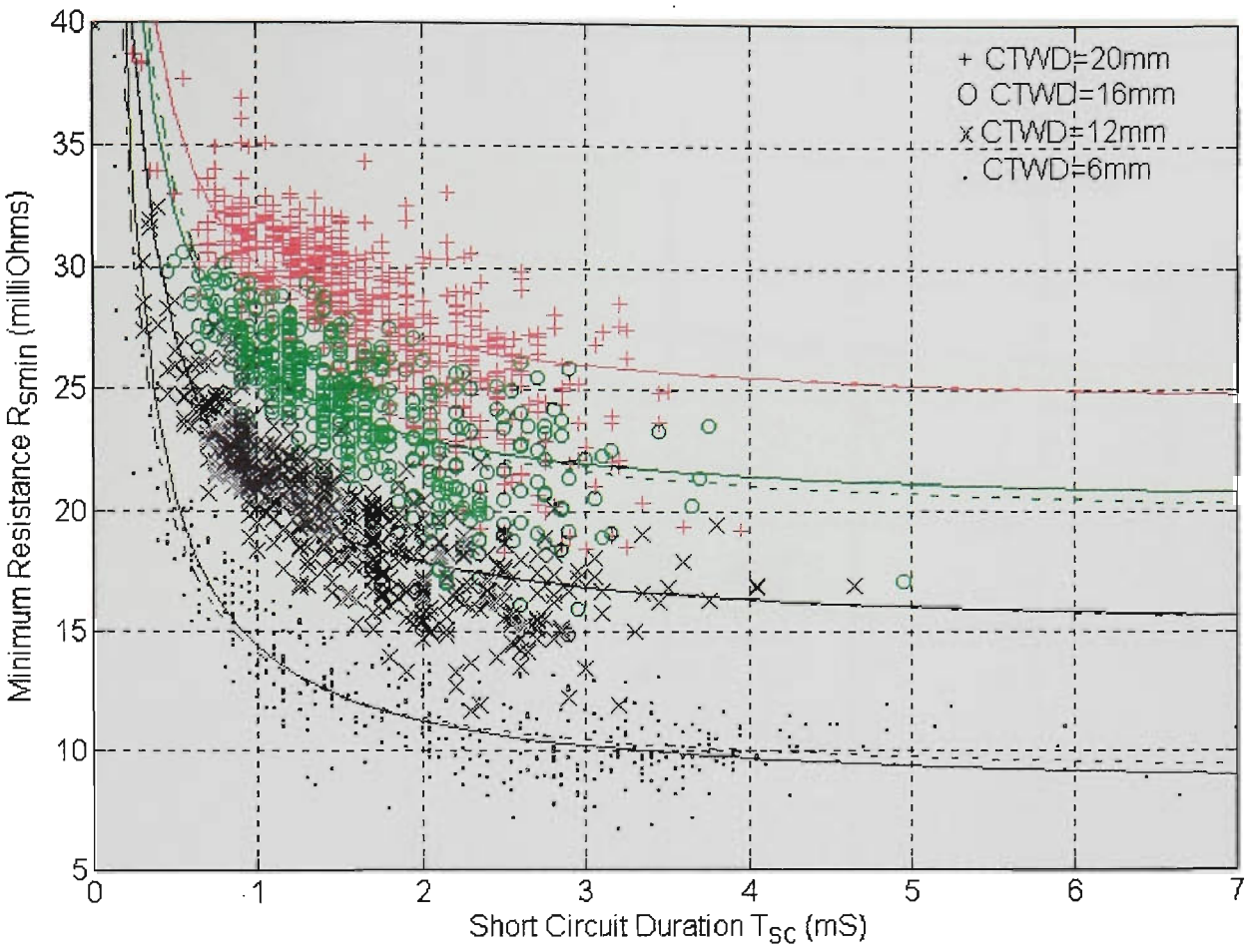

Figure 6.21 R_{smin} vs T_{sc} for CO_2 at 5.70 m/min

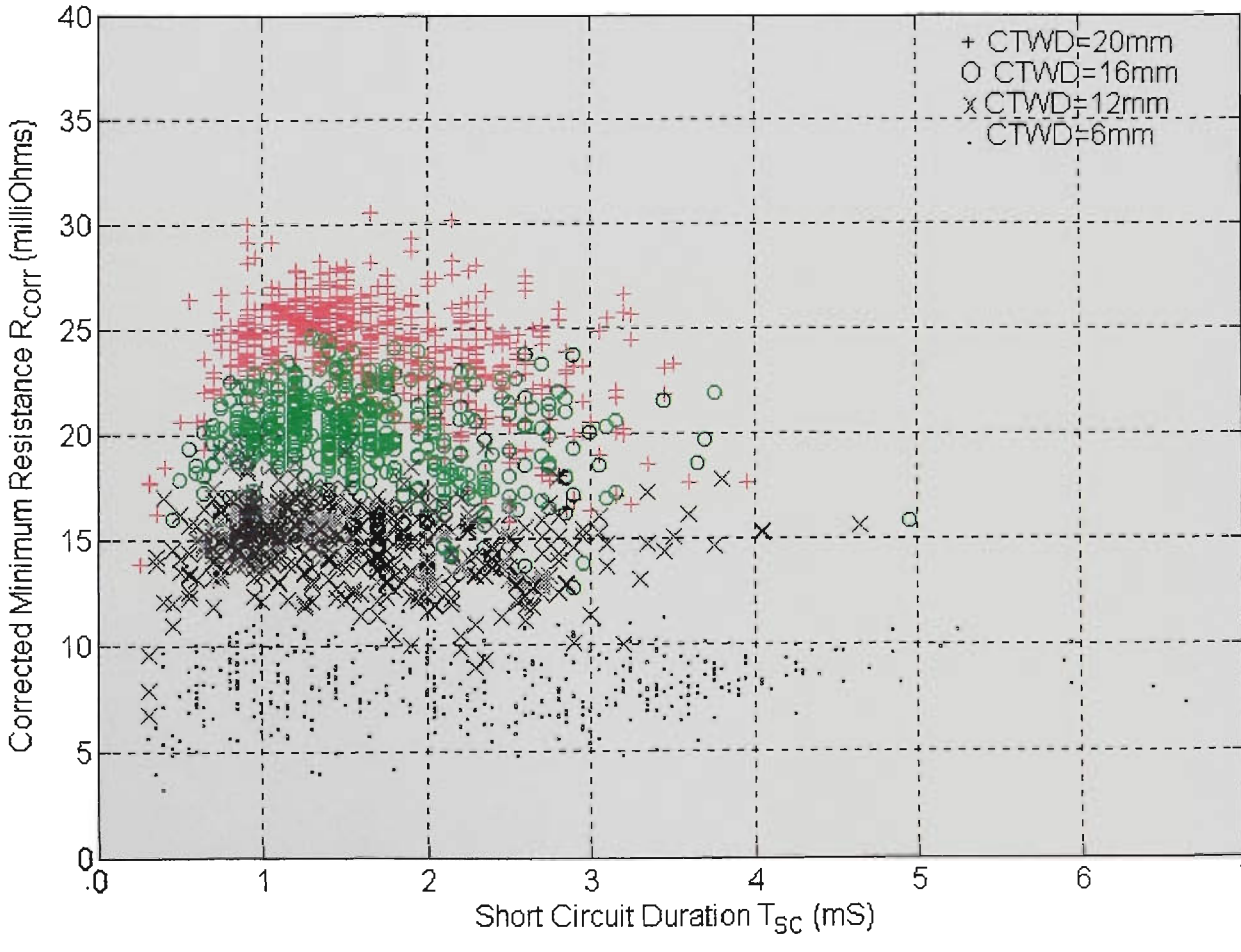

Figure 6.22 R_{corr} vs T_{sc} for CO_2 at 5.70 m/min

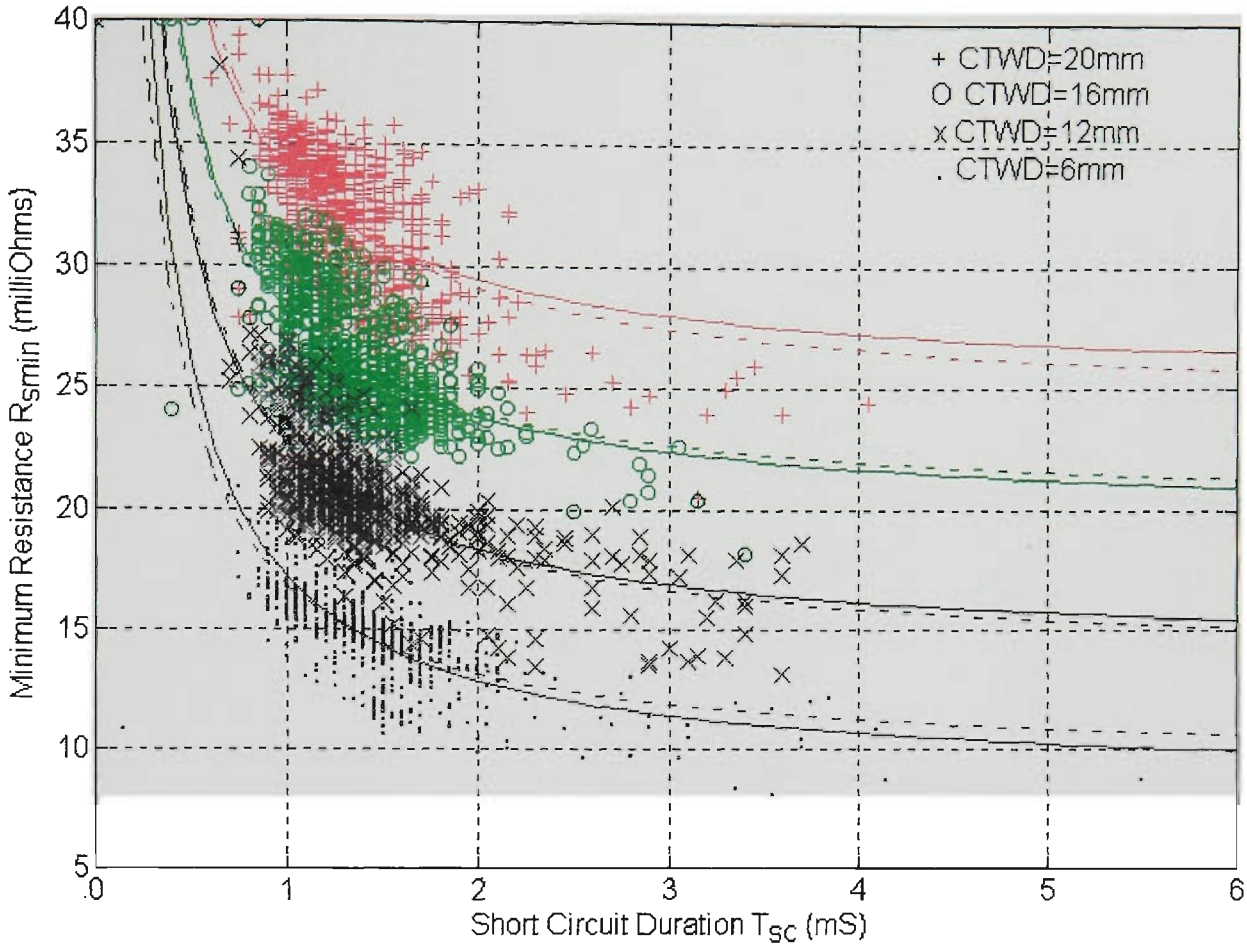

Figure 6.23 R_{smin} vs T_{sc} for Ar-23%CO_2 at 3.79 m/min

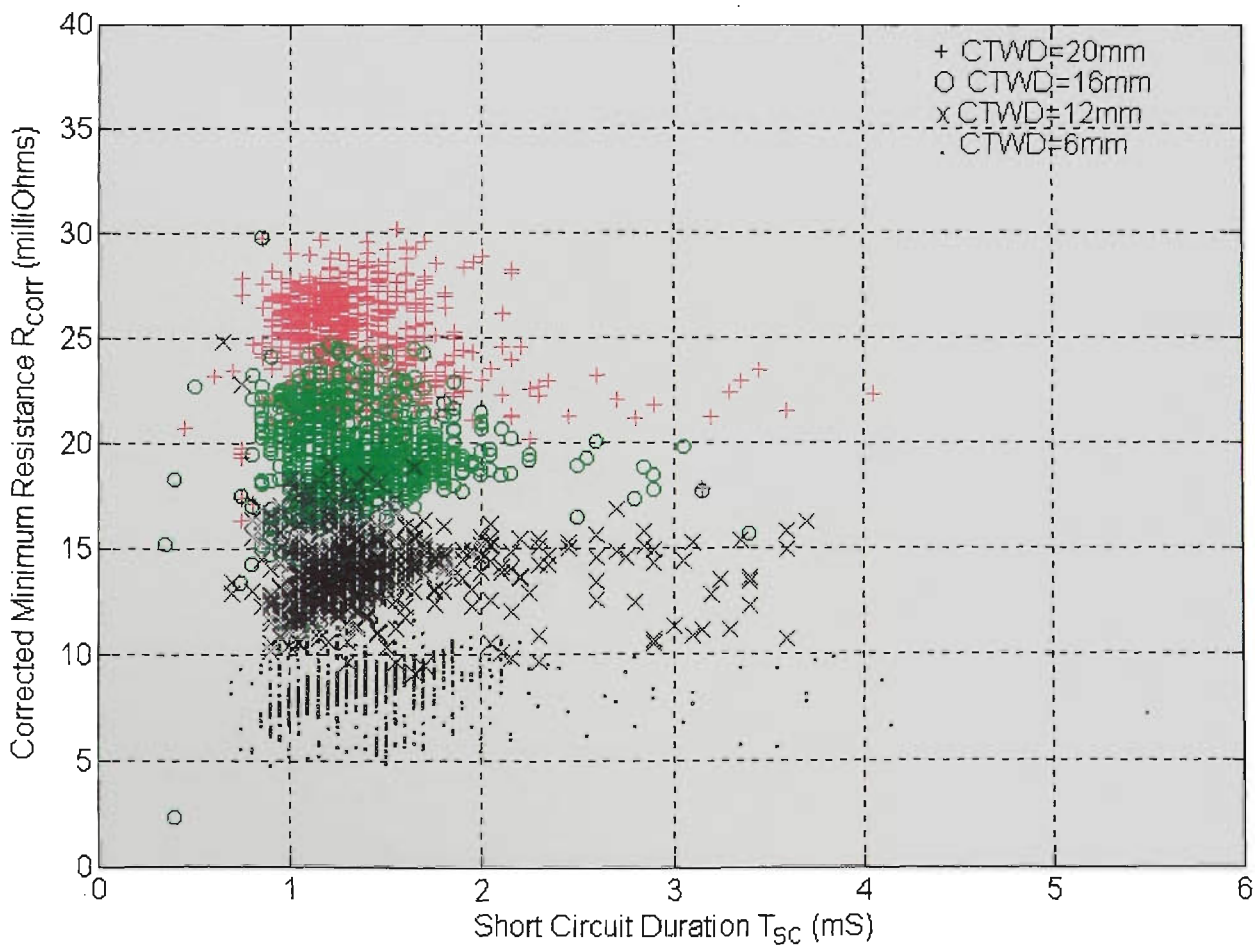

Figure 6.24 R_{corr} vs T_{sc} for Ar-23%CO_2 at 3.79 m/min

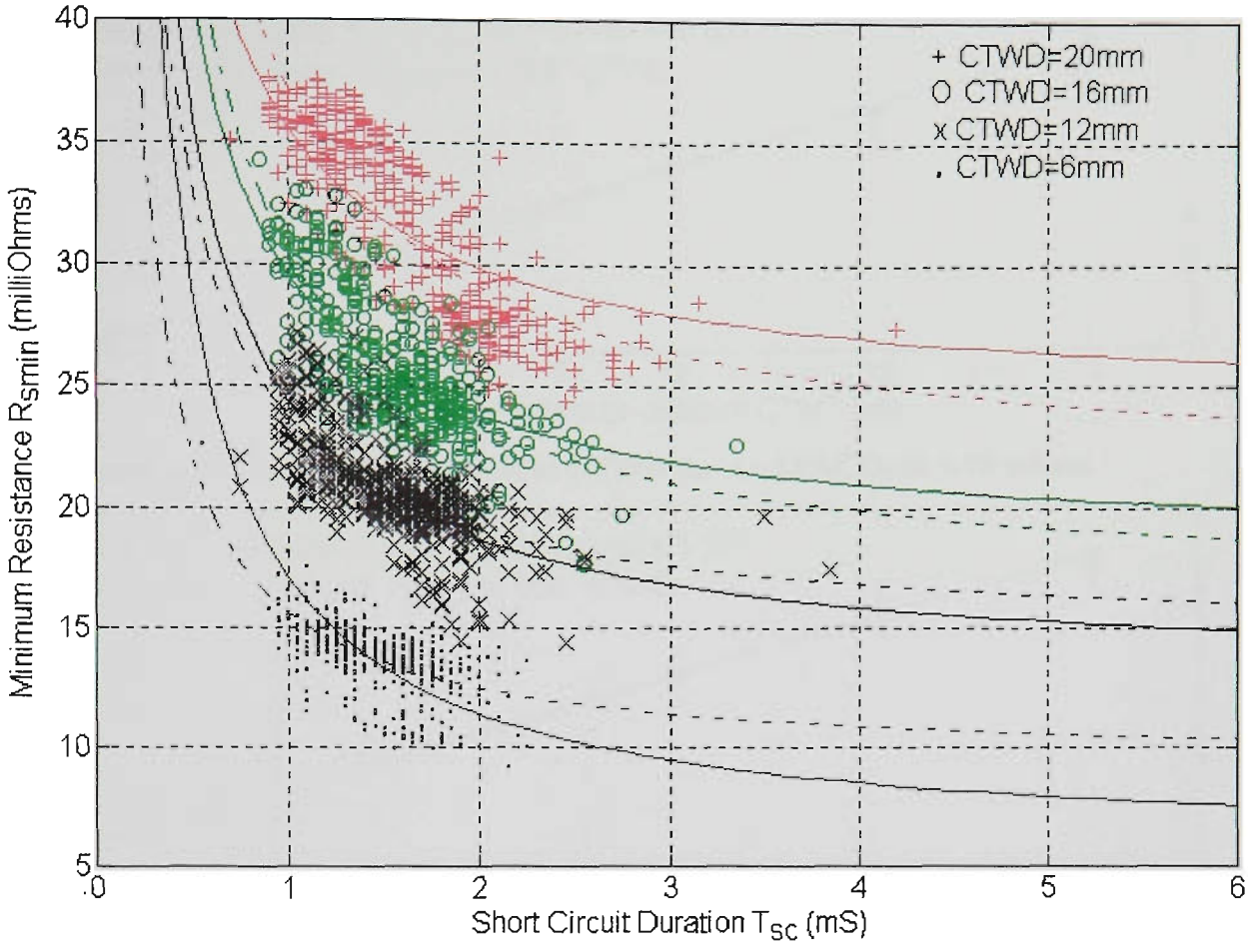

Figure 6.25 R_{smin} vs T_{sc} for Ar-23%CO_2 at 1.87 m/min

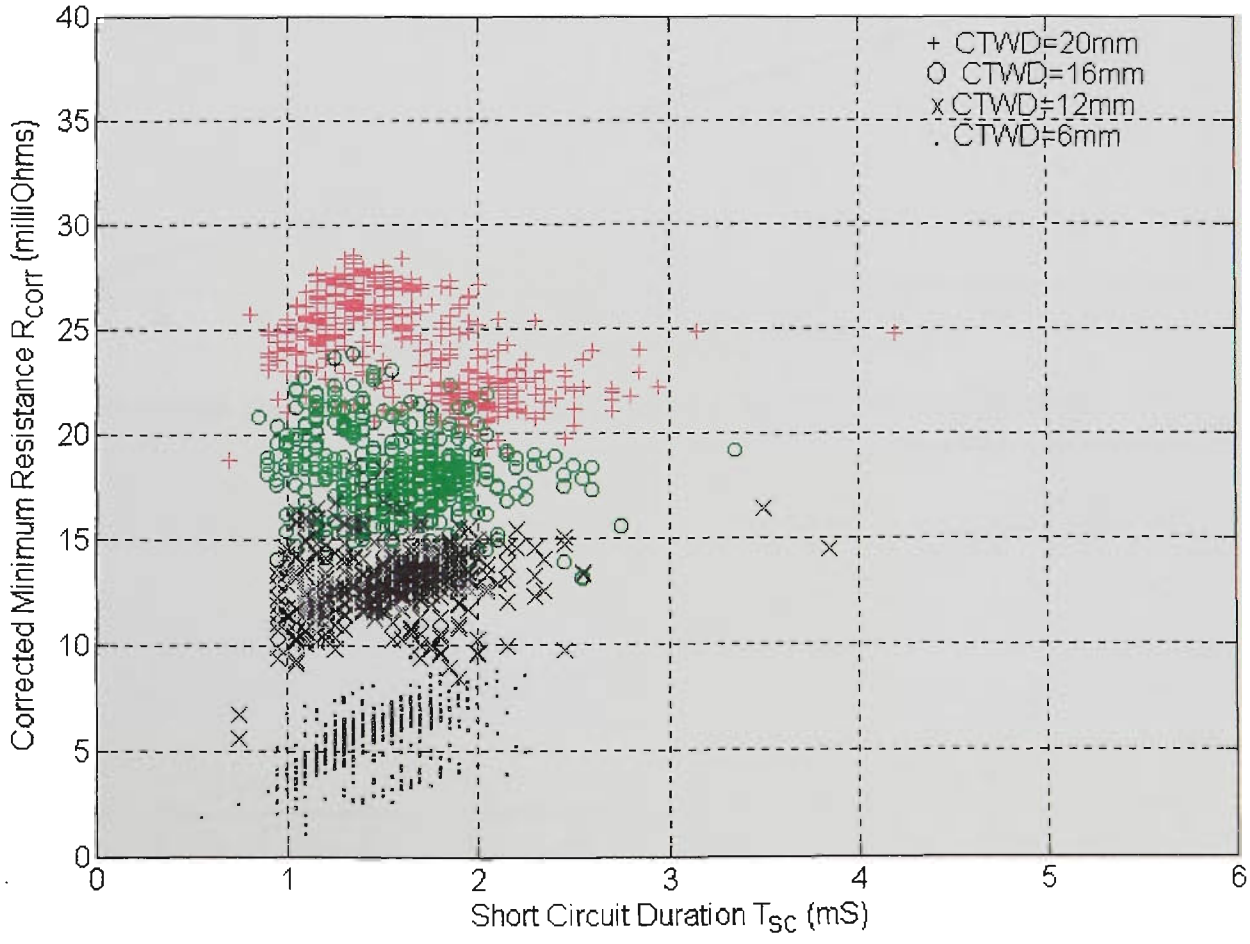

Figure 6.26 R_{corr} vs T_{sc} for Ar-23%CO_2 at 1.87 m/min

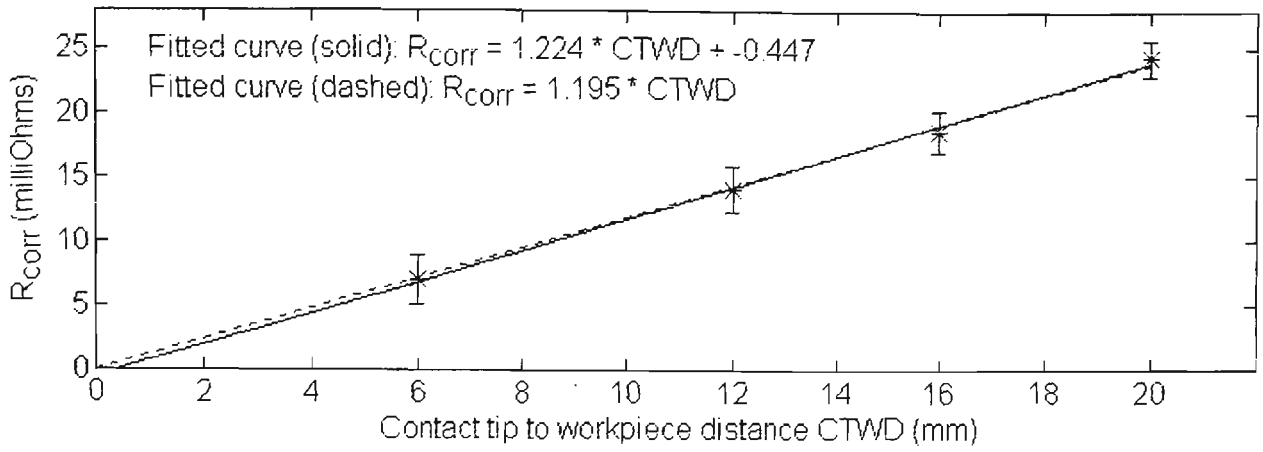

Figure 6.27 Corrected resistance vs CTWD for Ar-23%CO_2 at 5.70 m/min

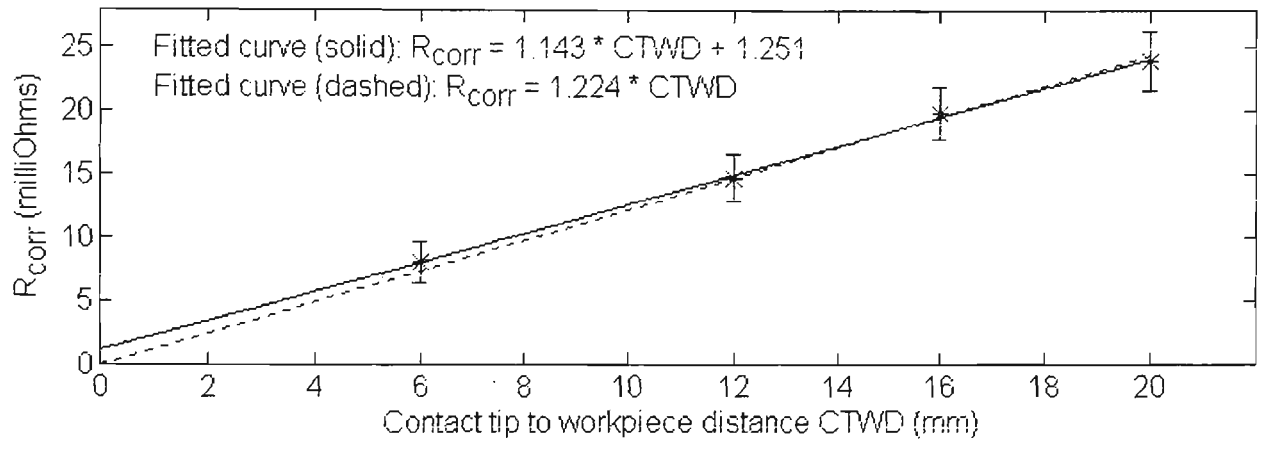

Figure 6.28 Corrected resistance vs CTWD for CO_2 at 5.70 m/min

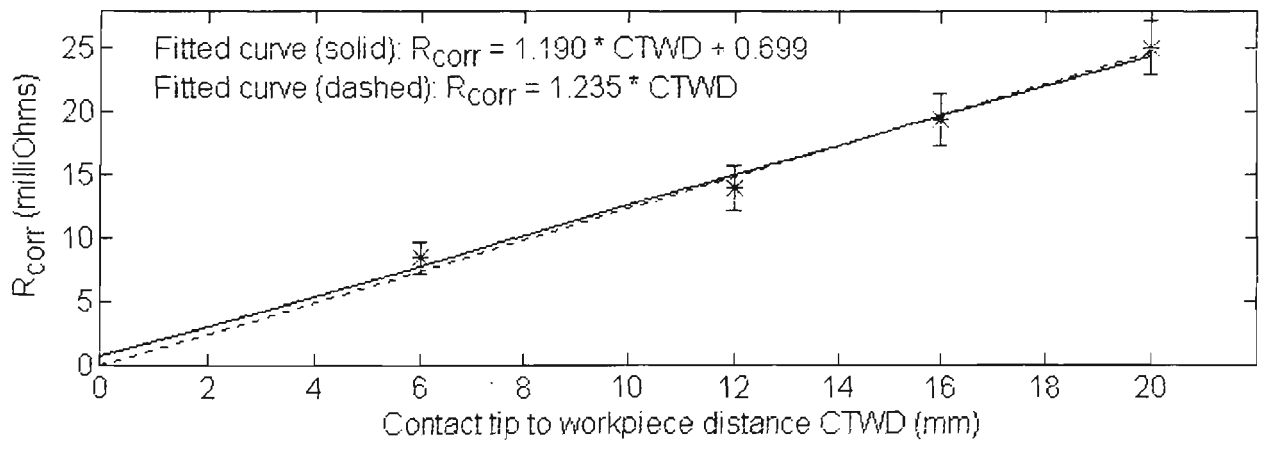

Figure 6.29 Corrected resistance vs CTWD for Ar-23%CO_2 at 3.79 m/min

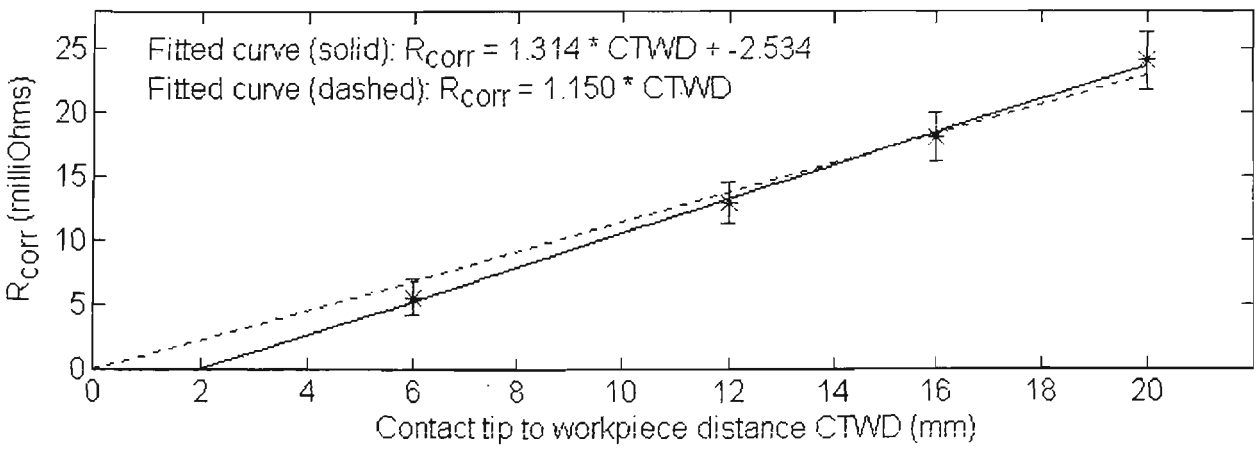

Figure 6.30 Corrected resistance vs CTWD for Ar-23%CO_2 at 1.87 m/min

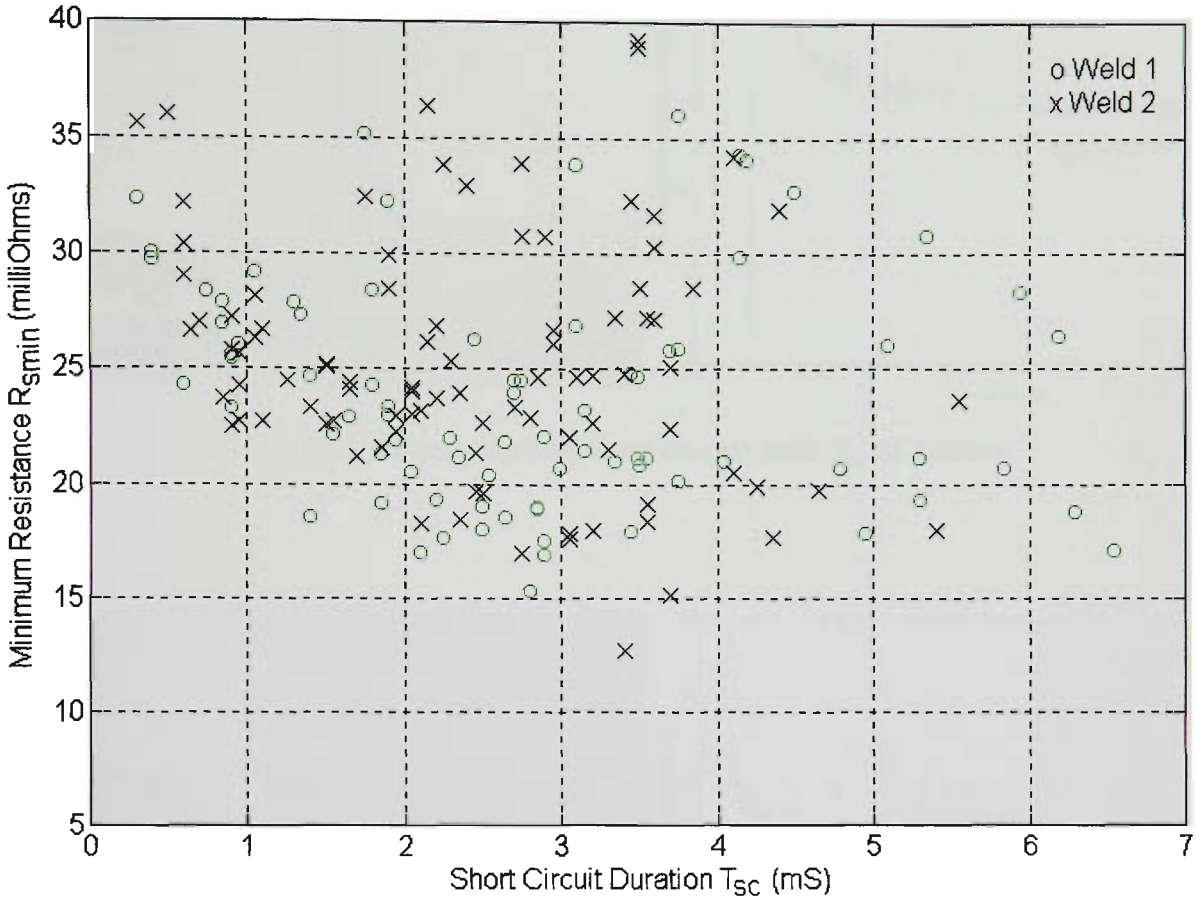

Figure 6.31 R_{smin} vs T_{sc} for unstable welds (Ar-23%CO_2, 5.70 m/min, CTWD=20mm)

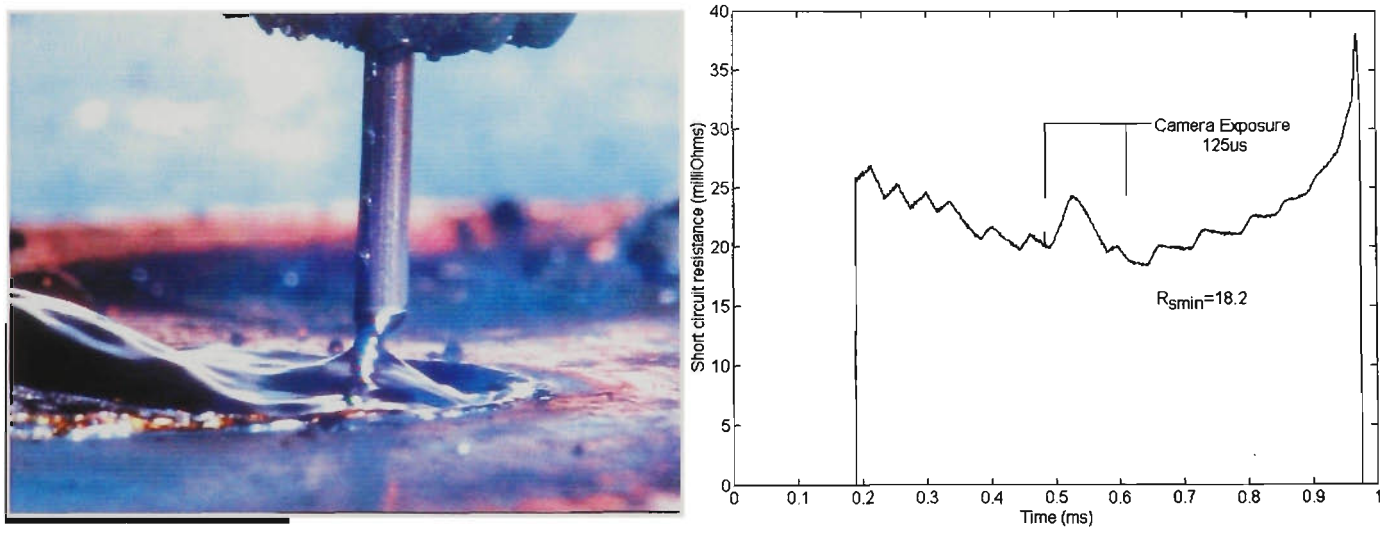

Figure 6.32 Photograph of short circuit with T_{sc} of 0.78ms

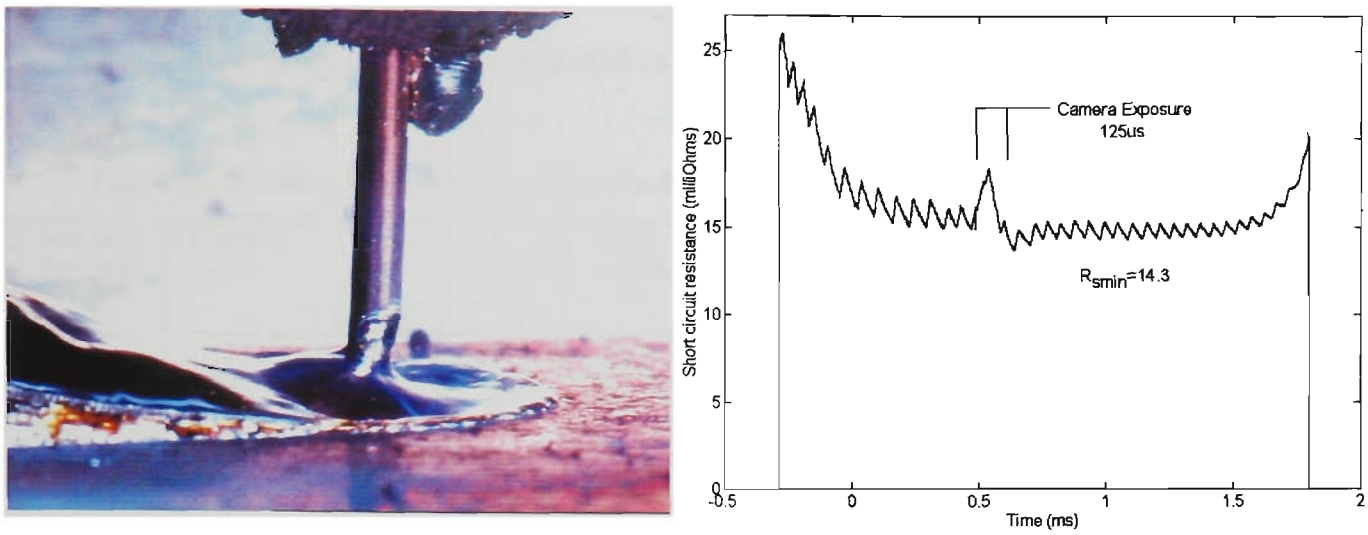

Figure 6.33 Photograph of short circuit with T_{sc} of 2.06ms

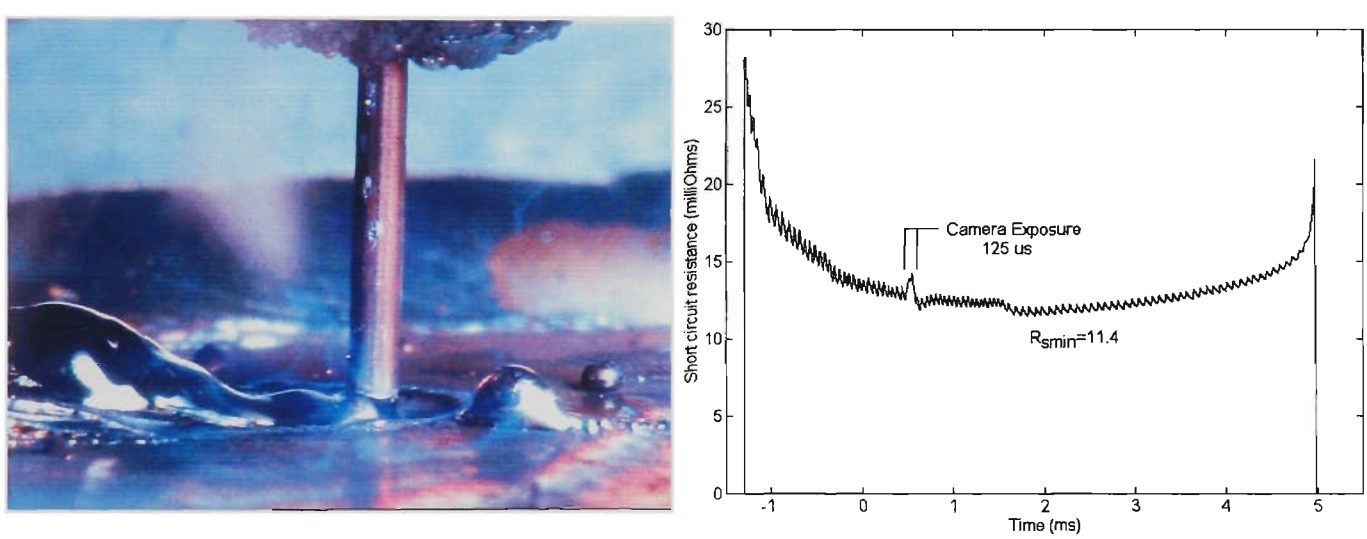

Figure 6.34 Photograph of short circuit with T_{sc} of 6.28ms

Appendix 7

This appendix contains Figures relevant to Chapter 7.

Table 7.1 Melting Rate Test Parameters for Ar-23%CO_2 Shielding Gas

Test No.	Iarc_max, Tarc_max (A, ms)	Iarc_min (A)	Wire Feed Rate (m/min)	L (CTWD) (mm)	Mean Current (A)	Average Arcing Current (A)	RMS Current (A)	Melting Rate using Eq 7.7 (m/min)	Melting Rate using Eq 7.1 (m/min)
1	350, 1.5	75	5.70	20	99.8	85.7	122.2	5.92	5.67
2	350, 1.5	40	5.70	20	84.6	69.9	123.0	5.39	4.54
3	350, 1.5	95	5.70	20	107.2	95.0	119.8	6.14	6.25
4	350, 3.5	75	5.70	20	99.2	89.7	123.1	6.11	5.62
5	275, 1.5	75	5.70	20	100.4	84.1	118.6	5.67	5.71
6	350, 1.5	75	5.70	16	107.3	92.5	132.4	5.99	5.79
7	350, 1.5	40	5.70	16	91.7	75.1	131.8	5.34	4.71
8	350, 1.5	105	5.70	16	119.7	106.1	133.1	6.51	6.70
9	350, 1.5	75	5.70	12	113.9	97.7	141.3	5.79	5.74
10	350, 1.5	40	5.70	12	109.0	86.7	149.4	5.66	5.42
11	350, 3.5	75	5.70	12	116.2	104.4	146.9	6.21	5.89
12	275, 1.5	75	5.70	12	115.3	90.5	137.9	5.42	5.83
13	350, 1.5	75	5.70	6	134.6	104.9	167.4	5.36	6.02
14	350, 1.5	40	5.70	6	142.3	84.5	186.8	5.03	6.43
15	350, 1.5	100	5.70	6	137.6	116.9	161.7	5.69	6.18
16	350, 1.5	25	1.87	12	33.8	28.1	68.5	1.54	1.37
17	350, 1.5	25	3.79	12	61.6	50.4	110.6	3.21	2.71
18	350, 1.5	50	5.70	12	106.4	87.8	144.1	5.52	5.26
19	375, 1.5	50	7.20	12	133.2	102.6	175.3	7.20	7.03

Table 7.2 Melting Rate Test Parameters for CO_2 Shielding Gas

Test No.	Iarc_max, Tarc_max (A, ms)	Iarc_min (A)	Wire Feed Rate (m/min)	L (CTWD) (mm)	Mean Current (A)	Average Arcing Current (A)	RMS Current (A)	Melting Rate using Eq 7.7 (m/min)	Melting Rate using Eq 7.1 (m/min)
1	350, 1.5	30	5.70	20	75.9	62.0	119.0	5.59	4.86
2	350,2.5	50	5.70	20	82.3	70.1	115.1	5.62	5.60
3	350, 2.5	75	5.70	20	88.0	75.7	113.8	5.73	6.31
4	350, 2.5	45	5.70	20	79.8	67.0	117.8	5.68	5.31
5	350, 2.5	60	5.70	20	85.0	74.3	117.3	5.89	5.93
6	350, 2.5	30	5.70	20	74.2	63.2	122.8	5.86	4.67
7	350, 1.5	30	5.70	16	82.9	66.1	127.8	5.45	4.80
8	350, 3.5	30	5.70	16	79.9	67.9	130.3	5.64	4.50
9	350, 1.5	60	5.70	16	95.0	78.3	127.5	5.83	6.08
10	350, 1.5	75	5.70	12	107.6	91.0	136.5	5.79	6.10
11	350, 1.5	50	5.70	12	102.4	80.7	141.9	5.68	5.60
12	350, 1.5	100	5.70	12	117.5	104.0	138.0	6.28	7.11
13	350, 1.5	90	5.70	6	134.8	96.0	171.8	5.37	5.56
14	350, 1.5	75	5.70	6	143.4	85.4	182.7	5.31	6.15

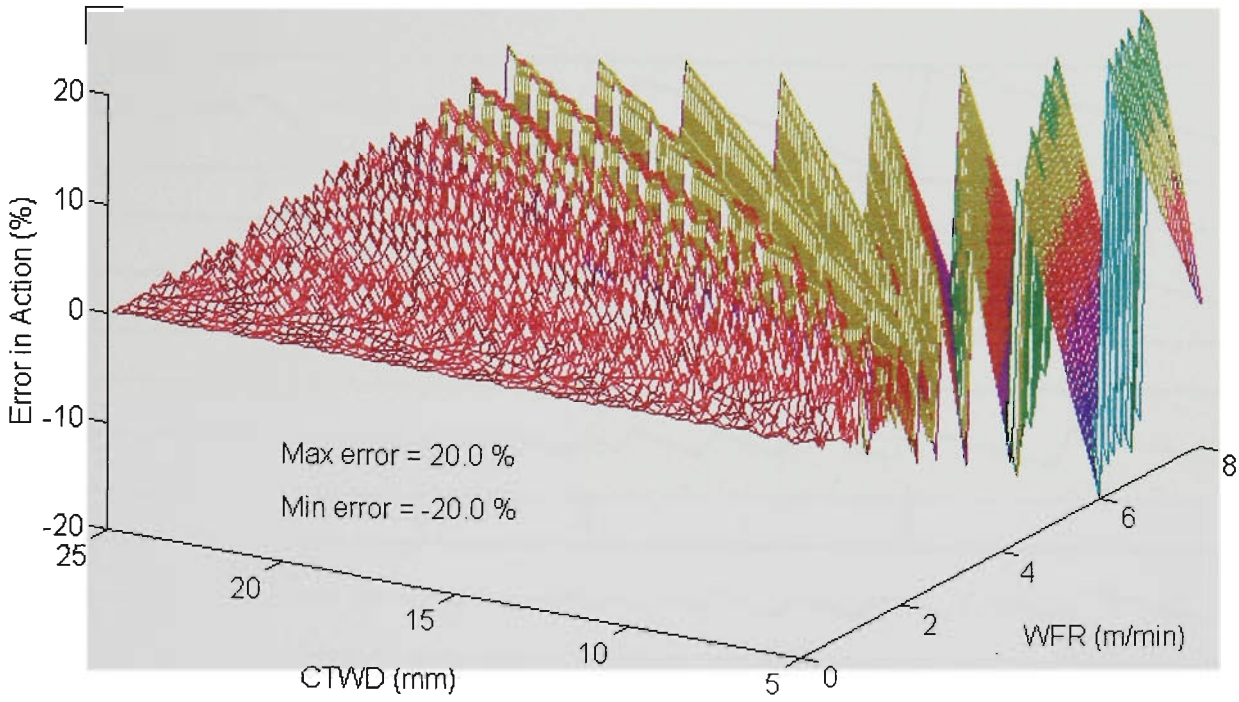

Figure 7.4 Percentage error in action integral vs CTWD & Wire feed rate (50μs sampling rate, 400 point array)

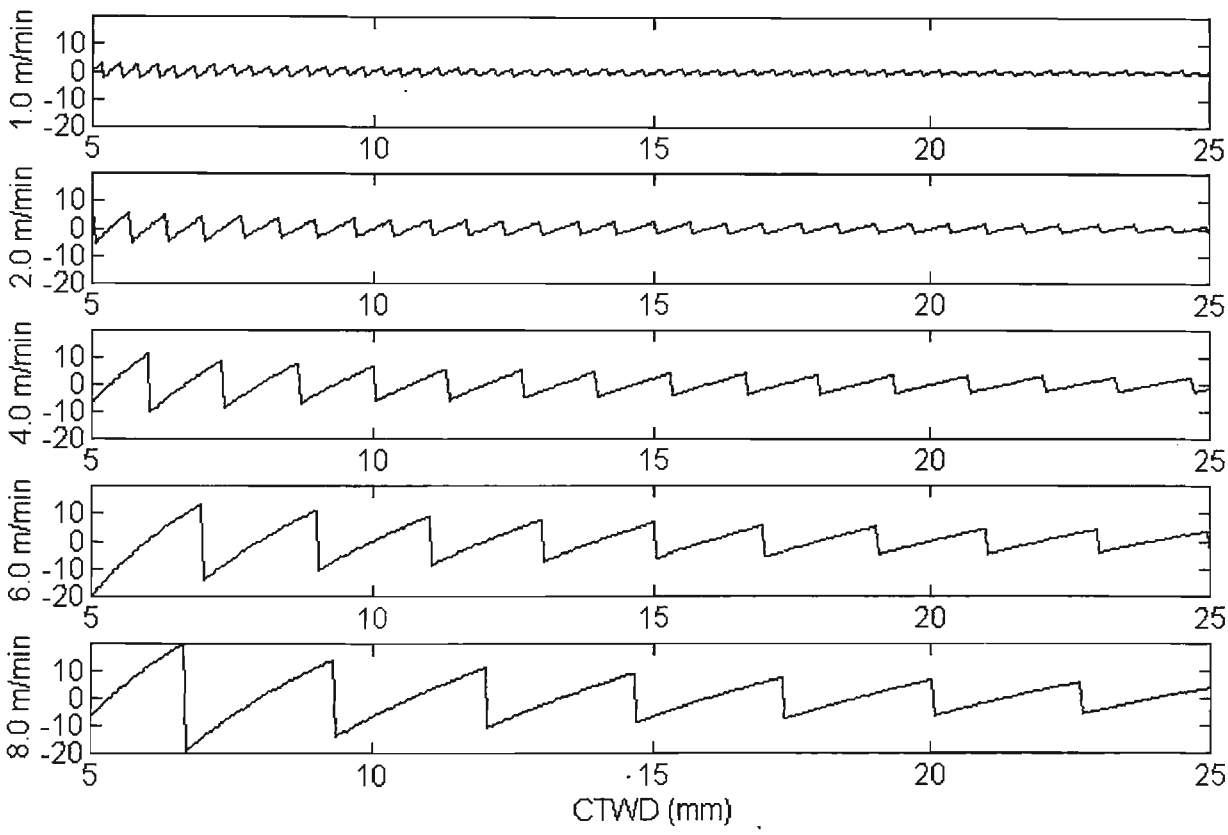

Figure 7.5 Percentage error in action integral vs CTWD as Wire feed rate varies (50μs sampling rate, 400 point array)

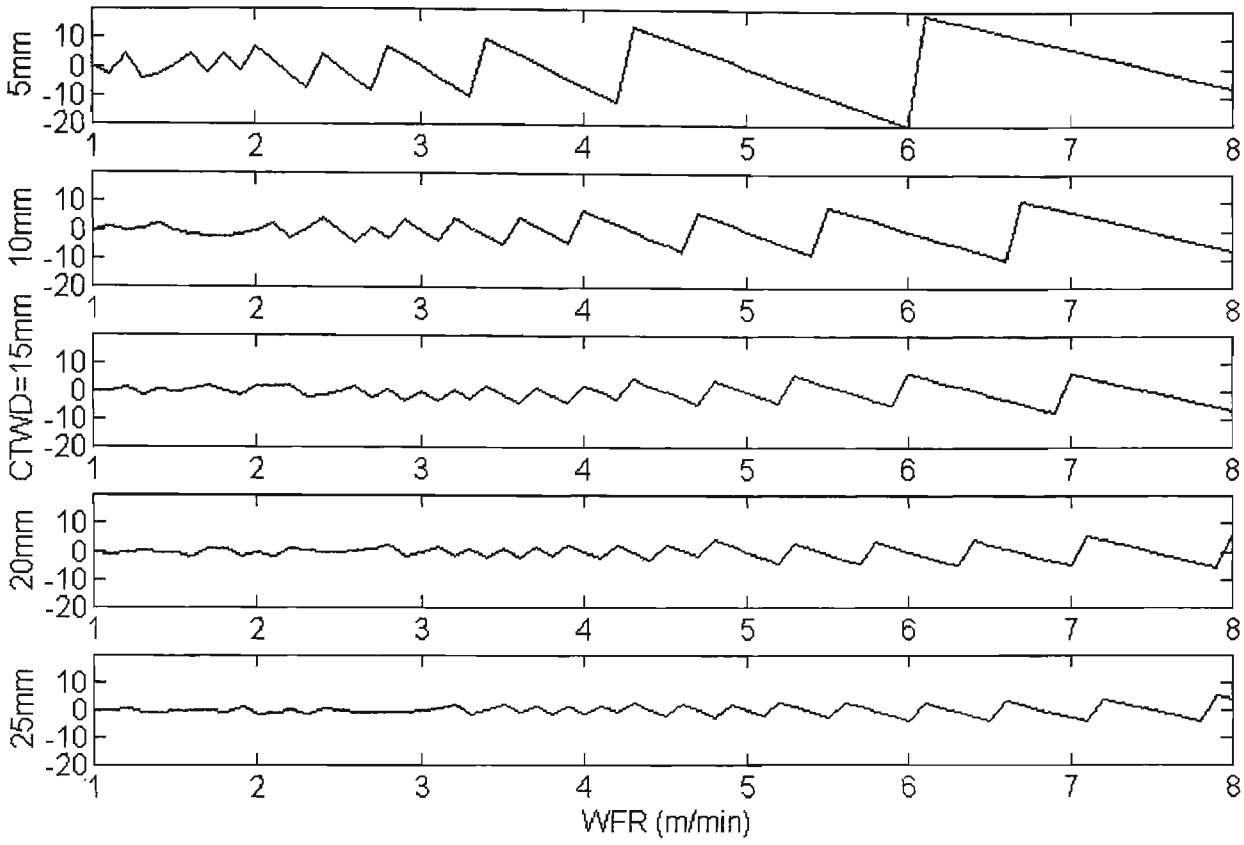

Figure 7.6 Percentage error in action integral vs Wire feed rate as CTWD varies (50μs sampling rate, 400 point array)

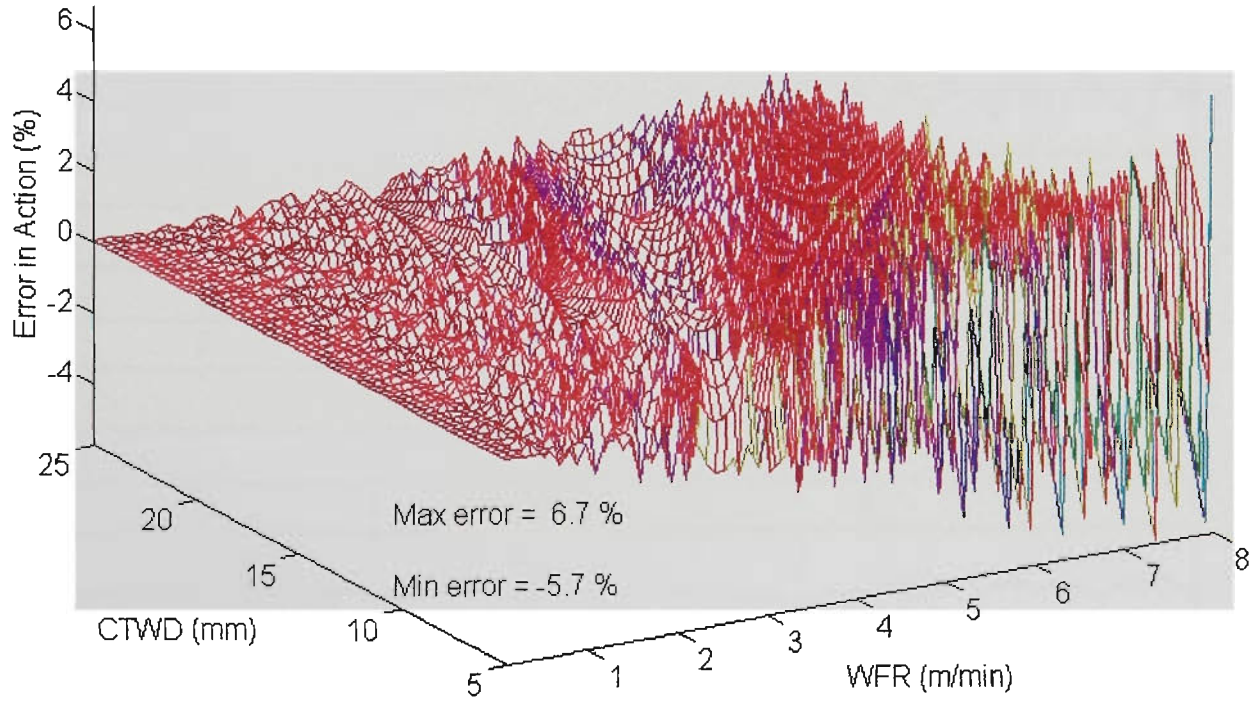

Figure 7.7 Percentage error in action integral vs CTWD & Wire feed rate (50μs sampling rate, 100 point array)

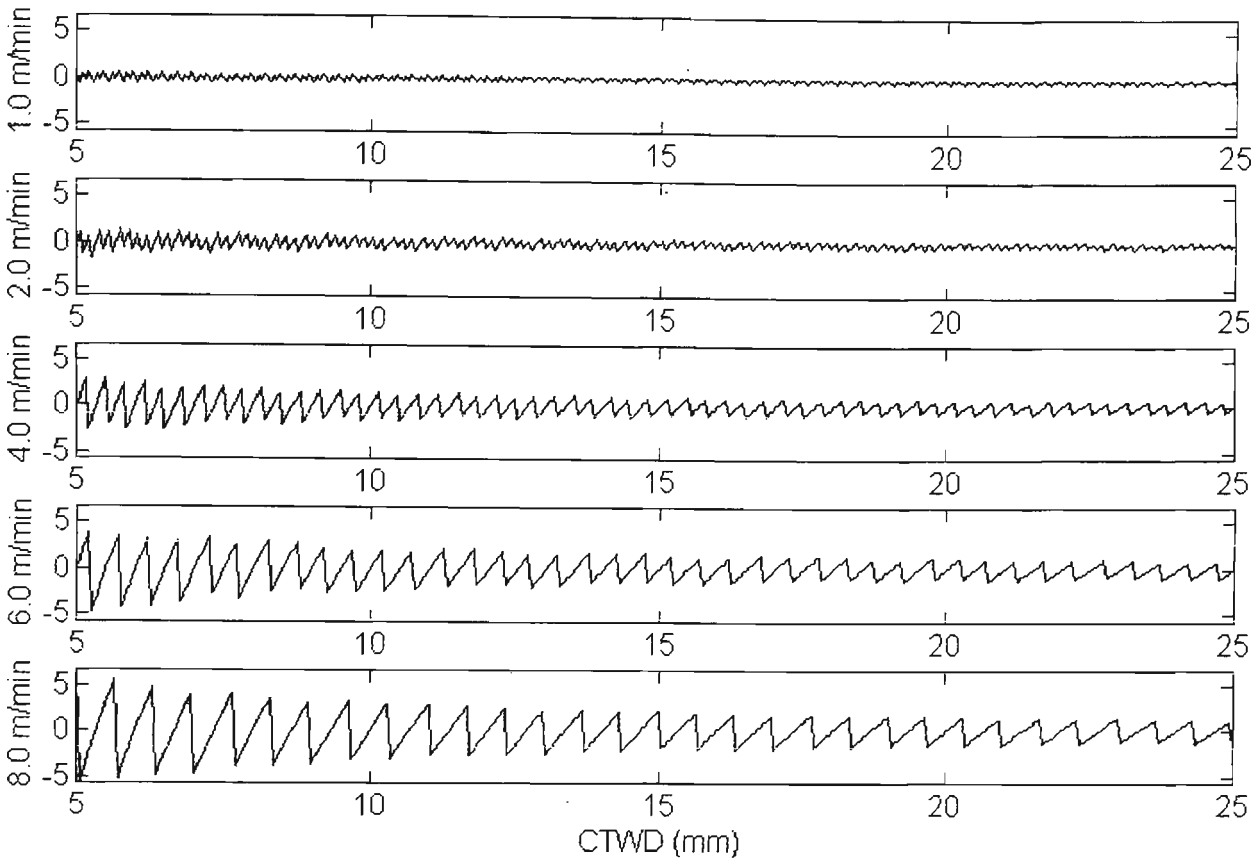

Figure 7.8 Percentage error in action integral vs CTWD as Wire feed rate varies (50μs sampling rate, 100 point array)

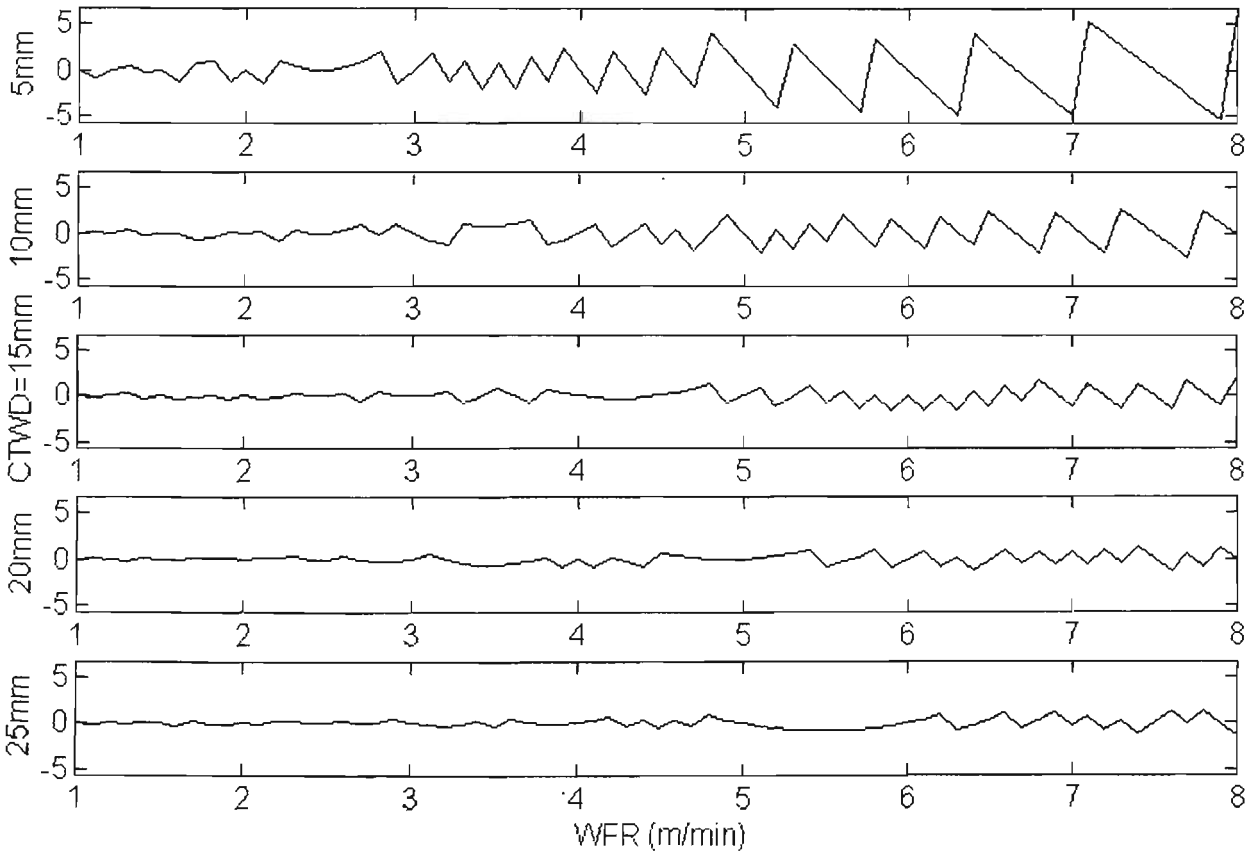

Figure 7.9 Percentage error in action integral vs Wire feed rate as CTWD varies (50μs sampling rate, 100 point array)

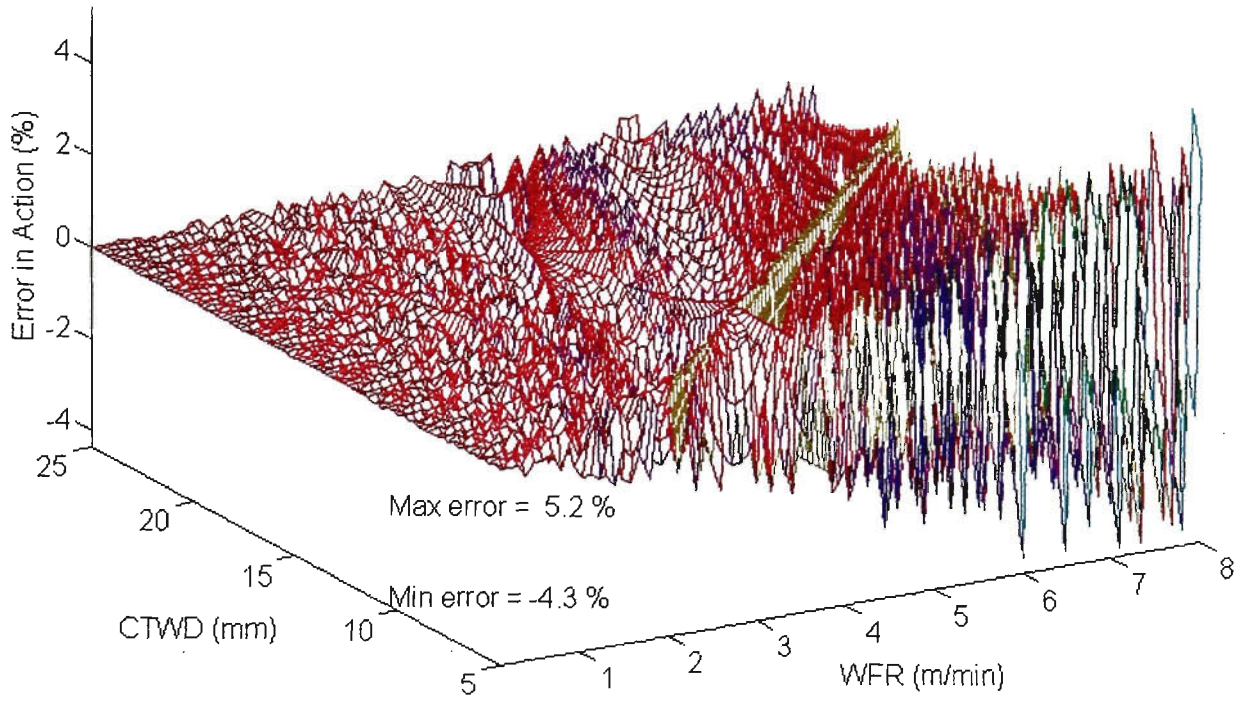

Figure 7.10 Percentage error in action integral vs CTWD & Wire feed rate (40μs sampling rate, 100 point array)

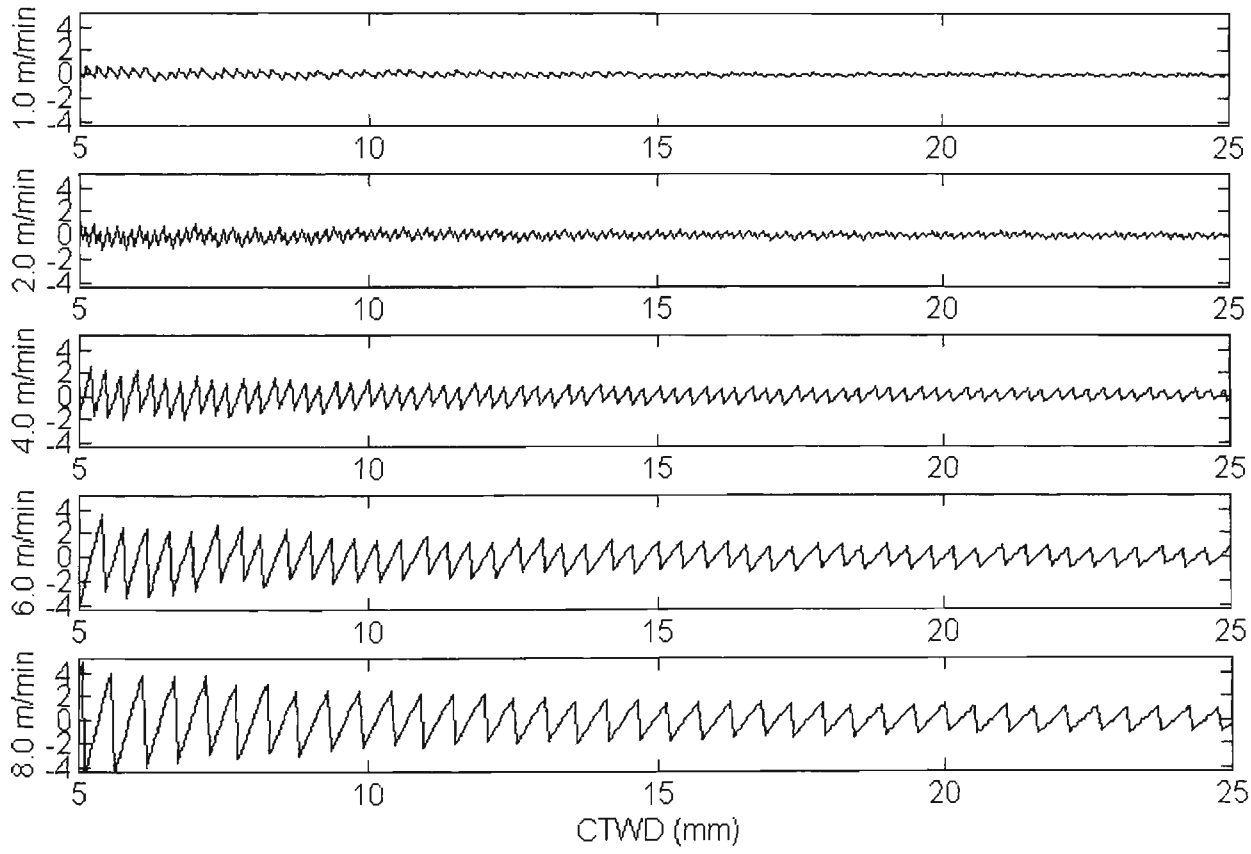

Figure 7.11 Percentage error in action integral vs CTWD as Wire feed rate varies (40μs sampling rate, 100 point array)

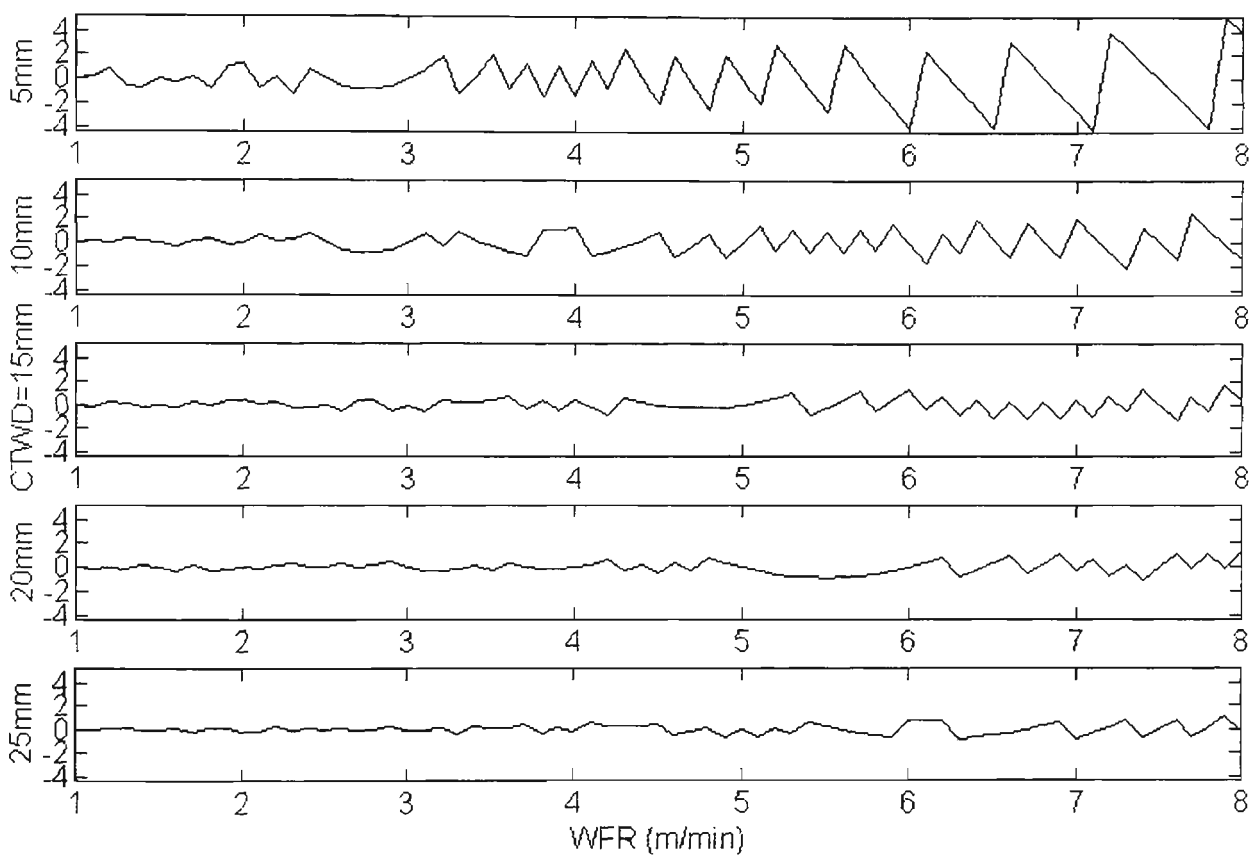

Figure 7.12 Percentage error in action integral vs Wire feed rate as CTWD varies (40μs sampling rate, 100 point array)

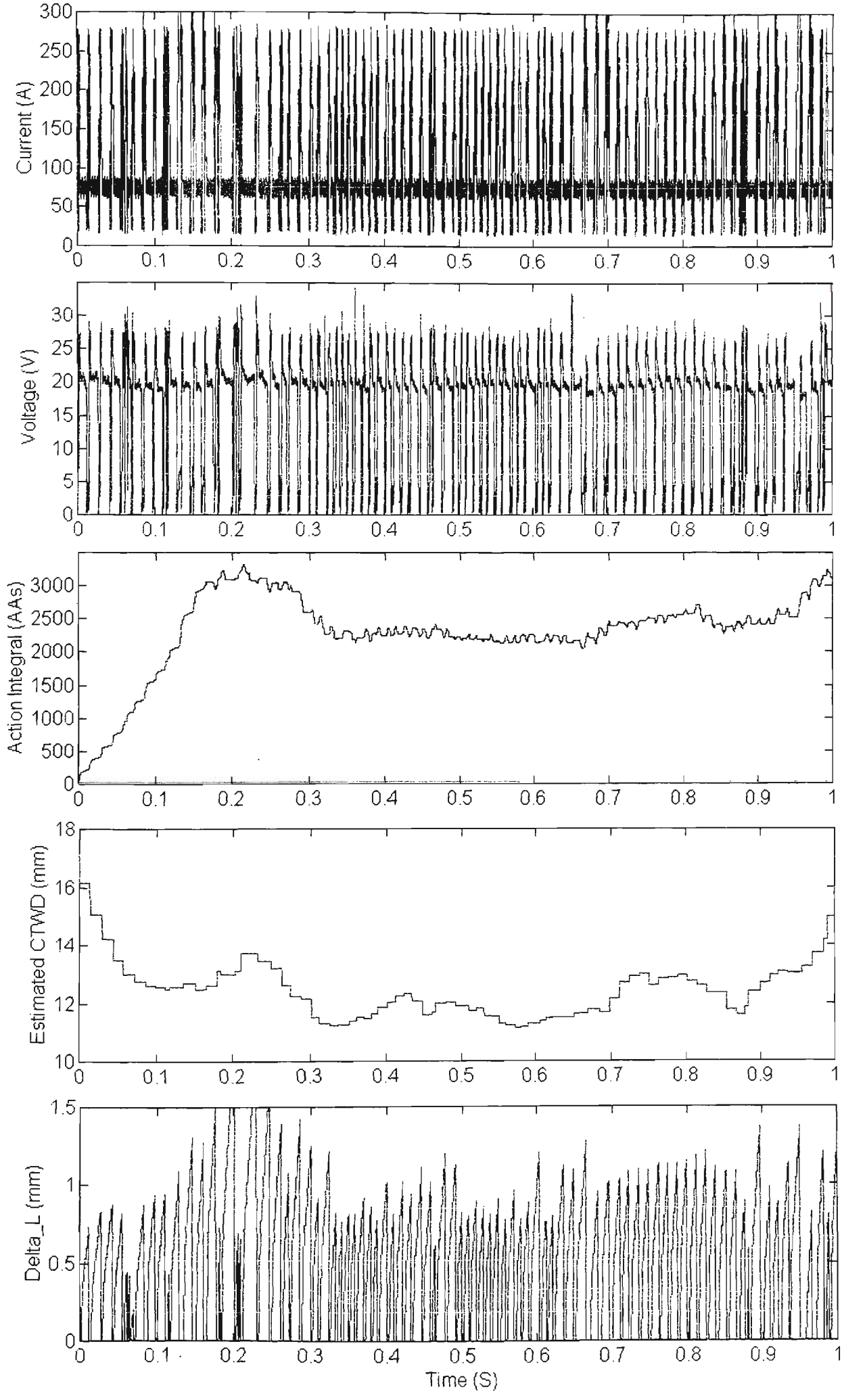

Figure 7.13 Offline simulation results for First Method (typical), 0.0-1.0 seconds

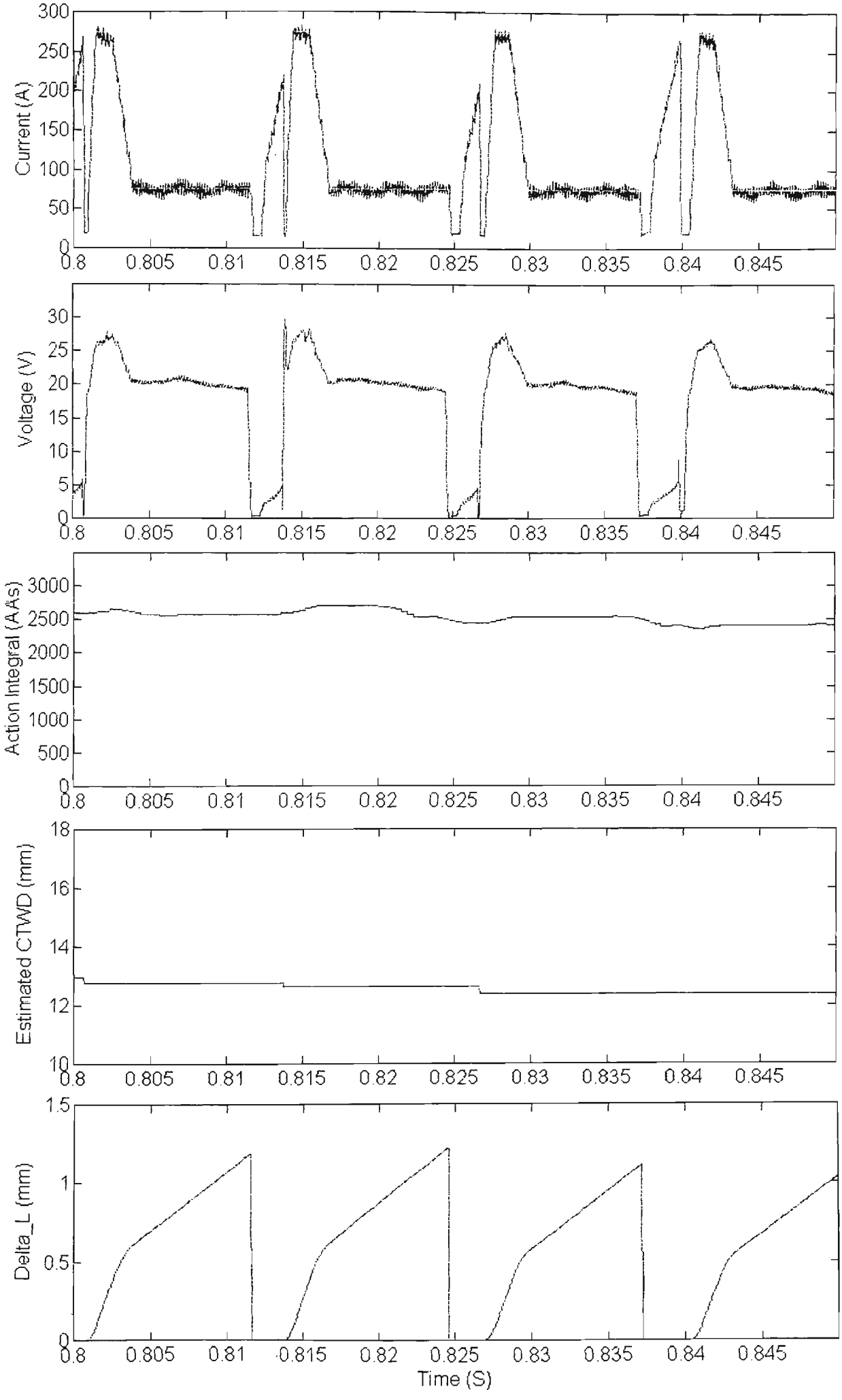

Figure 7.14 Offline simulation results for First Method (typical), 0.80-0.85 seconds

Table 7.5 Average Action for Tests in Ar-23%CO_2 and CO_2

Ar-23%CO_2 shielding gas			CO_2 shielding gas		
Test No.	**Average value of $H_L(\tau)$ from simulations (J/mm^3)**	**Bulk estimate of $H_L(\tau)$ from eqn 7.31 (J/mm^3)**	**Test No.**	**Average value of $H_L(\tau)$ from simulations (J/mm^3)**	**Bulk estimate of $H_L(\tau)$ from eqn 7.31 (J/mm^3)**
1	5.41	5.49	1	4.95	5.02
2	5.64	5.61	2	4.44	4.46
3	5.10	5.13	3	4.34	4.28
4	5.63	5.62	4	4.90	4.84
5	4.92	4.96	5	4.78	4.77
6	5.03	4.93	6	5.49	5.58
7	4.95	4.85	7	4.46	4.35
8	5.09	5.02	8	4.78	4.66
9	3.71	3.76	9	4.44	4.31
10	4.48	4.55	10	3.39	3.39
11	4.22	4.27	11	3.79	3.80
12	3.43	3.50	12	3.46	3.51
13	2.40	2.26	13	2.56	2.43
14	3.25	3.09	14	3.07	2.90
15	2.16	2.06			
16	2.31	2.33			
17	3.35	3.33			
18	3.95	3.98			
19	4.90	4.79			

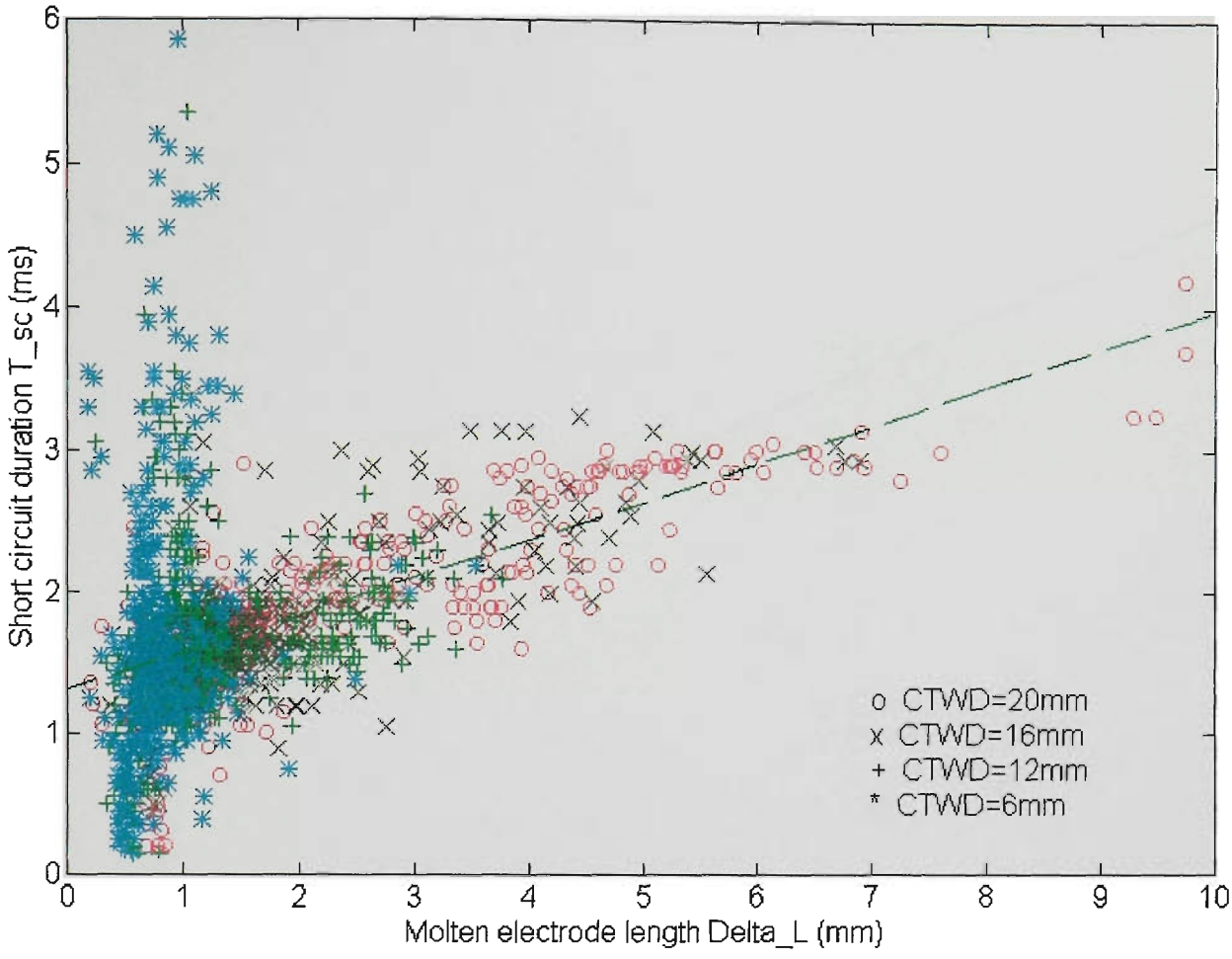

Figure 7.26 Short circuit duration T_sc versus ΔL (uncorrected) for Ar-23%CO_2

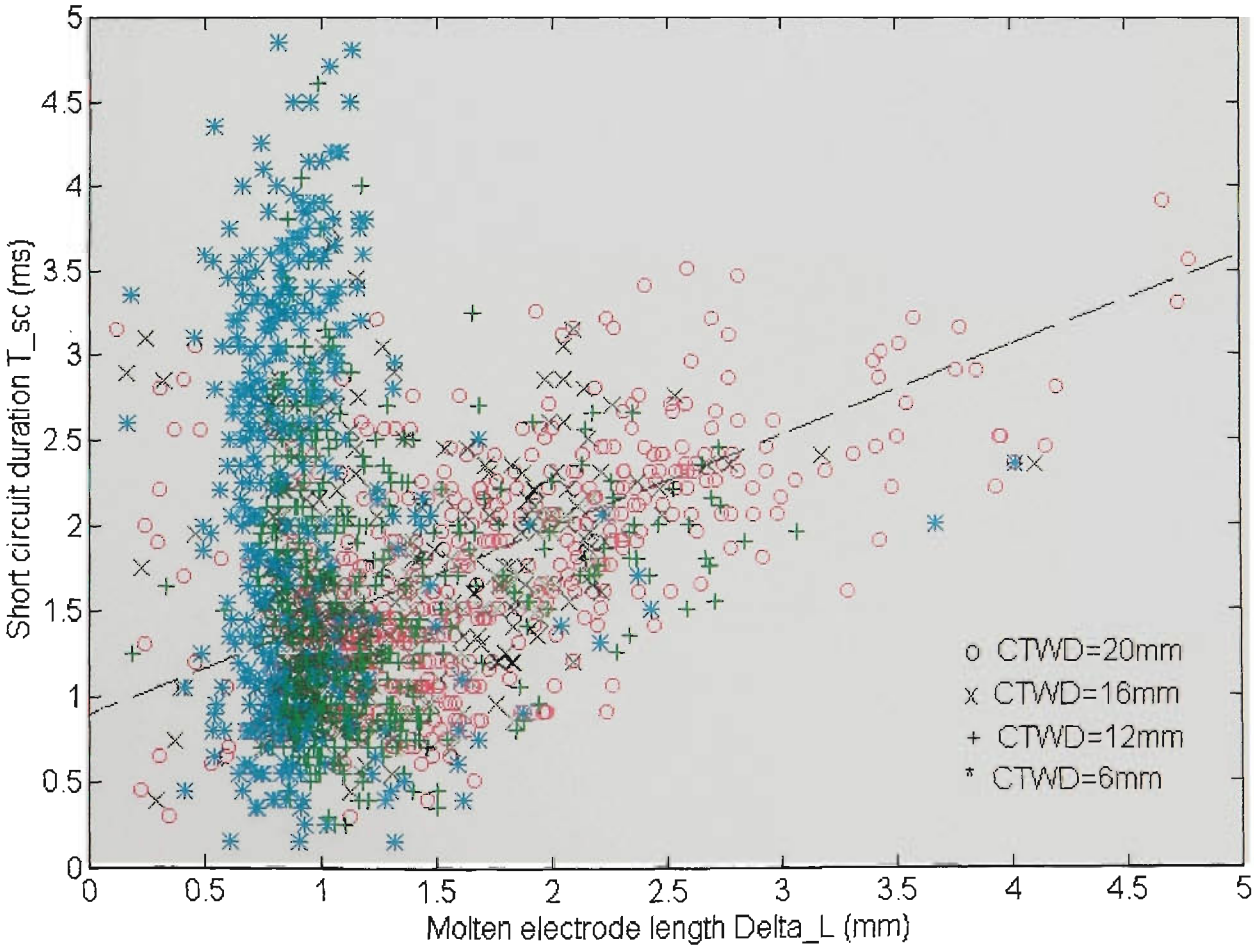

Figure 7.27 Short circuit duration T_sc versus ΔL (uncorrected) for CO_2

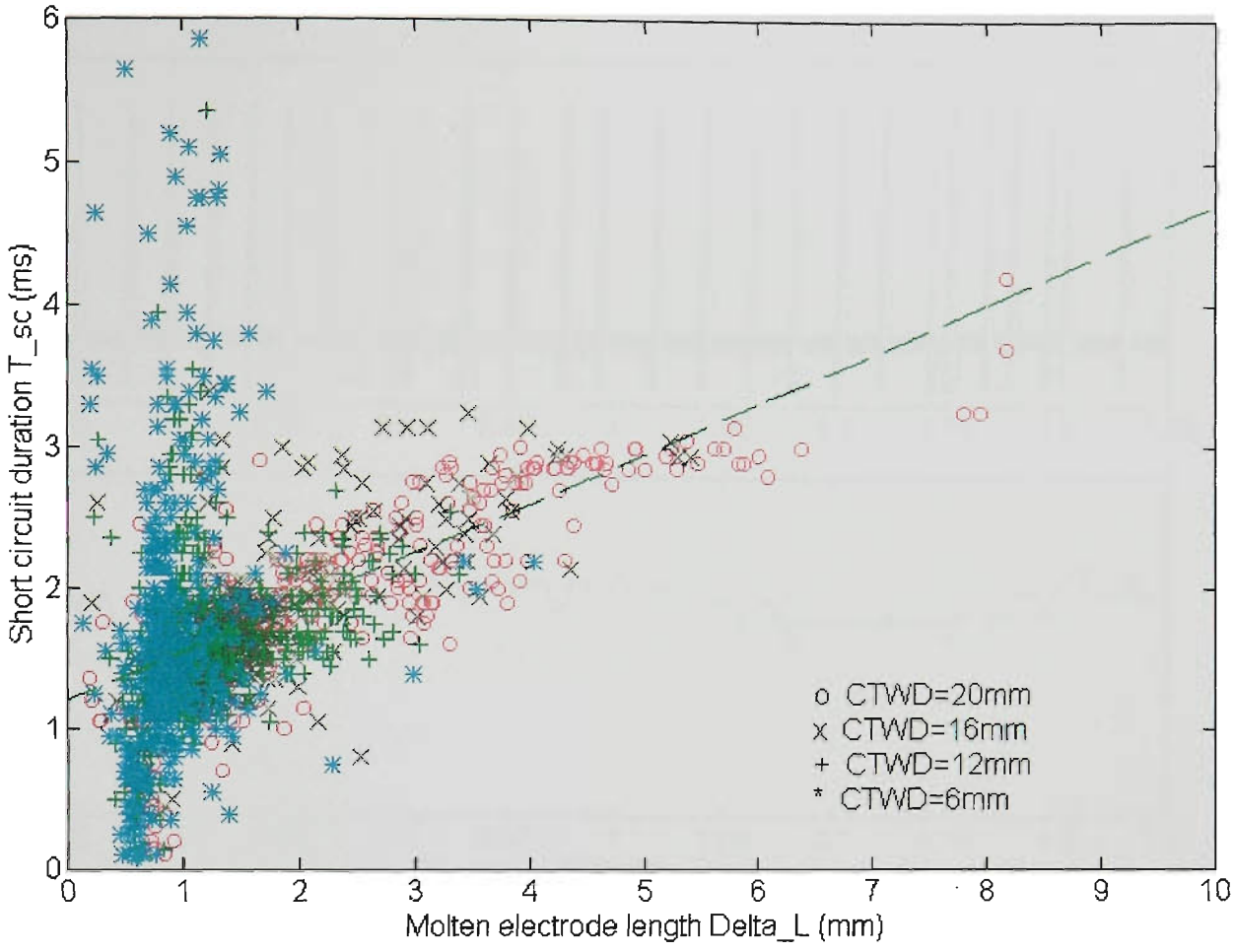

Figure 7.28 Short circuit duration T_sc versus ΔL (corrected) for Ar-23%CO_2

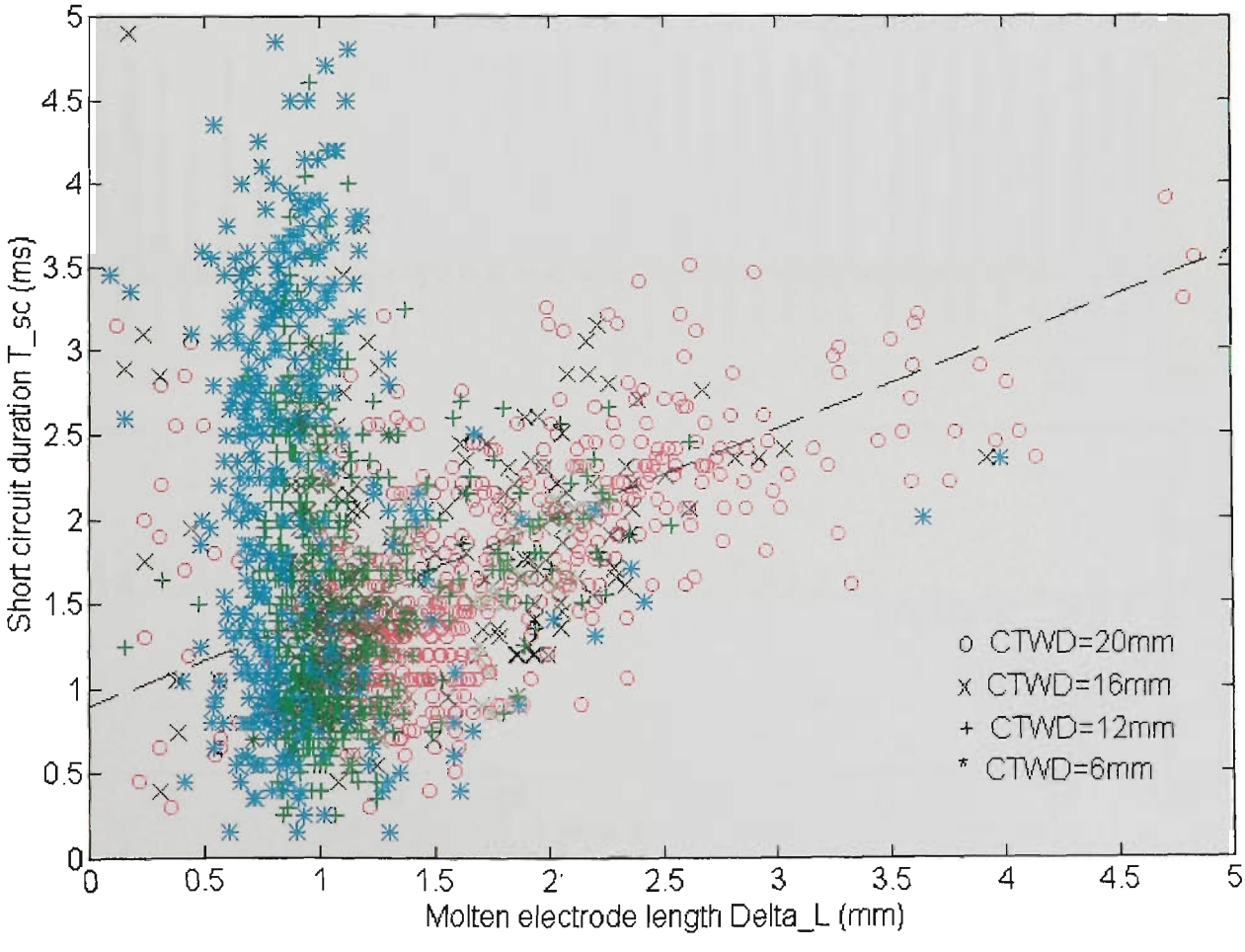

Figure 7.29 Short circuit duration T_sc versus ΔL (corrected) for CO_2

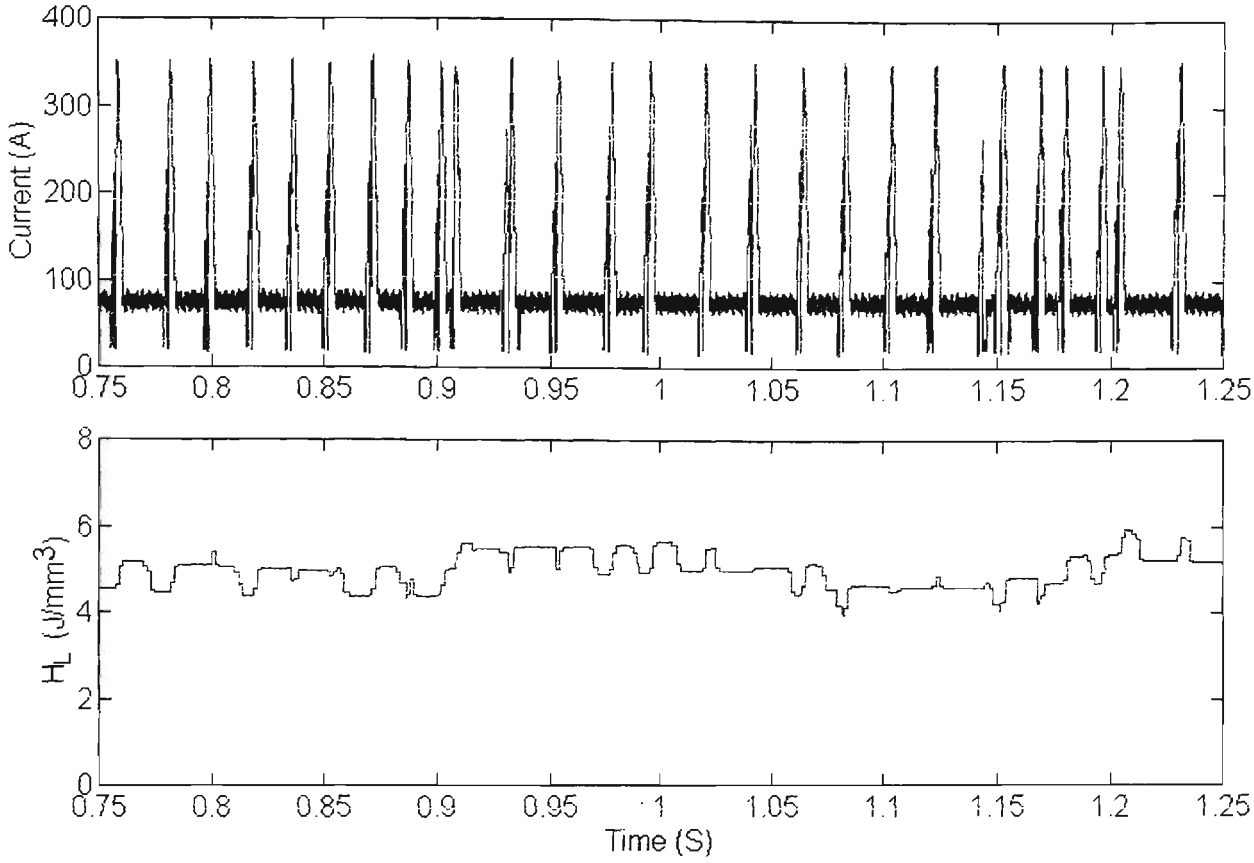

Figure 7.32 H_L evaluated for Test 6, Table 7.1 (CTWD=16mm)

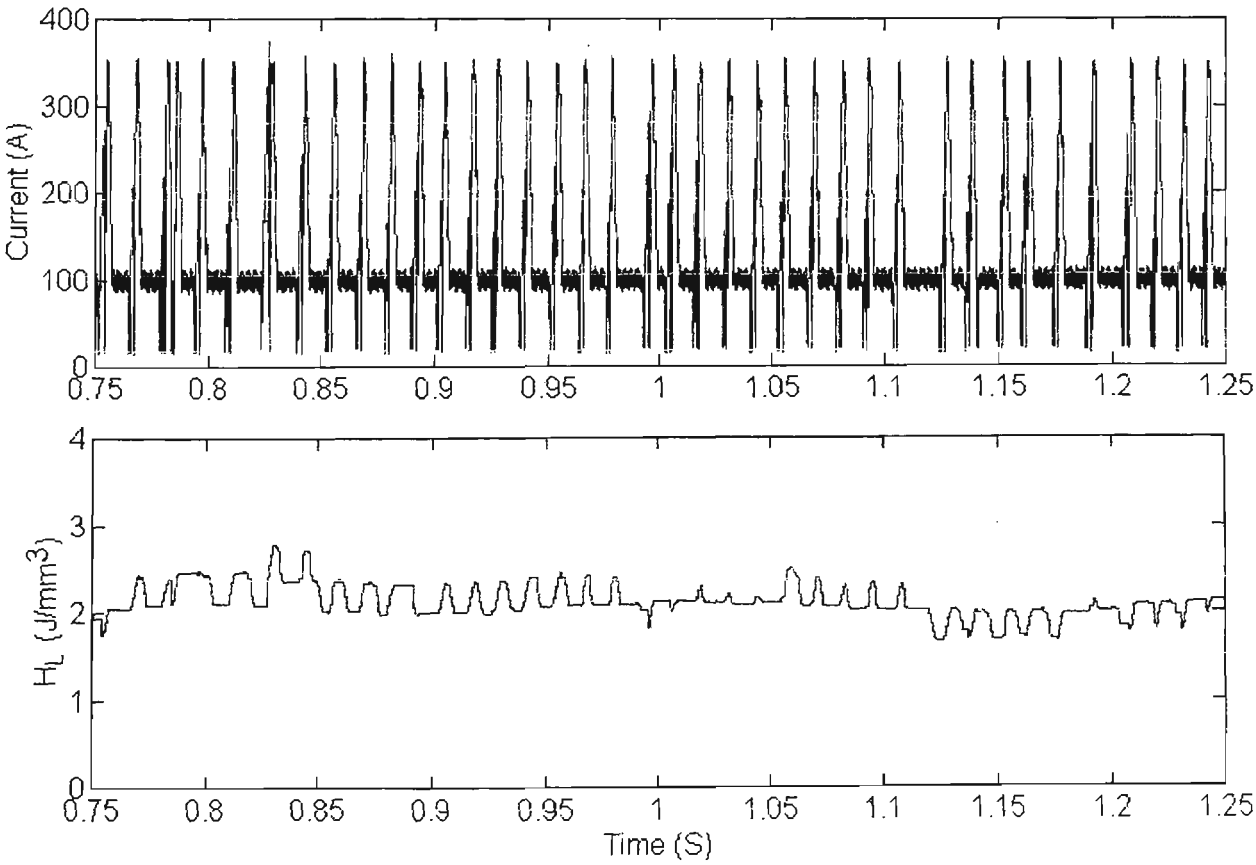

Figure 7.33 H_L evaluated for Test 15, Table 7.1 (CTWD=6mm)

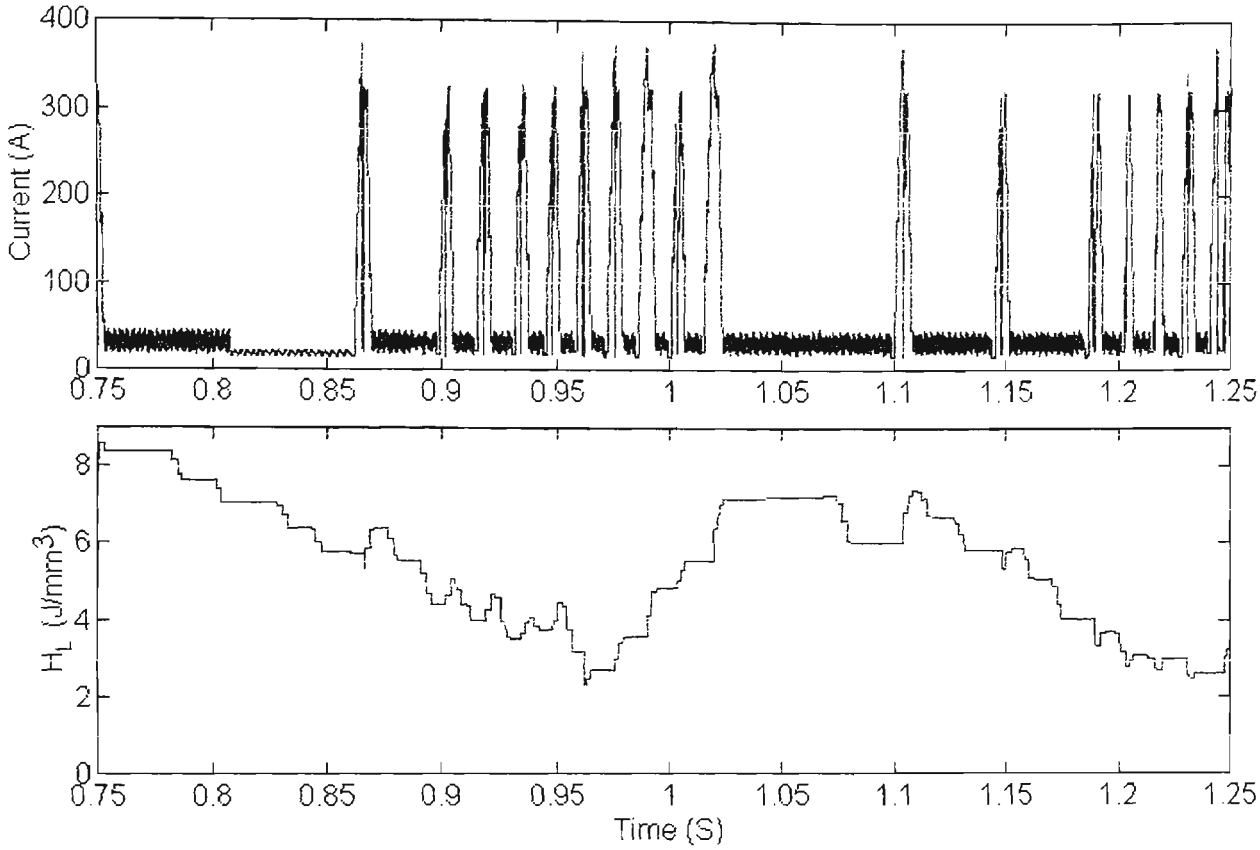

Figure 7.34 H_L evaluated for an unstable weld (CTWD=20mm)

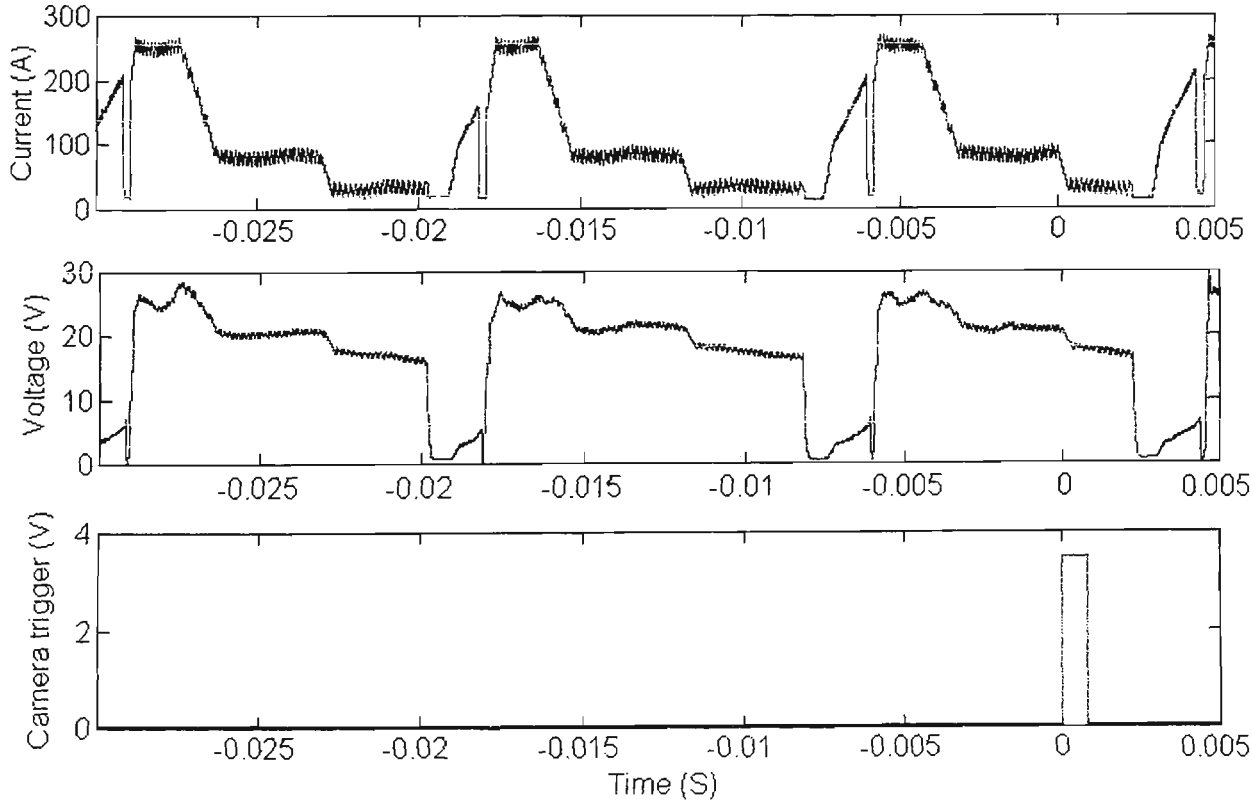

Figure 7.37 Current, voltage and camera trigger waveforms during typical photographic verification test

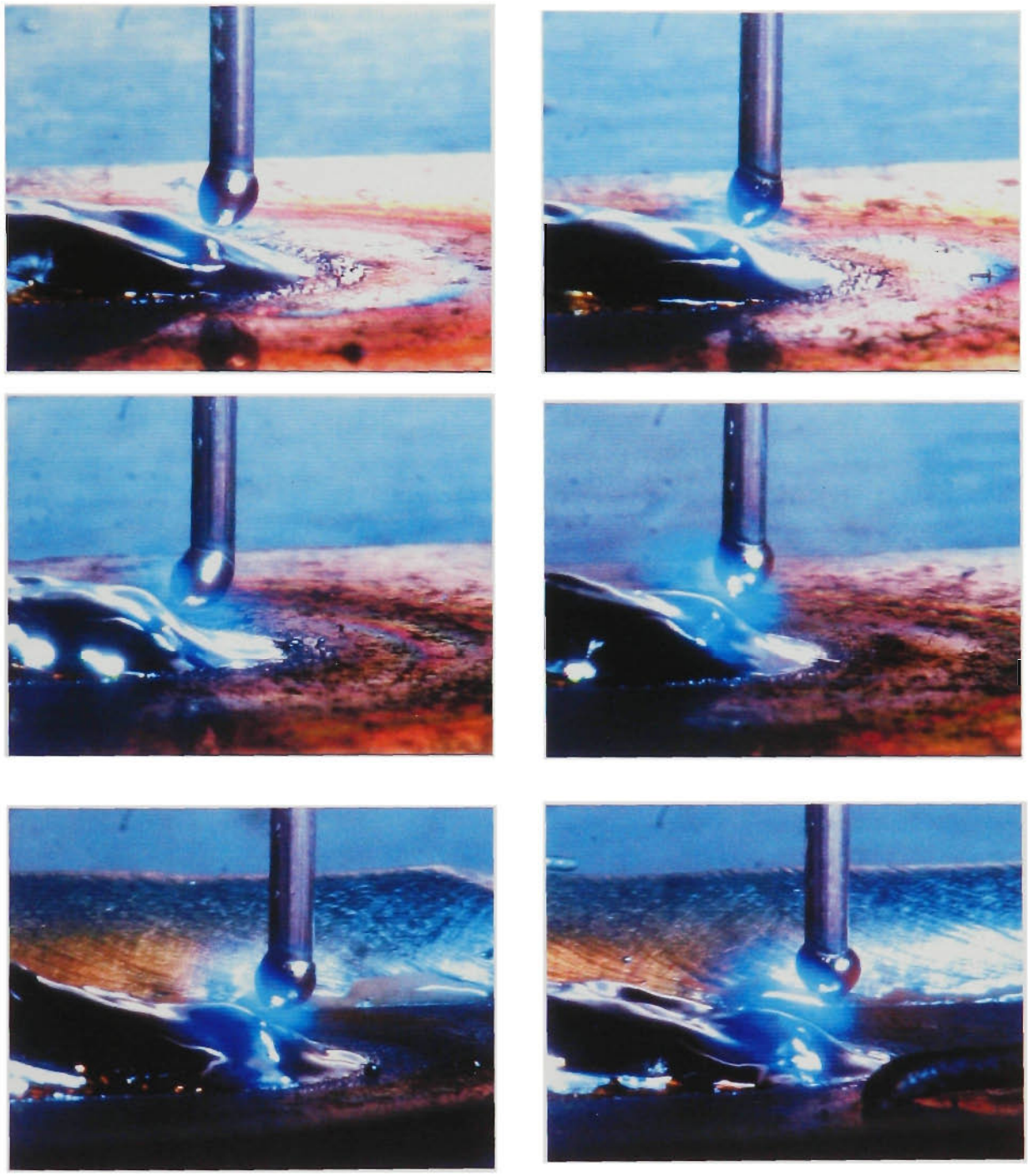

Figure 7.38 Typical photographs of droplet (when target reached)

Appendix 8

This appendix contains Figures relevant to Chapter 8.

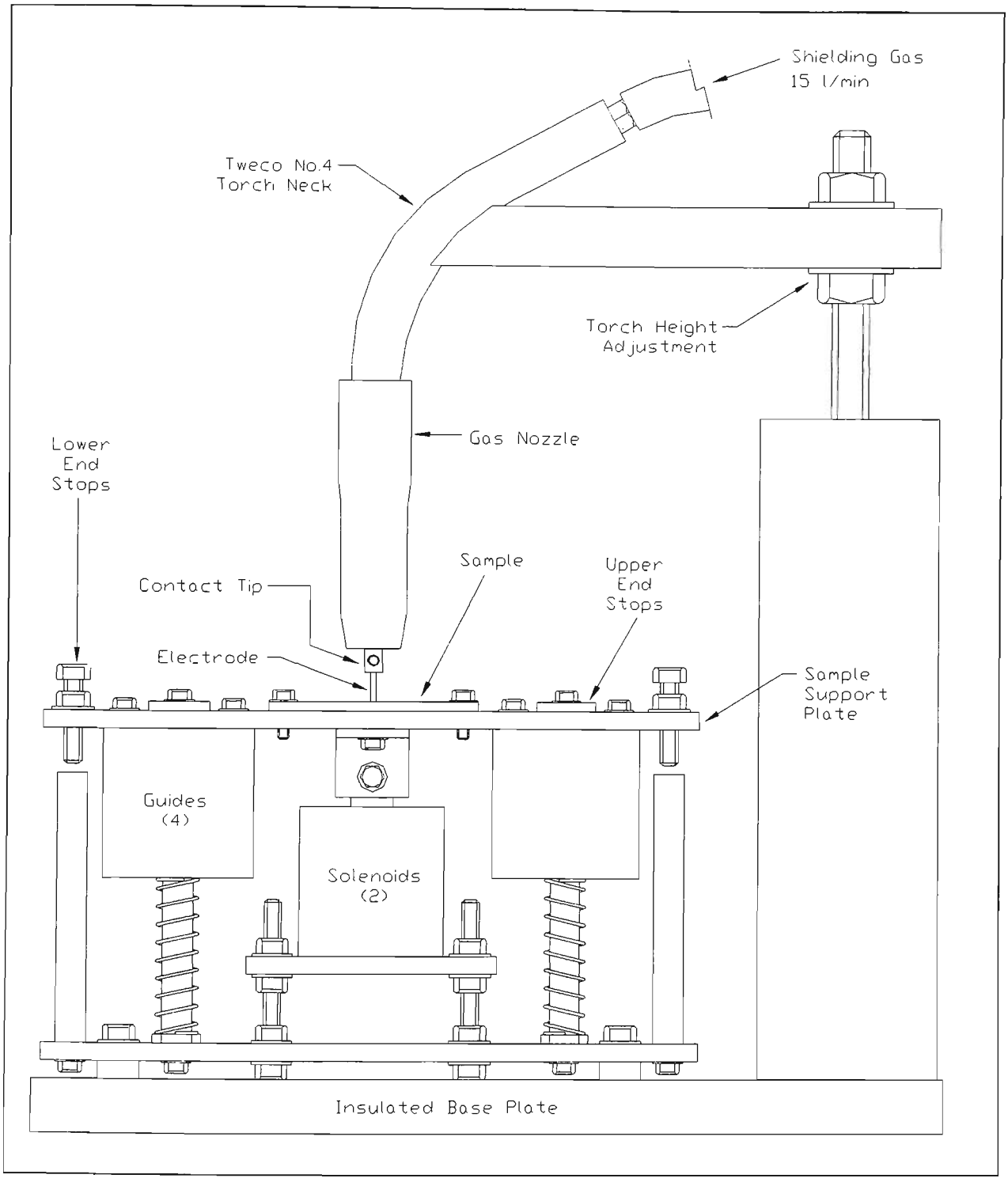

Figure 8.6 Mechanical arrangement of arc characterisation test rig

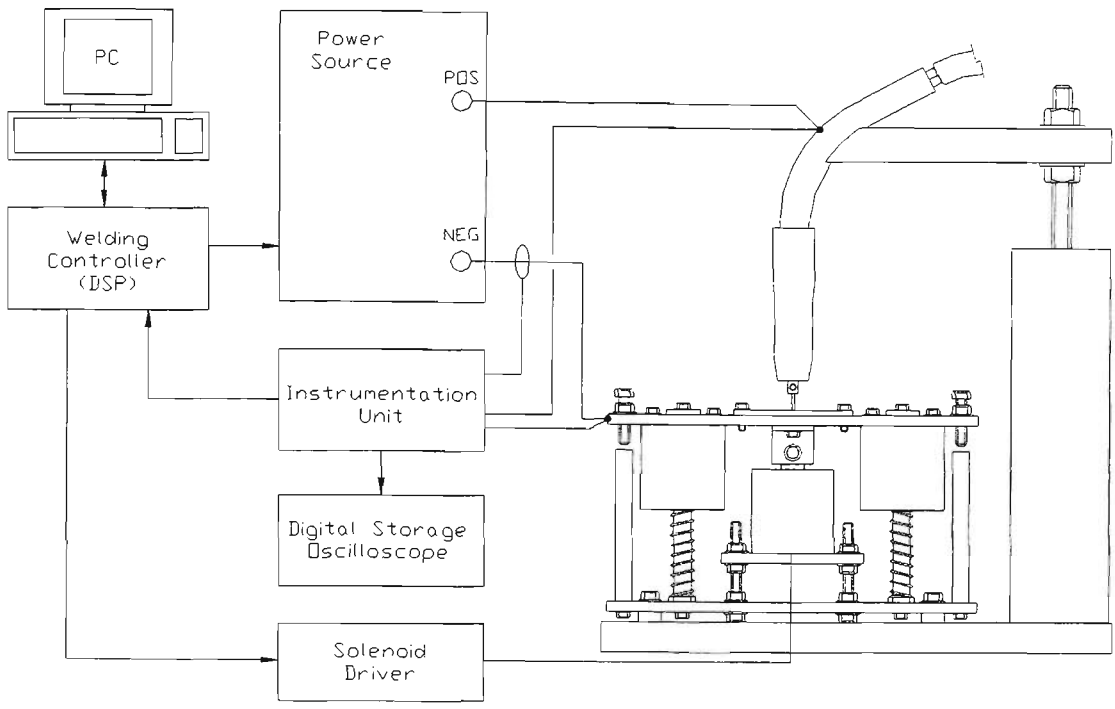

Figure 8.7 Electrical arrangement of arc characterisation test rig

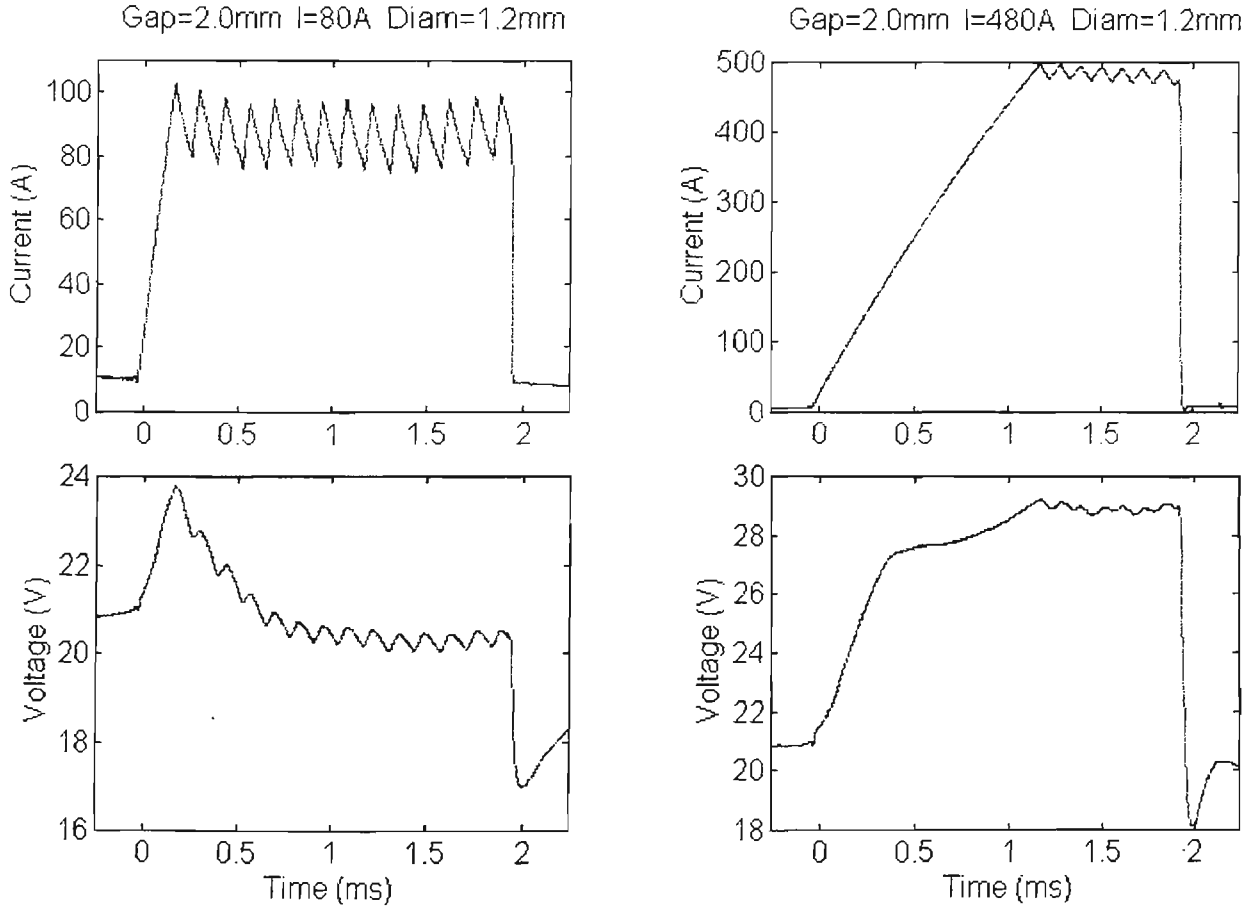

Figure 8.8 Typical voltage and current waveforms for tests (Ar-23%CO_2)

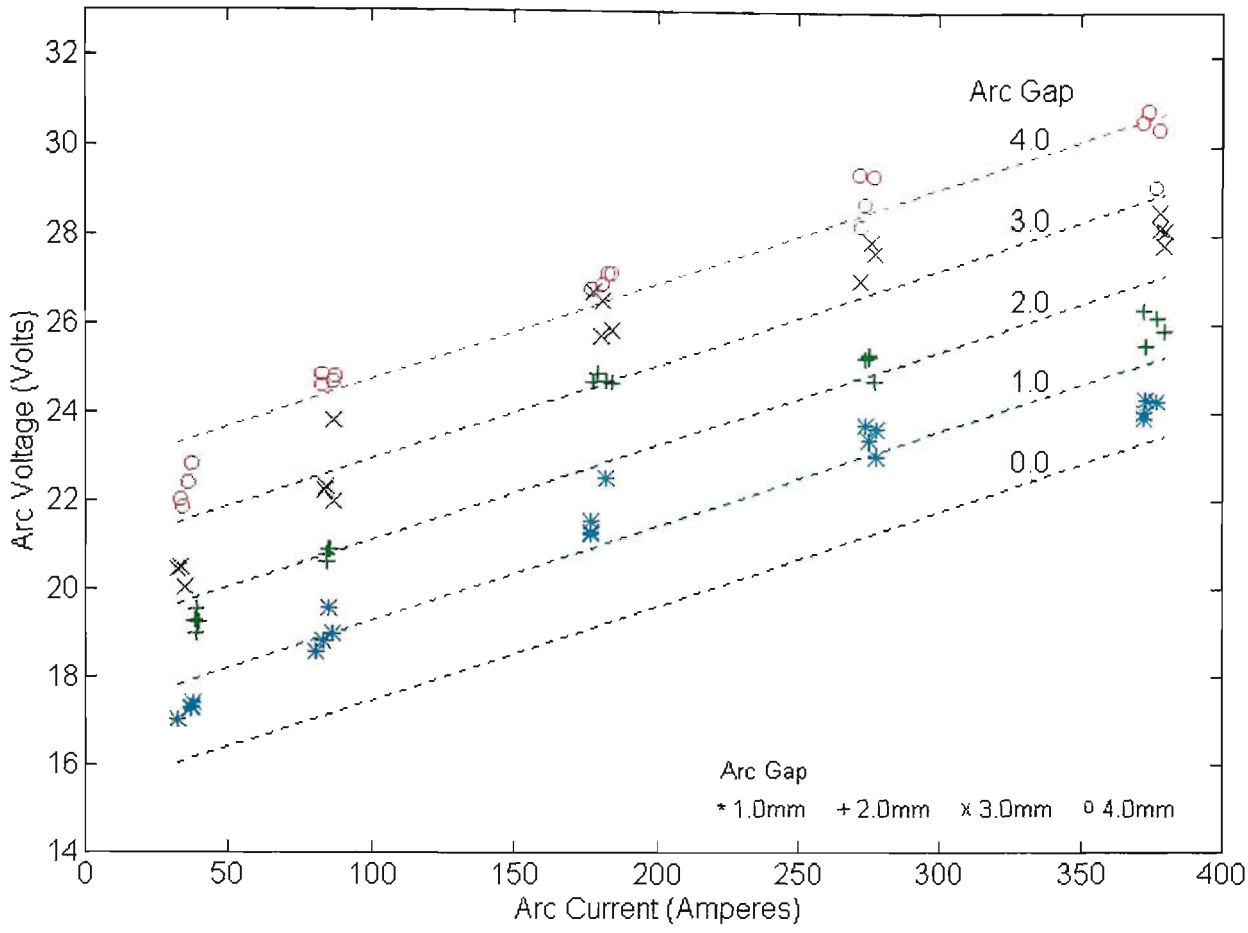

Figure 8.9 V-I characteristics for Ar-16%CO_2-3%O_2, 0.9mm MS electrode positive

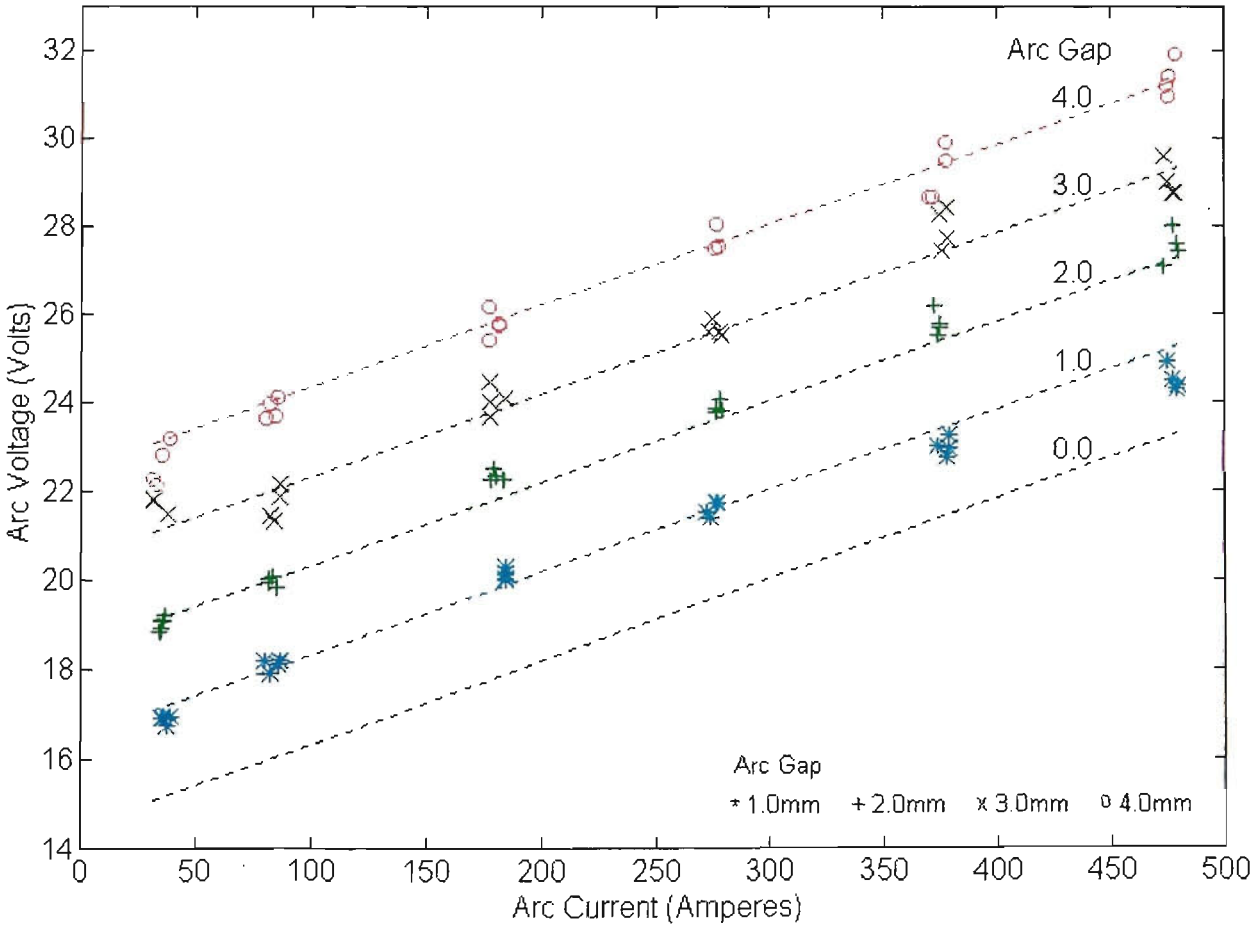

Figure 8.10 V-I characteristics for Ar-16%CO_2-3%O_2, 1.2mm MS electrode positive

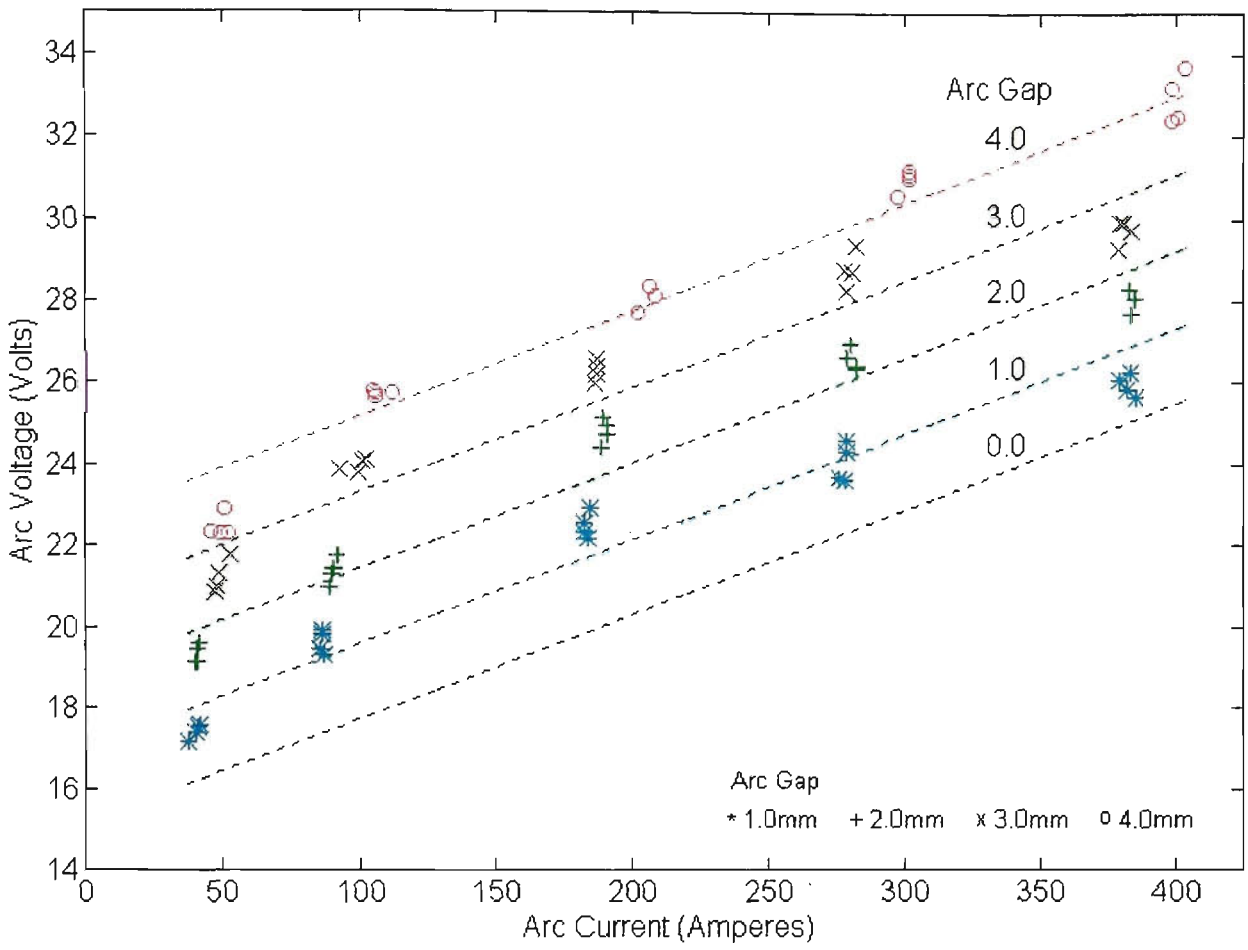

Figure 8.11 V-I characteristics for Ar-23%CO_2, 0.9mm MS electrode positive

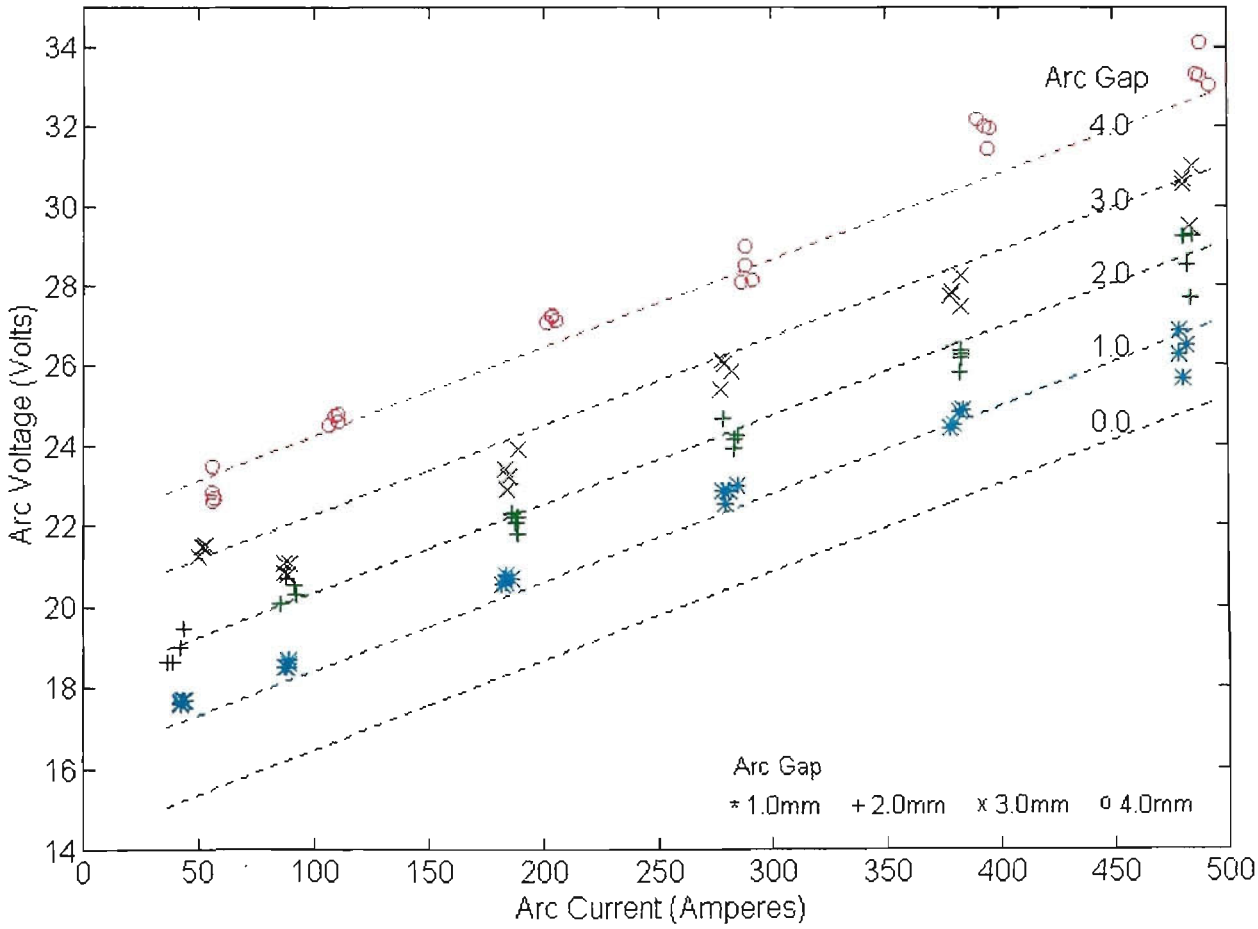

Figure 8.12 V-I characteristics for Ar-23%CO_2, 1.2mm MS electrode positive

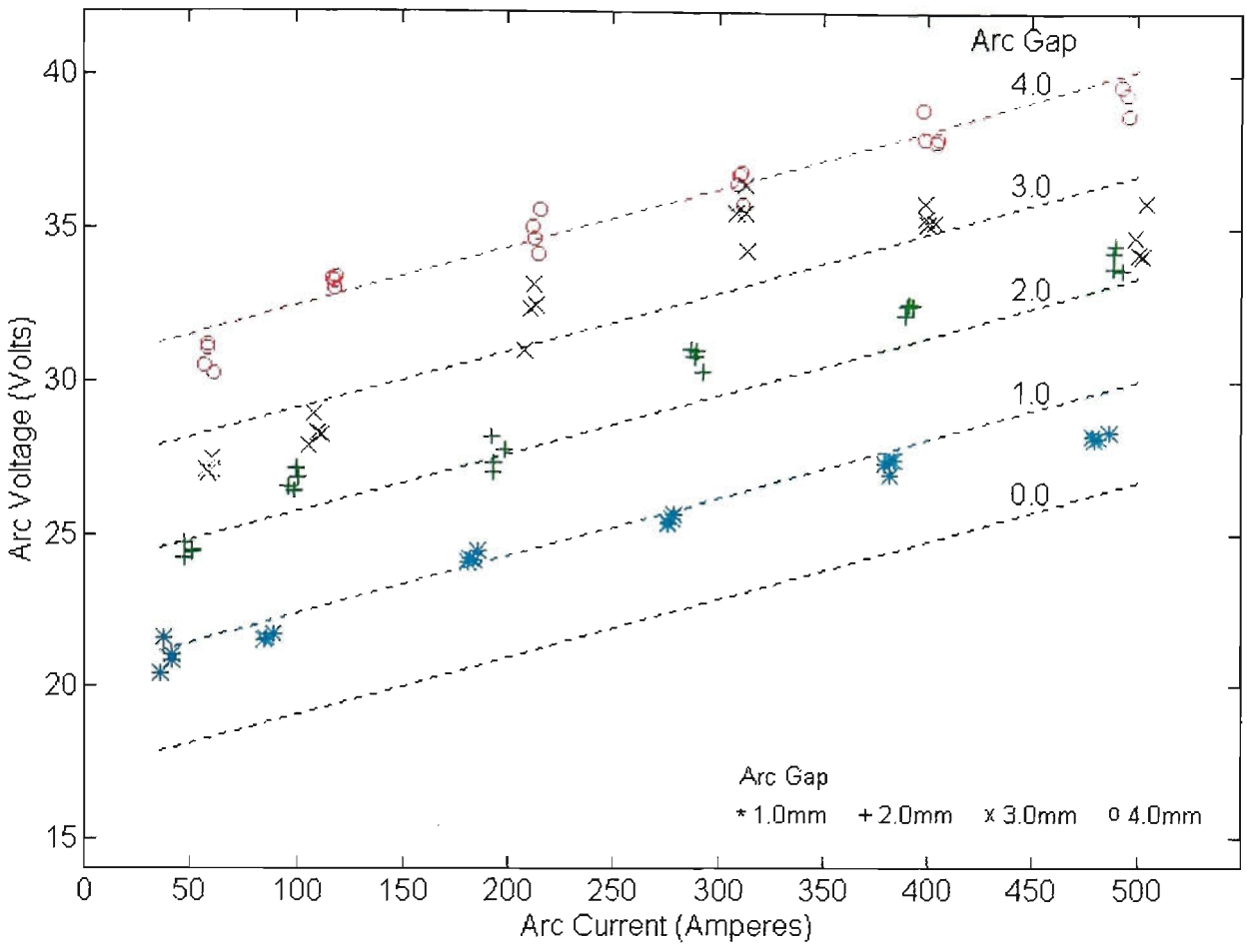

Figure 8.13 V-I characteristics for CO_2, 1.2mm MS electrode positive

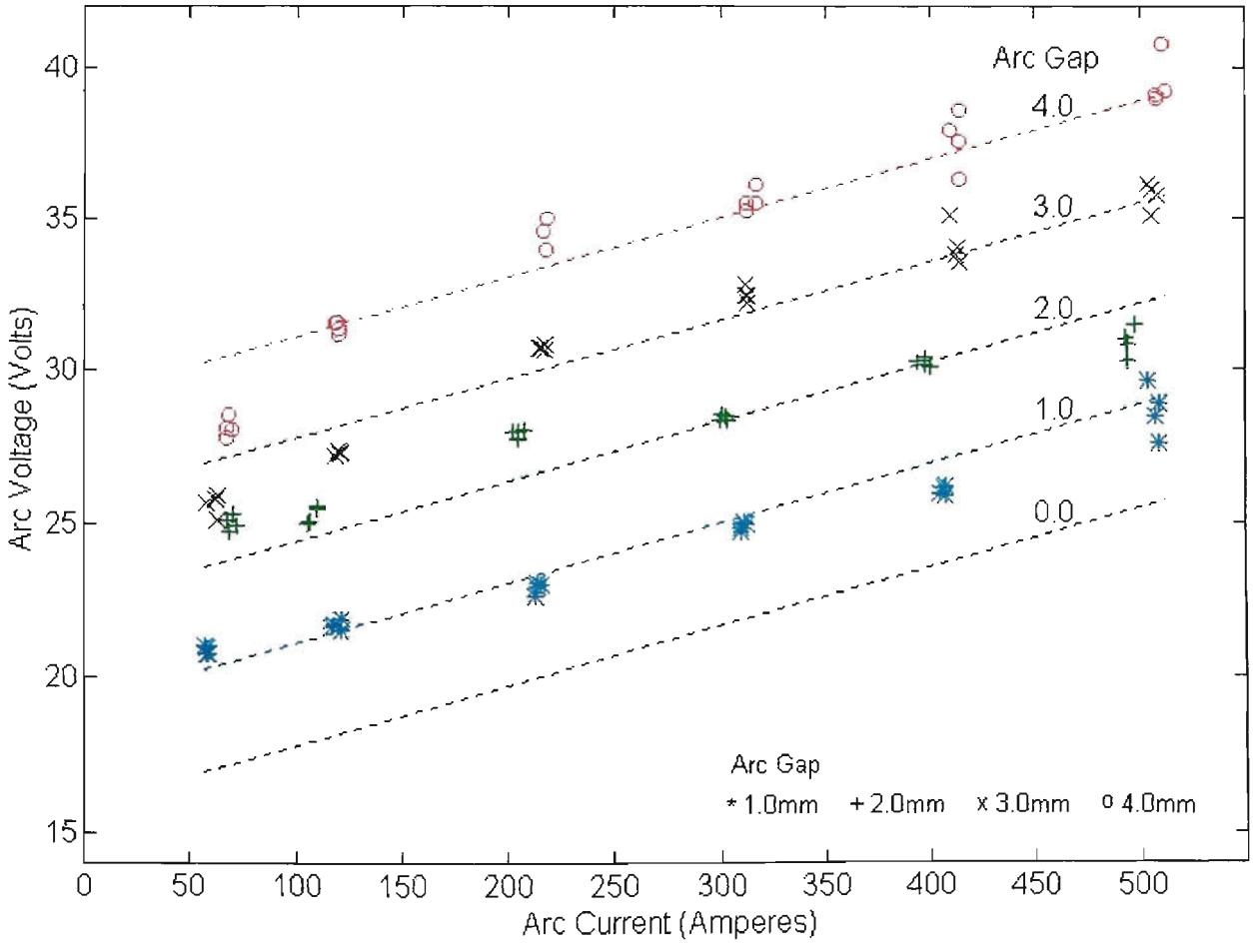

Figure 8.14 V-I characteristics for CO_2, 1.6mm MS electrode positive

Appendix 9

This appendix contains Figures relevant to Chapter 9.

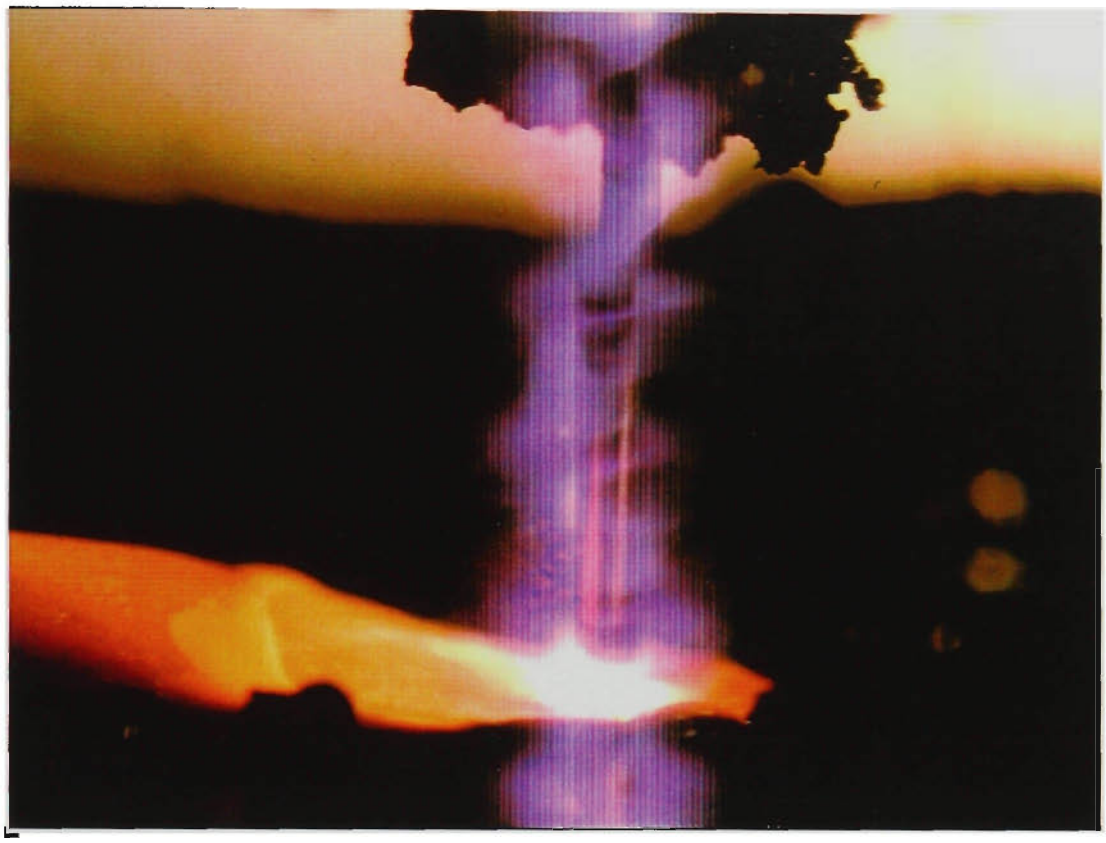

Figure 9.2 Exposure with 2.5kW floodlighting

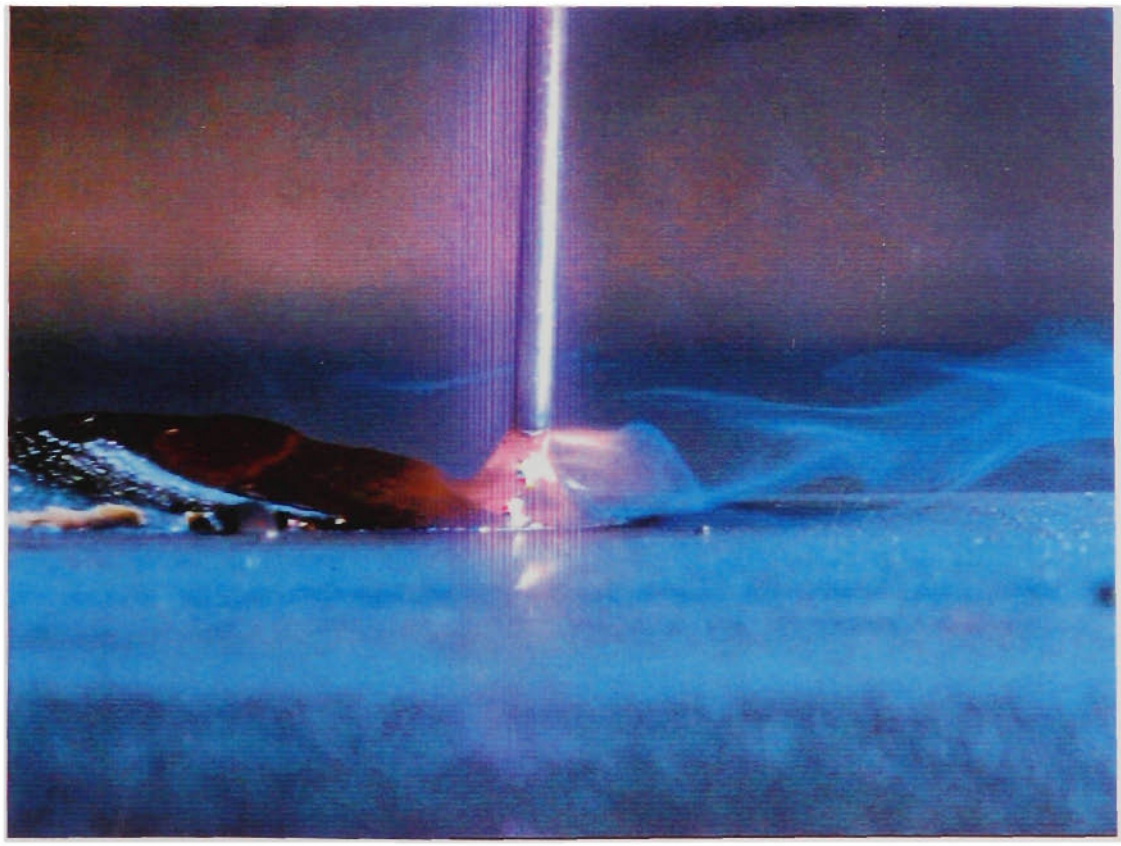

Figure 9.3 Exposure with commercial xenon flash unit

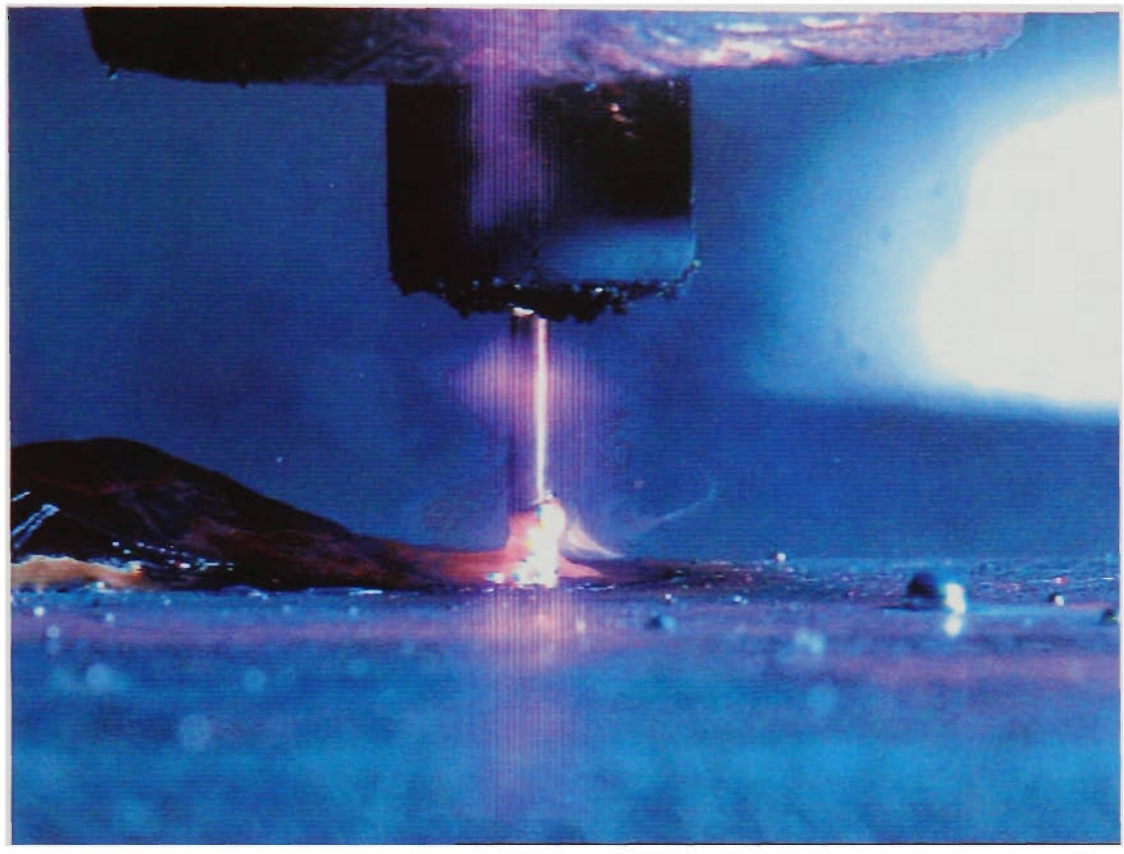

Figure 9.4 Exposure with commercial xenon flash unit

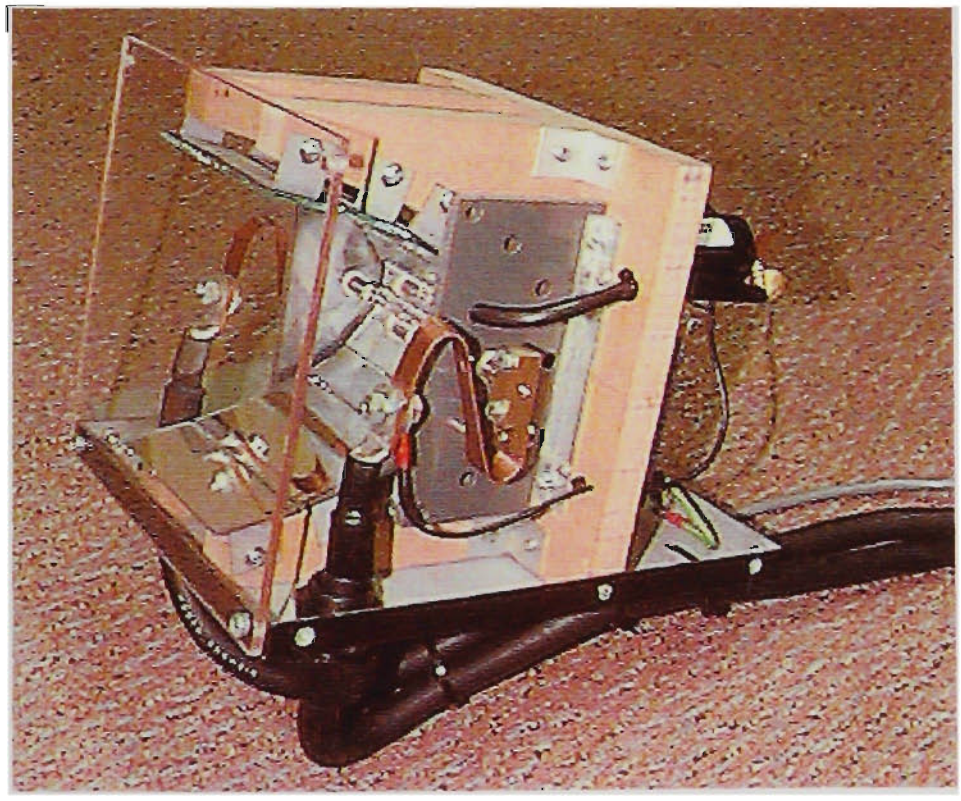

Figure 9.5 Photograph of first-design flash head

(cover removed)

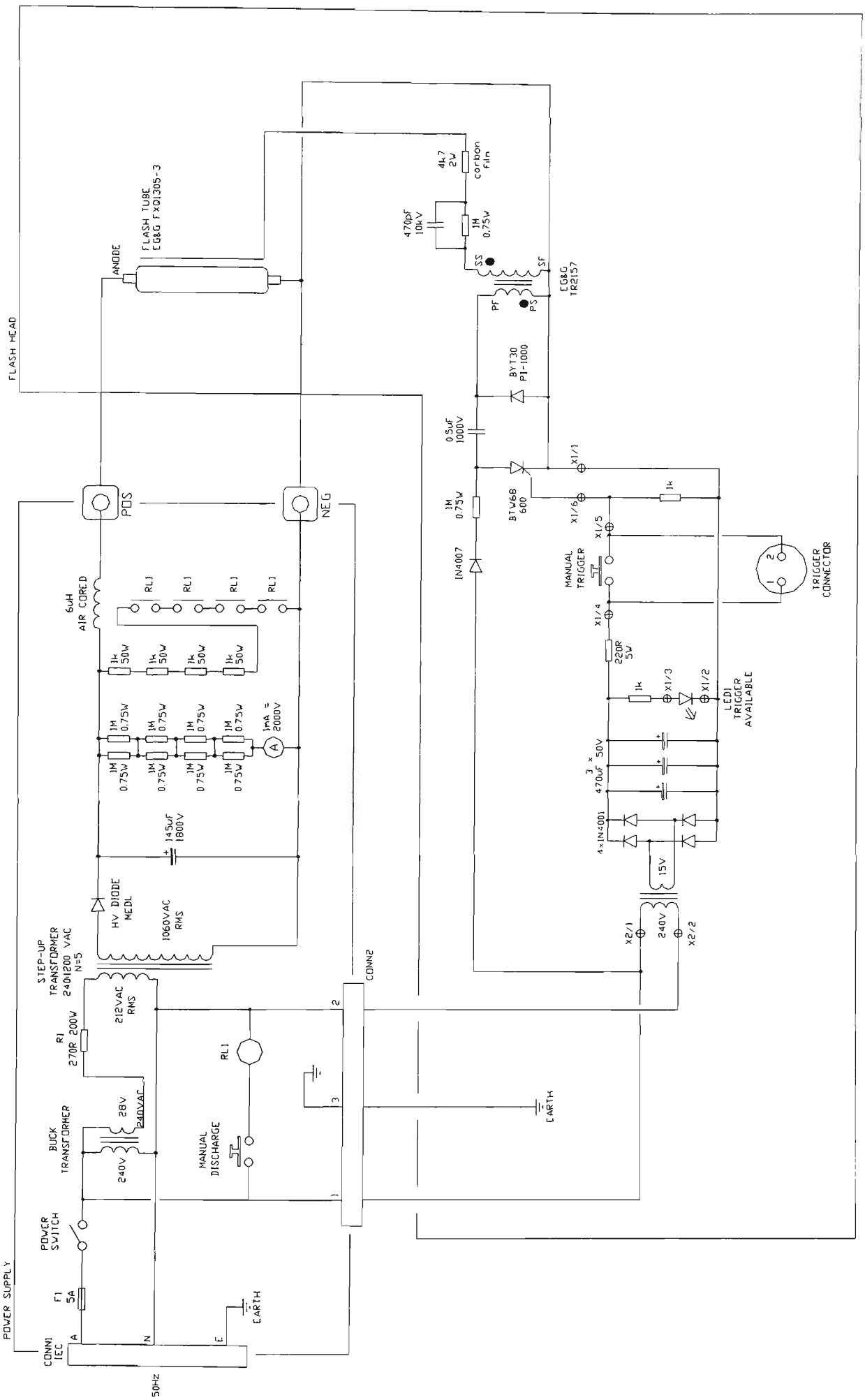

Figure 9.6 Schematic diagram of flash unit

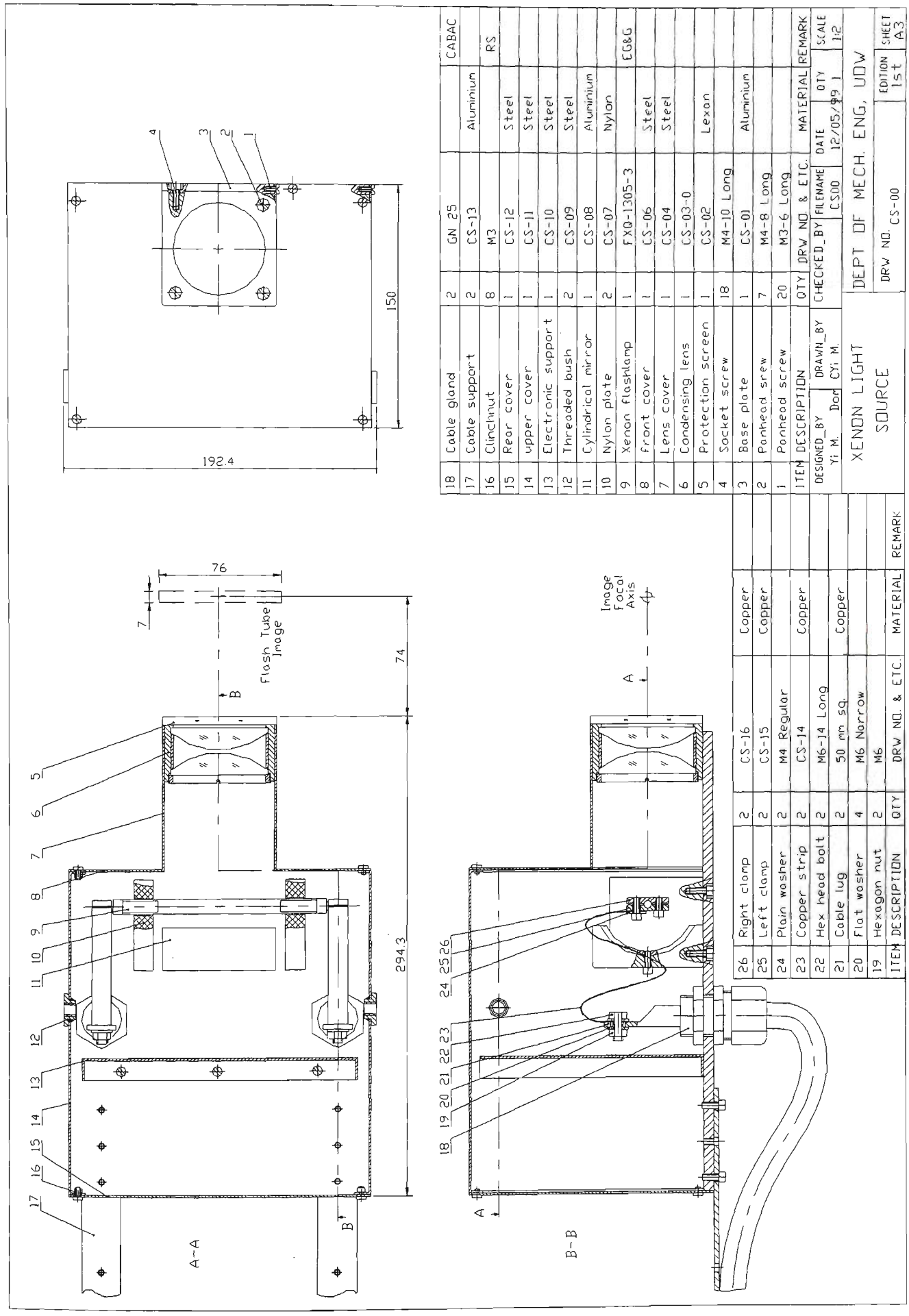

ITEM	DESCRIPTION	QTY	DRW NO. & ETC.	MATERIAL	REMARK
18	Cable gland	2	GN 25		CABAC
17	Cable support	2	CS-13	Aluminium	
16	Clinchnut	8	M3		RS
15	Rear cover	1	CS-12	Steel	
14	upper cover	1	CS-11	Steel	
13	Electronic support	1	CS-10	Steel	
12	Threaded bush	2	CS-09	Steel	
11	Cylindrical mirror	1	CS-08	Aluminium	
10	Nylon plate	2	CS-07	Nylon	
9	Xenon flashlamp	1	FXQ-1305-3		EG&G
8	Front cover	1	CS-06	Steel	
7	Lens cover	1	CS-04	Steel	
6	Condensing lens	1	CS-03-0		
5	Protection screen	1	CS-02	Lexan	
4	Socket screw	18	M4-10 Long		
3	Base plate	1	CS-01	Aluminium	
2	Panhead screw	7	M4-8 Long		
1	Panhead screw	20	M3-6 Long		
26	Right clamp	2	CS-16	Copper	
25	Left clamp	2	CS-15	Copper	
24	Plain washer	2	M4 Regular		
23	Copper strip	2	CS-14	Copper	
22	Hex head bolt	2	M6-14 Long		
21	Cable lug	2	50 mm sq.	Copper	
20	Flat washer	4	M6 Narrow		
19	Hexagon nut	2	M6		

Figure 9.9 Layout of second-design flash head (courtesy Y. Mao)

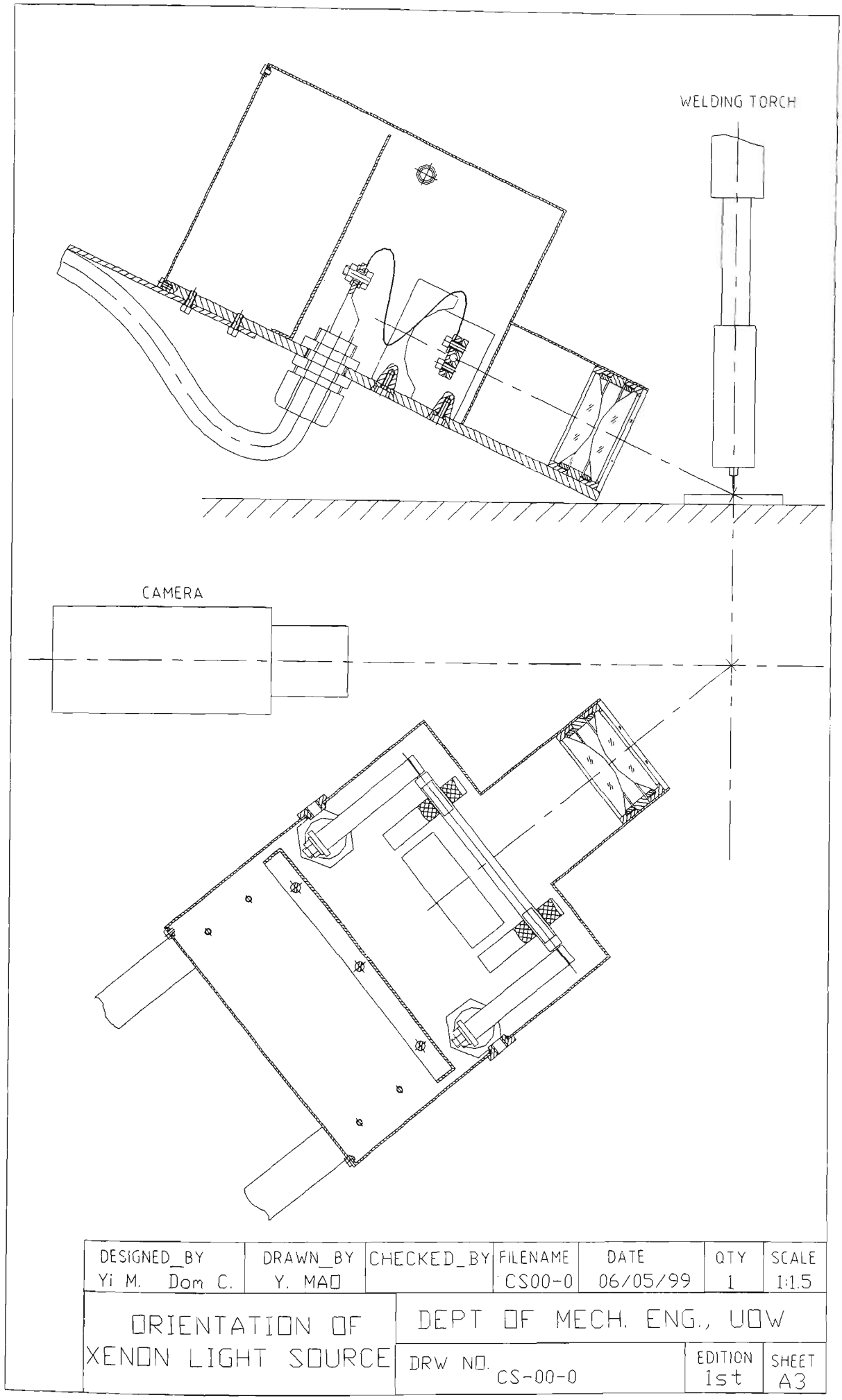

Figure 9.8 Optical Alignment of second-design flash head (courtesy Y. Mao)

Appendix 10

This appendix contains Figures relevant to Chapter 10.

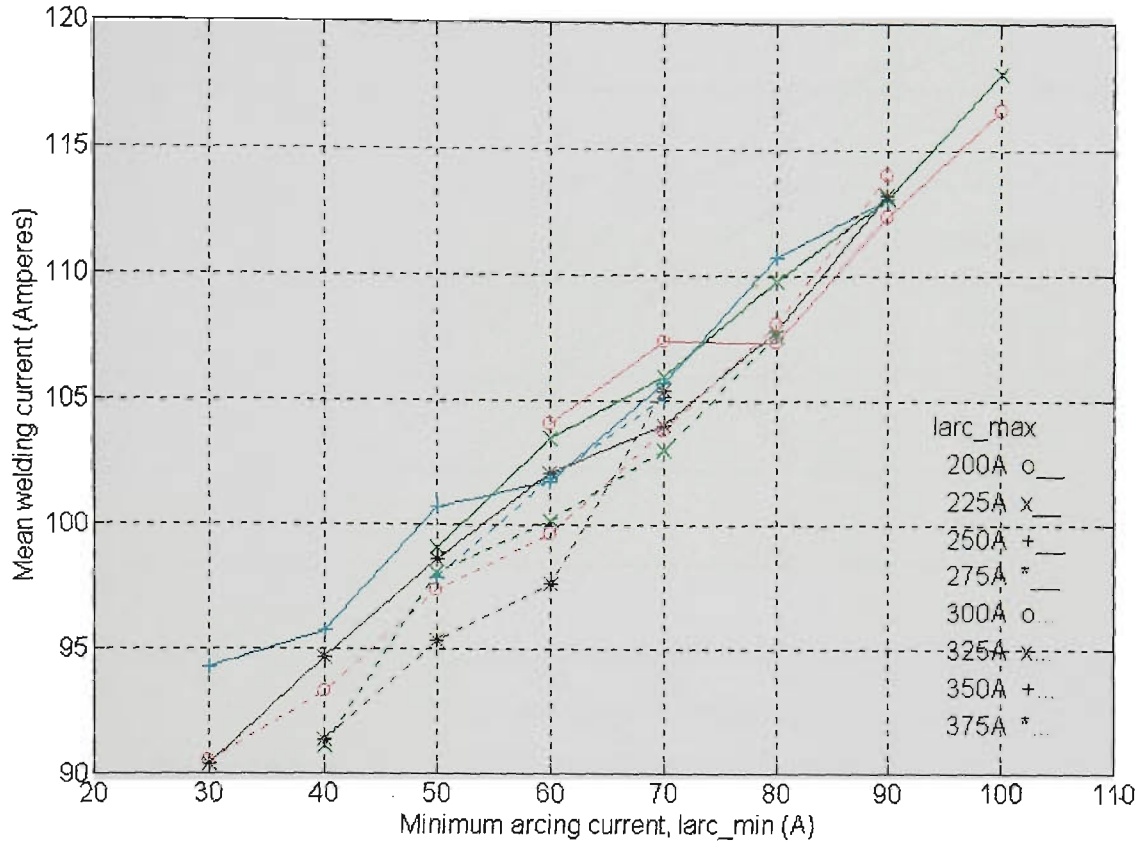

Figure 10.3 Mean welding current vs Iarc_min & Iarc_max
(Ar-23%CO_2, CTWD=16mm, WFR=5.7m/min, Travel=390mm/min)

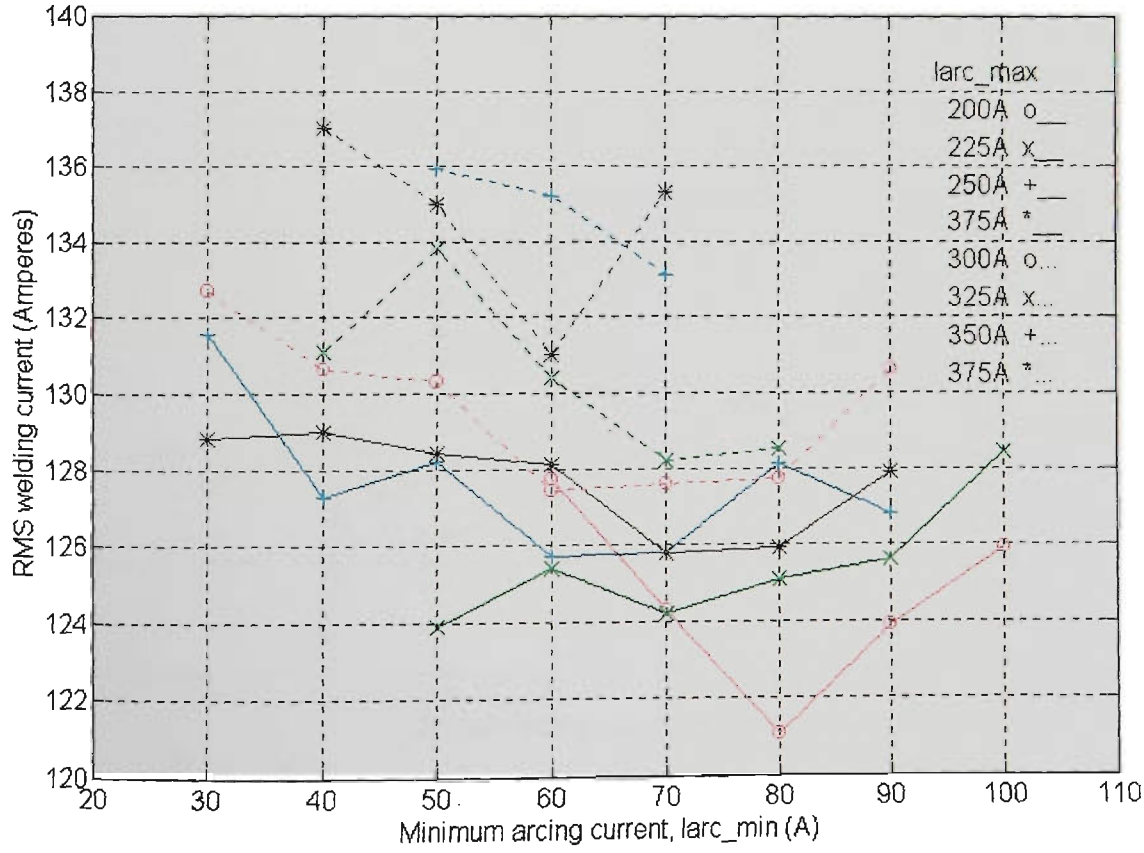

Figure 10.4 RMS welding current vs Iarc_min & Iarc_max
(Ar-23%CO_2, CTWD=16mm, WFR=5.7m/min, Travel=390mm/min)

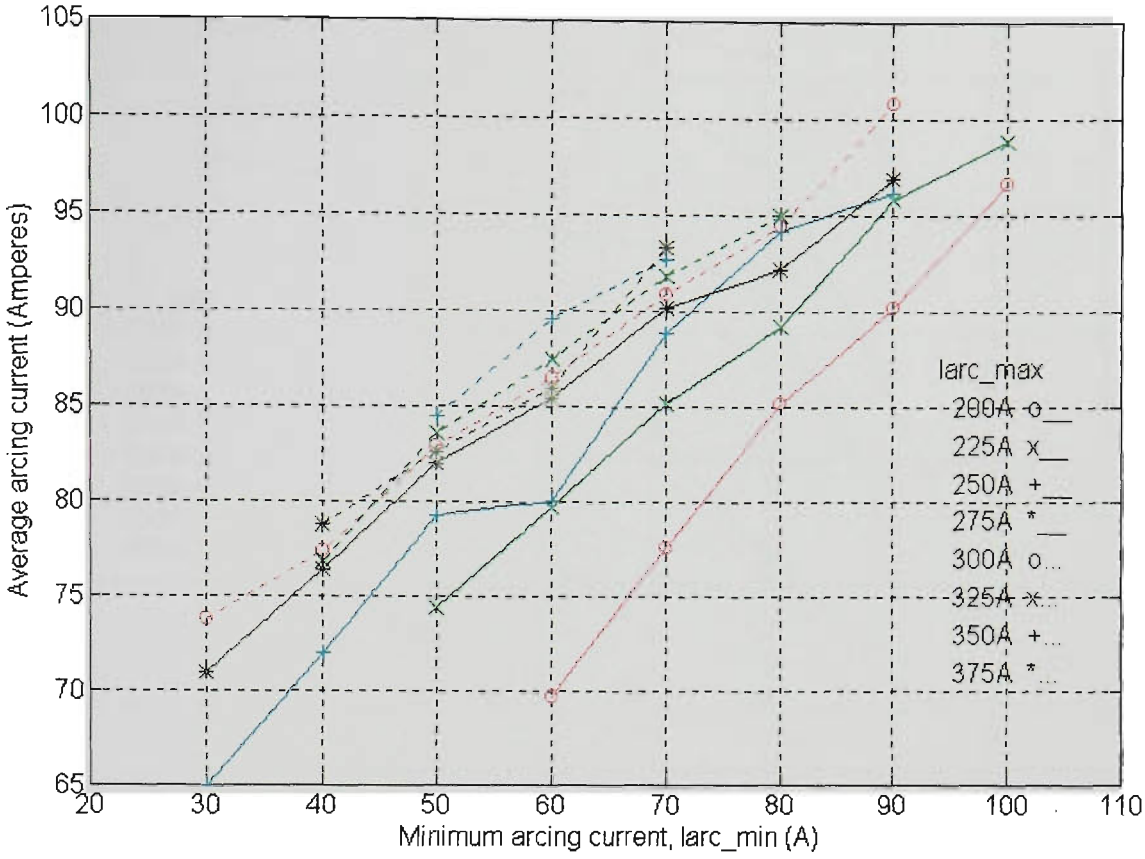

Figure 10.5 Average arcing current vs Iarc_min & Iarc_max

(Ar-23%CO_2, CTWD=16mm, WFR=5.7m/min, Travel=390mm/min)

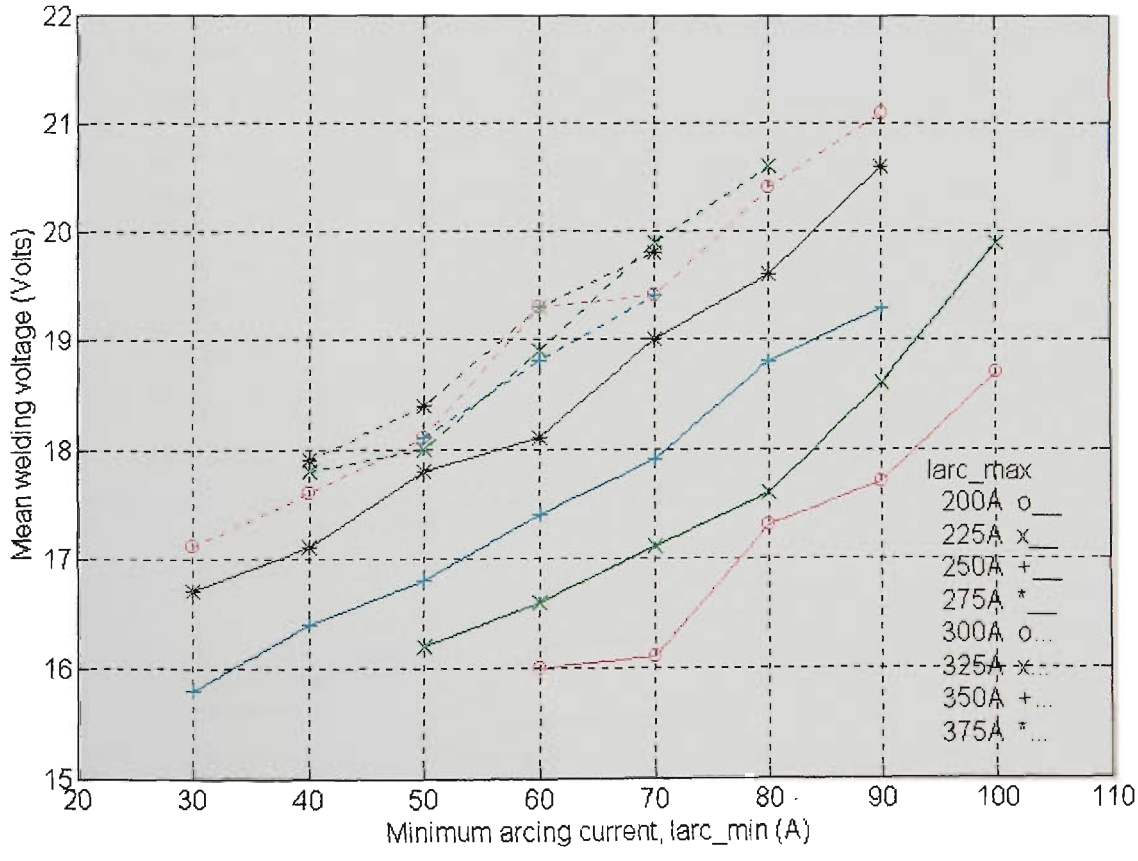

Figure 10.6 Mean voltage vs Iarc_min & Iarc_max

(Ar-23%CO_2, CTWD=16mm, WFR=5.7m/min, Travel=390mm/min)

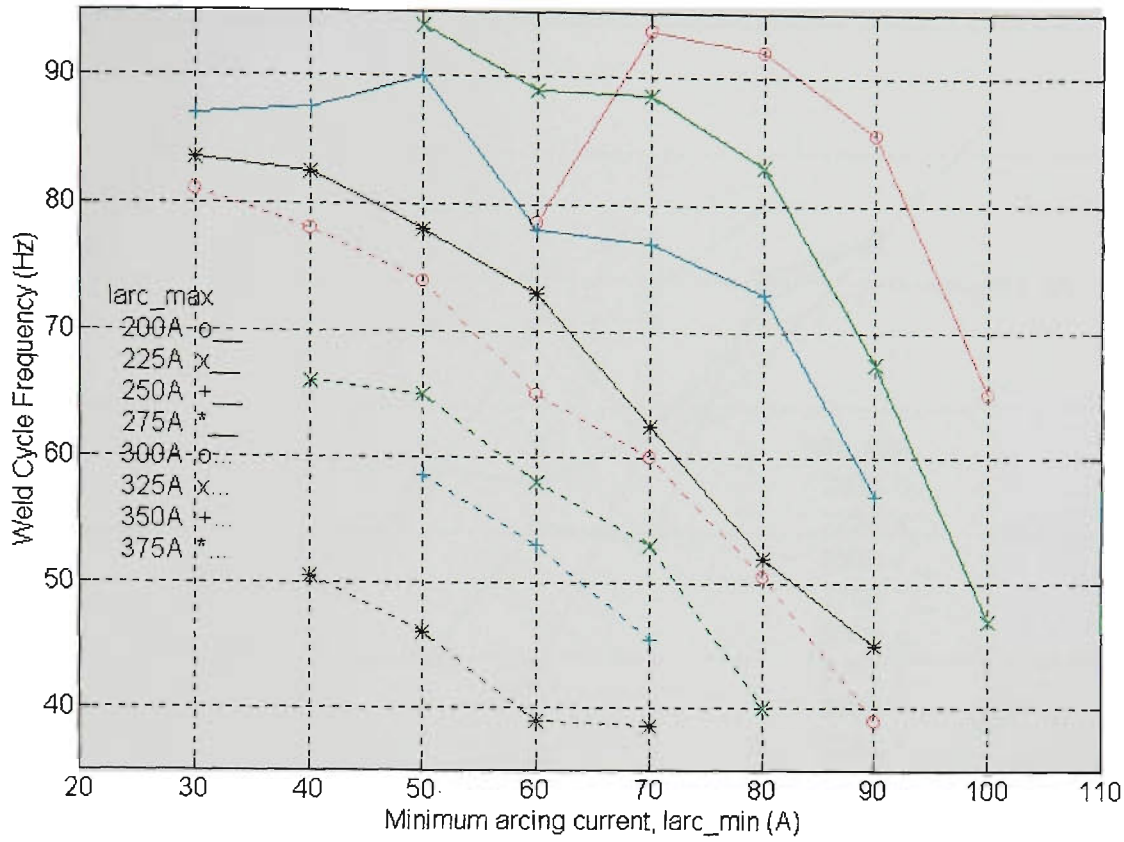

Figure 10.7 Average dipping frequency vs Iarc_min & Iarc_max
(Ar-23%CO_2, CTWD=16mm, WFR=5.7m/min, Travel=390mm/min)

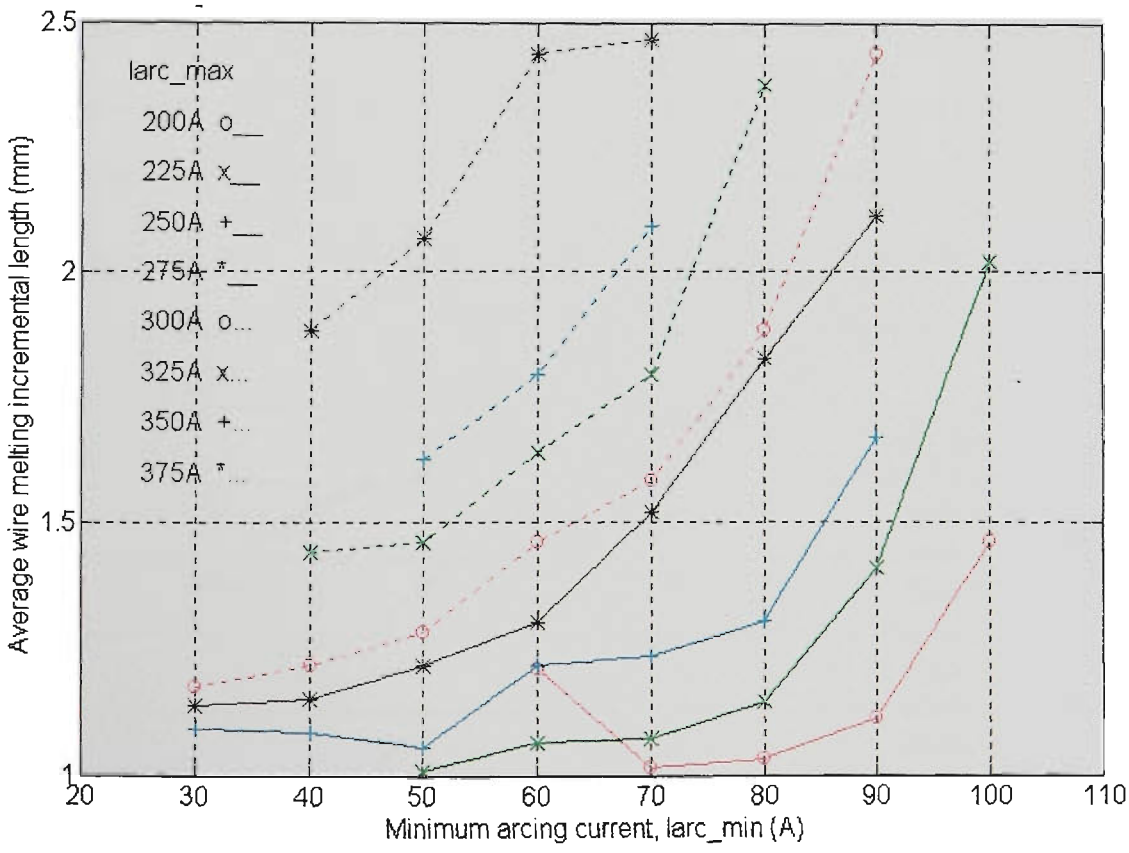

Figure 10.8 Avg wire melting incremental length ΔL vs Iarc_min & Iarc_max
(Ar-23%CO_2, CTWD=16mm, WFR=5.7m/min, Travel=390mm/min)

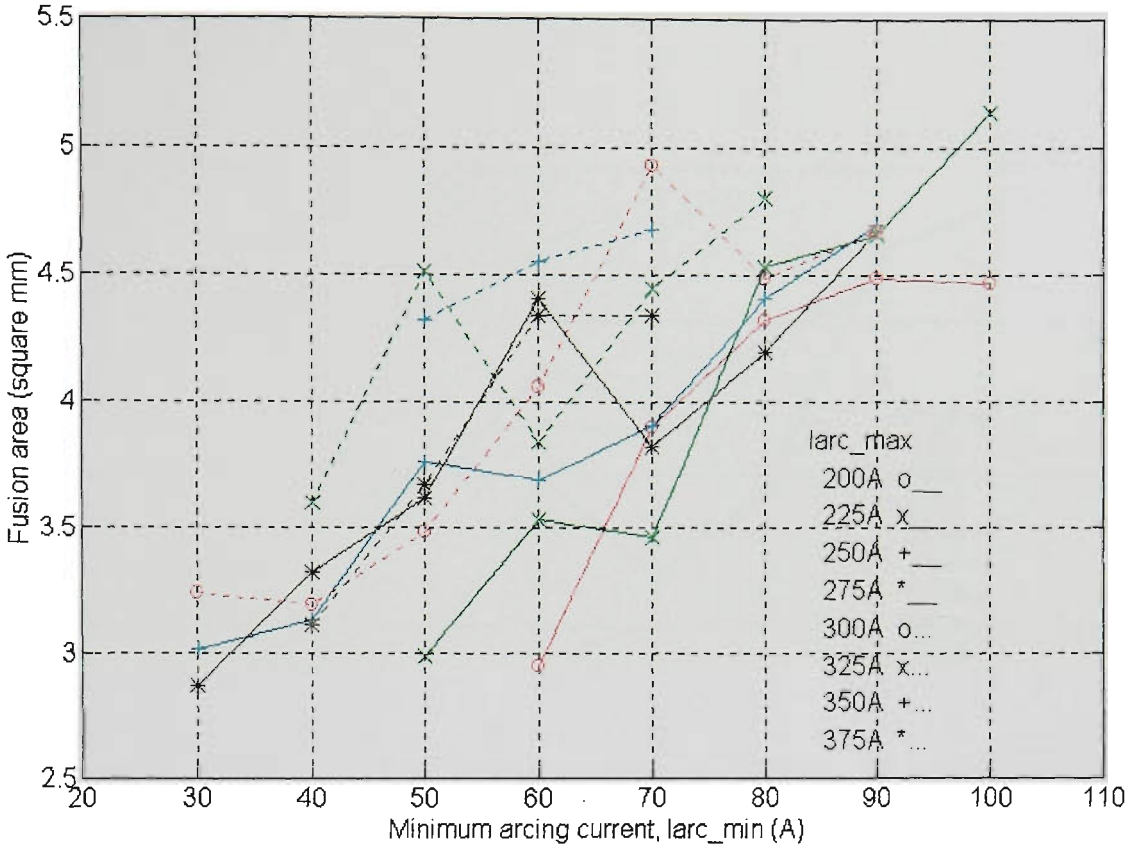

Figure 10.9 Fusion area vs Iarc_min & Iarc_max

(Ar-23%CO_2, CTWD=16mm, WFR=5.7m/min, Travel=390mm/min)

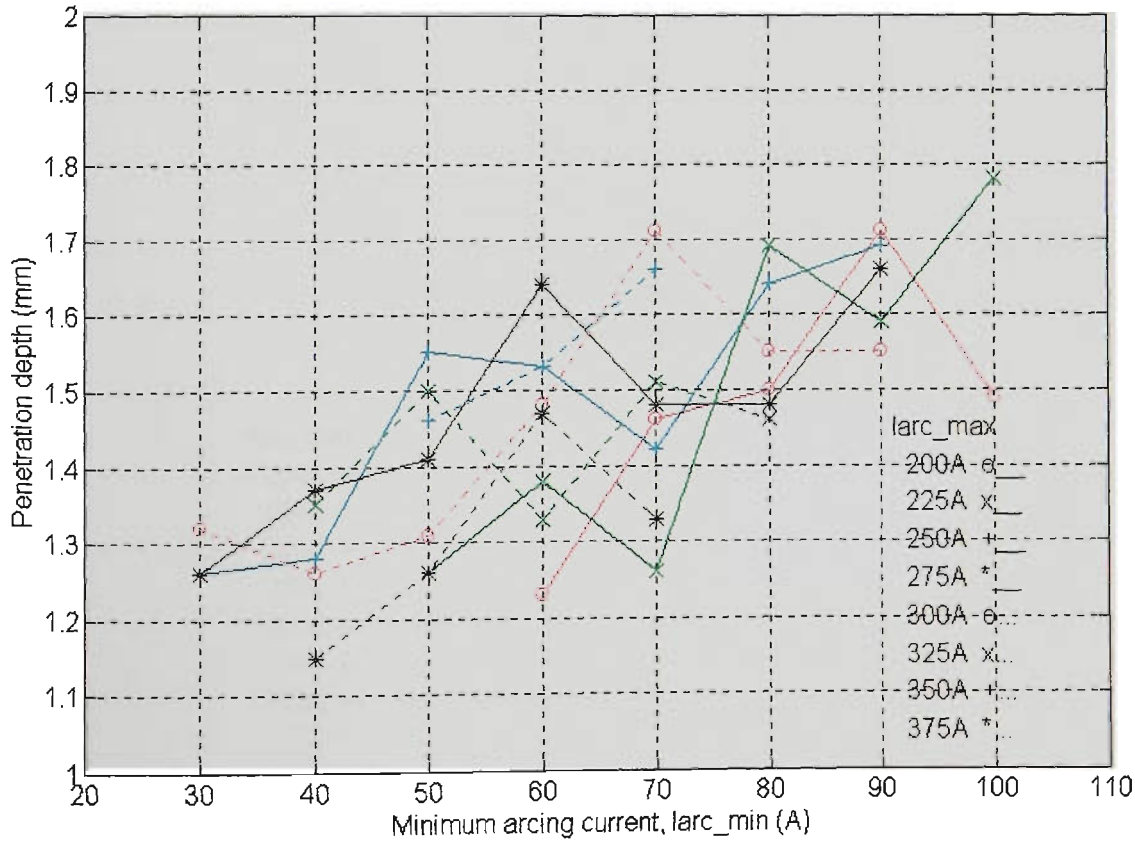

Figure 10.10 Penetration depth vs Iarc_min & Iarc_max

(Ar-23%CO_2, CTWD=16mm, WFR=5.7m/min, Travel=390mm/min)

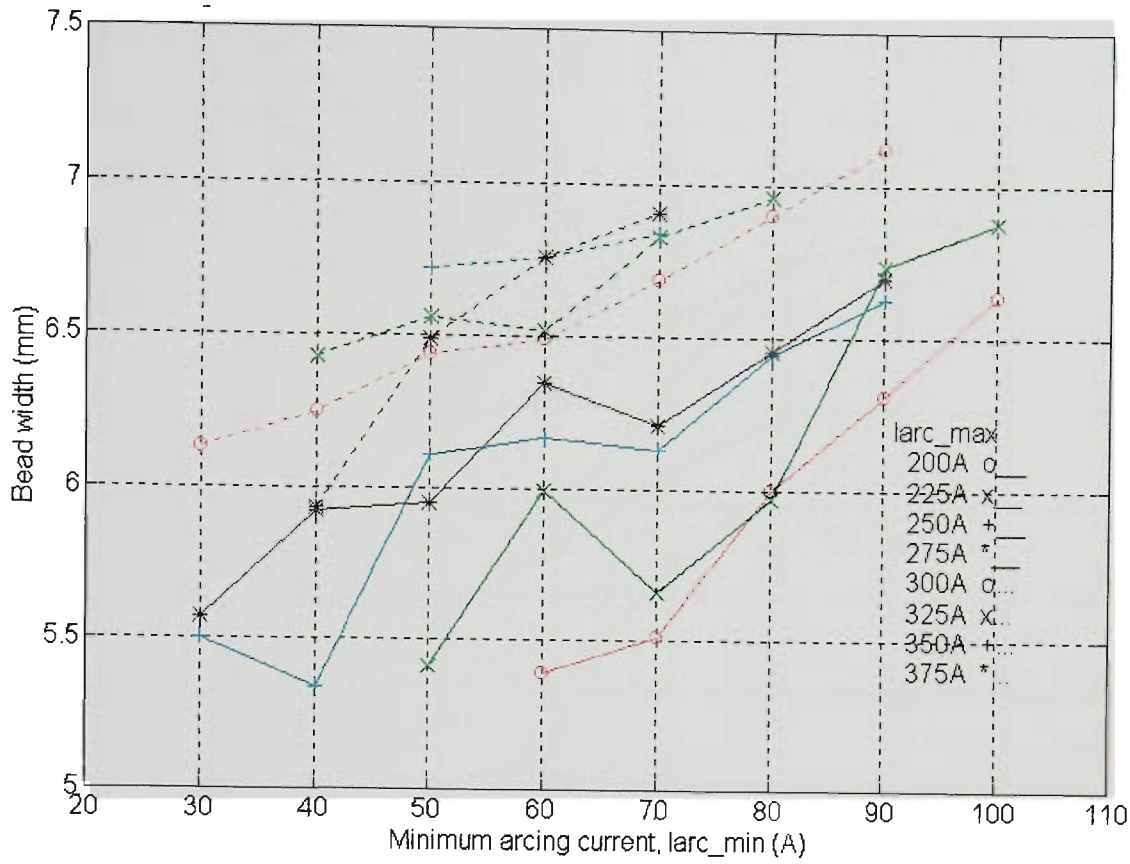

Figure 10.11 Weld bead width vs Iarc_min & Iarc_max
(Ar-23%CO_2, CTWD=16mm, WFR=5.7m/min, Travel=390mm/min)

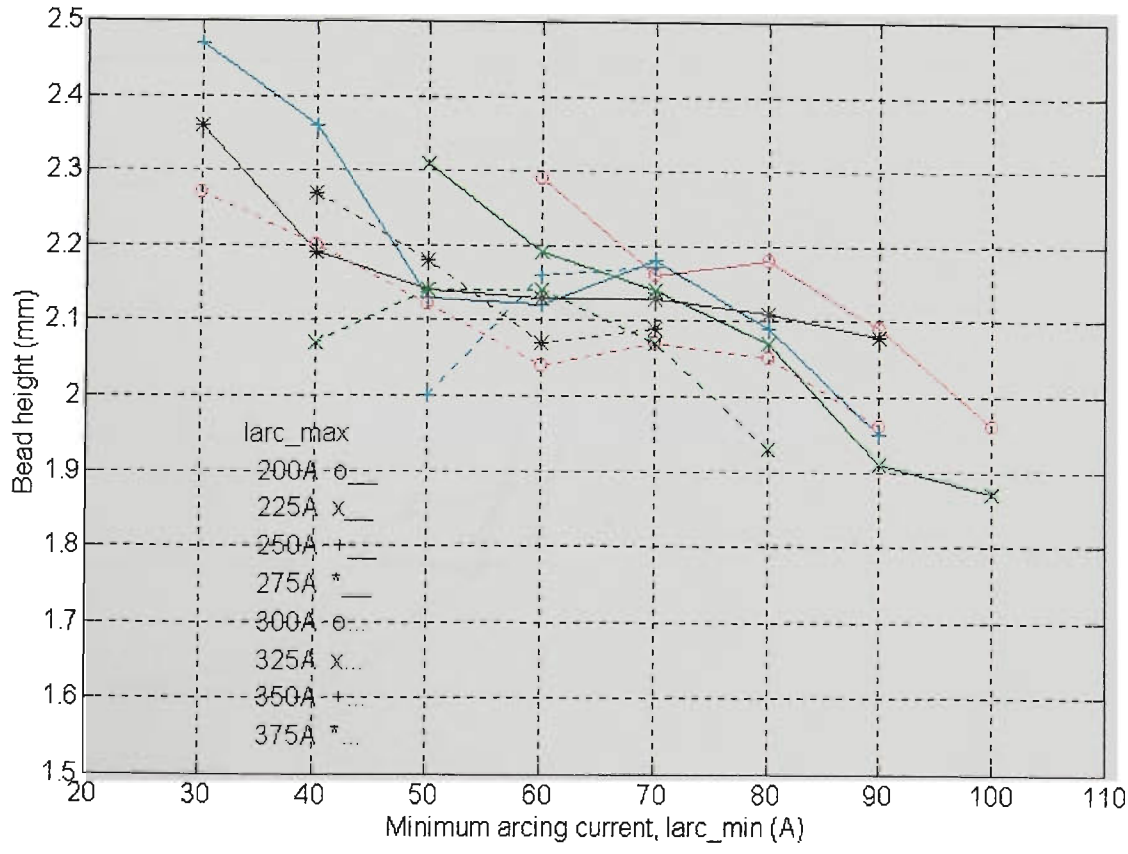

Figure 10.12 Weld bead height vs Iarc_min & Iarc_max
(Ar-23%CO_2, CTWD=16mm, WFR=5.7m/min, Travel=390mm/min)

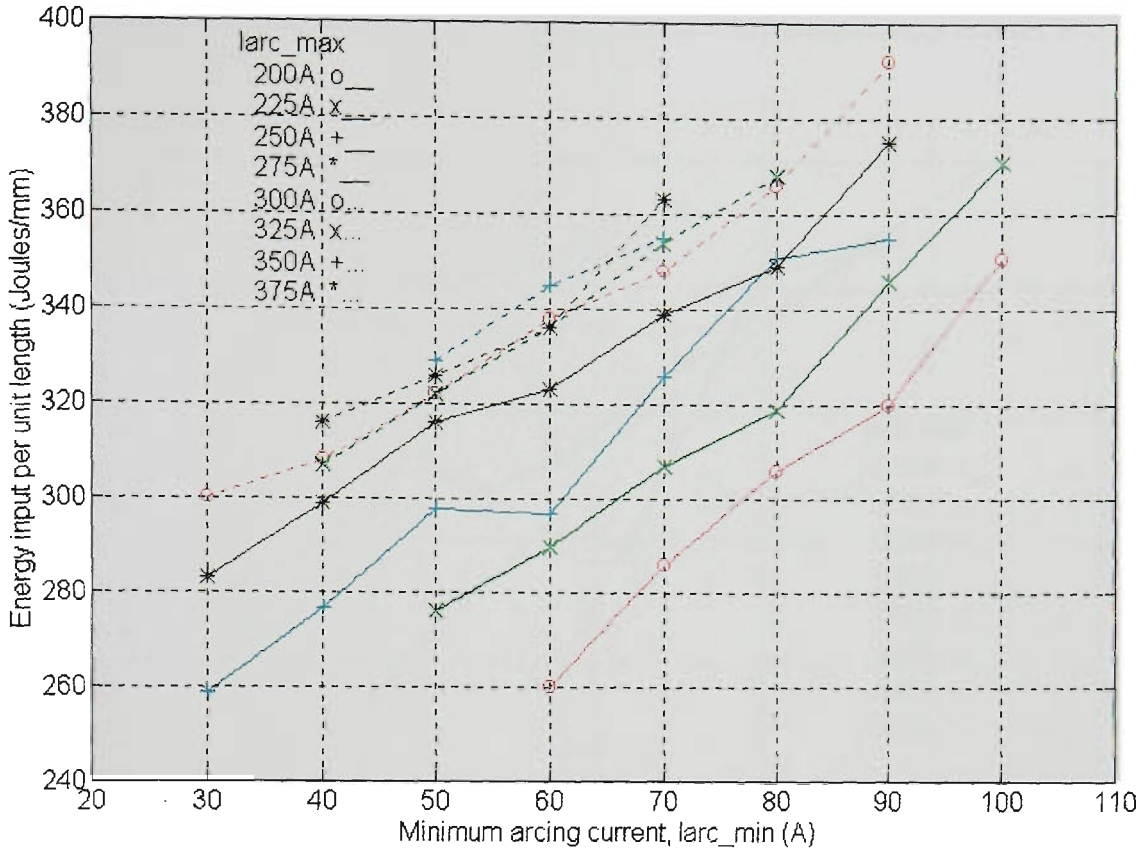

Figure 10.13 Energy input per unit length of weld vs Iarc_min & Iarc_max ($Ar-23\%CO_2$, CTWD=16mm, WFR=5.7m/min, Travel=390mm/min)

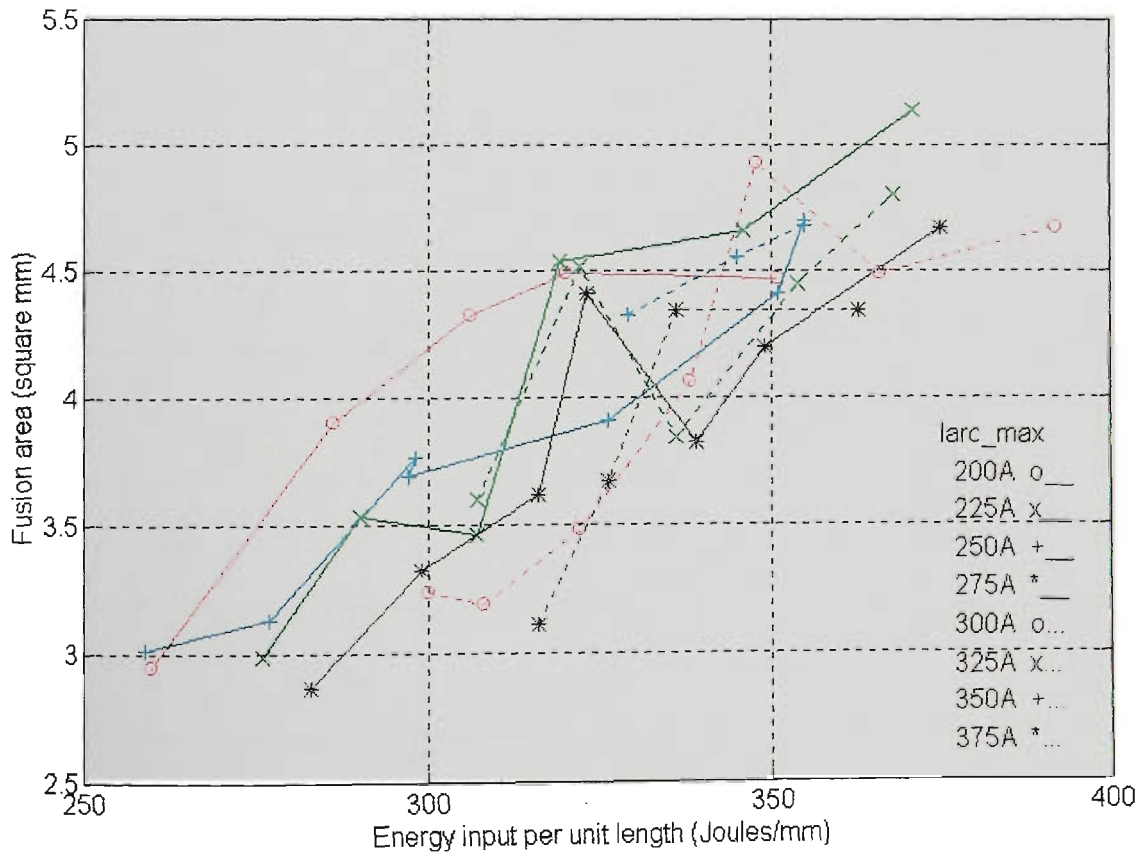

Figure 10.14 Fusion area vs Energy input per unit length of weld ($Ar-23\%CO_2$, CTWD=16mm, WFR=5.7m/min, Travel=390mm/min)

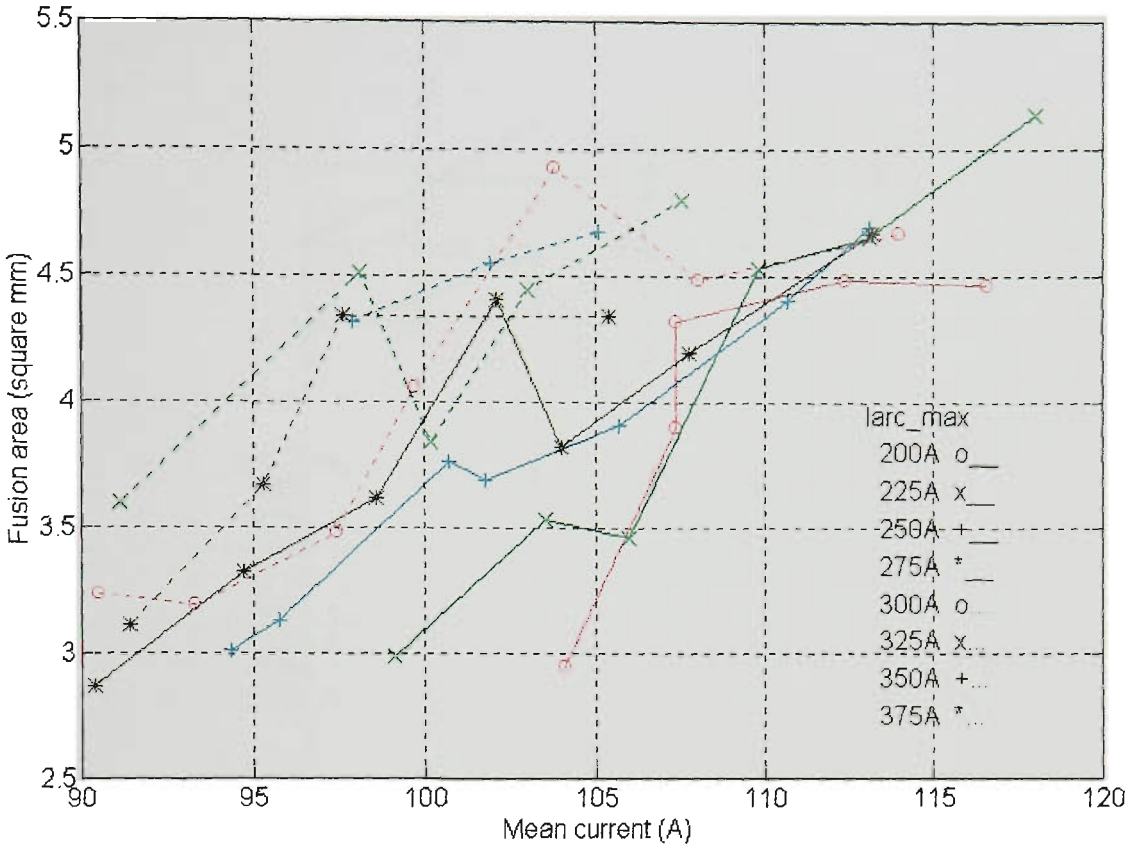

Figure 10.15 Fusion area vs Mean welding current

(Ar-23%CO_2, CTWD=16mm, WFR=5.7m/min, Travel=390mm/min)

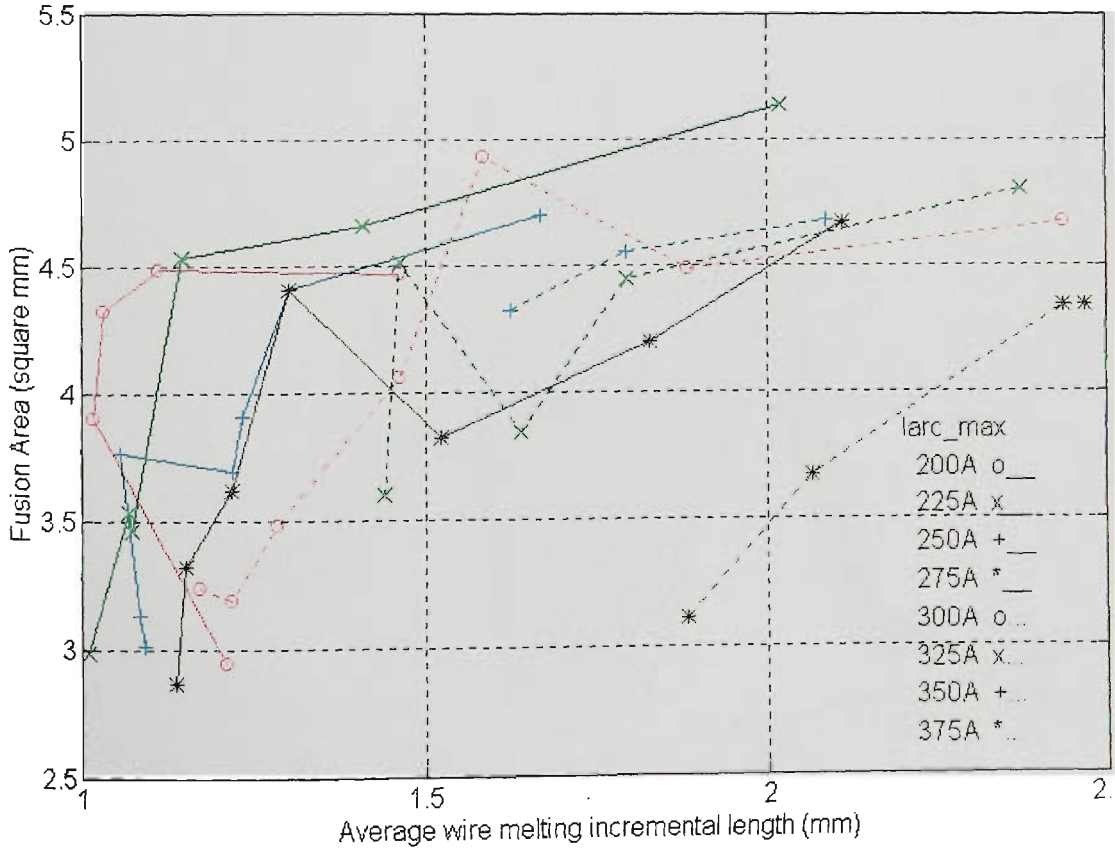

Figure 10.16 Fusion area vs Average wire melting incremental length ΔL

(Ar-23%CO_2, CTWD=16mm, WFR=5.7m/min, Travel=390mm/min)

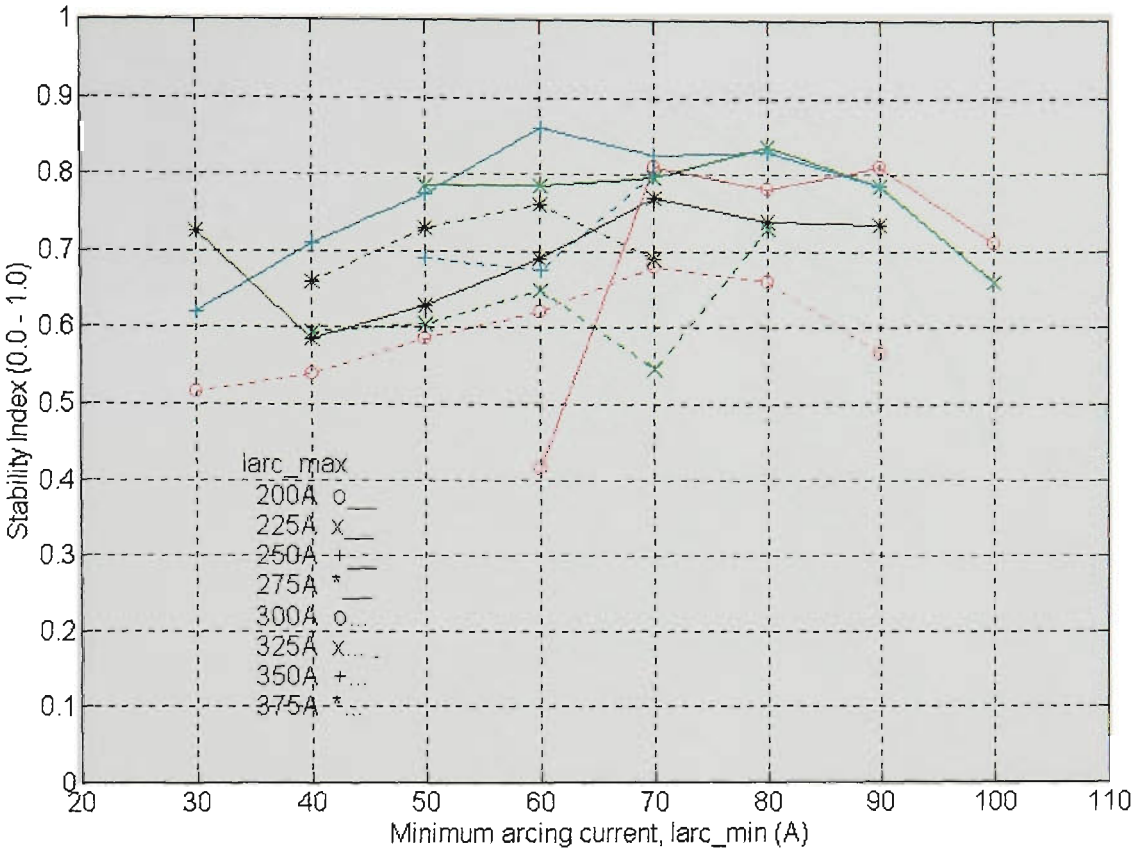

Figure 10.17 Stability index vs Iarc_min & Iarc_max (2D)

(Ar-23%CO_2, CTWD=16mm, WFR=5.7m/min, Travel=390mm/min)

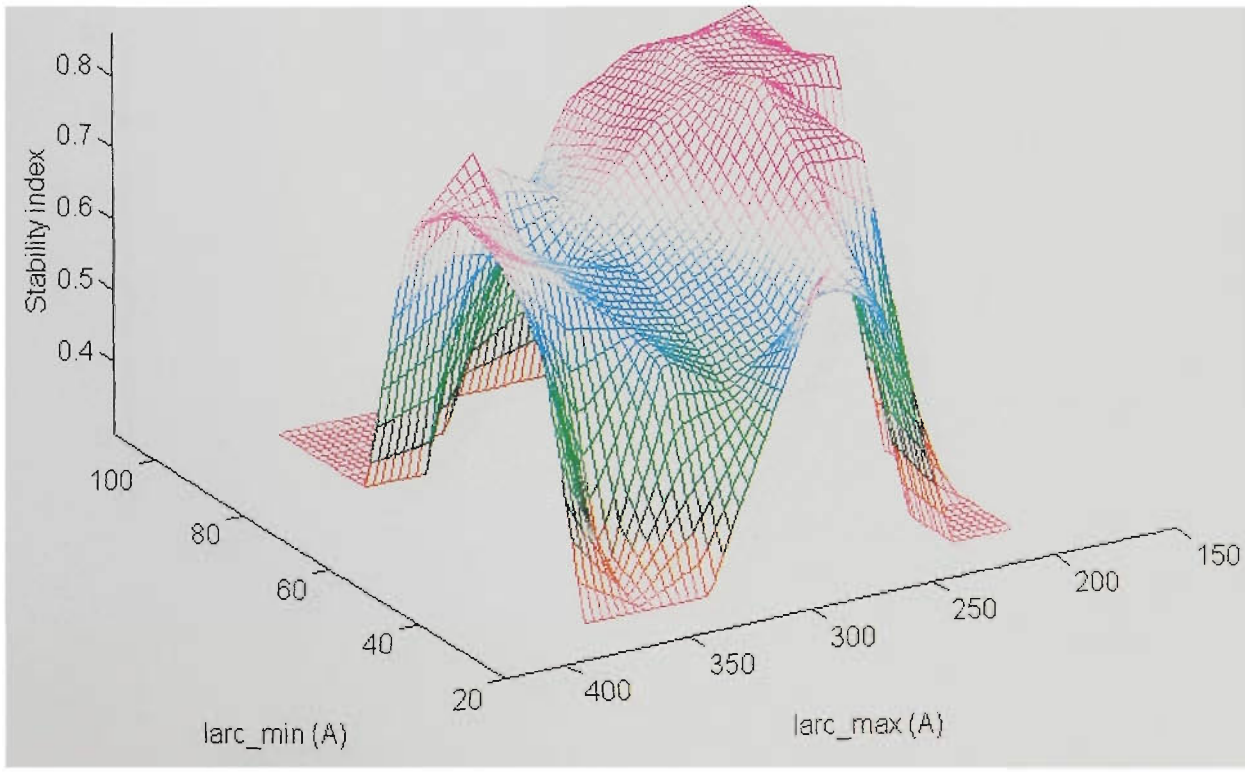

Figure 10.18 Stability index vs Iarc_min & Iarc_max (3D)

(Ar-23%CO_2, CTWD=16mm, WFR=5.7m/min, Travel=390mm/min)

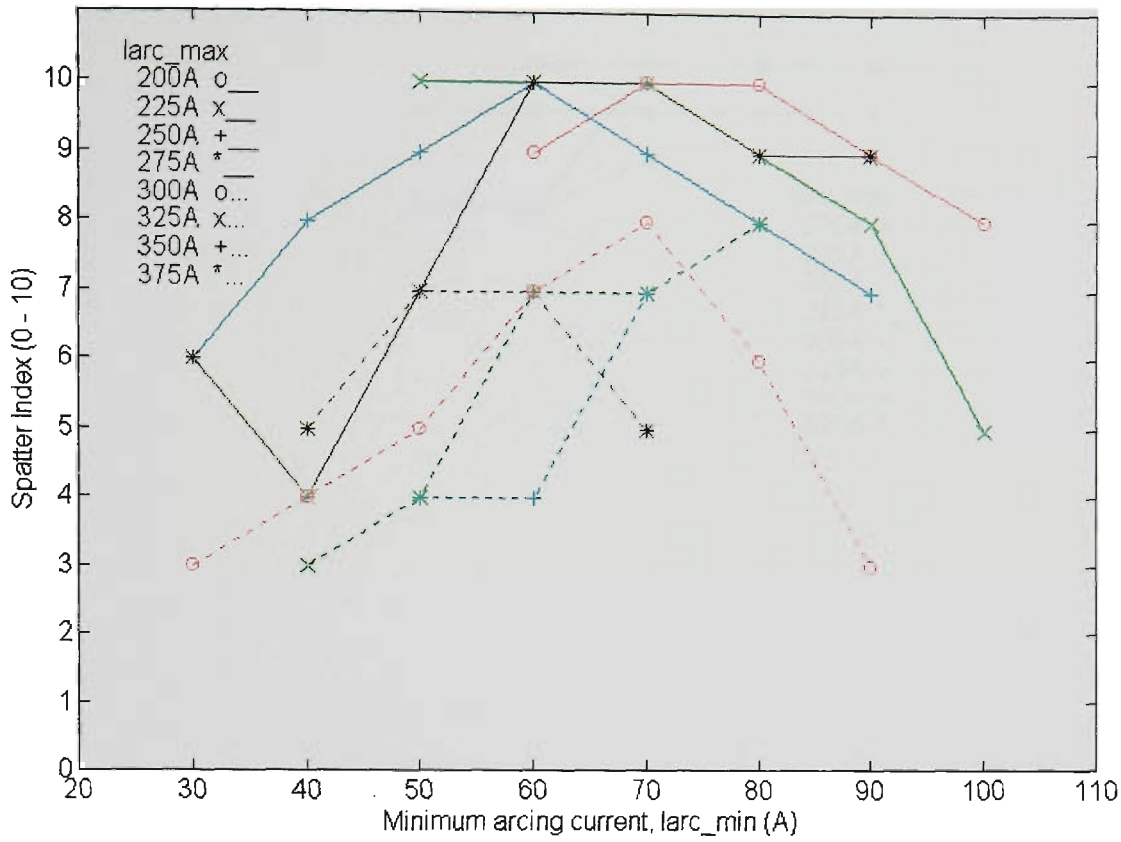

Figure 10.19 Spatter index vs Iarc_min & Iarc_max (2D)

(Ar-23%CO_2, CTWD=16mm, WFR=5.7m/min, Travel=390mm/min)

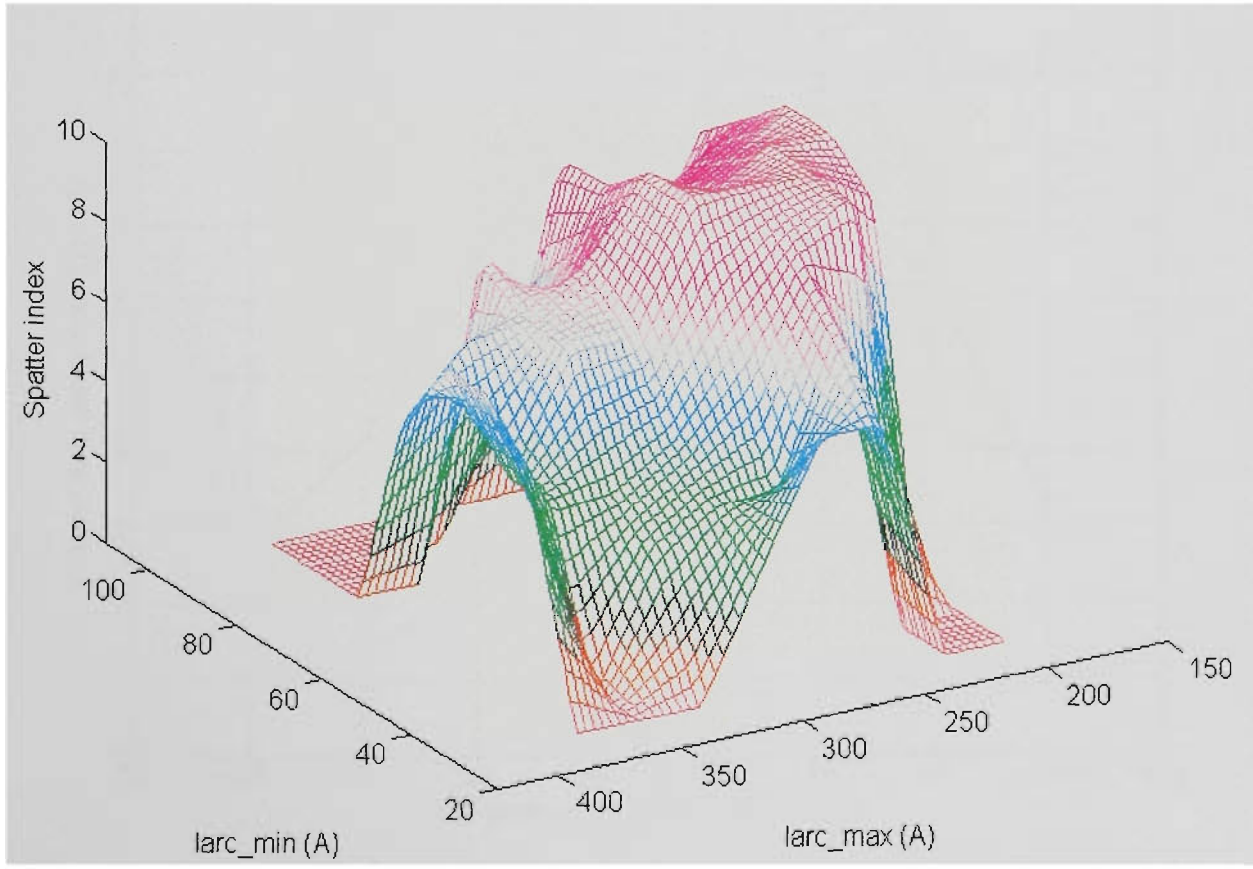

Figure 10.20 Spatter index vs Iarc_min & Iarc_max (3D)

(Ar-23%CO_2, CTWD=16mm, WFR=5.7m/min, Travel=390mm/min)

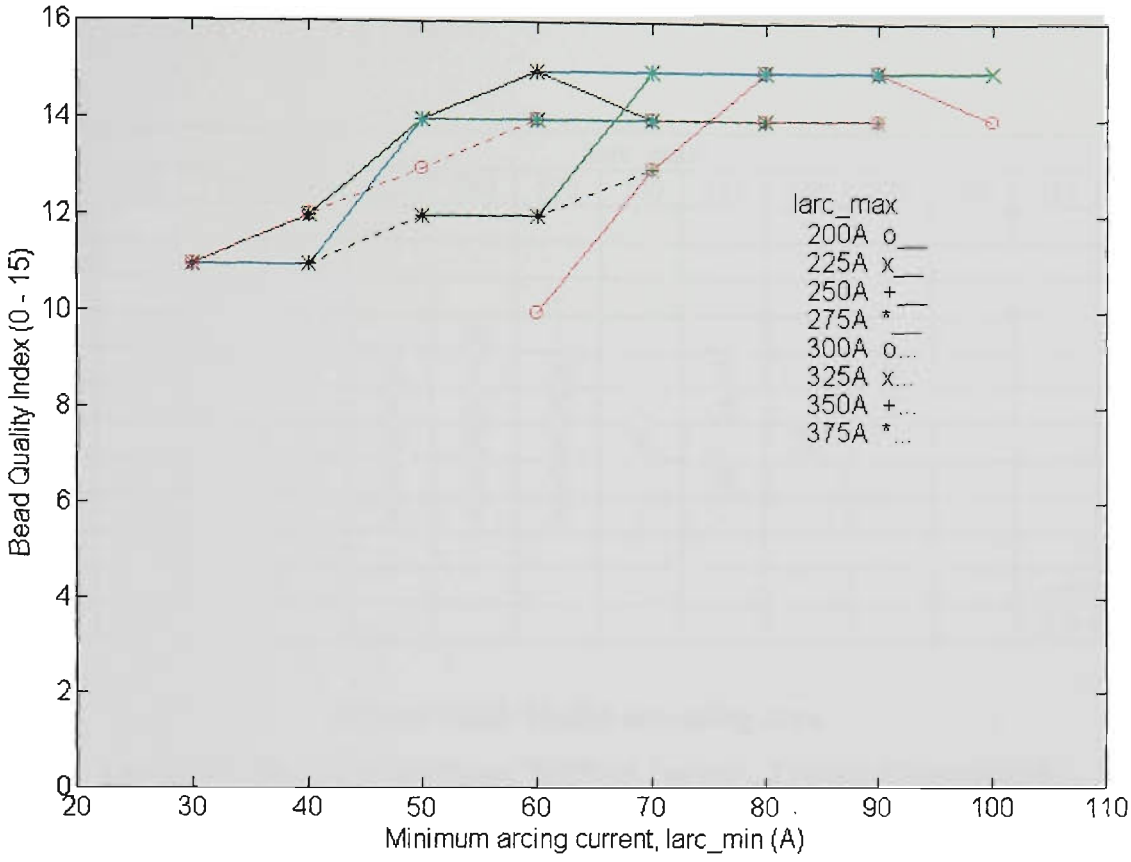

Figure 10.21 Bead quality index vs Iarc_min & Iarc_max
(Ar-23%CO_2, CTWD=16mm, WFR=5.7m/min, Travel=390mm/min)

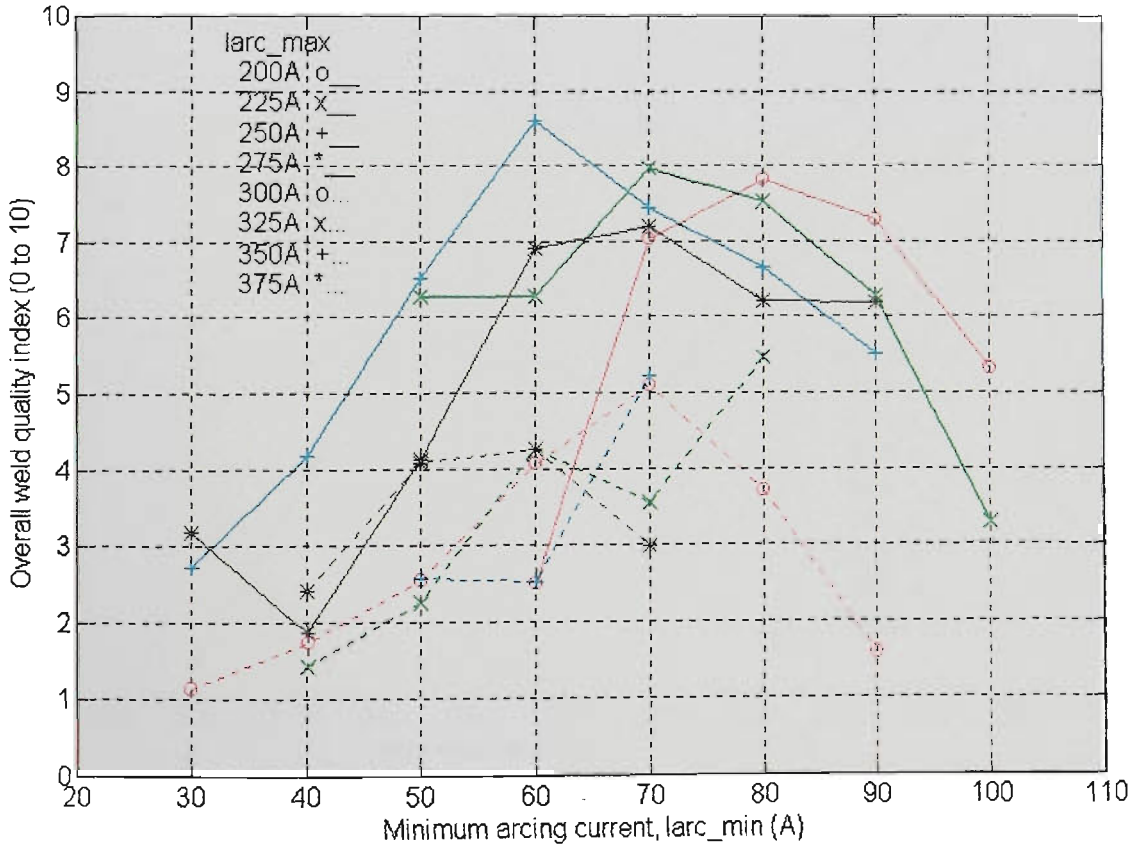

Figure 10.22 Weld overall quality index vs Iarc_min & Iarc_max
(Ar-23%CO_2, CTWD=16mm, WFR=5.7m/min, Travel=390mm/min)

Iarc_min	Iarc_max												
	150	175	200	225	250	275	300	325	350	375	400	425	450
10													
20													
30					-	-	-						
40					X	-	-	-		-			
50				X	X	X	-	X	-	X			
60			-	X	X	X	X	X	-	X			
70			X	X	X	X	X	-	X	-			
80			X	X	X	X	-	X					
90			X	X	X	X	-	-					
100			X	-									
110												- = tested	
120												X = useful	

Figure 10.23 Useful operating area

(Ar-23%CO_2, CTWD=16mm, WFR=5.7m/min, Travel=390mm/min)

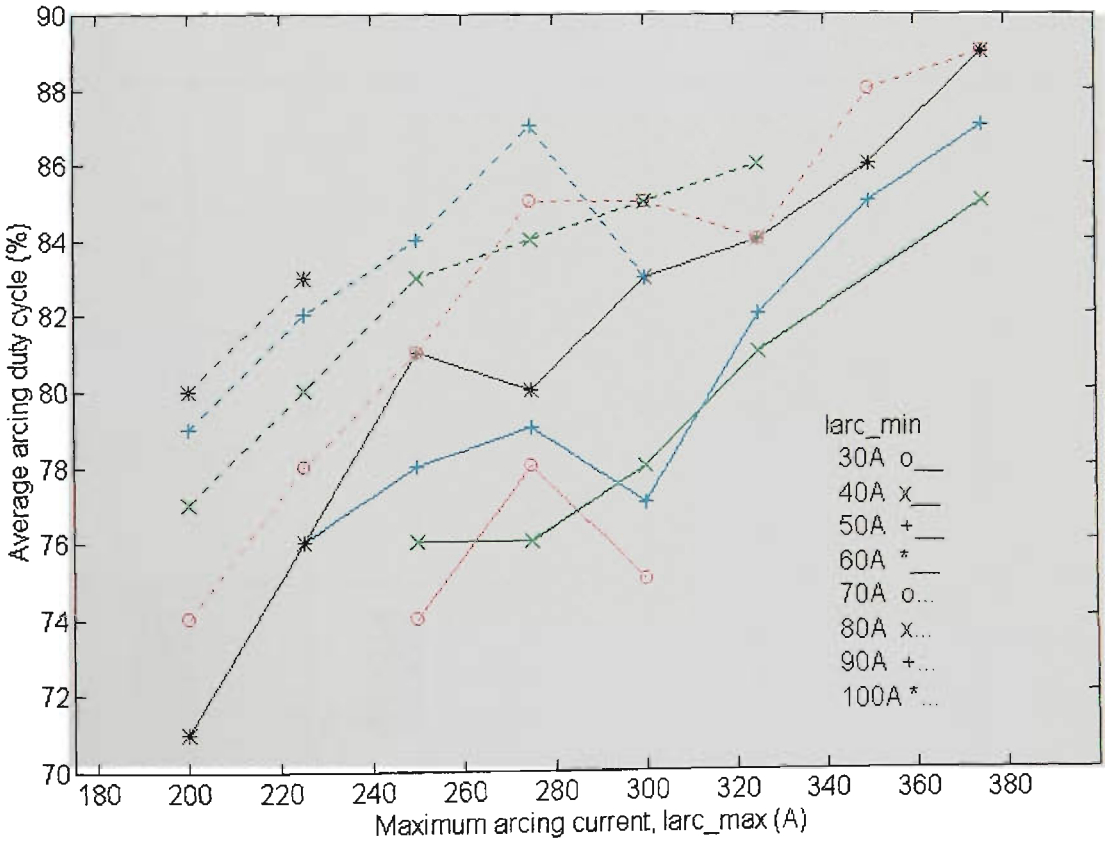

Figure 10.24 Arcing duty cycle vs Iarc_max & Iarc_min

(Ar-23%CO_2, CTWD=16mm, WFR=5.7m/min, Travel=390mm/min)

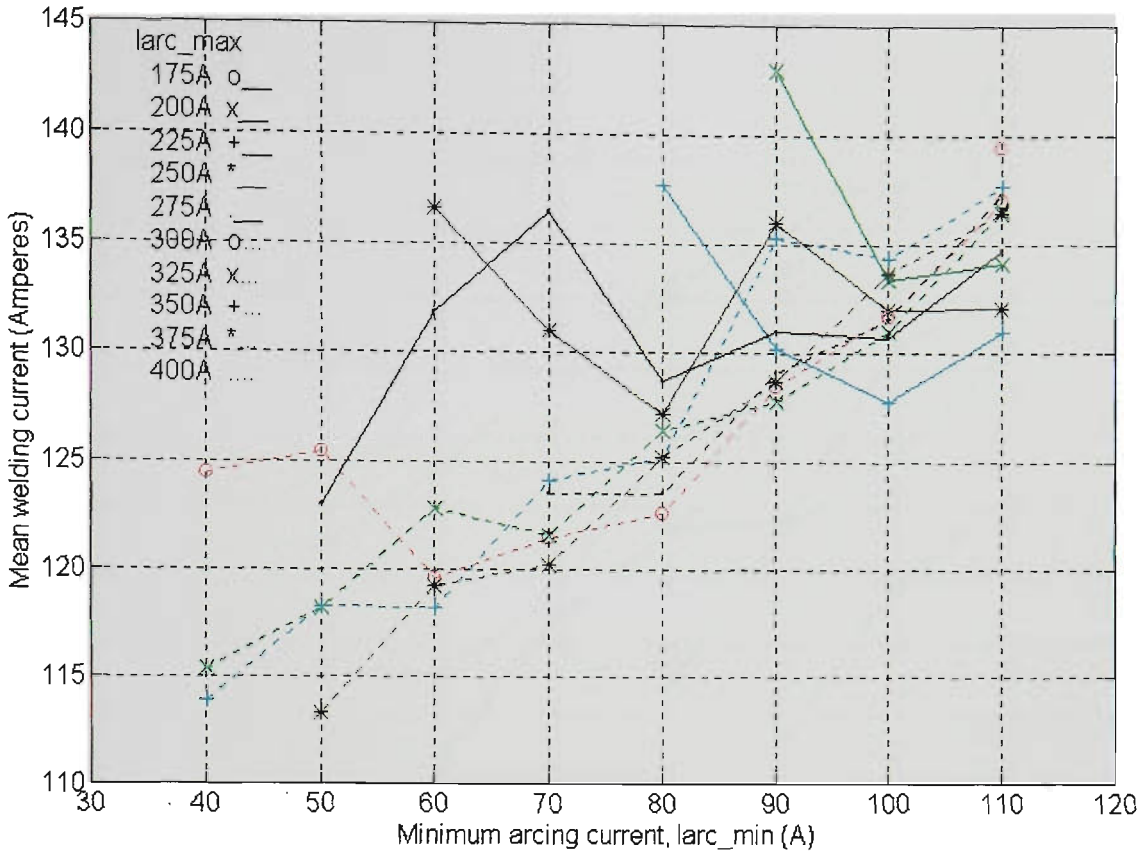

Figure 10.27 Mean welding current vs Iarc_min & Iarc_max

(Ar-23%CO_2, CTWD=8mm, WFR=5.7m/min, Travel=390mm/min)

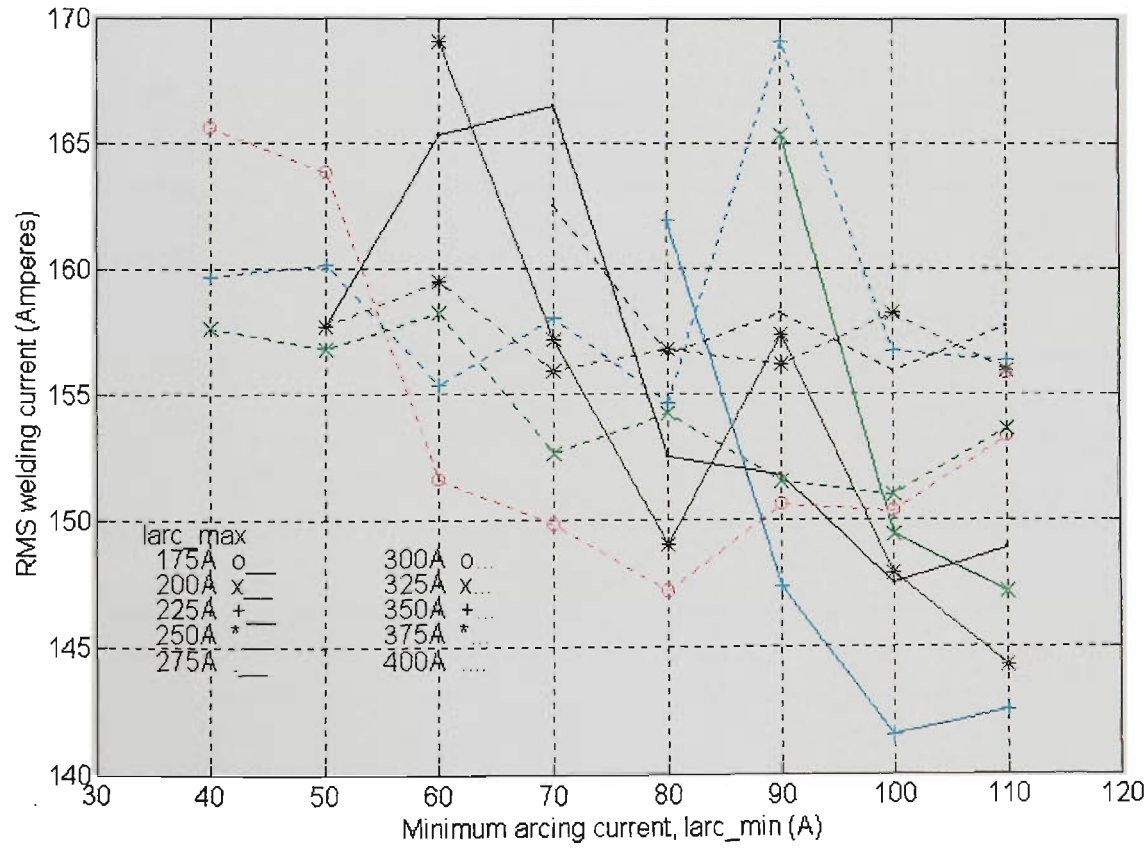

Figure 10.28 RMS welding current vs Iarc_min & Iarc_max

(Ar-23% CO_2, CTWD=8mm, WFR=5.7m/min, Travel=390mm/min)

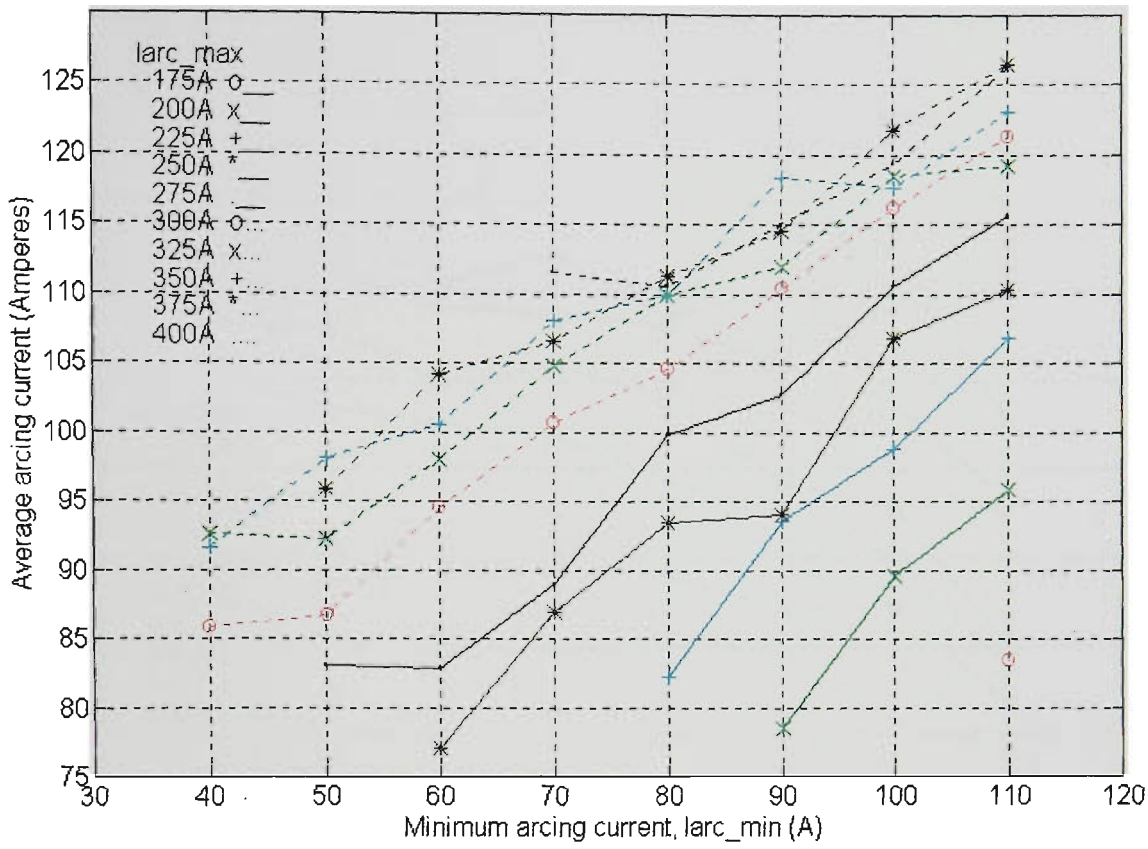

Figure 10.29 Average arcing current vs Iarc_min & Iarc_max

(Ar-23% CO_2, CTWD=8mm, WFR=5.7m/min, Travel=390mm/min)

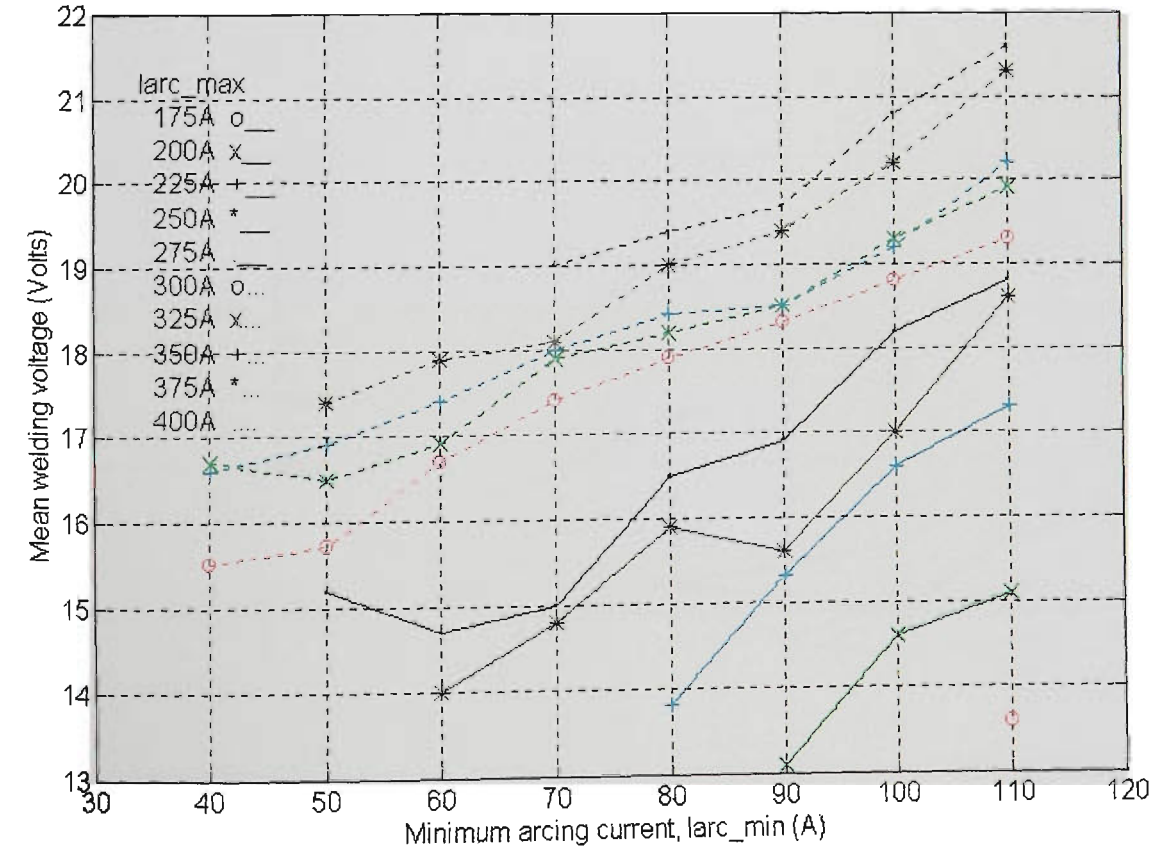

Figure 10.30 Mean voltage vs Iarc_min & Iarc_max

(Ar-23% CO_2, CTWD=8mm, WFR=5.7m/min, Travel=390mm/min)

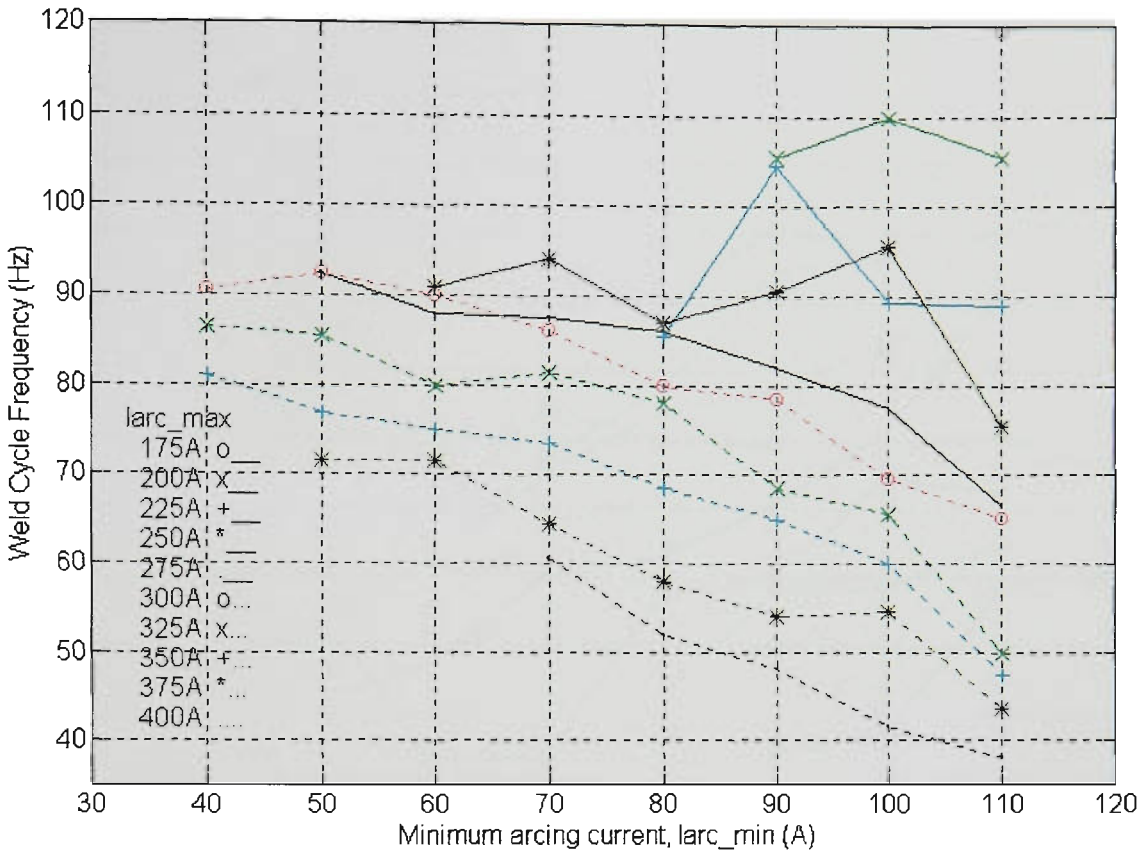

Figure 10.31 Average dipping frequency vs Iarc_min & Iarc_max (Ar-23% CO_2, CTWD=8mm, WFR=5.7m/min, Travel=390mm/min)

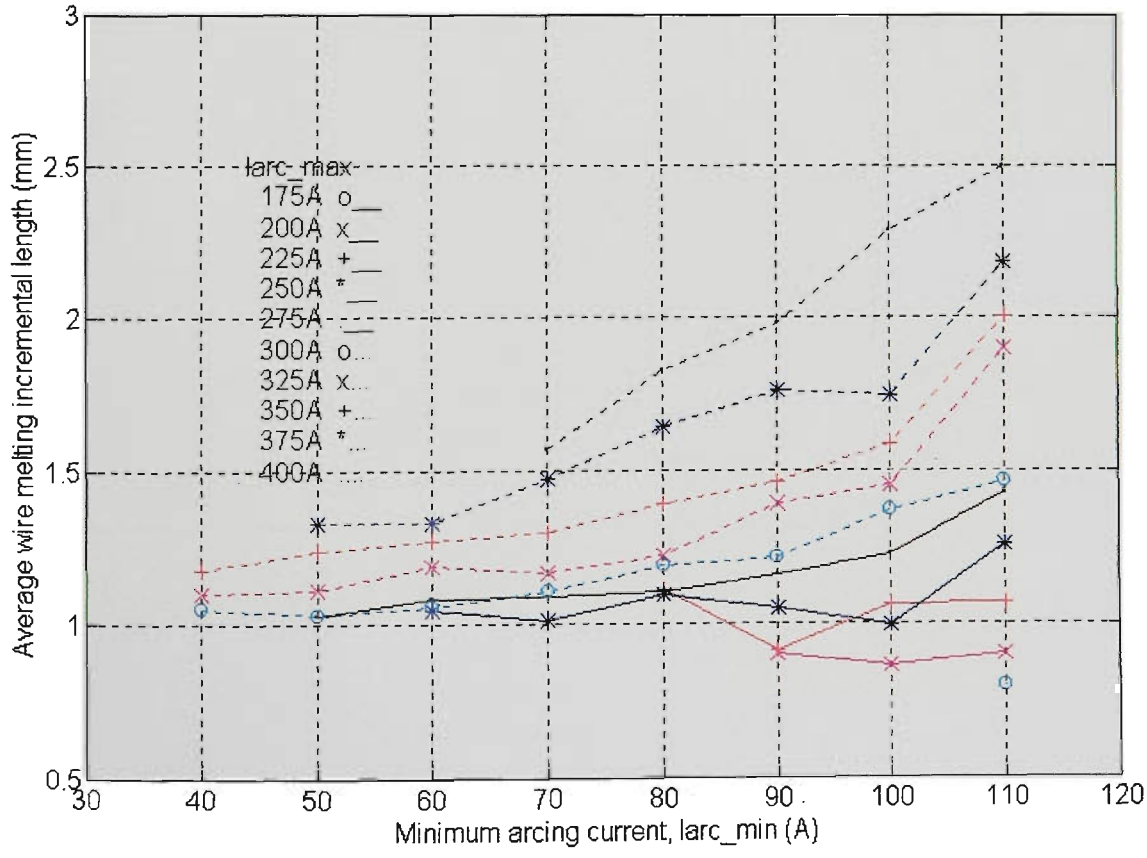

Figure 10.32 Avg wire melting incremental length ΔL vs Iarc_min & Iarc_max (Ar-23% CO_2, CTWD=8mm, WFR=5.7m/min, Travel=390mm/min)

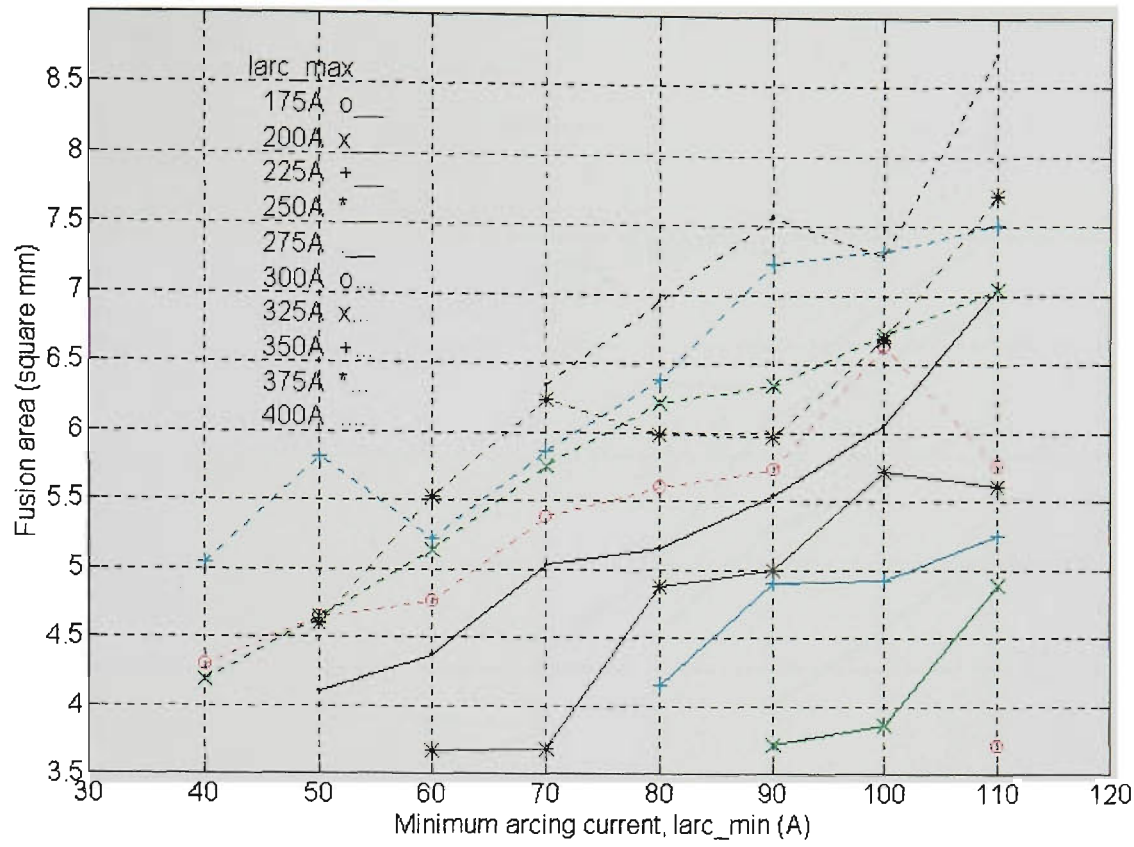

Figure 10.33 Fusion area vs Iarc_min & Iarc_max

(Ar-23% CO_2, CTWD=8mm, WFR=5.7m/min, Travel=390mm/min)

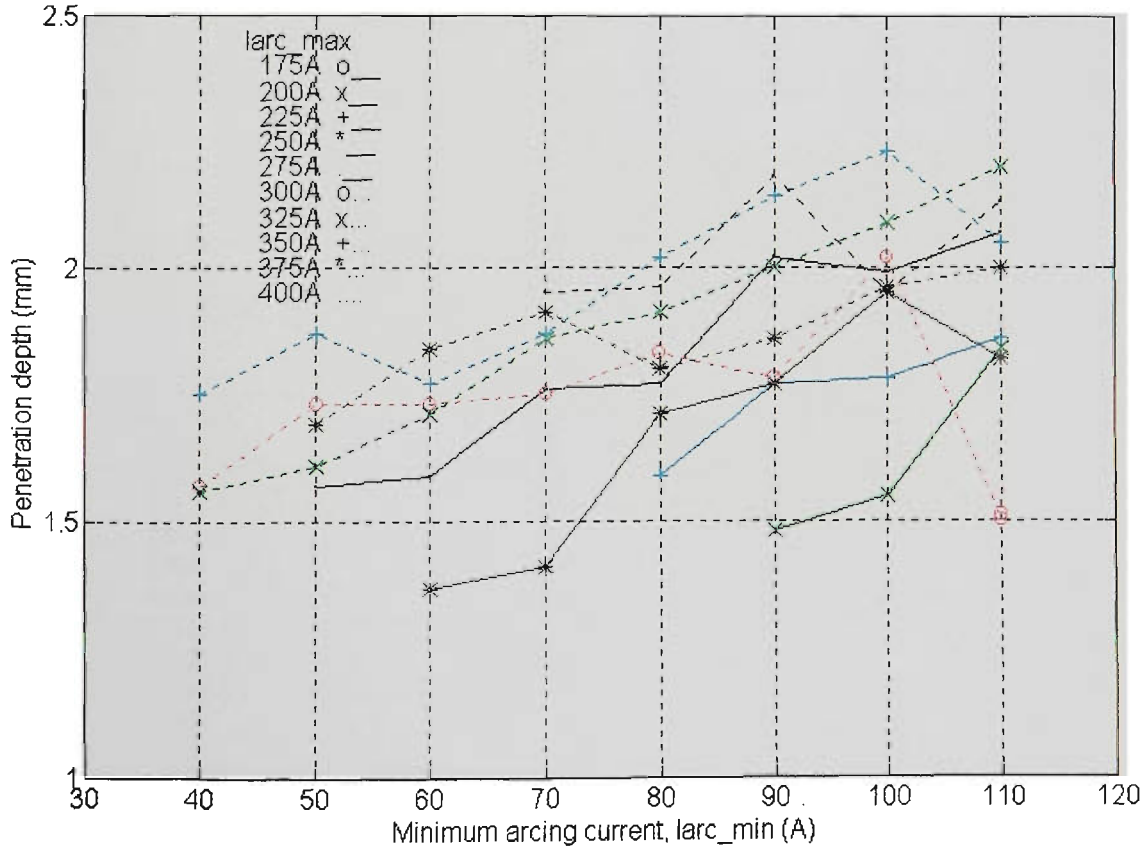

Figure 10.34 Penetration depth vs Iarc_min & Iarc_max

(Ar-23% CO_2, CTWD=8mm, WFR=5.7m/min, Travel=390mm/min)

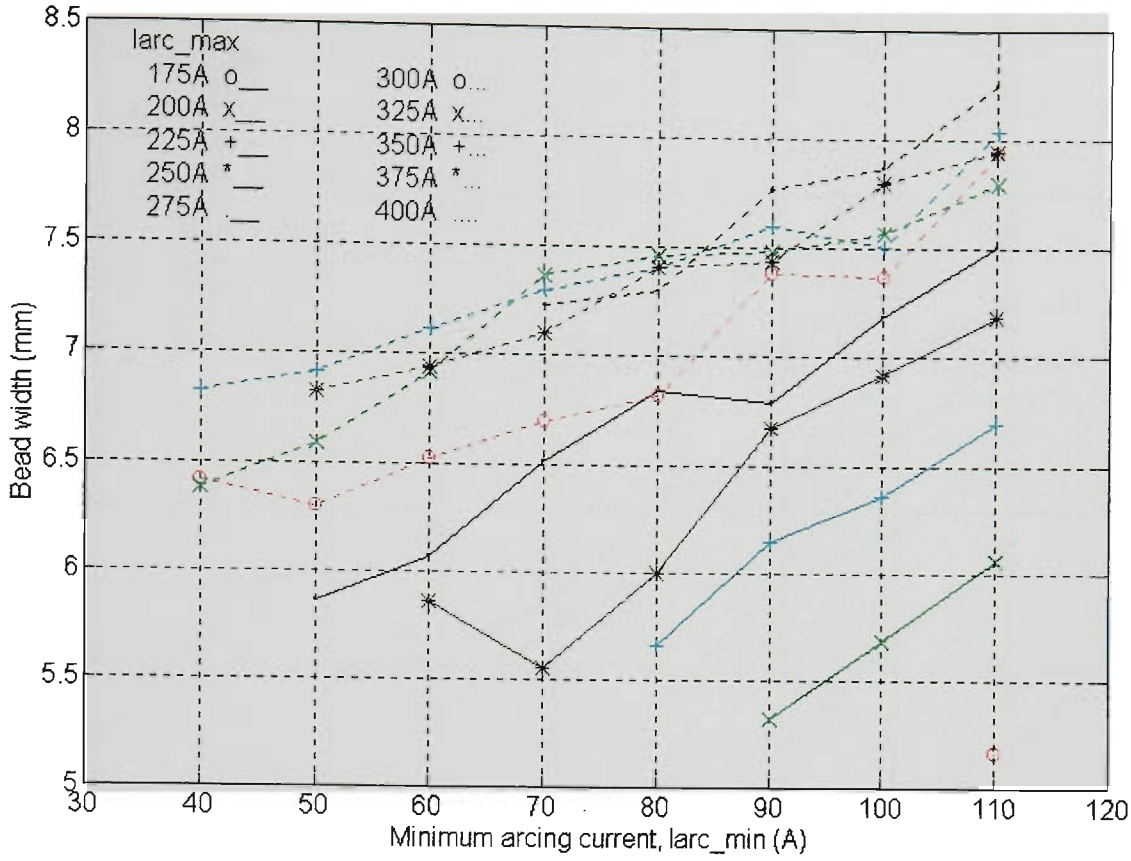

Figure 10.35 Weld bead width vs Iarc_min & Iarc_max

(Ar-23% CO_2, CTWD=8mm, WFR=5.7m/min, Travel=390mm/min)

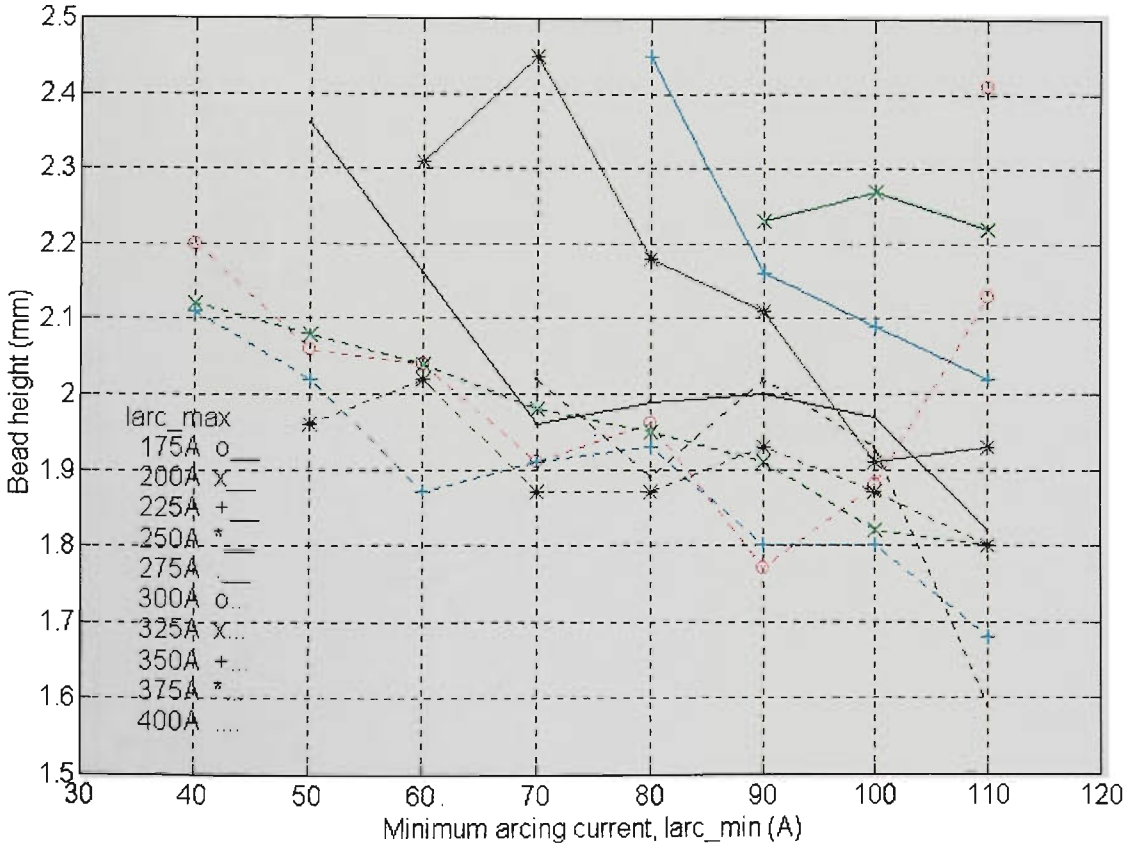

Figure 10.36 Weld bead height vs Iarc_min & Iarc_max

(Ar-23% CO_2, CTWD=8mm, WFR=5.7m/min, Travel=390mm/min)

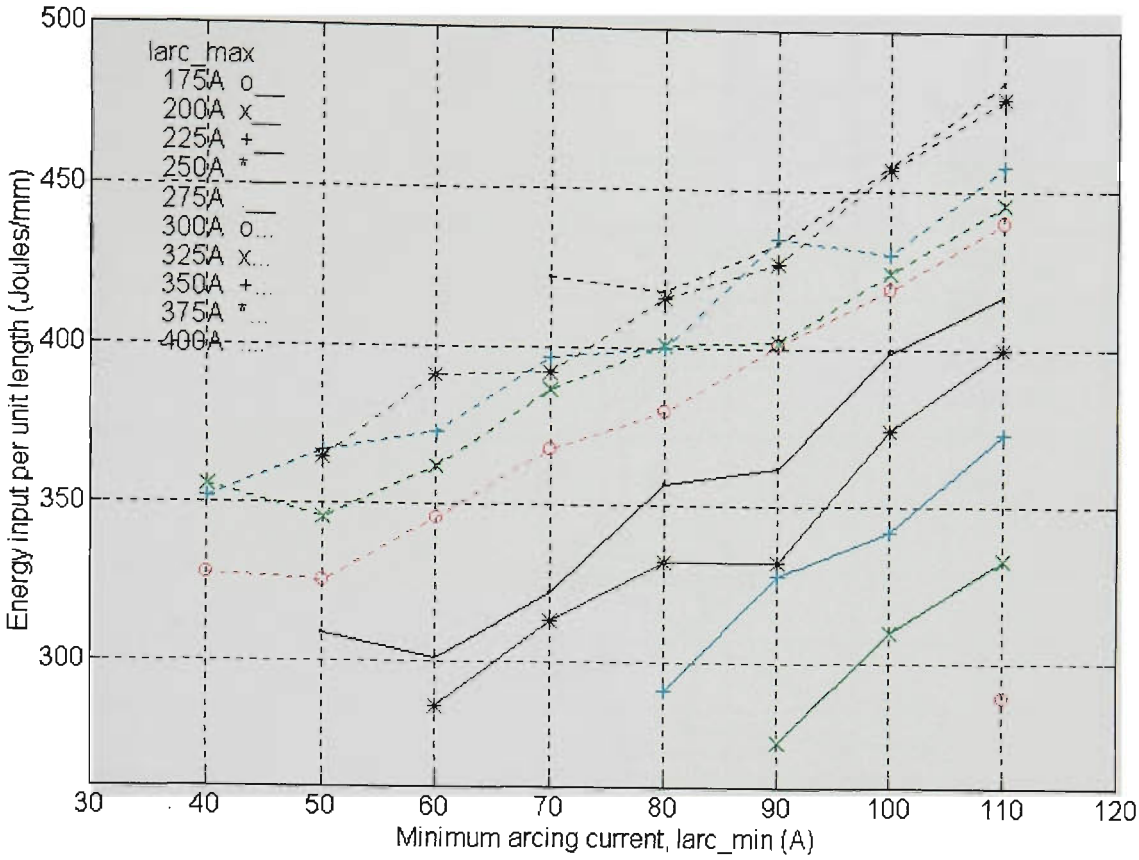

Figure 10.37 Energy input per unit length of weld vs Iarc_min & Iarc_max (Ar-23% CO_2, CTWD=8mm, WFR=5.7m/min, Travel=390mm/min)

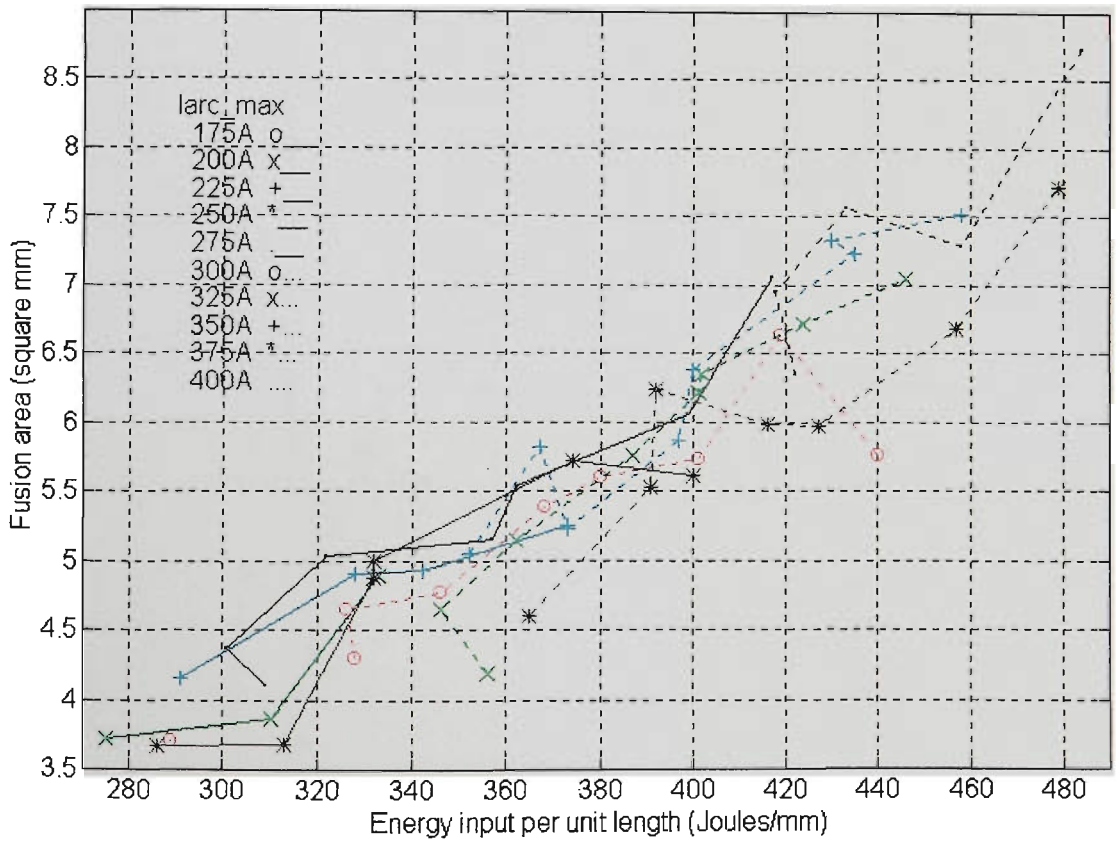

Figure 10.38 Fusion area vs Energy input per unit length of weld (Ar-23% CO_2, CTWD=8mm, WFR=5.7m/min, Travel=390mm/min)

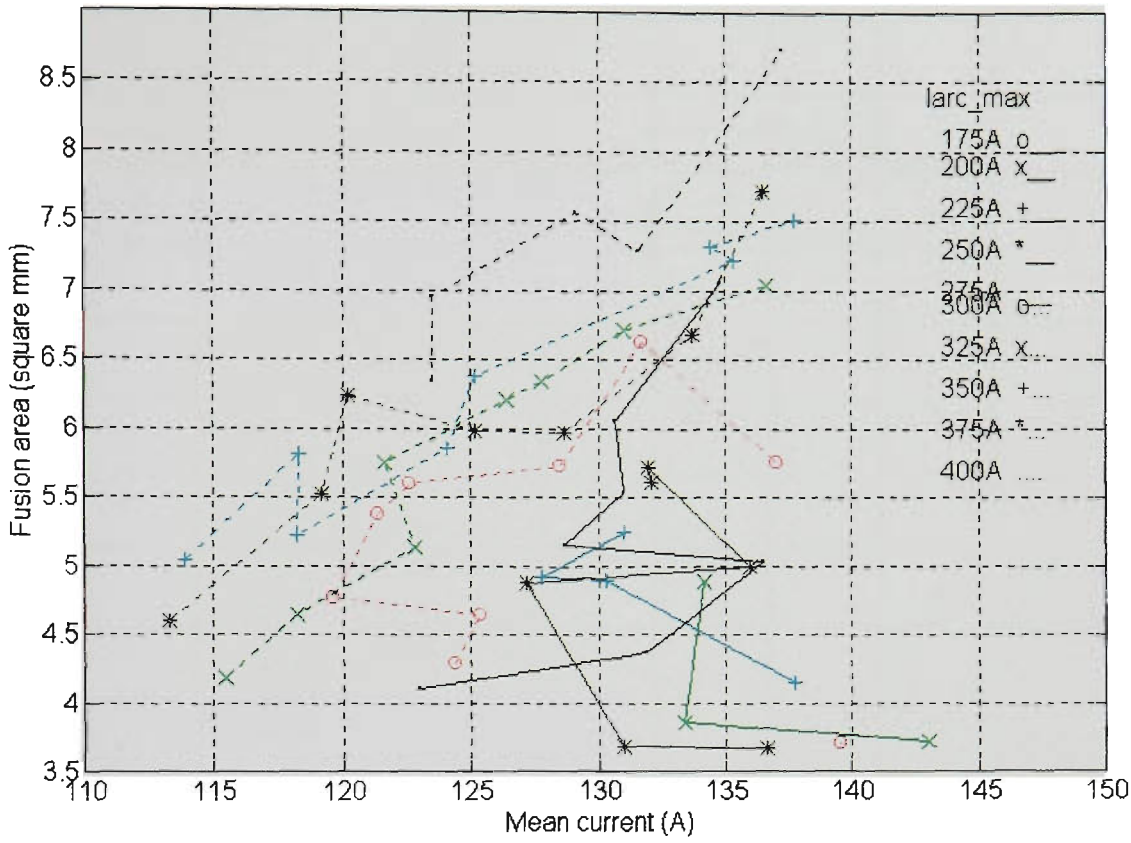

Figure 10.39 Fusion area vs Mean welding current

(Ar-23% CO_2, CTWD=8mm, WFR=5.7m/min, Travel=390mm/min)

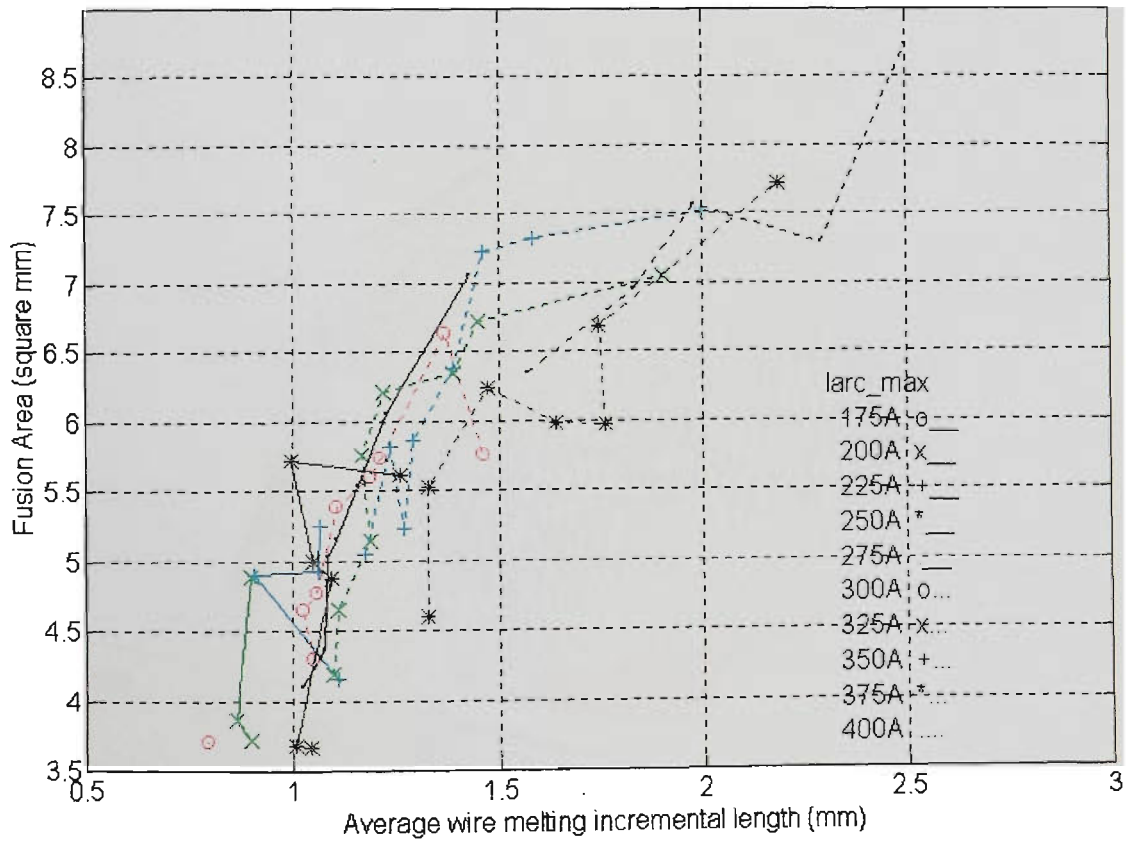

Figure 10.40 Fusion area vs Average wire melting incremental length ΔL

(Ar-23% CO_2, CTWD=8mm, WFR=5.7m/min, Travel=390mm/min)

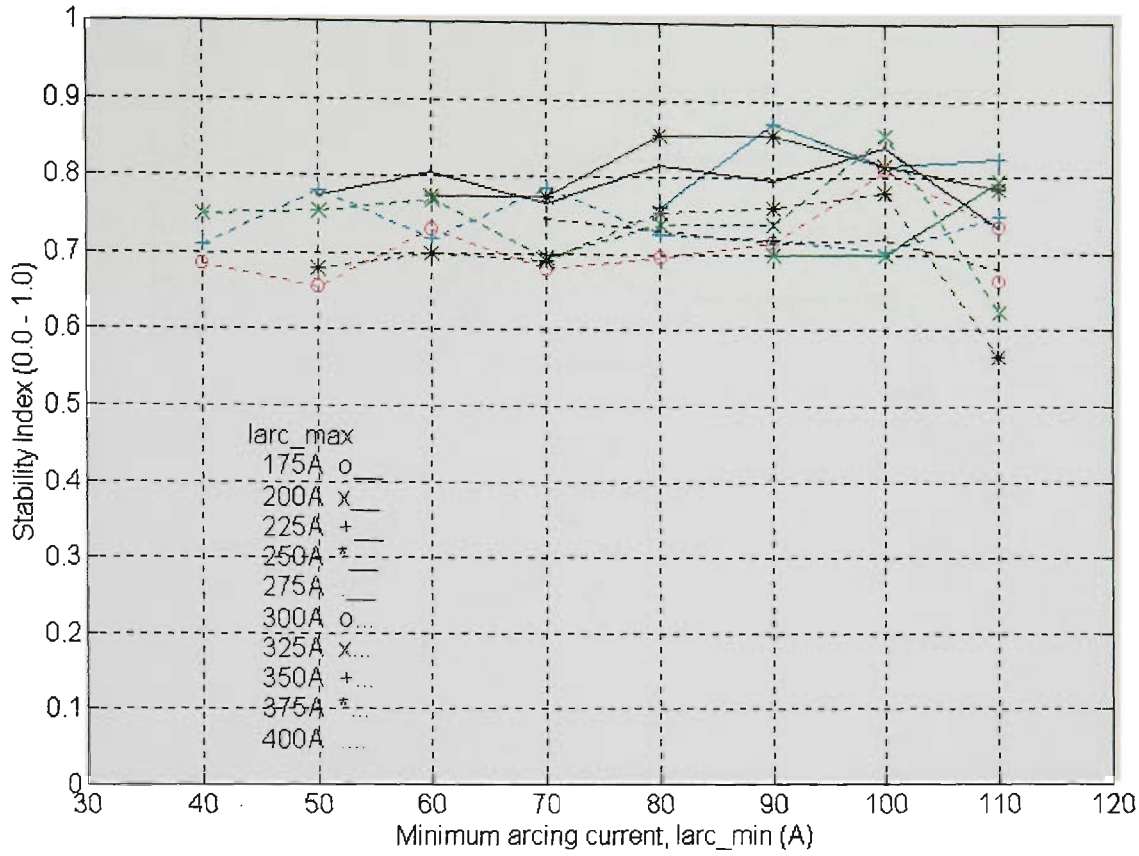

Figure 10.41 Stability index vs Iarc_min & Iarc_max (2D)

(Ar-23% CO_2, CTWD=8mm, WFR=5.7m/min, Travel=390mm/min)

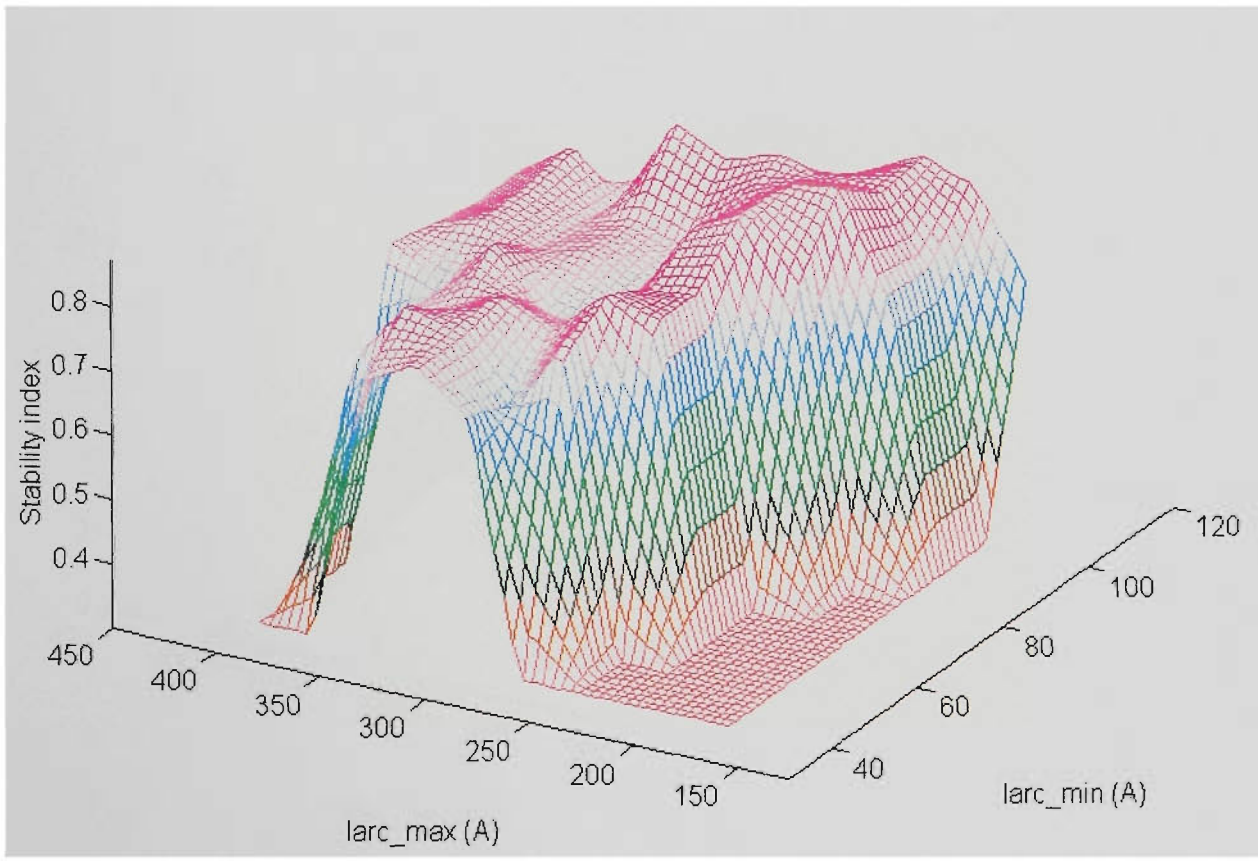

Figure 10.42 Stability index vs Iarc_min & Iarc_max (3D)

(Ar-23% CO_2, CTWD=8mm, WFR=5.7m/min, Travel=390mm/min)

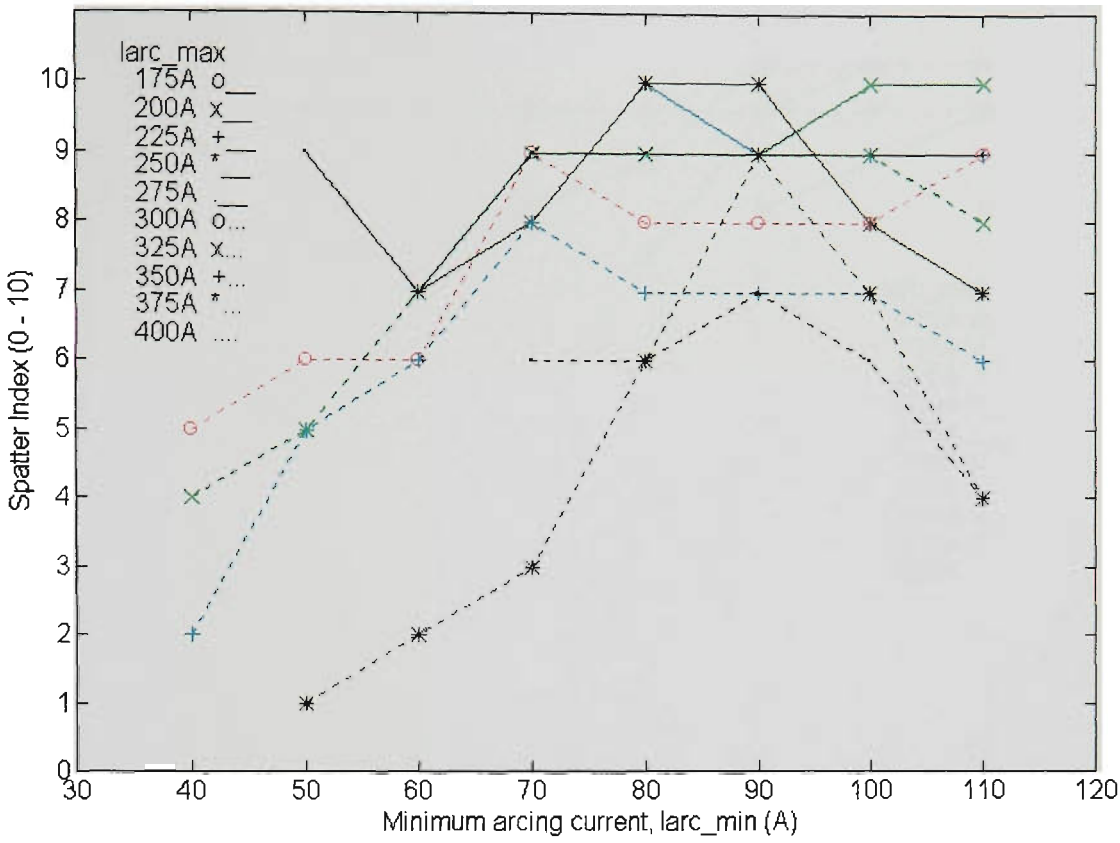

Figure 10.43 Spatter index vs Iarc_min & Iarc_max (2D)

(Ar-23% CO_2, CTWD=8mm, WFR=5.7m/min, Travel=390mm/min)

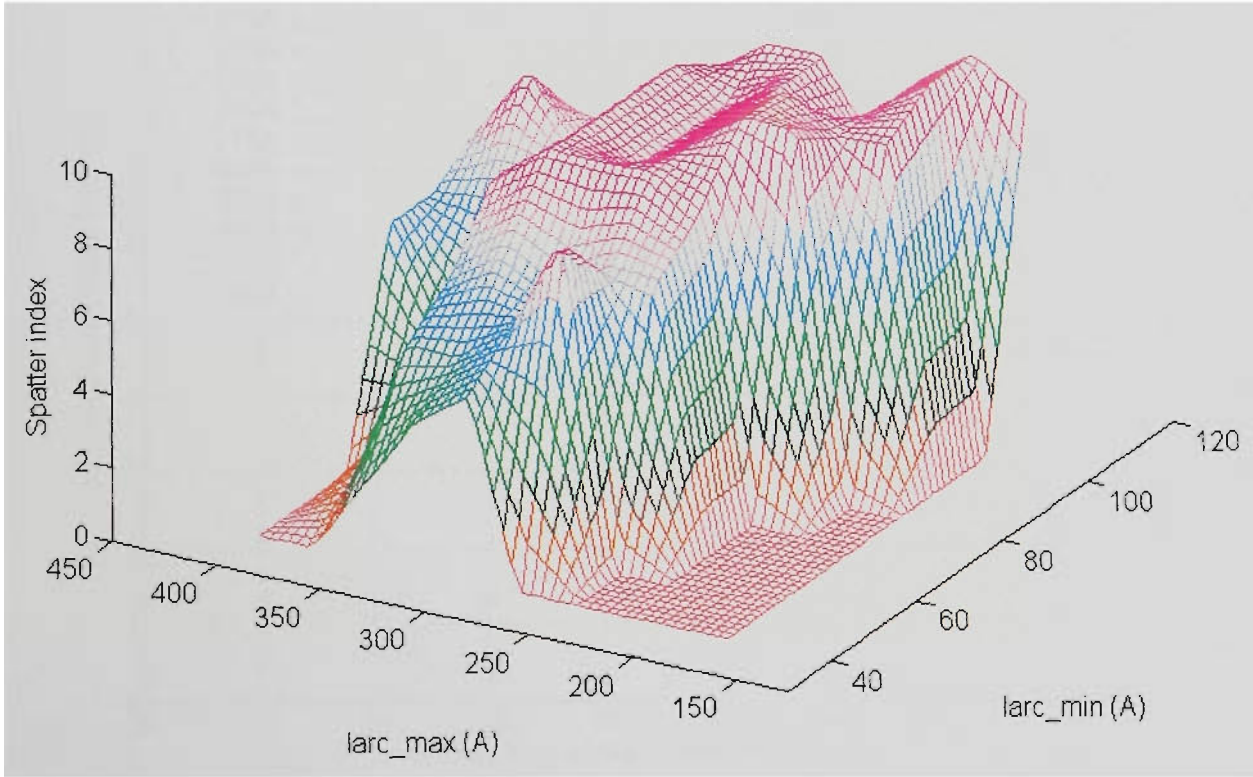

Figure 10.44 Spatter index vs Iarc_min & Iarc_max (3D)

(Ar-23% CO_2, CTWD=8mm, WFR=5.7m/min, Travel=390mm/min)

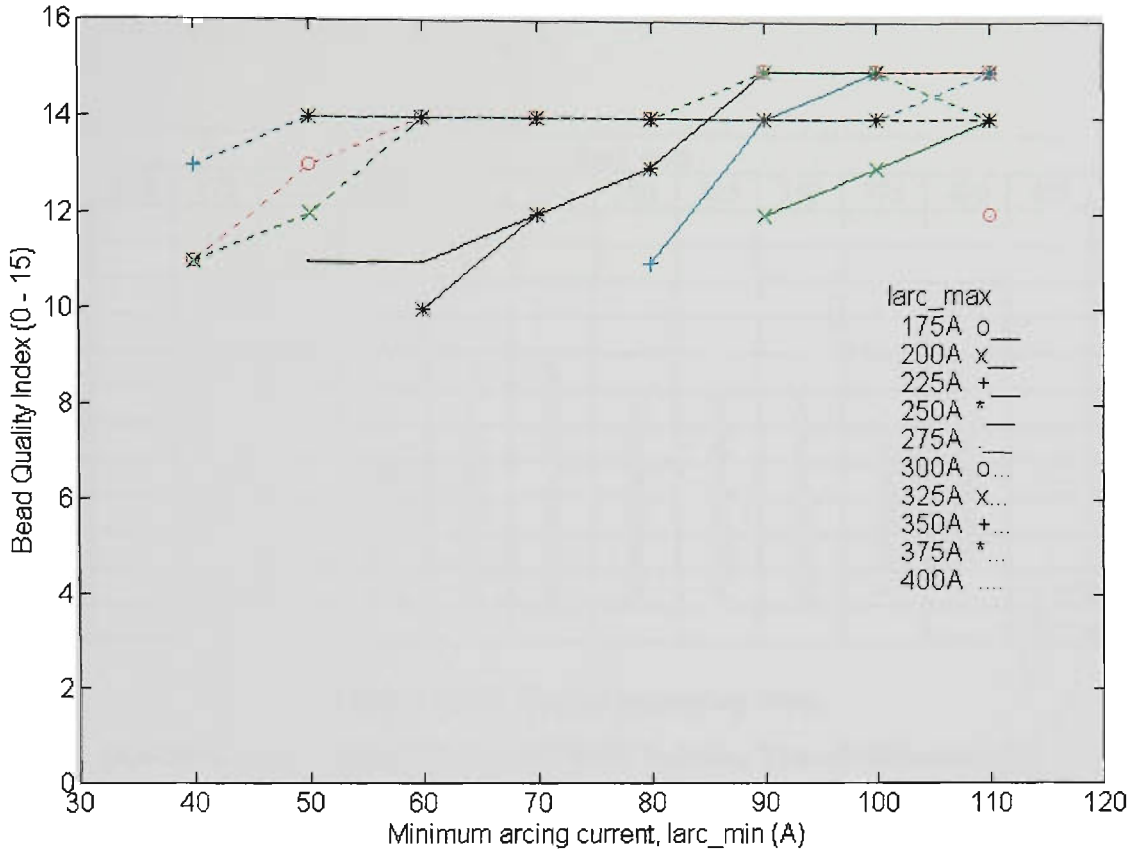

Figure 10.45 Bead quality index vs Iarc_min & Iarc_max

(Ar-23% CO_2, CTWD=8mm, WFR=5.7m/min, Travel=390mm/min)

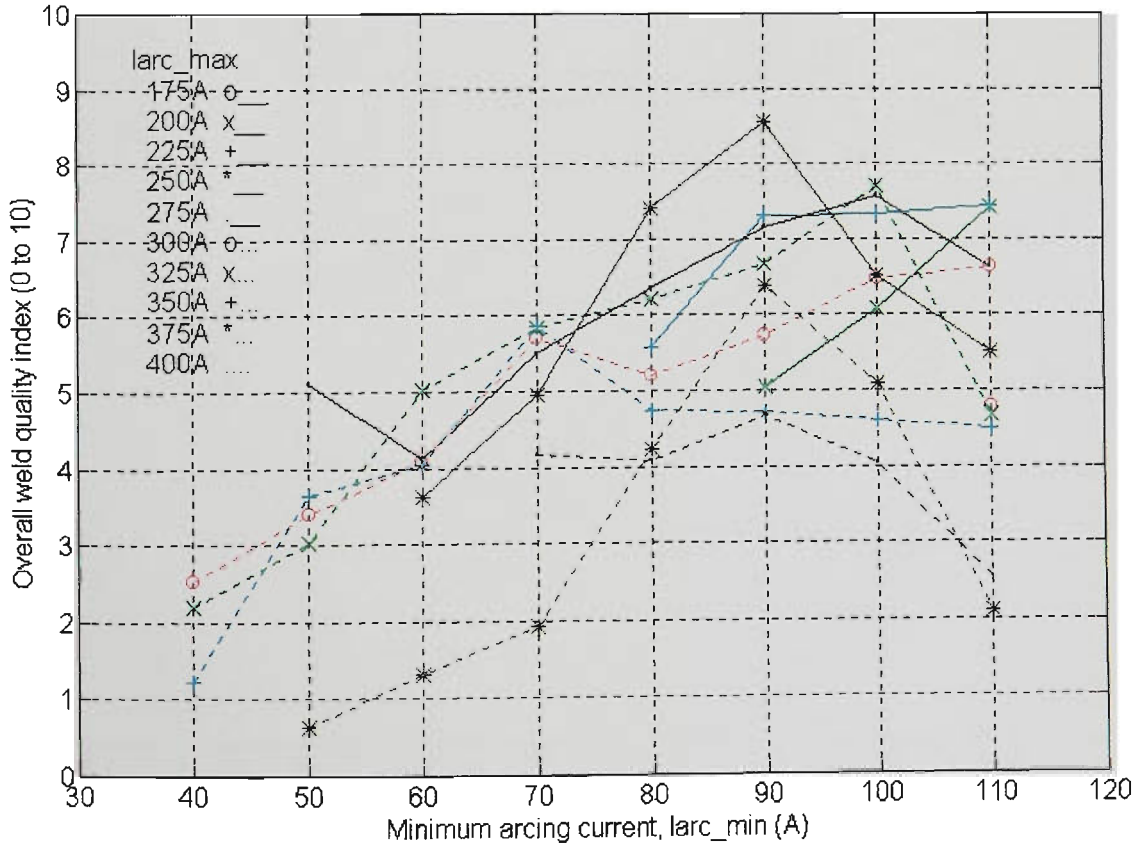

Figure 10.46 Weld overall quality index vs Iarc_min & Iarc_max

(Ar-23% CO_2, CTWD=8mm, WFR=5.7m/min, Travel=390mm/min)

Iarc_min	Iarc_max												
	150	175	200	225	250	275	300	325	350	375	400	425	450
10													
20													
30													
40							-	-	-				
50						X	-	-	-	-			
60					-	X	X	X	X	-			
70					X	X	X	X	X	-	X		
80				X	X	X	X	X	X	X	X		
90			X	X	X	X	X	X	X	X	X		
100			X	X	X	X	X	X	X	X	X		
110		X	X	X	X	X	X	X	X	-	-	- = tested	
120												X = useful	

Figure 10.47 Useful operating area

(Ar-23% CO_2, CTWD=8mm, WFR=5.7m/min, Travel=390mm/min)

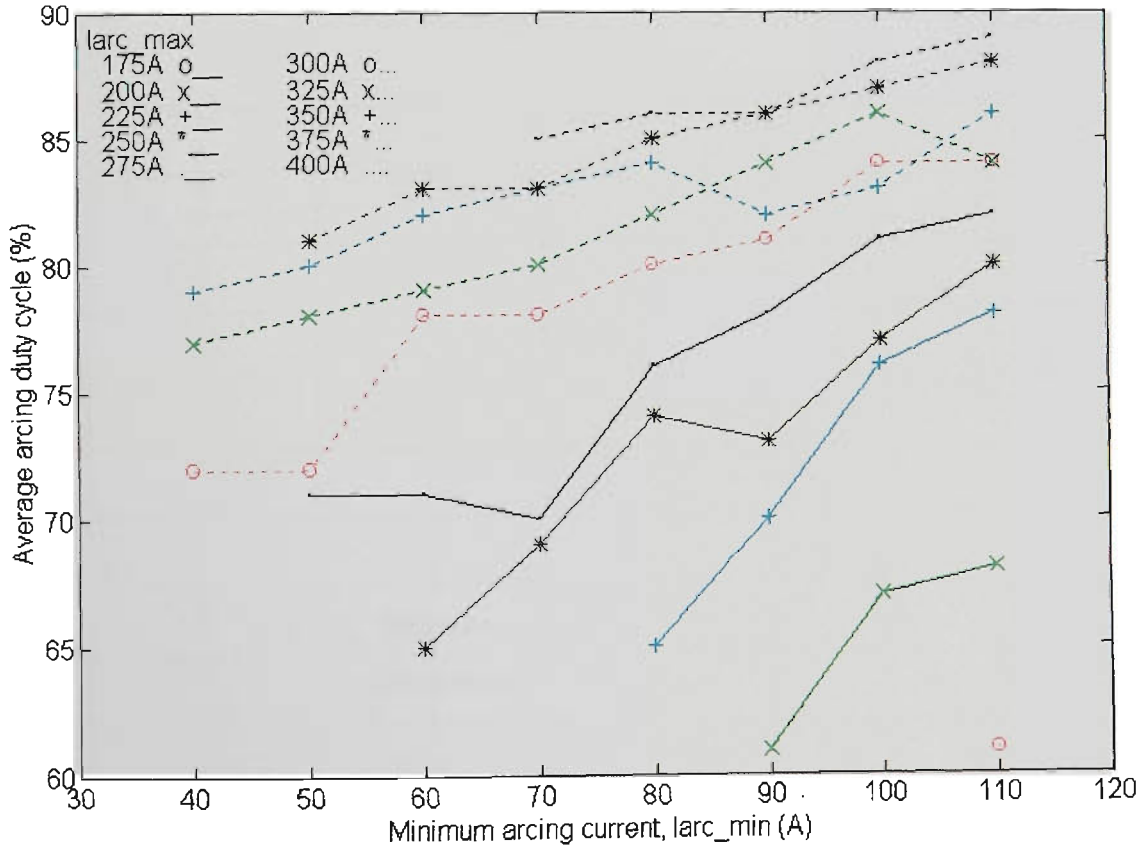

Figure 10.48 Arcing duty cycle vs Iarc_max & Iarc_min

(Ar-23% CO_2, CTWD=8mm, WFR=5.7m/min, Travel=390mm/min)

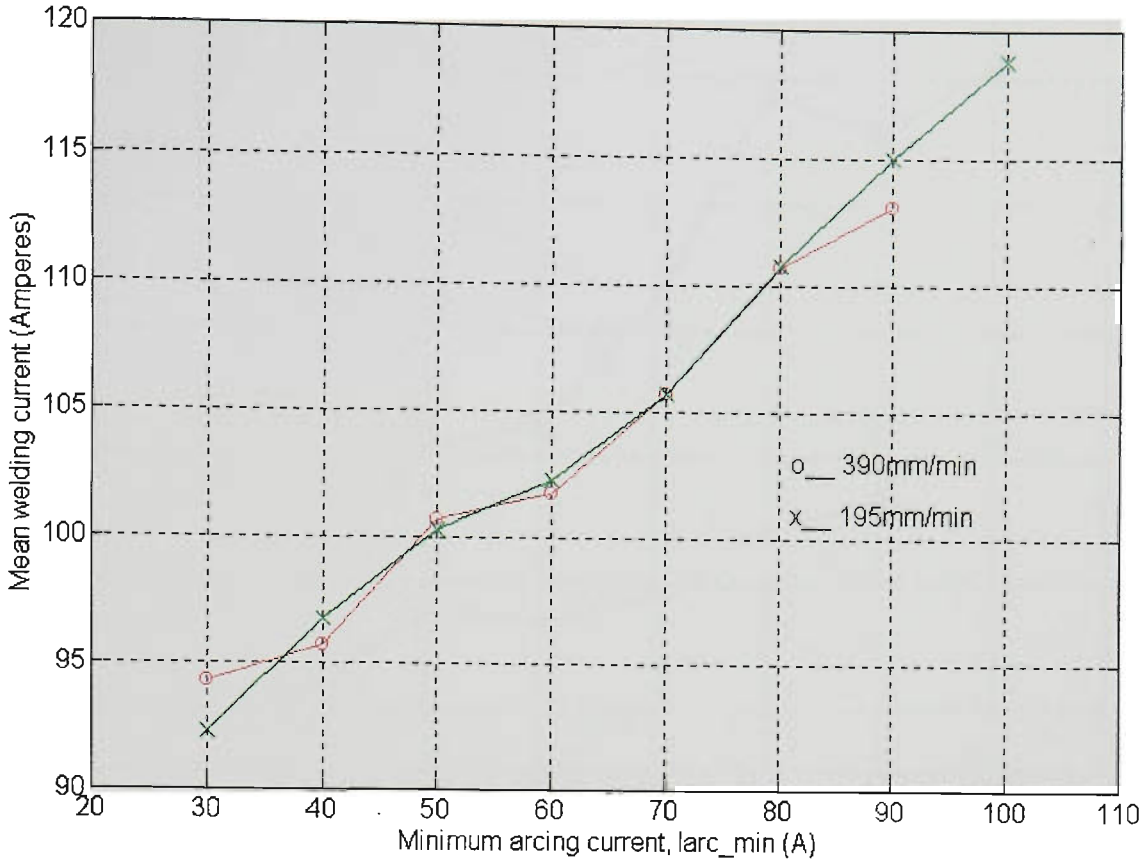

Figure 10.52 Mean welding currents for travel speeds of 195 & 390 mm/min (Ar-23% CO_2, CTWD=16mm, WFR=5.7m/min)

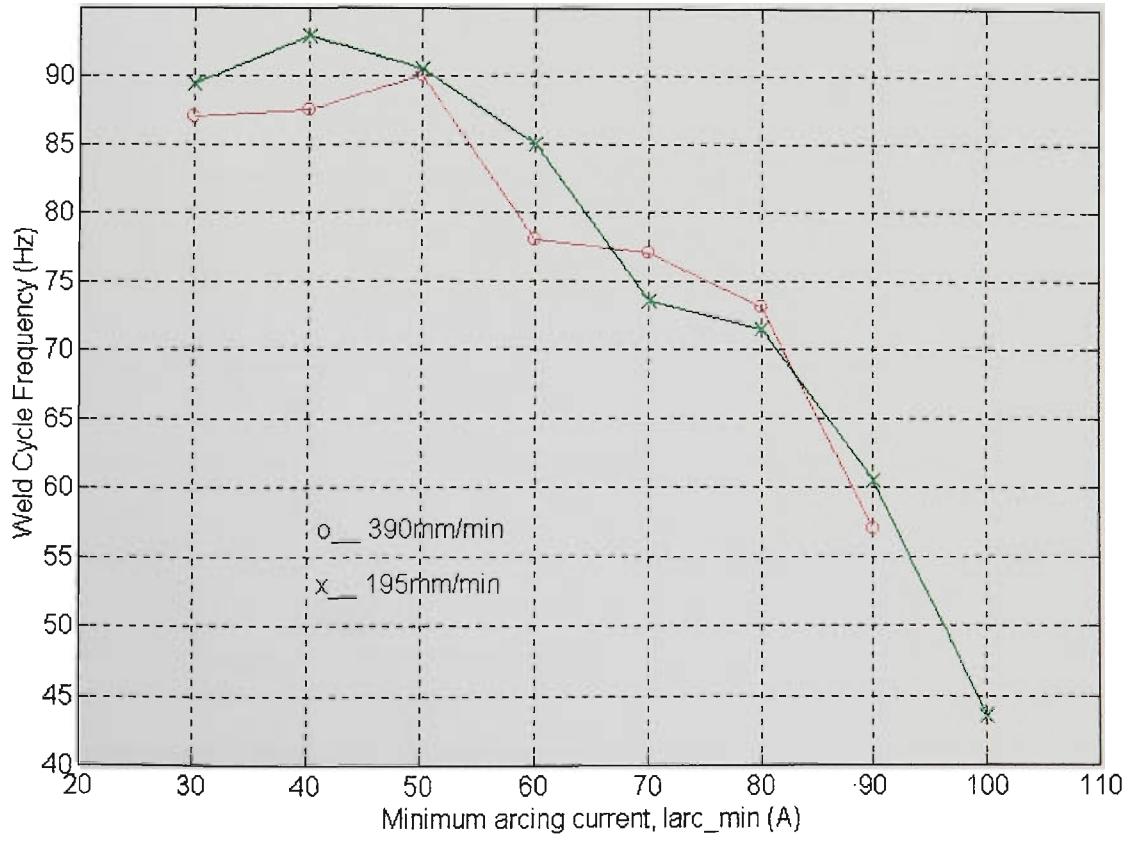

Figure 10.53 Average dipping frequencies for travel speeds of 195 & 390 mm/min (Ar-23% CO_2, CTWD=16mm, WFR=5.7m/min)

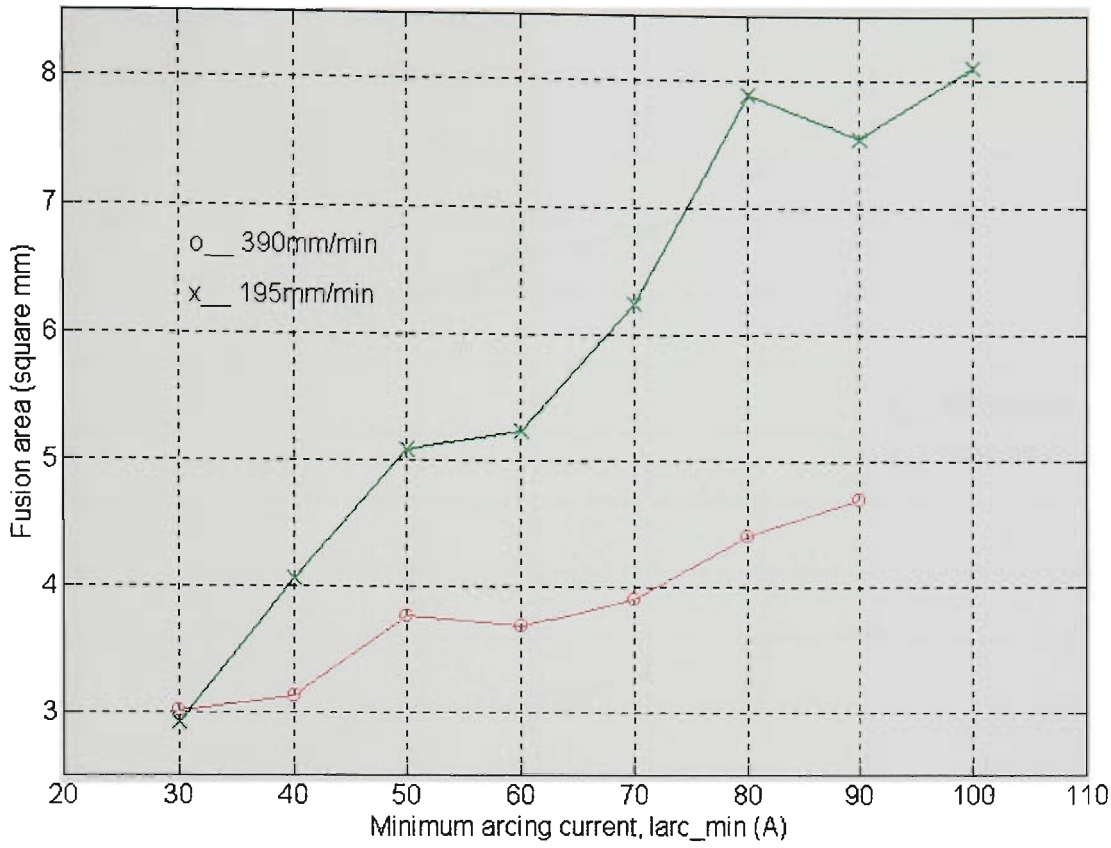

Figure 10.54 Fusion areas for travel speeds of 195 & 390 mm/min (Ar-23% CO_2, CTWD=16mm, WFR=5.7m/min)

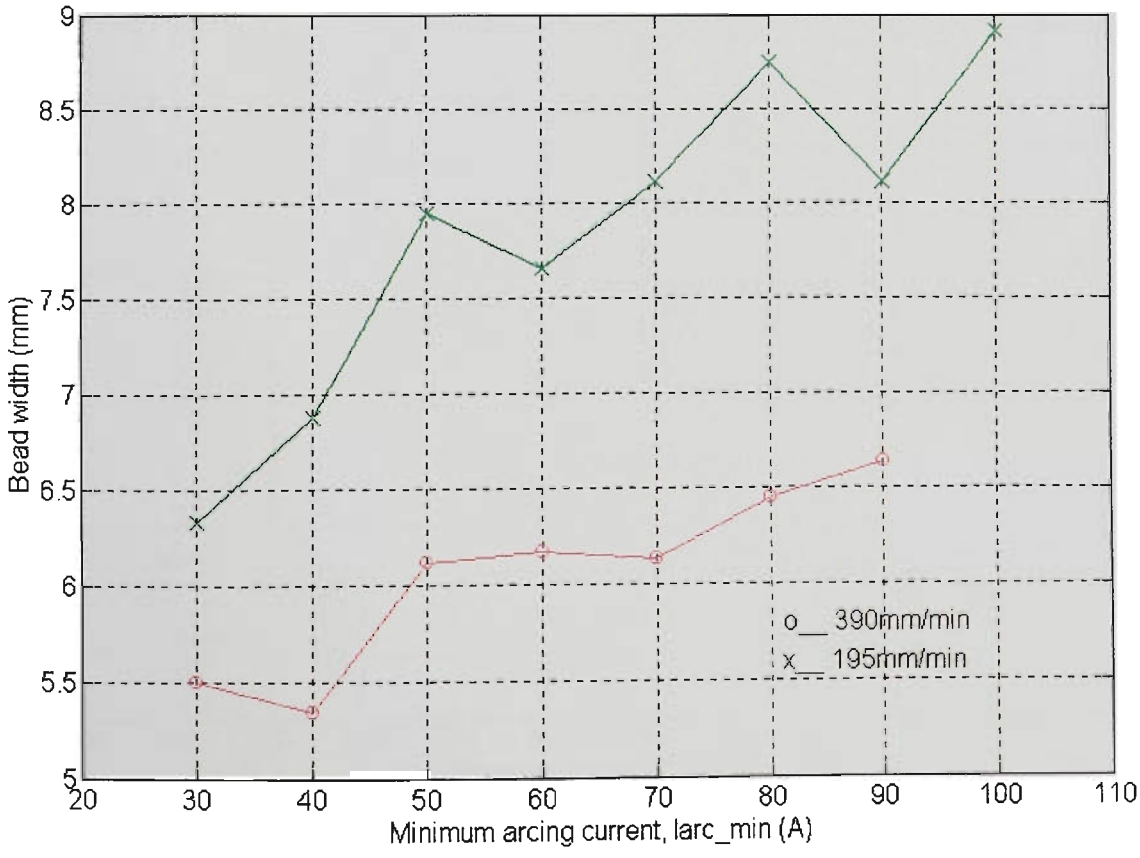

Figure 10.55 Bead widths for travel speeds of 195 & 390 mm/min (Ar-23% CO_2, CTWD=16mm, WFR=5.7m/min)

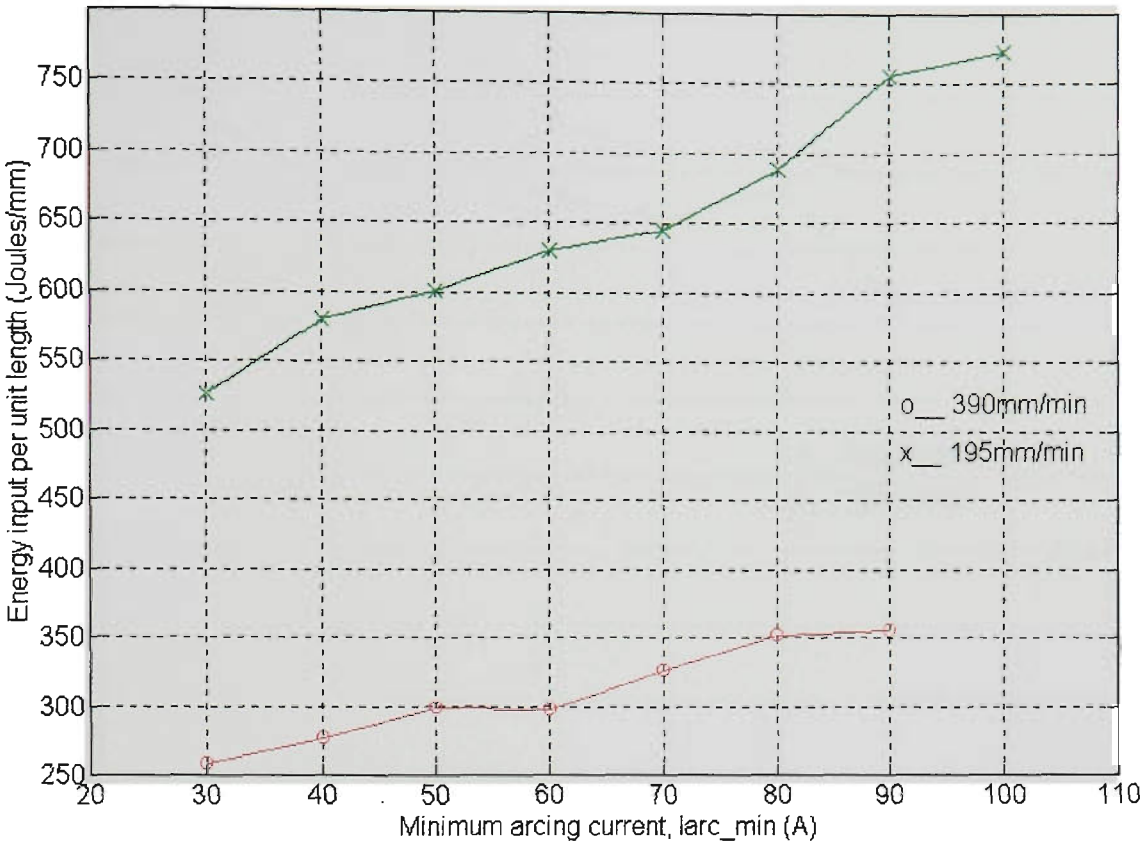

Figure 10.56 Energy inputs for travel speeds of 195 & 390 mm/min (Ar-23% CO_2, CTWD=16mm, WFR=5.7m/min)

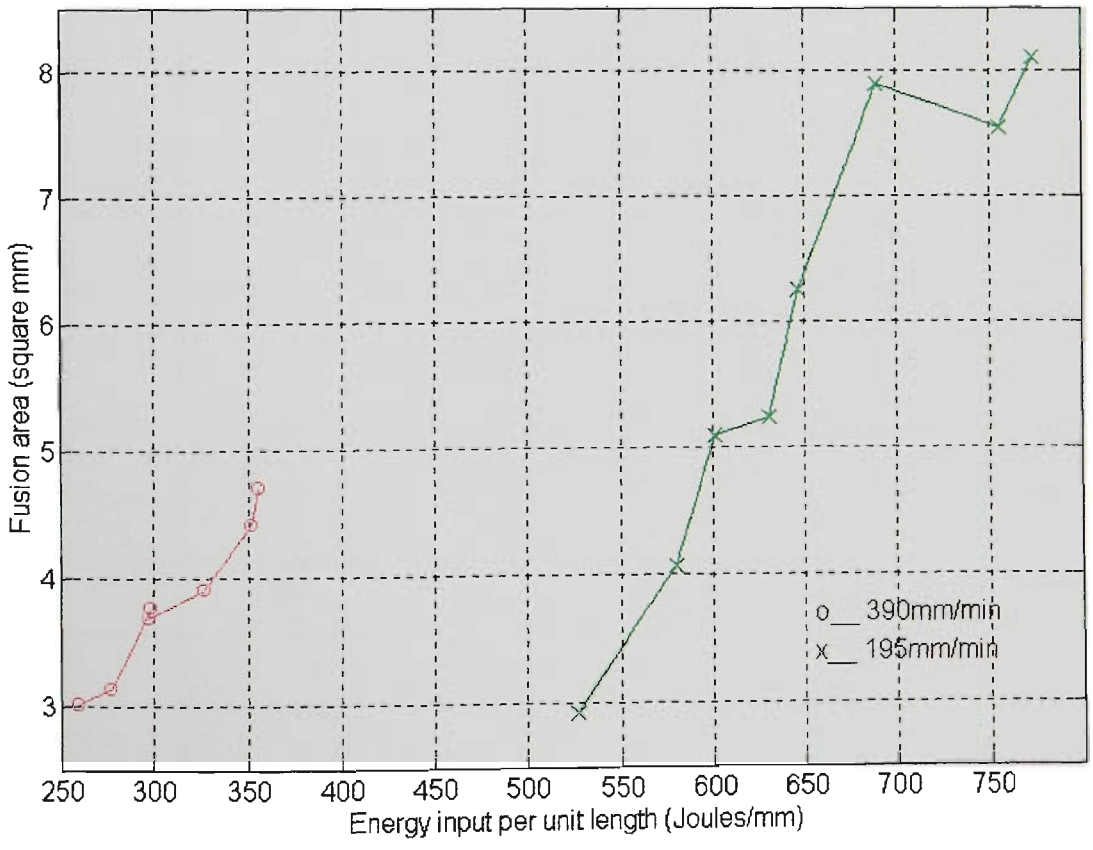

Figure 10.57 Fusion area vs Energy input for travel speeds of 195 & 390 mm/min (Ar-23% CO_2, CTWD=16mm, WFR=5.7m/min)

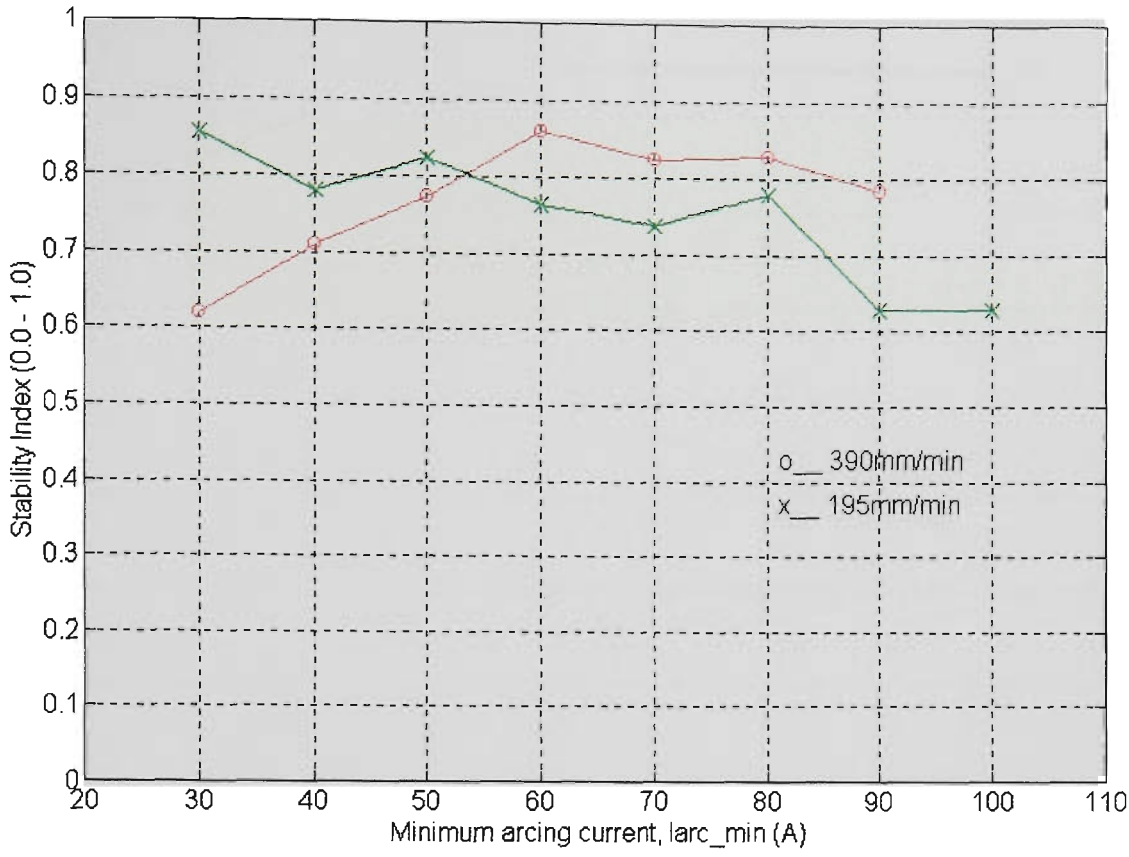

Figure 10.58 Stability indices for travel speeds of 195 & 390 mm/min (Ar-23% CO_2, CTWD=16mm, WFR=5.7m/min)

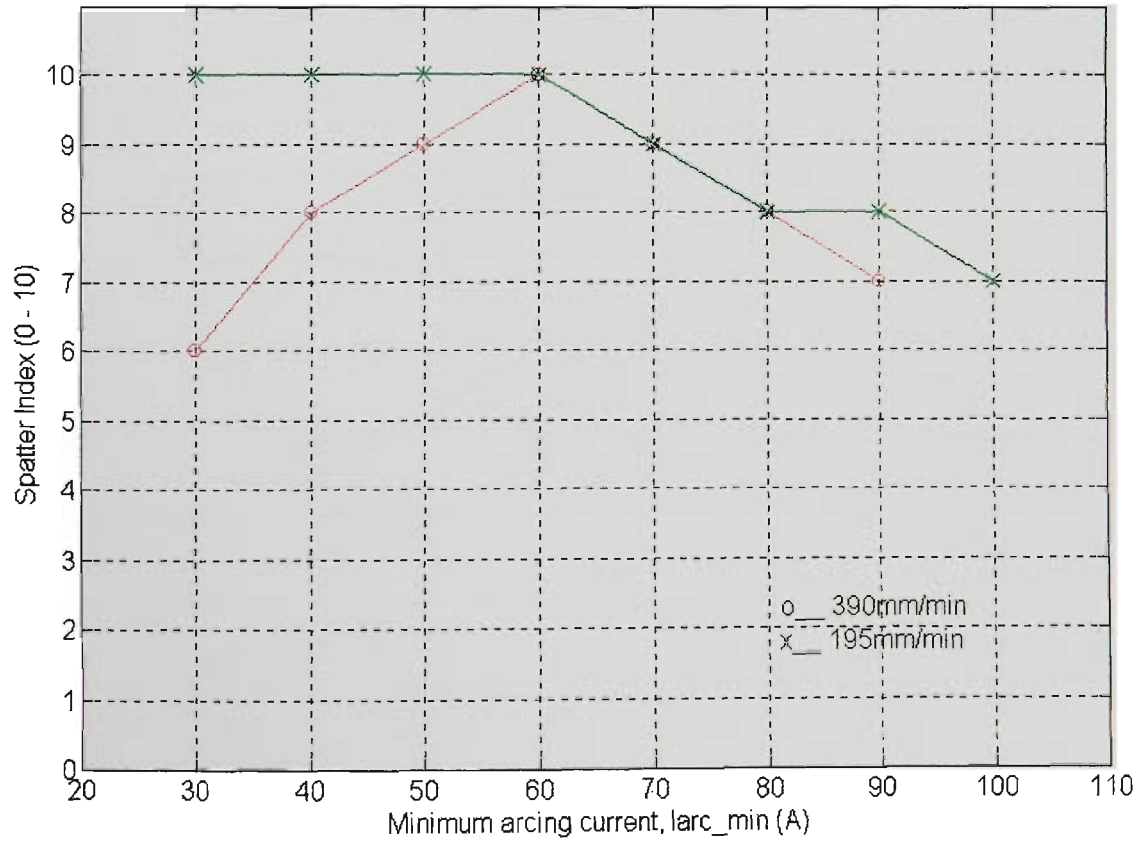

Figure 10.59 Spatter indices for travel speeds of 195 & 390 mm/min (Ar-23% CO_2, CTWD=16mm, WFR=5.7m/min)

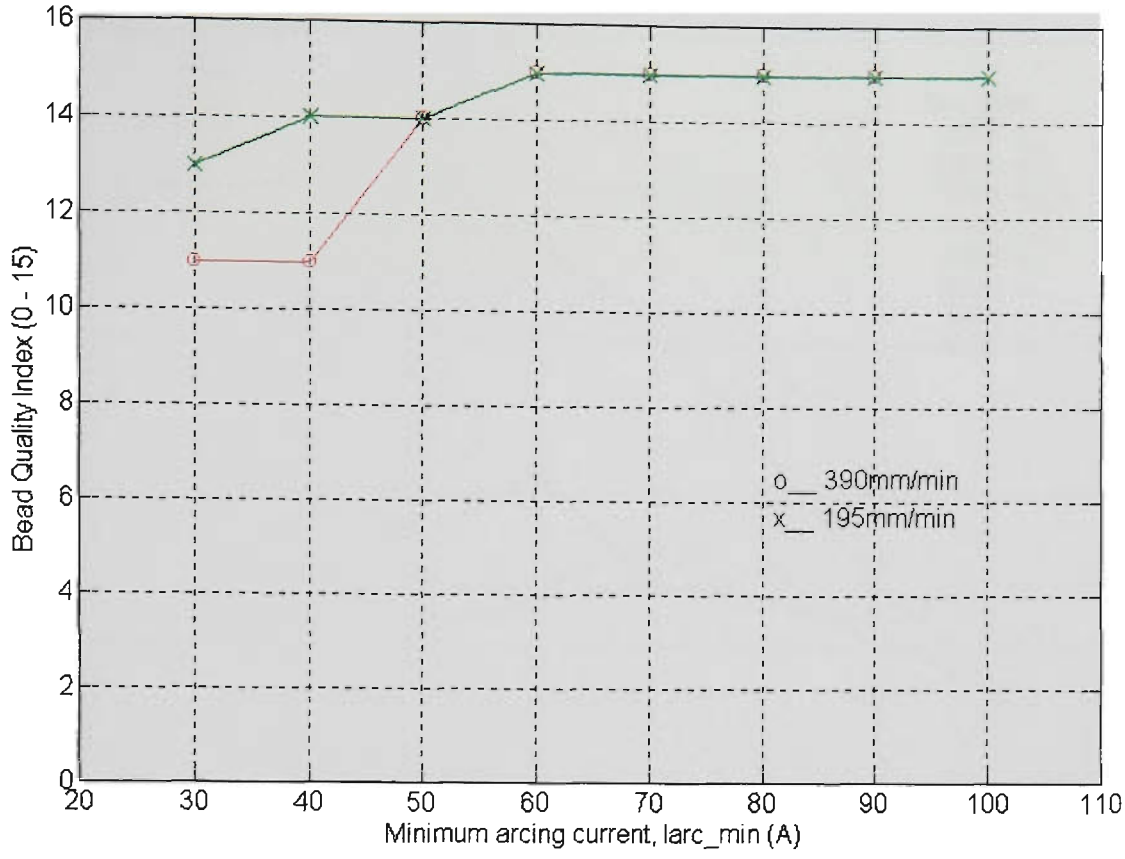

Figure 10.60 Bead quality indices for travel speeds of 195 & 390 mm/min (Ar-23% CO_2, CTWD=16mm, WFR=5.7m/min)

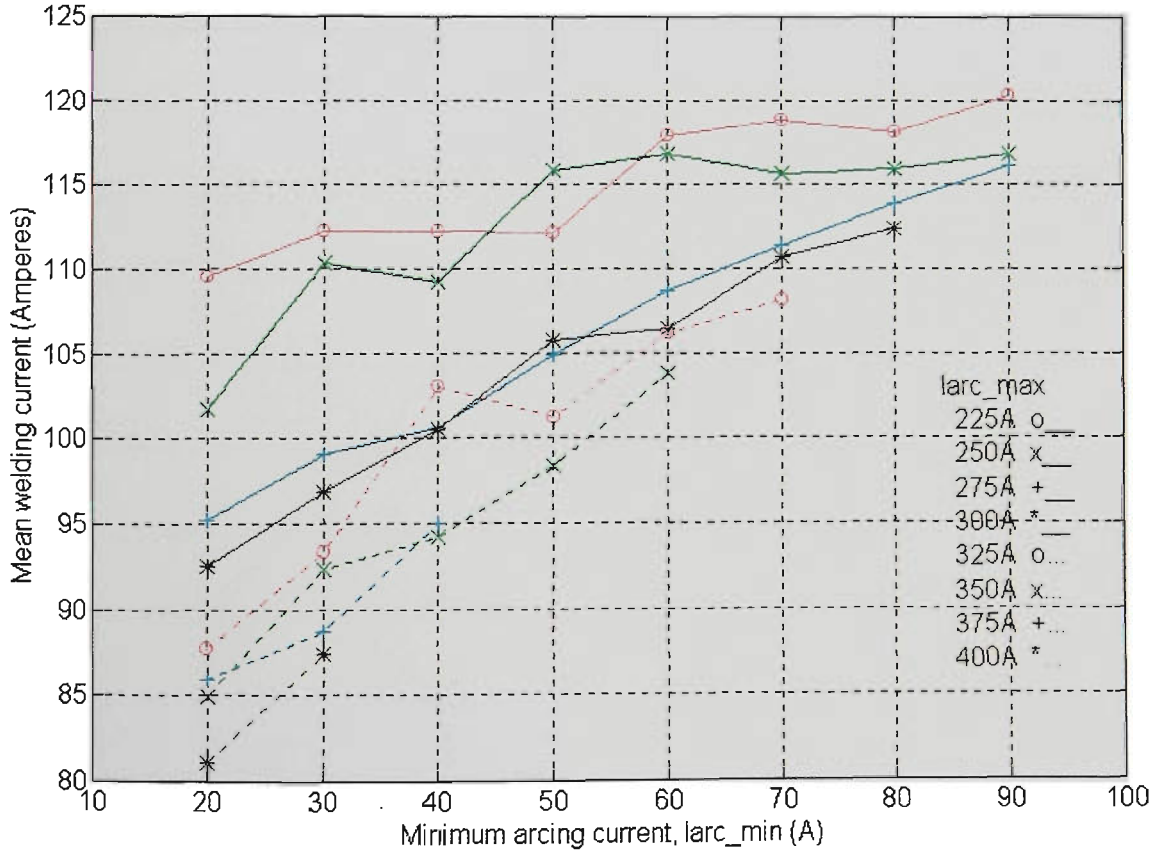

Figure 10.73 Mean welding current vs Iarc_min & Iarc_max (CO_2, CTWD=12mm, WFR=5.7m/min, Travel=195mm/min)

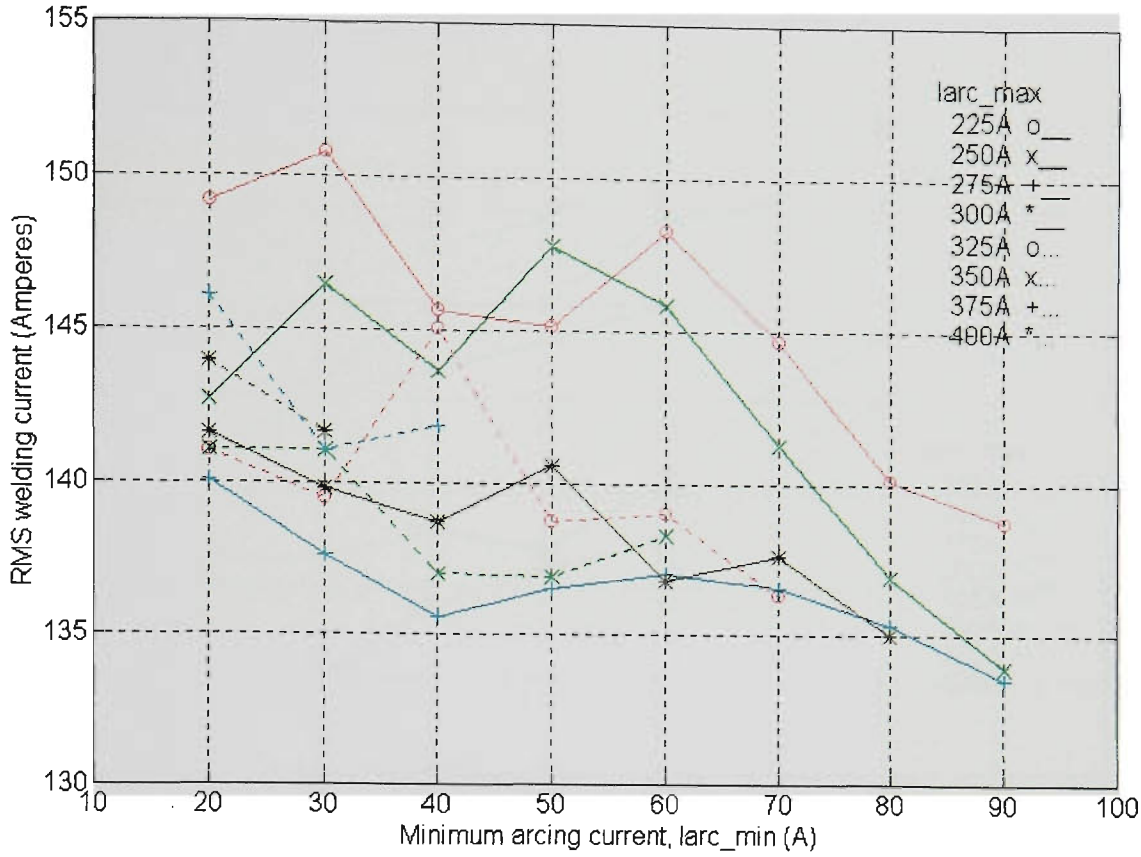

Figure 10.74 RMS welding current vs Iarc_min & Iarc_max (CO_2, CTWD=12mm, WFR=5.7m/min, Travel=195mm/min)

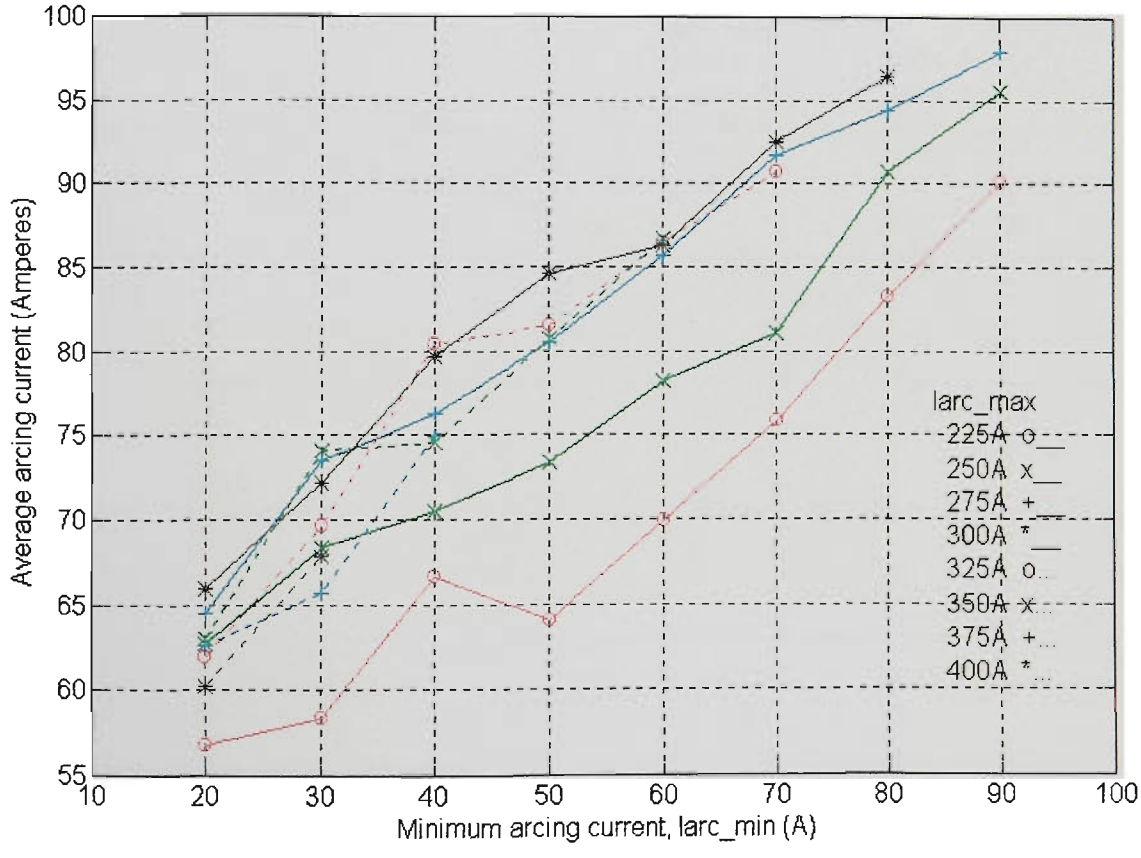

Figure 10.75 Average arcing current vs Iarc_min & Iarc_max (CO_2, CTWD=12mm, WFR=5.7m/min, Travel=195mm/min)

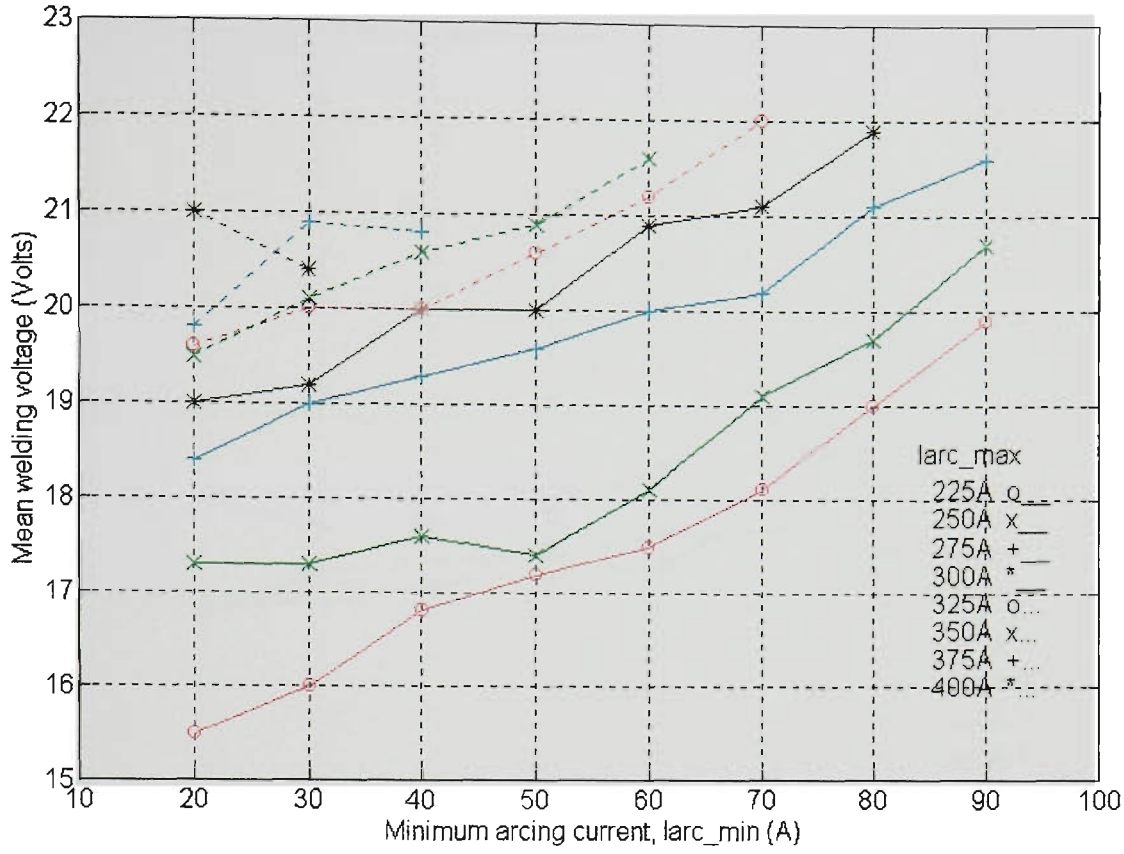

Figure 10.76 Mean voltage vs Iarc_min & Iarc_max

(CO_2, CTWD=12mm, WFR=5.7m/min, Travel=195mm/min)

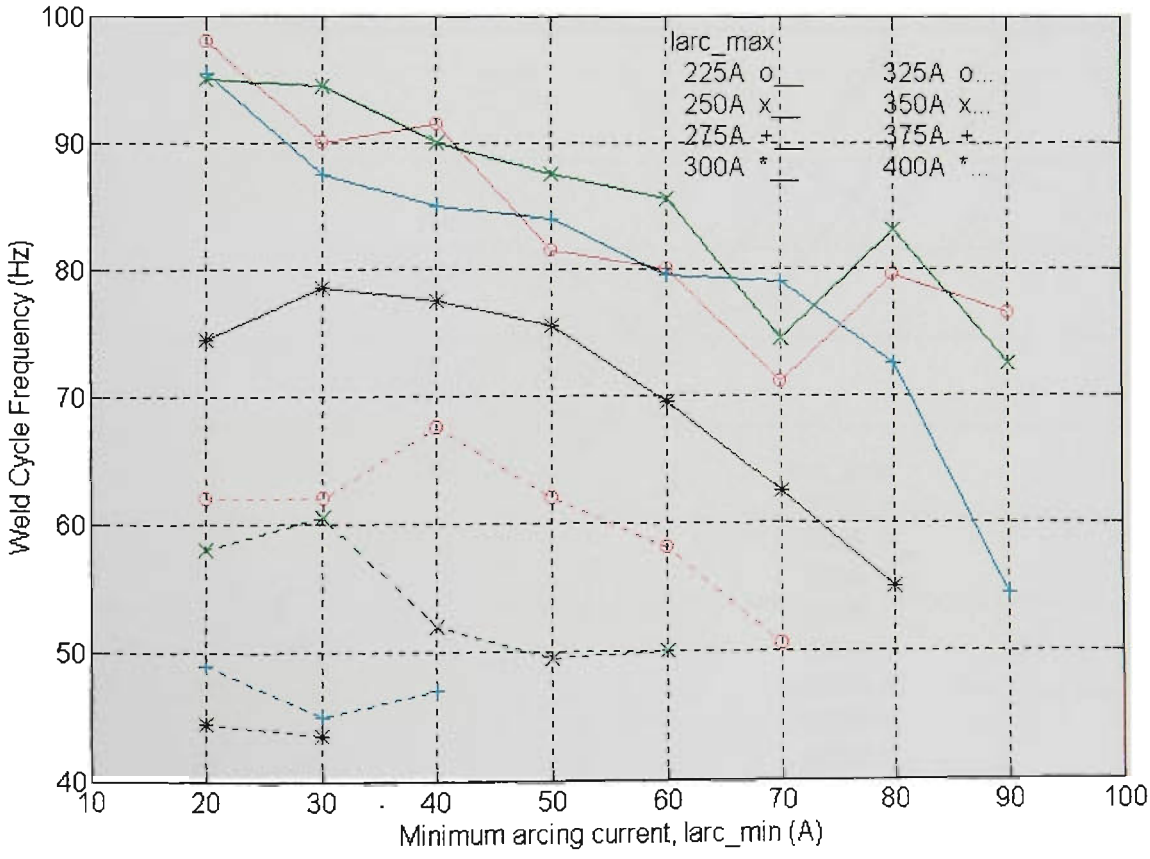

Figure 10.77 Average dipping frequency vs Iarc_min & Iarc_max

(CO_2, CTWD=12mm, WFR=5.7m/min, Travel=195mm/min)

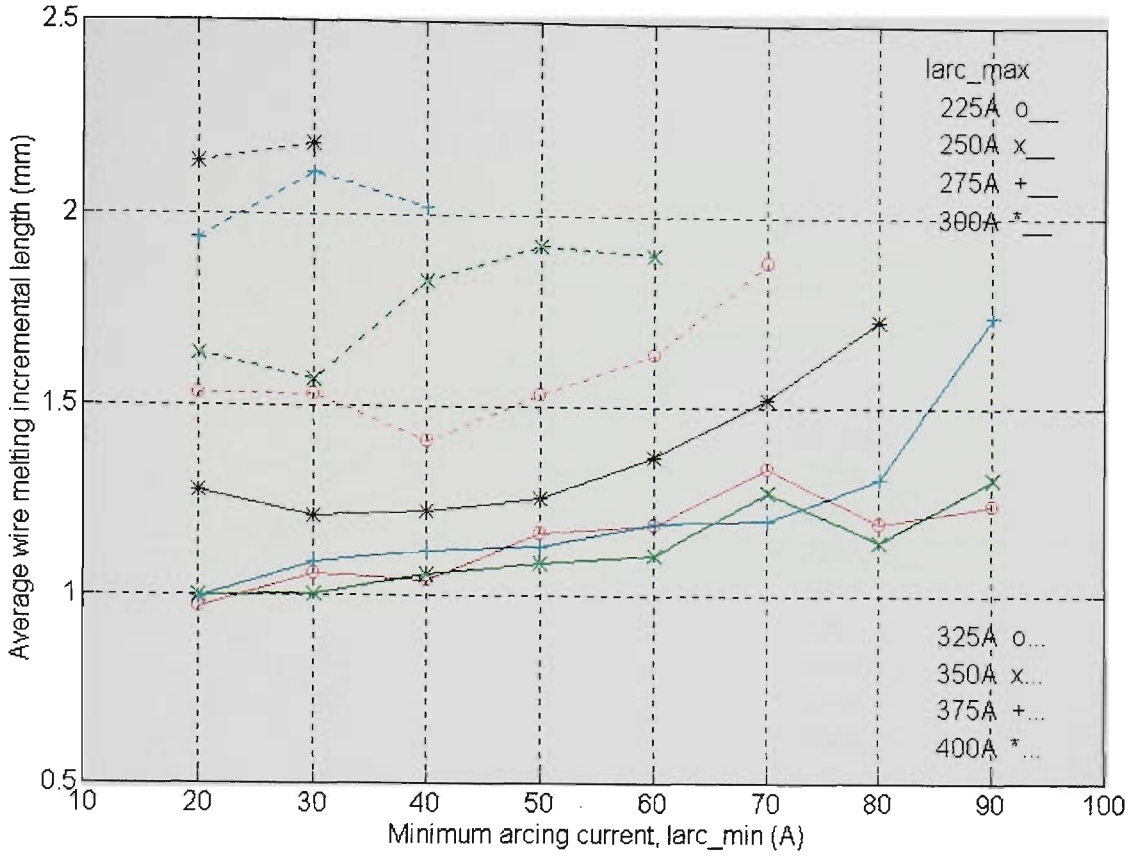

Figure 10.78 Avg wire melting incremental length ΔL vs Iarc_min & Iarc_max (CO_2, CTWD=12mm, WFR=5.7m/min, Travel=195mm/min)

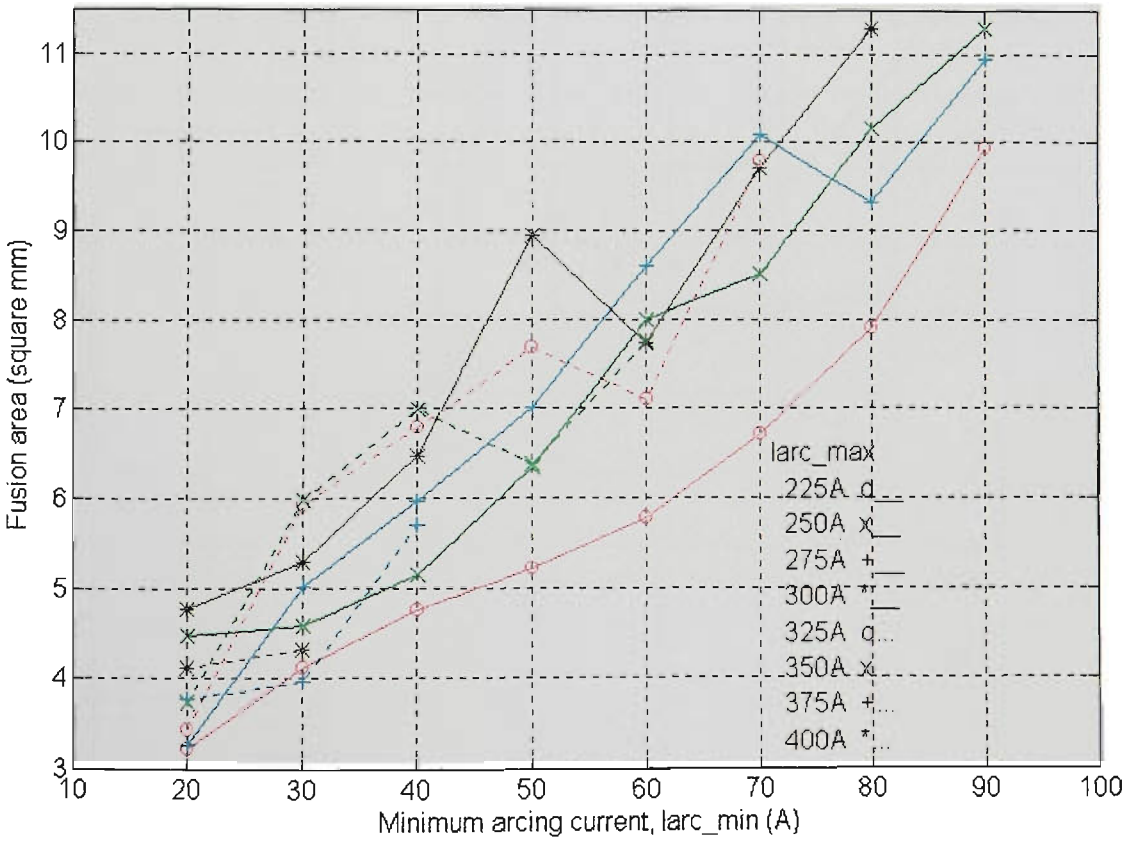

Figure 10.79 Fusion area vs Iarc_min & Iarc_max (CO_2, CTWD=12mm, WFR=5.7m/min, Travel=195mm/min)

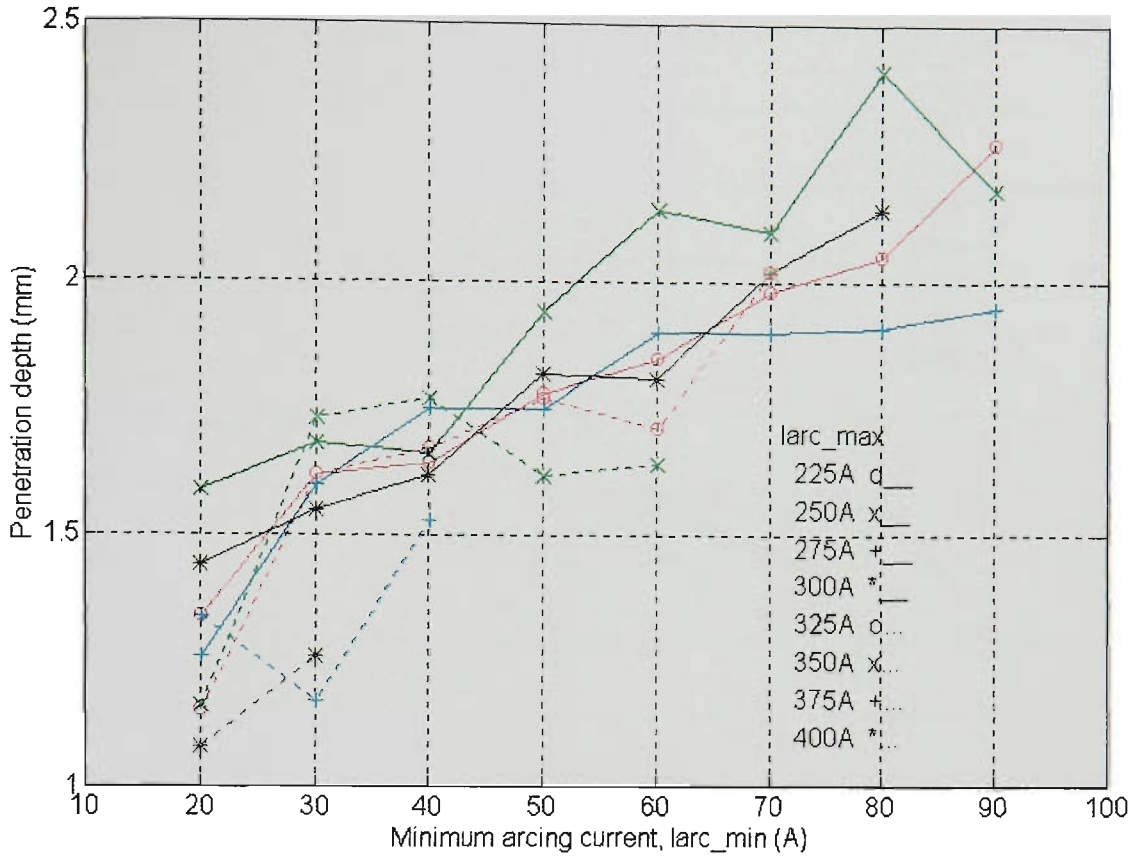

Figure 10.80 Penetration depth vs Iarc_min & Iarc_max
(CO_2, CTWD=12mm, WFR=5.7m/min, Travel=195mm/min)

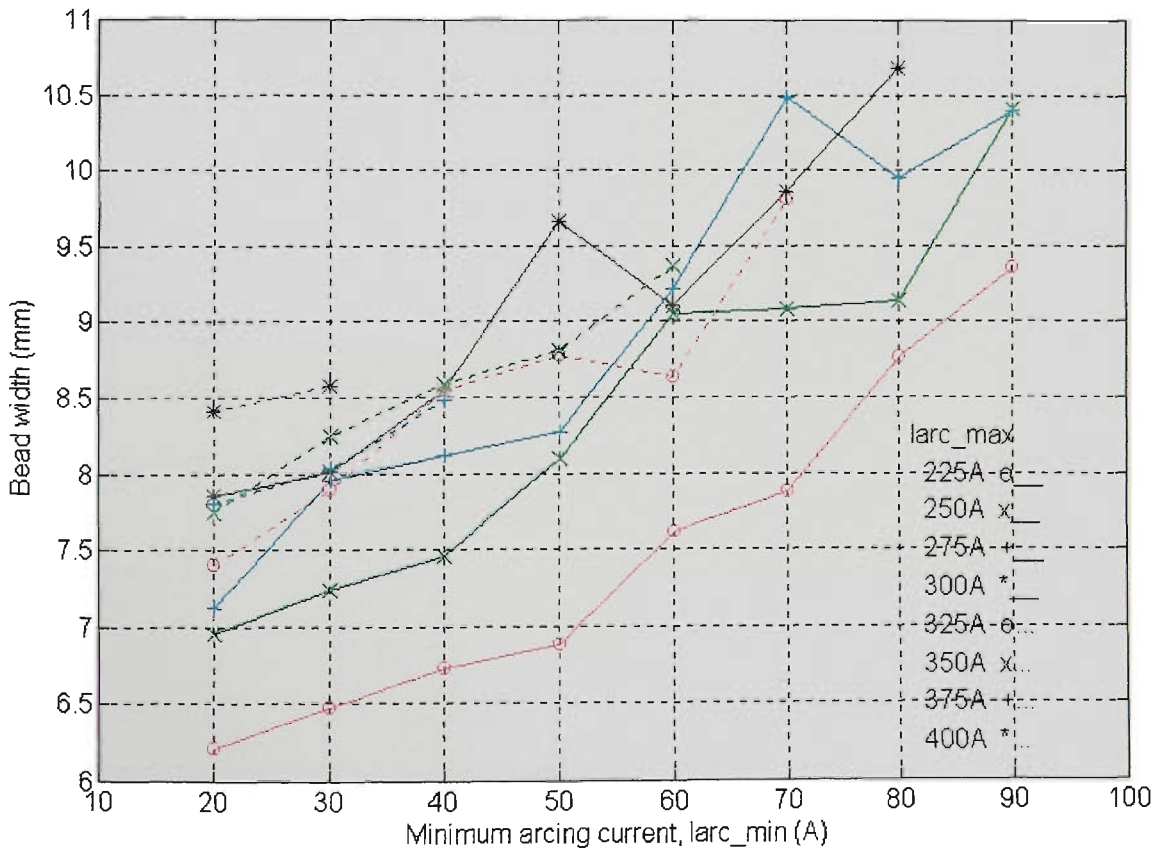

Figure 10.81 Weld bead width vs Iarc_min & Iarc_max
(CO_2, CTWD=12mm, WFR=5.7m/min, Travel=195mm/min)

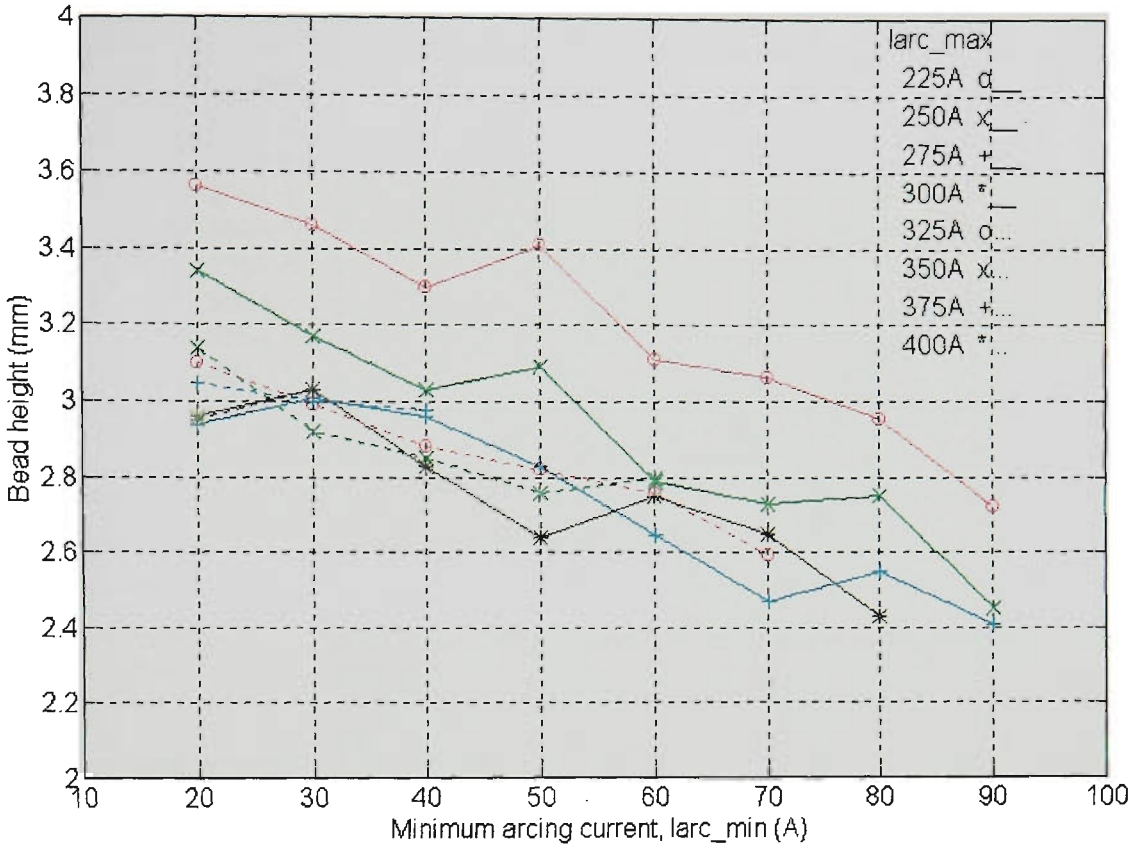

Figure 10.82 Weld bead height vs Iarc_min & Iarc_max

(CO_2, CTWD=12mm, WFR=5.7m/min, Travel=195mm/min)

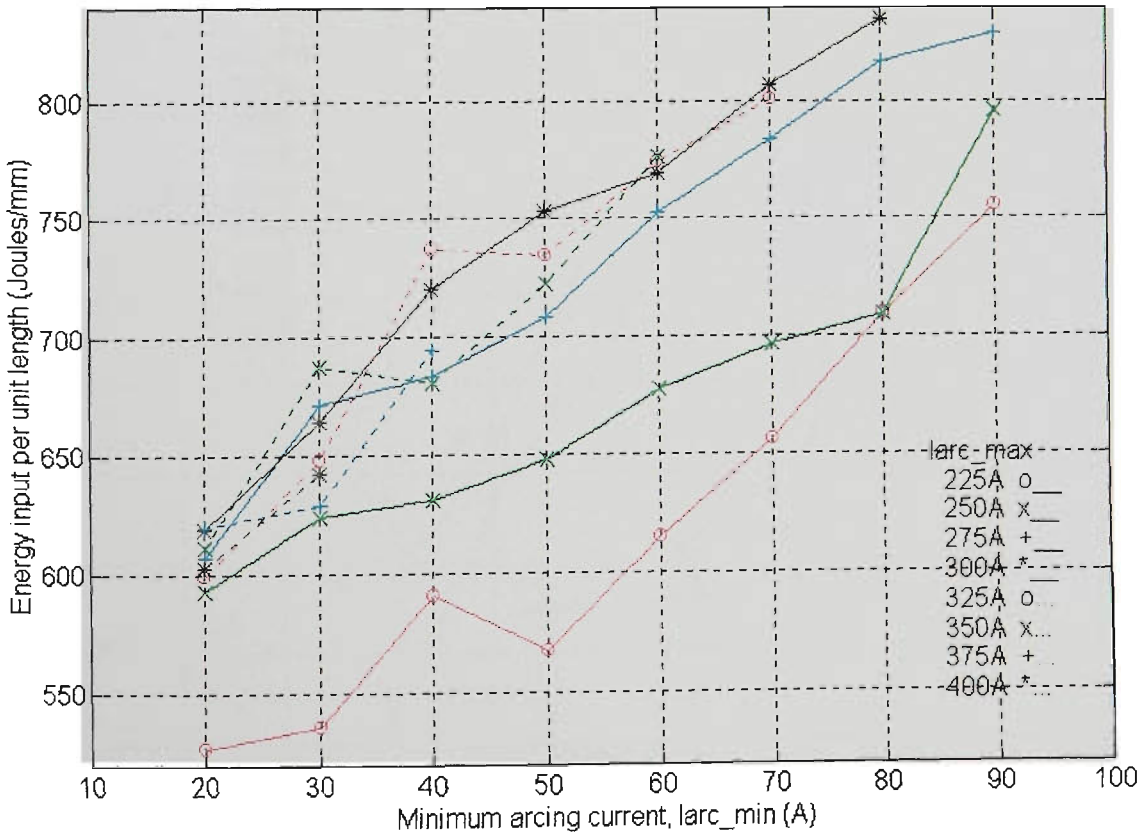

Figure 10.83 Energy input per unit length of weld vs Iarc_min & Iarc_max

(CO_2, CTWD=12mm, WFR=5.7m/min, Travel=195mm/min)

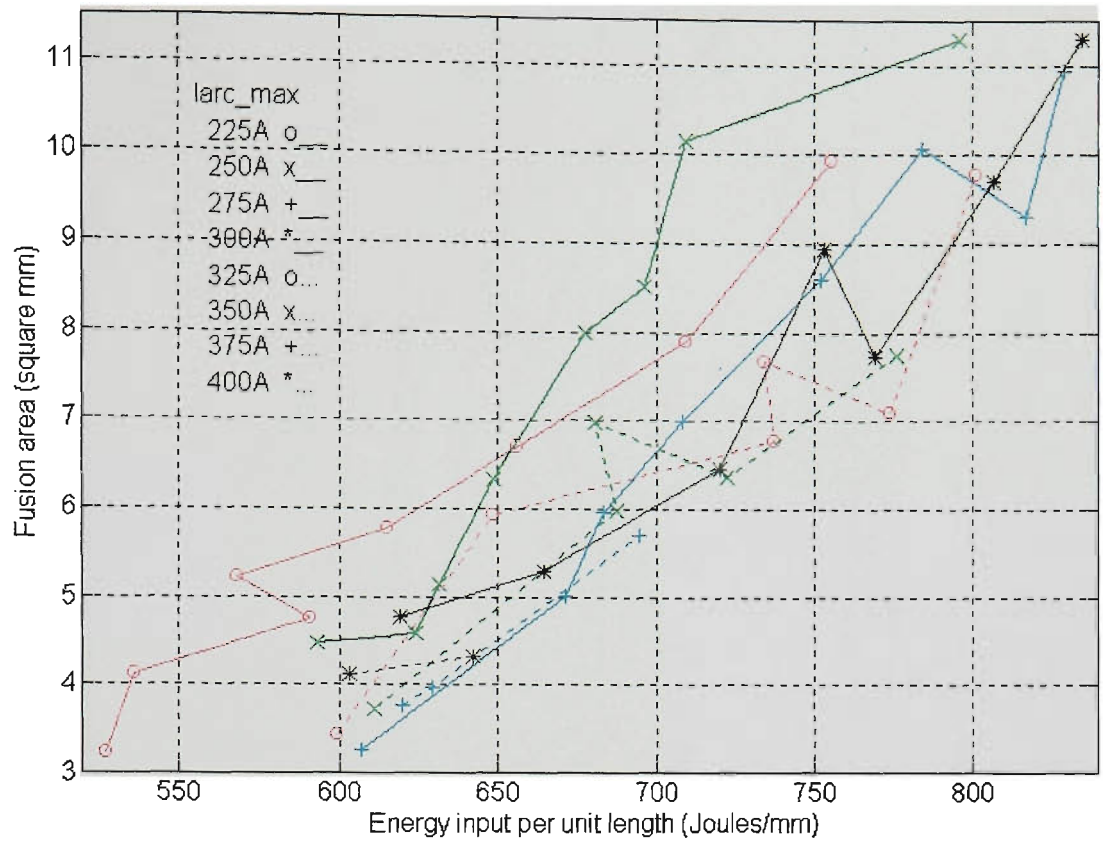

Figure 10.84 Fusion area vs Energy input per unit length of weld (CO_2, CTWD=12mm, WFR=5.7m/min, Travel=195mm/min)

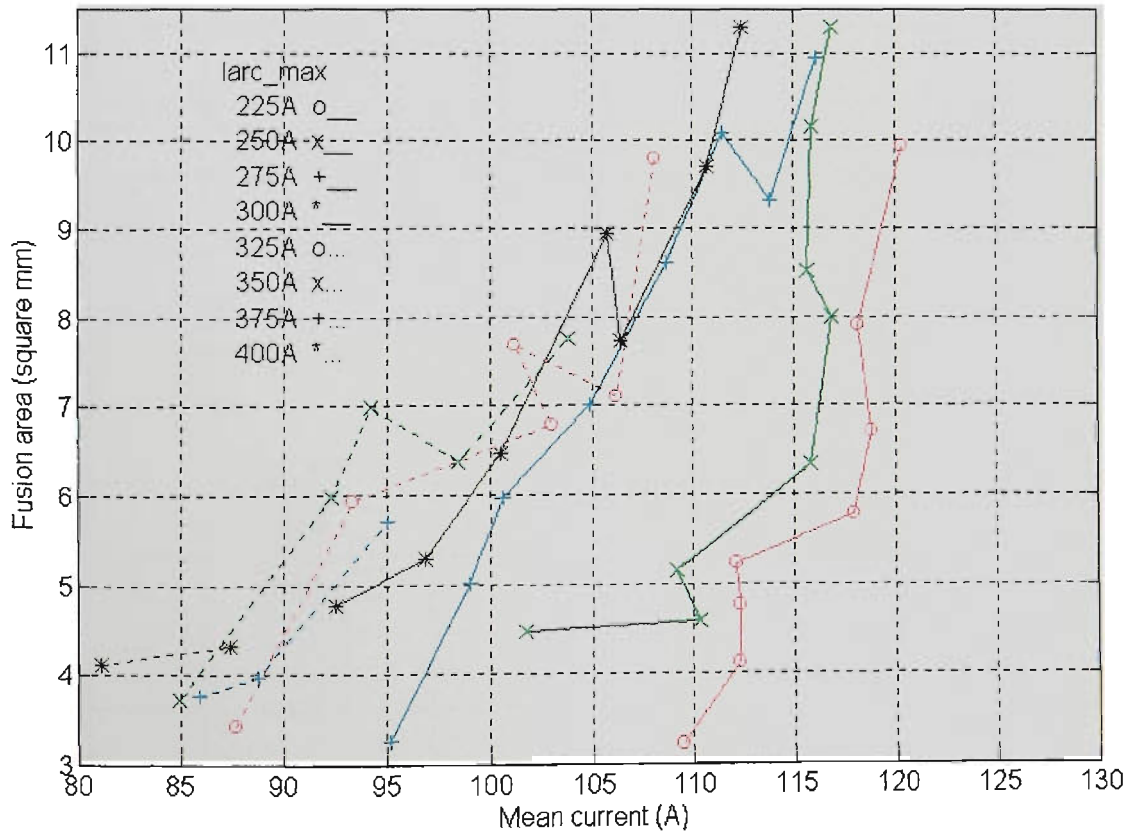

Figure 10.85 Fusion area vs Mean welding current (CO_2, CTWD=12mm, WFR=5.7m/min, Travel=195mm/min)

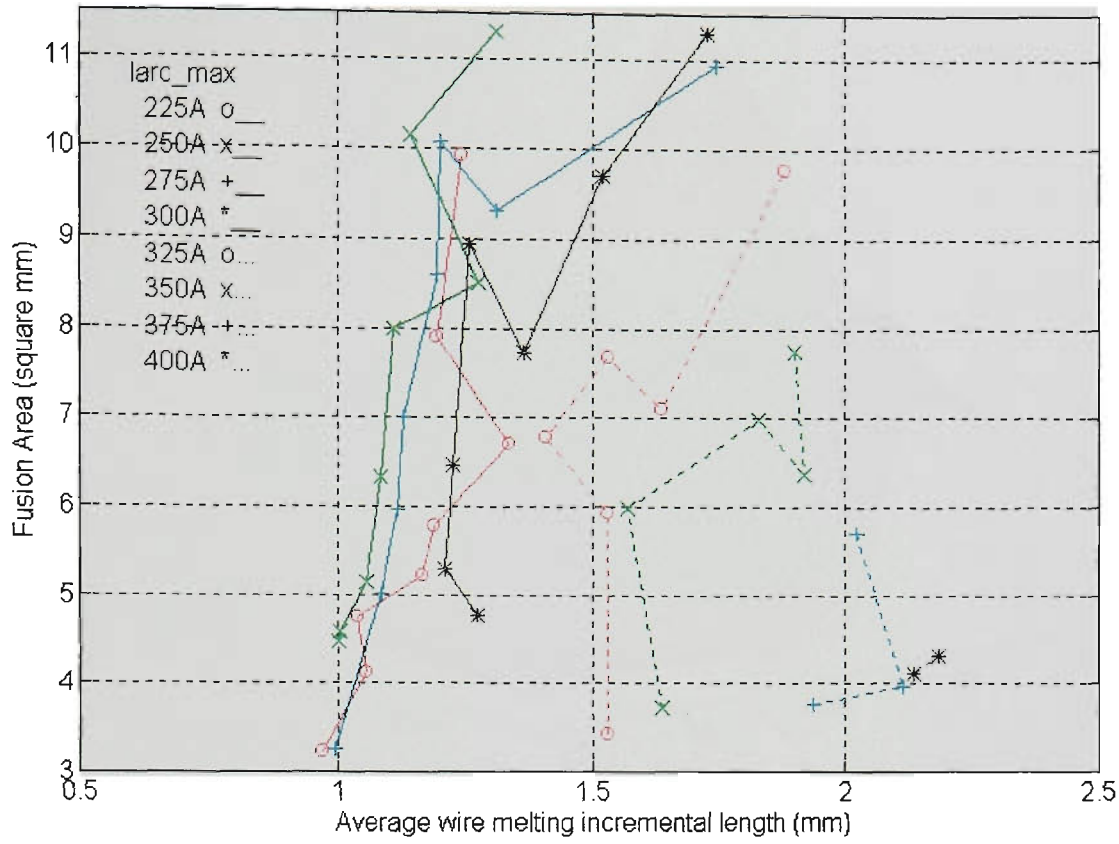

Figure 10.86 Fusion area vs Average wire melting incremental length ΔL (CO_2, CTWD=12mm, WFR=5.7m/min, Travel=195mm/min)

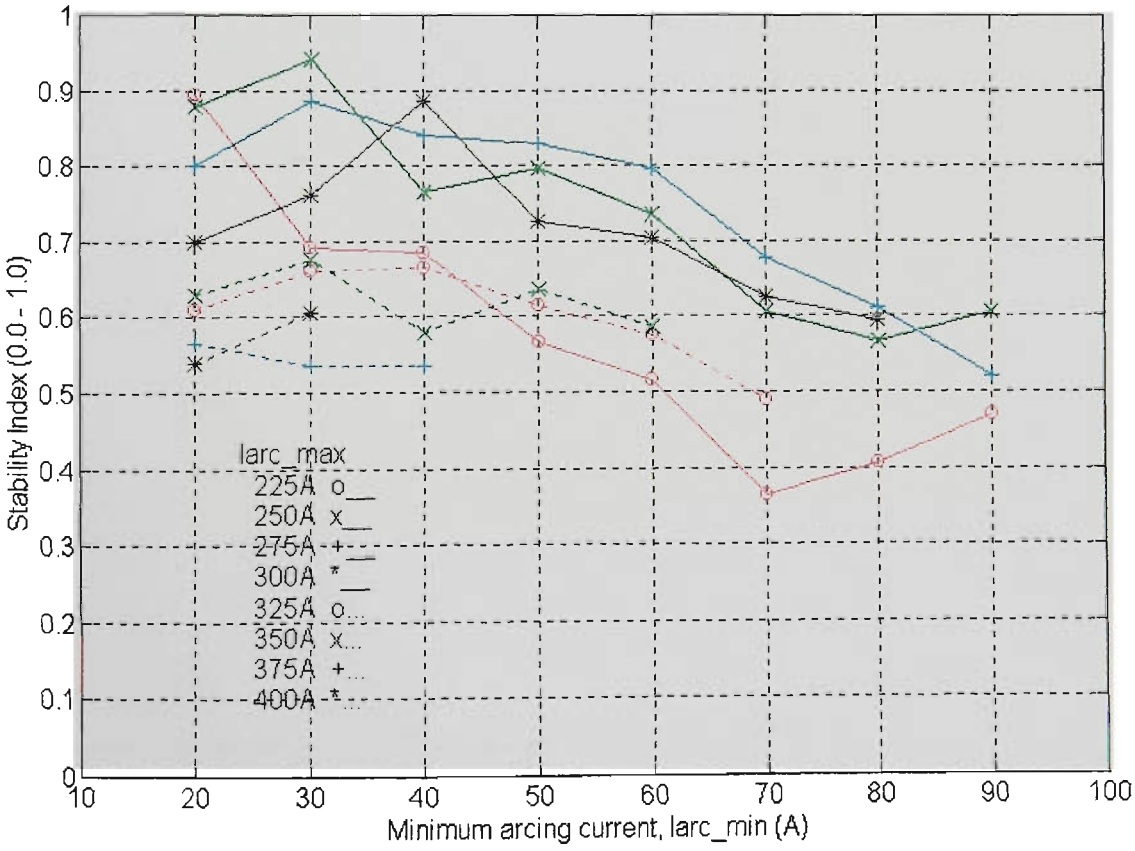

Figure 10.87 Stability index vs Iarc_min & Iarc_max (2D) (CO_2, CTWD=12mm, WFR=5.7m/min, Travel=195mm/min)

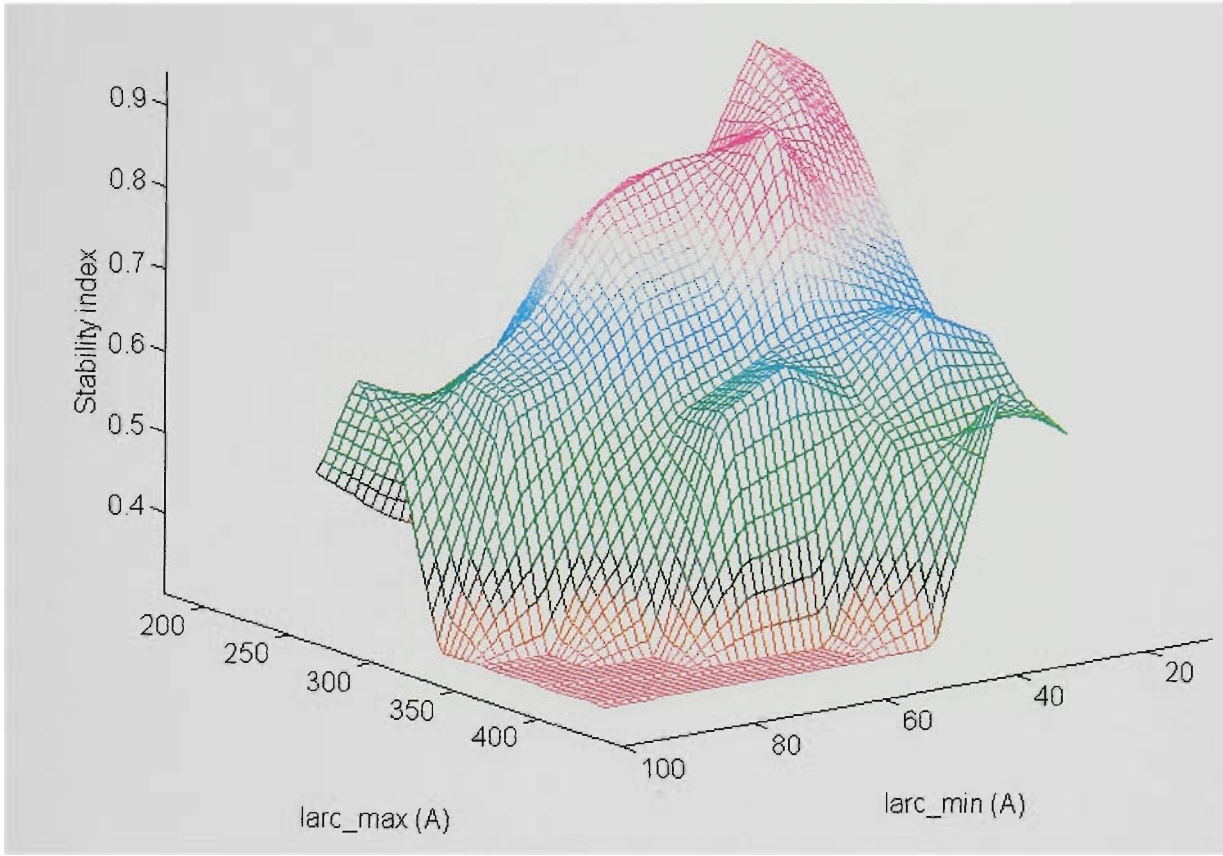

Figure 10.88 Stability index vs Iarc_min & Iarc_max (3D)
(CO_2, CTWD=12mm, WFR=5.7m/min, Travel=195mm/min)

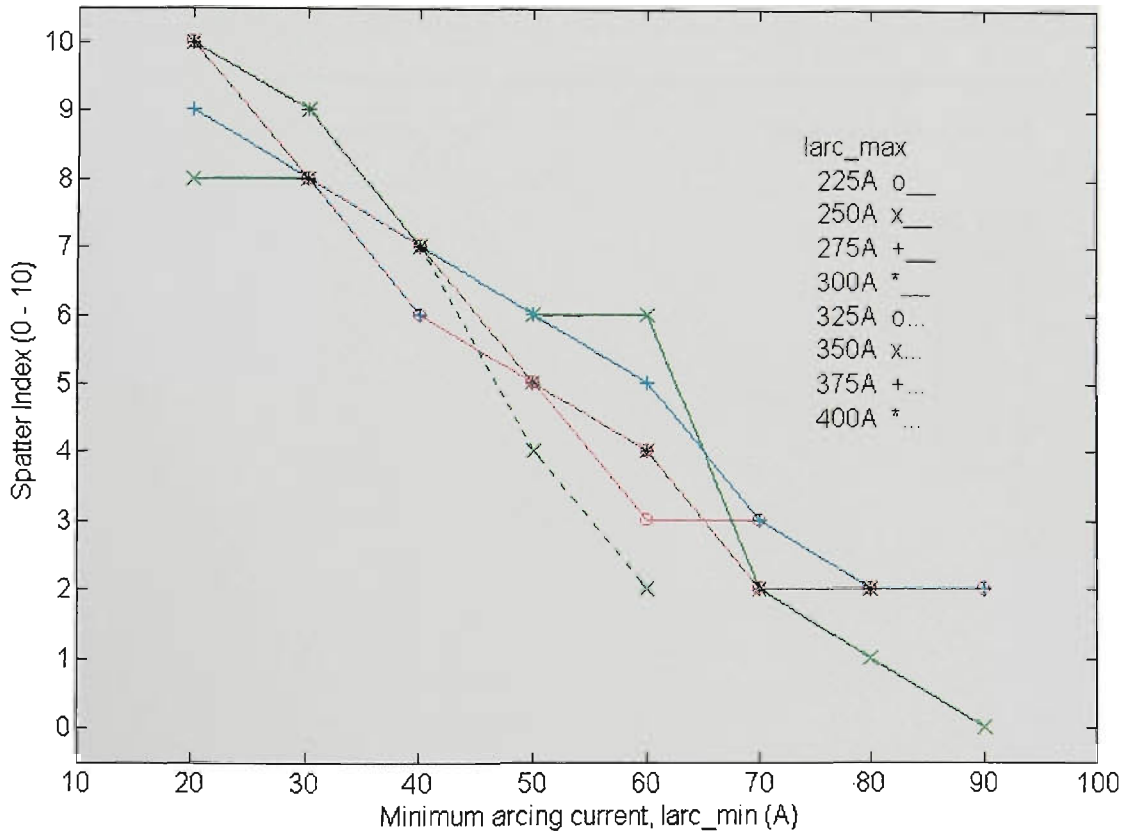

Figure 10.89 Spatter index vs Iarc_min & Iarc_max (2D)
(CO_2, CTWD=12mm, WFR=5.7m/min, Travel=195mm/min)

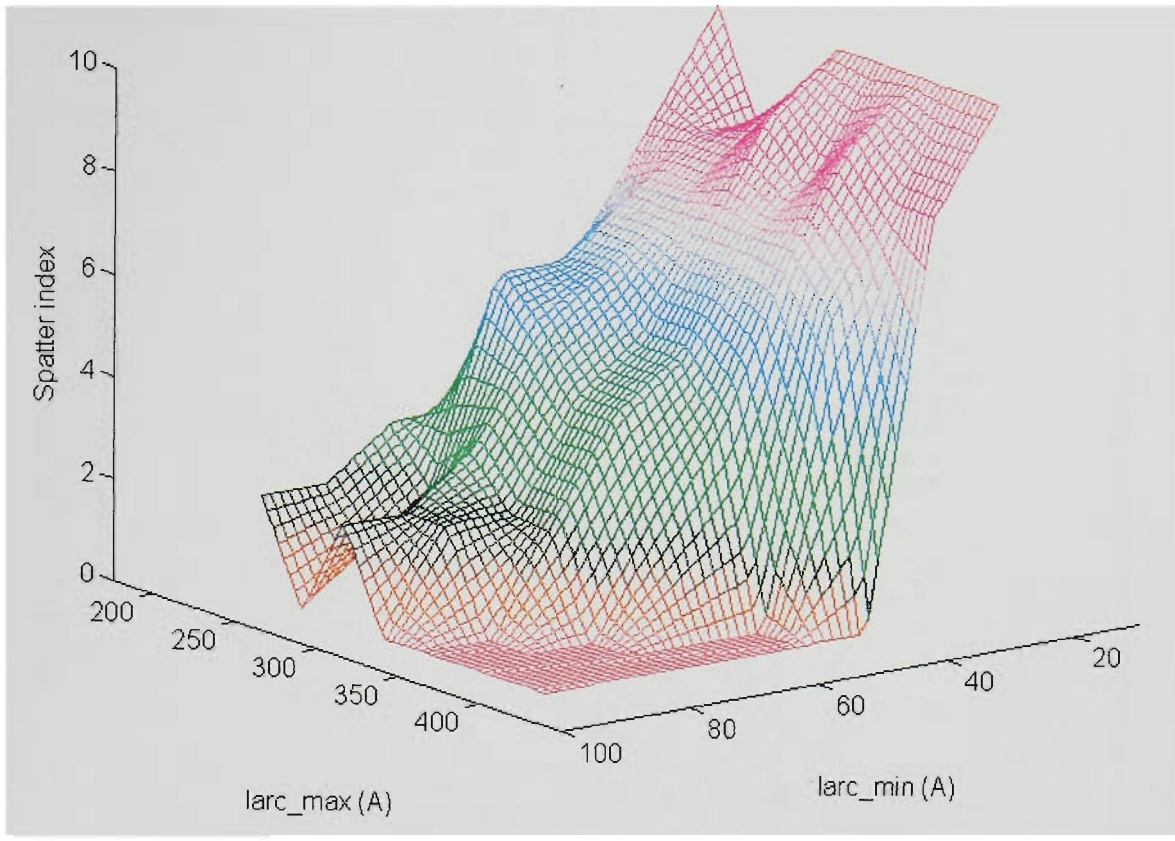

Figure 10.90 Spatter index vs Iarc_min & Iarc_max (3D)

(CO_2, CTWD=12mm, WFR=5.7m/min, Travel=195mm/min)

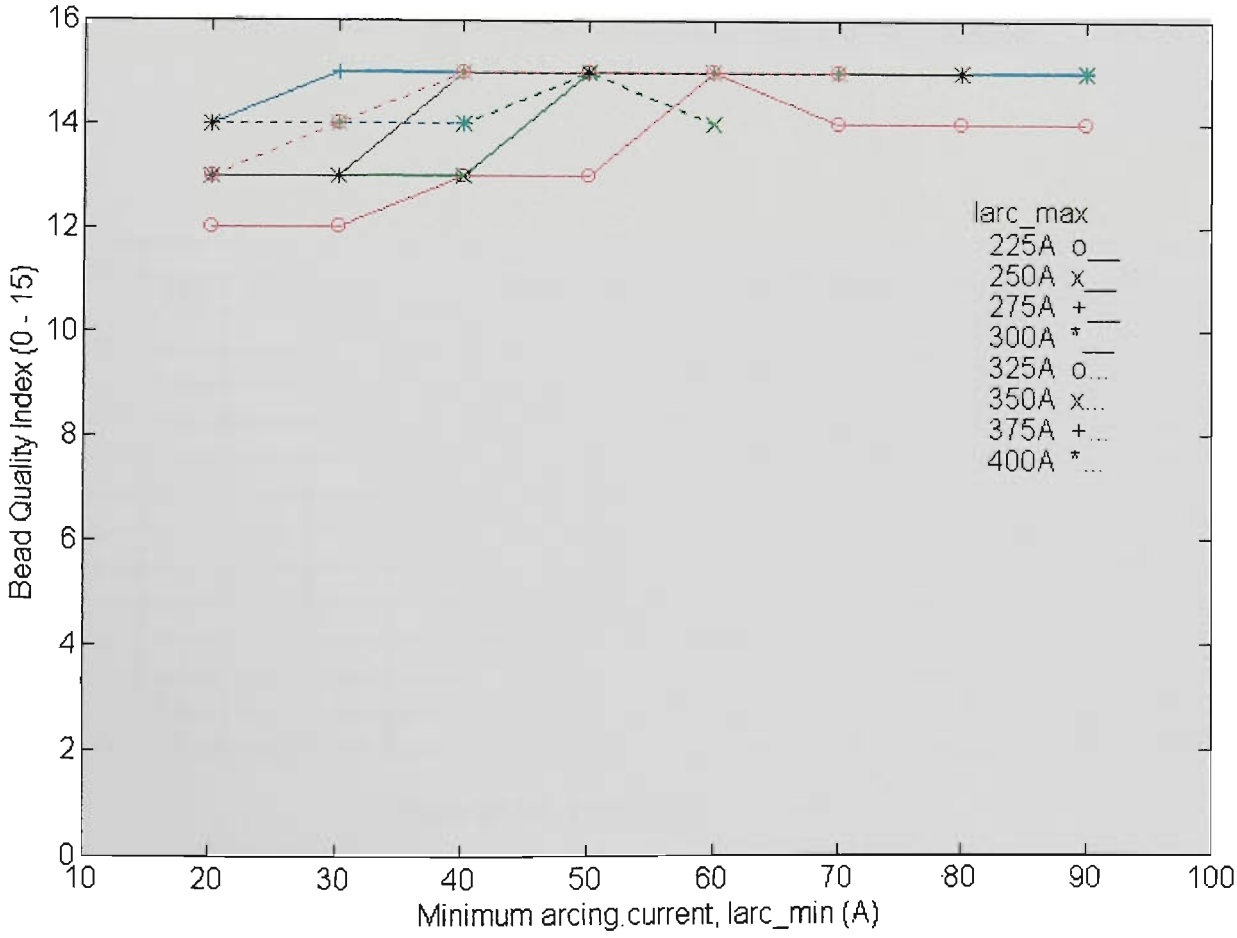

Figure 10.91 Bead quality index vs Iarc_min & Iarc_max

(CO_2, CTWD=12mm, WFR=5.7m/min, Travel=195mm/min)

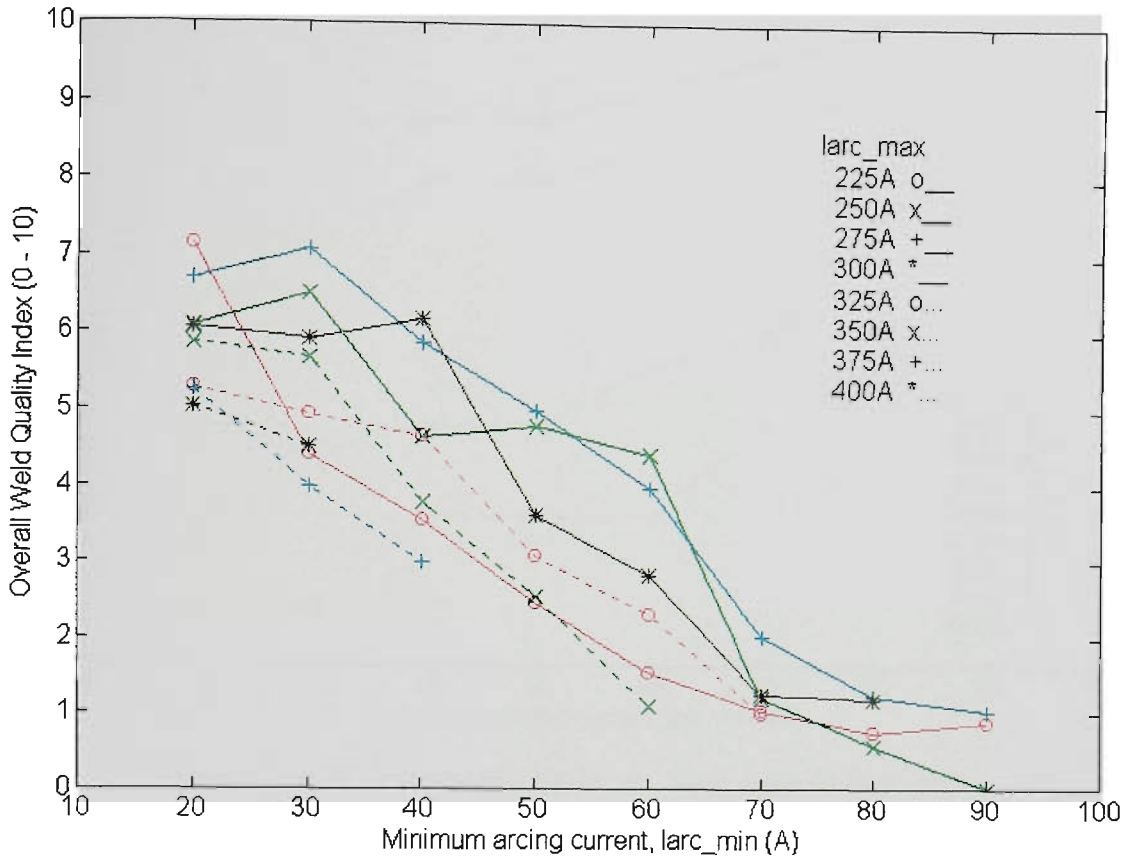

Figure 10.92 Weld overall quality index vs Iarc_min & Iarc_max

(CO_2, CTWD=12mm, WFR=5.7m/min, Travel=195mm/min)

Iarc_min	Iarc_max												
	150	175	200	225	250	275	300	325	350	375	400	425	450
10													
20				-	X	X	X	X	X	X	X		
30				-	X	X	X	X	X	X	X		
40				-	X	X	X	X	X	-			
50				-	X	X	X	-	-				
60				-	X	X	-	-	-				
70				-	-	-	-	-					
80				-	-	-	-						
90				-	-	-							
100													
110												- = tested	
120												X = useful	

Figure 10.93 Useful operating area

(CO_2, CTWD=12mm, WFR=5.7m/min, Travel=195mm/min)

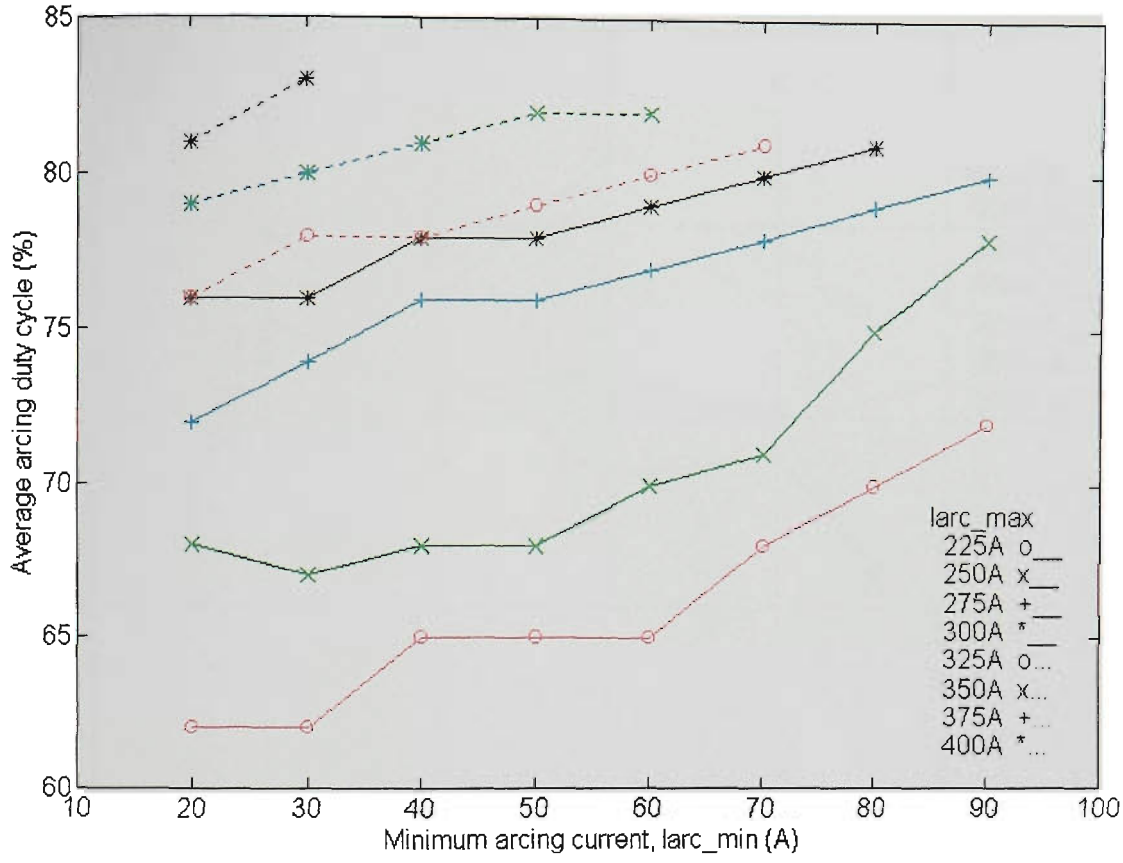

Figure 10.94 Arcing duty cycle vs Iarc_max & Iarc_min
(CO_2, CTWD=12mm, WFR=5.7m/min, Travel=195mm/min)

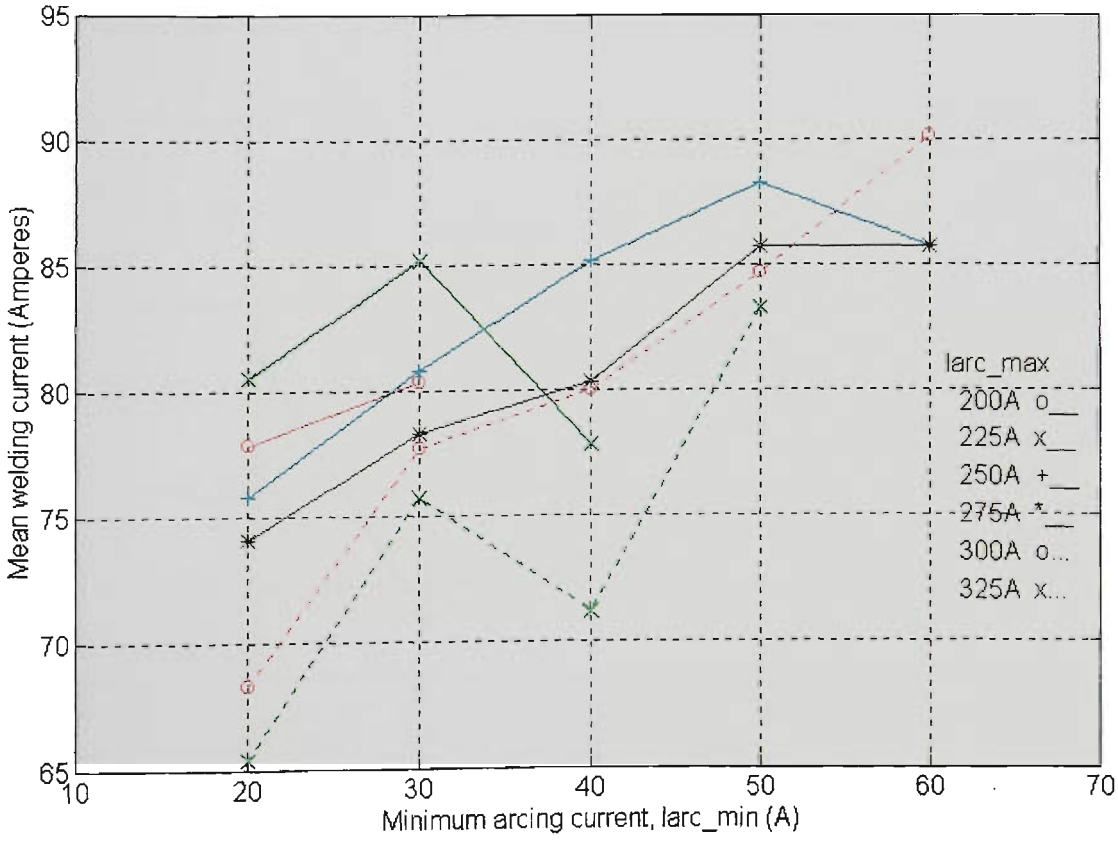

Figure 10.103 Mean welding current vs Iarc_min & Iarc_max
(CO_2, CTWD=20mm, WFR=5.7m/min, Travel=195mm/min)

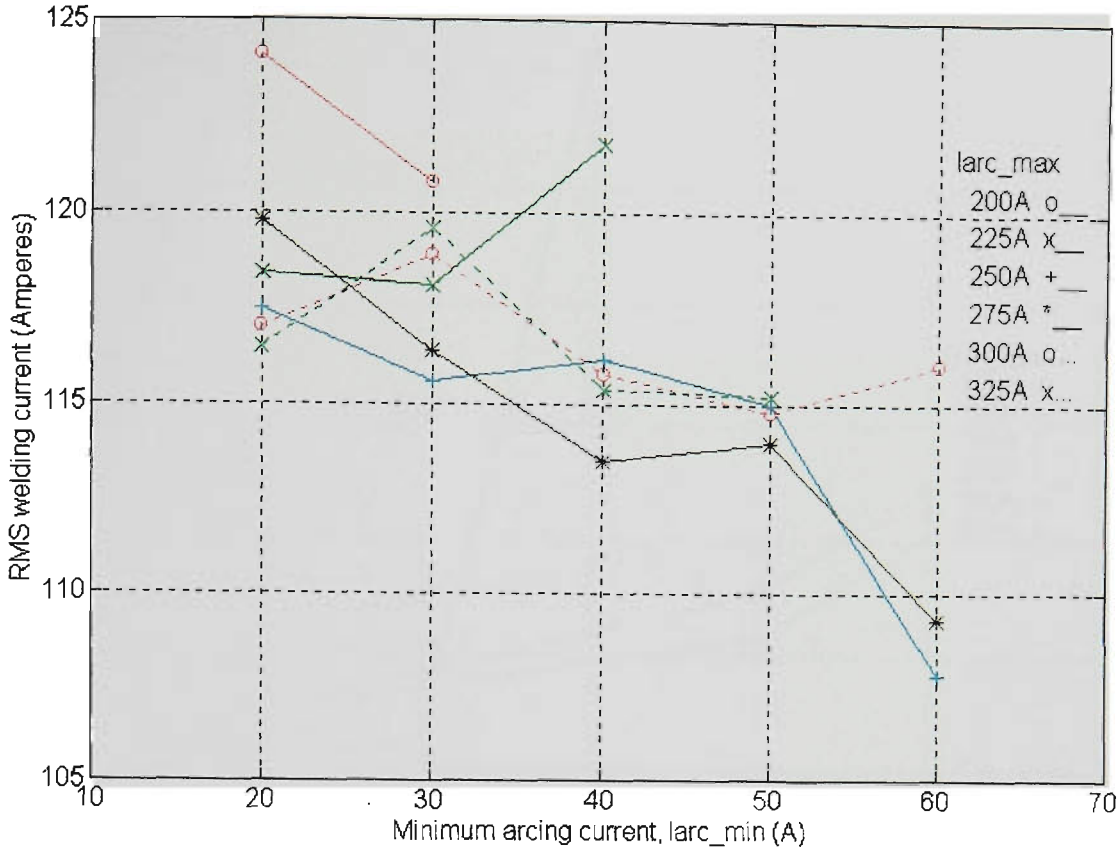

Figure 10.104 RMS welding current vs Iarc_min & Iarc_max (CO_2, CTWD=20mm, WFR=5.7m/min, Travel=195mm/min)

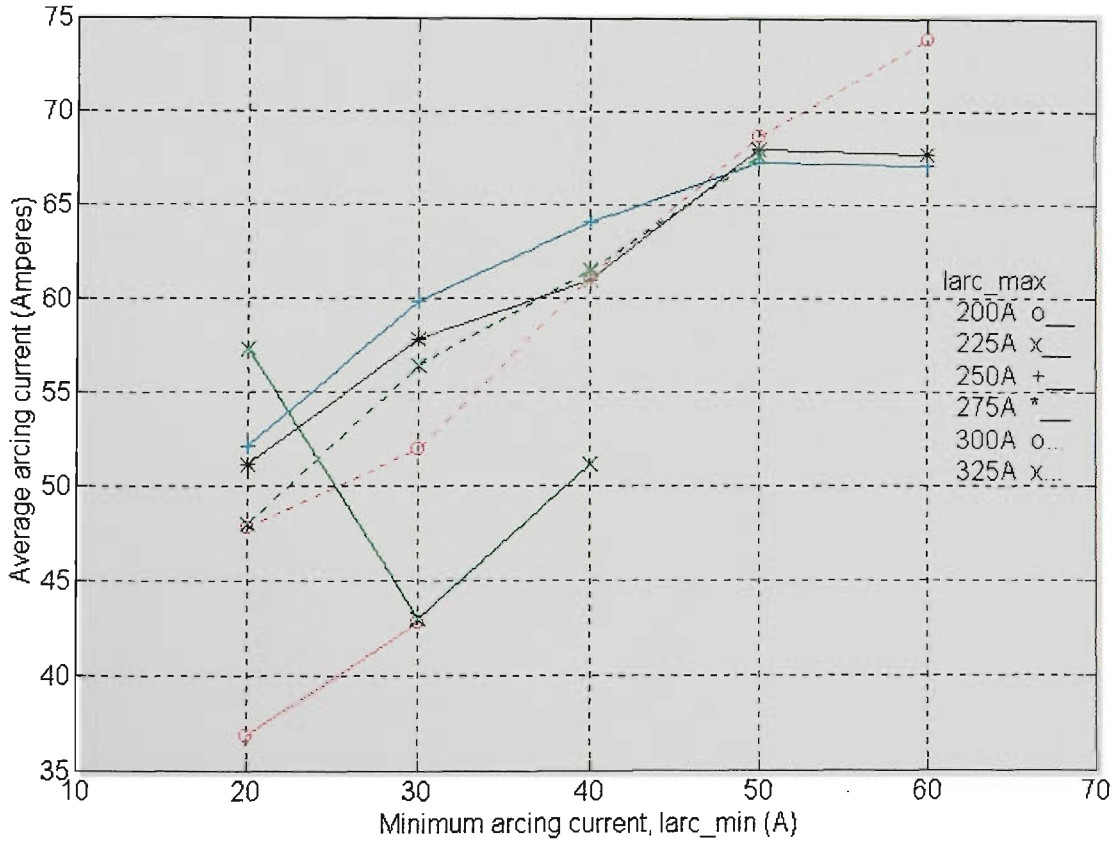

Figure 10.105 Average arcing current vs Iarc_min & Iarc_max (CO_2, CTWD=20mm, WFR=5.7m/min, Travel=195mm/min)

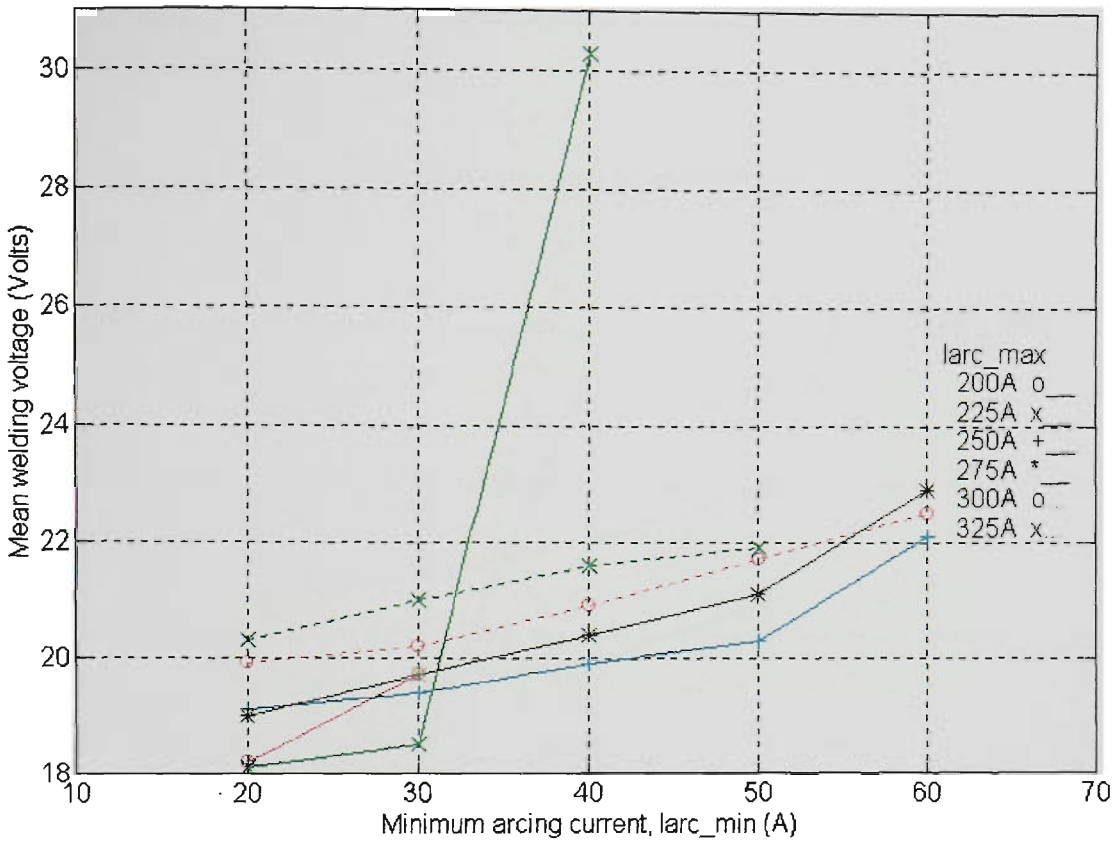

Figure 10.106 Mean voltage vs Iarc_min & Iarc_max

(CO_2, CTWD=20mm, WFR=5.7m/min, Travel=195mm/min)

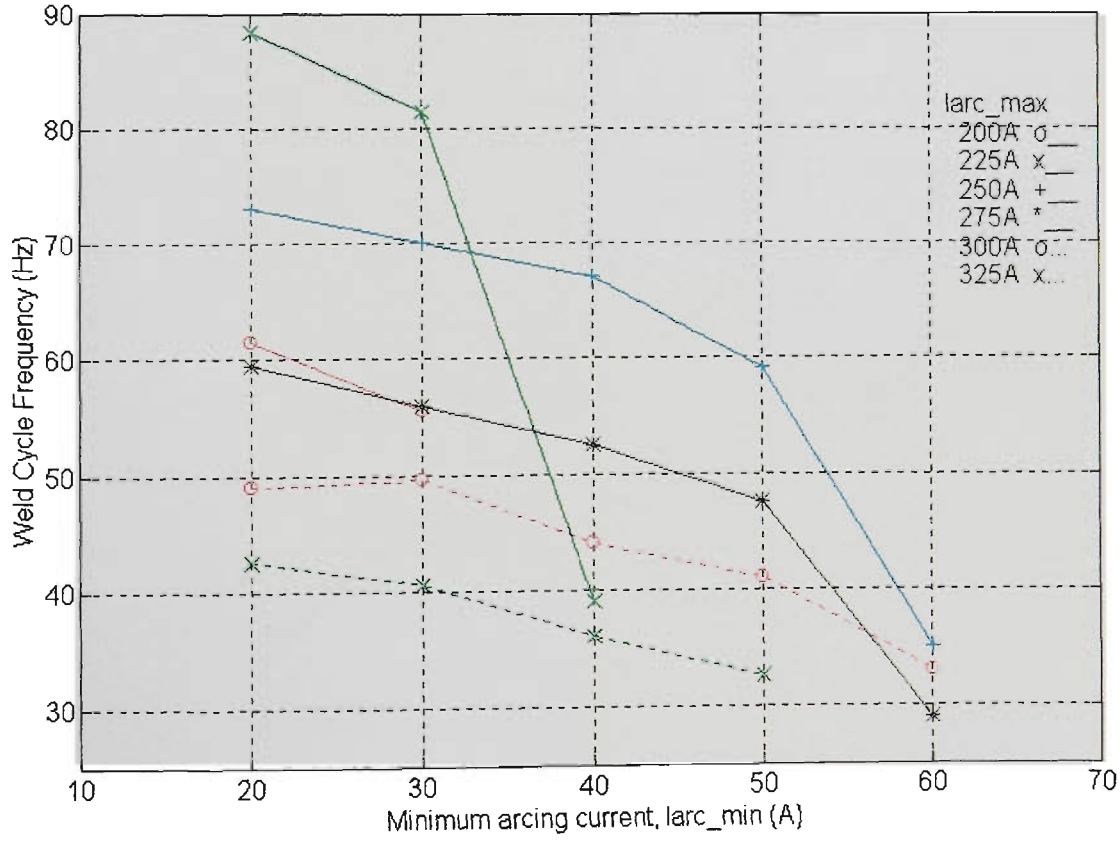

Figure 10.107 Average dipping frequency vs Iarc_min & Iarc_max

(CO_2, CTWD=20mm, WFR=5.7m/min, Travel=195mm/min)

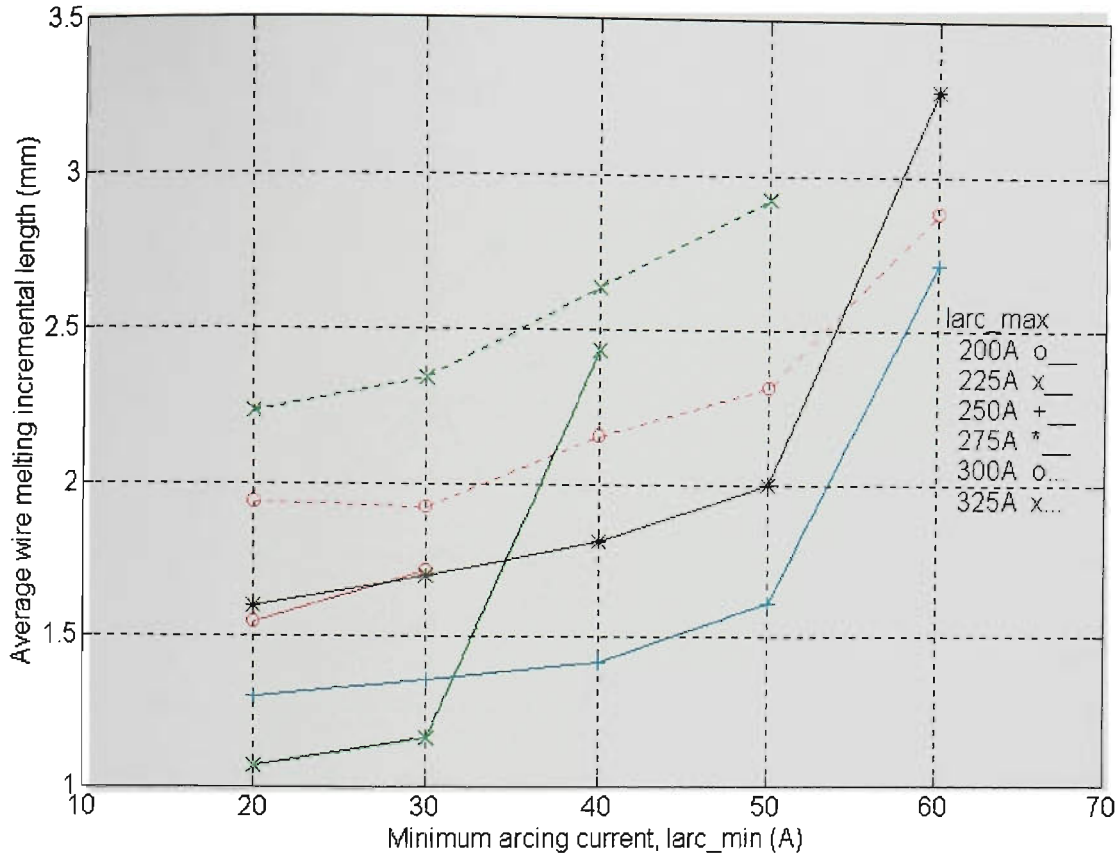

Figure 10.108 Avg wire melting incremental length ΔL vs Iarc_min & Iarc_max (CO_2, CTWD=20mm, WFR=5.7m/min, Travel=195mm/min)

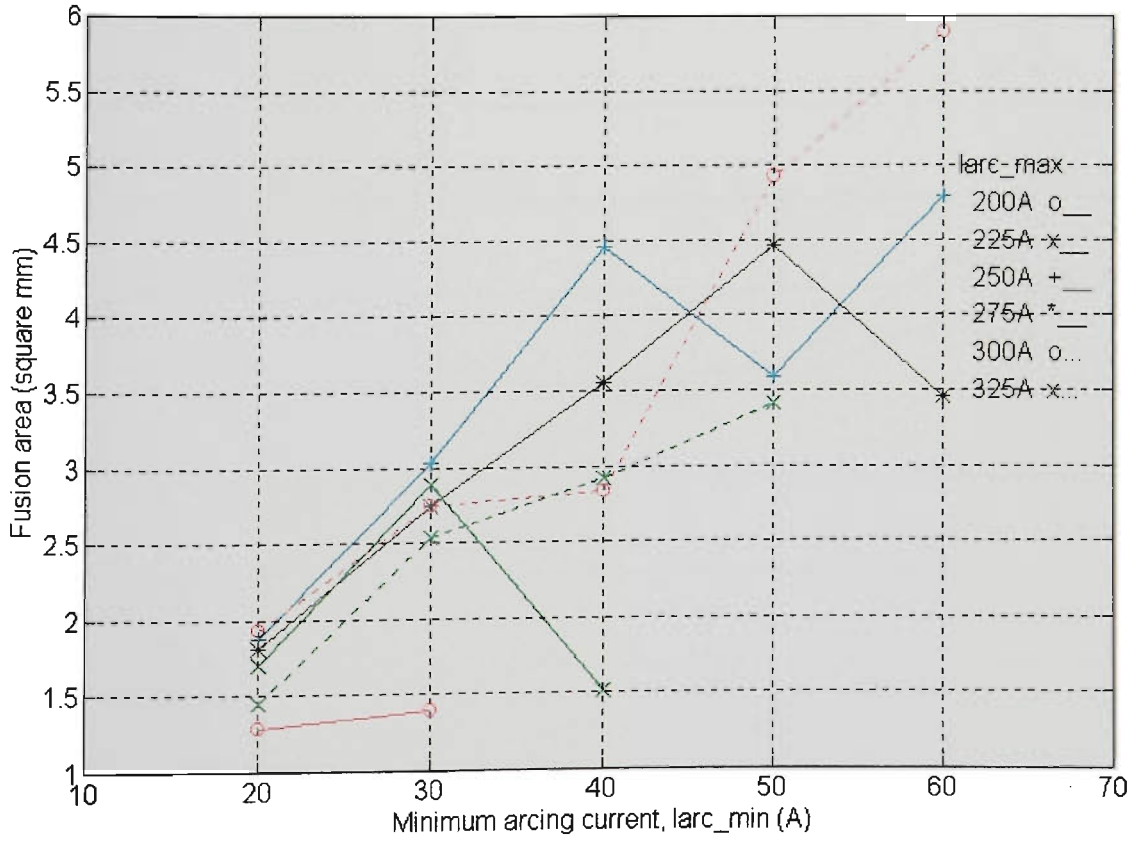

Figure 10.109 Fusion area vs Iarc_min & Iarc_max (CO_2, CTWD=20mm, WFR=5.7m/min, Travel=195mm/min)

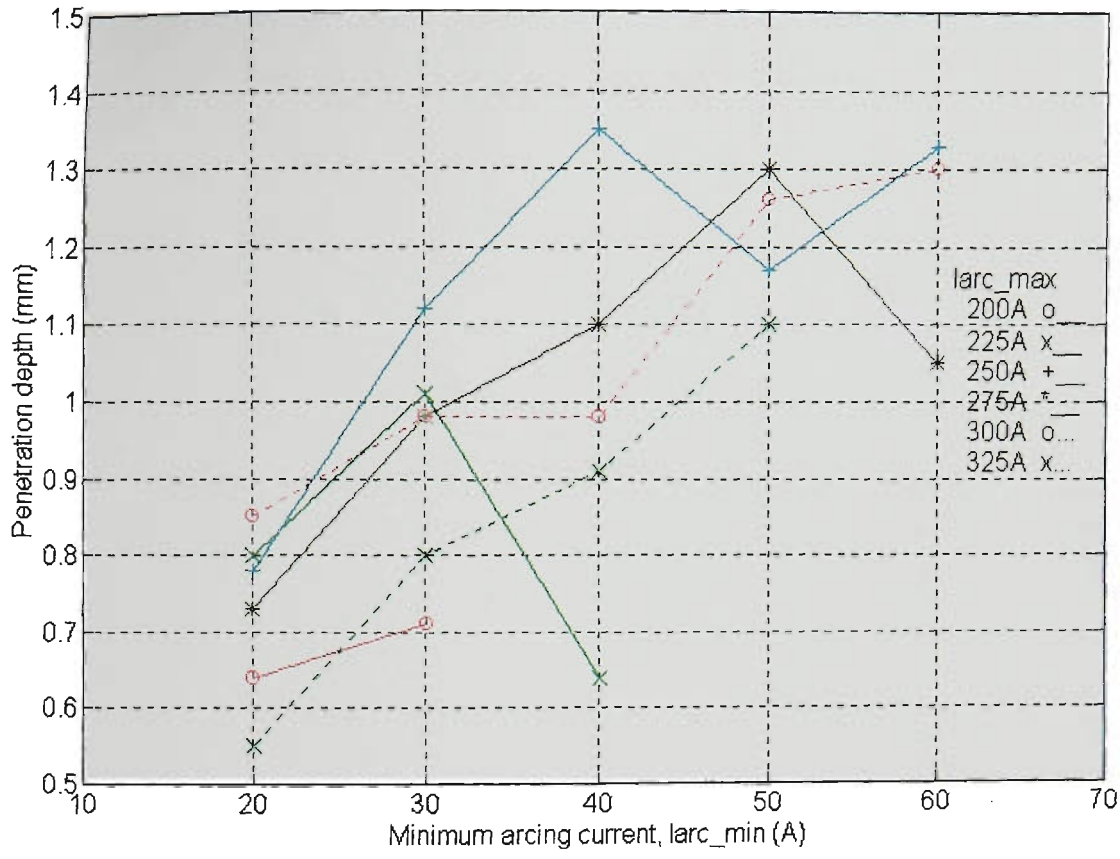

Figure 10.110 Penetration depth vs Iarc_min & Iarc_max
(CO_2, CTWD=20mm, WFR=5.7m/min, Travel=195mm/min)

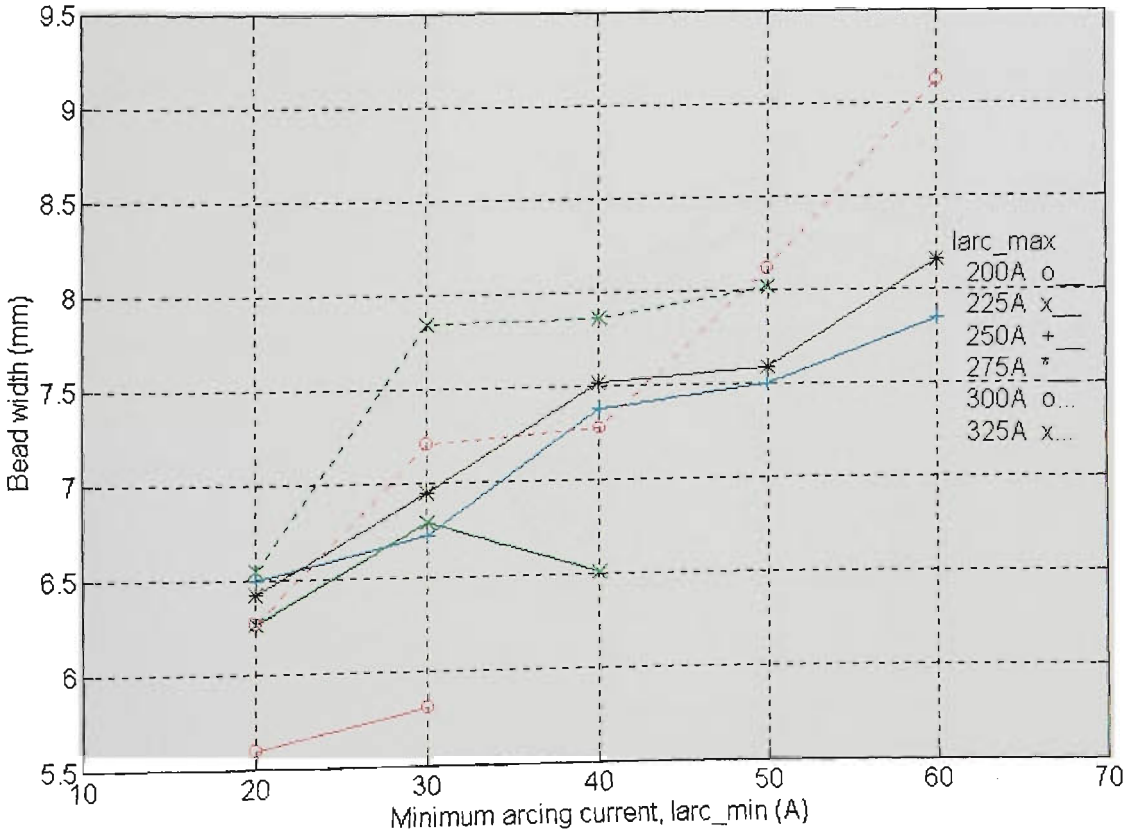

Figure 10.111 Weld bead width vs Iarc_min & Iarc_max
(CO_2, CTWD=20mm, WFR=5.7m/min, Travel=195mm/min)

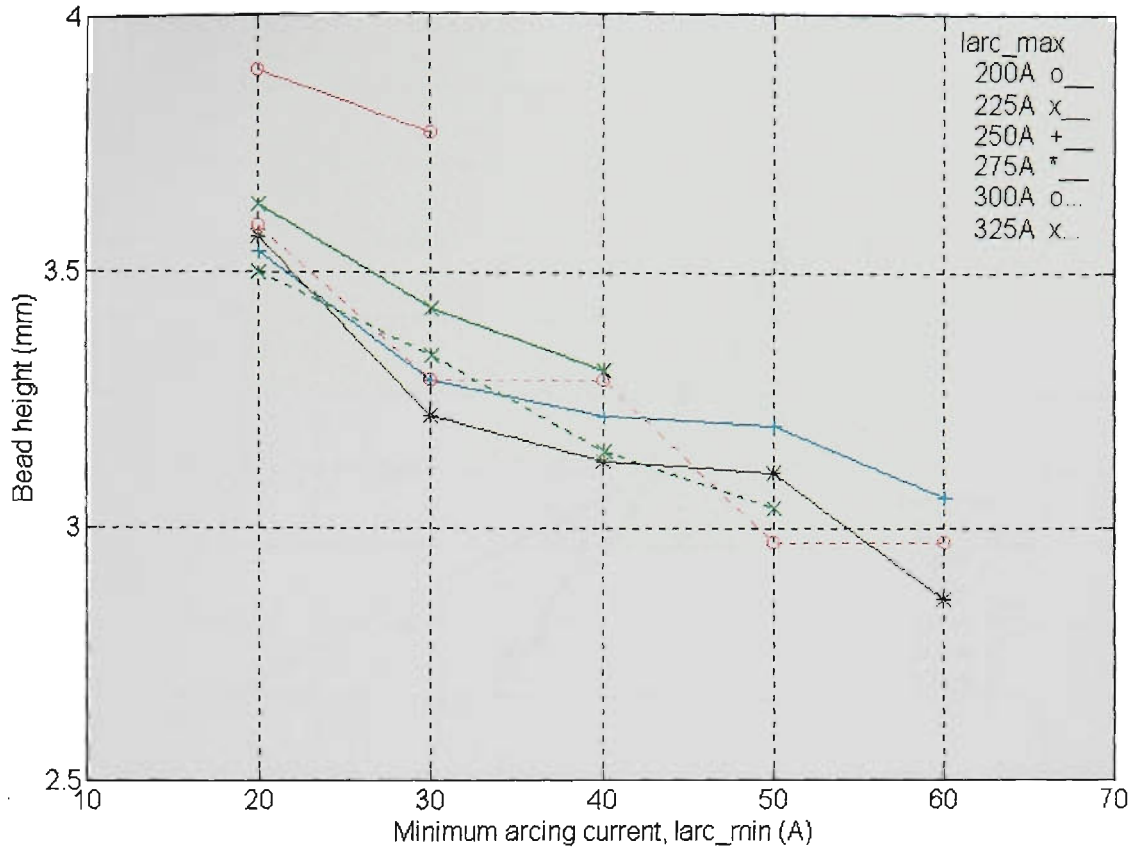

Figure 10.112 Weld bead height vs Iarc_min & Iarc_max
(CO_2, CTWD=20mm, WFR=5.7m/min, Travel=195mm/min)

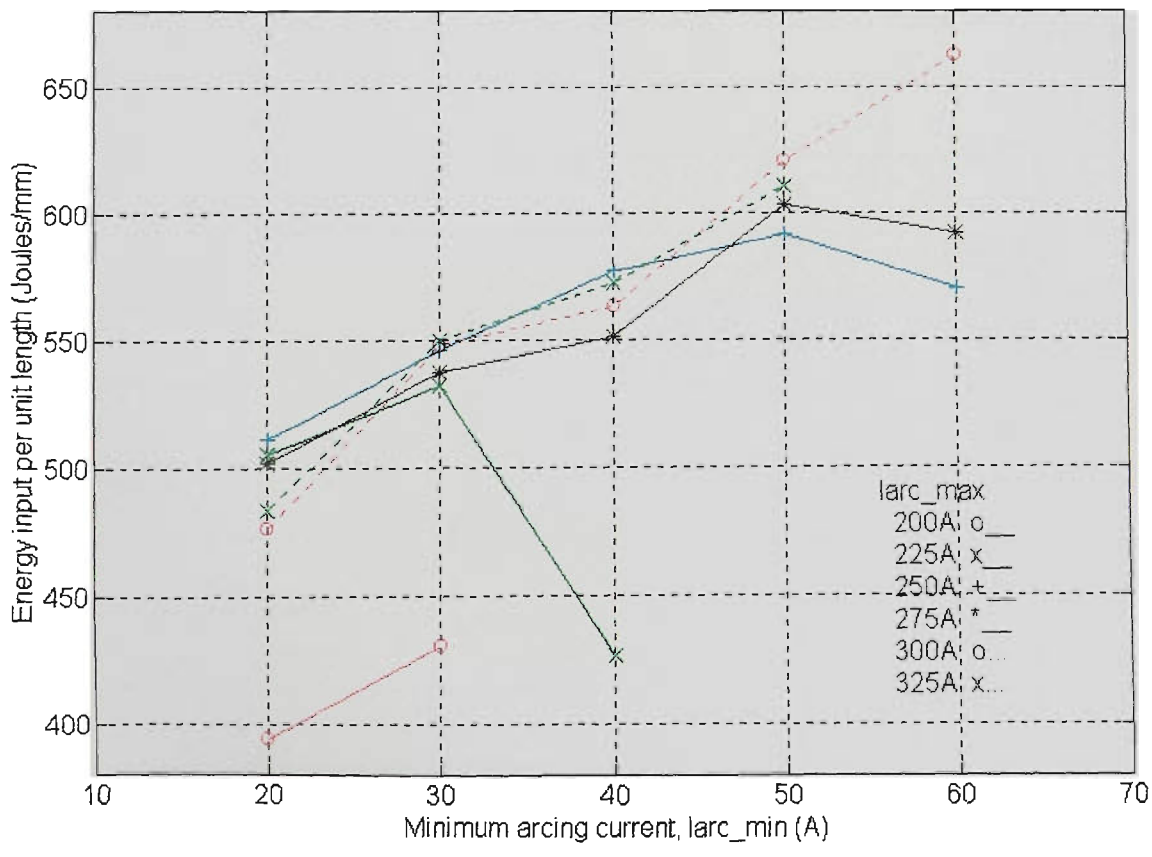

Figure 10.113 Energy input per unit length of weld vs Iarc_min & Iarc_max
(CO_2, CTWD=20mm, WFR=5.7m/min, Travel=195mm/min)

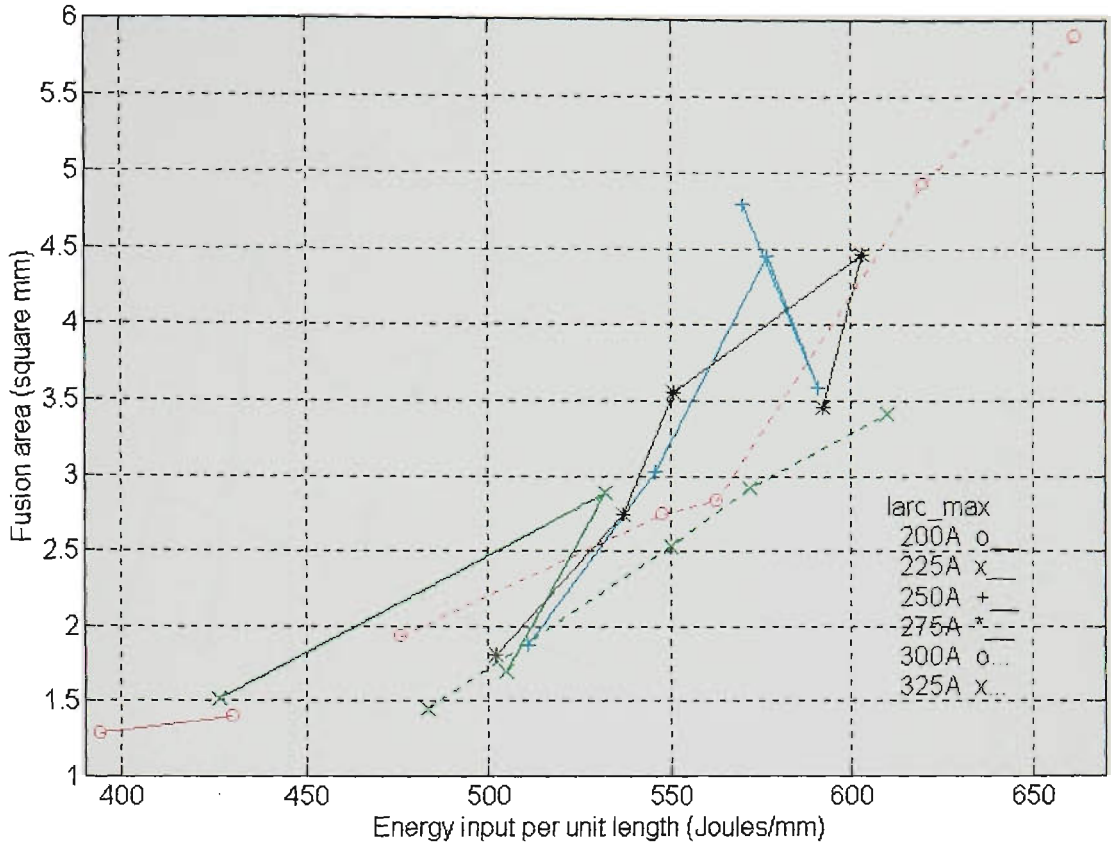

Figure 10.114 Fusion area vs Energy input per unit length of weld (CO_2, CTWD=20mm, WFR=5.7m/min, Travel=195mm/min)

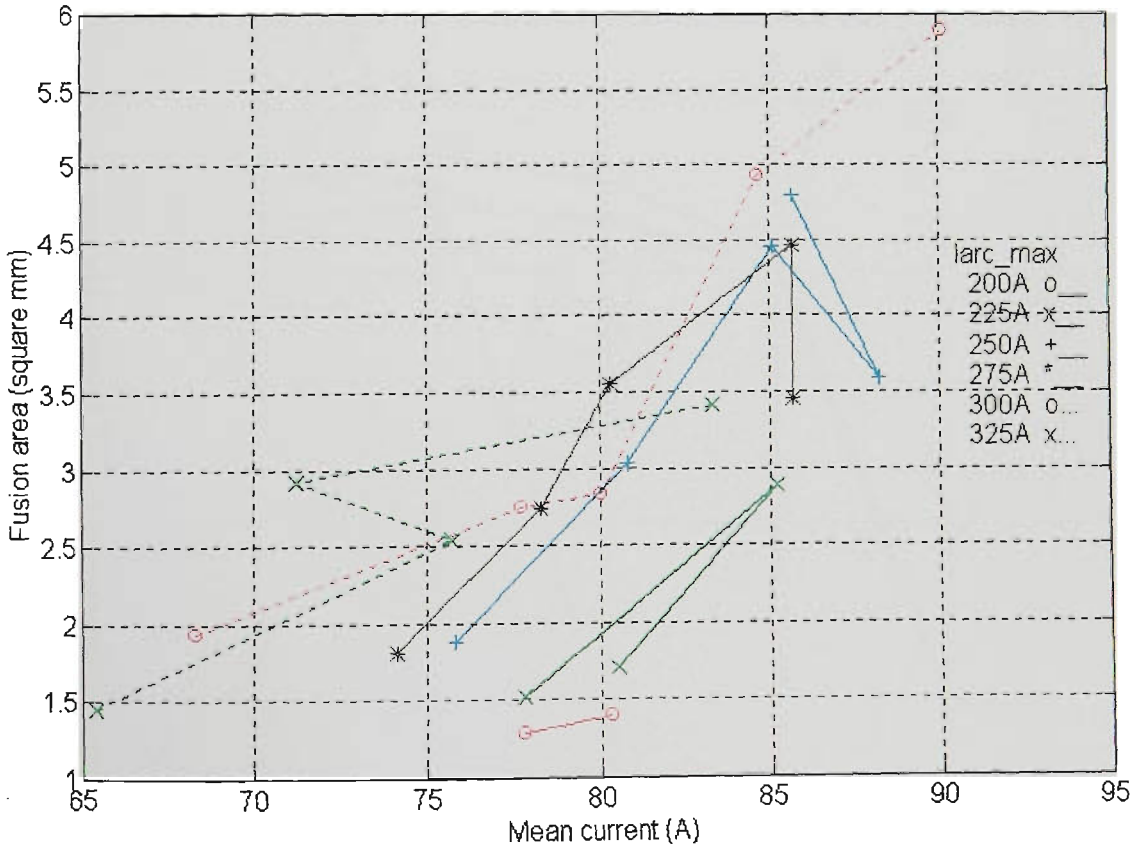

Figure 10.115 Fusion area vs Mean welding current (CO_2, CTWD=20mm, WFR=5.7m/min, Travel=195mm/min)

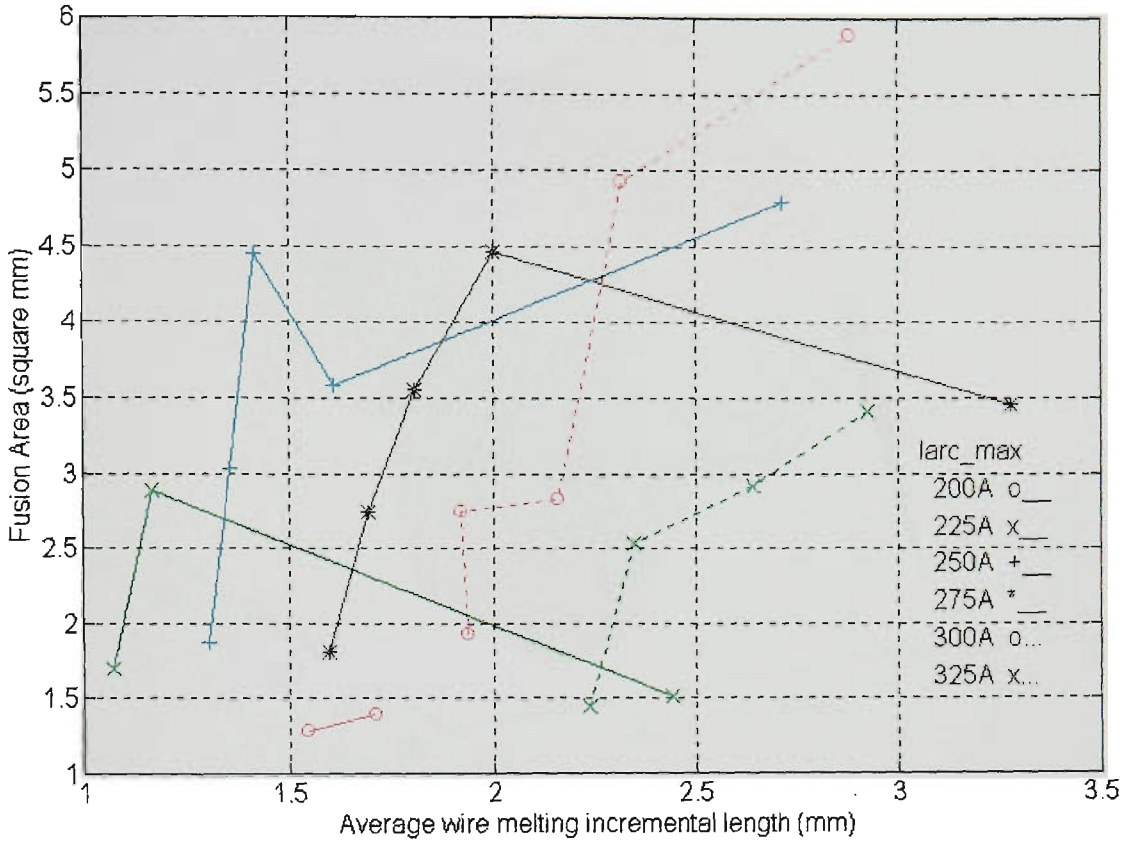

Figure 10.116 Fusion area vs Average wire melting incremental length ΔL (CO_2, CTWD=20mm, WFR=5.7m/min, Travel=195mm/min)

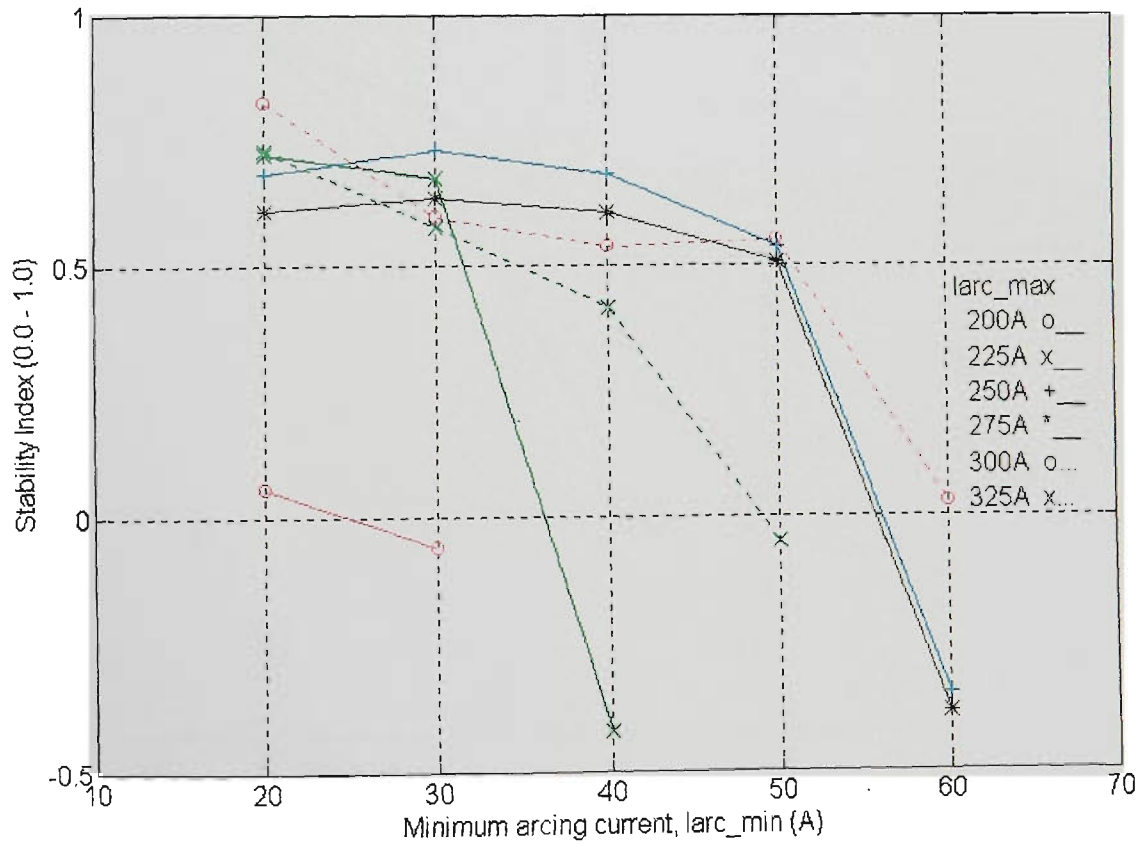

Figure 10.117 Stability index vs Iarc_min & Iarc_max (2D) (CO_2, CTWD=20mm, WFR=5.7m/min, Travel=195mm/min)

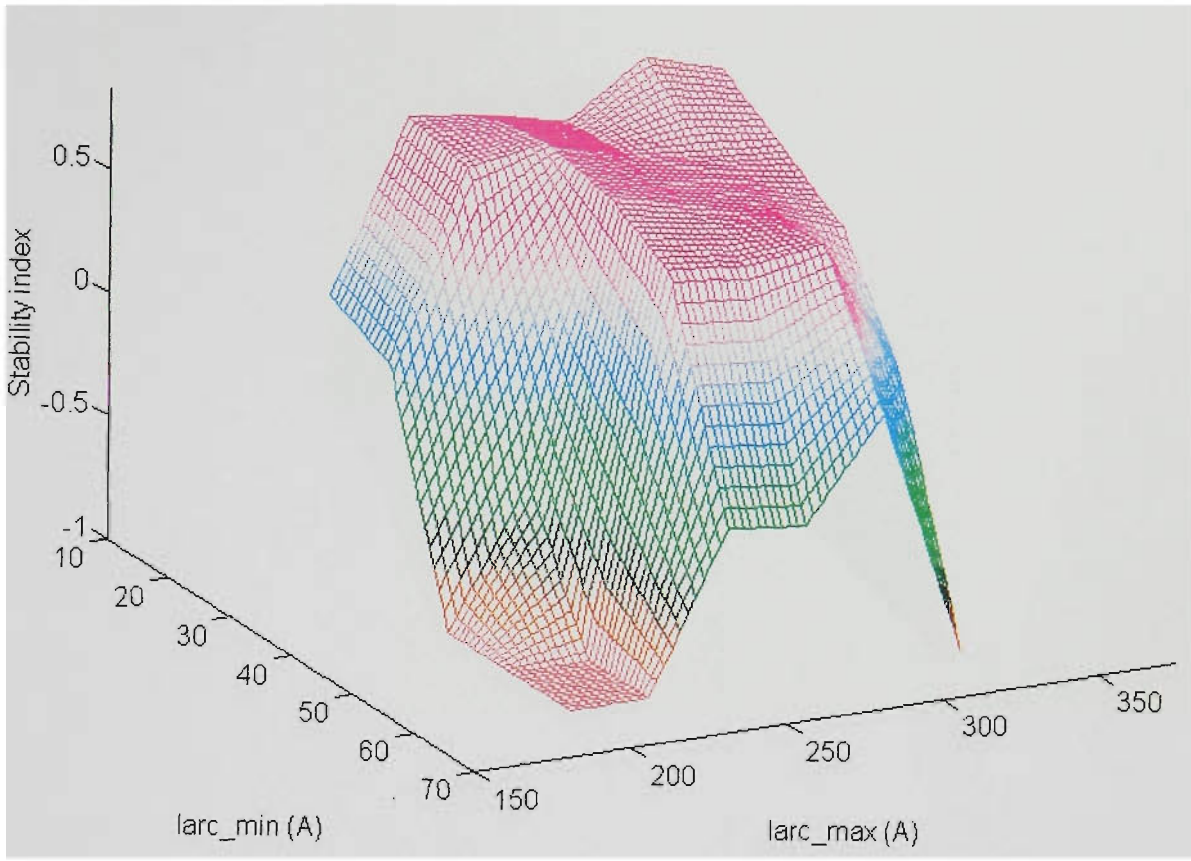

Figure 10.118 Stability index vs Iarc_min & Iarc_max (3D)
(CO_2, CTWD=20mm, WFR=5.7m/min, Travel=195mm/min)

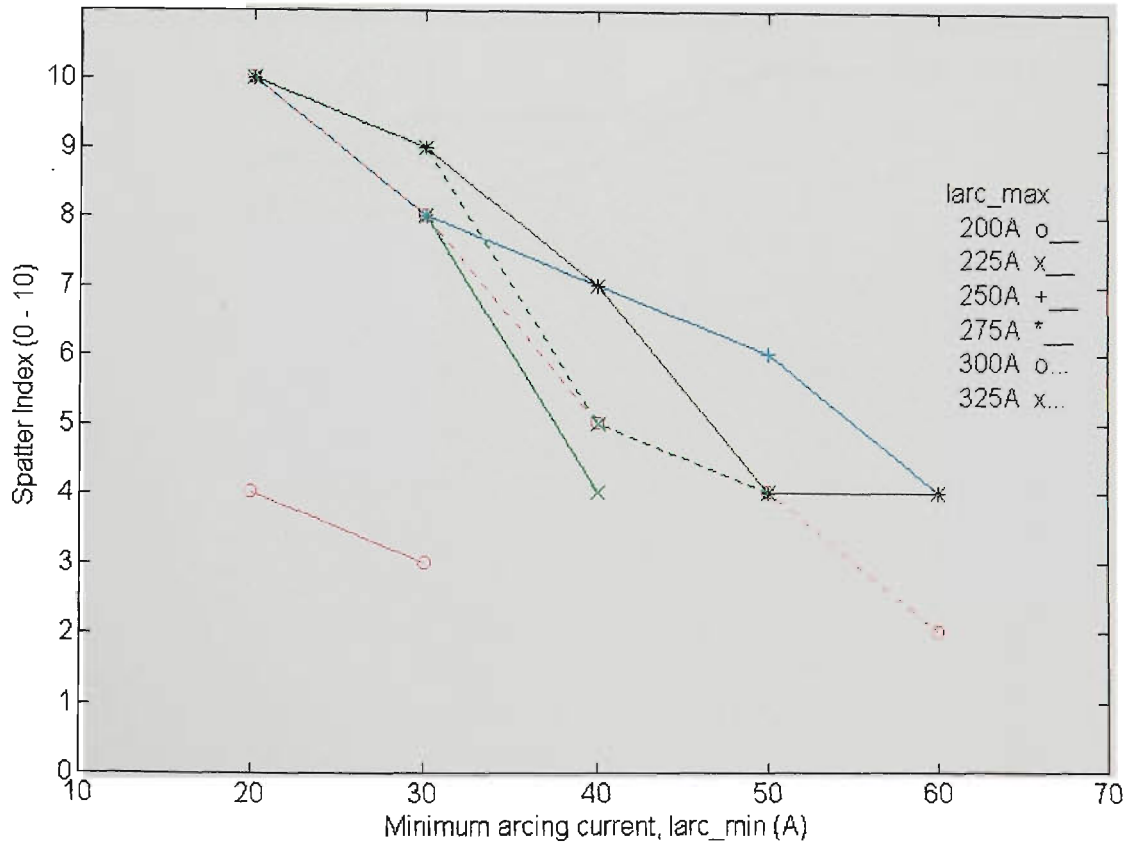

Figure 10.119 Spatter index vs Iarc_min & Iarc_max (2D)
(CO_2, CTWD=20mm, WFR=5.7m/min, Travel=195mm/min)

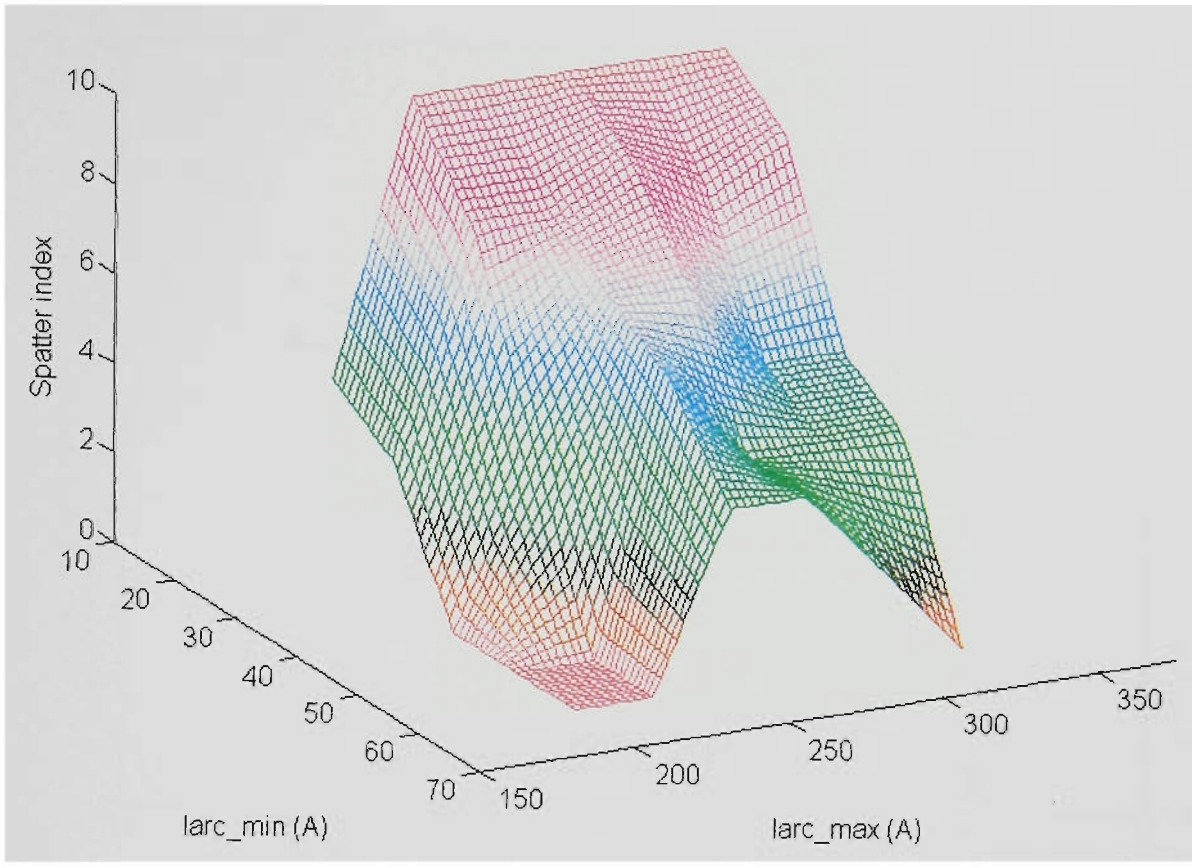

Figure 10.120 Spatter index vs Iarc_min & Iarc_max (3D)
(CO_2, CTWD=20mm, WFR=5.7m/min, Travel=195mm/min)

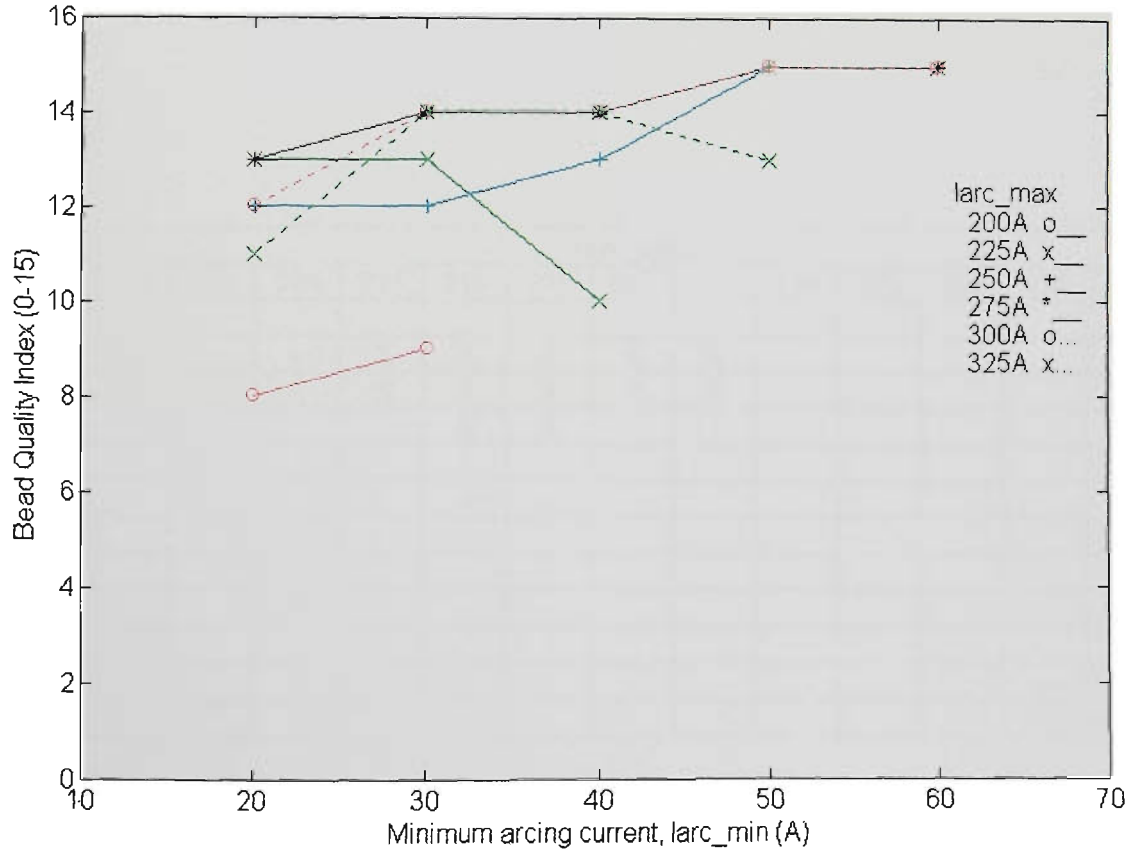

Figure 10.121 Bead quality index vs Iarc_min & Iarc_max
(CO_2, CTWD=20mm, WFR=5.7m/min, Travel=195mm/min)

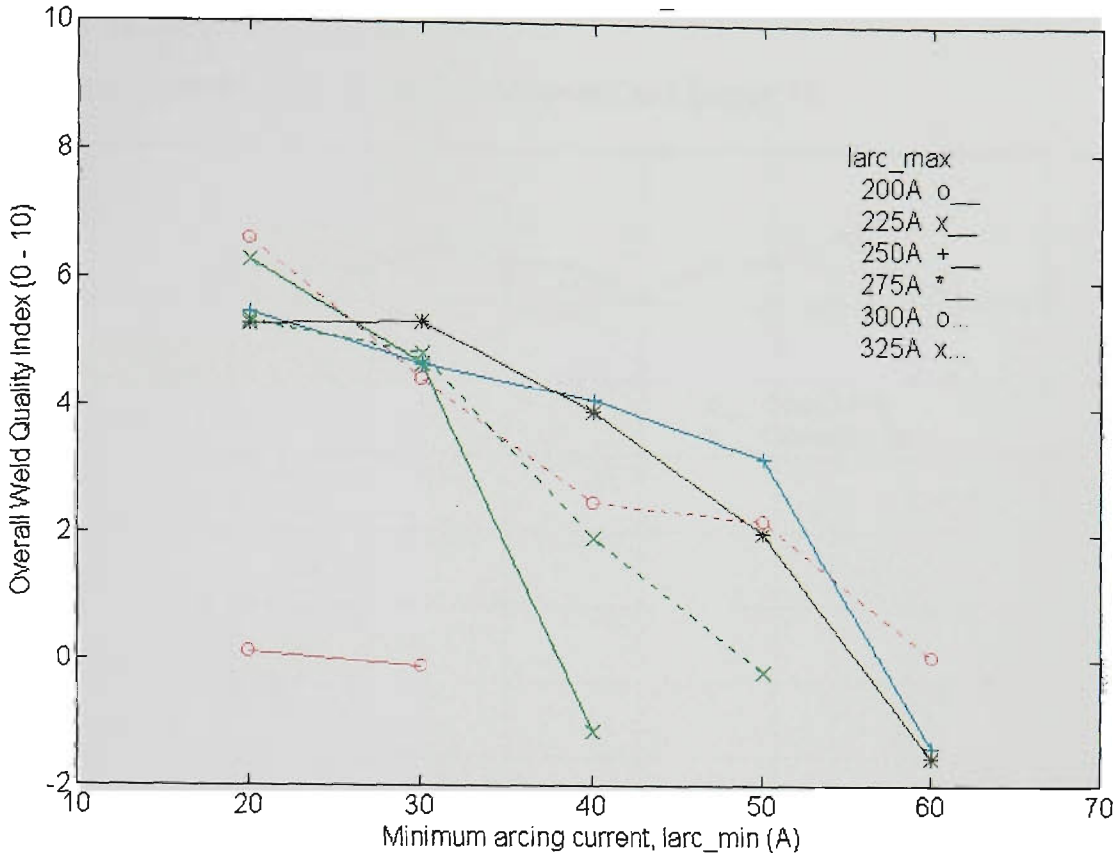

Figure 10.122 Weld overall quality index vs Iarc_min & Iarc_max (CO_2, CTWD=20mm, WFR=5.7m/min, Travel=195mm/min)

Iarc_min	Iarc_max												
	150	175	200	225	250	275	300	325	350	375	400	425	450
10													
20			-	X	X	X	X	X					
30			-	X	X	X	X	X					
40				-	X	X	-	-					
50					-	-	-	-					
60					-	-	-						
70													
80													
90													
100													
110												- = tested	
120												X = useful	

Figure 10.123 Useful operating area (CO_2, CTWD=20mm, WFR=5.7m/min, Travel=195mm/min)

Appendix 11

This appendix contains Figures relevant to Chapter 11.

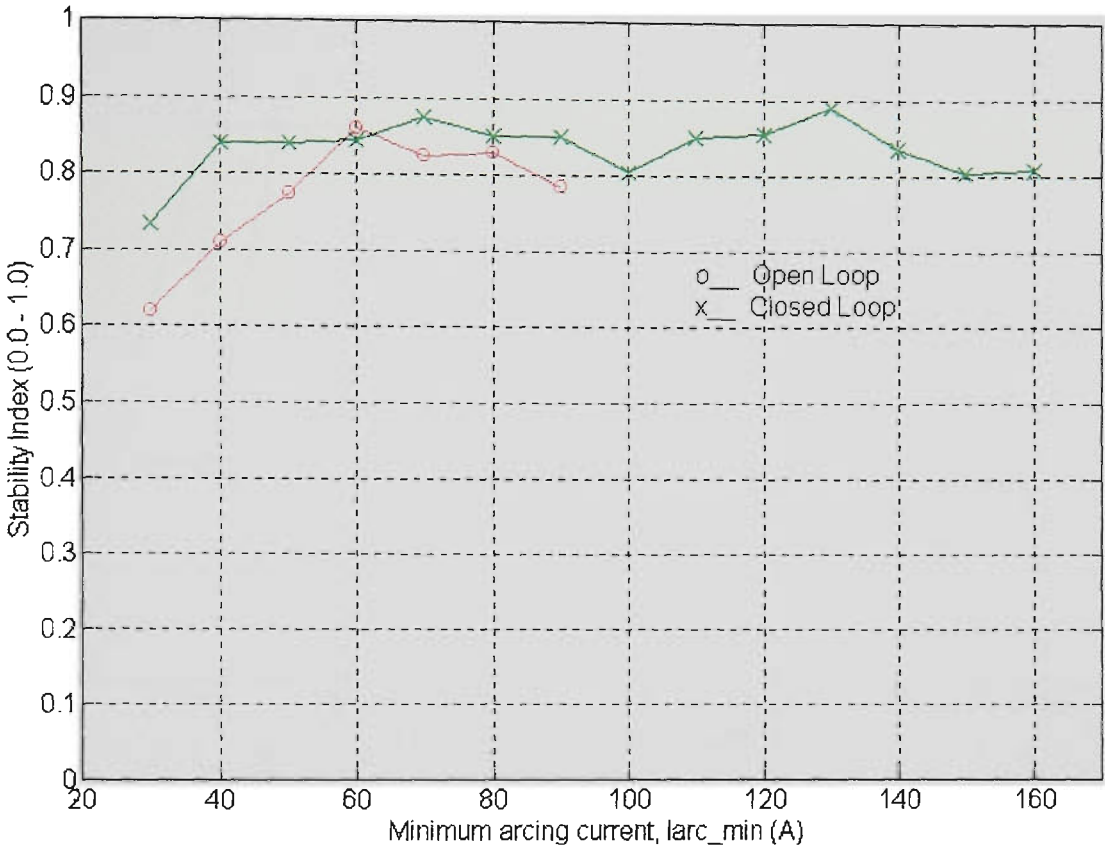

Figure 11.6 Stability index vs Iarc_min

(Ar-23%CO_2, CTWD=16mm, WFR=5.7m/min, Travel=390mm/min)

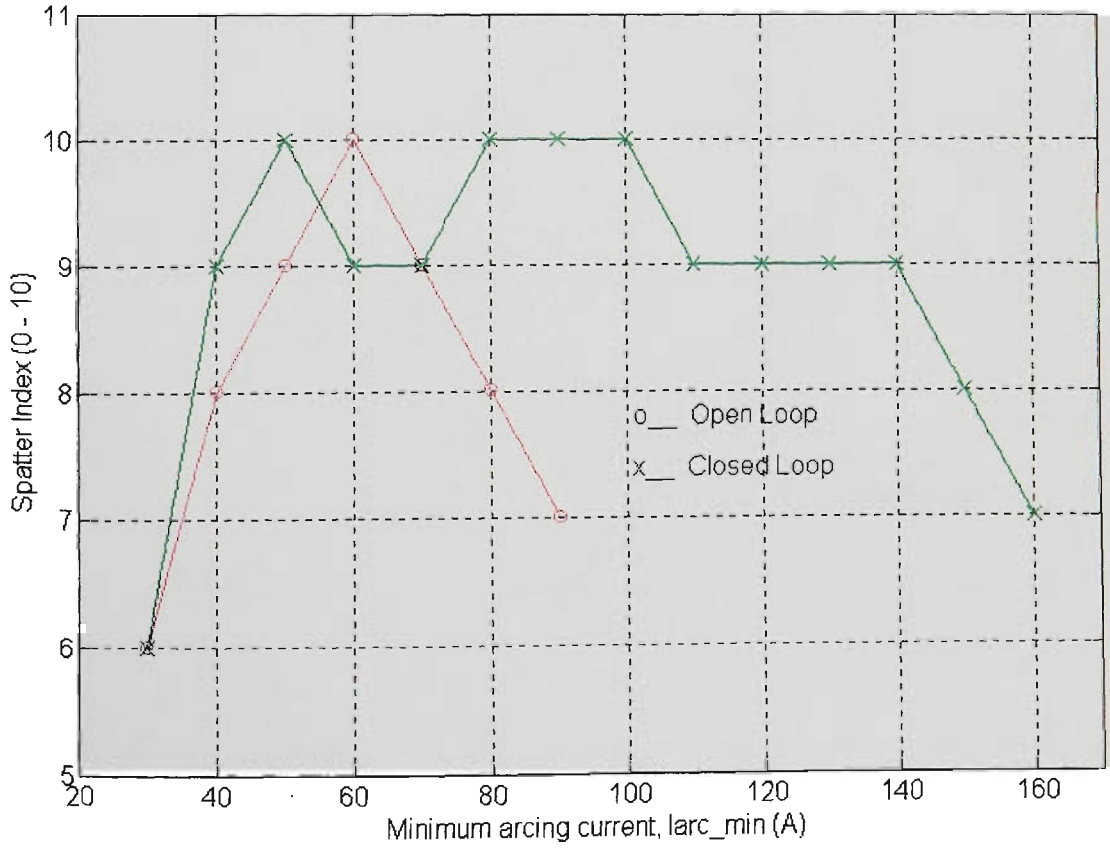

Figure 11.7 Spatter index vs Iarc_min

(Ar-23%CO_2, CTWD=16mm, WFR=5.7m/min, Travel=390mm/min)

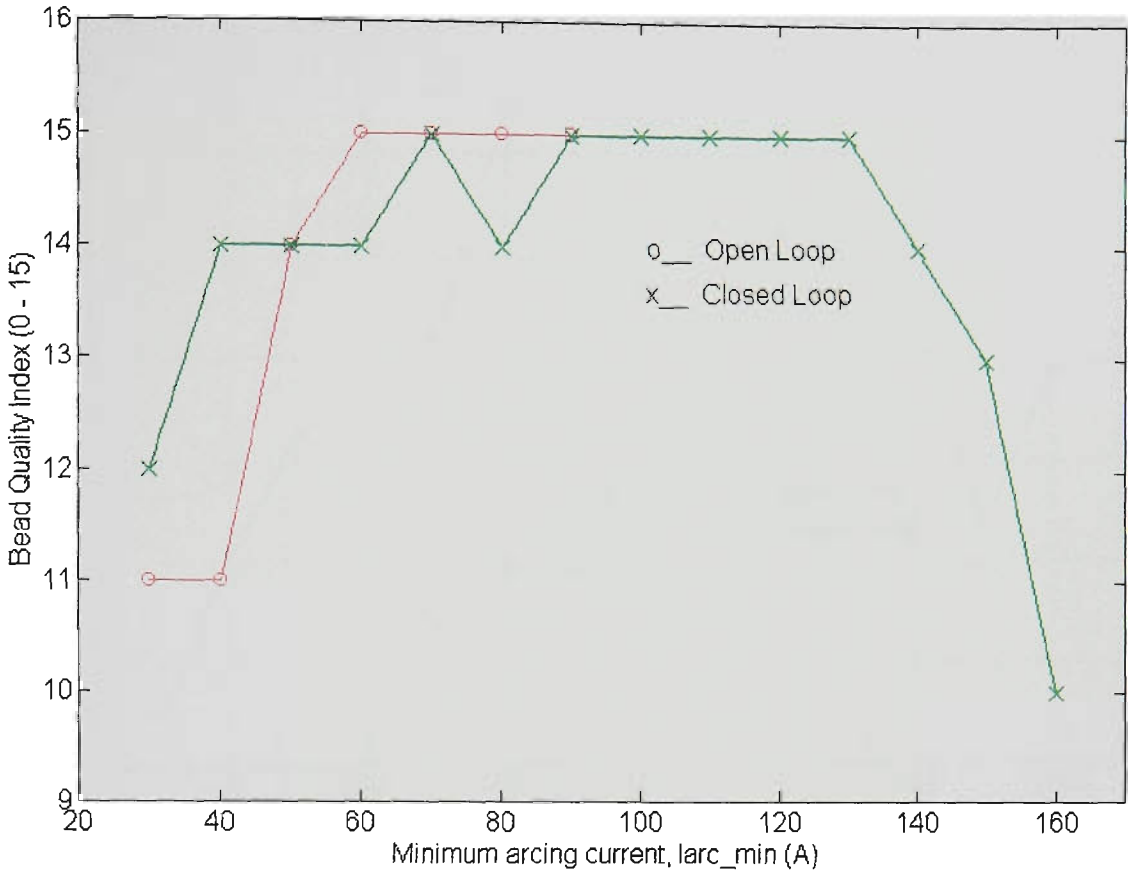

Figure 11.8 Bead quality index vs Iarc_min

(Ar-23%CO_2, CTWD=16mm, WFR=5.7m/min, Travel=390mm/min)

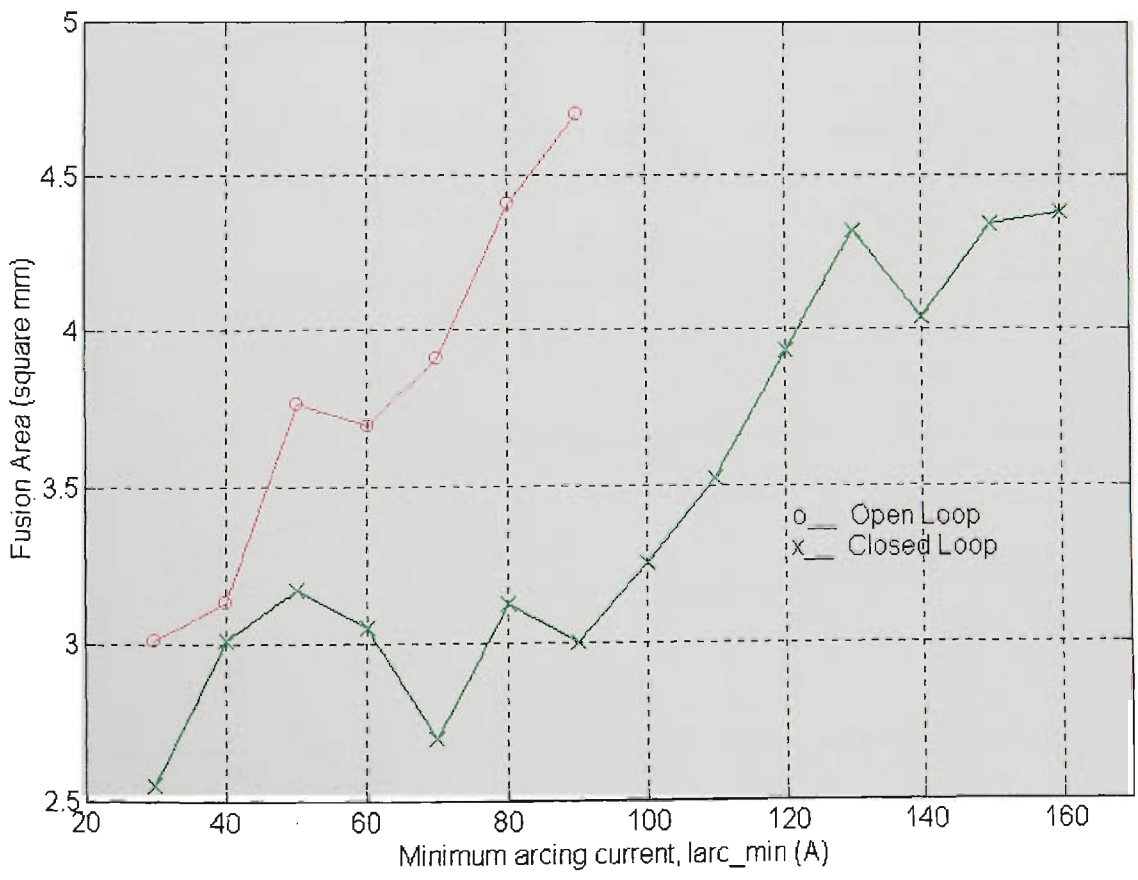

Figure 11.9 Fusion area vs Iarc_min

(Ar-23%CO_2, CTWD=16mm, WFR=5.7m/min, Travel=390mm/min)

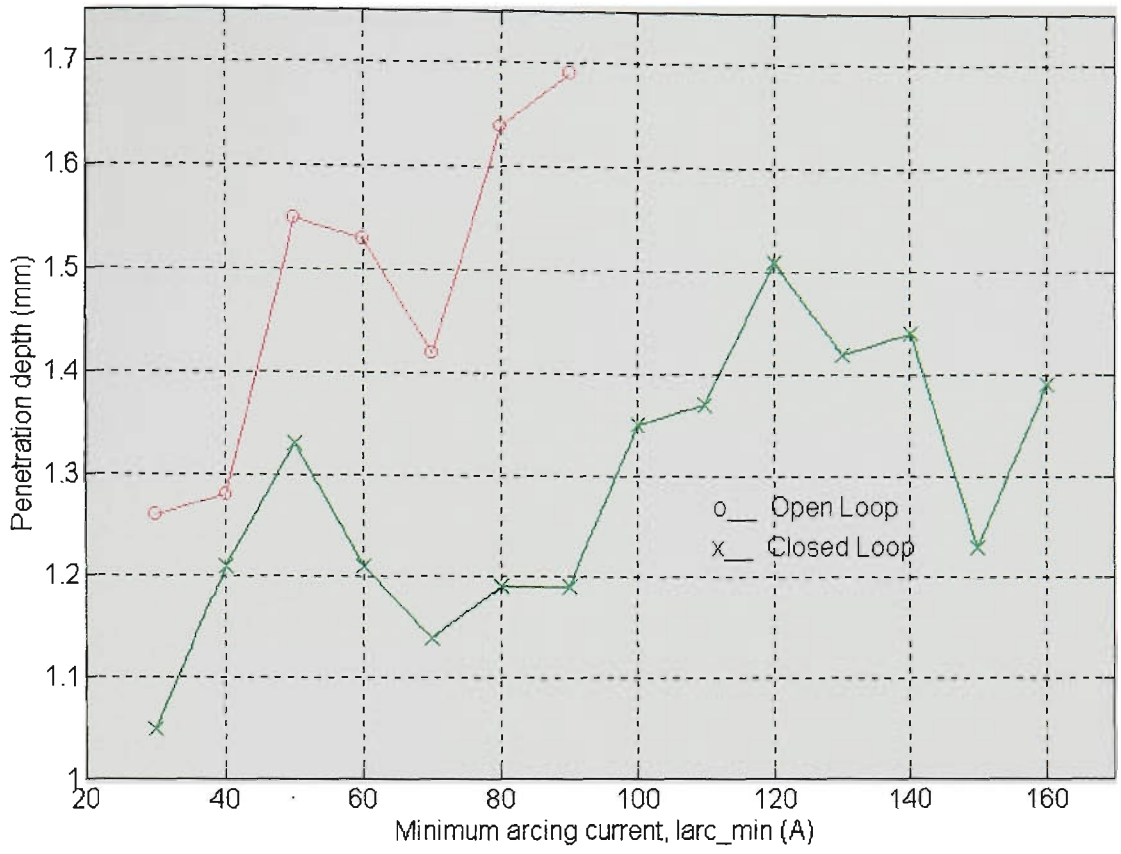

Figure 11.10 Penetration depth vs Iarc_min

(Ar-23%CO_2, CTWD=16mm, WFR=5.7m/min, Travel=390mm/min)

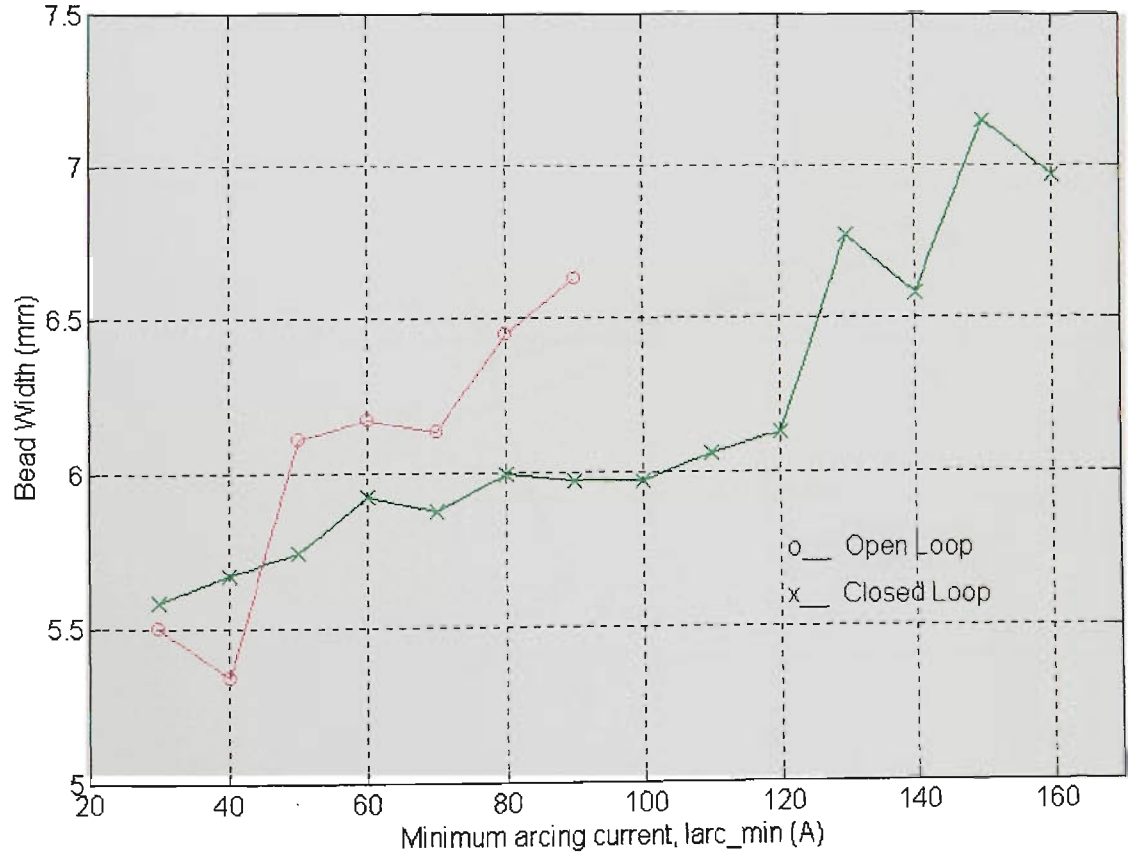

Figure 11.11 Bead width vs Iarc_min

(Ar-23%CO_2, CTWD=16mm, WFR=5.7m/min, Travel=390mm/min)

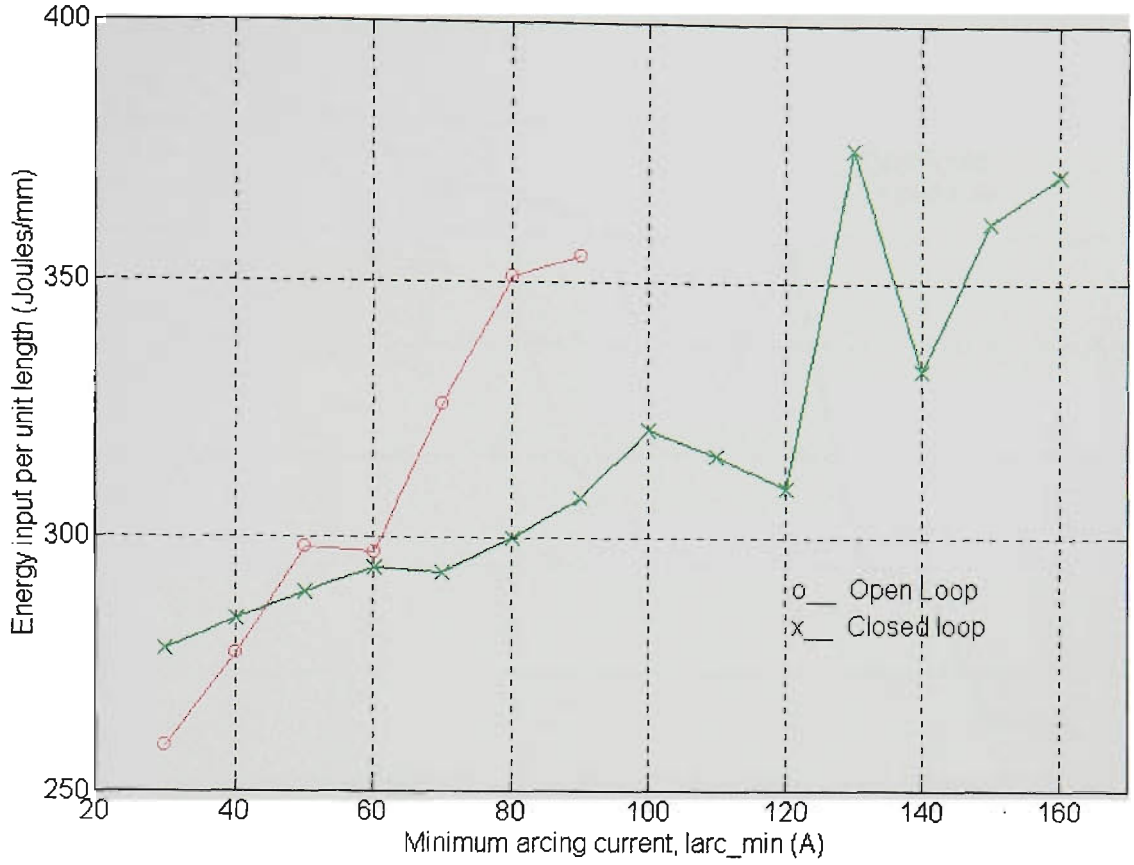

Figure 11.12 Energy input per unit length vs Iarc_min

(Ar-23%CO_2, CTWD=16mm, WFR=5.7m/min, Travel=390mm/min)

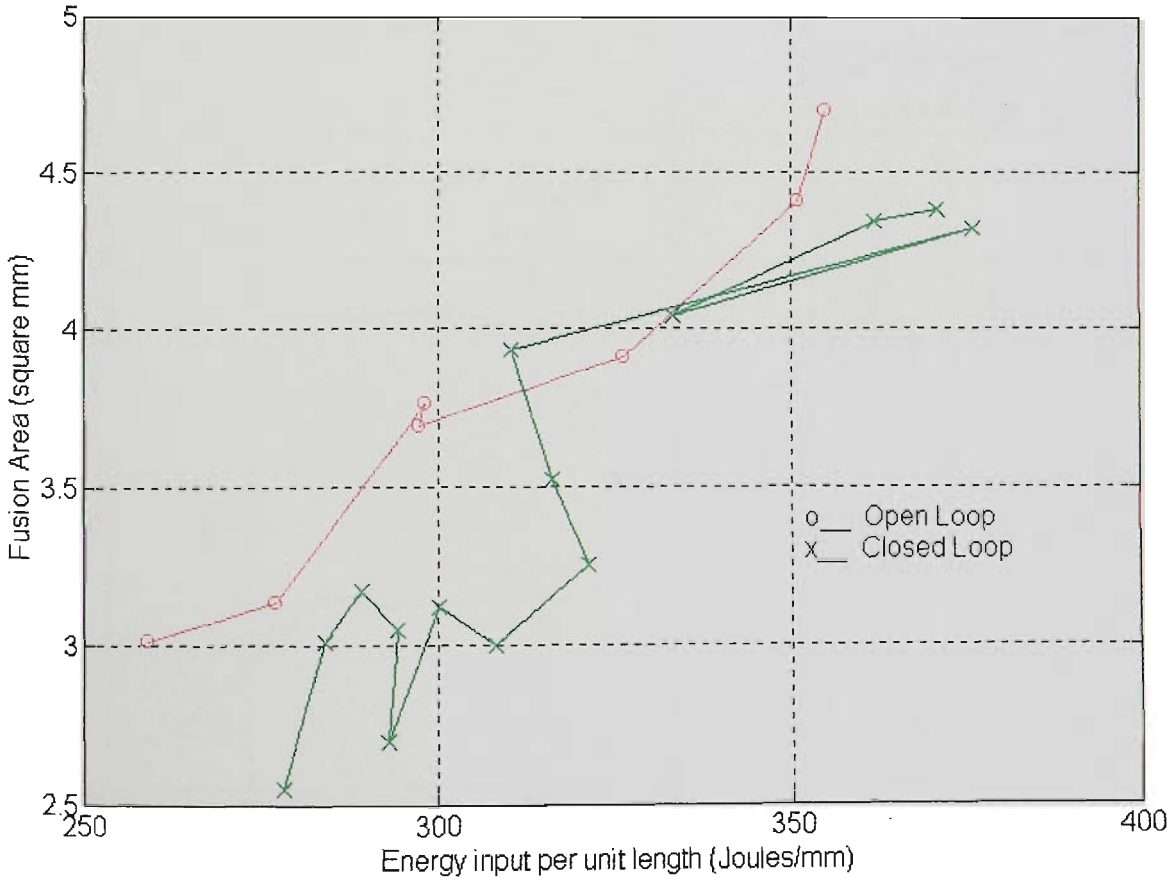

Figure 11.13 Fusion area vs Energy input per unit length

(Ar-23%CO_2, CTWD=16mm, WFR=5.7m/min, Travel=390mm/min)

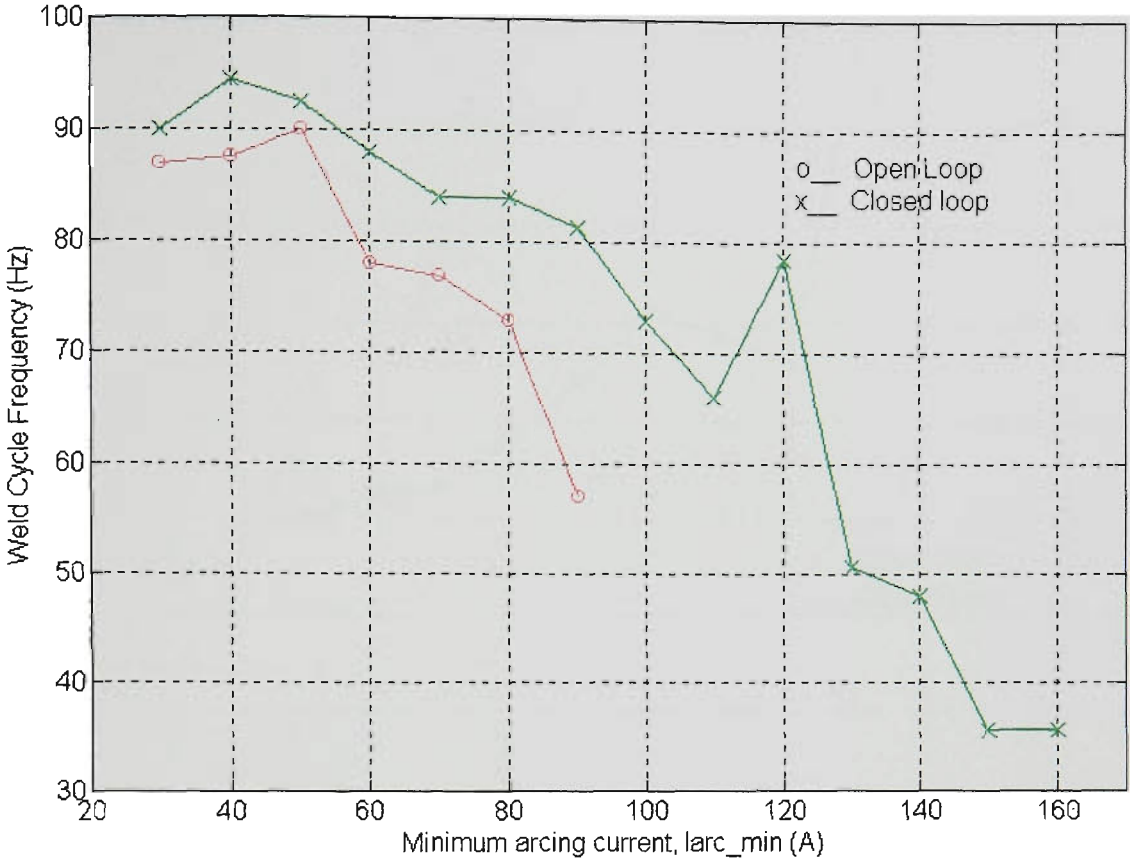

Figure 11.14 Average dipping frequency vs Iarc_min

(Ar-23%CO_2, CTWD=16mm, WFR=5.7m/min, Travel=390mm/min)

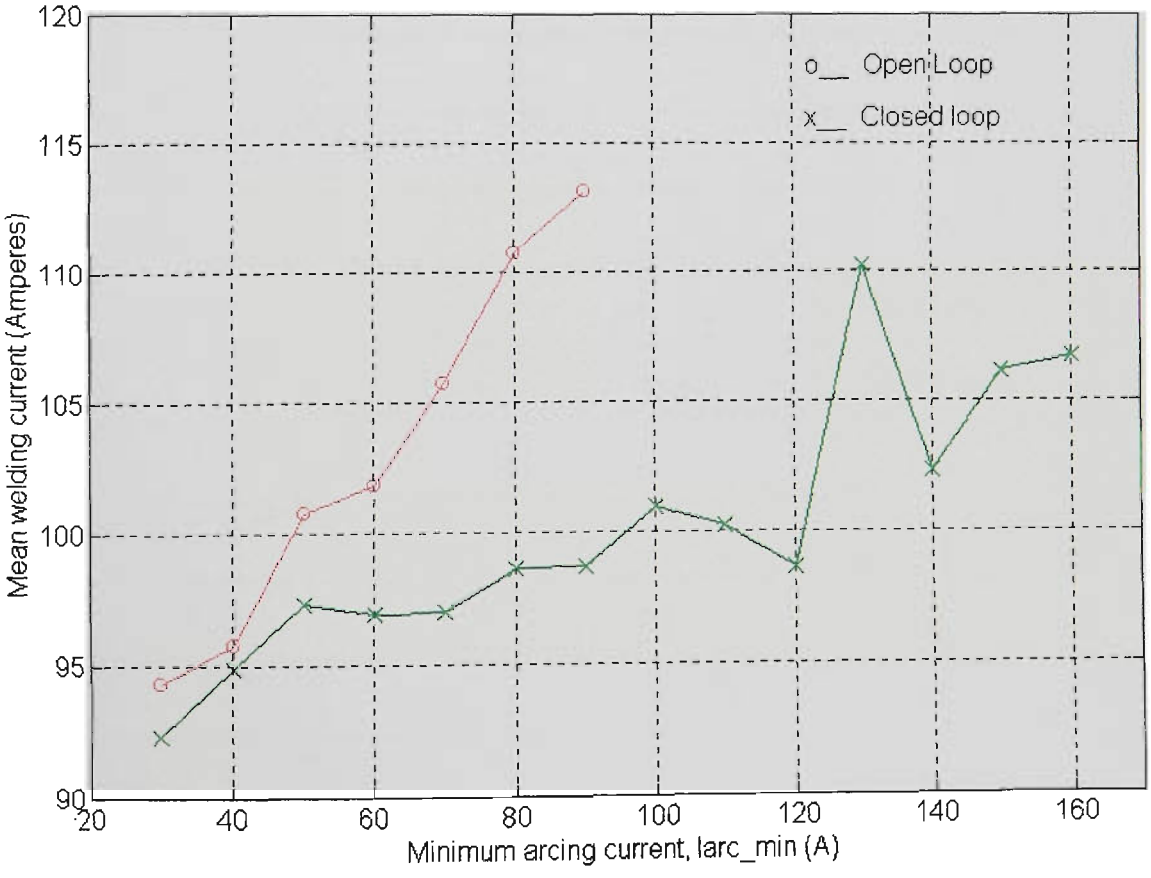

Figure 11.15 Mean welding current vs Iarc_min

(Ar-23%CO_2, CTWD=16mm, WFR=5.7m/min, Travel=390mm/min)

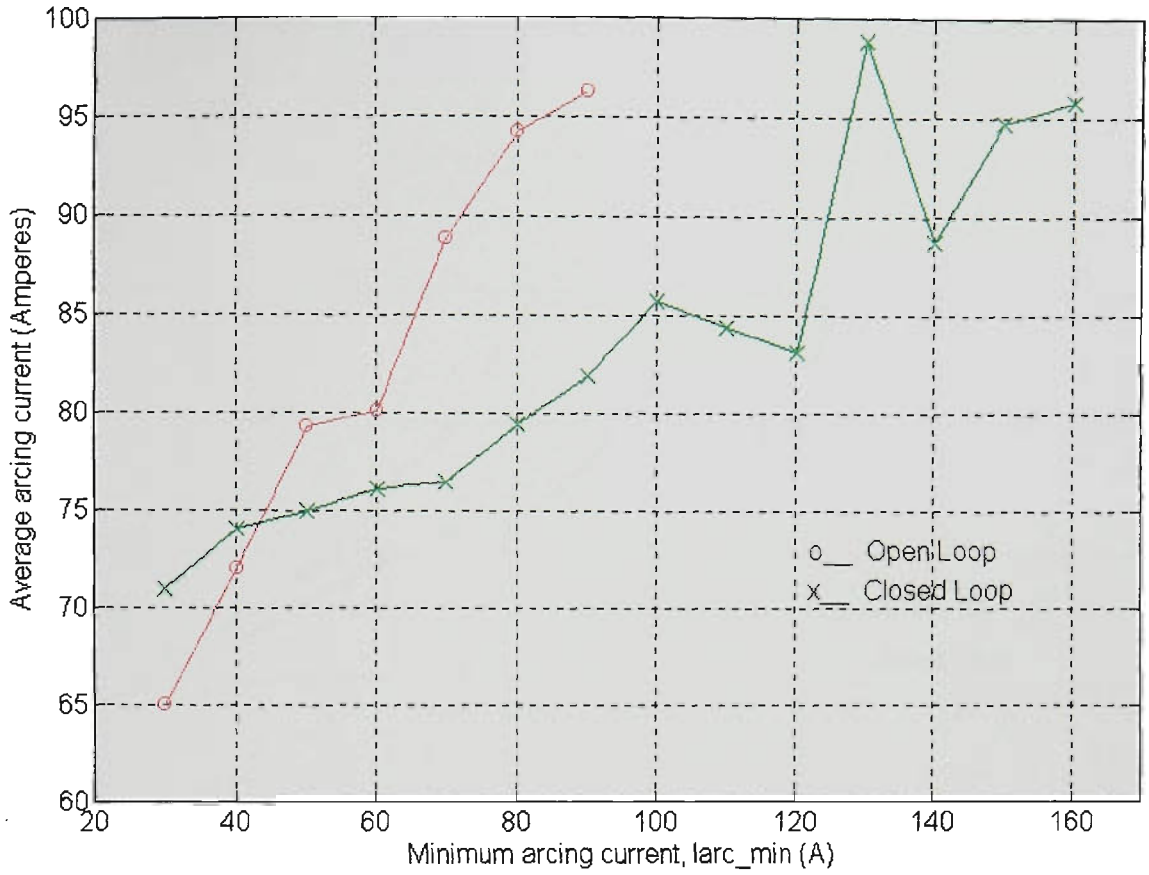

Figure 11.16 Average arcing current vs Iarc_min

(Ar-23%CO_2, CTWD=16mm, WFR=5.7m/min, Travel=390mm/min)

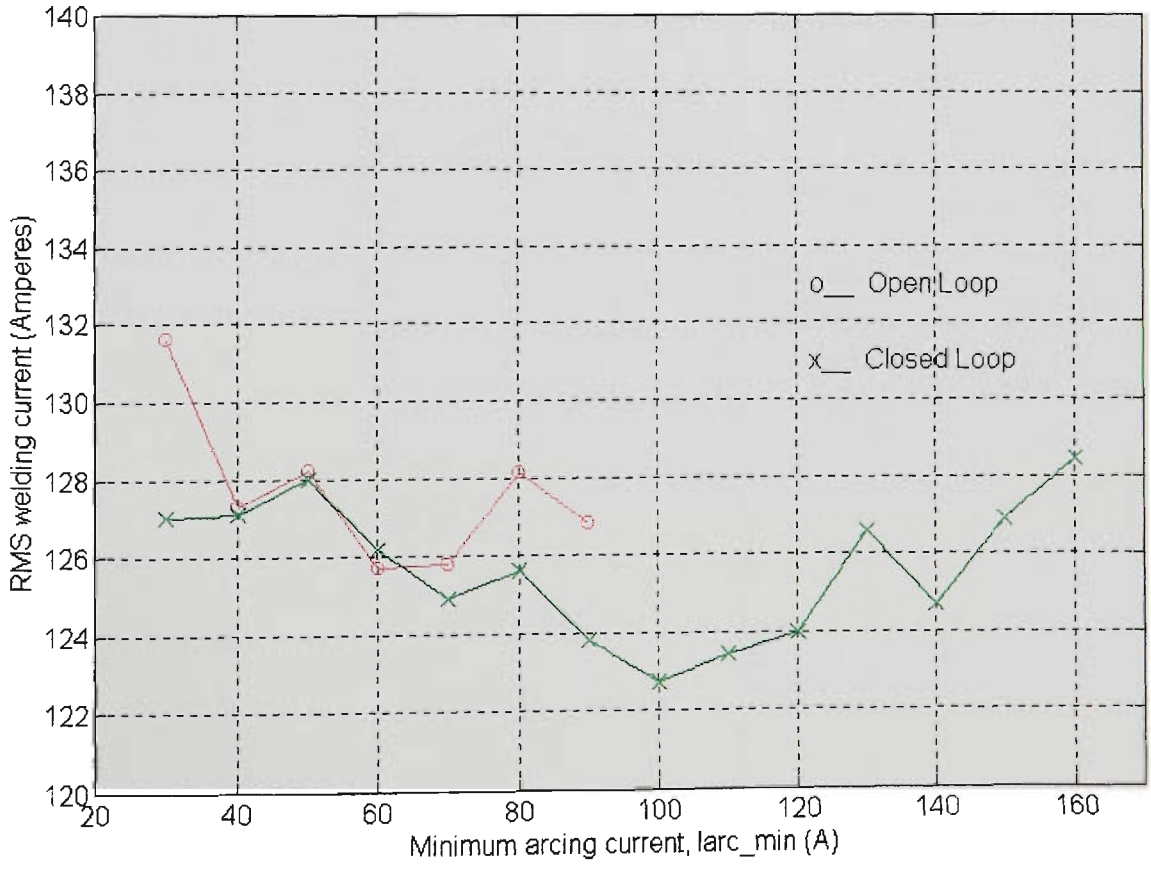

Figure 11.17 RMS welding current vs Iarc_min

(Ar-23%CO_2, CTWD=16mm, WFR=5.7m/min, Travel=390mm/min)

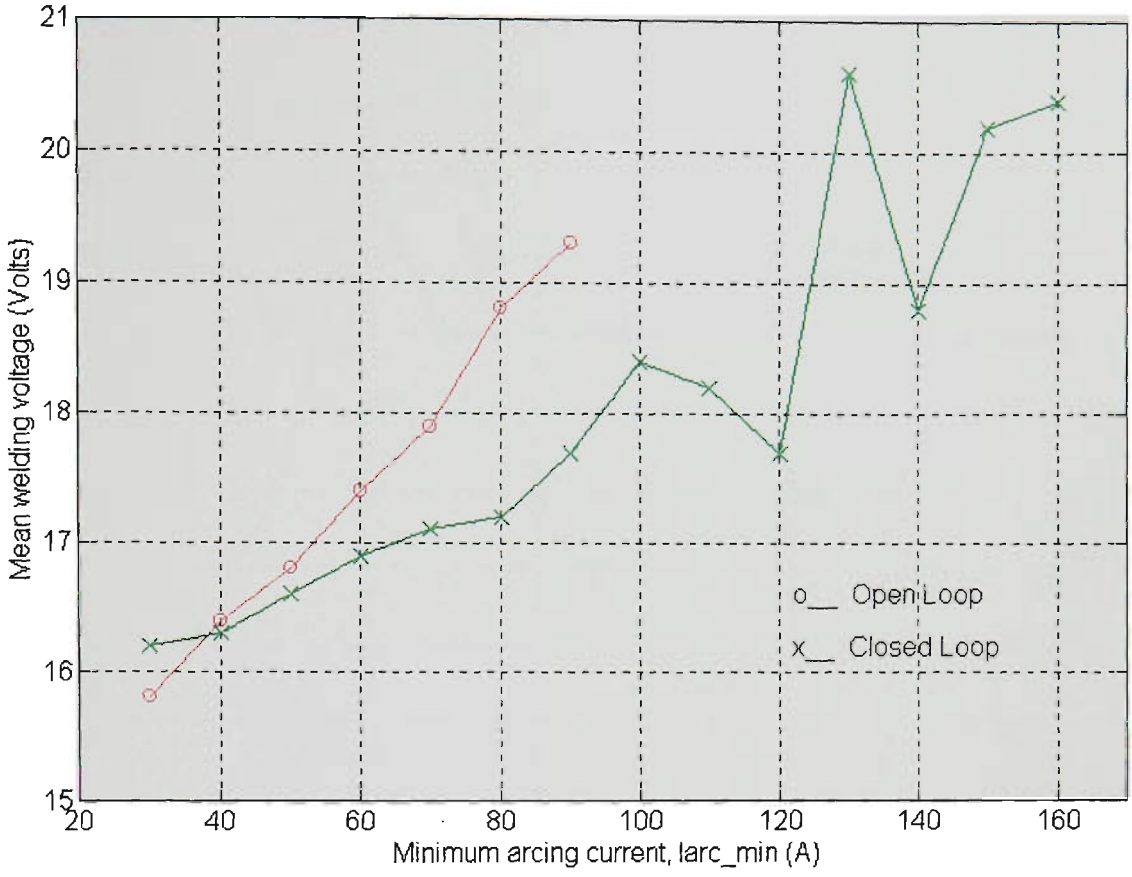

Figure 11.18 Mean welding voltage vs Iarc_min

(Ar-23%CO_2, CTWD=16mm, WFR=5.7m/min, Travel=390mm/min)

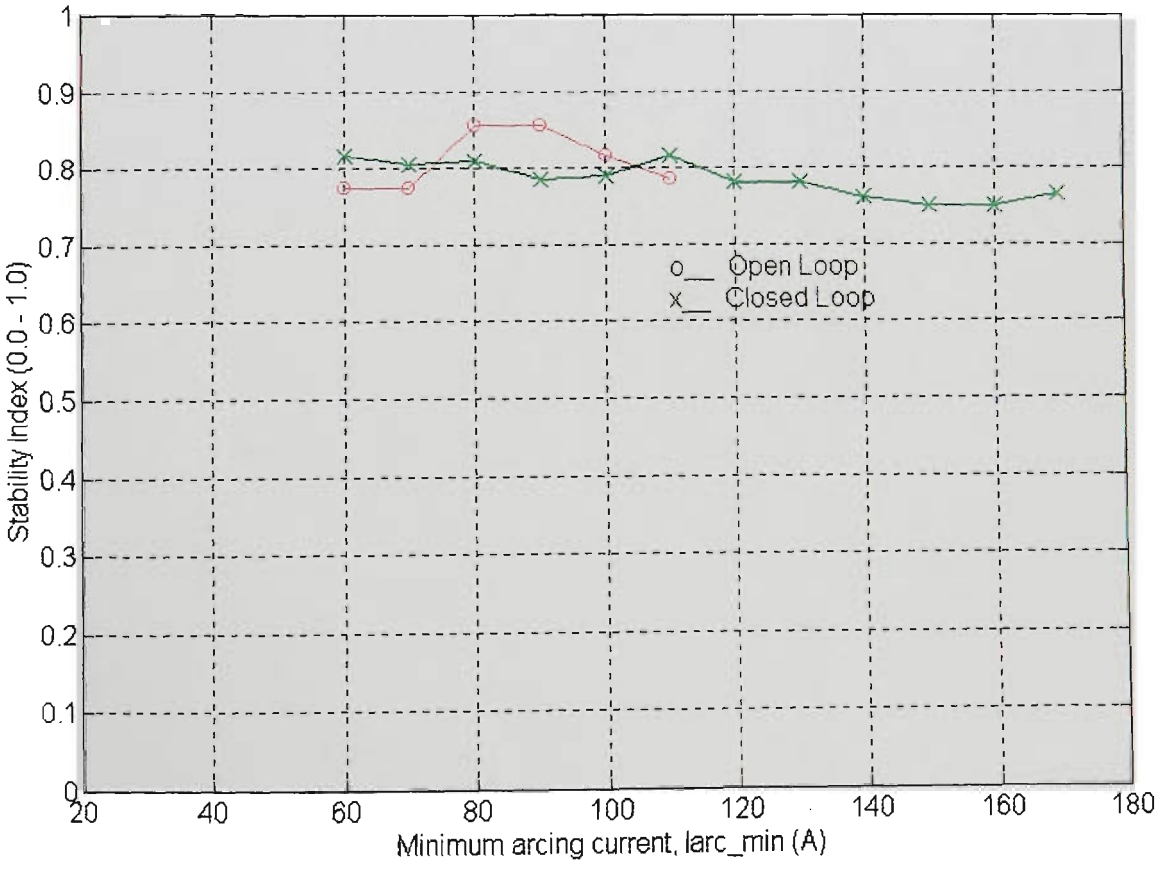

Figure 11.20 Stability index vs Iarc_min

(Ar-23%CO_2, CTWD=8mm, WFR=5.7m/min, Travel=390mm/min)

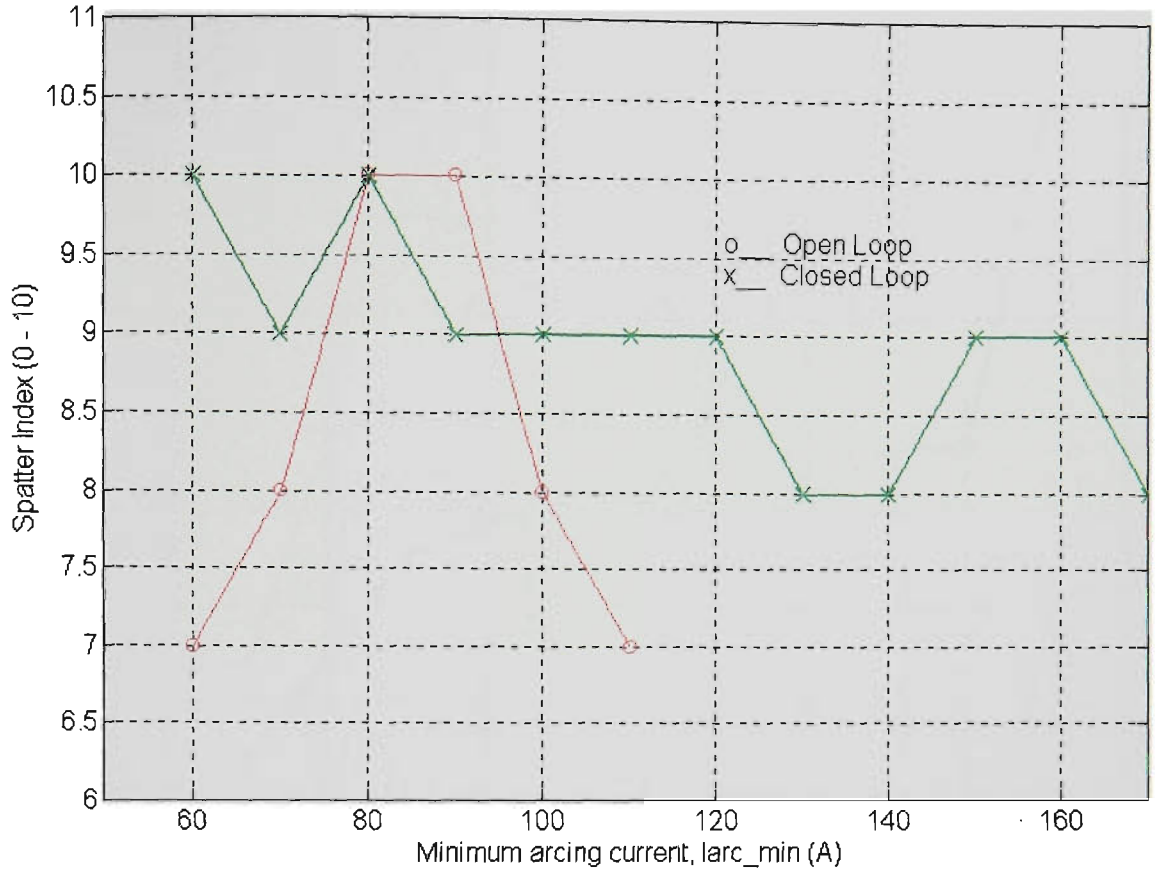

Figure 11.21 Spatter index vs Iarc_min

(Ar-23%CO_2, CTWD=8mm, WFR=5.7m/min, Travel=390mm/min)

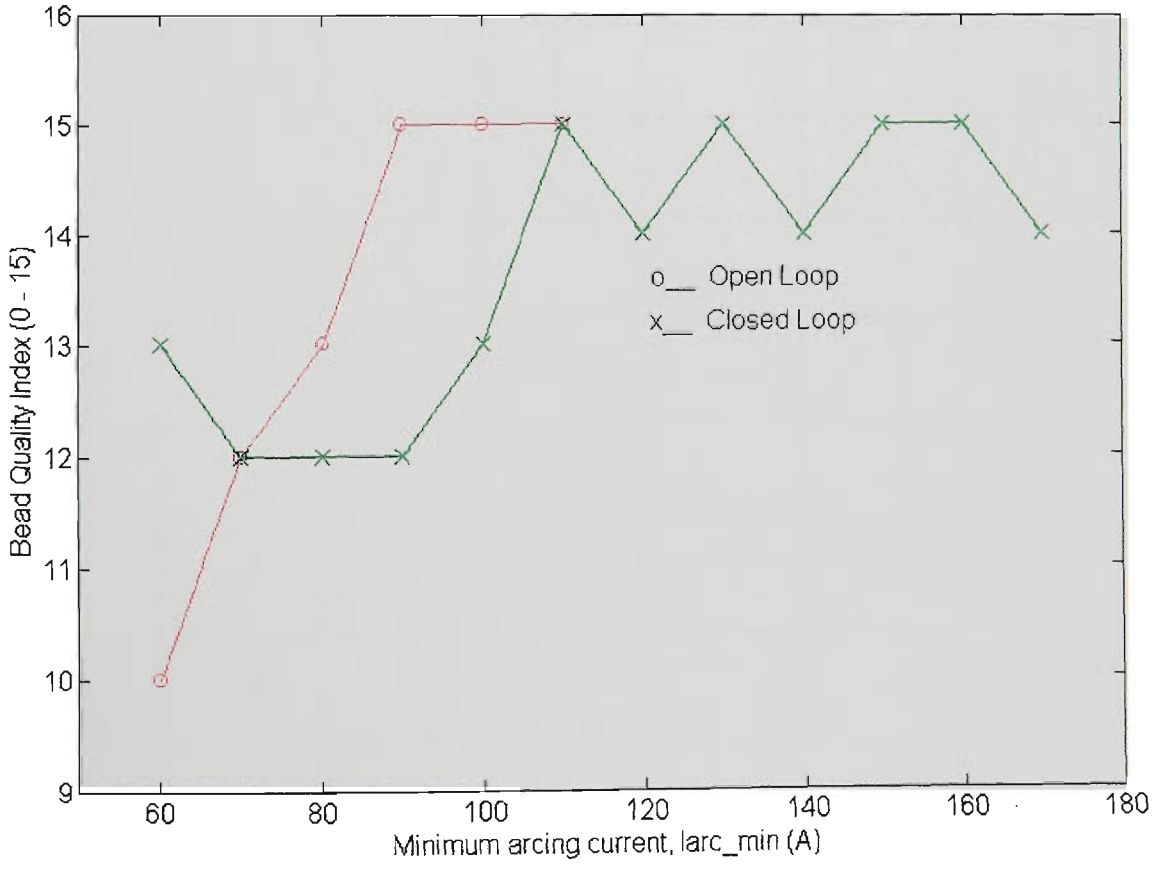

Figure 11.22 Bead quality index vs Iarc_min

(Ar-23%CO_2, CTWD=8mm, WFR=5.7m/min, Travel=390mm/min)

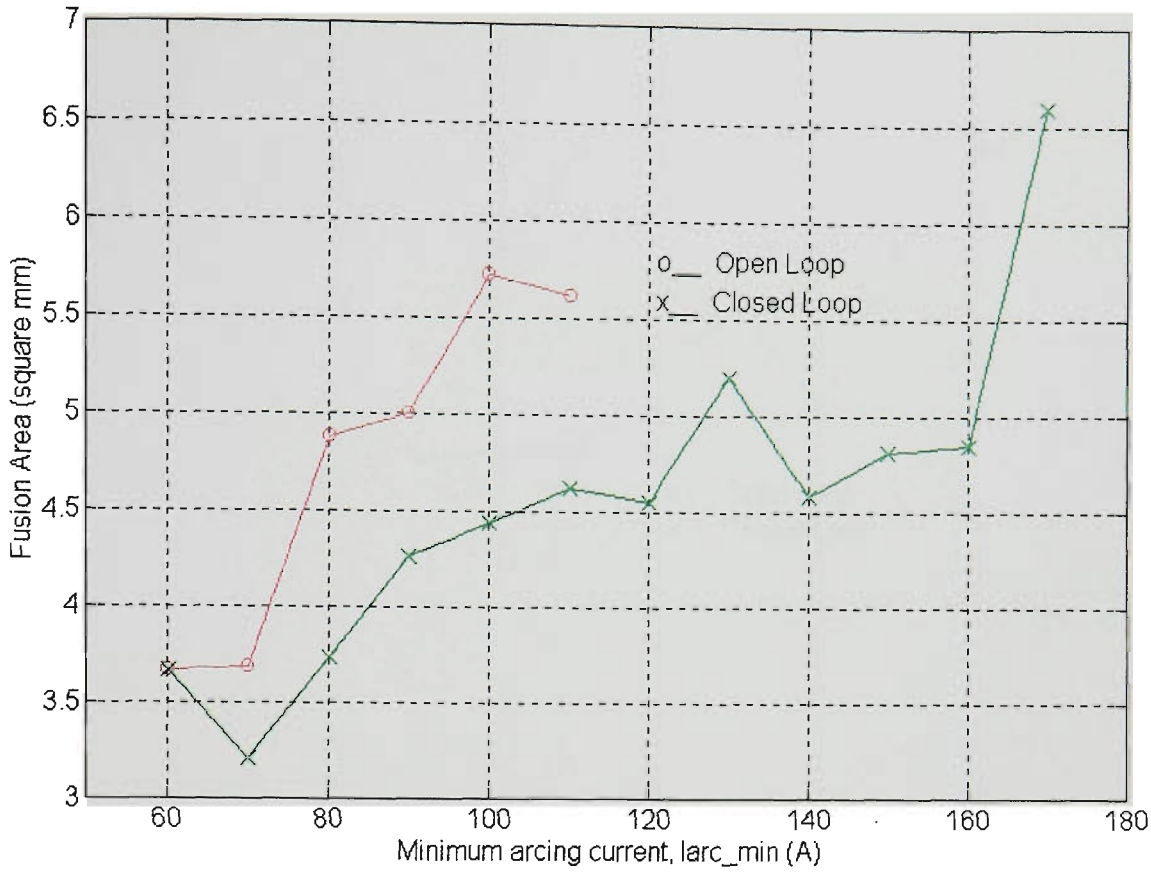

Figure 11.23 Fusion area vs Iarc_min

(Ar-23%CO_2, CTWD=8mm, WFR=5.7m/min, Travel=390mm/min)

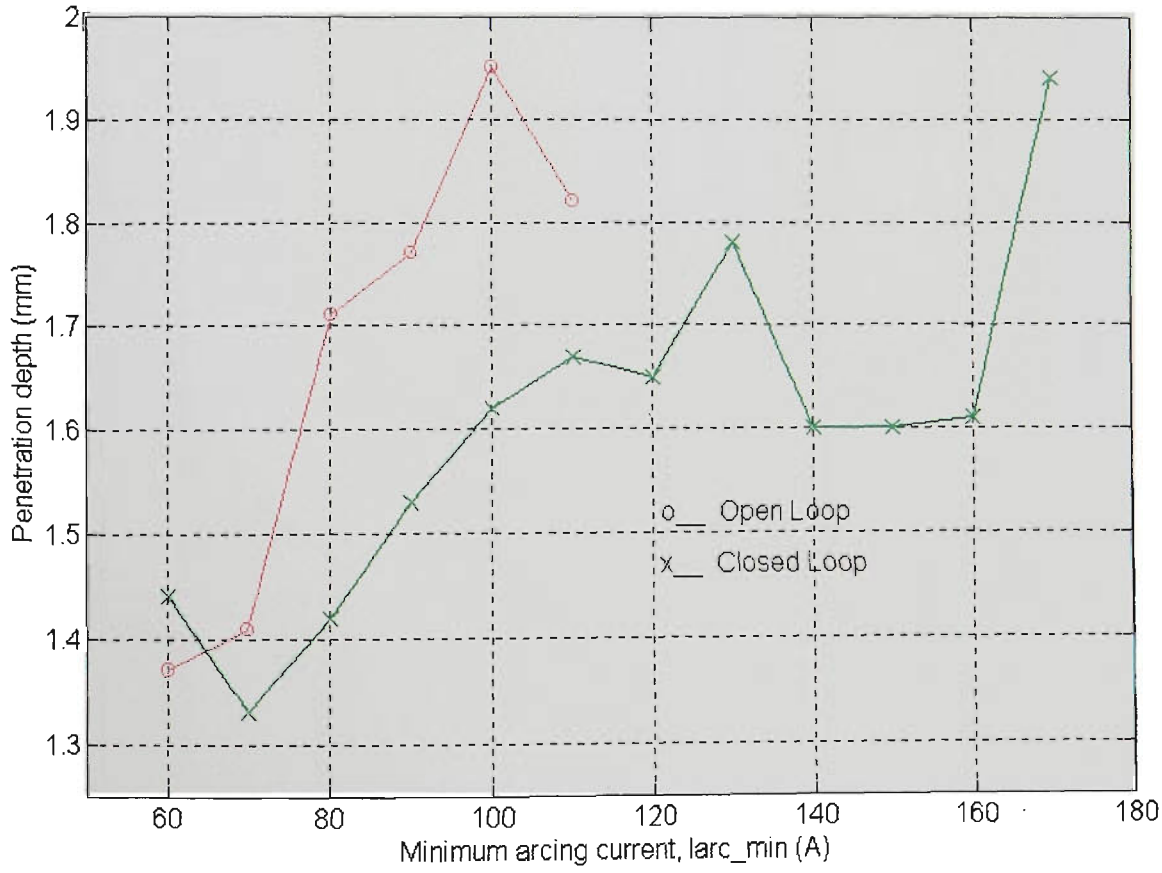

Figure 11.24 Penetration depth vs Iarc_min

(Ar-23%CO_2, CTWD=8mm, WFR=5.7m/min, Travel=390mm/min)

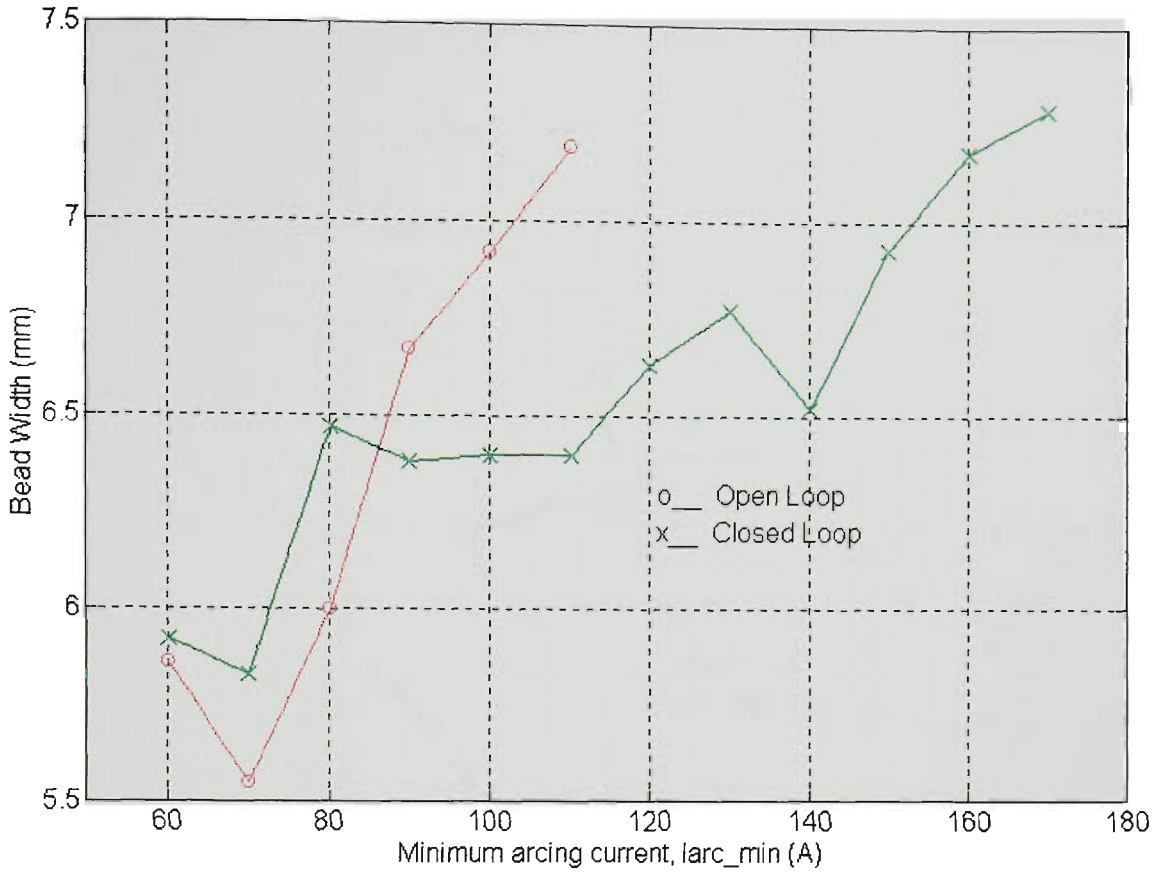

Figure 11.25 Bead width vs Iarc_min

(Ar-23%CO_2, CTWD=8mm, WFR=5.7m/min, Travel=390mm/min)

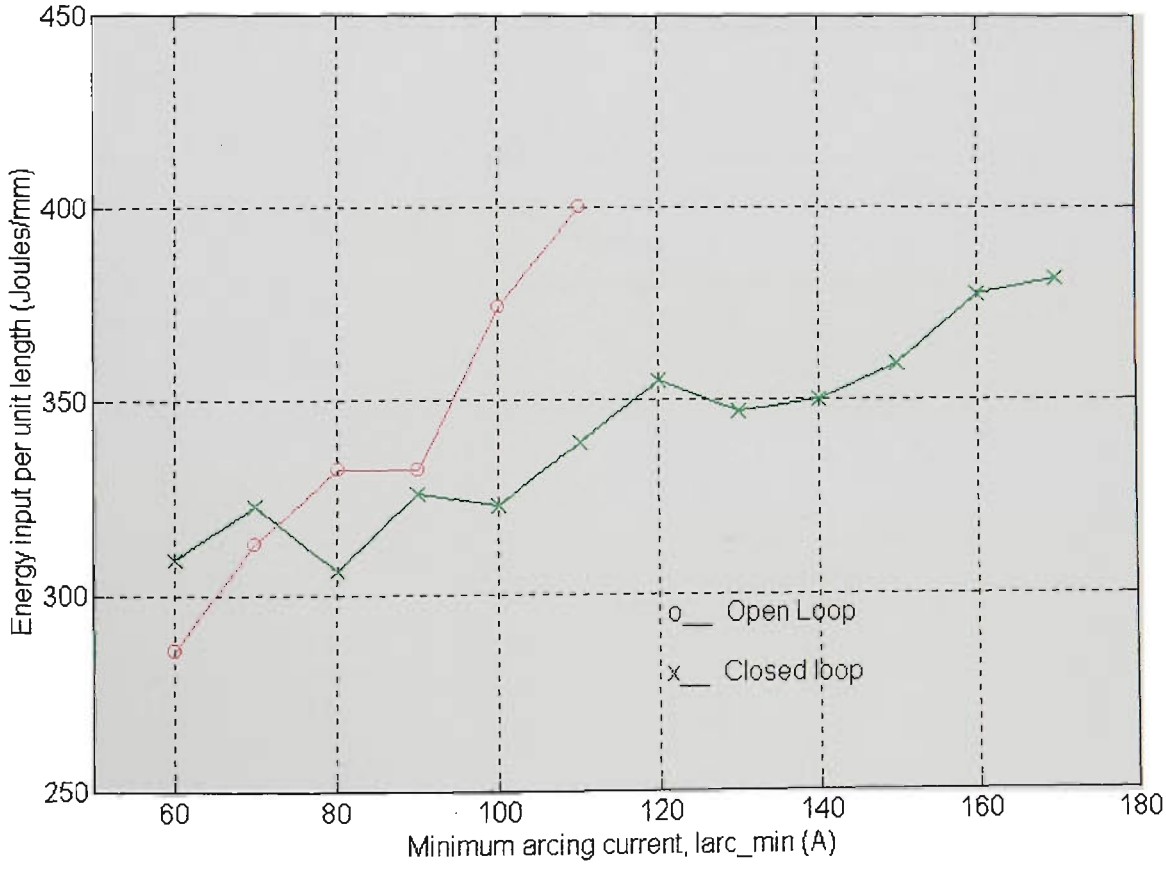

Figure 11.26 Energy input per unit length vs Iarc_min

(Ar-23%CO_2, CTWD=8mm, WFR=5.7m/min, Travel=390mm/min)

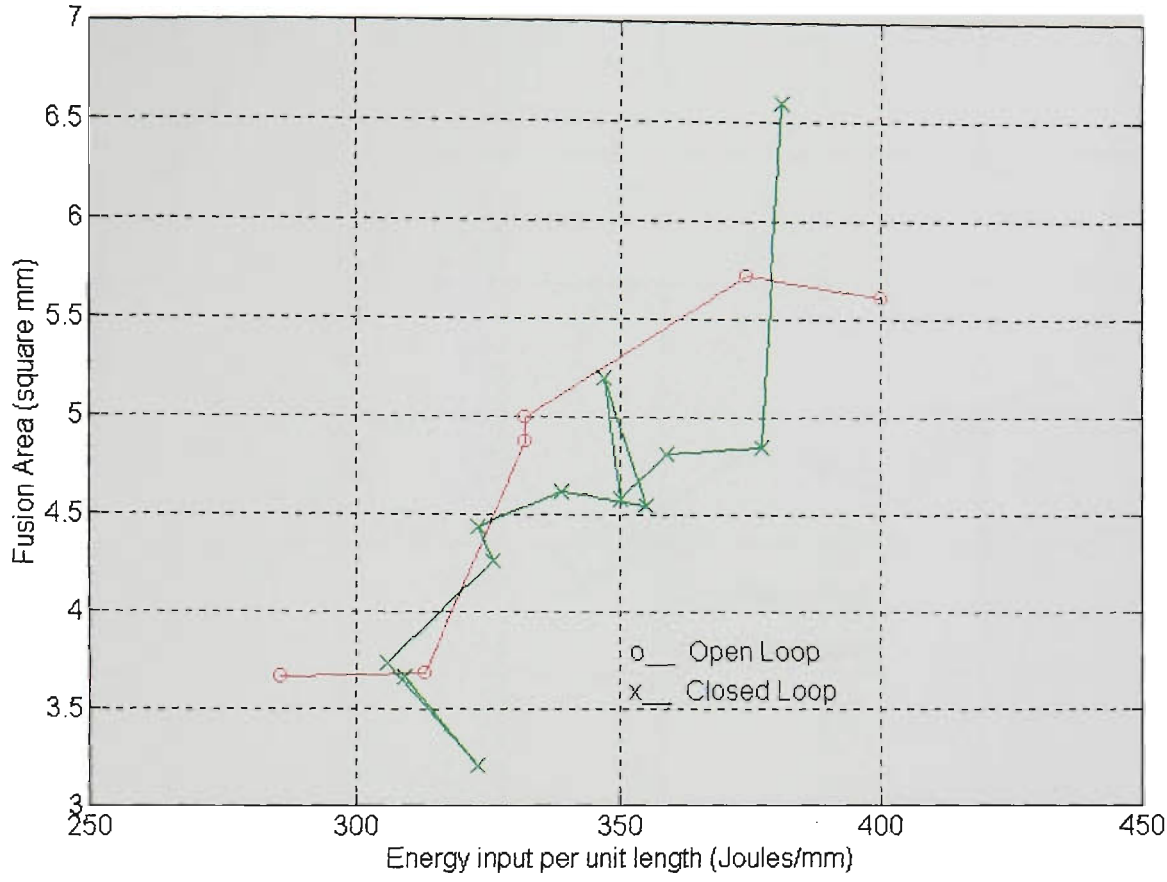

Figure 11.27 Fusion area vs Energy input per unit length
(Ar-23%CO_2, CTWD=8mm, WFR=5.7m/min, Travel=390mm/min)

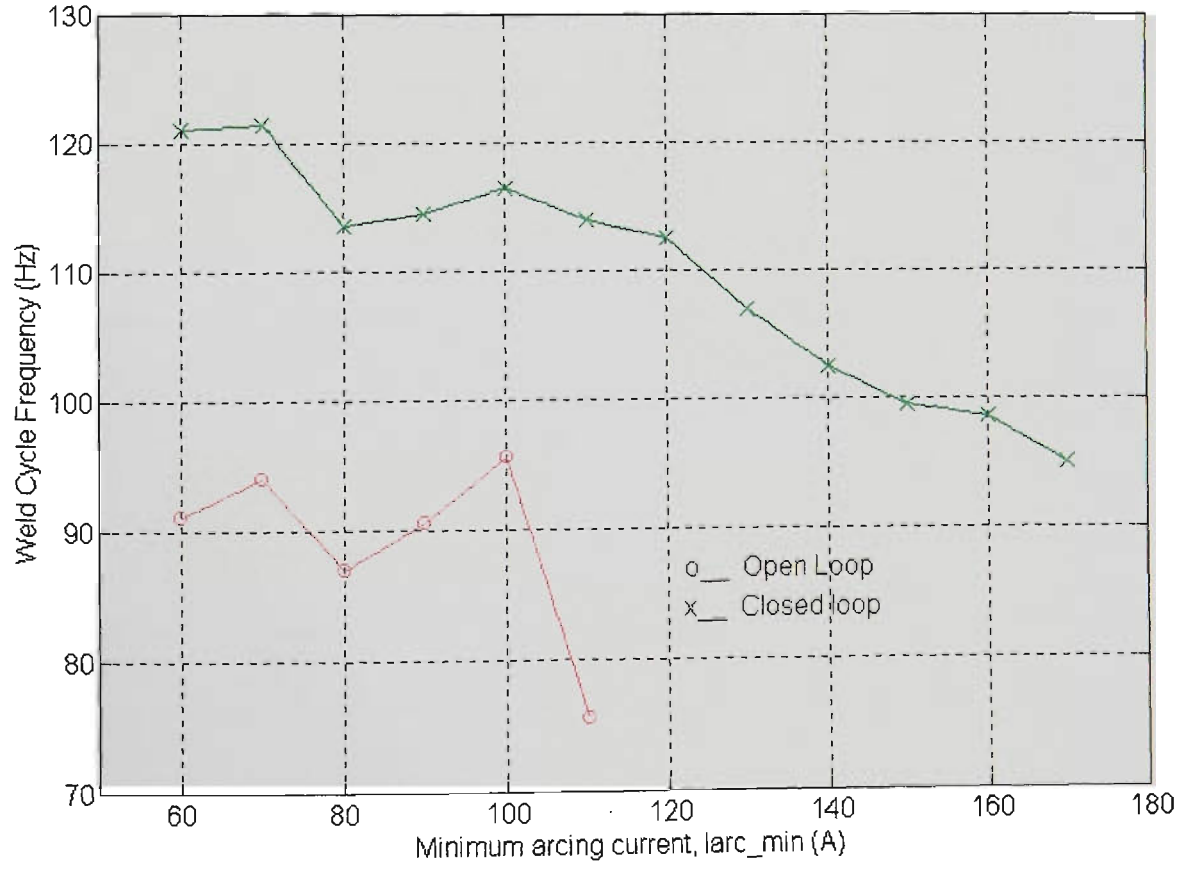

Figure 11.28 Average dipping frequency vs Iarc_min
(Ar-23%CO_2, CTWD=8mm, WFR=5.7m/min, Travel=390mm/min)

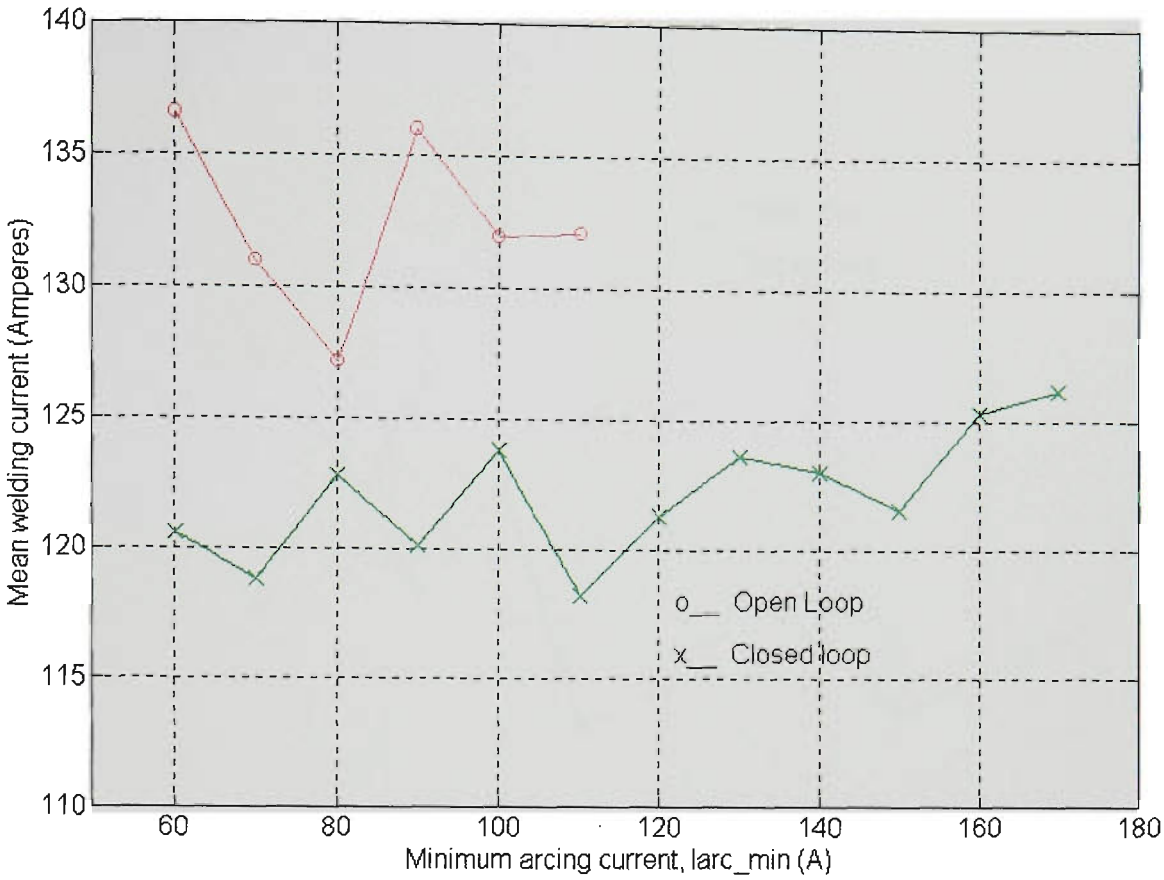

Figure 11.29 Mean welding current vs Iarc_min

(Ar-23%CO_2, CTWD=8mm, WFR=5.7m/min, Travel=390mm/min)

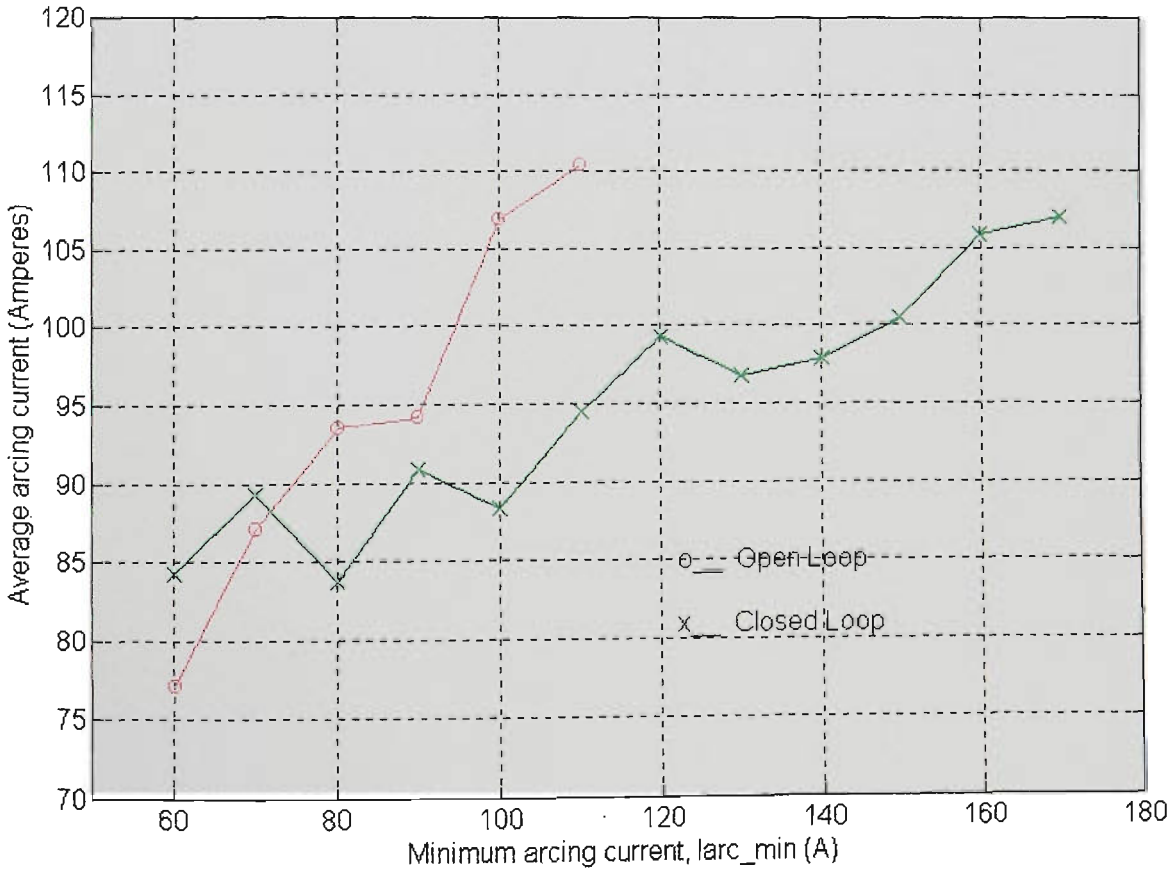

Figure 11.30 Average arcing current vs Iarc_min

(Ar-23%CO_2, CTWD=8mm, WFR=5.7m/min, Travel=390mm/min)

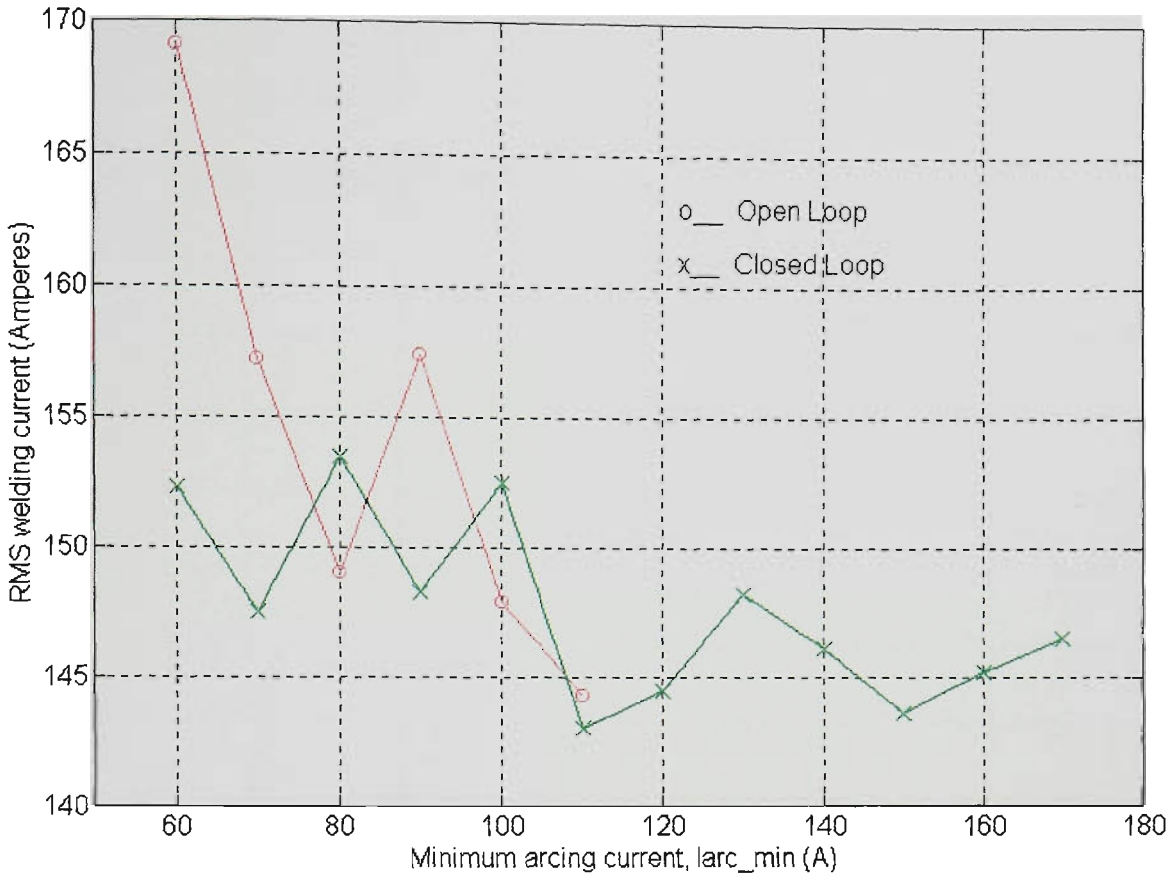

Figure 11.31 RMS current vs Iarc_min

(Ar-23%CO_2, CTWD=8mm, WFR=5.7m/min, Travel=390mm/min)

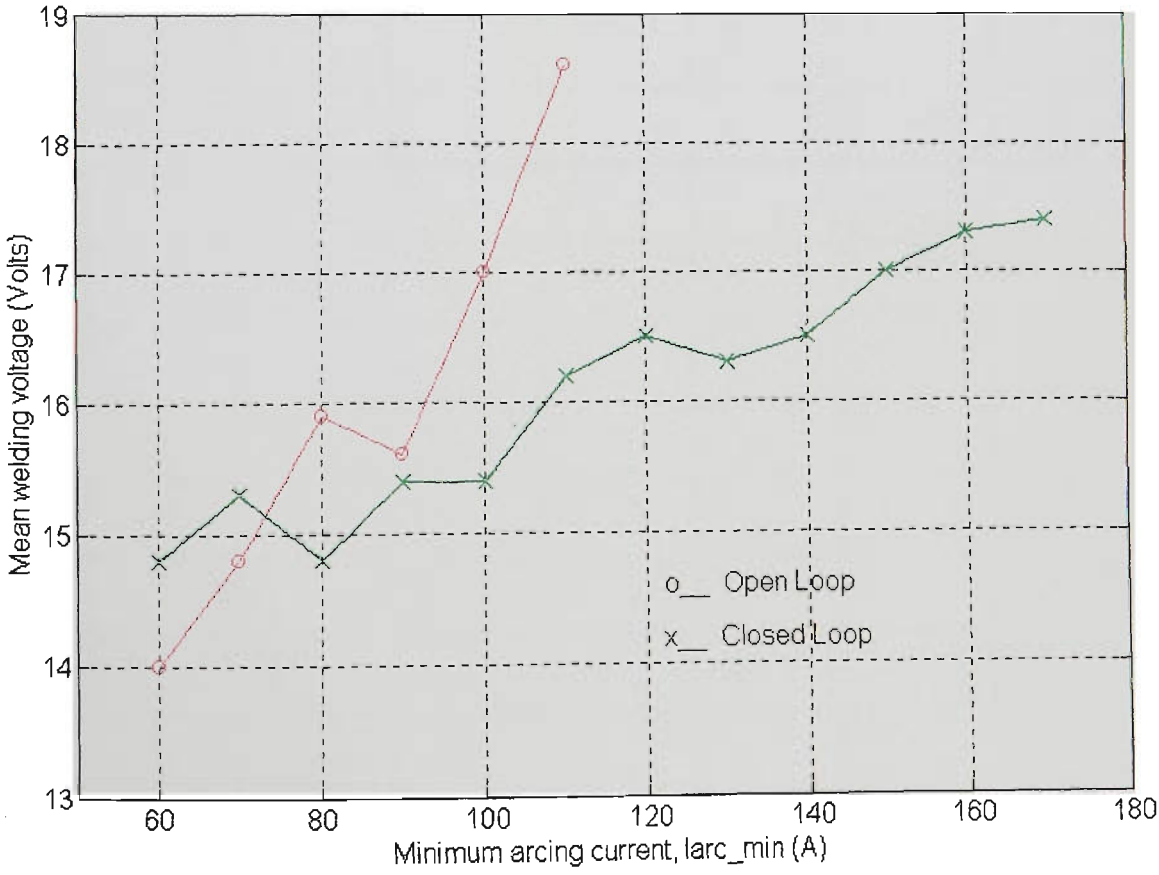

Figure 11.32 Mean voltage vs Iarc_min

(Ar-23%CO_2, CTWD=8mm, WFR=5.7m/min, Travel=390mm/min)

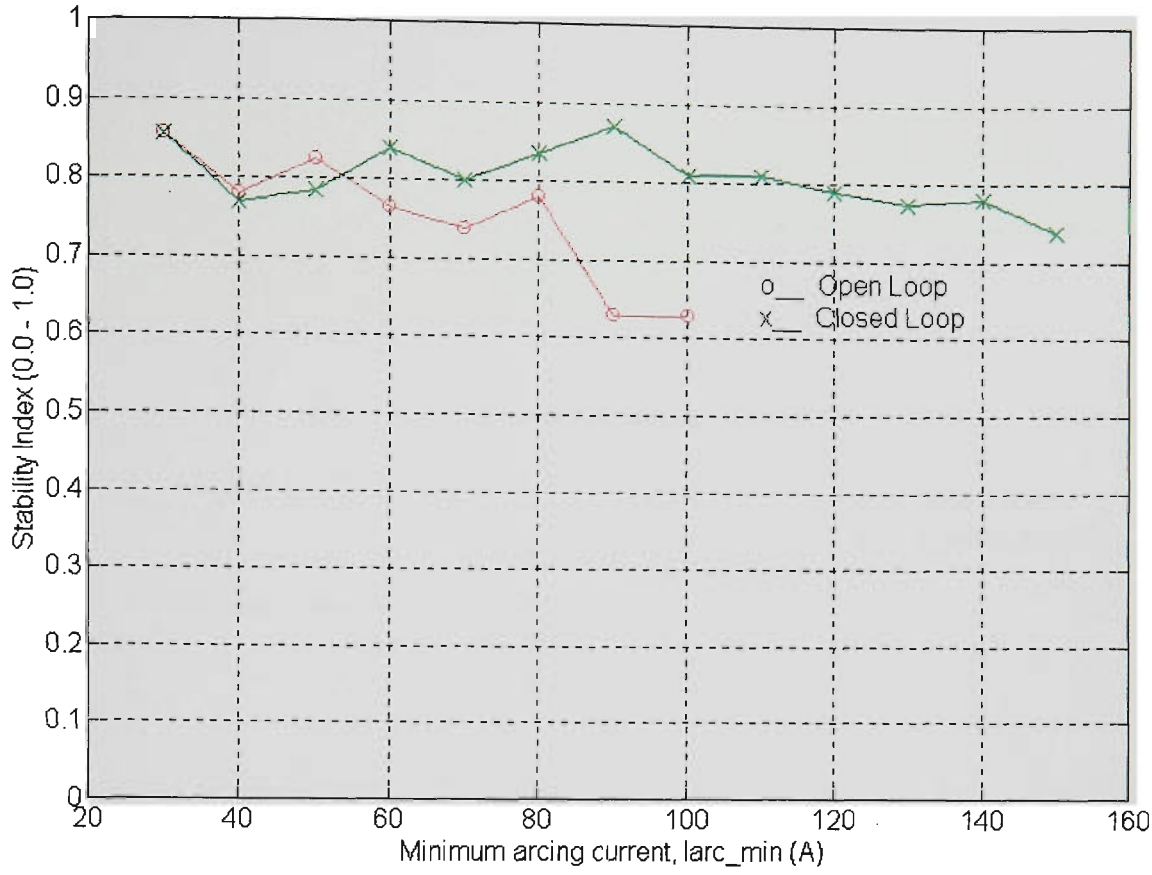

Figure 11.33 Stability index vs Iarc_min

(Ar-23%CO_2, CTWD=16mm, WFR=5.7m/min, Travel=195mm/min)

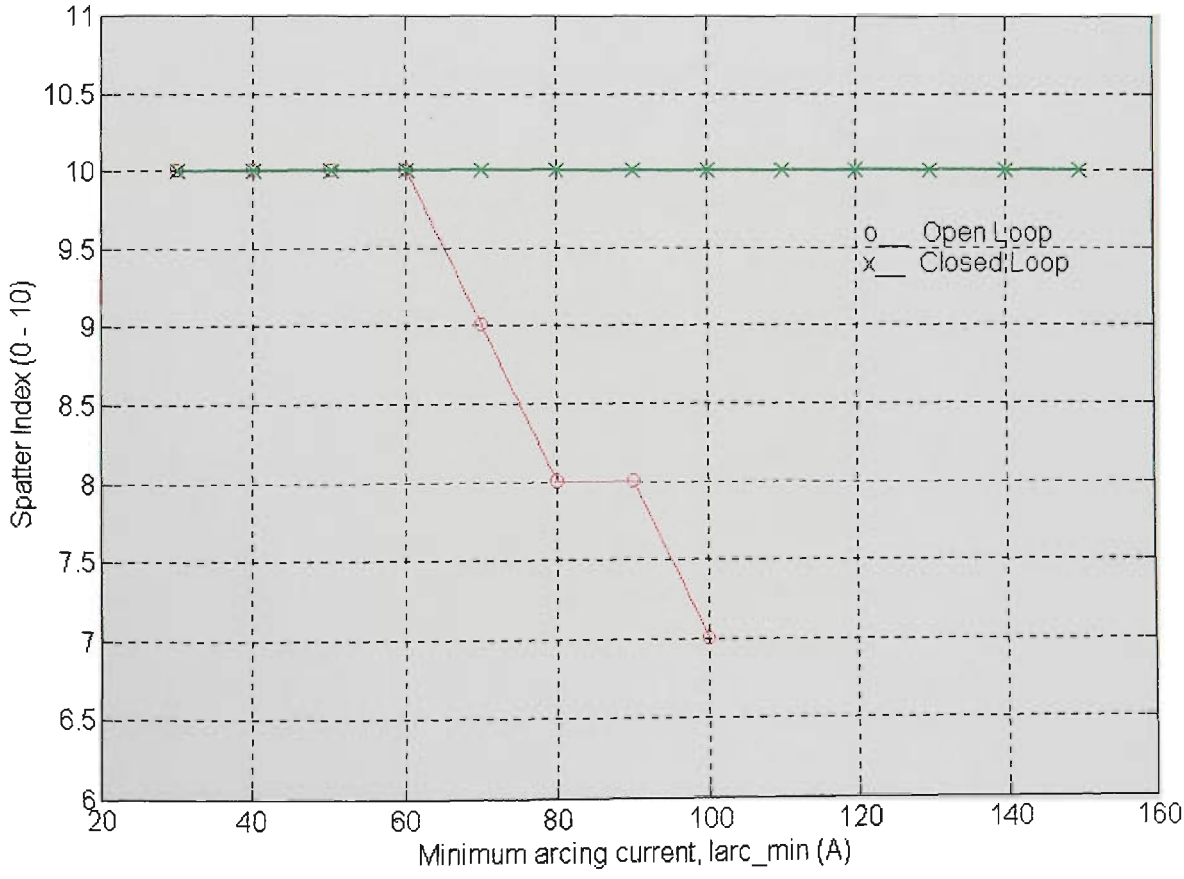

Figure 11.34 Spatter index vs Iarc_min

(Ar-23%CO_2, CTWD=16mm, WFR=5.7m/min, Travel=195mm/min)

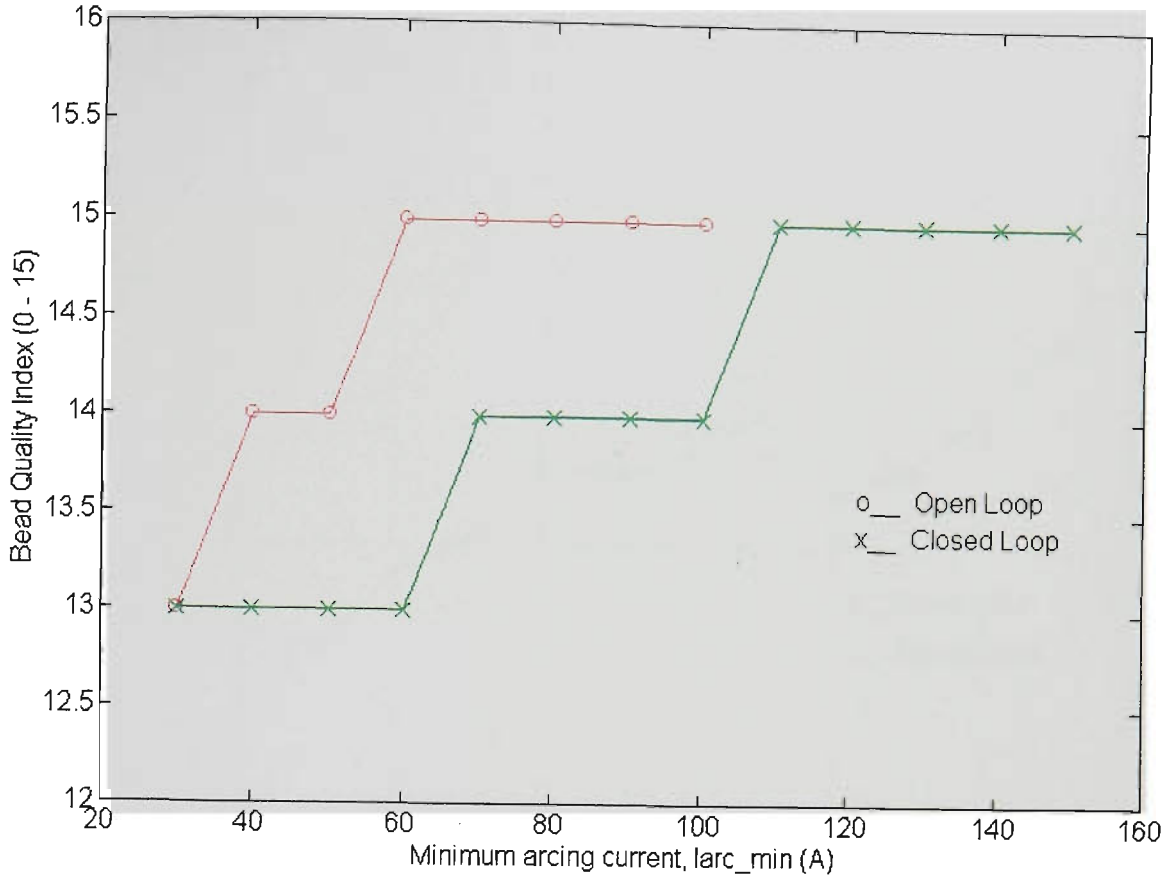

Figure 11.35 Bead quality index vs Iarc_min

(Ar-23%CO_2, CTWD=16mm, WFR=5.7m/min, Travel=195mm/min)

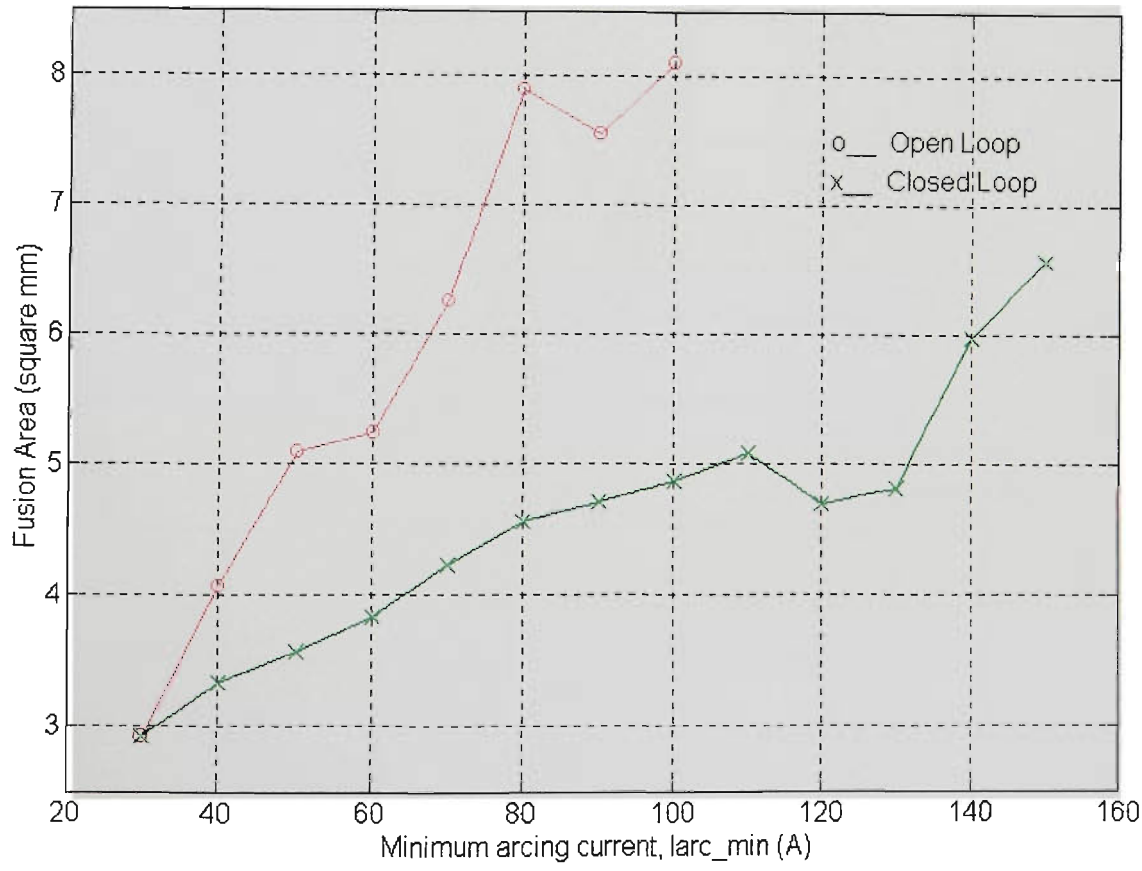

Figure 11.36 Fusion area vs Iarc_min

(Ar-23%CO_2, CTWD=16mm, WFR=5.7m/min, Travel=195mm/min)

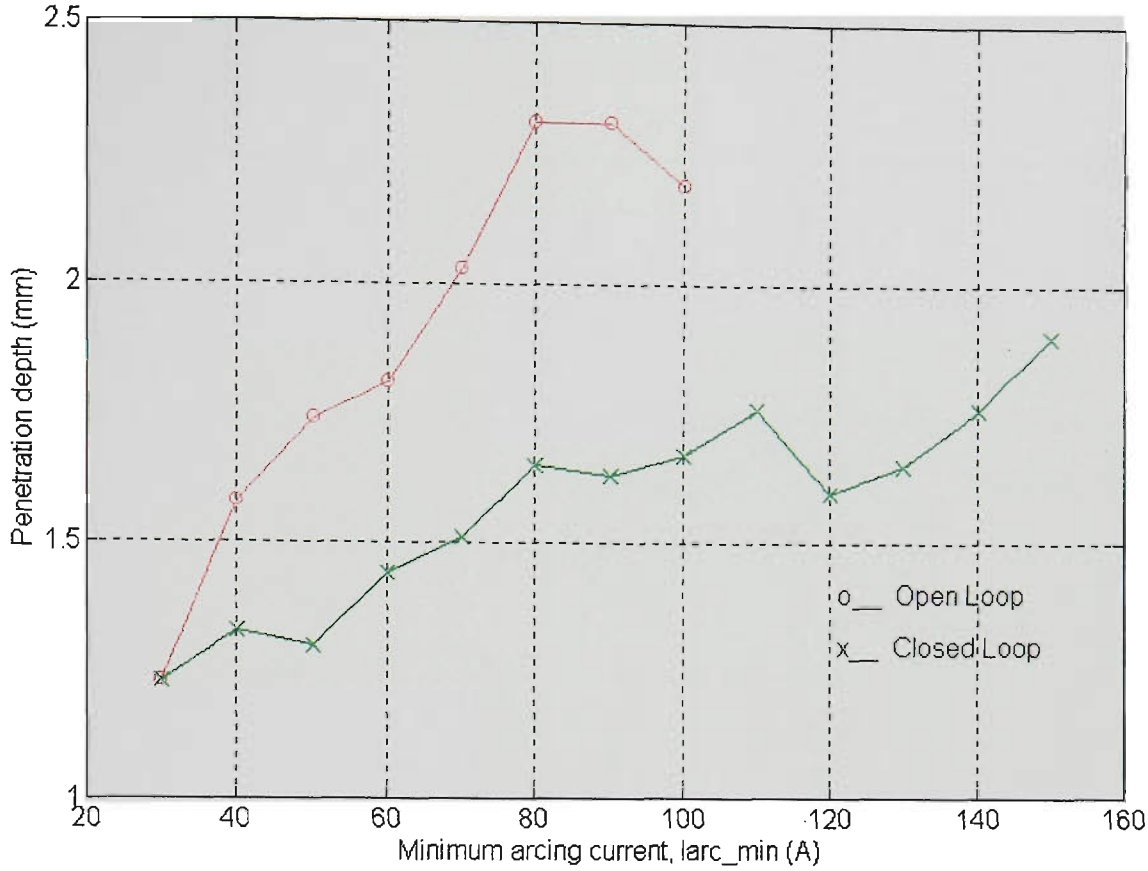

Figure 11.37 Penetration depth vs Iarc_min

(Ar-23%CO_2, CTWD=16mm, WFR=5.7m/min, Travel=195mm/min)

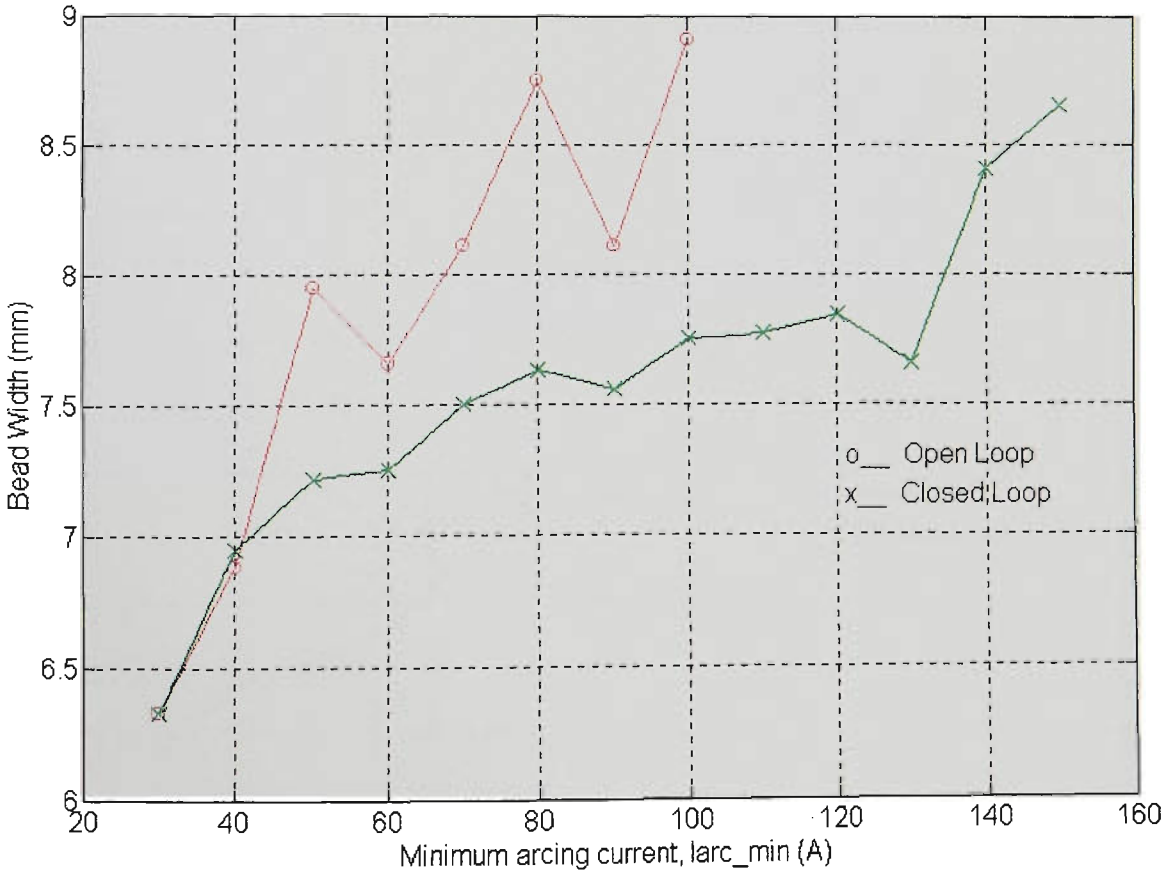

Figure 11.38 Bead width vs Iarc_min

(Ar-23%CO_2, CTWD=16mm, WFR=5.7m/min, Travel=195mm/min)

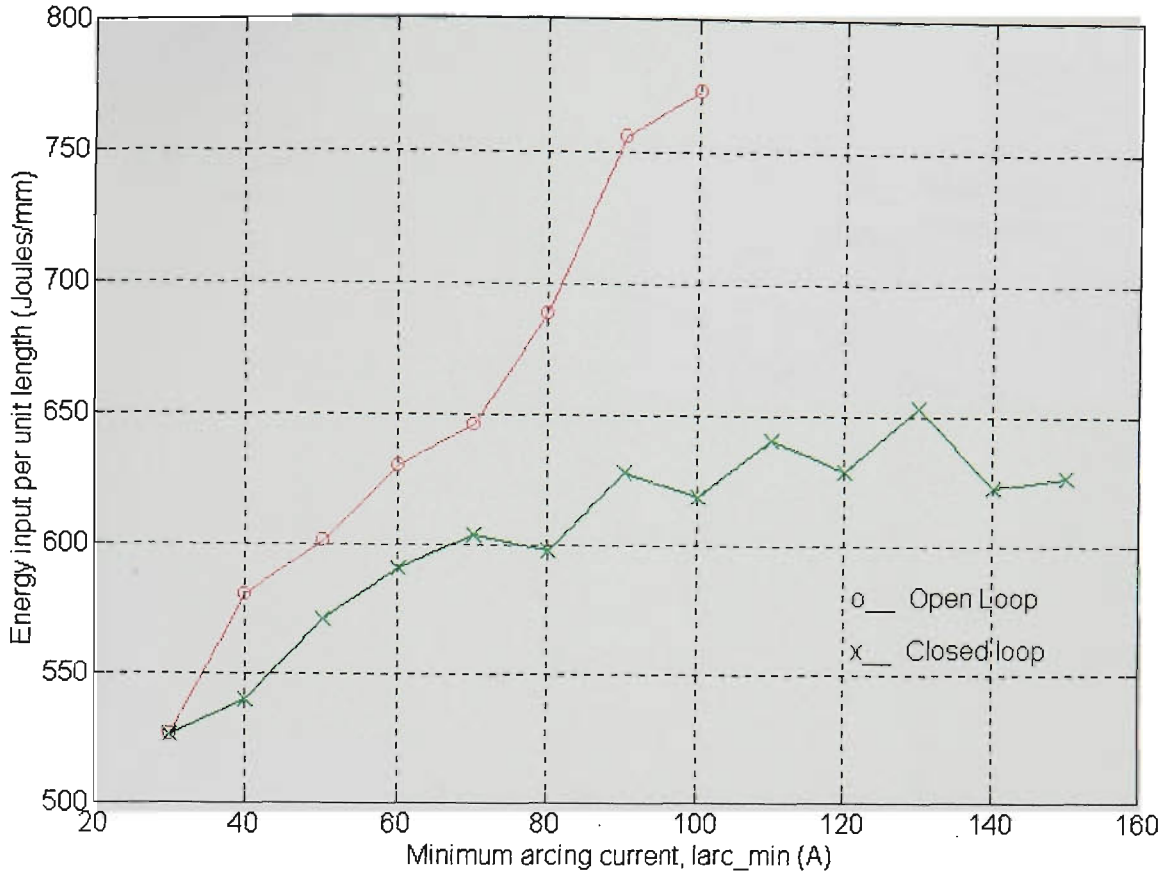

Figure 11.39 Energy input per unit length vs Iarc_min

(Ar-23%CO_2, CTWD=16mm, WFR=5.7m/min, Travel=195mm/min)

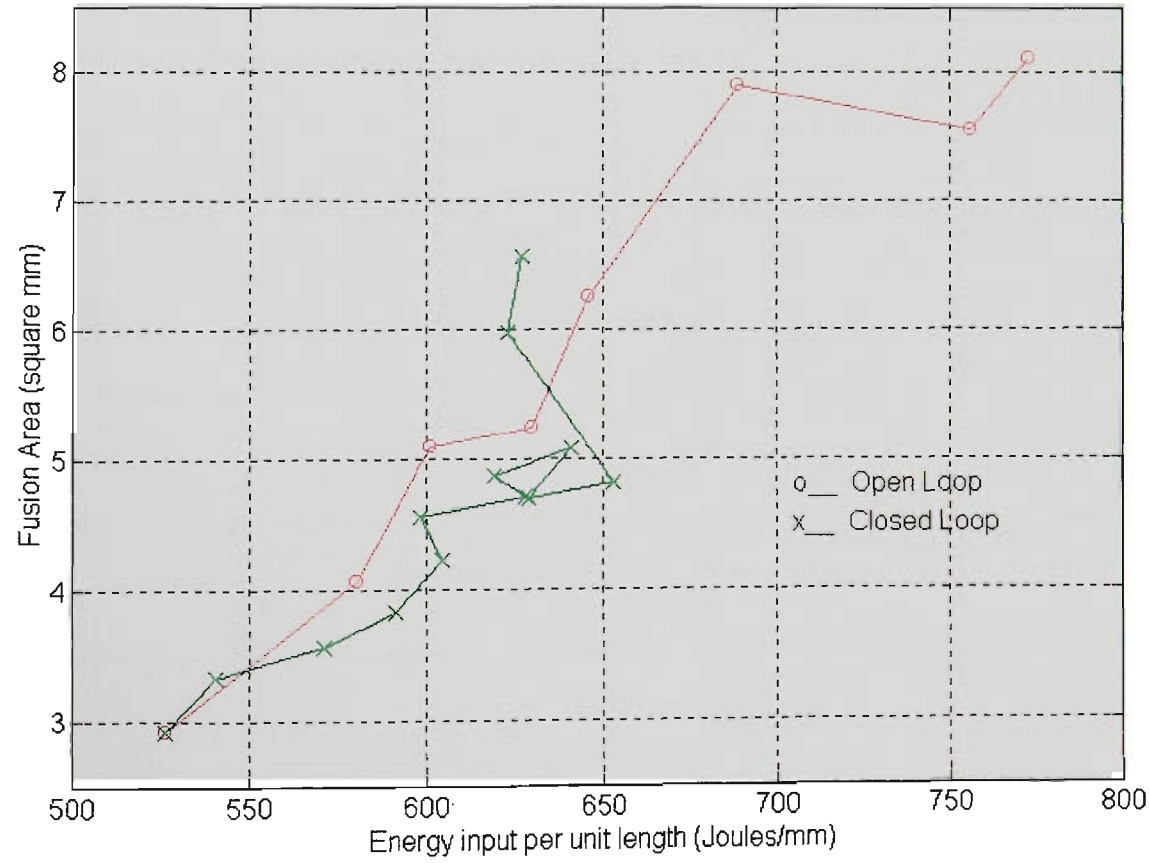

Figure 11.40 Fusion area vs Energy input per unit length

(Ar-23%CO_2, CTWD=16mm, WFR=5.7m/min, Travel=195mm/min)

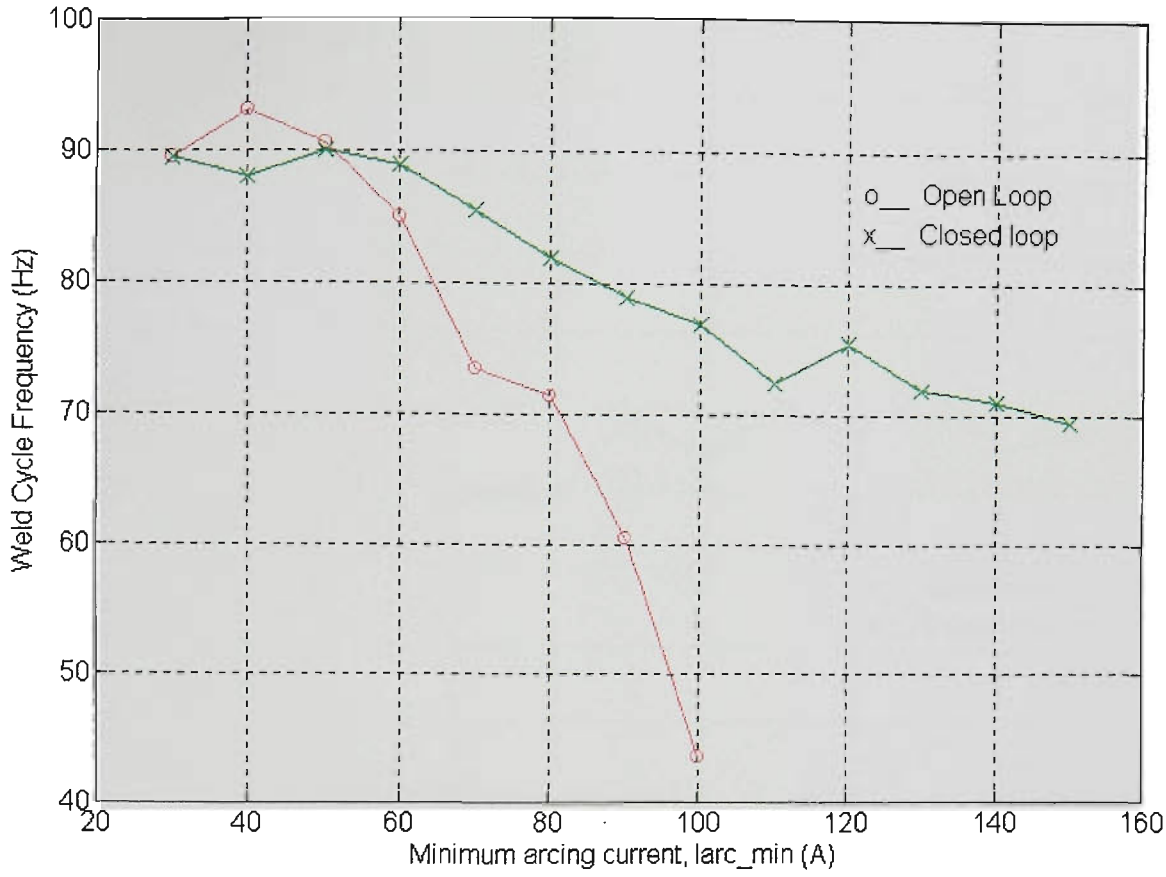

Figure 11.41 Average dipping frequency vs Iarc_min

(Ar-23%CO_2, CTWD=16mm, WFR=5.7m/min, Travel=195mm/min)

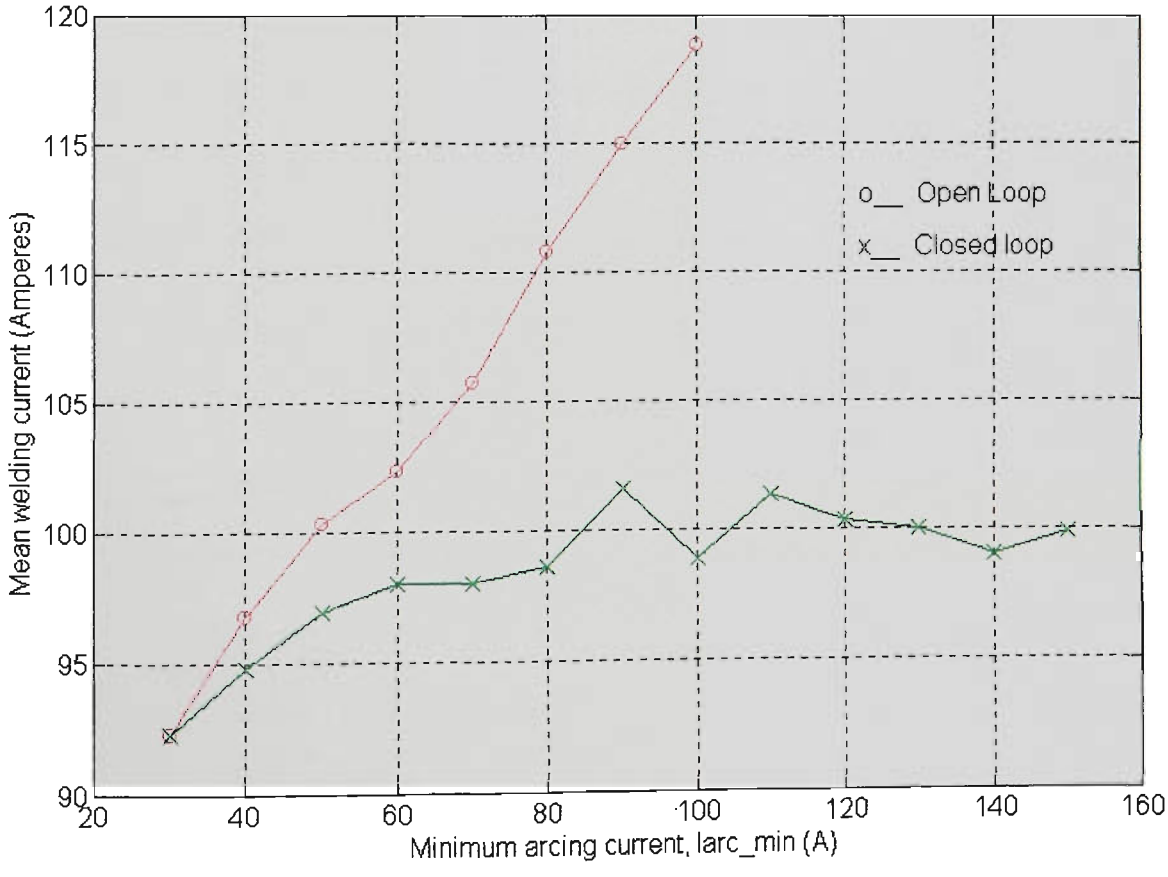

Figure 11.42 Mean welding current vs Iarc_min

(Ar-23%CO_2, CTWD=16mm, WFR=5.7m/min, Travel=195mm/min)

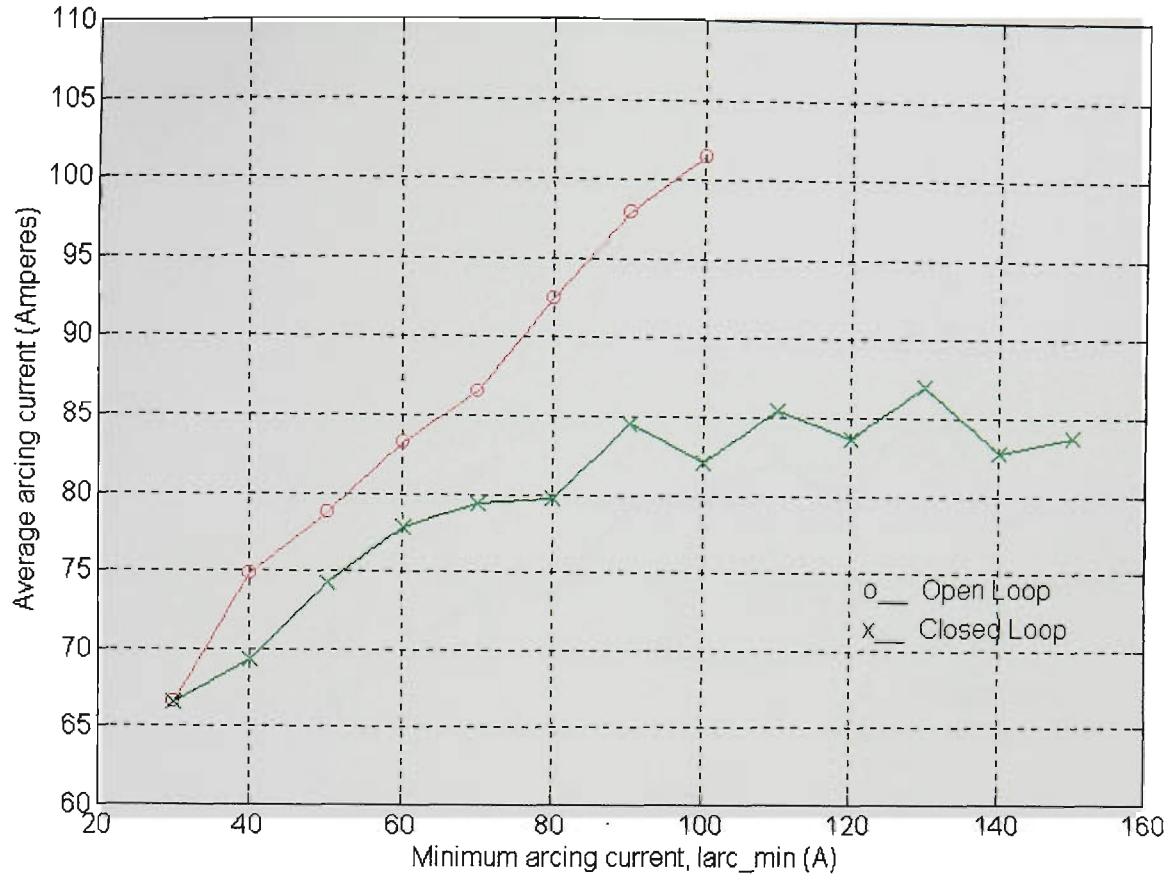

Figure 11.43 Average arcing current vs Iarc_min

(Ar-23%CO_2, CTWD=16mm, WFR=5.7m/min, Travel=195mm/min)

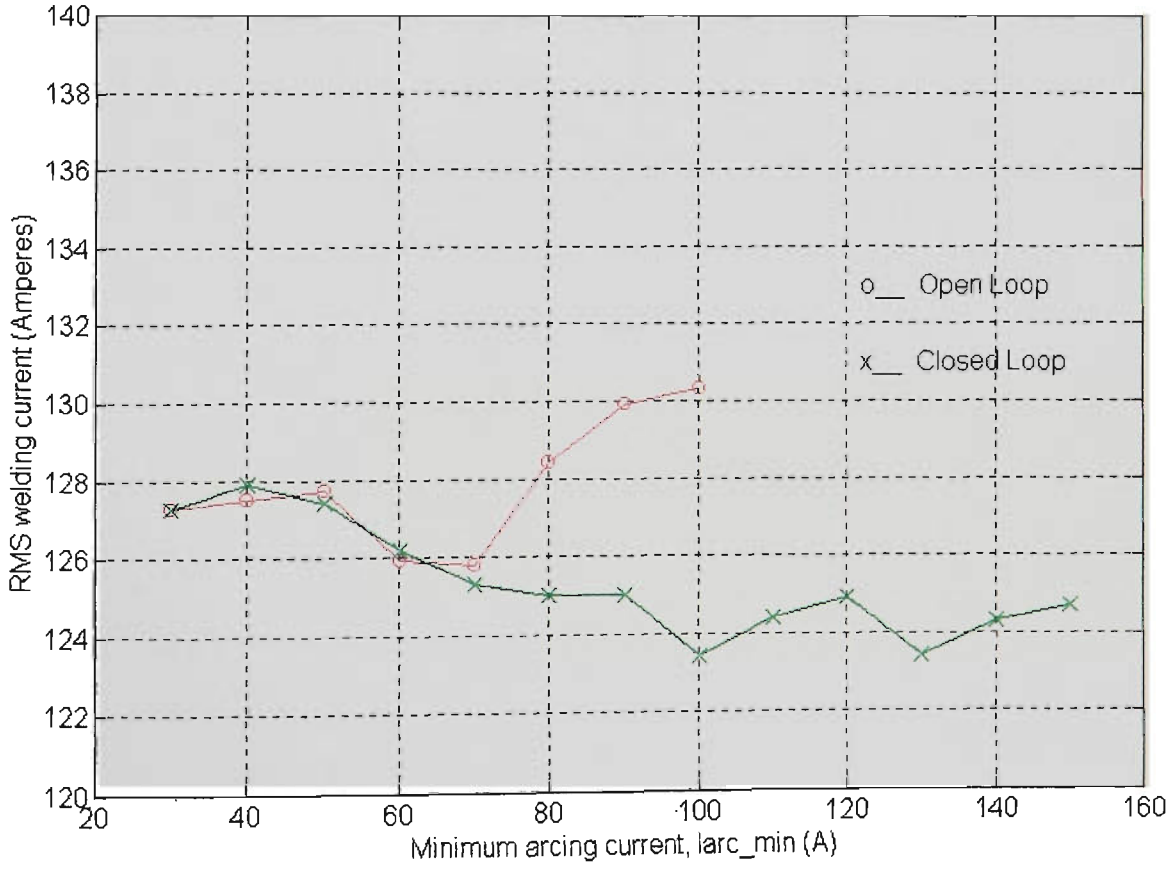

Figure 11.44 RMS current vs Iarc_min

(Ar-23%CO_2, CTWD=16mm, WFR=5.7m/min, Travel=195mm/min)

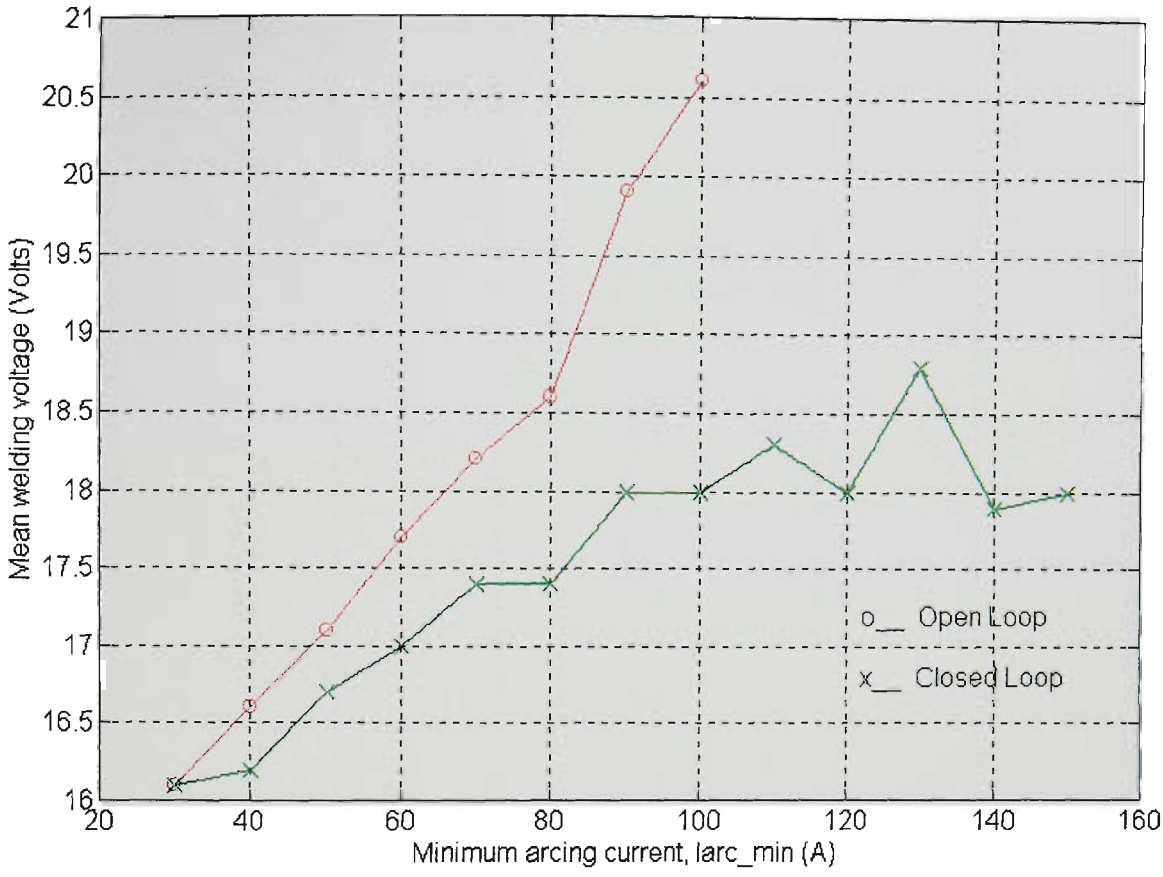

Figure 11.45 Mean voltage vs Iarc_min

(Ar-23%CO_2, CTWD=16mm, WFR=5.7m/min, Travel=195mm/min)

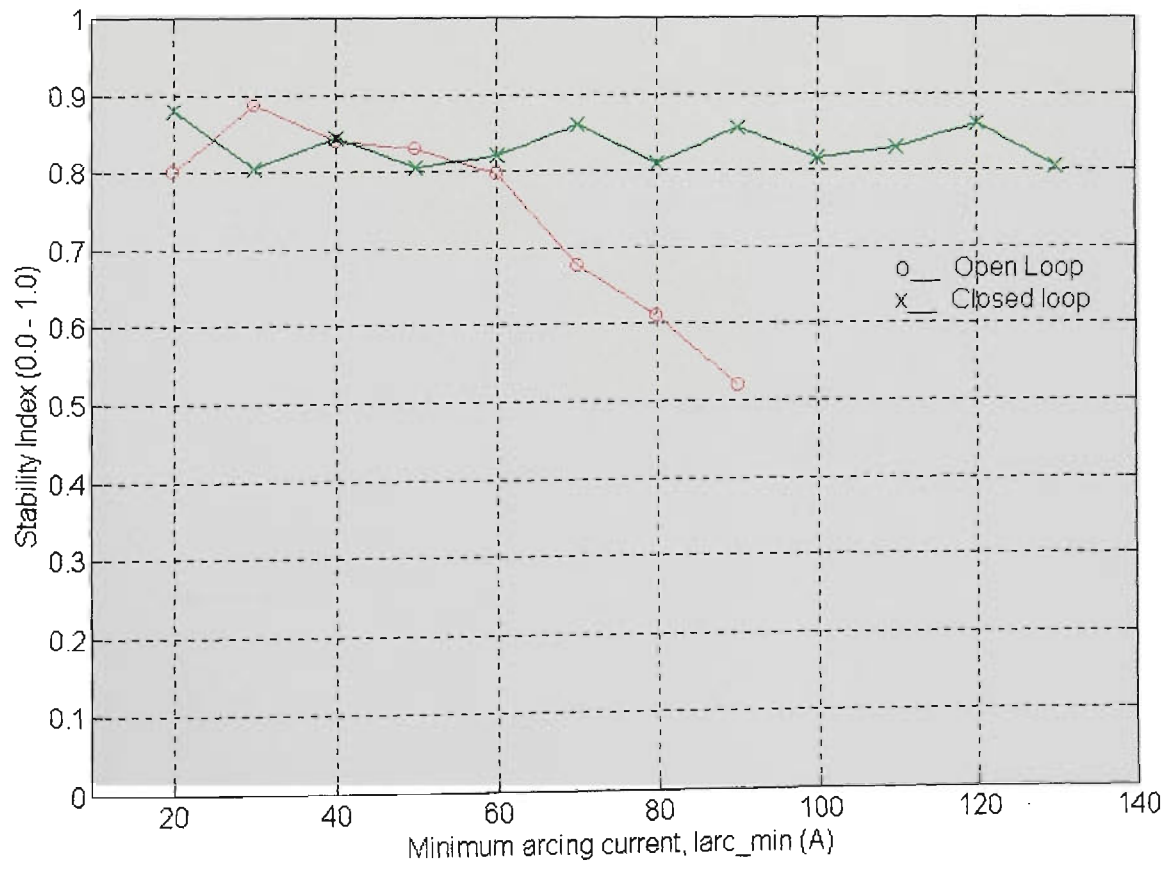

Figure 11.47 Stability index vs Iarc_min

(CO_2, CTWD=12mm, WFR=5.7m/min, Travel=195mm/min)

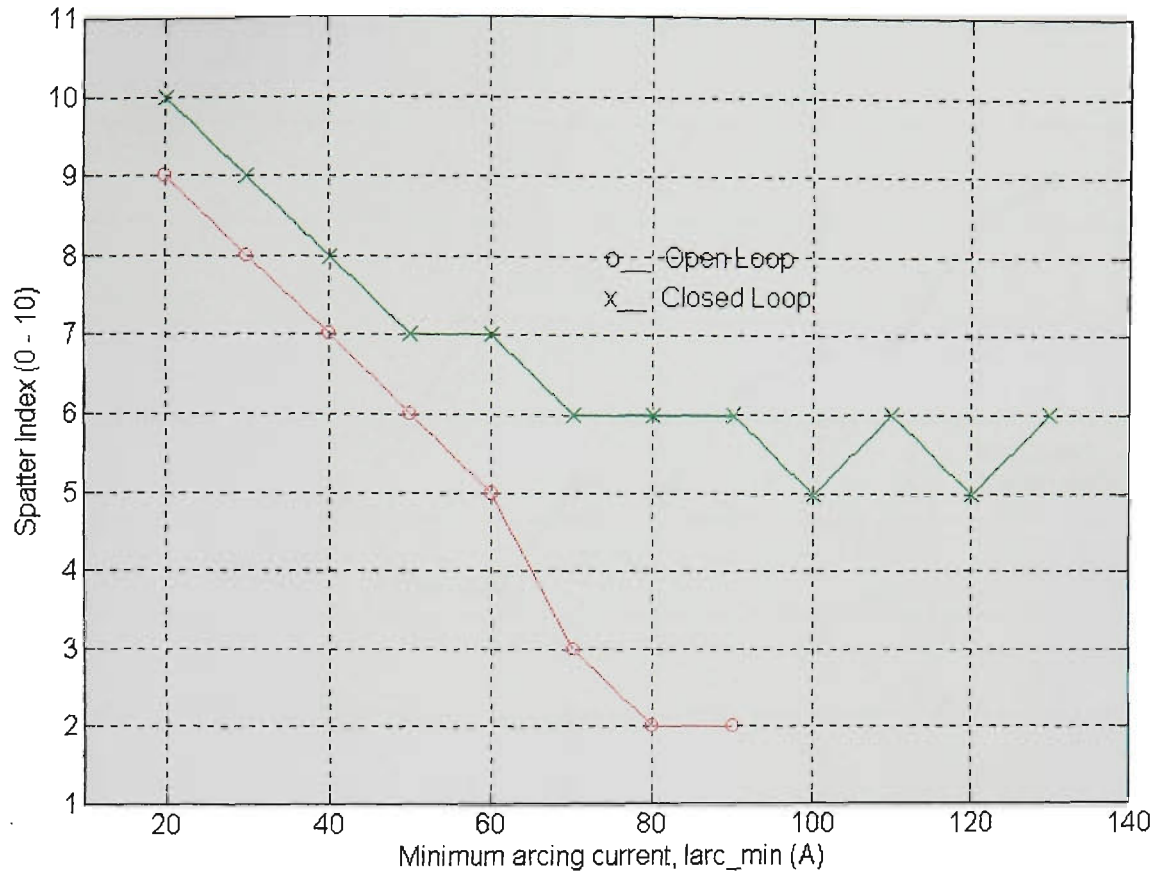

Figure 11.48 Spatter index vs Iarc_min

(CO_2, CTWD=12mm, WFR=5.7m/min, Travel=195mm/min)

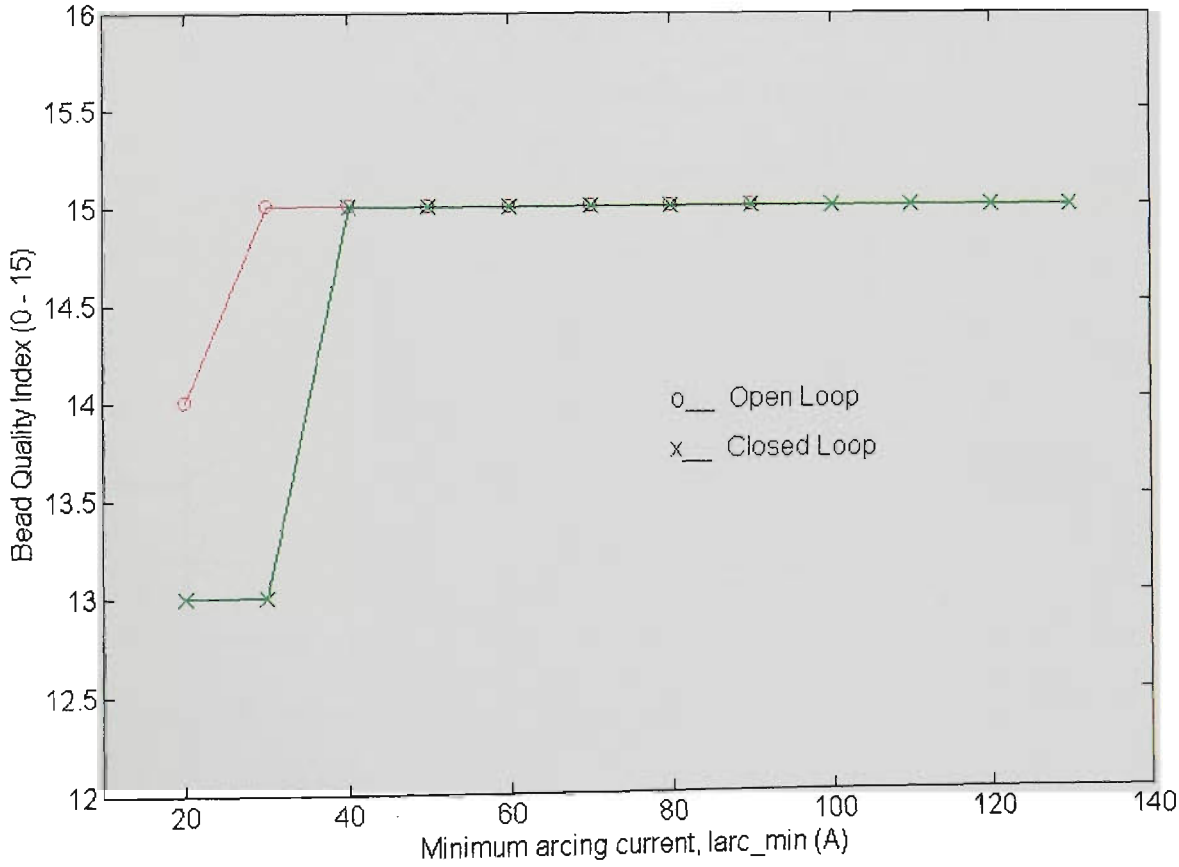

Figure 11.49 Bead quality index vs Iarc_min

(CO_2, CTWD=12mm, WFR=5.7m/min, Travel=195mm/min)

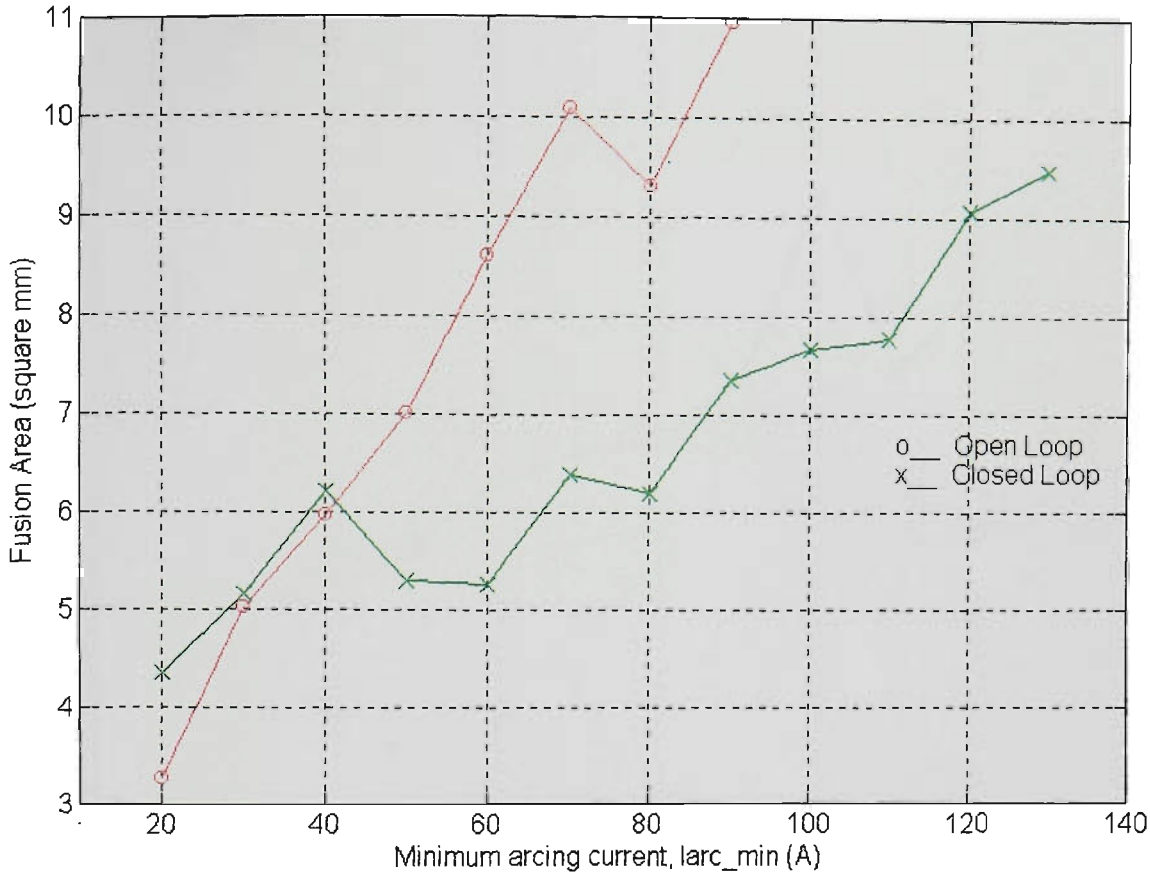

Figure 11.50 Fusion area vs Iarc_min

(CO_2, CTWD=12mm, WFR=5.7m/min, Travel=195mm/min)

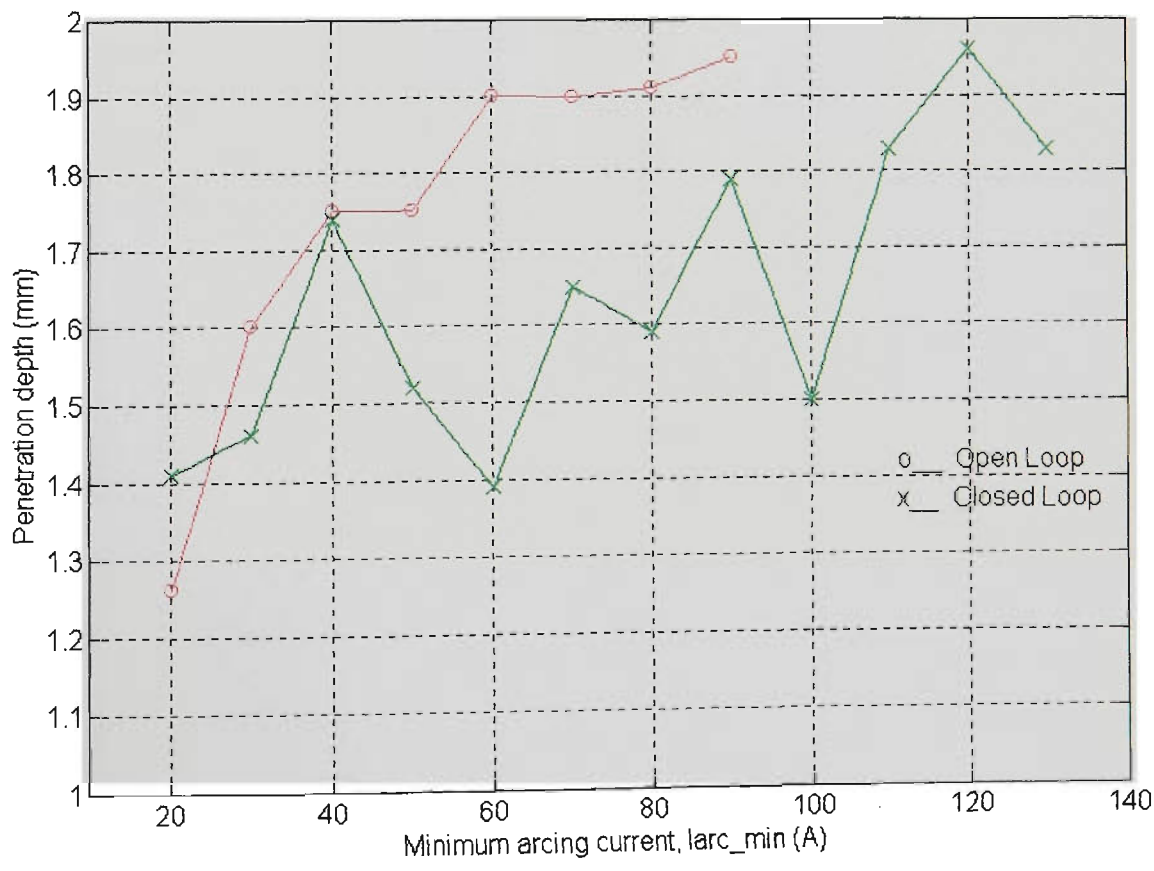

Figure 11.51 Penetration depth vs Iarc_min

(CO_2, CTWD=12mm, WFR=5.7m/min, Travel=195mm/min)

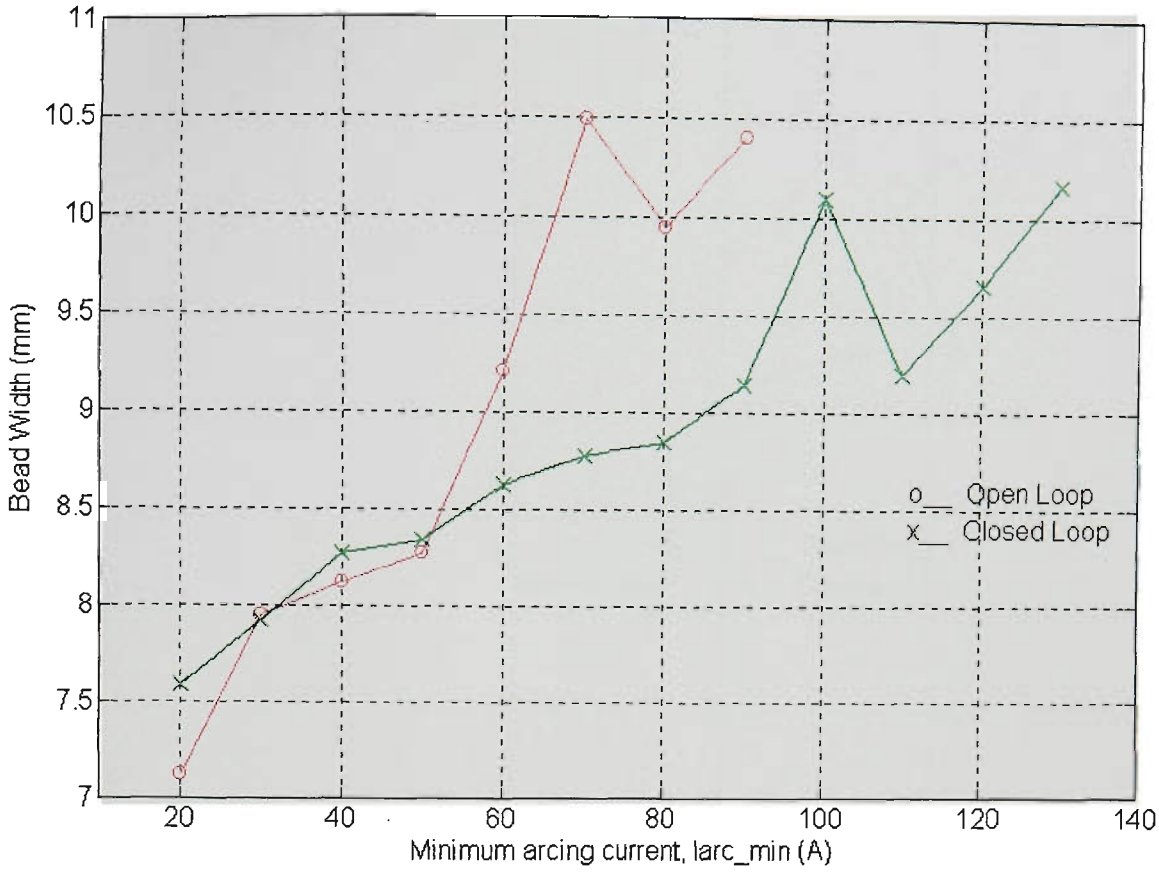

Figure 11.52 Bead width vs Iarc_min

(CO_2, CTWD=12mm, WFR=5.7m/min, Travel=195mm/min)

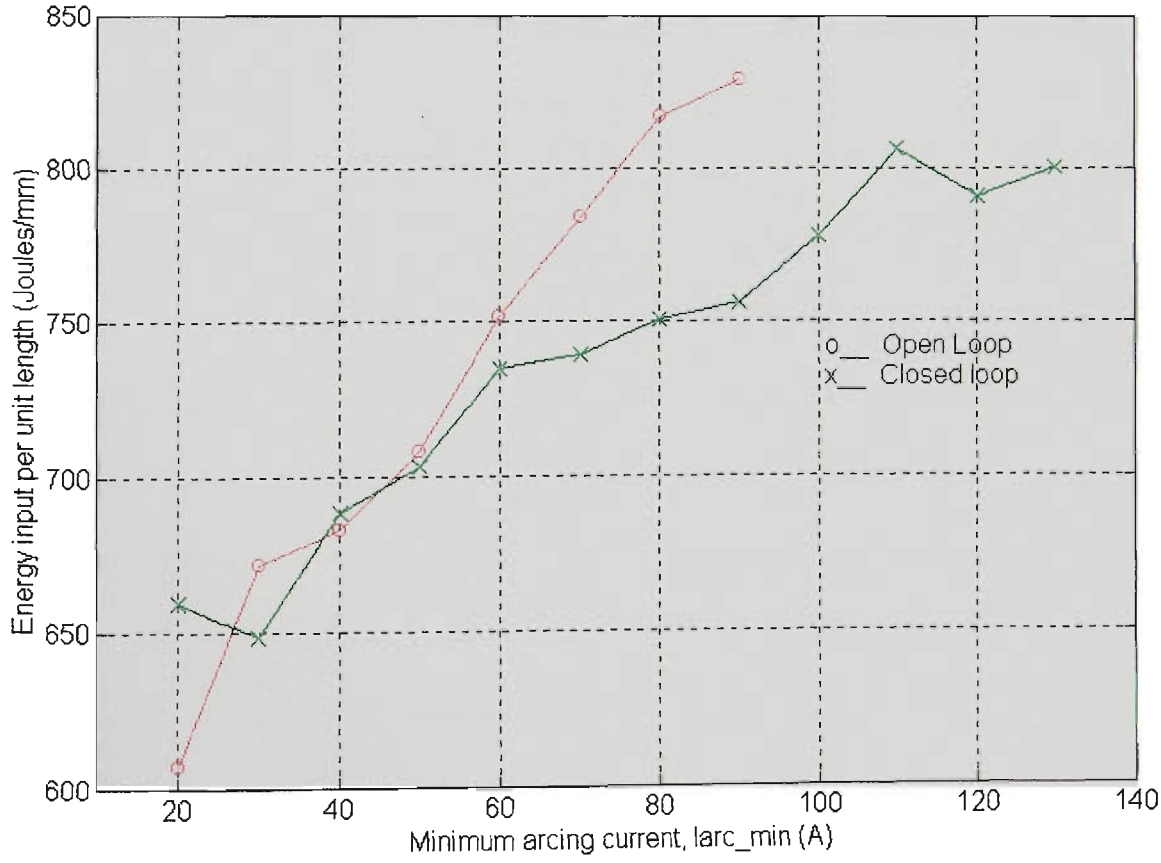

Figure 11.53 Energy input per unit length vs Iarc_min

(CO_2, CTWD=12mm, WFR=5.7m/min, Travel=195mm/min)

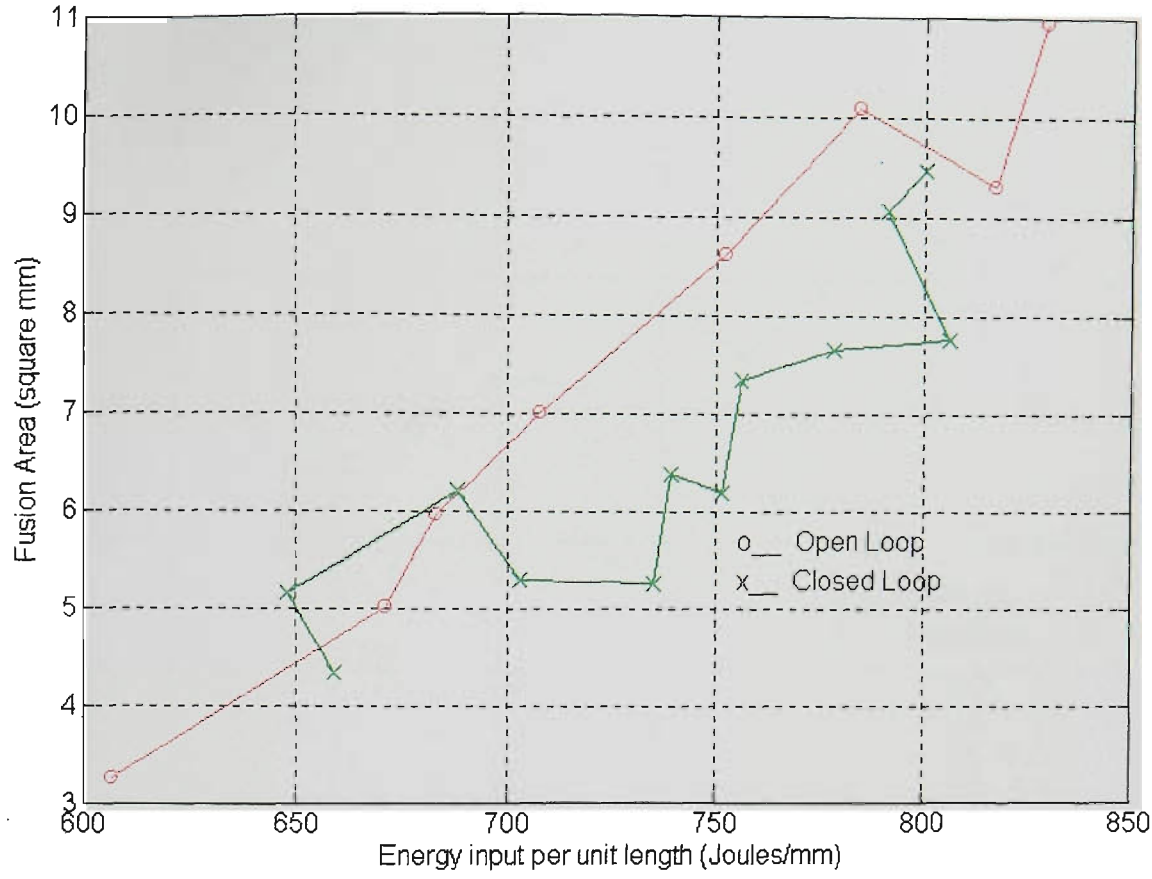

Figure 11.54 Fusion area vs Energy input per unit length

(CO_2, CTWD=12mm, WFR=5.7m/min, Travel=195mm/min)

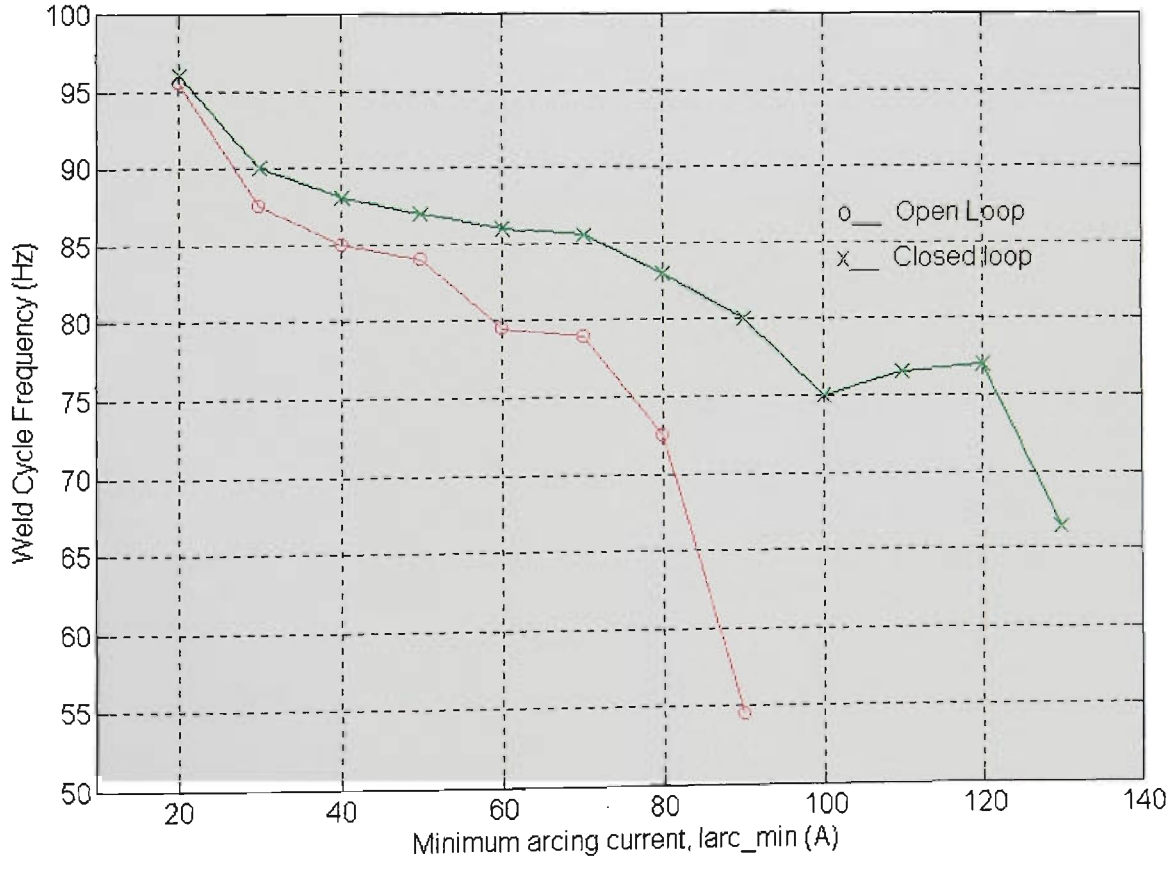

Figure 11.55 Average dipping frequency vs Iarc_min

(CO_2, CTWD=12mm, WFR=5.7m/min, Travel=195mm/min)

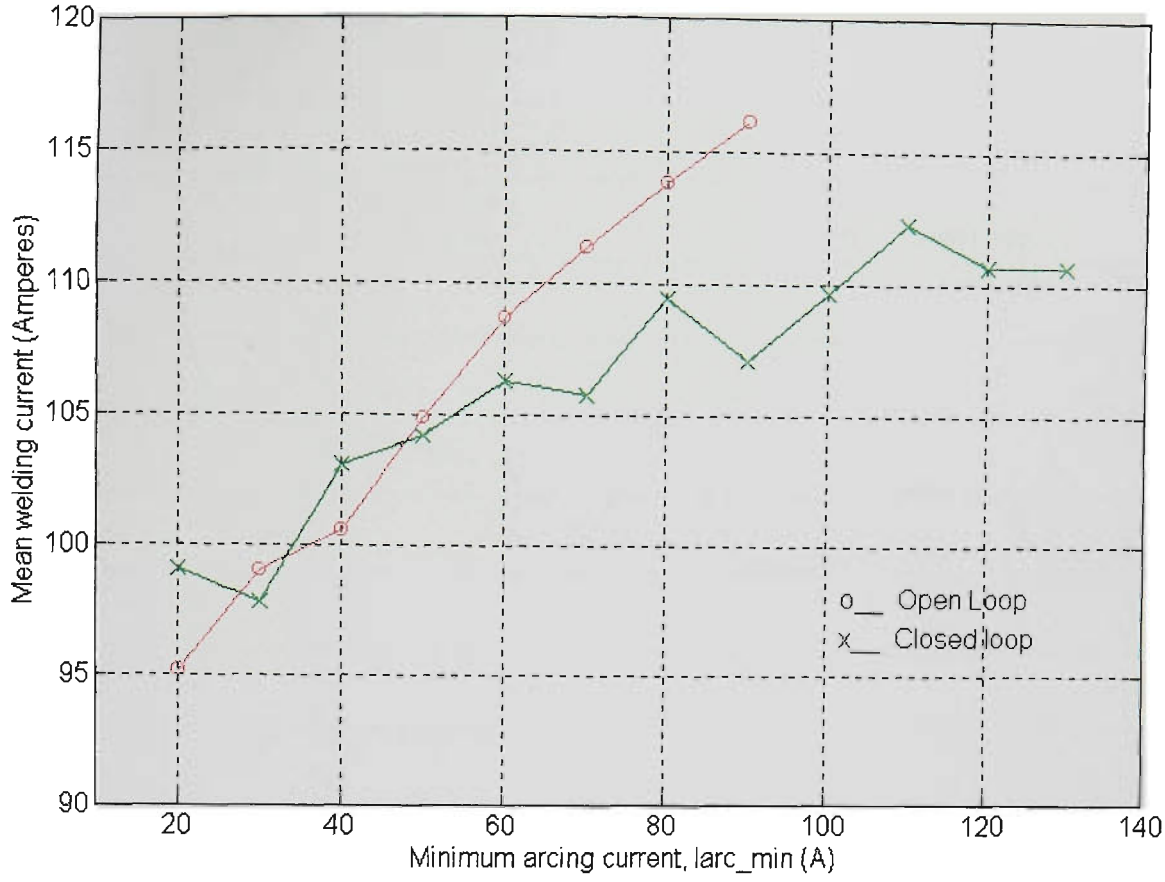

Figure 11.56 Mean welding current vs Iarc_min

(CO_2, CTWD=12mm, WFR=5.7m/min, Travel=195mm/min)

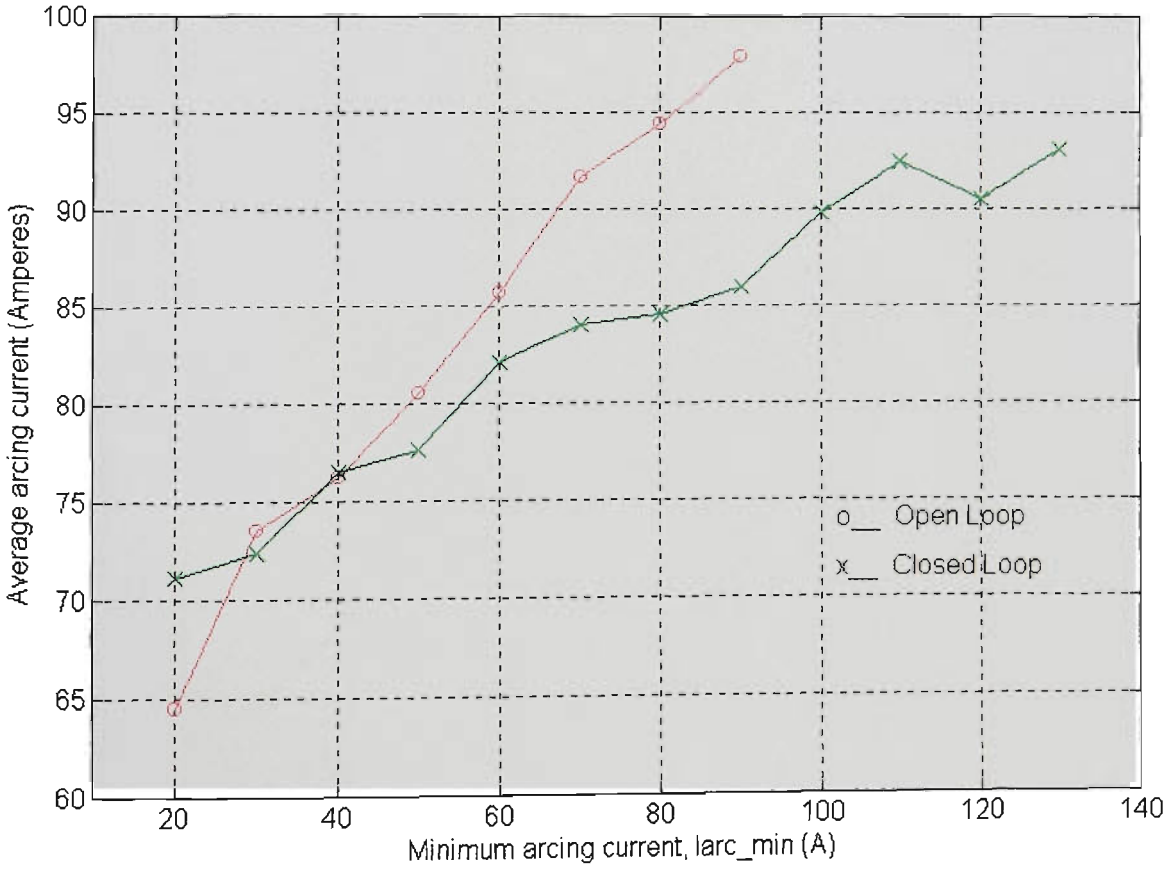

Figure 11.57 Average arcing current vs Iarc_min

(CO_2, CTWD=12mm, WFR=5.7m/min, Travel=195mm/min)

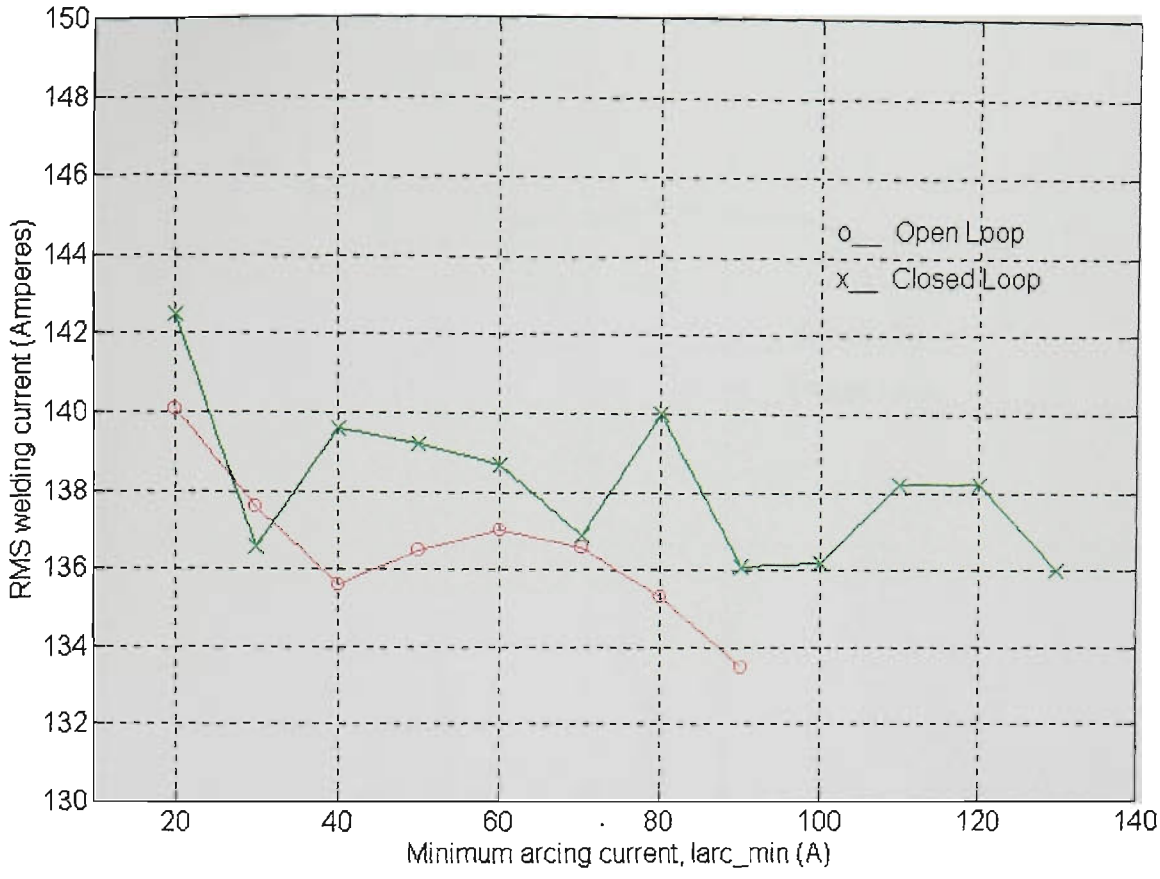

Figure 11.58 RMS current vs Iarc_min

(CO_2, CTWD=12mm, WFR=5.7m/min, Travel=195mm/min)

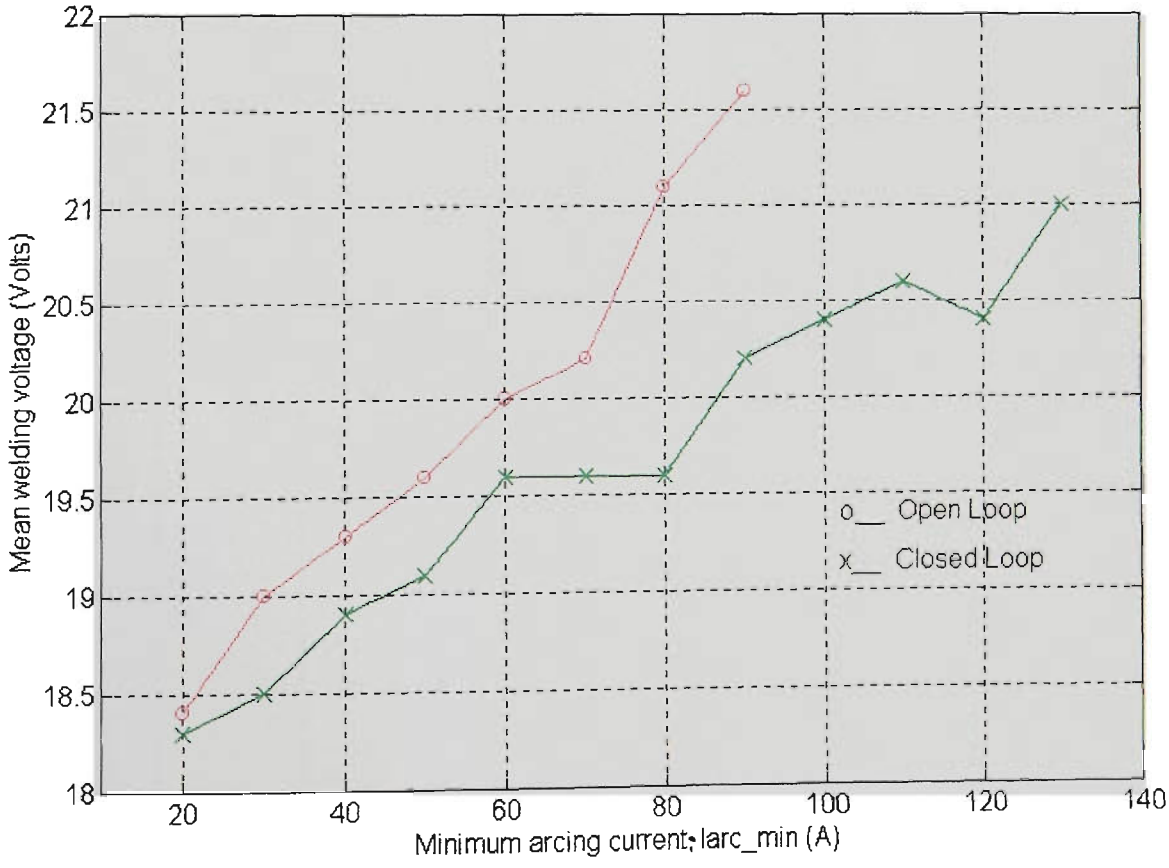

Figure 11.59 Mean voltage vs Iarc_min

(CO_2, CTWD=12mm, WFR=5.7m/min, Travel=195mm/min)

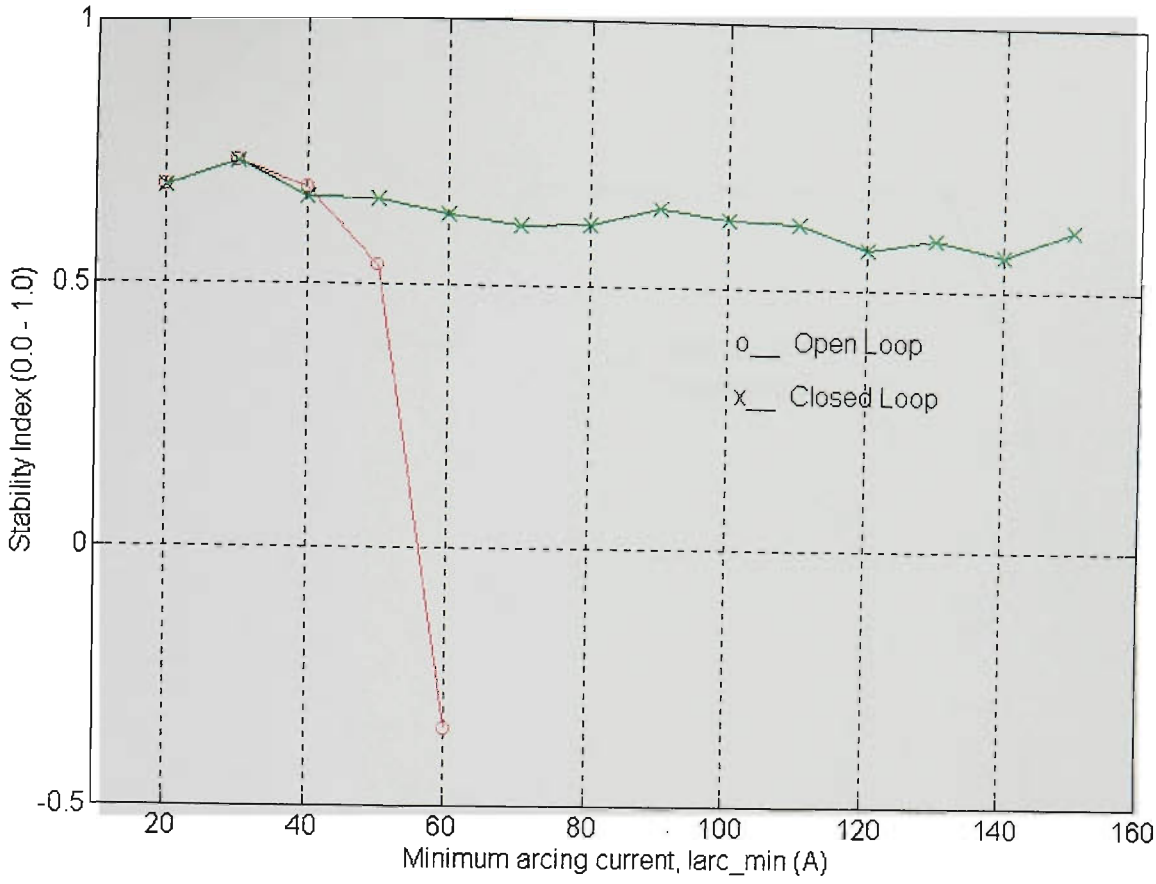

Figure 11.61 Stability index vs Iarc_min

(CO_2, CTWD=20mm, WFR=5.7m/min, Travel=195mm/min)

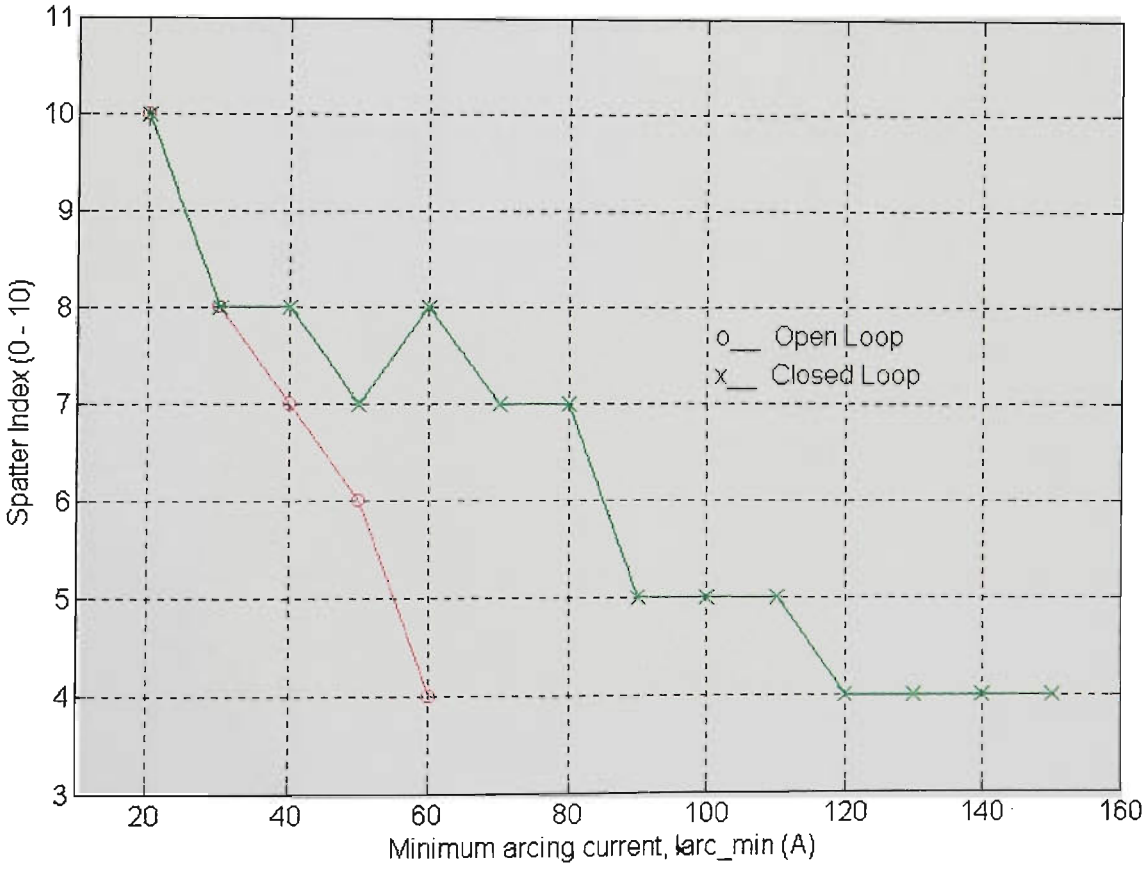

Figure 11.62 Spatter index vs Iarc_min

(CO_2, CTWD=20mm, WFR=5.7m/min, Travel=195mm/min)

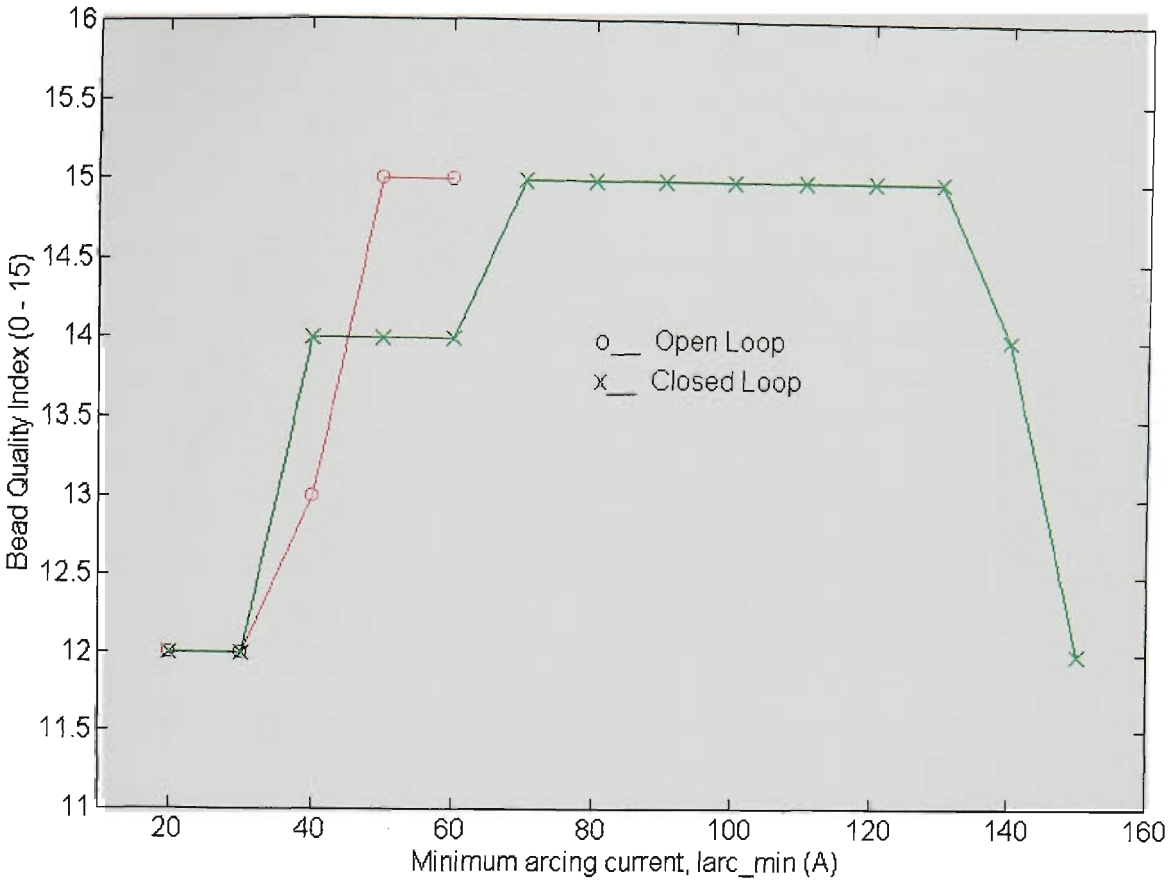

Figure 11.63 Bead quality index vs Iarc_min

(CO_2, CTWD=20mm, WFR=5.7m/min, Travel=195mm/min)

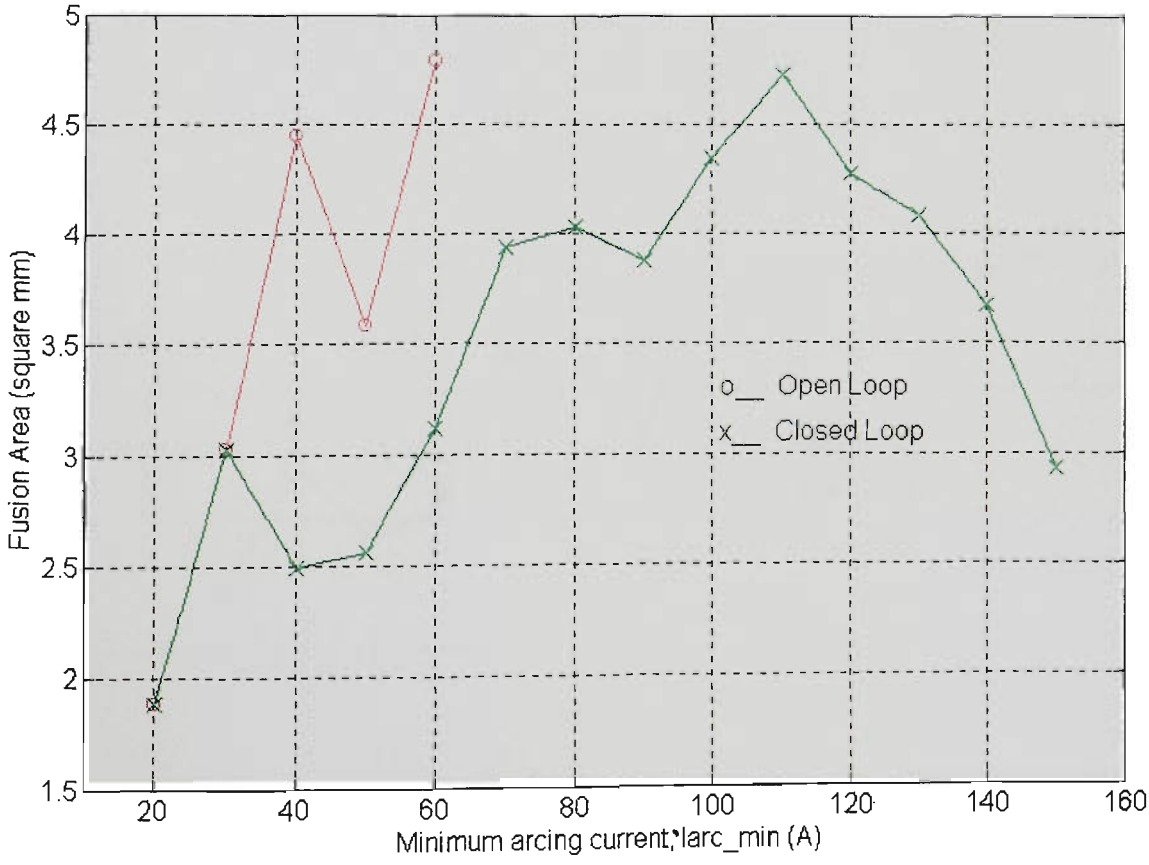

Figure 11.64 Fusion area vs Iarc_min

(CO_2, CTWD=20mm, WFR=5.7m/min, Travel=195mm/min)

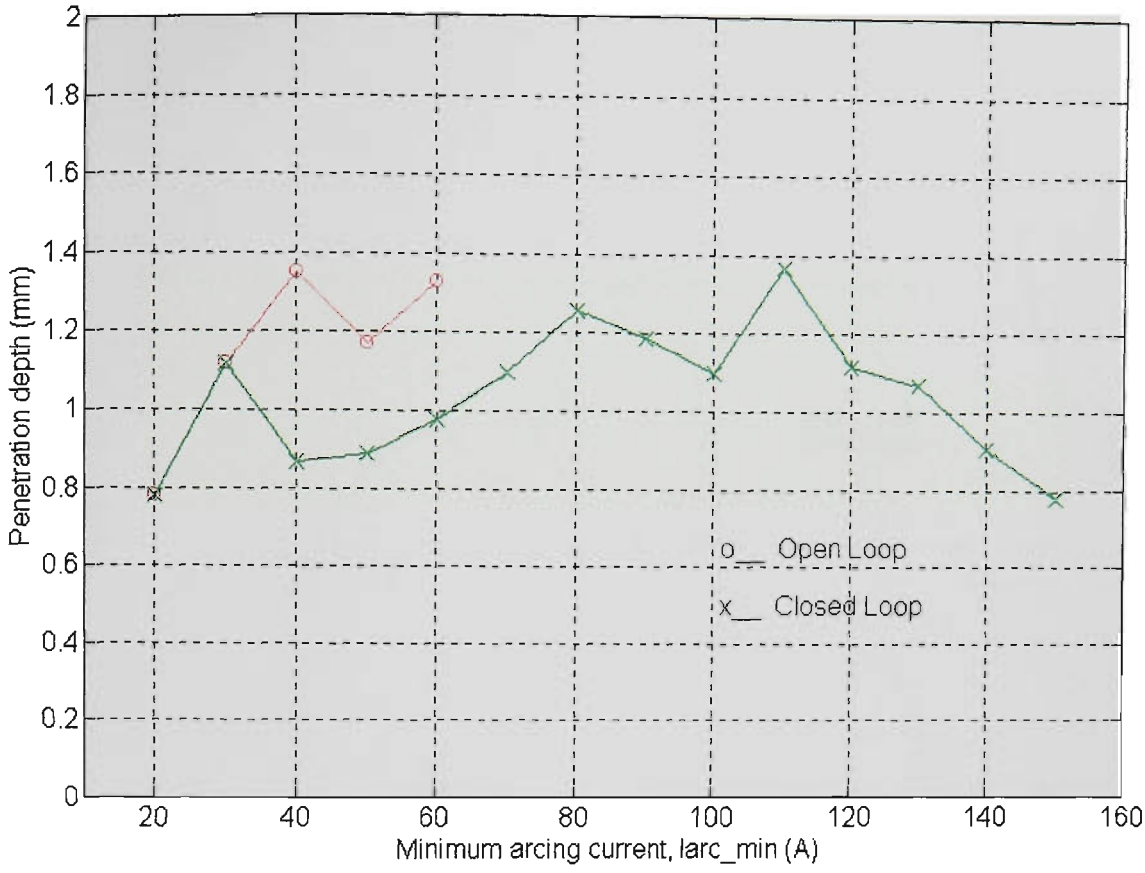

Figure 11.65 Penetration depth vs Iarc_min

(CO_2, CTWD=20mm, WFR=5.7m/min, Travel=195mm/min)

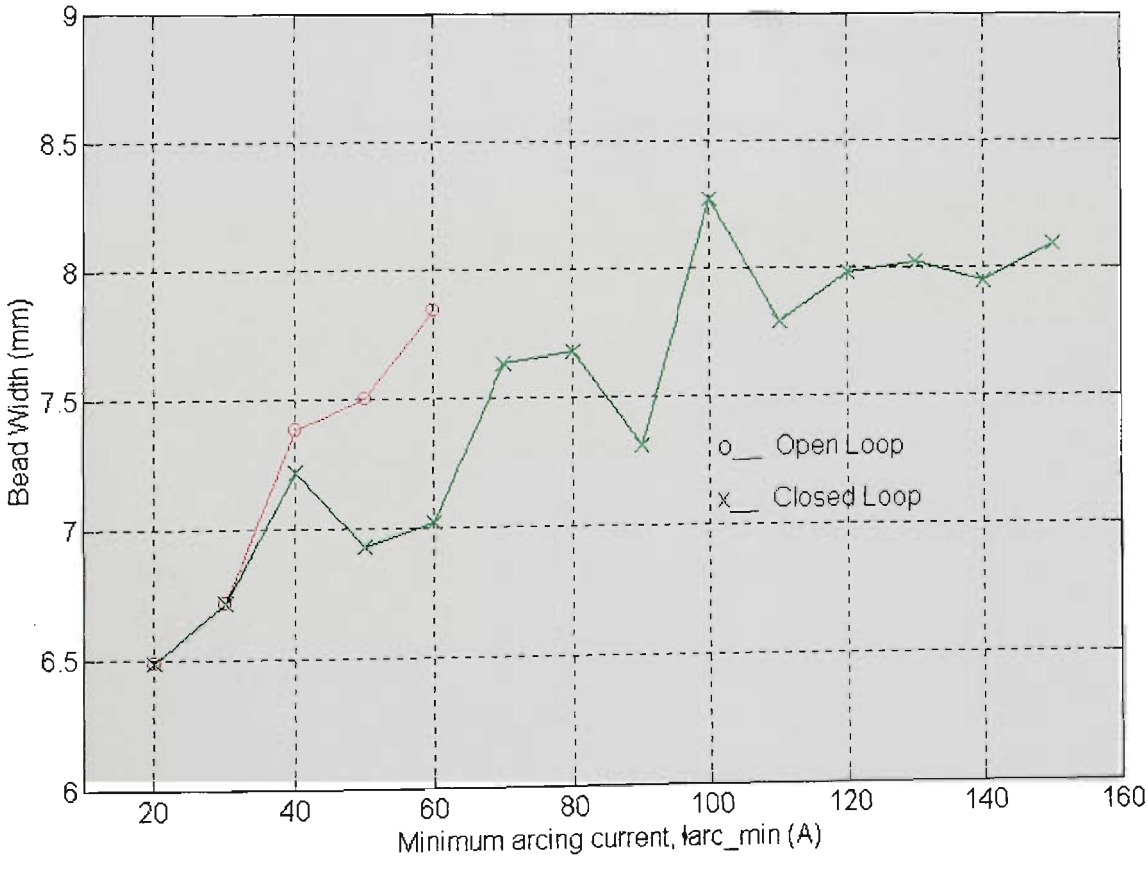

Figure 11.66 Bead width vs Iarc_min

(CO_2, CTWD=20mm, WFR=5.7m/min, Travel=195mm/min)

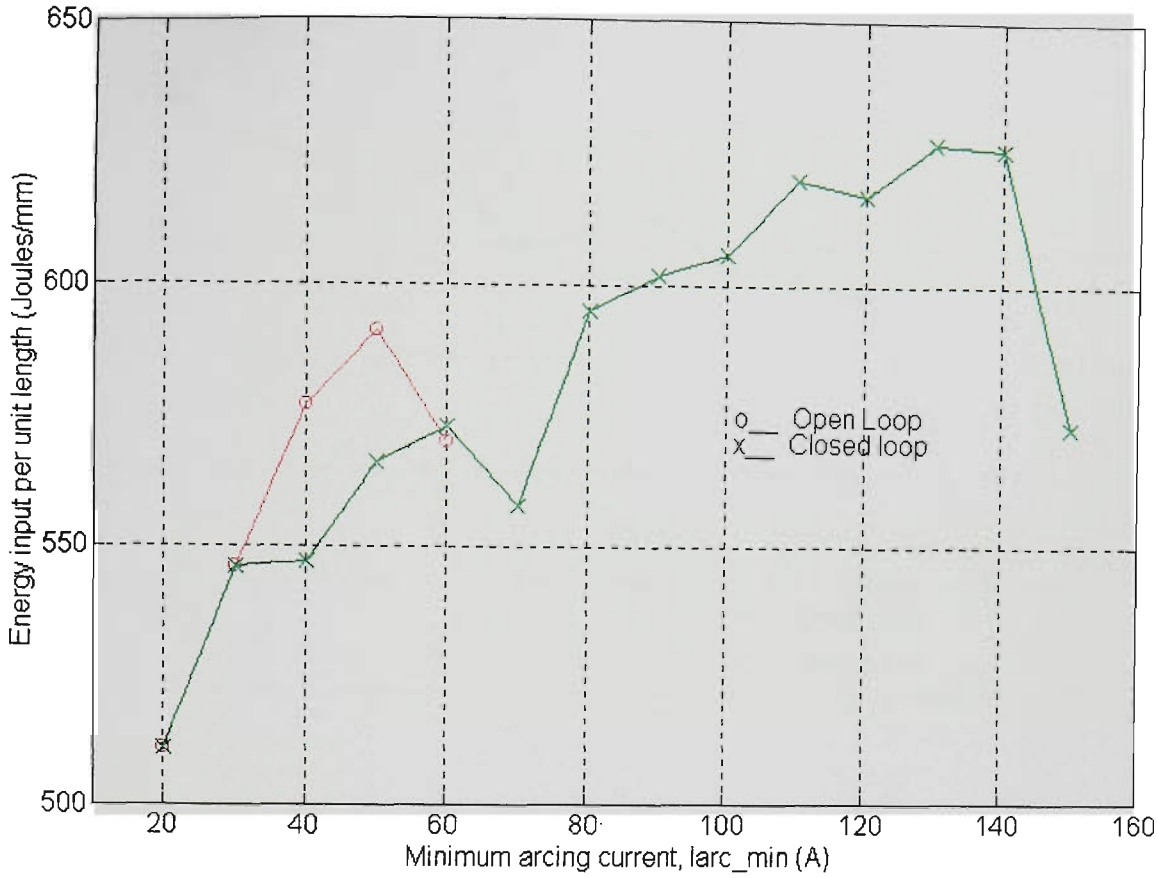

Figure 11.67 Energy input per unit length vs Iarc_min

(CO_2, CTWD=20mm, WFR=5.7m/min, Travel=195mm/min)

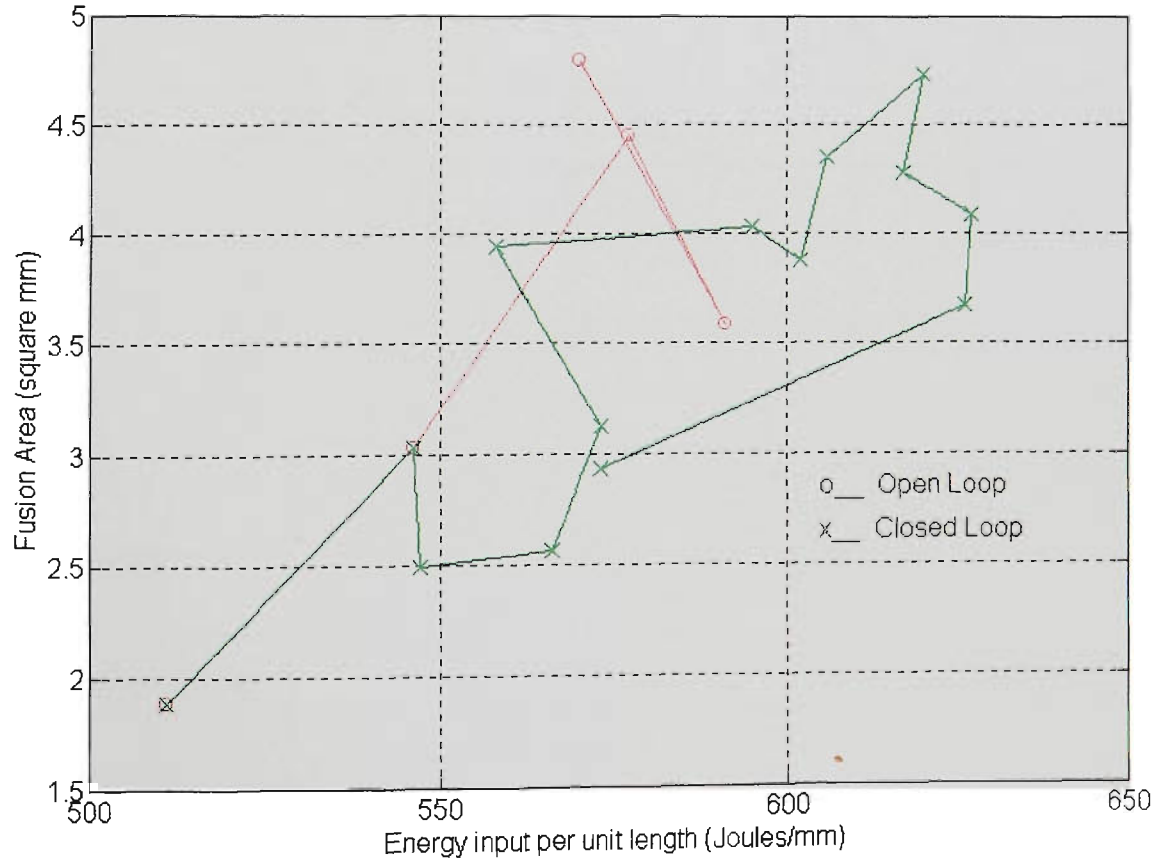

Figure 11.68 Fusion area vs Energy input per unit length

(CO_2, CTWD=20mm, WFR=5.7m/min, Travel=195mm/min)

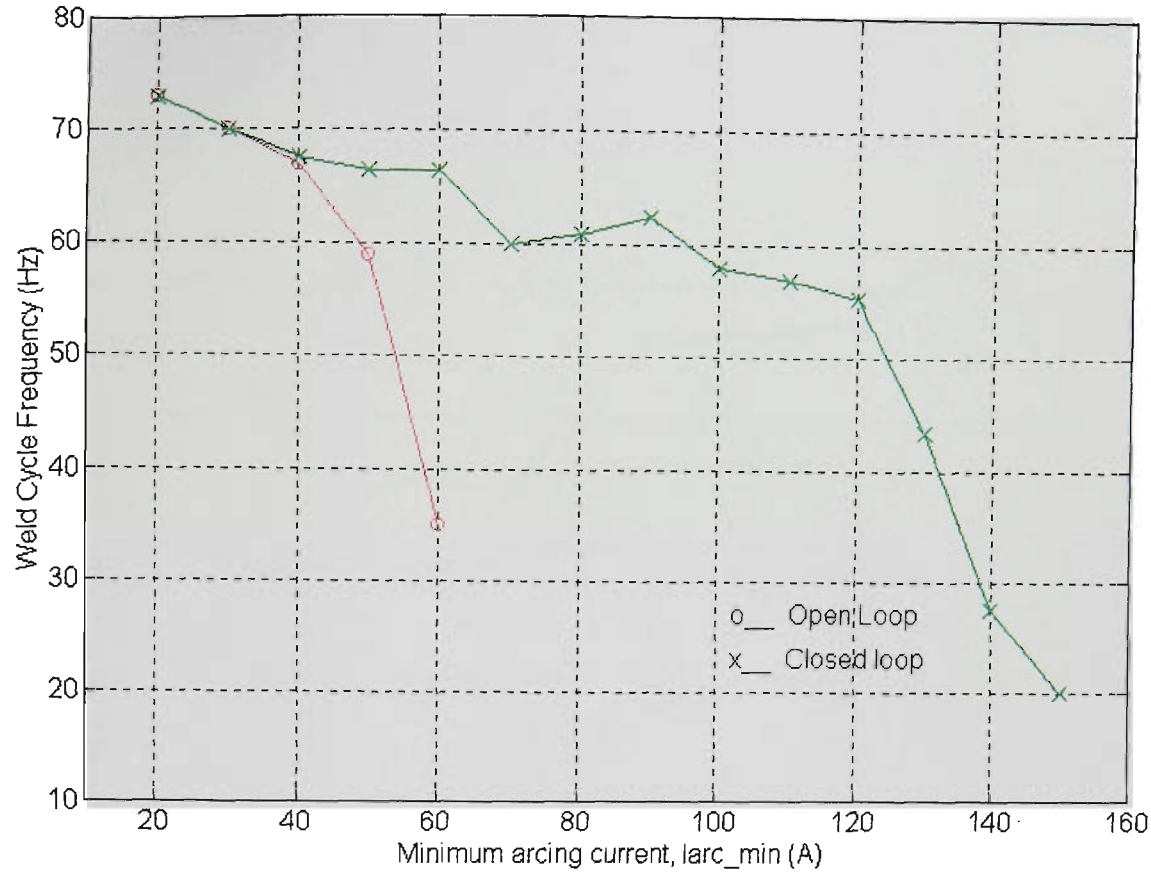

Figure 11.69 Average dipping frequency vs Iarc_min
(CO_2, CTWD=20mm, WFR=5.7m/min, Travel=195mm/min)

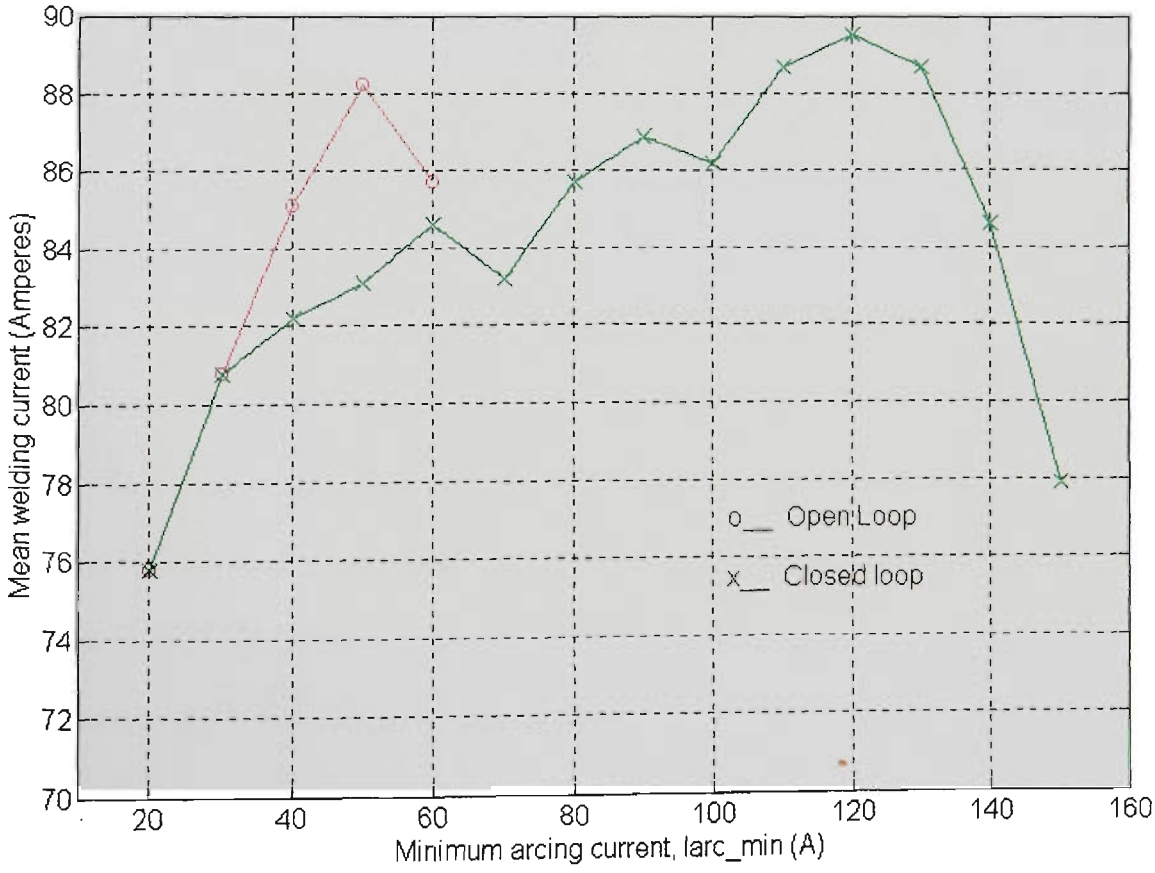

Figure 11.70 Mean welding current vs Iarc_min
(CO_2, CTWD=20mm, WFR=5.7m/min, Travel=195mm/min)

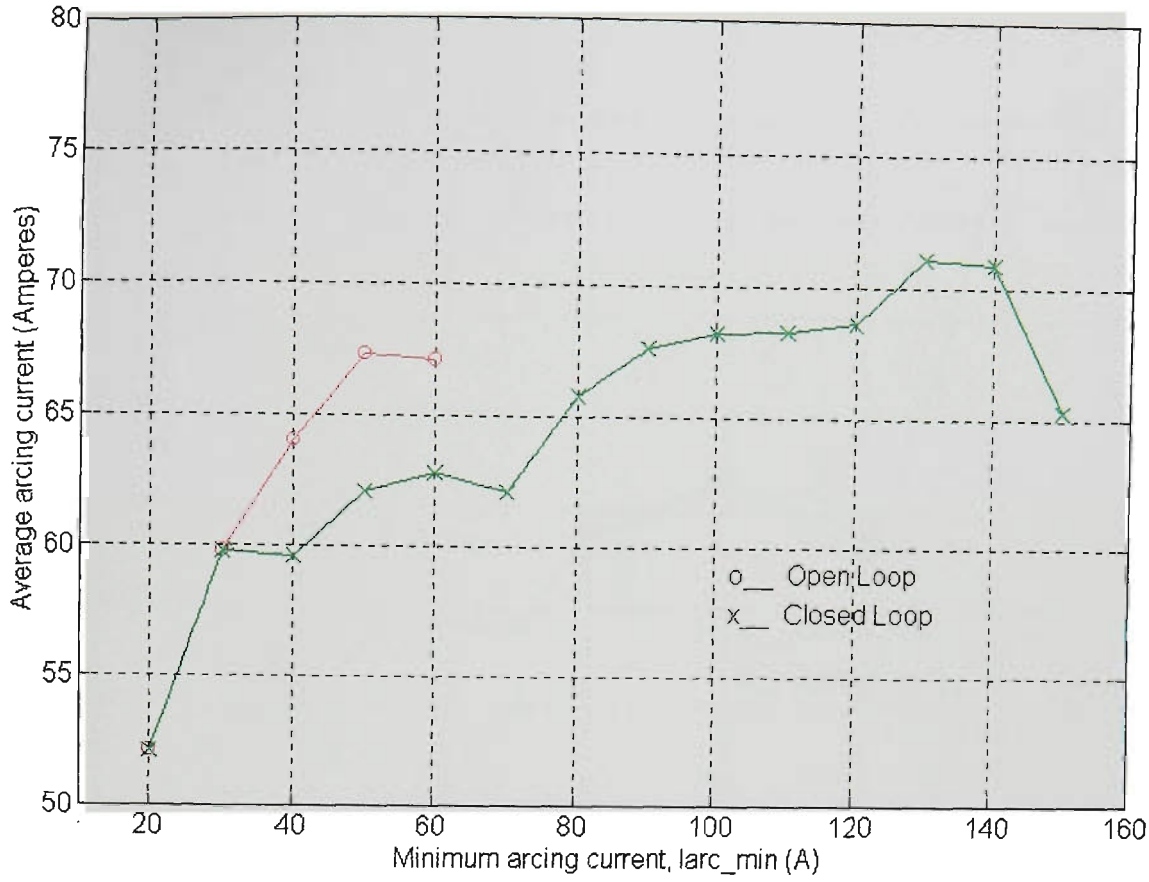

Figure 11.71 Average arcing current vs Iarc_min

(CO_2, CTWD=20mm, WFR=5.7m/min, Travel=195mm/min)

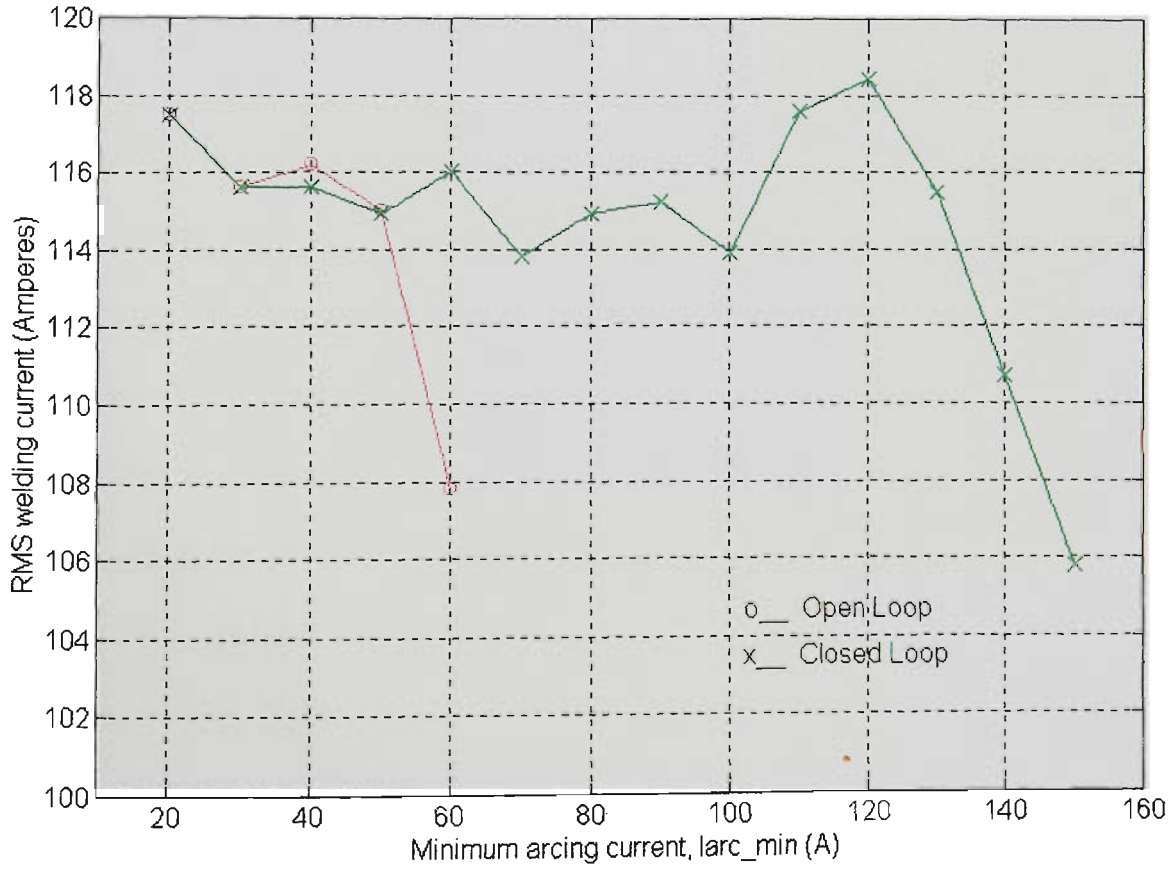

Figure 11.72 RMS current vs Iarc_min

(CO_2, CTWD=20mm, WFR=5.7m/min, Travel=195mm/min)

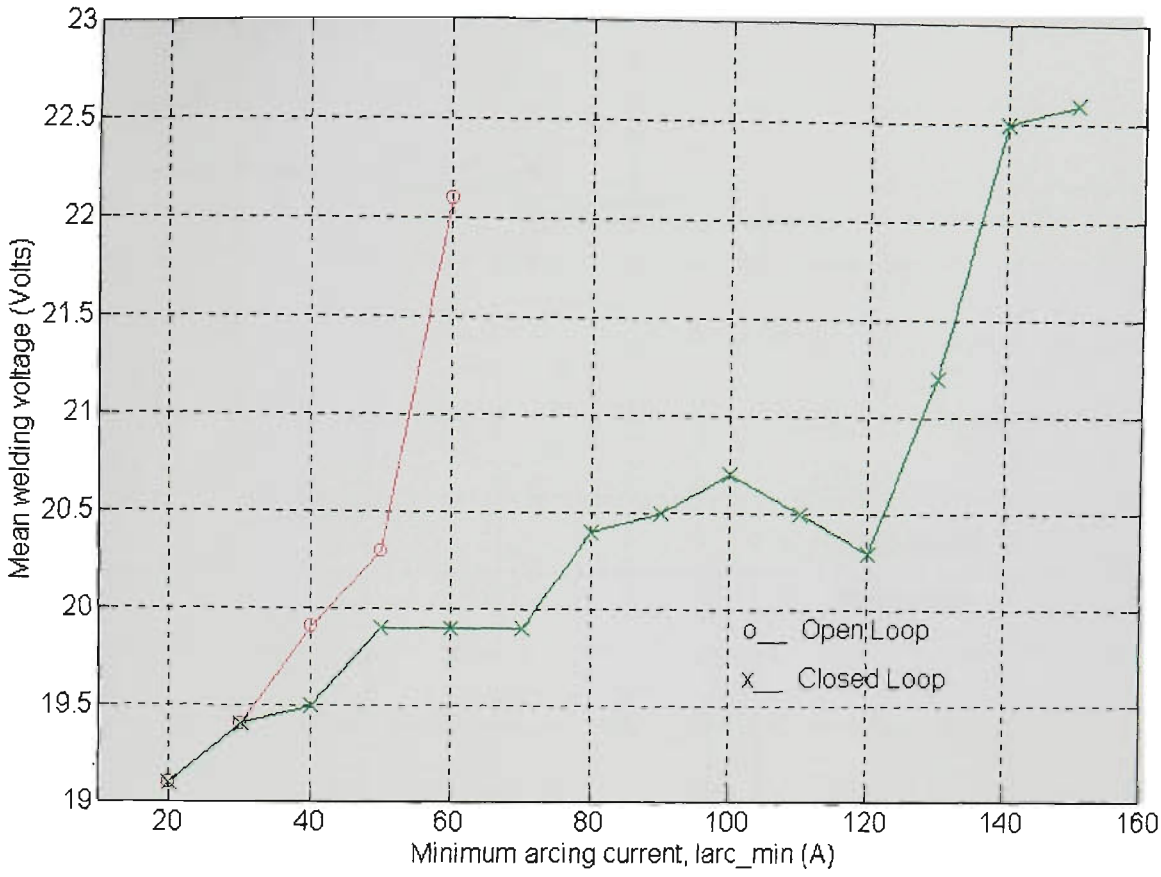

Figure 11.73 Mean voltage vs Iarc_min

(CO_2, CTWD=20mm, WFR=5.7m/min, Travel=195mm/min)

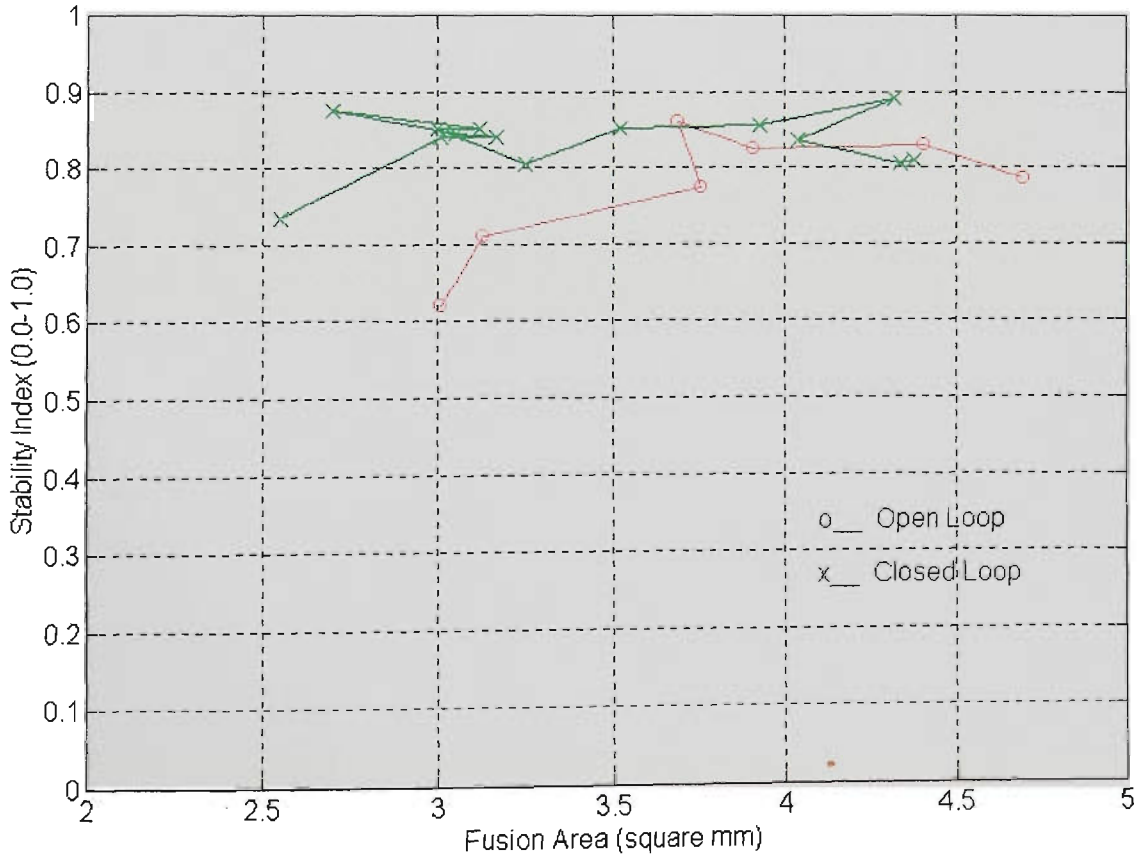

Figure 11.74 Stability index vs Fusion area

(Ar-23%CO_2, CTWD=16mm, WFR=5.7m/min, Travel=390mm/min)

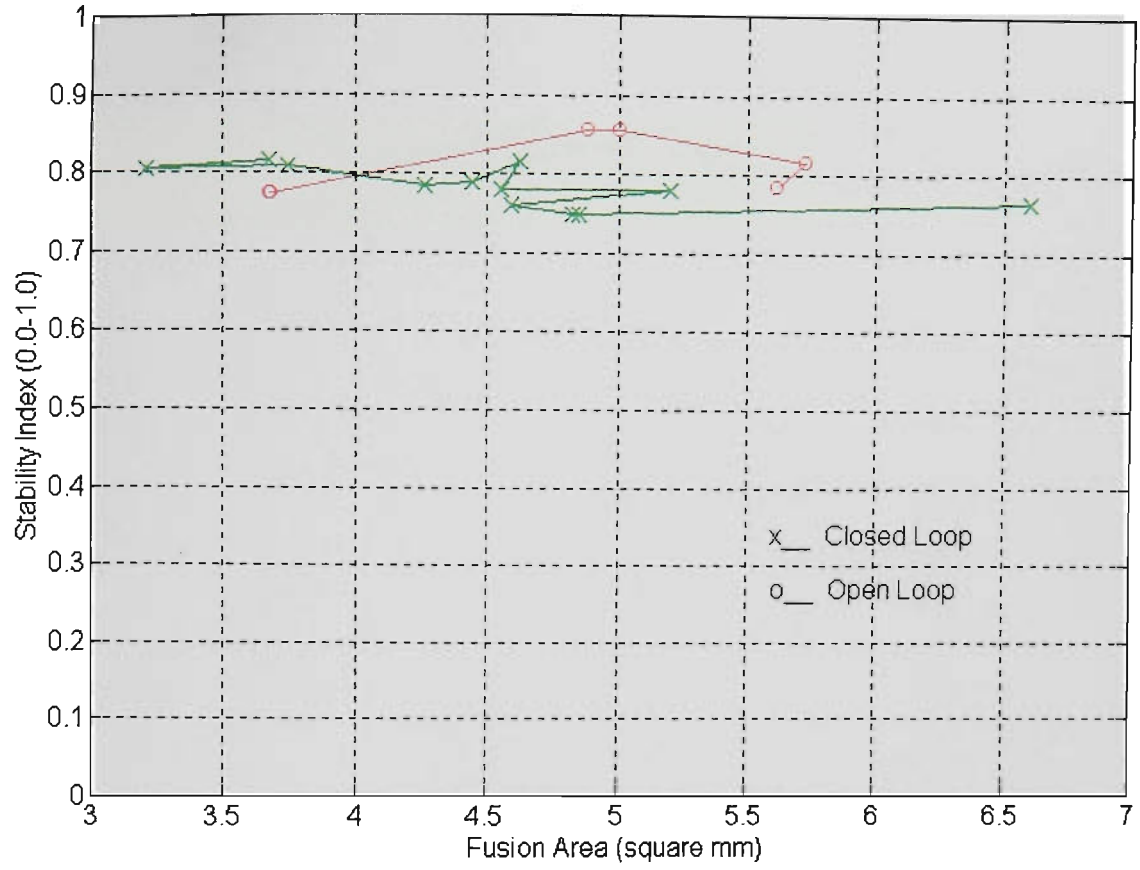

Figure 11.75 Stability index vs Fusion area

(Ar-23%CO_2, CTWD=8mm, WFR=5.7m/min, Travel=390mm/min)

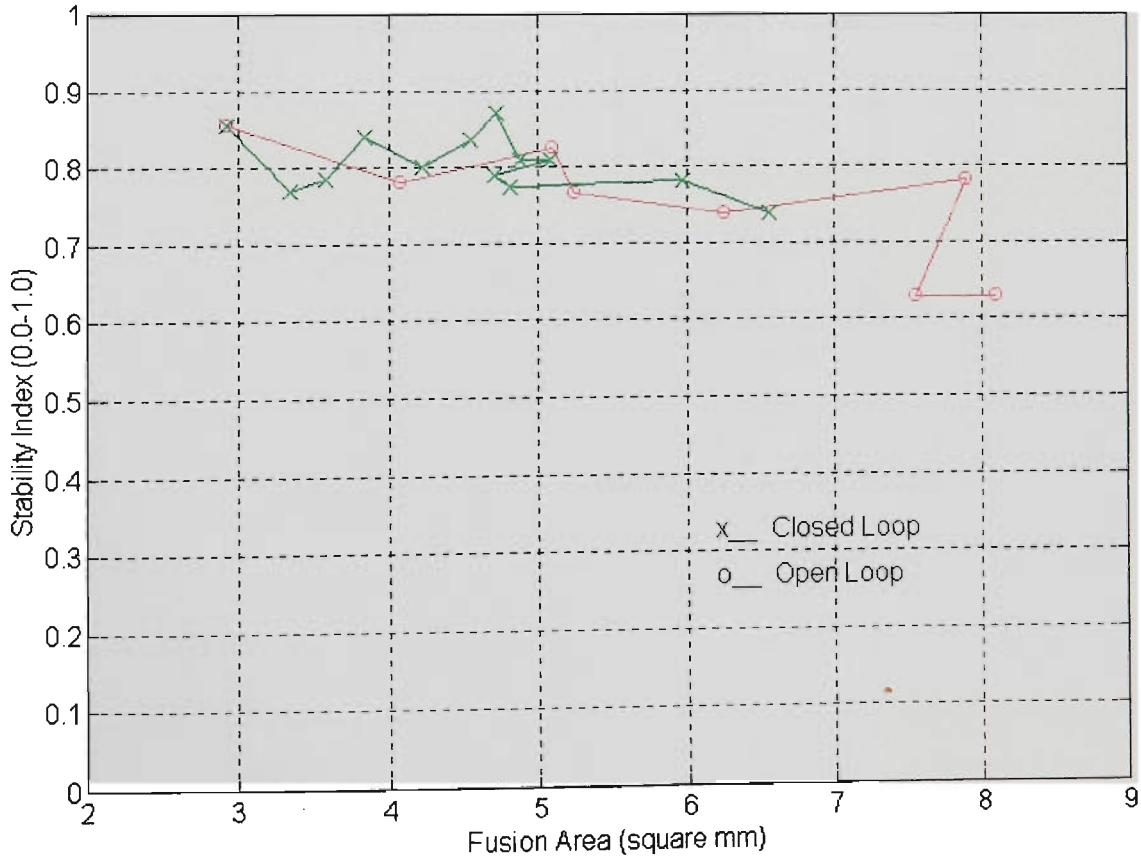

Figure 11.76 Stability index vs Fusion area

(Ar-23%CO_2, CTWD=16mm, WFR=5.7m/min, Travel=195mm/min)

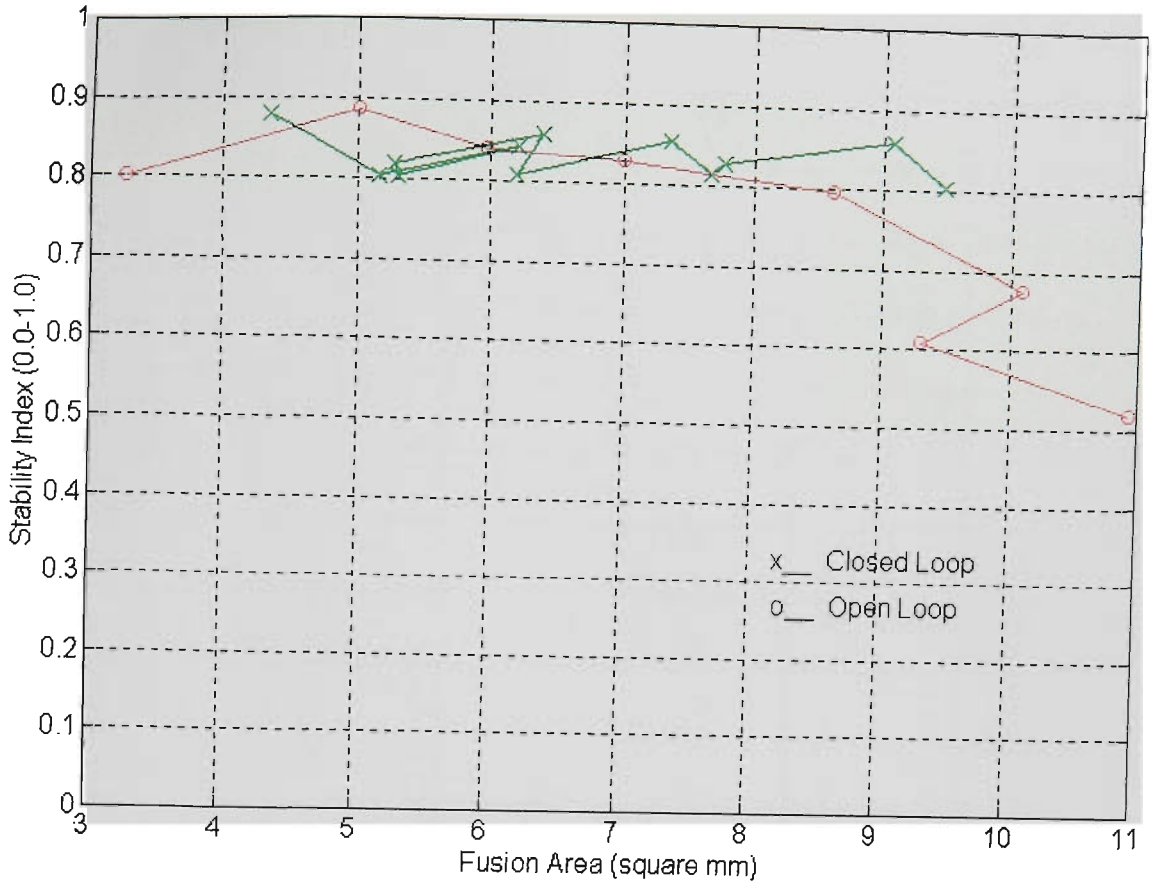

Figure 11.77 Stability index vs Fusion area

(CO_2, CTWD=12mm, WFR=5.7m/min, Travel=195mm/min)

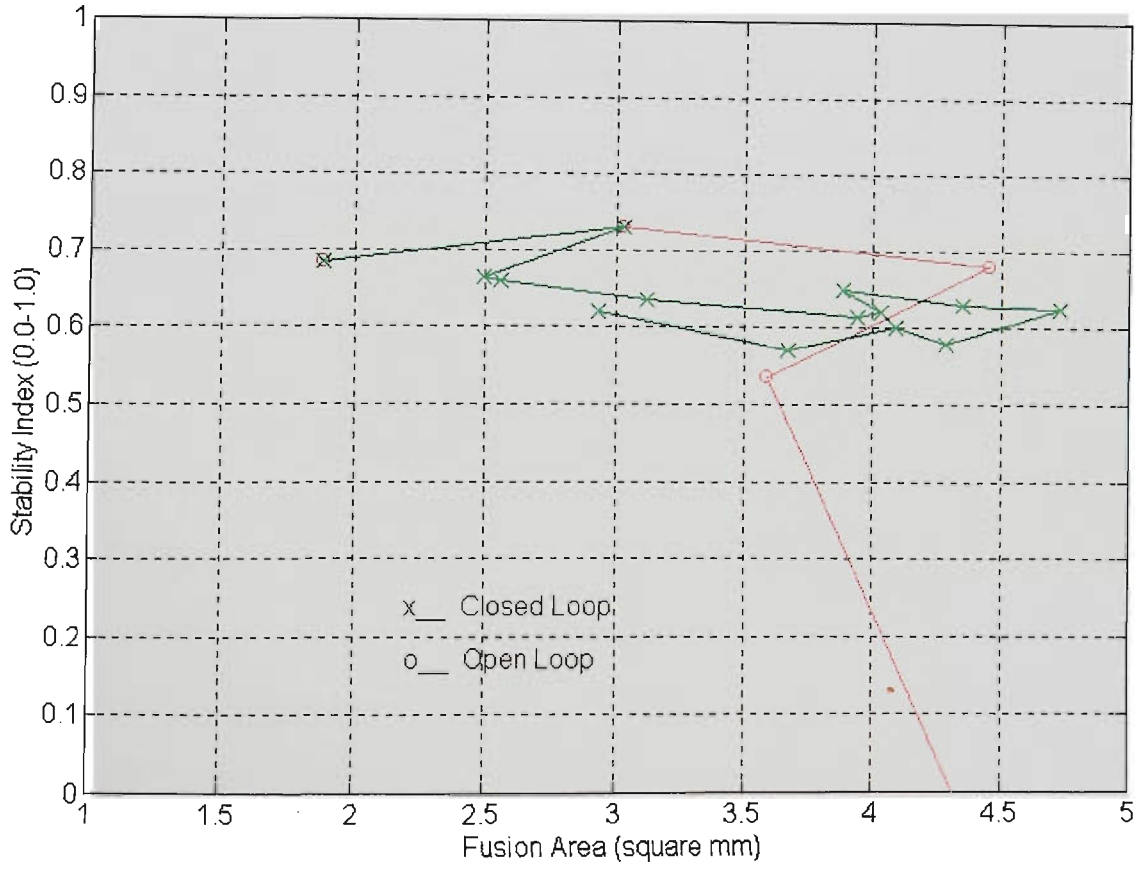

Figure 11.78 Stability index vs Fusion area

(CO_2, CTWD=20mm, WFR=5.7m/min, Travel=195mm/min)

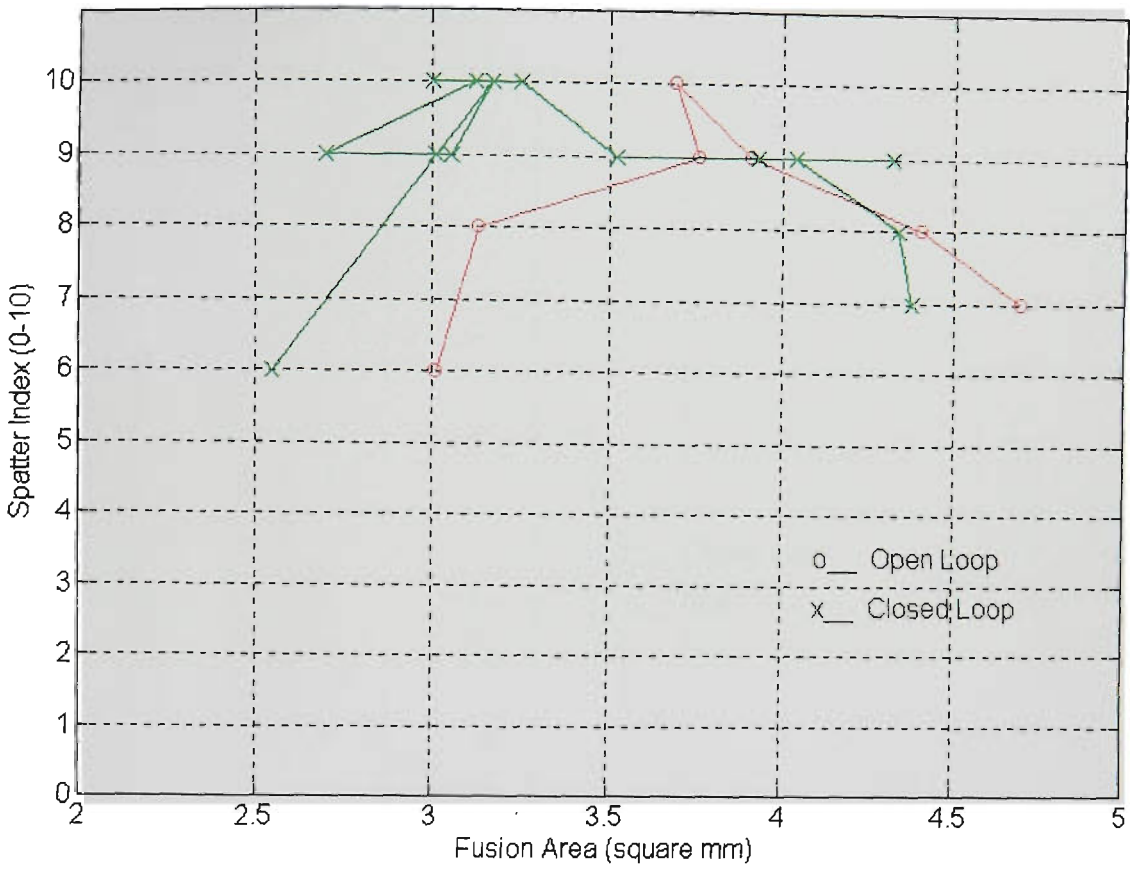

Figure 11.79 Spatter index vs Fusion area

(Ar-23%CO_2, CTWD=16mm, WFR=5.7m/min, Travel=390mm/min)

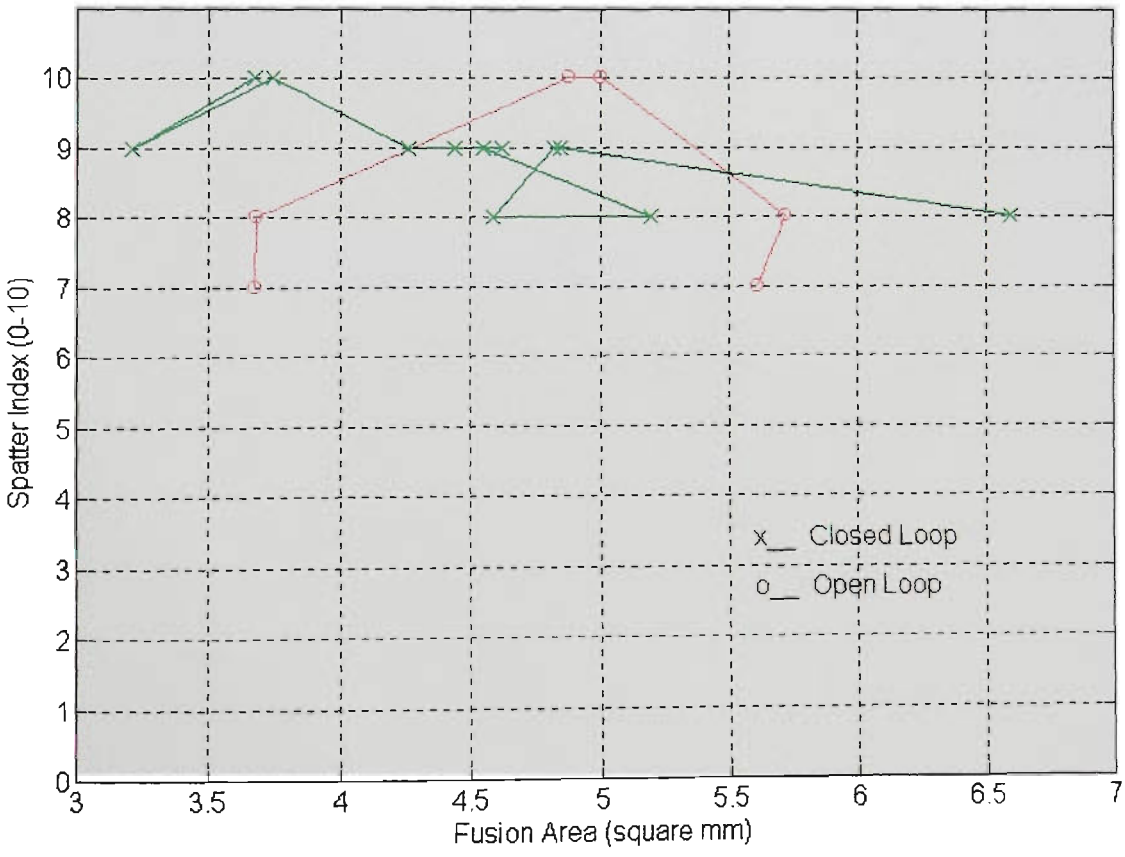

Figure 11.80 Spatter index vs Fusion area

(Ar-23%CO_2, CTWD=8mm, WFR=5.7m/min, Travel=390mm/min)

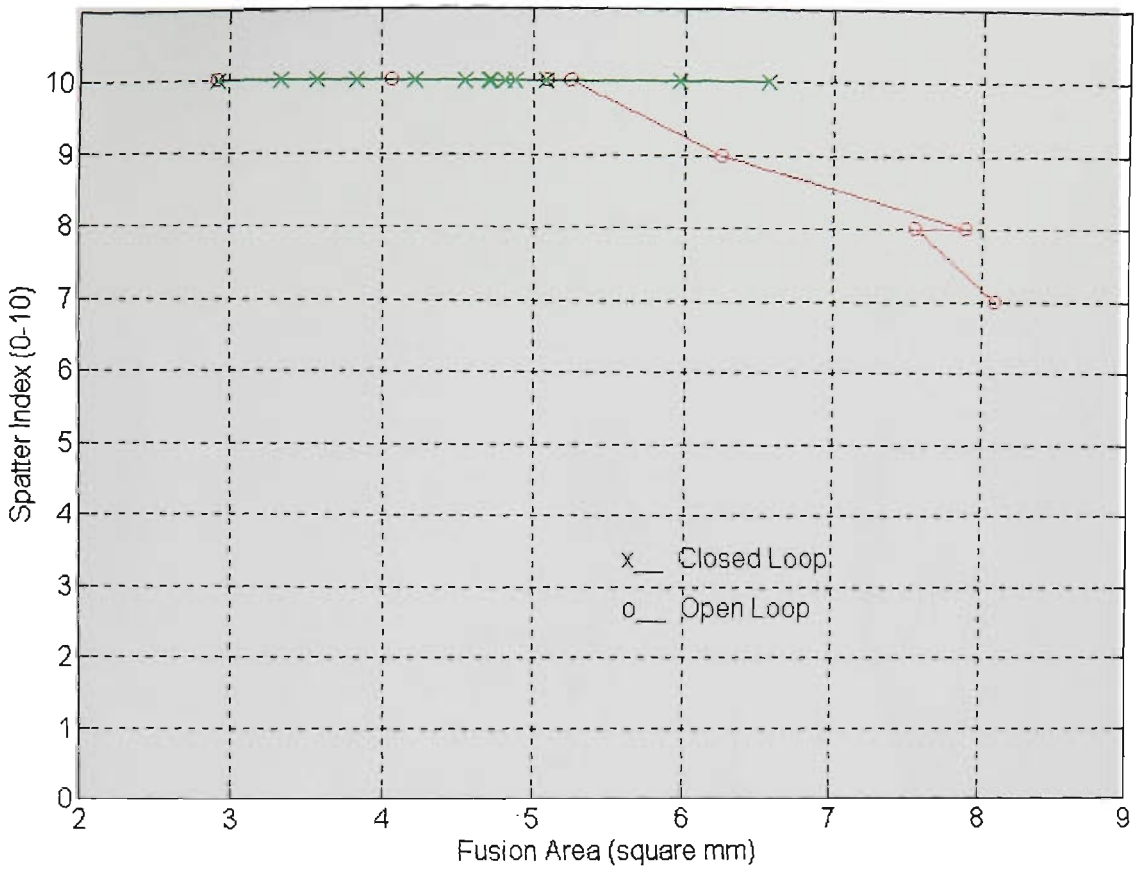

Figure 11.81 Spatter index vs Fusion area

(Ar-23%CO_2, CTWD=16mm, WFR=5.7m/min, Travel=195mm/min)

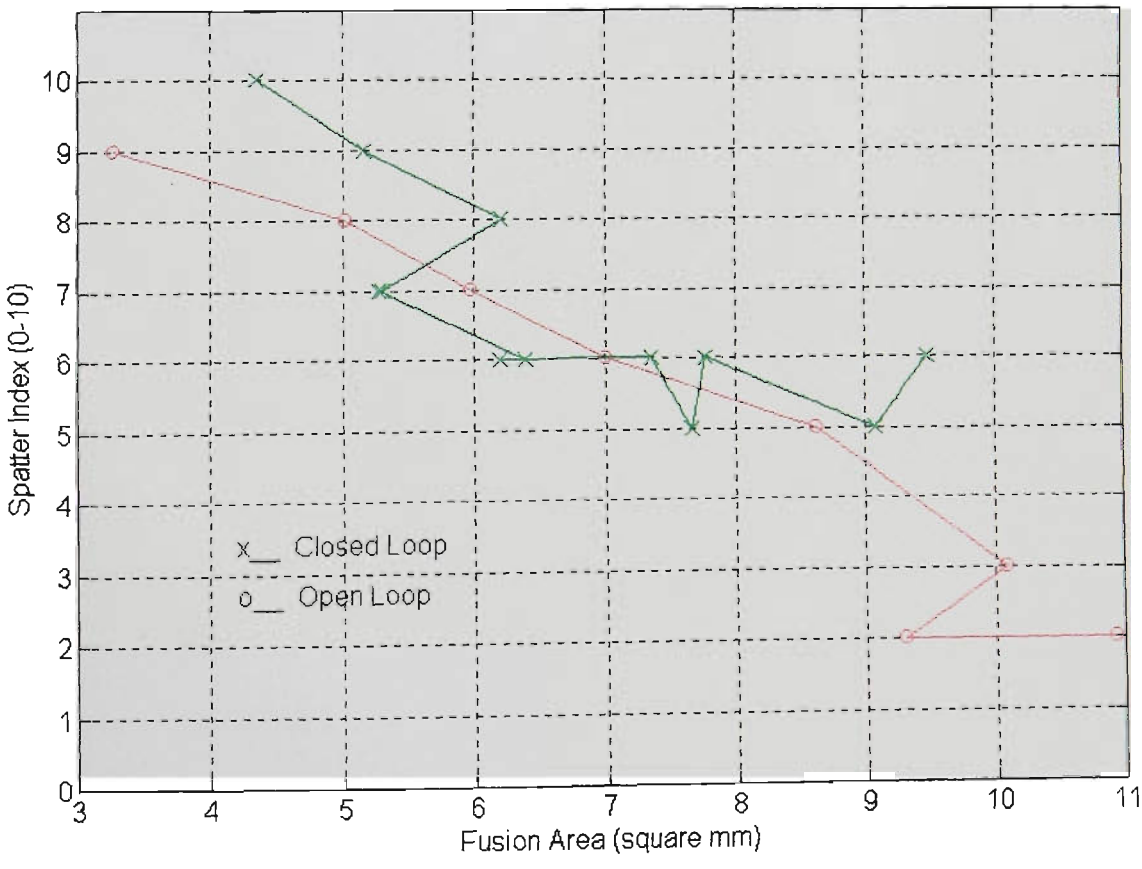

Figure 11.82 Spatter index vs Fusion area

(CO_2, CTWD=12mm, WFR=5.7m/min, Travel=195mm/min)

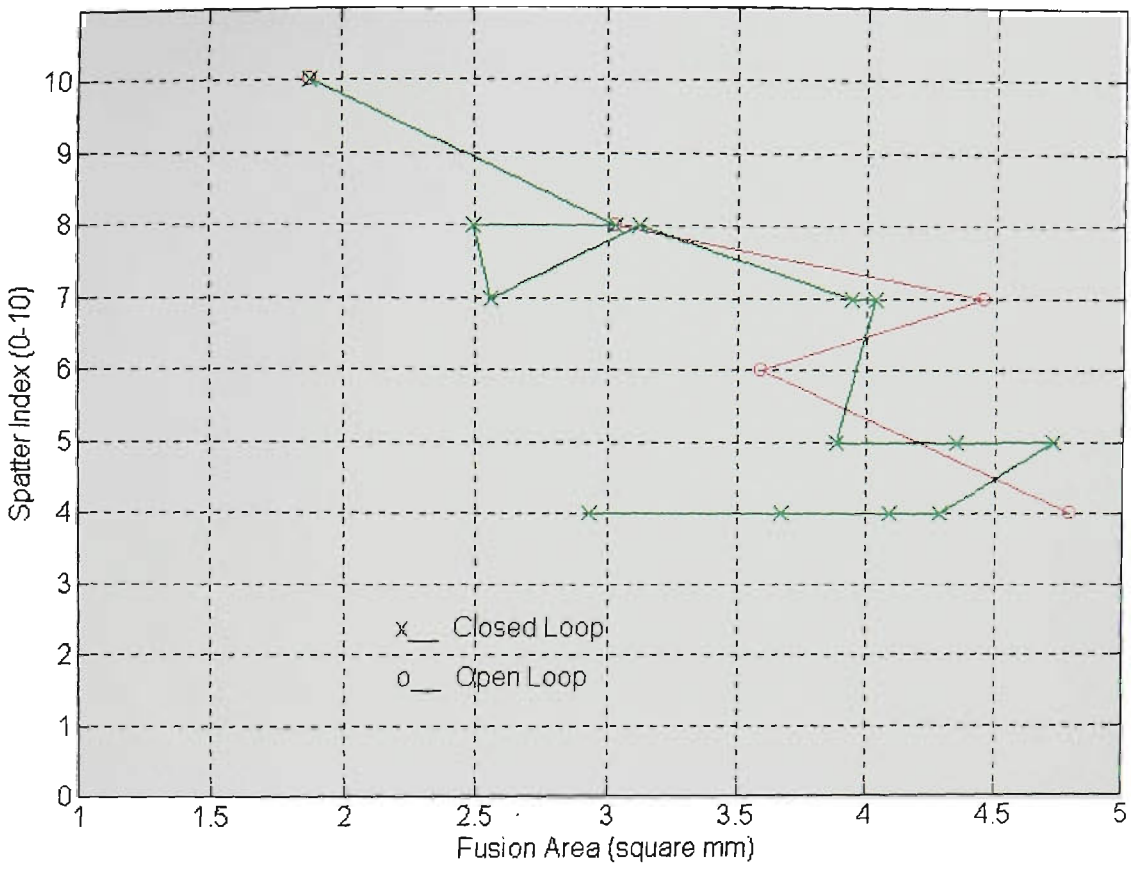

Figure 11.83 Spatter index vs Fusion area

(CO_2, CTWD=20mm, WFR=5.7m/min, Travel=195mm/min)